Impact of a Movable System-Bath Boundary on Photon and Phonon Correlations and Quantum Information in Hierarchically Modelled Open Systems.

A thesis submitted by

BEN S. HUMPHRIES

in partial fulfilment of the requirements for
the degree of Doctor of Philosophy.

UNIVERSITY OF EAST ANGLIA
SCHOOL OF CHEMISTRY

December 2023

© This copy of the thesis has been supplied on condition that anyone who consults it is understood to recognise that its copyright rests with the author and that use of any information derived there from must be in accordance with current UK Copyright Law. In addition, any quotation or extract must include full attribution.

Abstract

Non-perturbative methods are a powerful way of modelling open quantum systems (OQS). One such approach employed in chemical physics is the hierarchical equations of motion (HEOM). The flagship result of this thesis is the derivation of a new form of HEOM termed the Lorentz-Drude Undamped Oscillator HEOM (LDUO-HEOM), which is presented in the penultimate chapter. Preceding this is an analysis of historical methods of OQS (chapter 2) and the studies that have led to the realisation of the need for the LDUO-HEOM approach (chapters 3 and 4). Two different models are developed to establish the impact of keeping a molecular vibration in the Hamiltonian or moving it to the bath by modelling a simple molecular system. This is quantified through quantum information and quantum correlation metrics. Here 2D spectral lineshape is linked to non-Markovian memory effects. It is shown that the ellipticity of the peaks and the degree of non-Markovianity increase sharply when coupled to overdamped environments, or more gradually in underdamped environments, but with underdamped environments giving rise to greater non-Markovianity overall. We show that auxiliary density operators (ADOs) contain fundamental physical information that can offer new insight for terminating the HEOM, by reshaping the hierarchy volume to minimise the number of ADOs. Furthermore, second order quantum correlations are analysed. It is shown that phonon transitions modulate photon correlations at the vibrational mode frequency for continuously driven systems. If instead, the system is driven by a femtosecond pulsed laser we can see regions of intense vibrational stimulation within the correlations. The above methodologies are then applied to more complex systems such as molecular dimers. Finally, we present an analysis of the derived LDUO-HEOM through benchmark calculations of 2D electronic spectra and show it is a useful tool for modelling vibronic effects in ultrafast 2D spectroscopy.

Access Condition and Agreement

Each deposit in UEA Digital Repository is protected by copyright and other intellectual property rights, and duplication or sale of all or part of any of the Data Collections is not permitted, except that material may be duplicated by you for your research use or for educational purposes in electronic or print form. You must obtain permission from the copyright holder, usually the author, for any other use. Exceptions only apply where a deposit may be explicitly provided under a stated licence, such as a Creative Commons licence or Open Government licence.

Electronic or print copies may not be offered, whether for sale or otherwise to anyone, unless explicitly stated under a Creative Commons or Open Government license. Unauthorised reproduction, editing or reformatting for resale purposes is explicitly prohibited (except where approved by the copyright holder themselves) and UEA reserves the right to take immediate ‘take down’ action on behalf of the copyright and/or rights holder if this Access condition of the UEA Digital Repository is breached. Any material in this database has been supplied on the understanding that it is copyright material and that no quotation from the material may be published without proper acknowledgement.

Contents

List of Figures

List of Tables

Acknowledgements

The research presented in this thesis was completed using the High Performance Computing Cluster supported by the Research and Specialist Computing Support service at UEA. I wish to express my gratitude to all the members of this team.

First, I must thank my secondary supervisor Prof Emilian Părău who has been a steadfast support throughout the whole PhD. I also thank my temporary supervisor, and collaborator, Dr Magnus Borgh. His expertise has been invaluable, and I am hugely grateful for our collaborations. Also, I wish to thank Dr Joachim Seibt, whose discussion educated and affirmed in equal measure.

Similarly, I wish to thank my close friends, Silvana Matei, Connor Robbins, Ben Young-Longstaff, and Rob Woodward. It is no exaggeration to say that I owe them my life, and I am eternally grateful for their kindness, and support. In addition, I wish to thank Danny Netherwood, whose enthusiasm for research has been infectious. I am also grateful to my good friends Kirsty Nice and Dr David Pearce, we have spent much needed down-time together. I must also thank my Psychologist, Dr Natius Oelofsen, whose optimism, support, and innovative suggestions have led to fundamental mental and practical solutions.

I wish to thank Josh Kinslow and Natalia Gray. Their introduction to the Jones group has been very beneficial for my learning and morale. It is essential that I also thank my good friend, and colleague, Dr Dale Green. We have spent many years discovering the complexity of open quantum systems, and his boundless coding experience and emotional guidance have always been invaluable to me. I hope we collaborate again in the future.

My eternal gratitude goes to my primary supervisor, Dr Garth Jones, who has reignited my passion for scientific research. Garth has shown me overwhelming kindness and patience throughout the years, especially during my period of ill health, in addition to a vast wealth of knowledge and physical chemistry insight. In my mind, Garth and his group are the epitome of what a leader and collaborative group should be, and I am extremely grateful to have been a part of it. I hope we continue to collaborate in the future.

I wish to thank my family who have supported and saved me during some of the darkest periods of this research. It would have been impossible without them. Finally, I must thank my wonderful partner Fan Sun, and our Kasha Biscuit Sun, who have given me the strength to continue on.

Publications

Research undertaken as part of this thesis resulted in the following publications:

1. Green, D.; Humphries, B. S.; Dijkstra, A. G.; Jones, G. A. Quantifying Non-Markovianity in Underdamped versus Overdamped Environments and Its Effect on Spectral Lineshape. *J. Chem. Phys.* **2019**, *151* (17), 174112.

2. Humphries, B. S.; Green, D.; Jones, G. A. The influence of a Hamiltonian vibration versus a bath vibration on the 2D electronic spectra of a homodimer. *J. Chem. Phys.* **2022**, *156* (8), 084103.

3. Humphries, B. S.; Green, D.; Borgh, M. O.; Jones, G. A. Phonon Signatures in Photon Correlations. *Phys. Rev. Lett.* **2023**, *131* (14), 143601.

4. Humphries, B. S.; Kinslow, J. C.; Green, D.; Jones, G. A. The role of quantum information in HEOM trajectories. *J. Chem. Theory Comput.* **2024**, *submitted*.

5. Humphries, B. S.; Green, D.; Jones, G. A. The influence of system-bath boundary placement via Lorentz-Drude undamped hierarchical equations of motion. *J. Chem. Phys.* **2024**, *submitted*.

1 Introduction

Our current understanding of the natural world stems from simplified models of underlying physical processes. Whether it is macroscopic descriptions of fluid flow, or the microscopic dynamics of molecules, a reduction of the total degrees of freedom is a necessary compromise in nearly every model. For example, consider computing the dynamics of an N particle system. If we have initial positions and velocities for each particle and an equation of motion, derived from continuous microscopic variables, then moving one discrete time step forwards could be achieved. However, if it takes 1 byte of memory for each particle, then at the scale of even one mole (6.02×10^{23}) of molecules we would need 602 zettabytes (2^{70} bytes) of memory. Clearly this is not feasible. It would be tempting, therefore, to work in extremely simplified systems with a very small number of relevant variables. This could be achieved by isolating our N particles of interest so that there are no external particles, like air, and by making N very small. This kind of simplifying approximation clearly comes at the cost of realism, but perhaps the model still provides valuable physical insight about the system of interest. *The fine balance between full physical complexity and a reduction due to computational necessity is one of the intrinsic motivations for this thesis.*

The analogy which was used initially to describe a reduction in the number of relevant variables can be defined more rigorously as a closed system. If there is a particle (or particles) of interest within an impermeable box, modelled with a spatial coordinate X for the molecular/atomic position, and it is isolated from the wider universe then there will be a fixed magnitude of energy contained in the box. This energy may disperse throughout the constituent particles in any manner - perhaps as a Boltzmann distribution - but cannot dissipate. Figure 1.0.1 presents a schematic of the formally defined closed system.

The work in this thesis involves systems which relax this simplification, through reintroduction of environment degrees of freedom, by opening the quantum system. Open quantum system (OQS) models consist of two (or more) components, each in an independent coordinate, linked by a function which shares all coordinates. Typically, for a two component OQS there is a system of interest in a coordinate X, and an environment of molecules in a linearly independent coordinate Q [4]. Both constituents are individually closed, and are

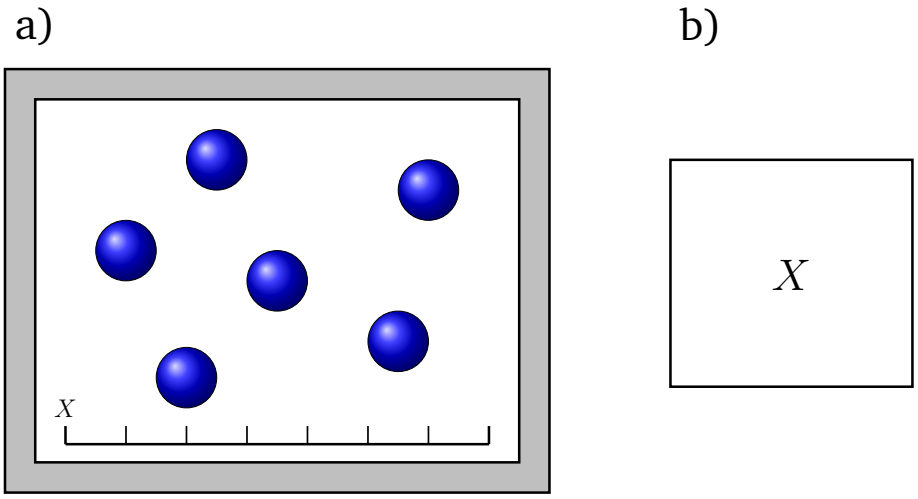

Figure 1.0.1: Schematic of a closed system. a) Physical interpretation: the outer wall is impermeable and all contained particles are modelled with a continuous positional coordinate, X. b) Mathematical interpretation: a closed system in coordinate X.

linked by an interaction term which depends on both molecular/atomic coordinates X and Q. Figure 1.0.2 presents a schematic of the formally defined OQS. In this way, a degree of physical realism is reintroduced as the primary system is now influenced by its surrounding environment and is free to dissipate energy out of the boundary encapsulating it. Generally, opening a model system comes at the expense of computational time, or a high memory requirement, unless other simplifications are introduced. An example of one such simplification is the introduction of a single continuous spectral density function which describes the summation of every environment particle. This function, $J(\omega)$, maps out the profile of an infinite number of weighted delta functions, and physically represents the overall behaviour of the environment ensemble at the cost of individual environment particle resolution. Such simplifications shift the computational bottleneck within simulations from the large Hamiltonians into mathematically challenging spectral distributions. This exemplifies the second intrinsic motivation of this thesis: *derivation and physical justification of further simplifying approximations or equations which allow computational simulation of memory intensive open systems.*

As modern experimental chemical physics and physical chemistry reach deeper and deeper into the microscopic, quantum, world it becomes increasingly important to be able to make use of OQS models. Genuine quantum behaviours are often very sensitive to perturbations of energy, or length scales of the system and as such stochastic degrees of freedom can not be easily omitted as in closed systems. OQS models lend themselves effectively to the modelling of quantum behaviour in Bose-Einstein condensates[5] formed through boson bunching, which are sensitive to the healing length (an intrinsic

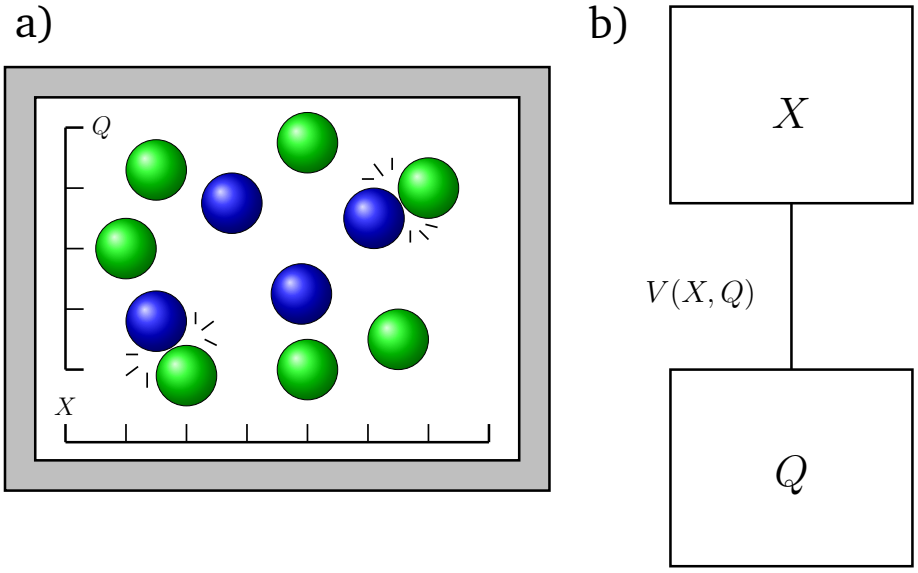

Figure 1.0.2: Schematic of an open system. a) Physical interpretation: the outer wall is impermeable and all system particles are modelled with a continuous positional coordinate, X, environment particles are modelled with a linearly independent continuous positional coordinate, Q. The two systems can interact through collision. b) Mathematical interpretation: a pair of individually closed systems in linearly independent coordinates, X and Q. The two components are coupled via $V(X, Q)$, resulting in an open total system.

length scale) of the system, and to models of antibunching effects in coherent boson beams, which are dependent on energy dissipation due to surrounding environment ensembles. In many physical regimes, which are typically inconsistent with closed system approximations, quantum observations can be entirely destroyed or obscured by environment modes. This leads to the final intrinsic motivation for this work: *application of OQS models to predict genuine quantum effects while using a set of equations and approximations which closely correlate to experimental physical parameters.*

But for what purpose do such models exist, and why are they relevant? Light and light-matter interactions are incredibly versatile tools for the transmission of information and energy, and for use as probes at scales ranging from microscopic to cosmic due[6,7], in part, to its quantum nature. Light moves rapidly, is easily generated, and has both wave and particle character. All such applications exploit the nature of quantum interference and entanglement to extract information regarding either the scattering body or the coherent source of radiation.

At the microscopic scale, the generation of light and the behaviour of light beams are routinely applied in the context of information transfer in fibre optic cables[8,9]. In order to maximise the efficiency and speed with which signals can be sent and received it is crucial to understand the process used to generate

coherent beams of light, and to understand how light interacts with materials and other coherent beams. These microscopic interactions can result in quantum effects emerging. Among the most striking examples is the experimental discovery of antibunching in the photon emission of fluorescing atoms which provided the first direct demonstration of the quantum properties of light[10]. This type of correlation measurement, which can be observed experimentally and calculated theoretically, is a reduction in the detection probability of a second photon immediately after the detection of a first. The second order correlation function, which is used to measure this probability, is a powerful statistical tool and is not limited to photons. It has been used to study a broad range of boson interactions, and light-matter interactions such as bunching and antibunching in transmission through waveguides[11] and in emission from plasmonic nanojunctions[12], pattern formation in photoinduced nucleation[13], photon-blockade effects in optical cavities[14–19] (including modified response at strong coupling)[20], atomic arrays, as well as super- atom behaviour in ensembles of quantum emitters[21–23]. Indeed, this correlation metric extends to correlation in phonons[24] including phonon blockade in opto-mechanical and spin-mechanical systems, magnons[25] including magnon-atom entanglement and photon-magnon blockade in a ferrimagnetic material coupled to a microcavity, and photon-phonon bunching and antibunching in a qubit-phonon-plasmon system under strong coupling. Higher order blockade effects and other complex dynamic behaviours are accessible through higher order correlation functions[26], and can be exploited for high-precision imaging[27].

On a cosmic scale, interferometry can be used to probe distances and the radii of celestial bodies through the disappearance of fringe patterns[28,29] as a consequence of quantum interference. In optical correlation experiments of either a single split beam of photons or a pair of beams, information regarding either the body scattering the coherent sources, or the distance between the sources, is extracted from the level of interference of the superimposed waves. If there is a phase difference between the beams of less than π during the period of observation, then clear fringe patterns emerge as a result of constructive and destructive interference. If this phase difference is greater than the critical value then no interference pattern will be observed upon interaction of these beams. By tuning the distance over which each beam travels, or the distance between slits inducing interference, the phase difference between the two beams can be controlled. This has lead to studies of celestial bodies through Michelson type interferometry and radio astronomy[6,30,31], cosmic background radiation[32,33] and gravity waves[34].

Excitation of molecules and the subsequent emission of light is regularly used for probing or tagging molecules in the condensed phase[35]. While both linear

and nonlinear spectroscopies are capable of differentiating vibrational and electronic transitions[36], two-dimensional optical spectroscopy (2DOS) is additionally able to separate homogeneous and inhomogeneous broadening. These processes, which are often depicted with Liouville pathways[37], have broadening which is dependent on the memory effects induced by the environment of the open quantum system. A third order signal, induced by interaction with three laser pulses, can be used to generate these Liouville pathways which describe changes in system population and coherence dynamically. 2DOS peaks which are static, or decay towards lower detection frequencies, exist in population pathways whereas oscillatory signals, which beat as a consequence of excited state superpositions, exist in coherence pathways. In a linear spectrum all environmental and system induced broadening is projected onto a single axis, and isolation of these components is difficult. In contrast 2DOS separates inhomogeneous, environmental, broadening onto the diagonal and homogeneous broadening, due to system transition uncertainty, onto the anti-diagonal axes through rephasing in photon echo techniques. Such an approach allows full resolution of each source of broadening so that diagonal static disorder and anti-diagonal electronic dephasing are independent. In this way, subtle movement of the OQS boundary which impacts quantum effects, and the structure of individual OQS models, can be observed through changes in diagonal and anti-diagonal lineshape.

Modern experimental and theoretical 2DOS methods can be performed over a full range of energies from low energy 2D infrared spectroscopy (2DIR) able to probe vibrational structure[38], through mid-energy 2D electronic spectroscopy (2DES) which offers insight into electronic and vibrational coupling known as vibronic coupling and purely electronic structure[39,40], to the highest energy 2D x-ray spectroscopy (2DXS) which probes fine structure[41] and dynamic modelling of conical intersections through transient redistribution of ultrafast electronic coherences in attosecond Raman signals (TRUECARS)[42–44]. In addition, further coupling regimes can be achieved through combinations such as: the combination of UV/vis and IR frequencies which leads to 2D electronic-vibrational (2DEV) and 2D vibrational-electronic (2DVE) spectroscopies which, similar to 2DES, considers explicit coupling of vibrational and electronic degrees of freedom[45–48]. The acute resolution of these combined approaches is particularly relevant in light harvesting complexes[45,49], dimers[50–52], exciton states in quantum wells[53–57], and quantum dots[58–63].

Resonance energy transfer (RET) is a nonradiative method of energy transmission between donor and acceptor sites in light-sensitive molecules. Such transfer is essential in light harvesting complexes and is common in pigment molecules, leading to a host of dye-derived, aggregate, models[52,64–74]. The strong dependence on the separation distance of the two sites in this

transfer makes electronically coupled excitonic species, termed *dimers*, ideal model molecules.

Historically, the modelling of aggregate systems was achieved through purely independent vibrational and electronic degrees of freedom, with the Born-Oppenheimer (adiabatic) approximation of quantum mechanics. However, more recent models account for these degrees of freedom and simultaneously include electronic-vibrational coupling in the system Hamiltonian resulting in a quenching of the electronic, J, coupling[75–77]. Such approaches, which are termed *nonadiabatic*, of modelling vibronic dimers additionally exhibit enhancement of vibrational coherences on the ground electronic state, and driven anticorrelated vibrations in excitation energy transfer (EET)[78–80]. Application of equivalent models has revealed a strong dependence on vibrational degrees of freedom of long-lived coherences in 2DES moreso than dependence on electronic degrees of freedom[81]. Furthermore, the importance of vibrational contributions are emphasised by the splitting of exciton states in heterodimers which leads to a rate enhancement of EET[82–86]. Work by Policht et al. has also demonstrated weak exciton transitions accessible through specific vibronic coherence processes[87]. More recently, nonadiabatic models have been further extended to include both weak and strong coupling regimes[88], and coupling with a full continuum of vibrational modes through path integrals[89]. Such quantum-classical methodologies transform the dimer coordinates into those of a simplified two level spin-Boson Hamiltonian[90] in the presence of a single bath which captures full vibrational complexity which is absent in weaker nonadiabatic, or adiabatic models. This demonstrates the oscillatory electronic cycle at the excitation energy between the monomer units of the dimer at physiological temperatures and that static disorder, introduced directly by the environment, results in asymmetric two-level-system configurations which suppress quantum behaviours such as tunnelling[89]. These findings are supported by loss of quantum effects at physiological temperatures, due to the rapid destruction of exciton-vibrational coherences by electronic dephasing[91–93]. In addition, rather than being a purely destructive influence, it has been suggested that environmental, static, disorder and inhomogeneous broadening contribute to prolonging the lifetime of observed coherences[94]. Another experimentally relevant parameter of importance is the pulse width. It has been shown that the finite width of the laser spectrum can lead to distortion of 2D spectra and significant changes in coherences[69,95–97]. However, it is shown that in the limit of long population time that the impulsive limit is sufficient.

Despite current emphasis on coherent mechanisms, it is worth noting the equal, if not greater, importance of incoherent mechanisms in EET which have been demonstrated for a series of photosynthetic molecules and generalised to a broad set of electronically coupled species[98–100]. It is demonstrated that

coherent beatings are delocalised vibrations on the ground state, interpreted as vibrational coherences and mixed electronic-vibrational coherences on the excited state, rather than long-lived electronic signals[97,98,101–106]. Irrespective of these effects, there is still broad interest in quantum coherent effects in EET and light-harvesting complexes for their potential applications in green energy.

The necessary complexity of a model OQS is dependent on the desired system, but can range from low complexity in exact models with few degrees of freedom, to highly technical approximations with many degrees of freedom. One such exact approach is the multimode Brownian oscillator (MBO) model, where the system-bath interaction is calculated using the perturbative cumulant expansion[37,107–111]. The cumulant expansion, in analogy with the spectral density[112–114], maps system variables onto harmonic oscillators and in this instance results in addition of non-Markovian memory effects which are usually inconsistent with perturbative theories[115]. An approximation of these dynamics, which constitute a thermodynamic composite with thermal bathentanglement[116–118], can be obtained via stochastic methods introducing random forcing due to the environment ensemble. Despite being less accurate than exact approaches, these approximations remain in good agreement with experimental results[119,120].

Perturbative theories involve generating approximate solutions to non-trivial problems through relation to solutions of a simpler, or more tractable, problem. Typically a solution is written as a power series of a small parameter, where the order zero component corresponds to the solution of the tractable problem, such that higher order additions of the expansion parameter introduce corrections which, when truncated, form the approximate solution. The benefit of this is that it increases the number of applicable systems which can be modelled, while also keeping the method of modelling simplistic and easily solvable. Such perturbative, approximate, methods generally make use of the Markov and Born approximations to guarantee solvability. The Markov approximation ensures that the equations of motion are time-local, numerically explicit, and subsequently have no memory effects. The Born approximation enforces a weak system-bath coupling in order to ensure system and environment components are separable, and can be written as a power series in terms of the system-bath interaction. Many forms of Markovian master equation, including Lindblad, and Redfield master equations[121–123] have been used to model multi-level electronic systems, closed systems, and OQSs with Markovian environment interactions such as for weakly coupled environments[124–127]. Based on the Markovian approximation, which is fundamental to these derivations, these methods are numerically explicit and therefore are necessarily time local equations. However, time locality is not explicitly intrinsic to perturbative equations, subsequently there have been works on non-local perturbative approaches[128,129].

Additionally, perturbative equations need not be Markovian as demonstrated by non-Markovian corrections to the standard Redfield equation[126].

In contrast, functions or variables which cannot be expanded as a power series through a perturbative theory are known as *non-perturbative*. The cost of removing the perturbation is that additional complexity is returned to the system and methods being solvable is not guaranteed, often leading to complex high order partial differential equations (PDEs). While this might seem counterproductive when our goal is simplification, this can often be mitigated by further more restrictive assumptions, in order to introduce strongly non-Markovian, quantum characteristics to OQS. This generally manifests itself as time non-locality in the equations of motion, meaning that the Markov approximation is invalidated. One approach to reaching solvable equations of motion is, in a manner analogous to the Born approximation, splitting the dynamics into fast and slow 'irrelevant' and 'relevant' parts. Through the Nakajima-Zwanzig projection operator[130,131] a pair of coupled equations of motion can be produced, which can be simplified to a time non-local, integro-differential master equation under the assumption that the system and environment are fully factorisable. Another approach involves the application of Itô calculus. By moving into a non-perturbative regime, significantly more sophisticated methodologies are required in order to generate useful equations of motion due to the intrinsic interdependence of historical states in numerically implicit schemes. Under similar simplifying assumptions as the Nakajima-Zwanzig master equation, it is possible to generate Kubo's stochastic Liouville equation[132,133], and the Fokker-Planck equation, or through introduction of friction incurred by a forcing operator one can generate a Langevin equation[134,135]. Each approach introduces non-Markovianity into the dynamics of the system of interest through stochastic variables, where subsequent modulation of the quantum system is regulated by the fluctuation-dissipation theorem[136,137]. Stochastic Gaussian processes introduce a drift and diffusion term into the equations of motion, which act as forcing variables and corrections to the dynamics. In such cases thermal, white noise, fluctuations (often characterised by successive weak interaction) are introduced which influences the system probability distribution resulting in Brownian motion and non-Markovianity. Application of these approaches has allowed for a mix of analytical and approximate OQS models with coloured noise baths, simplified correlations through Gaussian-Markovian noise, and strongly non-Markovian dynamics[138–141]. Additionally, nonadiabatic processes in the low temperature limit are accessible through quantum corrections to the Fokker-Planck equation[142].

Many non-perturbative equations of motion can also be generated through path integral approaches based on work by both Calderia and Leggett and

Feynman and Vernon[4,143,144]. The path integral generalises classical action and proposes that the most probable trajectory is a sum over an infinite number of quantum trajectories resulting in a quantum amplitude. The benefit of this formalism in OQSs is twofold: phase-like additions of trajectories can be extended to non-Markovian sums over an infinite number of historical trajectories, and the dynamics of stochastic processes, which model Brownian type motion, can be effectively computed and visualised through sums of infinite trajectories. Similar to the Fokker-Planck equation and Kubo's stochastic Liouville equation, derivation of these equations of motion takes considerably more effort because of the large complexity. Consequently, a range of additional assumptions are required, depending on the form of the equation of motion, to reach solvable equations of motion. Appendix D, considers the relationship between a series of Stochastic equations and their path integral counterparts. Path integral derived equations of motion, similar to other non-perturbative approaches, are often time non-local, and can take the form of high order integro-differential equations of motion with a non-Markovian memory kernel, which is the source of numerical implicit character, dependent on the form of the spectral density function[113,145,146]. However, this does not mean that all path integral derived methods are numerically implicit. Through simplifying approximations such as the Markovian, rotating wave, or Born approximations these methods reduce to being time-local equations of motion[147].

Kubo and Tanimura first derived the time-local hierarchical equations of motion in 1989[147] using the Feynman and Vernon path integral, for a Gaussian-Markovian bath[138,146,148]. The earliest derivations of this equation of motion employed restrictive assumptions including, weak coupling, high temperature, and uncorrelated initial conditions to ensure no bathentanglement[117,147]. Shortly after this the derivation was extended to allow for arbitrary spectral densities, correlated initial conditions, coloured non-Markovian noise, and strong system-bath coupling at low temperatures resulting in exact solutions for a full range of bath coupling strengths, timescales, and system temperatures with the exception of at the critical damping limit[118,149–152]. The HEOM was fully generalised through a derivation involving a cumulant expansion in 2020[139]. The treatment of the spectral density, and the subsequent nature of interactions between vibrational and electronic degrees of freedom, have been treated in two different ways: standard direct coupling as in the overdamped Hierarchical equation of motion (HEOM)[147], or through a canonical transform as in the underdamped HEOM[153]. These are two cases from the full limiting cases of the damping strength, which ranges from undamped methods where the vibration is in the system[154], overdamped for weakly coupled bath vibrations[155,156], through to underdamped for strongly coupled bath vibrations[153], including linear combinations of each approach[157]. In the former two cases the system-bath

boundary separates the electronic and vibrational degrees of freedom and system-bath coupling has to be introduced explicitly, whereas in the latter EOM the system-bath boundary is contained within the spectral density and coupling between the degrees of freedom arises naturally from the canonically transformed variables.

The broad appeal of the HEOM has led it to be applied in linear, and higher-order optical spectroscopies, including 2DIR, where multiple vibrational modes are coupled to the same or different thermal baths with the potential for correlated bath interactions[138,150,158,159], in the 2DES of pure Ehrenfest states[160], and 2DEV[161]. Additionally, HEOM methods have been employed in the studies of quasiparticles such as dissipatons[162], phonons through the phonon fluctuation spectrum[163], electron transfer[164], entanglement of qubits[116,117], and in models of excitonic aggregates for light harvesting[156,165–168]. In such models it is typical for electronic dephasing and vibrational relaxation processes to be separated into individually evolved baths which are coupled to nonadiabatic vibronic dimer Hamiltonians[169].

However, non-perturbative approaches, which make use of canonical transforms, are not the only way of introducing complex memory effects into OQSs. In direct contrast to the canonical transform, reaction coordinate approaches which incorporate a collective coordinate of the environment into the system Hamiltonian, allow access to important environmental properties. Such models have been employed by Iles-smith et al.[170] and demonstrate behaviour not present within standard perturbative approaches. In addition, Maguire et al.[171] have applied this model to the Franck-Condon physics of a two-level system, and McConnell et al.[172] in modelling electron counting experiments.

Each of the aforementioned intrinsic motivations are summarised through the hypotheses addressed in this work. In chapter 2, and appendix D, a broad review of contemporary theory and EOMs is considered in order to generate a sound understanding of the necessary approximations and assumptions used in the generation of fully non-Markovian equations of motion, derived through the path integral formalism. *Hypothesis 1: Through non-perturbative, modern, formalisms can model complexity be maximised in conjunction with a minimisation of computational effort?* Based on this, chapters 3 and 4 consider the impact on 2DES and quantum correlations of movement of the system-bath boundary using the HEOM. *Hypothesis 2: Are genuine quantum effects strongly impacted by system-bath boundary placement, and can these impacts be controlled by approximations and advanced formalisms?* This is achieved by implementation of the vibronic Hamiltonian for monomer and dimer systems into quantum dynamical simulations followed by calculation of necessary quantum metrics.

Finally, in chapter 5, the previous hypotheses are developed through the derivation of a new HEOM, the Lorentz-Drude Undamped Oscillator (LDUO) HEOM. This is proposed in order to confirm the equivalence between systems modelled with explicit vibrational structure versus canonically subsumed vibrations in the limit of zero vibrational mode damping. *Hypothesis 3: Through reduction to an undamped vibrational mode, can models with canonically subsumed vibrations become equivalent to those with explicit vibrational structure?*

2 Theoretical Methods

Mathematical Notation

Within this thesis there has been a considerable effort to maintain a consistent style of notation and nomenclature both within itself and as part of the wider work of the Jones group. A summary of rules regarding cases, fonts, and brackets is as follows:

1. Mathematical variables are written in italic font, for example x, including when they appear as a super/sub-script, such as Q_t.
2. Mathematical operators and names are written in roman font, for example $\mathrm{d}t$, including when they appear in super/sub-scripts, such as $\mathrm{H}_{\mathrm{A}}^{\mathrm{V}}$.
3. Bold font is reserved for vectors, for example $\mathbf{R}$. These are not usually given italic font as they are treated as a matrix (operator) of lower dimensions.
4. Hats and tildes are reserved for special cases of vectors, operators, and functions. For example a unit vector is denoted with a hat, and the Fourier transform of a function is denoted with a tilde. $\hat{\mathbf{R}}$, $f(t) \rightarrow \tilde{f}(\omega)$.
5. Round brackets $(,\ )$ are termed parentheses, when applicable. Square brackets $[,\ ]$ are termed brackets when applicable. Curly brackets $\{,\ \}$ are termed braces when applicable.
6. Brackets are reserved for functionals - functions of functions - with the exception of commutation relations, or bounds. Examples are $f[g(x)]$, $[\mathrm{H}, \rho] = \mathrm{H}\rho - \rho\mathrm{H}$, and $[-\infty, \infty]$ totally inclusive, or $[-\infty, \infty)$ partially inclusive.
7. Braces can be sorted into three cases. Firstly, they will be used for sets of vectors or functions, such as $\{x\}$. Secondly, they may be used as a placeholder, alongside a dot, for variables or functions within a definition, for example $\frac{\mathrm{d}\{\cdot\}}{\mathrm{d}t}$. Finally, they may rarely be used as a second kind of standard bracket in equations which are particularly long in order to differentiate a large number of parentheses.

Finally, the superscript (ν) is applied to computational parameters which have been converted to the units of wavenumbers via the multiplication by $(2\pi c)^{-1}$ for angular frequencies or c^{-1} for linear frequencies. This is in contrast to the notation traditionally adopted in the Jones group, such as in Green[173], of $\tilde{\{\cdot\}}$ which in this thesis is reserved for transformations of mathematical functions and variables such as through the Fourier transform.

2.1 Model Systems and Open Quantum Theory

Details of the theoretical methods used in this thesis are presented in this chapter. A general description of open quantum system methods and (non-)Markovianity is followed by details of the total Hamiltonian, separated into the system, bath and field components.

2.1.1 Closed Systems

Closed systems, in the Feynman and Vernon[4] sense as depicted in figure 1.0.1, are completely defined by a time-dependent wavefunction, $\psi(t)$. This function is a formal solution of the Schrödinger equation, (D.1.1.2), or when written in vector form it is a formal solution of equation (2.1.1). The vectorised equation is a generalisation which transforms the wavefunction into a column vector, $|\psi(t)\rangle$, such that physical observables for the system are operators which act on the constituent Hilbert space.

$$i\hbar\frac{\mathrm{d}}{\mathrm{d}t}|\psi(t)\rangle = \mathrm{H}|\psi(t)\rangle\,, \tag{2.1.1}$$

is an equation of motion (EOM) for the dynamics of the wavefunction where $\hbar = \frac{h}{2\pi}$, h is Planck's constant, $i = \sqrt{-1}$, and $\mathrm{H}(t)$ is the Hamiltonian for the closed system. EOMs are models designed to predict the behaviour of physical systems, and can range from exact equations such as the Schrödinger equation for a single hydrogen atom to complex approximations of ensembles of molecules like the Hierarchical equations of motion (HEOM), see section 2.5.4. In all cases, EOMs are generated from intrinsic theories, approximations, and assumptions about the physical properties which they aim to replicate. This thesis aims to explore these factors in detail in section, 2.5, in order to thoroughly understand model behaviour and their regimes of applicability.

Computational models generated from continuous EOMs are more amenable when constructed in a discrete, vectorised, framework consisting of operators and matrices. As such, the wavefunction for a state at a time t, can be constructed in a

numerically explicit fashion from an initial condition and an evolution operator:

$$|\psi(t)\rangle = \mathrm{U}(t, t_0)\,|\psi(t_0)\rangle\,. \tag{2.1.2}$$

A numerically explicit operator, such as U, processes an evolution in a step-wise fashion where each step depends solely on previously determined steps. As a consequence of this the evolution operator is defined as an integral over a continuous time variable, s,

$$\mathrm{U}(t, t_0) = \mathrm{T}_{\leftarrow} \exp\Big(-\frac{i}{\hbar}\int_{t_0}^{t} \mathrm{H}(s)\,\mathrm{d}s\Big), \tag{2.1.3}$$

and a chronological time ordering operator, $\mathrm{T}_{\leftarrow}$.

Even within a closed system it is important to be able to model a number of molecules simultaneously. This leads to the introduction of the density operator for mixed states, which is addressed fully in appendix D.1.2,

$$\rho(t) = \sum_i p_i\,|\psi_i(t)\rangle\,\langle\psi_i(t)|\,. \tag{2.1.4}$$

Here, each molecule in a state $|\psi_i(t)\rangle$ has an occupation probability p_i, such that the total probability is $\sum_i p_i = 1$. If any of $\{p_i\}$ is equal to unity then the state being described is *pure*. In contrast, the superposition of a number of pure states is a *mixed* state, with purity defined as $\mathrm{Tr}(\rho^2)$. It is also possible to write a mixture of mixed states in the form of a density matrix:

$$\rho(t) = \sum_{ij} p_i p_{ij}\,|\psi_{ij}(t)\rangle\,\langle\psi_{ij}(t)|\,, \tag{2.1.5}$$

where introduction of the density matrix of a mixed state yields

$$\rho(t) = \sum_i p_i \rho_i. \tag{2.1.6}$$

This powerful mathematical construction is already a dramatic improvement on computing an ensemble particle by particle as the density matrix is now able to describe a statistical ensemble of many moles. This is a consequence of the Hilbert space of the Hamiltonian containing the energy levels of individual molecules within the ensemble.

This results in the standard form of the density operator, which is used throughout this thesis. The diagonal elements of this matrix are the ensemble *populations*, and correspond to the proportion of the ensemble which is in a given state. Consequently, diagonal elements $\in \mathbb{R}^+$ such that the trace of the density matrix is one. The off-diagonal elements of the density matrix, $\in \mathbb{C}$, are termed *coherences* and define the interferences between different basis states of

the system. When the coherences are non-zero the system is in a *superposition* of the constituent basis states. The evolution of the density matrix can be generated through application of a pair of evolution operators, resulting in the Liouville-von Neumann equation (discussed in full detail in section D.1.2), through an analogous, numerically explicit, process to state evolution (2.1.2):

$$\rho(t) = \mathrm{U}(t, t_0)\rho(t_0)\mathrm{U}^{\dagger}(t, t_0), \tag{2.1.7}$$

$$= \mathrm{T}_{\leftarrow} \exp\Big(-\frac{i}{\hbar}\int_{t_0}^{t} \mathcal{L}_{\mathrm{LVN}}(s)\, \mathrm{d}s\Big)\rho(t_0), \tag{2.1.8}$$

where $\mathcal{L}_{\mathrm{LVN}}$ is the Liouville evolution superoperator.

This closed system has a total Hamiltonian $\mathrm{H}(t)$ dependent only on the basis state energies and time. However, in the theory of Open Quantum Systems (OQS) Hamiltonian operators are typically constructed in the interaction picture such that there is an interaction between the system variables and variables of an environment,

$$\mathrm{H}(t) = \mathrm{H}_0 + \mathrm{H}_{\mathrm{I}}(t). \tag{2.1.9}$$

This splits the system into a time-independent contribution describing the system in the absence of interaction, and a time-dependent contribution describing the effect of the interaction.

2.1.2 Open Quantum Systems

Open systems, in the Feynman and Vernon sense as depicted in figure 1.0.2, consist of two or more formally closed systems in independent coordinates which are linked through an interaction term dependent on the coordinates of all coupled systems. A wide range of EOMs exist for modelling the equally broad array of open systems, and the dynamics can be approximate or exact. For simple systems, such as the Jaynes-Cummings Hamiltonian[174,175] for a two-level atom interacting with an optical cavity, there is an analytical solution, however many other treatments involve making simplifying assumptions to produce complex memory effects from large systems. Generally, all degrees of freedom within an open system cannot be treated explicitly, therefore it is usual to construct the total system as a composite of constituent Hilbert spaces where the environment degrees of freedom are simplified[113]. The total Hamiltonian for an open system is an extension of equation (2.1.9) and takes the form

$$\mathrm{H}(t) = \mathrm{H}_{\mathrm{S}} \otimes \mathrm{I}_{\mathrm{B}} + \mathrm{I}_{\mathrm{S}} \otimes \mathrm{H}_{\mathrm{B}} + \mathrm{H}_{\mathrm{SB}}(t), \tag{2.1.10}$$

$\mathrm{H}_i, \mathrm{I}_i \in \{\mathrm{S}, \mathrm{B}\}$, where I_i is the identity operator for the component i. Here, the time-independent component is split into system and environment contributions, each in their own coordinates, and tensored with the dimensions

of the other component. In this way the full Hilbert space is a composite of the constituent degrees of freedom, $\mathcal{H}_{\mathrm{SB}} = \mathcal{H}_{\mathrm{S}} \otimes \mathcal{H}_{\mathrm{B}}$. A reduced density matrix in terms of individual degrees of freedom can be obtained by computing a partial trace over the density matrix. In the case of a partial environmental trace, the system reduced density operator is

$$\rho_{\mathrm{S}}(t) = \mathrm{Tr}_{\mathrm{B}}\Big(\mathrm{U}(t_0,t)\rho(t_0)\mathrm{U}^{\dagger}(t_0,t)\Big). \tag{2.1.11}$$

In an open system with a Hamiltonian in the form of equation (2.1.10), the full dynamics are intrinsically altered by the behaviour of the time-dependent interaction contribution. Depending on the form of this interaction the dynamics can be a small deviation from thermal equilibrium, or fundamentally altered by a complex entanglement[a] of the system and environment. The vast difference in behaviour between these cases makes considering the full range of choices in full generality almost impossible, hence, it is usual to apply simplifying approximations or assumptions about the nature of the interaction Hamiltonian. If the system-bath interaction is very small, then we can apply the weak coupling approximation, often called the Born approximation. This assumes that the environment interaction is a small perturbation to the overall dynamics such that it can be treated as time independent. This corresponds to qubits, or two-level-systems (TLSs) subjected to relatively weak dissipation[176]. This assumption is often used in conjunction with an, approximate, perturbative expansion technique of the interaction coupling strength in which it is natural to assume that high order couplings can be neglected leading to EOMs like the Redfield Master equation[121] - D.1.5. Alternatively, if the coupling between the system and bath is strong then the bath contributions must be fully time dependent and cannot be simplified with the Born approximation. Instead, simplifications based on the scale of the reduced density operator are considered which leads to sets of coupled EOMs as in the Nakajima-Zwanzig equation[130,131] D.1.3. Finally, it is possible to consider the full degrees of freedom, with fully time-dependent interactions, using non-perturbative methods such as the Fokker-Planck equation[177,178] D.1.9, or via stochastic forcing D.1.8. The drawbacks of such an approach, discussed in detail in appendix D.1, are that advanced calculus is required to generate the EOM.

In all cases, it can be beneficial to make an additional choice regarding the separability of the degrees of freedom of the initial state of the system and bath. A standard approximation is to use uncorrelated (factorisable) initial conditions,

$$\rho(t_0) = \rho_{\mathrm{S}}(t_0) \otimes \rho_{\mathrm{B}}(t_0), \tag{2.1.12}$$

[a] This is an entanglement of system and bath variables, analogous to entanglement that is the interdependence of a pair of (or many) particle states. Later this is referred to as 'bathentanglement' to differentiate it. This concept is equivalent to that which is discussed in Dijkstra et al.[117]

which corresponds to systems that are initially separated from the environment. Again, the alternative is a fully correlated initial condition where the system and environment have mixed degrees of freedom, which corresponds to an equilibrium state. This requires an alteration to non-perturbative techniques through the resolvent[149] such as in the arbitrary spectral density HEOM (ASD-HEOM) 2.5.4.3.

2.1.3 Quantum Dynamical Maps

When considering systems with a strongly correlated system and environment it is useful to consider an operator, analogous to the unitary evolution operator, but which acts solely on system degrees of freedom. This operator is known as a quantum *dynamical map*, $\phi_{\mathrm{M}}(t)$. For a weakly interacting system which is simplified by application of the Born approximation, the dynamical map is

$$\rho_{\mathrm{S}}(t) = \phi_{\mathrm{M}}(t)\rho_{\mathrm{S}}(t_0) = \mathrm{Tr}_{\mathrm{B}}\Big(\mathrm{U}(t_0,t)(\rho_{\mathrm{S}}(t_0)\otimes\rho_{\mathrm{B}})\mathrm{U}^{\dagger}(t_0,t)\Big), \tag{2.1.13}$$

fully incorporating the impact of the environment on the system of interest. In order to rigorously define evolution of the reduced density operator through dynamical maps, we must establish when it can be effectively applied. We have already considered a generalisation of theory from continuous microscopic variables to matrices in which physical observables correspond to operating on the system Hilbert space. Similarly, we can consider a generalisation of classical observables in phase space to quantum observables in a C^*-algebra. In Quantum Mechanics the state of a physical system, $|\phi(t)\rangle$, is a linear functional which is acting on an abstract C^*-algebra, and physical observables are hermitian elements of the same algebra. Since states define probabilities of occupation every eigenvalue must be non-negative, and additionally we require that operating on these states with a linear functional must not alter the trace. We can rationalise this by considering the probabilities within the density matrix: it is required that the total probability is unchanged and positive during the course of an evolution. It is because of these properties that quantum dynamical maps are said to be Hermiticity, trace, and positivity preserving. This leads to the definition of *positivity*: if the density matrix elements, $\rho_{nn} > 0 \ \forall\, n$ and $\phi_{\mathrm{M}}(\rho_{nn})$ are also $> 0 \ \forall\, n$ then ρ is positive and the dynamical map, ϕ_{M}, is positivity preserving. Unfortunately, this definition is not enough to describe all physical evolutions. For example, the eigenvalues of a quantum entangled[b] qubit under the influence of the partial transpose operation, are negative[179]. To rectify this, the definition is extended to *complete-positivity*, whereby dynamical maps must not only be positive in the degrees of freedom of the system, but also systems where these degrees of freedom are a subset. For our purposes this

[b] The usual definition of entanglement, as opposed to the specific case of bathentanglement.

asserts that the dynamical map transforms physical states, with positive probabilities, to other physical states for the total degrees of freedom not just for the reduced degrees of freedom of ρ_S. When a dynamical map is completely positive it is called a *quantum channel*, and it is through these channels that the system and environment interact.

2.1.4 The Environment

The work in this thesis considers a total ensemble with a very small system and an environment contribution which is many orders of magnitude larger. This is typical in condensed phase spectroscopy and quantum optics where the system of interest may consist of a small number of molecules or particles relative to an environment which is effectively infinite, such as the solvent of a dilute solution. To model this we construct the environment as a continuum of modes, such that the degrees of freedom are infinite, called a *reservoir*. This reservoir is then initialised to a thermal equilibrium distribution, as would be typical in experiments, which is known as a *bath*. Throughout this thesis the environment is assumed to be infinite with respect to the system of interest, and initially in a thermal equilibrium meaning that the terms bath and environment can be used interchangeably. This highlights the benefit of the theory of open quantum systems: the evolution of the reduced density operator may be computed, taking into account the interaction with the infinite bath degrees of freedom, without the need to propagate the continuum of bath modes.

When a system of interest is coupled to a bath, the once closed system is now free to dissipate energy between the constituent parts, resulting in a damping of the reduced density operator. This system damping lends itself readily to modelling with a classical stochastic forcing, therefore Langevin or Stochastic EOMs, which are discussed fully in D.1.7 and D.1.8, are natural choices for modelling these systems. Within this thesis, we aim to discuss quantum information and quantum correlations, and both are impacted directly by this source of damping. In models of Nuclear Magnetic Resonance (NMR) spectroscopy this damping refers to both T_1 type dissipation and T_2^* type dephasing, and in models of boson counting experiments the damping refers to a loss of quantum correlation in time resulting in a classical correlation at thermal equilibrium. T_1 dissipation and the loss of quantum correlation occur as a consequence of the transfer of energy from the system of interest into the bath resulting in system relaxation and can be considered as longitudinal relaxation[138]. In contrast, T_2^* dephasing is a consequence of transverse relaxation which manifests as a modulation of the potential energy surface along the coordinate without a vertical translation (transition)[138]. In addition, dephasing and the loss of quantum correlation are linked through coherence.

Excitation typically occurs over a range of frequencies, through the application of a broadband laser pulse, resulting in a number of simultaneous excited states moving as a wavepacket within the potential[180,181]. Loss of coherence within the superposition leads to uncertainty of the associated transition frequency and an increased spectral broadening as the signal decays. Similarly, in boson counting experiments continuous driving by a laser field results in a loss of coherence which emerges as quantum antibunching.

The magnitude of damping introduced within these models is of particular importance as it is a crucial indicator for quantum behaviour. Within spectroscopy, damping, and the associated lineshape broadening, is attributed to memory effects arising from the OQS dynamics. Within models of optical coherence the level of damping, and relative level of vibrational relaxation, is intrinsically linked to the level of quantum antibunching. Therefore, the amount of damping is quantified through the correlation function, which is discussed in detail in section 2.2.2.2. Low order correlation functions[31] can be used to track system and bath timescales, and in particular the bath relaxation timescale has a profound impact on the level of damping. This quantity defines the length of time required for the bath to return to its equilibrium distribution after a perturbation, and physically represents a solvent stabilisation effect. When the timescale of the bath reorganisation is very fast with respect to the system relaxation, the system-bath interaction behaves as a thermally averaged, time-independent constant. However, if the timescales of the system and the bath are of equivalent order, the system-bath interaction is fully time-dependent. This can lead to complex dynamics as the bath may be at any stage through the equilibration process when the system relaxation occurs. In this instance, a finite history of the state of the system will have been imprinted into the partially equilibrated bath. The history, which is free to recur at a later point in the evolution of the system, is known to impact the dynamics and is termed a *memory* effect.

Memory effects can be formally extended using the definitions of dynamical maps. In a system completely devoid of memory effects, corresponding to an instantaneous return to equilibrium with respect to the system, the dynamical map for the evolution can be divided into time increments. This results in an additive property analogous to numerically explicit calculations

$$\phi_{\mathrm{M}}(t_0)\phi_{\mathrm{M}}(t_1) = \phi_{\mathrm{M}}(t_0 + t_1), \quad t_0, t_1 > 0, \tag{2.1.14}$$

and means that the map is invertible[182]. Under these circumstances we can call this map strictly *divisible* such that

$$\phi_{\mathrm{M}}(t, t_0) = \phi_{\mathrm{M}}(t, t_1)\phi_{\mathrm{M}}(t_1, t_0), \quad t > t_1 > t_0, \tag{2.1.15}$$

as long as ϕ_{M} is completely-positive and trace preserving (CPTP, discussed in 2.1.3)[183]. This dynamical map is equivalently known as a semigroup and may be converted into exponential form as in Breuer[113]

$$\phi_{\mathrm{M}}(t) = \exp(\mathcal{L}_{\mathrm{g}} t). \tag{2.1.16}$$

Here $\mathcal{L}_{\mathrm{g}}$ is the *generator* analogous to an evolution superoperator. This particular generator is in a form suitable for an OQS with a time-independent interaction, such as in the Lindblad master equation discussed fully in D.1.6. If the generator is time-dependent then the dynamical map can be written as

$$\mathrm{V}(t, t_0) = \mathrm{T}_{\leftarrow} \exp\Big(\int_{t_0}^{t} \mathcal{L}_{\mathrm{g}}(s)\, \mathrm{d}s \Big), \tag{2.1.17}$$

with

$$\mathrm{V}(t, t_1)\mathrm{V}(t_1, t_0) = \mathrm{V}(t, t_0). \tag{2.1.18}$$

The addition of propagators in this manner is another statement of the definition of a fully divisible dynamical map as in equation (2.1.15). This property is sufficient for it to be a numerically explicit operation. Additionally, divisible dynamical maps imply that the underlying process is Markovian, obeying the Markov property, and have no memory effects.

2.1.5 Markovianity

The memory of a system is formalised through the Markov property which itself is a statement that a stochastic process is memoryless if its evolution is independent of its history. When considering an arbitrary discretised evolution, the classical Markov property is equivalent to being numerically explicit: each state depends solely on the previous state in time. This means that any process which evolves following a scheme such that successive steps depend on more than one previous time step are termed *non-Markovian* and do not satisfy the Markov property. Markovianity is summarised in figure 2.1.1, which shows a maximally non-Markovian process.

This form of Markovianity, based on classical probability theory, bestows the property of time-locality to EOMs for Markovian processes. This is because the Markov property behaves in a numerically explicit manner such that Markovian governing equations have no memory. In contrast, this implies that non-Markovian EOMs or EOMs suitable of dealing with complex system-bath interactions must have time non-local governing equations.

As a consequence of the fragile nature of quantum measurements, the definition of Markovianity from classical probability must be extended.

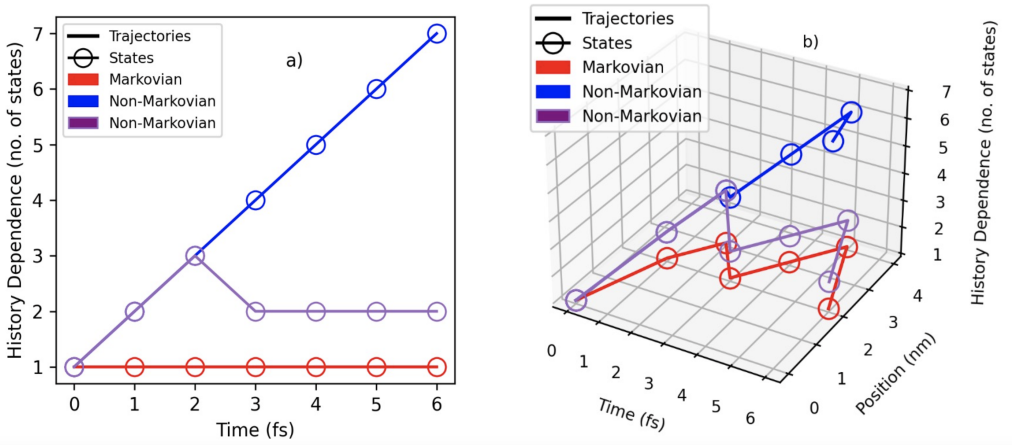

Figure 2.1.1: a) Schematic of Markovianity depicting history dependence as a function of 'number of previous state dependencies' and time. Blue is maximally non-Markovian, and red fully Markovian. b) Schematic of Markovianity additionally including the independent spatial coordinate.

Classically, it is possible to generate accurate probabilities for every individual time-step in an evolution. However, under the formulation of quantum mechanics, the same is not true for a wavefunction based theory, which collapses upon observation. In order to generalise the concept of Markovianity to quantum Markovianity, first it is worth noting the ambiguity surrounding both classical and quantum forms of Markovianity. While a rigorous re-definition of every form of classical and quantum Markovianity is beyond the scope of this thesis, it is worth highlighting the findings of Li et al.[183] who discuss a wide array of definitions of Markovianity. The definition used within this thesis most closely matches the definitions of Divisibility, (2.1.15), and Dynamical Semigroups, (2.1.14), despite similarities to the definition based on the Gorini–Kossakowski–Sudarshan–Lindblad (GKSL) master equation, section D.1.6. The definition of quantum Markovianity used in this thesis maintains the spirit of formal, classical, Markovianity but is applied to the reduced system of interest rather than the full system. Instead of strict consideration of CPTP maps, this form relies more heavily on the transfer of *information* along quantum channels with specific emphasis on the direction of transfer[184]. Such a procedure can be verified experimentally by periodically assessing the state of an initial condition throughout system evolution by the application of tomography[185].

Information can be understood as the complement of the entropy of a system: it is a statement of the total uncertainty and disorder. In a perfectly ordered crystal structure it will be possible to have maximum information about the system as a consequence of minimal entropy. Conversely, the observer has minimum information about a thermal mixture of completely indistinguishable, degenerate, molecules. As the level of disorder in a system decreases, such as

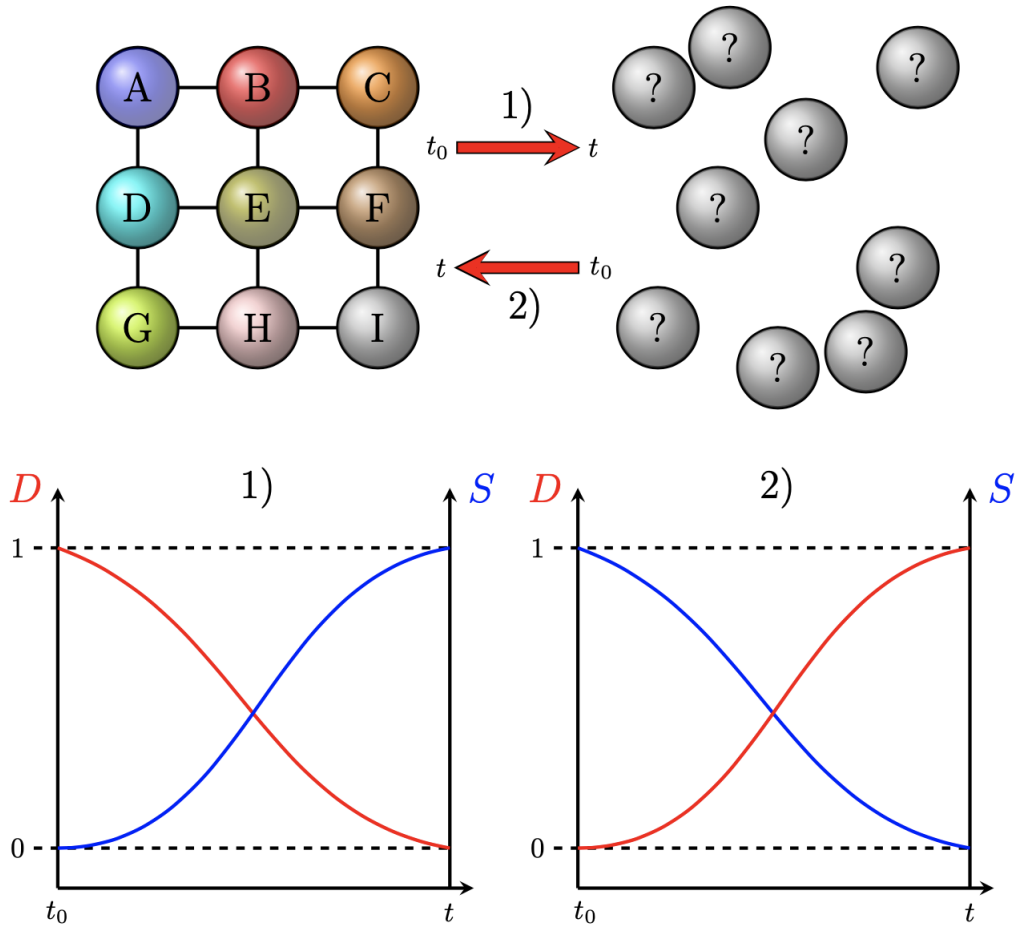

Figure 2.1.2: Schematic depicting the bounds of distinguishability. 1) Evolution from an ordered lattice structure at t_0 into the condensed phase at t. 2) Evolution from the condensed phase at t_0 to an ordered lattice at t. The two graphs depict the corresponding bounds of the Von Neumann entropy, S, and the trace distance metric, D.

during a chemical phase transition, the quantum uncertainty of physical observables decreases in proportion to the increase of quantum information. The Von Neumann entropy, a generalisation of classical Shannon entropy, is measured as

$$S(\rho) = -k_{\mathrm{B}}\mathrm{Tr}\Big(\rho\ln\rho\Big). \tag{2.1.19}$$

As such, the entropy of a pure state (discussed in D.1.2) is zero, corresponding to the occupation of a single *distinguishable* state. Whereas, a completely mixed state has an even distribution of occupations among many states, which are indistinguishable from one another, such that the entropy is greater than zero. Information and distinguishability are summarised as a schematic is figure 2.1.2.

In OQSs, the structure of the Hilbert space leads to an additional restriction on the magnitude of Von Neumann entropy. Since the system and bath are correlated during evolution and the Hilbert space takes the form $\mathcal{H}^{(1)(2)} = \mathcal{H}^{(1)} \otimes \mathcal{H}^{(2)}$, the

entropy exhibits a subadditivity condition[185,186]

$$|S(\rho^{(1)}) - S(\rho^{(2)})| \leq S(\rho^{(1)(2)}) \leq S(\rho^{(1)}) + S(\rho^{(2)}), \tag{2.1.20}$$

which is sometimes referred to as a *triangle inequality* in analogy with the side lengths of a triangle in euclidean geometry. This is a demonstration of the fact that a positive correlation between component parts of a composite system results in an increase of information and a loss of entropy. In addition to subadditivity, quantum entropy exhibits strong subadditivity[186] when the composite system consists of three parts:

$$S(\rho^{(1)(2)(3)}) + S(\rho^{(2)}) \leq S(\rho^{(1)(2)}) + S(\rho^{(2)(3)}). \tag{2.1.21}$$

The entropy is also characterised by the fact that it is concave, which means that the entropy of a mixture serves as an upper bound for the sum of the entropies of its constituent parts,

$$S\left(\sum_j p_j \rho_j\right) \geq \sum_j p_j S(\rho_j), \tag{2.1.22}$$

with non-equal ρ_j. In practice this means that the entropy of a mixture of states is higher, and the total system more disordered, than for the sum of the entropy of its parts.

From the foundation of information a *metric* on the space of density matrices is constructed which considers the statistical distance between states corresponding to a quantification of the distinguishability. For a pair of classical probability distributions, compared at an initial time, this metric is known as the Kolmogorov distance. This metric can be generalised for application on quantum states, ρ_1 and ρ_2, with probabilities, p_1 and p_2, to the Helstrom (Bures) metric[187]

$$\Delta_{\mathrm{H}}(\rho_1, \rho_2) = \mathrm{Tr}|p_1\rho_1 - p_2\rho_2|, \tag{2.1.23}$$

where $|\mathrm{A}| = +\sqrt{\mathrm{A}^\dagger \mathrm{A}}$. Within this thesis we consider a simplified version of the Helstrom metric, the trace distance metric, which applies to quantum states which are equally probable, $p_1 = p_2 = \frac{1}{2}$:

$$D(\rho_1, \rho_2) = \frac{1}{2}\mathrm{Tr}|\rho_1 - \rho_2|. \tag{2.1.24}$$

This metric is bounded by $[0, 1]$ such that identical, indistinguishable states with parallel supports have $D(\rho_1, \rho_2) = 0$, and completely distinguishable, orthogonal states have $D(\rho_1, \rho_2) = 1$. States are said to be *orthogonal* when their support, or subspace of eigenvectors with non-trivial eigenvalues, are also orthogonal. A depiction of the bounding cases of $D(\rho_1, \rho_2)$ are shown in

schematic 2.1.2.

The action of a CPTP-map on the trace distance causes a contraction, meaning that system states become less distinguishable during the course of an evolution,

$$D(\rho_1(t), \rho_2(t)) \leq D(\rho_1(t_0), \rho_2(t_0)), \quad \text{when} \quad t > t_0. \tag{2.1.25}$$

A decrease in quantifiable distinguishability through the course of an evolution is a necessary and sufficient condition for the loss of quantum information and an increase in the system entropy. The information which is gained by the bath results in imprinting of system states on the bath degrees of freedom, or as a change of state[185]. If the loss of information through the course of an evolution is strictly monotonic, then the quantum channel must be a divisible semigroup which obeys the Markov property. This is the formal definition of a Markovian process as defined by authors including Breuer et al.[113,185]. Subsequently, any process which does not have a strictly monotonic loss of information must incur a transfer of information from the bath to the system. This transfer, which invalidates the divisibility condition, facilitates a build-up of correlation over a finite history which manifest as memory effects. Such processes are termed *non-Markovian*.

Breuer, Laine, and Piilo[188] further develop this concept into a quantification of the non-Markovianity of an open quantum system. The total magnitude and direction of information travel is ascertained through the information flux

$$\sigma = \frac{\mathrm{d}}{\mathrm{d}t} D(\rho_1(t), \rho_2(t)). \tag{2.1.26}$$

Next, the Markovian contributions, which have negative flux due to the monotonic loss of information, are discarded leaving the non-Markovian flux. Integration of this quantity over time produces a measure of the total information which is returned to the system from the bath,

$$\mathcal{N} = \max_{\rho_{1,2}} \int \sigma(t)\, \mathrm{d}t. \tag{2.1.27}$$

Based on this construction, any system which is purely Markovian will have $\mathcal{N} = 0$, while any process with a degree of non-Markovianity will have $\mathcal{N} > 0$. This measure is used in chapter 3 to measure the impact on quantum information metrics (and their respective physical processes) of the movement of the system-bath boundary within a hierarchical model.

2.1.6 Field Interactions

Applications such as quantum optical coherence measurements and spectroscopy involve the excitation of the open quantum system by the external electric field of an incident laser. To correctly account for the interaction of the system degrees of freedom with the laser field, an external field Hamiltonian must be added to the models. In section 4.1 we consider quantum correlations generated by a laser with a single frequency, and this is extended in section 4.2 to a Gaussian bandwidth. Similar to the Hamiltonian structure (2.1.10) of the theory of open quantum systems, quantum electrodynamics (QED) postulates that the time-independent field energy will be introduced through $\mathrm{H_F}$, and the time dependent system-field interaction will be introduced through $\mathrm{H_{SF}}(t)$. Ideally, we would employ a fully QED theory which combines a quantum EOM, such as the Schrödginer equation (D.1.1.2), with a quantum treatment of radiation in terms of quantised photons. In the weak-coupling limit between the radiation and the system, perturbative expansions of the coupling strength are particularly useful as higher order interaction terms can be safely neglected with minimal impact on the model. However, when the coupling strength is large, as in many boson counting experiments which use resonant field frequencies[189,190], perturbative approaches fail. Rather than employing a full quantum mechanical treatment, which requires a large Hilbert space, we employ an approximate method of modelling the system-field interaction. If the size of the electromagnetic subspace is limited such that there are few photon modes then a floquet model could be introduced[191]. This theory is analogous to the Nakajima-Zwanzig projection operator (discussed in D.1.3) where fundamental components of the solution are factorised based on their timescale or magnitude. However, rather than limit the photon subspace, we propose the application of semi-classical theory where the system of interest is computed fully quantum mechanically and the radiation is modelled as a classical field through Maxwell's equations[191]. Under this approximation the Hamiltonian of the reduced system is supplemented by the time-dependent system-field interaction Hamiltonian, $\mathrm{H_{SF}}(t)$, within the generator $\mathcal{L}_\mathrm{g}$ (2.1.17). This leads to a general master EOM of the form

$$\frac{\mathrm{d}\rho_\mathrm{S}}{\mathrm{d}t} = \mathcal{L}_\mathrm{g}\rho_\mathrm{S}(t) = -\frac{i}{\hbar}[\mathrm{H_S} + \mathrm{H_{SF}}(t), \rho_\mathrm{S}(t)] + \mathrm{D}[\rho_\mathrm{S}(t)], \tag{2.1.28}$$

where the first set of square brackets denote the commutator, and where $\mathrm{D}[\rho_S(t)]$ is an arbitrary relaxation superoperator defining the interaction with the bath. The form of D is discussed fully in appendix D.1.6.

Accordingly, the models in this thesis are built from fundamental theory and its necessary approximations such that they follow a scheme as depicted in figure 2.1.3. There is an open quantum system, which consists of a bath

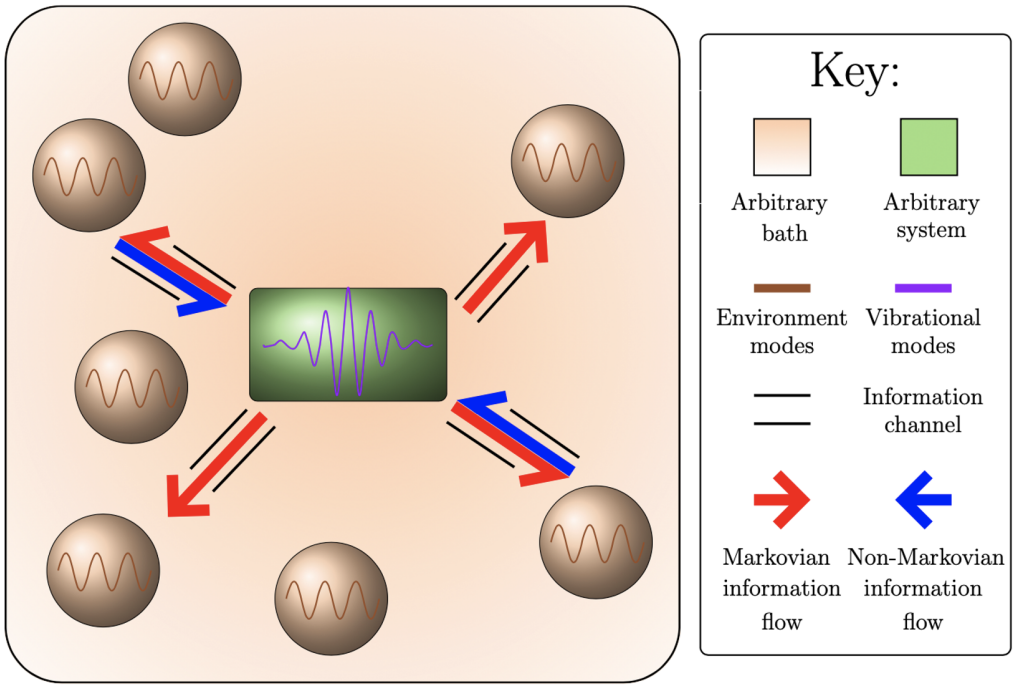

Figure 2.1.3: A schematic of the model system applied in this thesis: an open quantum system with a phononic bath allowing for non-Markovian memory effects. The green Hamiltonian of the system can be substituted for any of the vibronic molecules discussed in this section.

(solvent) and system of interest (solute) which are free to interact. This system is free to behave in a Markovian or non-Markovian manner. Interacting with this is a classically modelled incident laser field which places the system in a superposition of excited states. The influence of the bath then acts to damp the excited state wavepacket leading to dephasing and a dissipation of energy back into the bath. Dependent on the timescales of these fundamental processes the system is free to exhibit non-Markovian memory effects. This model is adequate for modelling time-resolved spectroscopic methods which currently are of the order of attoseconds, and for probing vibrational correlations in optical coherence experiments which are of the order of 100 wavenumbers.

2.2 The Hamiltonian

2.2.1 System Hamiltonian

2.2.1.1 Vibronic Monomer

Consider a two electronic energy level system, or monomer, with a ground state, S_0, and an excited state, S_1. The lower energy state vector is denoted $|g\rangle$ and the excited state vector, $|e\rangle$, found at an energy $\hbar\omega_{eg}$ above the ground state allowing

for the construction of a Hamiltonian,

$$\mathrm{H}_{\mathrm{M}}^{\mathrm{S}} = |g\rangle\, \mathrm{h}_g\, \langle g| + |e\rangle\, \mathrm{h}_e\, \langle e|\,, \tag{2.2.1}$$

with $\mathrm{h}_i,\ i \in \{g, e\}$ being the nuclear Hamiltonian for the vibrational contribution,

$$\mathrm{h}_g = \sum_j \left(\frac{\mathrm{p}_j^2}{2m_j} + \frac{1}{2} m_j \omega_j^2 \mathrm{q}_j^2 \right), \tag{2.2.2}$$

$$\mathrm{h}_e = \hbar\omega_{eg} + \sum_j \left(\frac{\mathrm{p}_j^2}{2m_j} + \frac{1}{2} m_j \omega_j^2 (\mathrm{q}_j - d_j)^2 \right), \tag{2.2.3}$$

and where $\{m_j\}$, $\{\mathrm{p}_j\}$, and $\{\mathrm{q}_j\}$ are respectively the mass, momentum and coordinate of the jth vibrational mode, with an associated frequency of $\{\omega_j\}$. The total Hamiltonian is denoted M to indicate that it is for a monomer, and the fact that it incorporates the coupling between the fundamental electronic degrees of freedom and the local vibrations, excluding rotational and translational contributions, makes it *vibronic*[192]. Each independent vibrational mode is modelled as a harmonic oscillator coupled to the electronic degrees of freedom. Each state has a respective potential energy surface, $V_i,\ i \in \{g, e\}$, and the excited state potential energy minimum is displaced relative to the ground state minimum by d_j along the coordinate q_j. Similarly, $\hbar\omega_{eg}$, is the energy of transition between the lowest vibrational levels of the two states, and $\hbar\omega_j$ is the energy of transition to the first vibrational excited state within each potential.

The potential energy surface can be non-dimensionalised by substituting the quantum harmonic oscillator into the Schrödinger equation (D.1.1.2) resulting in an intrinsic energy scale of $\hbar\omega_j$, an intrinsic lengthscale of $\sqrt{\frac{\hbar}{m_j\omega_j}}$ and the ground state energy of the oscillator, $\frac{\hbar\omega_j}{2}$. Hence the dimensionless coordinates are,

$$\tilde{\mathrm{p}}_j = \left(\sqrt{\hbar m_j \omega_j} \right)^{-1} \mathrm{p}_j, \tag{2.2.4}$$

$$\tilde{\mathrm{q}}_j = \left(\sqrt{\frac{m_j\omega_j}{\hbar}} \right) \mathrm{q}_j, \tag{2.2.5}$$

$$\tilde{d}_j = \left(\sqrt{\frac{m_j\omega_j}{\hbar}} \right) d_j, \tag{2.2.6}$$

and the nuclear Hamiltonians are expressed in the occupation number representation, via the intrinsic energy scale and ground state energy, as

$$\mathrm{h}_g = \sum_j \hbar\omega_j \left(\mathrm{b}_j^\dagger \mathrm{b}_j + \frac{1}{2} \right), \tag{2.2.7}$$

$$\mathrm{h}_e = \hbar(\omega_{eg} + \lambda) + \sum_j \hbar\omega_j \left(\mathrm{b}_j^\dagger \mathrm{b}_j - \frac{\tilde{d}_j}{\sqrt{2}} (\mathrm{b}_j + \mathrm{b}_j^\dagger) + \frac{1}{2} \right), \tag{2.2.8}$$

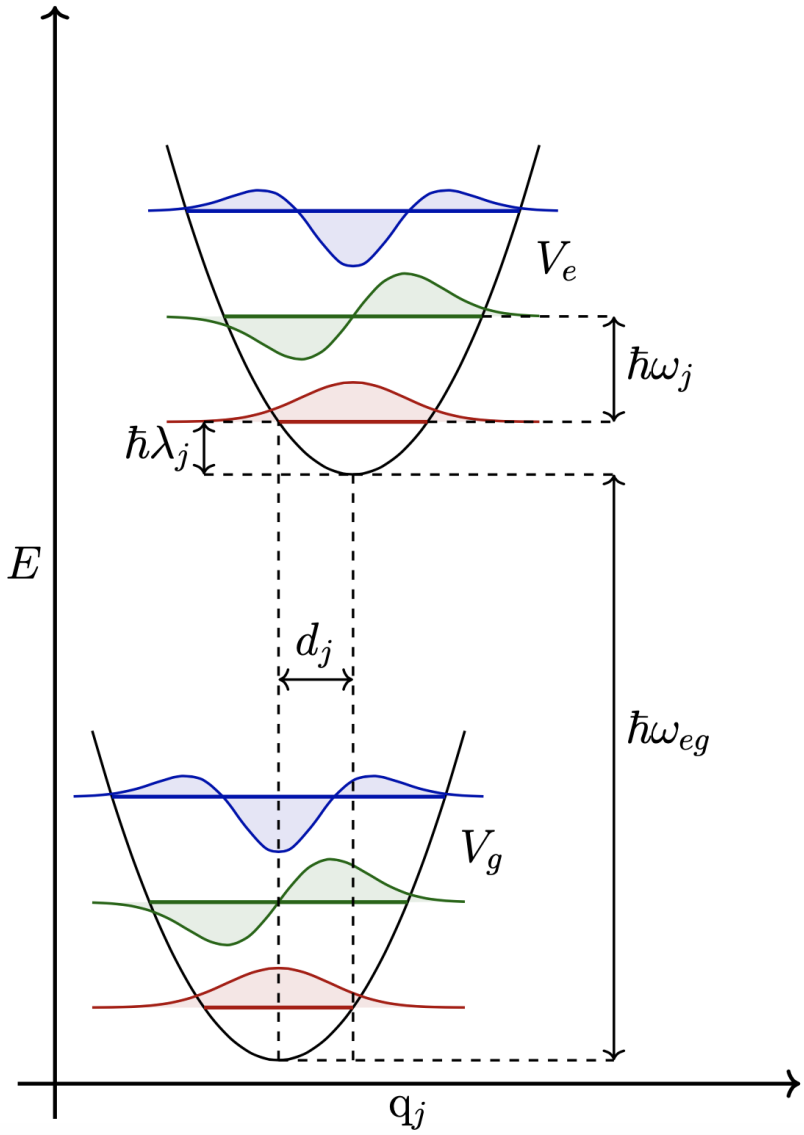

Figure 2.2.1: Potential energy surface of a vibronic monomer where the pair of electronic states are each coupled to the jth vibrational mode. Diabatic levels are coloured and have the appropriate bound quantum harmonic oscillator eigenstates overlaid.

where the second quantised form vibrational creation and annihilation operators, $\mathrm{b}_j^\dagger$ and b_j, are,

$$\mathrm{b}_j^\dagger = \sqrt{\frac{m_j\omega_j}{2\hbar}}\left(\mathrm{q}_j - \frac{i}{m_j\omega_j}\mathrm{p}_j\right) = \frac{1}{\sqrt{2}}(\tilde{\mathrm{q}}_j - \tilde{\mathrm{p}}_j), \tag{2.2.9}$$

$$\mathrm{b}_j = \sqrt{\frac{m_j\omega_j}{2\hbar}}\left(\mathrm{q}_j + \frac{i}{m_j\omega_j}\mathrm{p}_j\right) = \frac{1}{\sqrt{2}}(\tilde{\mathrm{q}}_j + \tilde{\mathrm{p}}_j), \tag{2.2.10}$$

and obey the boson commutation relation

$$[\mathrm{b}_j, \mathrm{b}_k^\dagger] = \delta_{jk}, \tag{2.2.11}$$

where δ_{jk} is the Kronecker delta. Consequently, this expresses the value of the

matrix element of the commutator for the indices j and k, and is a scalar.

The excited state displacement, $\tilde{d}_j$ induces a reorganisation energy of $\hbar\lambda_j$ in the fundamental electronic transition of the system and corresponds to the additional energy required to reach the equilibrium geometry of the product state. The potential energy surface (PES) for a vibronic monomer is shown in figure 2.2.1. Each vibrational mode couples to the electronic degrees of freedom linearly upon excitation, which is most evident in second quantised form (equation (2.2.8)) through terms proportional to the non-dimensional displacement, and is strongly dependent on the system basis. The system basis is a set of orthonormal eigenvectors (kets) which lead to a spectrum of energy levels dependent on the system Hilbert space. Upon linear coupling there is no change in either the reduced mass or frequency of the mode[193].

For an arbitrary number, N, of vibrational modes, the nuclear contribution to the system Hamiltonian is

$$|n\rangle = |\nu_0\nu_1 \dots \nu_{N-1}\rangle\,, \tag{2.2.12}$$

which corresponds to the extension of the vibrational subspace via a tensor product for each mode. $|\nu_j\rangle$, are the eigenstates of the vibrational number operator for the jth mode, such that,

$$\mathrm{b}_j^\dagger \mathrm{b}_j\,|\nu_j\rangle = \nu_j\,|\nu_j\rangle\,, \tag{2.2.13}$$

and

$$\mathrm{b}_j\,|n\rangle = \sqrt{\nu_j}\,|\nu_0, \dots, \nu_j - 1, \dots, \nu_{N-1}\rangle\,, \tag{2.2.14}$$

$$\mathrm{b}_j^\dagger\,|n\rangle = \sqrt{\nu_j + 1}\,|\nu_0, \dots, \nu_j + 1, \dots, \nu_{N-1}\rangle\,. \tag{2.2.15}$$

In this basis the ground state nuclear Hamiltonian, h_g, is diagonal containing no off-diagonal elements, such that $\mathrm{h}_g\,|n\rangle = E_n\,|n\rangle$, with energies

$$E_n = \sum_j^N \hbar\omega_j(\nu_j + \frac{1}{2}). \tag{2.2.16}$$

In contrast, the nuclear excited state Hamiltonian, h_e, is coupling dependent, and contains off-diagonal elements. Subsequent physical manifestations of the coupling are unique to the choice of basis.

This vibrational basis taken in conjunction with the electronic degrees of freedom through a tensor product constitutes the full monomer wavefunction

and represents the localisation of energy in a particular electronic state[194,195]

$$\psi_{\mathrm{M}}(t) = \psi_{\mathrm{M}}^{(\mathrm{ele})}(t) \cdot \psi_{\mathrm{M}}^{(\mathrm{vib})}(t), \tag{2.2.17}$$

which is equivalent to

$$|\psi_{\mathrm{M}}^{\mathrm{S}}\rangle = |\alpha\rangle \otimes |n\rangle = |\alpha, n\rangle\,, \tag{2.2.18}$$

where $\alpha \in \{g, e\}$. This is denoted, S, for *site* basis, which gets its name from the non-stationary superposition of vibrational states, forming a wavepacket, *localised* within the excited electronic potential. Additionally, this is an expression of the approximation that electronic charge redistribution can occur instantaneously relative to the motion of the nuclear degrees of freedom. This is often known as the first-order Herzberg-Teller expansion[196,197], or the Born-Oppenheiemer approximation. Consequently, there is no coupling between the electronic and vibrational degrees of freedom beyond that which is explicitly induced by the displacement of the excited state potential.

The vibronic coupling present in this model induces a total reorganisation energy dependent on the strength of the coupling, which is often quoted in terms of the Huang-Rhys parameter, S_j^{HR}, so that it takes the form

$$\hbar\lambda = \sum_j \lambda_j = \sum_j S_j^{\mathrm{HR}} \omega_j, \tag{2.2.19}$$

with

$$S_j^{\mathrm{HR}} = \tfrac{1}{2}\tilde{\mathrm{d}}_j^2 = \frac{m_j \omega_j d_j^2}{2\hbar}. \tag{2.2.20}$$

Physically this parameter, sometimes also called the electron nuclear coupling strength, represents the mean number of phonons in a coherent state that has been displaced by the reorganisation energy from that of the the vacuum distribution[198]. The Huang-Rhys parameter can additionally be generated directly from the overlap integrals of the quantum harmonic oscillator eigenstates of the ground and excited vibrational states[77]

$$S_j^{\mathrm{HR}} = \frac{|\,\langle e, 1_j | g, 0_j\rangle\,|^2}{|\,\langle e, 0_j | g, 0_j\rangle\,|^2}, \tag{2.2.21}$$

where the shorthand $|n\rangle = |0_0, 0_1, \ldots, \nu_j, \ldots, 0_{N-1}\rangle = |\nu_j\rangle$ denotes the vibrational quantum number where all modes are in the ground state except for the jth mode. These brakets, referred to as overlap integrals, are the Frank-Condon factors.

If we consider a monomer with the electronic singlet states,

$$\mathrm{S}_0 = |g\rangle = \begin{pmatrix} 1 \\ 0 \end{pmatrix}, \quad \mathrm{S}_1 = |e\rangle = \begin{pmatrix} 0 \\ 1 \end{pmatrix}, \tag{2.2.22}$$

coupled to a vibrational mode with a pair of vibrational levels, the monomer Hamiltonian is,

$$\mathrm{H}_{\mathrm{M}}^{\mathrm{S}} = \frac{\hbar\omega_0}{2}\begin{pmatrix} 1 & 0 & 0 & 0 \\ 0 & 3 & 0 & 0 \\ 0 & 0 & \frac{2}{\omega_0}(\omega_{eg}+\lambda)+1 & -\sqrt{2}d_0 \\ 0 & 0 & -\sqrt{2}d_0 & \frac{2}{\omega_0}(\omega_{eg}+\lambda)+3 \end{pmatrix}. \tag{2.2.23}$$

The choice of basis is fundamental to the nature of the off-diagonal elements within the Hamiltonian. In the site basis, the focus is on a localisation of states onto a particular potential energy surface. As a result, the states exist as a superposition. This can result in stationary states when $d_0 > 0$ because the linearly independent states depend on the system coupling, or non-stationary states. When $d_0 = 0$ the linearly independent solutions are the pure states and coupled combinations are non-stationary. As this description involves explicit forms for the off-diagonal coupling elements it is equivalent to a *diabatic* basis description. We could, however, consider a basis in which the focus is on stabilisation of the states such that these states are eigenstates of the molecular Hamiltonian, equation (2.2.25). This basis is known as the *vibronic* basis, for a monomer, and is considered as a *delocalised* basis of *adiabatic* eigenstates. The vibronic basis is the basis of eigenvalues and therefore is stationary when the states are pure. This means that the vibronic (adiabatic) basis is stationary, and the diabatic basis *may* be stationary if the eigenstates are a superposition of many levels. From this construction it is possible to generate both a diagonal Hamiltonian, and energy levels which are molecular state experimental observables, which exist in delocalised combinations of diabatic levels. This means that the energy levels behave as a hybridisation of diabatic states. If we allow the monomer excited state to be displaced by a non-zero value of d_0 then this basis of eigenstates is still equally valid, but is shifted to a new position of lowest energy and will have correspondingly altered eigenstates. Given this, a general site basis Hamiltonian can be written in terms of the eigenvalues of the basis of stationary states, ϵ_k, as

$$\mathrm{H}_{\mathrm{M}}^{\mathrm{S}} = \sum_k \epsilon_k \left|\psi_{\mathrm{M},k}^{\mathrm{V}}\right\rangle \left\langle\psi_{\mathrm{M},k}^{\mathrm{V}}\right|. \tag{2.2.24}$$

The vibronic basis Hamiltonian, identified by a superscript V, is achieved through diagonalisation of the site basis Hamiltonian via the unitary transformation matrix, $\mathrm{U}_{\mathrm{M}}^{\mathrm{VS}}$,

$$\mathrm{H}_{\mathrm{M}}^{\mathrm{V}} = (\mathrm{U}_{\mathrm{M}}^{\mathrm{VS}})^{\dagger}\mathrm{H}_{\mathrm{M}}^{\mathrm{S}}\mathrm{U}_{\mathrm{M}}^{\mathrm{VS}}, \tag{2.2.25}$$

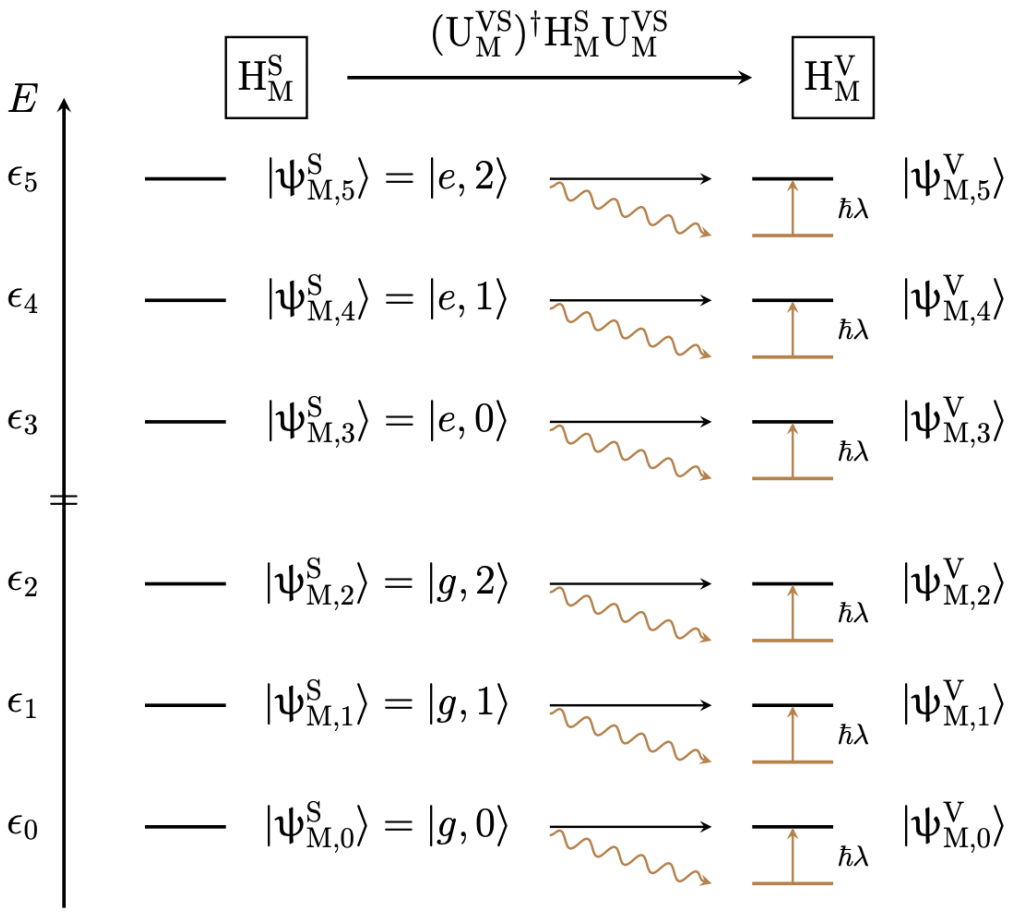

Figure 2.2.2: Transformation of the vibronic monomer Hamiltonian from the site to vibronic basis alters the wavefunction coefficients while maintaining the state energy unless the energy of reorganisation is omitted.

where

$$\mathrm{U}_{\mathrm{M}}^{\mathrm{VS}} = \sum_{k} |\psi_{\mathrm{M},k}^{\mathrm{V}}\rangle \langle\psi_{\mathrm{M},k}^{\mathrm{S}}| \,. \tag{2.2.26}$$

It is possible to change basis in this manner for any operator through an equivalent transformation, substituting the Hamiltonian for the required operator within equation (2.2.25).

Transformation of the Hamiltonian into the vibronic basis from the site basis alters the wavefunction coefficients but, unless the reorganisation is omitted in the nuclear Hamiltonian of the excited state (2.2.8), the state energy is maintained[76,77]. This means that site and vibronic basis energy levels for a vibronic monomer have equivalent energies.

In order to employ this scheme computationally, it is required to numerically diagonalise the Hamiltonian. To avoid significant truncation errors in the matrix elements, which manifest as a divergence of higher energy levels, a large number of vibrational levels must be included. Within this thesis diagonalisation of a vibronic monomer is achieved by including vibrational levels up to $\nu_j = 9$ before

a reduced number are extracted for use in any further computation or analysis.

This construction of a self-contained molecular system with electronic and vibrational degrees of freedom such that it can act as a chromophore, is termed a *vibronic monomer* and is the fundamental constituent of a *vibronic dimer*.

2.2.1.2 Electronically Coupled Aggregates

In order to explore the impact of electronic coupling on the quantum correlations in a pair of models with differing system-bath boundary placement in chapter 4, as a test of hypotheses 1 and 2, vibronic theory is extended to include aggregate species.

In the condensed phase, where molecules interact readily, the features of localisation and delocalisation in model bases are exacerbated as a consequence of additional electronic coupling. The result of this is that molecules are able to transfer electronic energy from a donor site to an acceptor site over a range of distances. At the longest range the coupling is expressed as a radiative transfer via emission and absorption of a photon of light, whereas at the shortest range, radiationless mechanisms dominate which lead to excitonic structures[199–202]. The radiationless energy transfer involves a Coulombic dipole-dipole interaction, modelled with Förster theory, whereby a semi-classical first order perturbation approximation induces instantaneous coupling. Despite these necessary approximations, the semi-classical model still fundamentally depicts a quantum process as discussed in Jones et al.[203]. At a shorter range still, there is a quantum mechanical exchange interaction as a consequence of direct overlap of the wavefunctions of the donor and acceptor sites, described by Dexter theory[201,204,205].

In direct analogy to the localisation of non-stationary states onto a particular PES within vibronic monomers, localisation occurs within dimer species. The electronic coupling between constituent monomer units within the aggregate allows a localisation of non-stationary states across both monomers on specific donor and acceptor sites on either monomer unit within the aggregate. In equivalence with the delocalised, vibronic, basis for monomers, the states of a vibronic dimer can be transformed into delocalised hybridisations of diabatic energy levels in the *exciton* basis. In this basis the focus is on the electronically delocalised exciton states of the aggregate as opposed to localised sites within the molecule. This makes these models particularly useful for addressing the controversy surrounding oscillating features within 2DES which suggest a coherent mechanism may be amplifying the rate of EET quantum mechanically[98,206–208].

The formation of an electronically coupled aggregate, whether it be through spatial separation or direct covalent bonding, has electronic coupling typically modelled following the work of Michael Kasha[209]. In this model, the molecular dipoles are approximated as infinitesimal points with a coupling, J, given by the Förster coupling equation, in order to describe the formation of Frenkel excitons[205,209]. For monomers A and B with associated transition dipole moments $\boldsymbol{\mu}_{\mathrm{A}}$ and $\boldsymbol{\mu}_{\mathrm{B}}$, the electronic coupling is

$$J = \frac{\kappa_{\mathrm{AB}}|\boldsymbol{\mu}_{\mathrm{A}}||\boldsymbol{\mu}_{\mathrm{B}}|}{4\pi\varepsilon_r\varepsilon_0 R^3}, \tag{2.2.27}$$

where the orientation factor of the two molecules is

$$\kappa_{\mathrm{AB}} = \hat{\boldsymbol{\mu}}_{\mathrm{A}} \cdot \hat{\boldsymbol{\mu}}_{\mathrm{B}} - 3(\hat{\boldsymbol{\mu}}_{\mathrm{A}} \cdot \hat{\mathbf{R}})(\hat{\boldsymbol{\mu}}_{\mathrm{B}} \cdot \hat{\mathbf{R}}), \tag{2.2.28}$$

with $\boldsymbol{\mu}_{\{\cdot\}} = |\boldsymbol{\mu}_{\{\cdot\}}|\hat{\boldsymbol{\mu}}_{\{\cdot\}}$, and where the displacement separating the monomers is $\mathbf{R} = R\hat{\mathbf{R}}$, ε_0 is the vacuum permittivity, and ε_r is the permittivity of the solvent[200,205]. Additional discussion about the transition dipole moments can be found in section 2.2.3.3.

The localised exciton states, are generated as a consequence of positive and negative perturbations of the energy of the combined monomer excited state by the electronic coupling, leading to an energy separation of $2J$. The exciton basis is particularly powerful for dimers as it is able to describe the adiabatic hybrid states, which are otherwise described as diabatic states on spatially distinct locations in the aggregate. When the combination of local monomer excited states results in a positive, symmetric, combination (as a result of matching phase) an optically bright $|e^+\rangle$ state is generated. Whereas, when the monomer excited states are out-of-phase, contributions from the respective transition dipole are anti-symmetric and cancel resulting in a dark $|e^-\rangle$ exciton state. Figure 2.2.3 shows the splitting of the exciton states alongside the doubly excited, $|f\rangle$, state where the exciton-exciton interaction which causes a minor shift in the transition frequencies is neglected[210].

Based on the relative orientation of the two monomer transition dipole moments two different types of aggregate can form, as shown in figure 2.2.4: J- and H-aggregates. When the transition dipole moments are arranged 'head-to-tail' the electronic coupling is negative, $J < 0$, and the lower energy configuration corresponds to the bright, symmetric exciton. Correspondingly, the dark exciton is the higher energy state, with an antisymmetric arrangement. J-aggregates, as a consequence of their strengthened transition dipole moment, are characterised by a red shift of the linear absorption spectrum and an increased radiative decay rate compared to the monomer species as the fluorescing population is enhanced by rapid relaxation mediated by the exciton state. In large aggregate systems the amplified fluorescing population

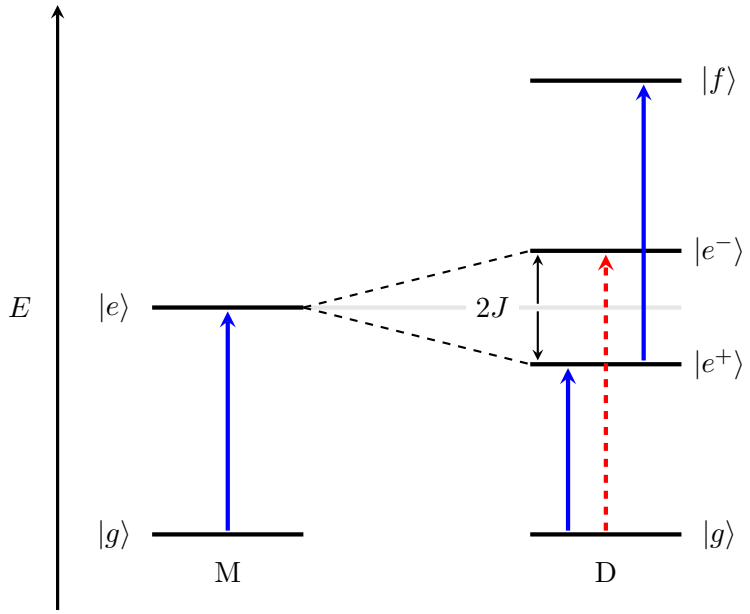

Figure 2.2.3: Energy level diagram for J-aggregate formation. The electronic coupling of monomers, M, forms two exciton states, $|e^+\rangle$ and $|e^-\rangle$, separated by $2J$ and a doubly excited state, $|f\rangle$. Allowed transitions are shown by solid blue arrows and forbidden transitions by dashed red arrows.

accumulates enough for the phenomenon of superradiance to occur[205]. In contrast, when the transition dipole moments are arranged in a 'side-by-side' configuration, the electronic coupling is positive, $J > 0$, resulting in the symmetric, bright, exciton state being at higher energy than the antisymmetric, dark, state. Subsequently, H-aggregates are characterised by a blue shift of the linear absorption spectrum and a decrease in fluorescence, as the dominant pathways for relaxation are via internal conversion and intersystem crossing mechanisms[201,205,211,212].

This model is not limited to standard aggregates. Recent adaptations of the Kasha model, involving non-standard aggregate geometries, have reproduced conventional behaviour from purely the charge transfer states and Dexter exchange interactions[201,205]. Despite these strengths, invalidation of the approximation that system conditions change slowly enough for the final Hamiltonian to be in its corresponding eigenstate, makes it impossible to account for molecular vibrations. As interest in molecular vibrations within open systems continues, advances beyond the traditional adiabatic approximation of Förster theory will be necessary[78,80].

2.2.1.3 Vibronic Dimer

In order to extend the framework of a vibronic monomer to allow for the study of a vibronic dimer, the Hilbert space must be expanded to accommodate vibrational

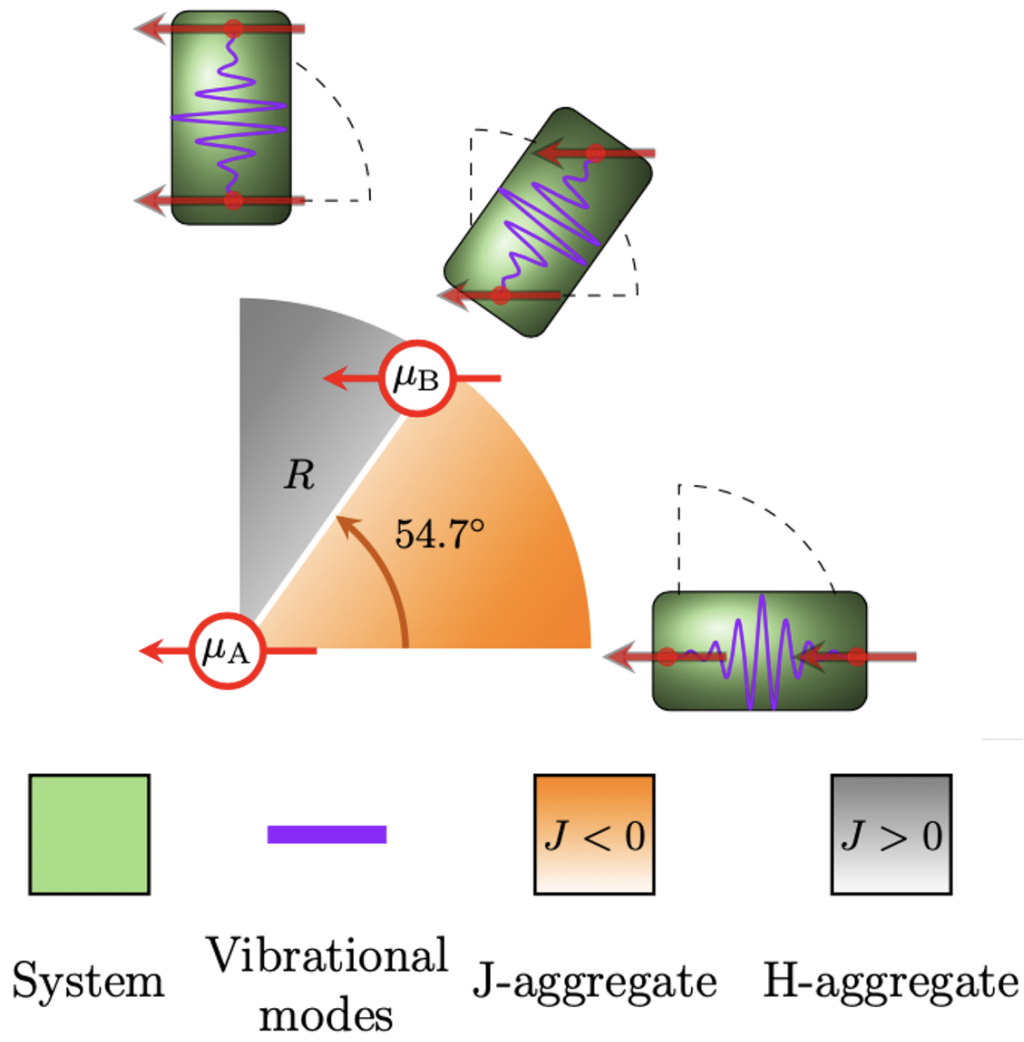

Figure 2.2.4: Two monomer transition dipole moments placed R apart and at an angle $\in [0°, 90°]$. For fixed R and parallel transition dipole moments, increasing from $0°$ (collinear) to $90°$ results in a transition from a J- to an H-aggregate, with the boundary at the magic angle, $54.7°$.

degrees of freedom from both monomer units. From equation (2.2.1), the site basis monomer Hamiltonian, the composite Hilbert space is further extended as a tensor product of monomer states,

$$|\psi_{\mathrm{D}}^{\mathrm{S}}\rangle = |\alpha_{\mathrm{A}}, n_{\mathrm{A}}\rangle \otimes |\alpha_{\mathrm{B}}, n_{\mathrm{B}}\rangle\,, \tag{2.2.29}$$

with α denoting the electronic state, and n the state of the N vibrational modes. As for the vibronic monomer denoted M, here D denotes the dimer subspace and A and B identify the constituent monomers. The total site basis dimer Hamiltonian is then,

$$\begin{aligned} \mathrm{H}_{\mathrm{D}}^{\mathrm{S}} &= \mathrm{H}_{\mathrm{MA}}^{\mathrm{S}} \otimes \mathrm{I}_{\mathrm{MB}} + \mathrm{I}_{\mathrm{MA}} \otimes \mathrm{H}_{\mathrm{MB}}^{\mathrm{S}} \\ &+ J \sum_{n_{\mathrm{A}}, n_{\mathrm{B}}} \Big(|e, n_{\mathrm{A}}, g, n_{\mathrm{B}}\rangle \langle g, n_{\mathrm{A}}, e, n_{\mathrm{B}}| + |g, n_{\mathrm{A}}, e, n_{\mathrm{B}}\rangle \langle e, n_{\mathrm{A}}, g, n_{\mathrm{B}}| \Big), \end{aligned} \tag{2.2.30}$$

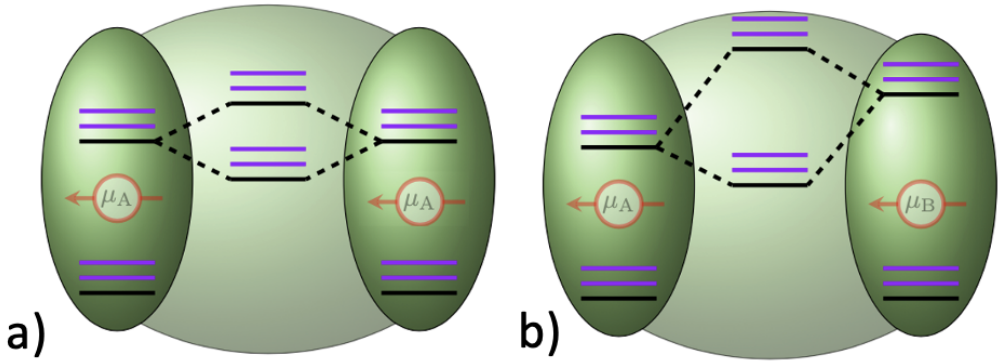

Figure 2.2.5: A schematic of a) a vibronic homodimer, and b) a vibronic heterodimer. In both cases the dipoles are oriented so that a J-aggregate is formed. The purple levels depict vibrational levels.

where $\mathrm{I}_{\mathrm{M}\{\cdot\}}$ is the identity operator over the full monomer degrees of freedom[68,78,81,102]. This results in a summation of the two monomer Hamiltonians with the addition of an electronic coupling between states with equivalent vibrational quanta[81,205] and electronic excitation is transferred between monomers. As such, the dimer Hamiltonian in the site basis is a composite Hilbert space spanning the doubly ground, $|g, n_{\mathrm{A}}, g, n_{\mathrm{B}}\rangle$, singly excited, $|e, n_{\mathrm{A}}, g, n_{\mathrm{B}}\rangle$ and $|g, n_{\mathrm{A}}, e, n_{\mathrm{B}}\rangle$, and doubly excited, $|e, n_{\mathrm{A}}, e, n_{\mathrm{B}}\rangle$, states of the total dimer, and contains coherence terms which are a combination of vibrational and electronic coupling. Figure 2.2.5 depicts a homo- and hetero-dimer constructed from these equations.

The site basis Hamiltonian is diagonalised in a manner equivalent to that of the vibronic monomer, resulting in a delocalised superposition of adiabatic eigenstates in the *exciton* basis. This transformation applies the unitary transformation matrix

$$\mathrm{H}_{\mathrm{D}}^{\mathrm{E}} = (\mathrm{U}_{\mathrm{D}}^{\mathrm{ES}})^{\dagger} \mathrm{H}_{\mathrm{D}}^{\mathrm{S}} \mathrm{U}_{\mathrm{D}}^{\mathrm{ES}}, \tag{2.2.31}$$

where

$$\mathrm{U}_{\mathrm{D}}^{\mathrm{ES}} = \sum_{k} |\psi_{\mathrm{D},k}^{\mathrm{E}}\rangle \langle \psi_{\mathrm{D},k}^{\mathrm{S}}| , \tag{2.2.32}$$

and where $|\psi_{\mathrm{D},k}^{\mathrm{E}}\rangle$ are the eigenstates of the site basis dimer Hamiltonian which can be written in terms of energies, ϵ_k, as

$$\mathrm{H}_{\mathrm{D}}^{\mathrm{S}} = \sum_{k} \epsilon_k |\psi_{\mathrm{D},k}^{\mathrm{E}}\rangle \langle \psi_{\mathrm{D},k}^{\mathrm{E}}| . \tag{2.2.33}$$

This theory is constructed in full generality so that it is suitable for both homo- and hetero-dimers with all possible couplings. Application to homodimers is considered in section 3.2 and a range of homo, and hetero, dimers and monomer-lattices are studied in section 4.4. The composite site basis

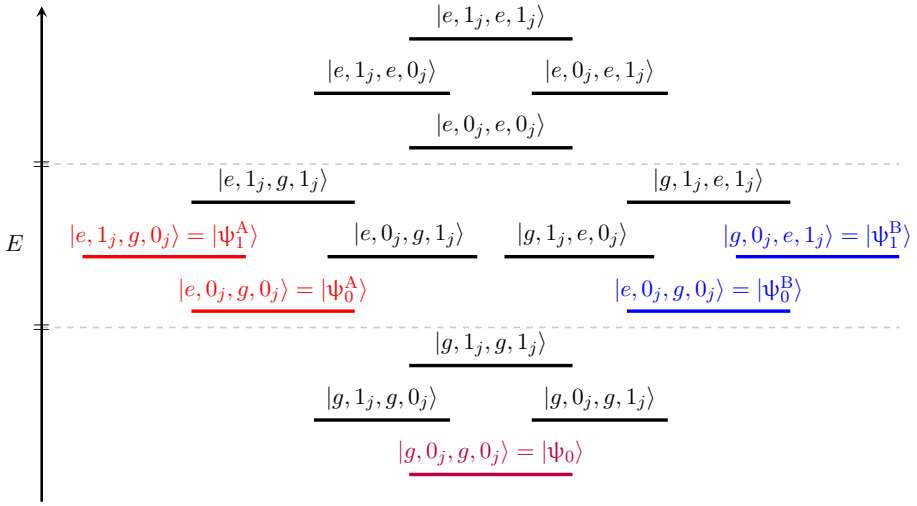

Figure 2.2.6: Energy level diagram of the composite site basis states for the jth mode of a vibronic homodimer. The ground and singly excited states, with zero or one quanta of vibrational energy in the excited state, and with no vibrational excitation in the electronic ground state are highlighted and assigned the aforementioned shorthand.

Hamiltonian is shown in figure 2.2.6 for a homodimer, and the shorthand discussed in the text is applied in order to highlight the doubly ground state, singly excited zero vibration states and singly excited single vibrational states. The already large site basis Hamiltonian for a vibronic monomer

$$\dim\left(\left(2(\nu+1)^N\right)^1 \times \left(2(\nu+1)^N\right)^1\right), \tag{2.2.34}$$

is considerably increased to

$$\dim\left(\left(2(\nu+1)^N\right)^2 \times \left(2(\nu+1)^N\right)^2\right), \tag{2.2.35}$$

where N is the number of vibrational modes and the highest vibrational quantum number of the mode is ν, when applied to a vibronic dimer. This results in a significant increase in computational cost when attempting to diagonalise the Hamiltonian. To counteract this, it is standard to neglect states in which the electronic ground state has an associated quanta of vibrational energy, reducing the composite site basis states to a single doubly ground state, $|\psi_0\rangle$, and vibronic states in which each monomer is vibrationally excited in isolation, $|\psi_\nu^{\mathrm{A/B}}\rangle$, $\nu \in \{0,1\}$, as shown in figure 2.2.6.

Despite the reduction in number of basis states, the full range of electronic and vibrational coupling can still be achieved within the model as would be expected of the full composite basis. Through application of the shorthand in figure 2.2.6, linear, symmetric $(+)$ and antisymmetric $(-)$ combinations of the

site basis wavefunctions result in exciton states[76],

$$|\psi_\nu^{\pm}\rangle = \frac{|\psi_\nu^{\mathrm{A}}\rangle \pm |\psi_\nu^{\mathrm{B}}\rangle}{\sqrt{2}}. \tag{2.2.36}$$

As is explained by Ottiger et al.[76] the influence of the vibrational modes on the electronic coupling leads to a quenching effect proportional to the Frank-Condon factors for the two monomers,

$$J_{\mathrm{Vib}} = J \langle\psi_\nu^{\mathrm{A}}|\psi_0\rangle \langle\psi_\nu^{\mathrm{A}}|\psi_0\rangle . \tag{2.2.37}$$

Subsequently, the limits of the overlap integrals minimise or maximise the electronic coupling leading to strong and weak coupling regimes. When vibrational coupling is minimal, synonymous with $\tilde{d}_j \sim 0$, there is a limited quenching effect and a minimised reduction in J known as the *strong coupling* limit. Alternatively, when vibrational coupling is maximised, synonymous with $\tilde{d}_j > 0$ such that $\hbar\lambda_j > J$, there is a strong quenching effect which reduces the electronic coupling. This regime is known as the *weak coupling* limit. These regimes represent a movement from strongly delocalised exciton states over both monomer units (coherent) to weakly delocalised (incoherent) dominated by nonadiabatic coupling[213].

2.2.1.3.1 Strong Coupling Limit

When the magnitude of vibrational coupling is small, or $\tilde{d}_j \to 0$, the ground and excited state PESs will tend towards perfect alignment, resulting in the Frank-Condon factors for purely electronic transitions being maximised, $\langle\psi_0^{\mathrm{A}}|\psi_0\rangle \to 1$. Contrastingly, because of the large number of nodes centred around the origin within the bound eigenstates of the quantum harmonic oscillator for $\nu > 0$, the overlap integrals relative to the ground state are minimised, $\langle\psi_\nu^{\mathrm{A}}|\psi_0\rangle \to 0$. This coupling regime is characterised by an electronic coupling strength which is greater than the magnitude of vibrational coupling, $\hbar\lambda_j < J$, which allows the predicted Davydov splitting of $2J$ between the exciton states to manifest, as in figure 2.2.3.

An example energy level diagram for a generalised H-aggregate, in the strong coupling limit, is considered in figure 2.2.7. As discussed in section 2.2.1.2, there is a bright symmetric exciton state which is higher in energy than the associated dark state. Additionally, the large positive coupling results in a band structure where exciton states are grouped with their corresponding vibronic levels. Evidence for this grouping has been presented by Ottiger et al.[76], where the forbidden transition into the lower, antisymmetric, exciton was accessed through breaking the inversion symmetry with an isotopic substitution.

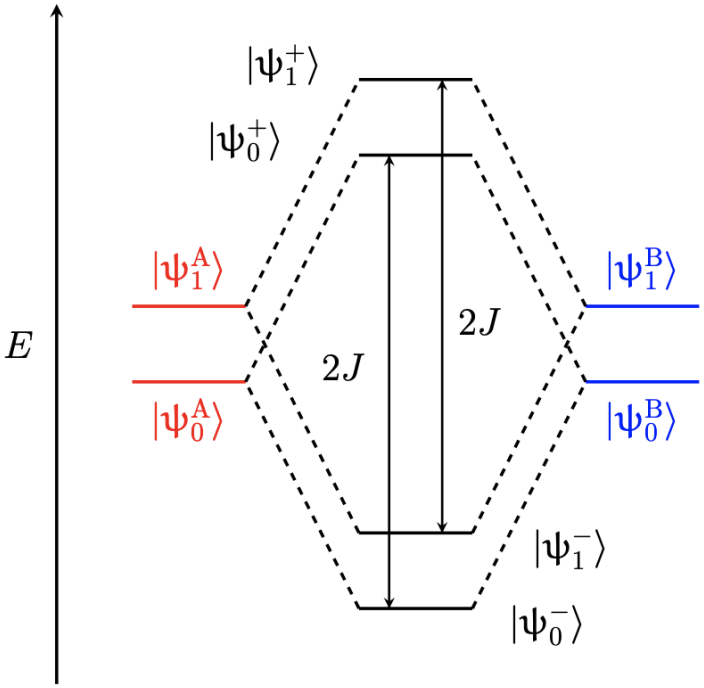

Figure 2.2.7: Formation of exciton states in an H-aggregate in the strong coupling limit.

2.2.1.3.2 Weak Coupling Limit

When the vibrational coupling is larger than zero, away from the strong coupling limit such that $\tilde{d}_j > 0$, the overlap integrals for the quantum harmonic oscillator eigenstates when $\nu > 0$ become non-zero resulting in fractional Frank-Condon factors. The weak coupling limit is characterised by vibrational coupling greater than the electronic coupling strength, $\hbar\lambda_j > J$ and a significant quenching[76,77]. As shown in figure 2.2.8, rather than forming a band structure, because of the reduced electronic coupling, J_{vib}, the splitting of twice the quenched coupling strength produces a vibronic progression of the monomer into pairs of exciton states. Again, this effect is demonstrated by the work of Ottiger et al.[76].

As the structure of excitonic systems depends so heavily on the placement of the vibrational levels within the model systems, and the strength of the electronic and vibrational couplings, it stands to reason that they should be very sensitive to the movement of vibrational levels - as occurs during the movement of the system-bath boundary. For this reason, in sections 3.2 and 4.4 we consider models of homodimers and a range of electronically coupled molecules during the course of moving the system-bath boundary through the canonical transform.

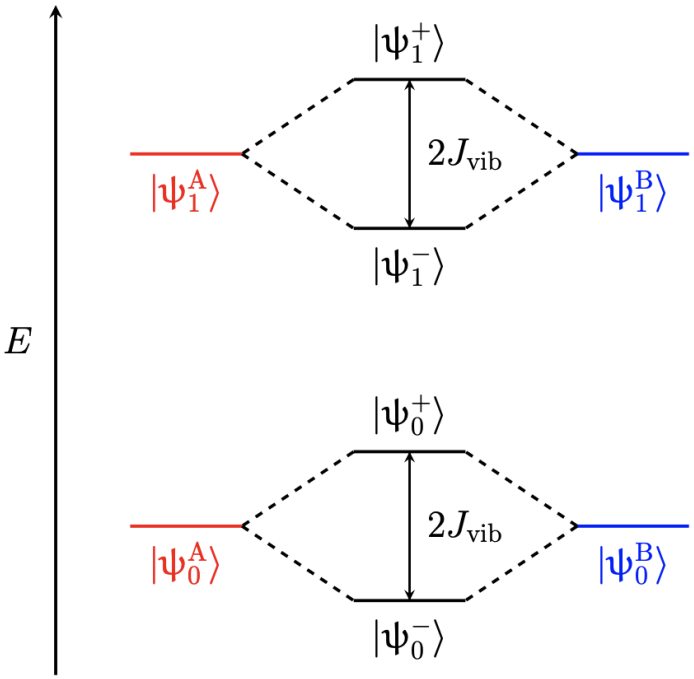

Figure 2.2.8: Formation of exciton states in an H-aggregate in the weak coupling limit. Red and blue basis states have equivalent energy to those in figure 2.2.7, demonstrating the difference in coupling strength.

2.2.2 Bath Interaction Hamiltonian

As discussed in chapter 1, an open system introduces a coupling to a wider environment through the introduction of environment degrees of freedom. However, when the scale of the bath is orders of magnitude larger than the system of interest, such as in systems of interest embedded within a solvent or wider protein structure, the question becomes, how best to model this vast number of degrees of freedom? As discussed in section D.1.8, and D.1.6, Stochastic EOMs are a powerful way of describing Brownian motion subject to a stochastic forcing which is useful in the application of OQS. The bath interaction Hamiltonian is developed by extending the classical Langevin equation, for application in a quantum regime, through the Caldeira-Leggett model. In this description it is assumed that the system-bath interaction is weak which allows the bath to be modelled as an infinite assembly of harmonic oscillators, assuming a continuous spectrum of noise[143,214]. Returning to a form of the total Hamiltonian, equivalent to equation (2.1.10), we note that the Hamiltonian is split into three contributions: the system, the bath, and their interaction,

$$\mathrm{H} = \mathrm{H_S} + \mathrm{H_B} + \mathrm{H_{SB}}. \tag{2.2.38}$$

The system-bath interaction Hamiltonian, following Feynman and Vernon formalism from chapter 1[4], is a bilinear coupling between the system and bath

coordinates,

$$\mathrm{H_{SB}} = -\sum_{n,\nu} g_{n,\nu}\mathrm{x}_{n,\nu}\mathrm{B}_n, \tag{2.2.39}$$

where n denotes the number of independent baths each containing a continuum of harmonic modes, ν, B_n is the system coordinate, $\mathrm{x}_{n,\nu}$ is the bath coordinate, and $g_{n,\nu}$ is the associated bath coupling strength. The corresponding bath Hamiltonian is

$$\mathrm{H_B} = \sum_{n,\nu}\Big(\frac{\mathrm{p}_{n,\nu}^2}{2m_{n,\nu}} + \frac{1}{2}m_{n,\nu}\omega_{n,\nu}^2\mathrm{x}_{n,\nu}^2\Big), \tag{2.2.40}$$

where the mass, momentum, and mode frequency are $m_{n,\nu}$, $\mathrm{p}_{n,\nu}$, and $\omega_{n,\nu}$, respectively. It is common to group the bath interaction Hamiltonian with the bath Hamiltonian[109,112,113,148], as they share dependence in the secondary coordinate of interest, the bath, through

$$\mathrm{H_S}(\mathrm{B}_n) + \mathrm{H_B}(\mathrm{x}_{n,\nu}) + \mathrm{H_{SB}}(\mathrm{B}_n, \mathrm{x}_{n,\nu}) = \mathrm{H_S}(\mathrm{B}_n) + \mathrm{H_I}(\mathrm{B}_n, \mathrm{x}_{n,\nu}), \tag{2.2.41}$$

where

$$\mathrm{H_I} = \sum_{n,\nu}\left(\frac{\mathrm{p}_{n,\nu}^2}{2m_{n,\nu}} + \frac{1}{2}m_{n,\nu}\omega_{n,\nu}^2\Big(\mathrm{x}_{n,\nu} - \frac{g_{n,\nu}\mathrm{B}_n}{m_{n,\nu}\omega_{n,\nu}^2}\Big)^2\right), \tag{2.2.42}$$

$$= \sum_{n,\nu}\left(\frac{\mathrm{p}_{n,\nu}^2}{2m_{n,\nu}} + \frac{1}{2}m_{n,\nu}\omega_{n,\nu}^2\mathrm{x}_{n,\nu}^2 - g_{n,\nu}\mathrm{x}_{n,\nu}\mathrm{B}_n + \frac{g_{n,\nu}^2\mathrm{B}_n^2}{2m_{n,\nu}\omega_{n,\nu}^2}\right). \tag{2.2.43}$$

The combination of the two Hamiltonians in this way introduces a third component, a correction of the system potential, which is equivalent to the reorganisation energy of the vibrational modes included in the system Hamiltonian in section 2.2.1.1. This Hamiltonian correction is denoted $\mathrm{H_{Sc}}$,

$$\mathrm{H_{Sc}} = \sum_{n,\nu}\frac{g_{n,\nu}^2}{2m_{n,\nu}\omega_{n,\nu}^2}\mathrm{B}_n^2 = \sum_{n,\nu}\eta_n\mathrm{B}_n^2, \tag{2.2.44}$$

where η_n is the reorganisation energy of bath n. The distribution of coupling strengths, associated with the bath modes, corresponds to a spectral distribution, known as the *spectral density function* when a continuous function is used to map the continuum profile, for each bath[109,112,113]

$$J_n(\omega) = \pi\sum_{\nu}\frac{g_{n,\nu}^2}{2m_{n,\nu}\omega_{n,\nu}}\delta(\omega - \omega_{n,\nu}), \tag{2.2.45}$$

where δ is the delta function. From this spectral distribution, it is possible to

calculate the total reorganisation energy for each bath, as[215]

$$\eta_n = \frac{1}{\pi}\int_0^\infty \frac{J_n(\omega)}{\omega}\,\mathrm{d}\omega. \tag{2.2.46}$$

2.2.2.1 Bath Coupling Operators

The nature of the system-bath coupling introduced by the vibrational and electronic degrees of freedom are significantly different, and correspond to different physical processes, such that it is logical to separate their interactions into a pair of independent baths, indexed n. When $n = 1$ the bath accounts for electronic coupling and corresponds to electrostatic interactions between the system molecules and fluctuating charges in the surrounding bath structure, for example in protein or solvent structures[91]. This affects the electronic excited states of the system such that the bath coupling operators, in the site basis, for the electronic environment are

$$\mathrm{B}^{\mathrm{S}}_{1,\mathrm{M}} = \sum_n |e,n\rangle\langle e,n|\,, \tag{2.2.47}$$

for a monomer and,

$$\mathrm{B}^{\mathrm{S}}_{1,\mathrm{D}} = \sum_{n_\mathrm{A},n_\mathrm{B}} \Big(|g,n_\mathrm{A},e,n_\mathrm{B}\rangle\langle g,n_\mathrm{A},e,n_\mathrm{B}| + |e,n_\mathrm{A},g,n_\mathrm{B}\rangle\langle e,n_\mathrm{A},g,n_\mathrm{B}| + 2\,|e,n_\mathrm{A},e,n_\mathrm{B}\rangle\langle e,n_\mathrm{A},e,n_\mathrm{B}| \Big), \tag{2.2.48}$$

for a dimer. These couplings contain no off-diagonal elements and subsequently describe the impact of stochastic bath motion on the transition frequencies between electronic states, which leads to T_2^* pure dephasing, as discussed in section 2.1.2.

Vibrational environment coupling, induced by a bath of phonons with an index of 2, describes the impact of a continuum of bath modes on the system vibrational motion. The vibrational perturbation of the system vibrational states in this way, as would be present for a solvent environment or a large protein molecule, leads to both dissipation and dephasing. It is important to note, however, that within this thesis the standard form of IVR, where energy is redistributed amongst system degrees of freedom, is more specific and is termed *vibrational relaxation* to distinguish it from the specific case of loss to the bath. Consequently, the most general case, where the phonon bath mediates energy loss into the bath degrees of freedom is IVR. The phonon environment does acquiesce vibrational relaxation, but the degrees of freedom to which the energy is lost are deemed to be specifically part of the bath, not the system degrees of freedom.

The coupling operators for the vibrational bath, in the site basis, are

$$\mathrm{B}^{\mathrm{S}}_{2,\mathrm{M}} = \mathrm{I}_{\mathrm{el}} \otimes \sum_j \tilde{\mathrm{q}}_j = \mathrm{I}_{\mathrm{el}} \otimes \sum_j \left(\frac{\mathrm{b}_j + \mathrm{b}_j^\dagger}{\sqrt{2}} \right), \tag{2.2.49}$$

for a monomer, where the identity operator over the electronic degrees of freedom is $\mathrm{I}_{\mathrm{el}} = \sum_\alpha |\alpha\rangle\langle\alpha| \,,\ \alpha \in \{g, e\}$, and

$$\mathrm{B}^{\mathrm{S}}_{2,\mathrm{D}} = \mathrm{B}^{\mathrm{S}}_{2,\mathrm{MA}} \otimes \mathrm{I}_{\mathrm{MB}} + \mathrm{I}_{\mathrm{MA}} \otimes \mathrm{B}^{\mathrm{S}}_{2,\mathrm{MB}}, \tag{2.2.50}$$

for a dimer[91,112,113]. This introduces a bilinear coupling between the system vibrational modes, $\tilde{\mathrm{q}}_j$, and the bath vibrational modes, $\mathrm{x}_{2,\nu}$, as in equation (2.2.39) and physically corresponds to longitudinal and transverse, T_1 and T_2 respectively, vibrational relaxation[138,216]. It is possible to add additional T_2^* pure dephasing as a consequence of the phononic bath modes, but it would require the inclusion of a square-linear coupling $\propto g_{2,\nu}\mathrm{x}_{2,\nu}\tilde{\mathrm{q}}_j^2$ which is neglected in most models. As we do not need any additional pure dephasing to be added to our model, we neglect the square-linear coupling in equation (2.2.49).

As in section 2.2.1.1, the bath coupling operators for the phonon environment are transformed into their respective vibronic/exciton bases through unitary transformations,

$$\mathrm{B}^{\mathrm{V}}_{2,\mathrm{M}} = (\mathrm{U}^{\mathrm{VS}}_{\mathrm{M}})^\dagger \mathrm{B}^{\mathrm{S}}_{2,\mathrm{M}} \mathrm{U}^{\mathrm{VS}}_{\mathrm{M}}, \tag{2.2.51}$$

$$\mathrm{B}^{\mathrm{E}}_{2,\mathrm{D}} = (\mathrm{U}^{\mathrm{ES}}_{\mathrm{D}})^\dagger \mathrm{B}^{\mathrm{S}}_{2,\mathrm{D}} \mathrm{U}^{\mathrm{ES}}_{\mathrm{D}}, \tag{2.2.52}$$

where the bath coupling operators for the electronic environment, B_1, are positive diagonal operators and do not change under this transformation.

Further avenues of relaxation, such as relaxation of electronic levels, can be incorporated through additional bath coupling operators. This example, which corresponds to fluorescence and phosphorescence due to spontaneous photon emission would require its own index, 3, and coupling operators[193]. However, as the timescale of such luminescence is at least an order of magnitude slower than dephasing and vibrational relaxation processes ($\sim$ ns versus $\sim$ fs), which are of particular significance to the work in this thesis, it is omitted.

2.2.2.2 Spectral Density

A spectral distribution, which contains the coupling strength and frequency associated with each bath mode in the environment ensemble, is the discrete form of the continuum of harmonic modes. This is approximated as a continuous, analytical, function by tracing the maxima of each delta function within equation (2.2.45). There is not one general form for the spectral density

function, as bath behaviour varies dramatically with a number of parameters such as temperature and viscosity/friction. However, it is possible for this function to be measured experimentally[114,217], and for a range of analytical forms to be constructed, which match the physical observables, based upon a phenomenological damping parameter, γ, which controls the friction of the bath.

The profile of the harmonic modes control the time-dependence of the system-bath interaction through the correlation function[37,138,149,153],

$$L_n^{(\alpha)}(t) = \frac{\hbar}{\pi}\int_0^\infty J_n(\omega)\left(\coth\Big(\frac{\beta\hbar\omega}{2}\Big)\cos\omega t - i\sin\omega t\right)\mathrm{d}\omega. \tag{2.2.53}$$

The correlation function of system-bath interaction, which is fundamental to the fluctuation-dissipation theorem, models the rate of decay of bath correlations subject to dissipation and thermal fluctuation[218,219]. The timescale for this decay, τ_c, is equivalent to the time taken for the bath to return to equilibrium after being perturbed. As discussed in section 2.1.5 the Markovian limit is synonymous with disparate correlation times between the system and bath, particularly when the bath correlation time is very short, and the non-Markovian limit is when the correlation times are of the same order and allow the formation of memory effects. When the number of bath modes is low and the spectral density is effectively discretised, the regular oscillation of the bath acts to restore the coherence of the reduced system which is associated with the time, τ_R. When the spectral density is smooth and continuous, due to an infinite limit of modes within the ensemble, the recurrence time increases until it is significantly larger than the system relaxation timescale. In such a limit, the restoration timescale can be safely neglected unless the spectral density features non-standard coupling between specific modes, such as for highly structured spectral densities, resulting in the persistence of periodic motion[148].

Highly structured spectral densities are often found in non-standard experimental parameter regimes such as systems at high temperatures or strongly coupled to external fields[220–222], but typically, at room temperature the spectral density for biological and chemical systems is Ohmic:

$$J_n(\omega) = \eta_n\omega\exp\Big(-\frac{\omega}{\omega_c}\Big), \tag{2.2.54}$$

dependent on the coupling strength, η_n, and the cutoff frequency, ω_c[91,148,223]. This can be written more generally as,

$$J_n(\omega) = \eta_n\frac{\omega^s}{\omega_c^{s-1}}\exp\Big(-\frac{\omega}{\omega_c}\Big), \tag{2.2.55}$$

where s is a unitless parameter $\in \mathbb{R}^+$ which shifts the focus of the bosonic mode

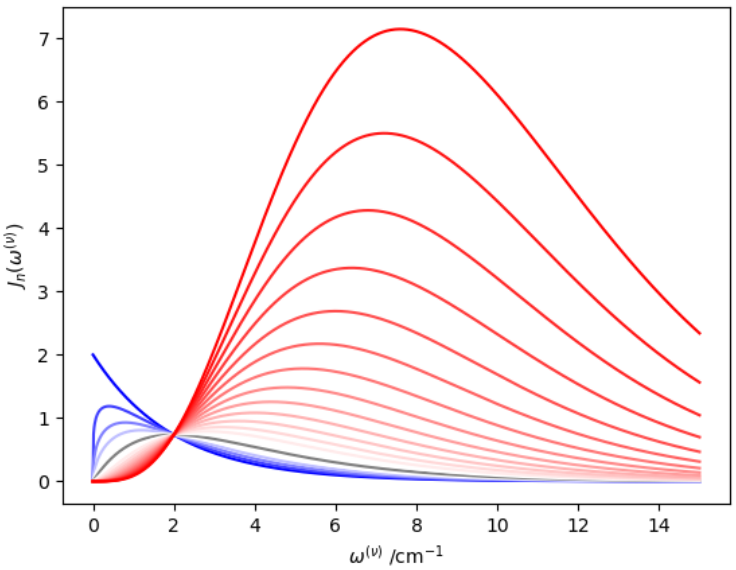

Figure 2.2.9: Spectral densities for a range of s values, while η_n is set to unity, ranging from sub-Ohmic in blue to Ohmic in gray, and super-Ohmic in red. In this depiction, $\eta_n = 1\ \mathrm{cm}^{-1}$, $\omega_c = 2\ \mathrm{cm}^{-1}$, and s is between 0 and 4, increasing in increments of 0.2. The mutual point of intersection for all the spectral densities is at ω_c.

coupling. When $s = 1$ this is the Ohmic spectral density, which is linear for low frequencies and decays exponentially for high frequencies. When $s < 1$ or $s > 1$ this is termed sub- or super-Ohmic respectively, and they focus heavily on either low or high frequencies relative to ω_c. A range of spectral densities for different values of s are depicted in figure 2.2.9. Sub-Ohmic spectral densities are applied in solid-state dynamics and super-Ohmic spectral densities find application in supersensitive quantum sensors[112,185,215,224–226]. Ohmic spectral densities are so commonplace because, while they are predominantly Markovian, for large couplings, non-constant correlation decay rate and associated non-Markovian behaviour become evident[138,227].

A spectral function which is linear for low frequencies and decays rapidly for higher frequencies is not restricted to this form of analytical expression. It is possible to further generalise the Ohmic form of the spectral density to

$$J_n(\omega) = \eta_n \omega j_c(\omega), \tag{2.2.56}$$

where

$$\lim_{\omega \to 0} j_c(\omega) = 1, \tag{2.2.57}$$

$$\lim_{\omega \to \infty} j_c(\omega) = 0, \tag{2.2.58}$$

because open quantum system dynamics tend to be characterised by low frequency environment mode interactions. The Lorentz-Drude form of the Ohmic spectral density, which is also particularly commonly used, satisfies these criteria and takes the form

$$J_n(\omega) = 2\eta_n \frac{\omega\Lambda_n}{\omega^2 + \Lambda_n^2}. \tag{2.2.59}$$

This form of the spectral density focuses coupling strength at lower frequency modes, with a peak at $\omega = \Lambda_n$, where $\Lambda_n^{-1} = \tau_c^{(n)}$ [113,219,228]. The system bath coupling strength is temperature dependent and takes the form[37],

$$\eta_n = \frac{\hbar\Delta_n^2}{2k_{\mathrm{B}}T}, \tag{2.2.60}$$

where k_{B} is the Boltzmann constant, and T is the temperature, but is constant across all n within this thesis. This is because all baths are part of a total system at a given temperature[c]. As discussed in section 2.2.2.1, electrostatic interactions between the system and environment result in perturbation of the electronic excited state PES, termed dephasing. This manifests as a fluctuation of the transition frequency by Δ_n, around its equilibrium value, over time,

$$\omega_{eg}(t) = \omega_{eg} + \delta\omega(t), \tag{2.2.61}$$

shown in figure 2.2.10.

The autocorrelation function of the perturbed transition frequency, which is equivalent to the correlation function for system-bath interaction, can be calculated through

$$L_n^{(\alpha)}(t) = \langle \delta\omega_n(t)\delta\omega_n(0)\rangle = \Delta_n^2 \exp\Big(-\frac{t}{\tau_c^{(n)}}\Big), \tag{2.2.62}$$

assuming Gaussian-Markov statistics, involving a normal distribution of frequencies and a short correlation time[37,138,147]. Additional discussion of this form of the correlation function is found in section 2.2.2.2.1. These approximations result in the formation of an *overdamped* bath where the relative sizes of Δ_n and $\tau_c^{(n)}$ produce the *homogeneous* and *inhomogeneous* limits, which represent the thermally averaged and static limits of the environment. When the correlation time of the environment is very short with respect to the system timescale then the system-bath interaction will be constant leading to homogeneous broadening on 2DES proportional to T_2^*. In contrast, when the environment timescale is a similar order of magnitude to that of the system, then individual sub-environments, or localised inhomogeneities, will appear and the 2DES will broaden into a normal distribution corresponding to delta

[c] It is possible to construct models with individual baths at differing temperatures, but these would constitute separate closed sections of the system with respect to each other.

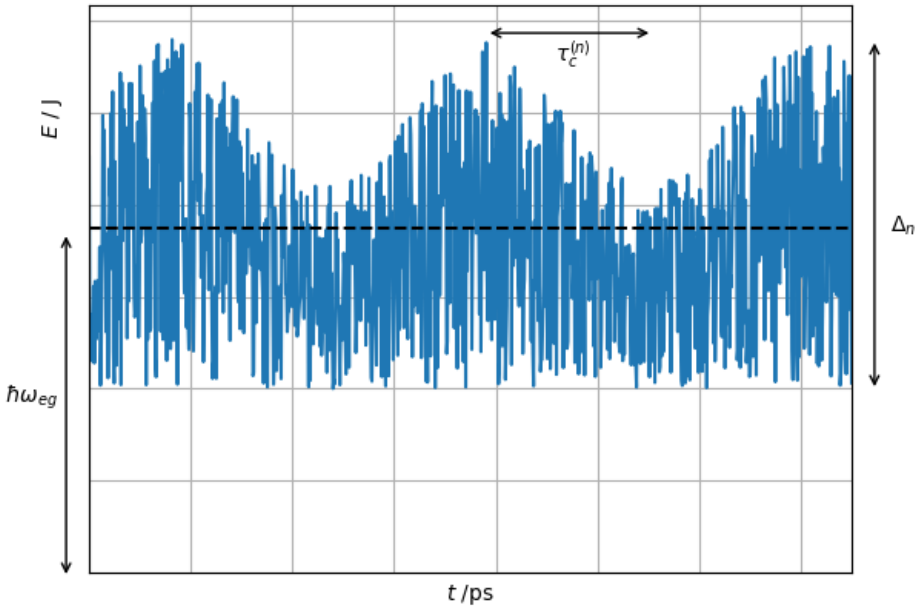

Figure 2.2.10: Modulation of the fundamental transition frequency of the system, ω_{eg}, as a result of coupling to the bath. The amplitude of the fluctuations is measured by Δ_n for the nth bath, with the associated correlation time $\tau_c^{(n)} = \Lambda_n^{-1}$.

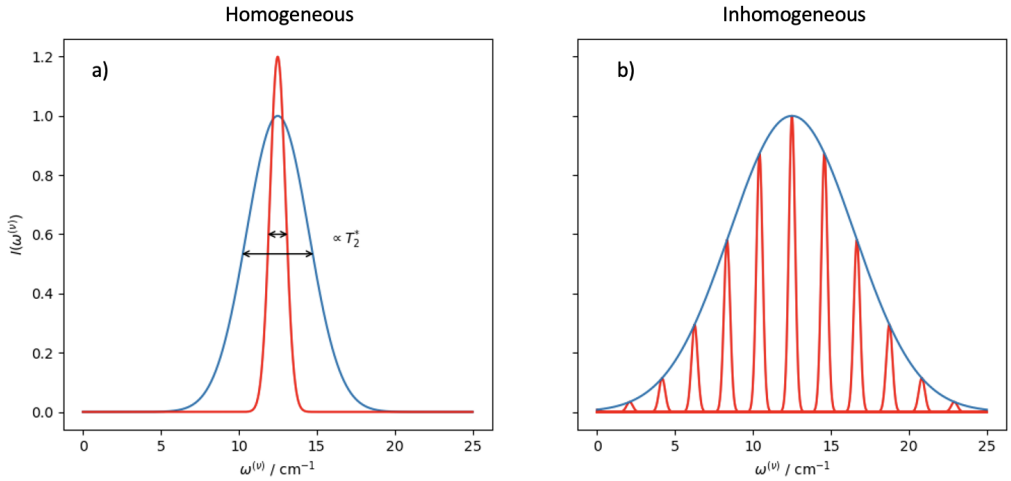

Figure 2.2.11: A depiction of homogeneous and inhomogeneous broadening of an arbitrary peak within a linear spectrum, dependent on the dephasing T_2^* and the range of transition frequencies of the ensemble, respectively.

functions at each transition frequency present in the ensemble[229]. These concepts are depicted in figures 2.2.10 and 2.2.11 and discussed at length in the context of the results in chapter 3.1. Application of an overdamped spectral density to a system is typically used to introduce an inhomogeneity in the system-bath interactions across the total system[138,157,230].

Alternatively, the spectral density can be highly structured and contain explicit dependence on certain bath modes, which are particularly strongly coupled, and which are weakly damped. This kind of spectral density is referred to as *underdamped*, in reference to the weakly damped modes, and are modelled by underdamped Brownian oscillators of the form[37,153],

$$J_n(\omega) = \frac{2\eta_n\gamma_n\omega_{0n}^2\omega}{(\omega_{0n}^2-\omega^2)^2+(\gamma_n\omega)^2}. \tag{2.2.63}$$

This involves a change of variables, termed a *canonical transformation*, which subsumes a minor oscillatory mode in coordinates independent of the environment into the environment degrees of freedom. In this instance the mode is a strongly coupled system mode, ω_0, which is itself coupled to a Lorentz-Drude bath, and is subsumed into the spectral density[138,164,219]. The relevance of such a transformation is that it preserves the form of Hamilton's equations, and by extension the Euler-Lagrange equation, during the change of coordinates. The Euler-Lagrange equations are fundamental to variational calculus and EOMs for systems where the aim is to minimise or maximise a functional, such as in open quantum systems. This type of invariance is also discussed in section D.1 and 2.5.4.1.2. The canonical transform, which is the fundamental mediator of system-bath boundary movement, is explored in depth in the analysis of spectral lineshape, 3.1, the detailed analysis of quantum information 3.2, 3.3, and quantum correlations 4.3 during the course of boundary movement.

An underdamped spectral density has a sharp peak at the subsumed mode frequency, ω_0, which has a small magnitude of broadening due to the damping parameter, γ. An example underdamped spectral density, and its associated correlation function, are shown in figure 2.2.12 b) and a). In the limit of zero damping the full-width-at-half-maximum (FWHM) parameter, $2\sqrt{2\ln 2}\cdot\sigma_\omega$, tends to zero and b) becomes a delta function for an entirely *undamped* oscillator. In this limit, the decay of the correlation function also vanishes, leaving a pure oscillation in a).

The formal definition of underdamped bath motion is that the bath friction be much smaller than the subsumed mode frequency, $\gamma \ll \omega_0$, producing prominent oscillations in the correlation function. On increasing the damping parameter there is a hybrid regime in which the spectral density behaves as neither limiting

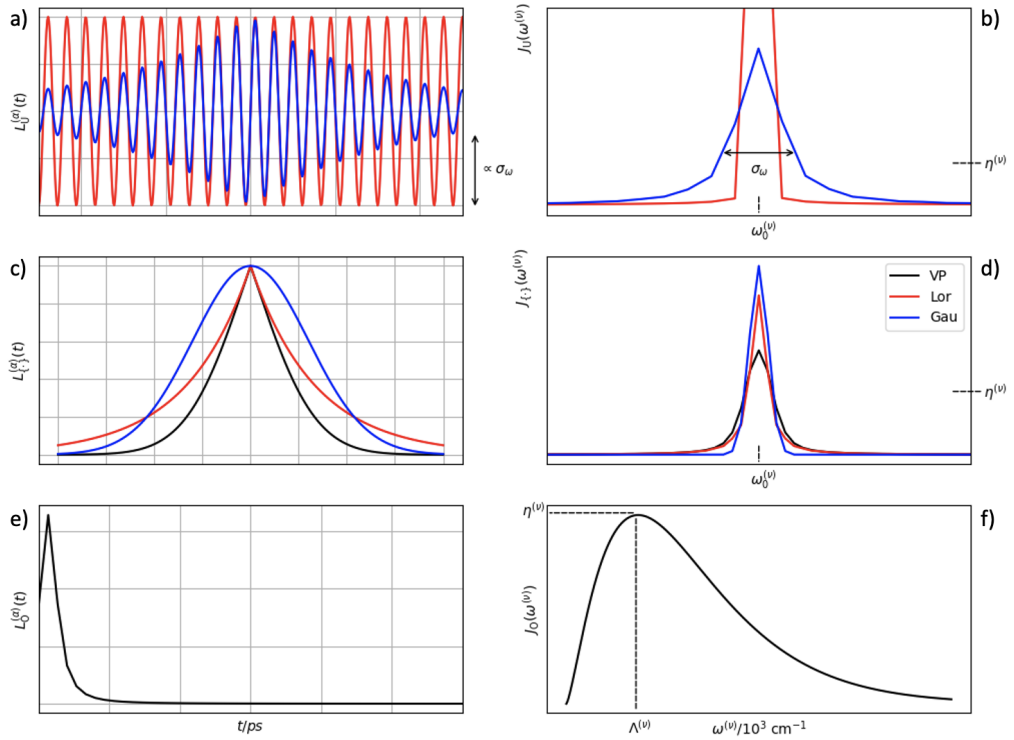

Figure 2.2.12: a) correlation function $L_{\mathrm{U}}^{(\alpha)}(t)$ and the corresponding spectral density b) Underdamped spectral density, $J_{\mathrm{U}}(\omega)$. c) Voigt profile correlation function, $L_{\mathrm{VP}}^{\alpha}(t)$, and the associated d) intermediate damping spectral density, $\gamma \sim \omega_0$, termed $J_{\mathrm{VP}}(\omega)$. e) Overdamped correlation function, $L_{\mathrm{O}}^{(\alpha)}(t)$, and the associated spectral density, f) overdamped spectral density, $J_{\mathrm{O}}(\omega)$. Within d) VP denotes Voigt Profile, Lor Lorentzian, and Gau Gaussian.

case, but rather as a convolution of the two, $\gamma \sim \omega_0$. The spectral density, therefore, becomes the convolution of a Gaussian and Lorentzian which is known as a *Voigt profile* and the correlation function both decays and oscillates. This non-limiting regime is depicted in figure 2.2.12 c) and d), and discussed again in section F. When the damping is significantly larger, so that it is in the overdamped limit, then $\gamma \gg \omega_0$ and the oscillating component of the correlation function vanishes returning the system to Lorentz-Drude form where,

$$\Lambda_n = \frac{\omega_{n0}^2}{\gamma_n} = (\tau_c^{(n)})^{-1}, \tag{2.2.64}$$

for the nth bath and where ω_{n0} is the subsumed mode for this bath. The overdamped limit is shown in figure 2.2.12 e) and f) and presents the decay from equation (2.2.62).

The power of the canonical transform, and the reason it is so useful in an OQS setting, is that it offers a way of simplifying the Hamiltonian complexity without introducing further approximations or assumptions[d]. Subsuming a fundamental

[d] Strictly, dimer systems may need to have a corrected energy to account for vibronic quenching. However, this is neither an approximation or assumption, but a choice which is corrected for.

vibration reduces the system degrees of freedom as underdamped modes maintain a description of the damped vibrational motion without the need to include the vibrational degrees of freedom explicitly in the Hamiltonian. However, in a computational setting where the total underdamped spectral density, J_{tot}, is split into a pair of components, J_{O} (equivalent to equation (2.2.59)) to control the system-bath inhomogeneity and bath mediated dephasing, and J_{U} (equivalent to equation (2.2.63)) to introduce the strongly coupled mode, additional damping is unavoidable. This is as a consequence of the phenomenological damping parameter, which is strictly non-zero to ensure convergence of standard hierarchies, for two baths being intrinsically larger than that of a single bath. It is currently unclear whether the mathematical equivalence of the underlying theory extends to computational models under the influence of many other approximations and assumptions, especially in the presence of a canonical source of damping[2,231]. In section 3.2 we perform a detailed study of the system-bath boundary movement and qualitatively ascertain the level of equivalence. Subsequently, we study highly sensitive quantum behaviours, of coherence and memory effects, under the influence of a movable system bath boundary in sections 3.2, 3.3 and 4.3. Finally, we quantify the mathematical equivalence through a study of the canonical damping in the zero limiting case, in chapter 5.

2.2.2.2.1 Cumulant Expansion

Typically, the system-bath interaction correlation function, (2.2.53), is generated through the cumulant expansion technique. This is an expansion, similar to a perturbative expansion, which applies to statistical descriptions of random variables, making it particularly useful when dealing with an equilibrium value perturbed by thermal fluctuation[37,232,233]. Physically, this corresponds to a mapping of the system of interest onto a collection of oscillatory modes, modelled as harmonic oscillators[37]. For a statistical variable, x_{st}, the average of its exponential can be written as an expansion in terms of moments, i.e. physical observables multiplied by a distance raised to a power,

$$\langle \exp(ikx_{\mathrm{st}}) \rangle = \sum_{j}^{\infty} \frac{(ik)^j}{j!} \langle x_{\mathrm{st}}^j \rangle \,. \tag{2.2.65}$$

Which is equivalent to an expression in terms of cumulants,

$$\langle \exp(ikx_{\mathrm{st}}) \rangle = \exp\left(\sum_{j}^{\infty} \frac{(ik)^j}{j!} c_j(x_{\mathrm{st}}) \right), \tag{2.2.66}$$

where $c_j(x_{\mathrm{st}})$ is the jth cumulant function. Cumulants are equivalent to moments such that the first three cumulants represent the mean, variance, and skewness

of the random variable:

$$c_1(x_{\mathrm{st}}) = \langle x_{\mathrm{st}} \rangle \,, \tag{2.2.67}$$

$$c_2(x_{\mathrm{st}}) = \langle x_{\mathrm{st}}^2 \rangle - \langle x_{\mathrm{st}} \rangle^2 \,, \tag{2.2.68}$$

$$c_3(x_{\mathrm{st}}) = \langle x_{\mathrm{st}}^3 \rangle - 3 \langle x_{\mathrm{st}} \rangle \langle x_{\mathrm{st}}^2 \rangle + 2 \langle x_{\mathrm{st}} \rangle^3 \,. \tag{2.2.69}$$

The reason behind using this approach is that, for random variables which obey Gaussian statistics (a normal distribution), all cumulants with an index $n > 2$ vanish, and this technique converges particularly rapidly. This makes this technique especially useful for open systems with an exponential function basis in which convergence is paramount.

In particular, for the time-ordered correlation function, which is an average over a fluctuating trajectory,

$$L_n^{(\alpha)}(t) = \left\langle \exp_{\leftarrow} \left(-i \int_0^t \delta\omega_n(t') \, \mathrm{d}t' \right) \right\rangle , \tag{2.2.70}$$

$$\approx \exp(c_{1,n}(t) + c_{2,n}(t)), \tag{2.2.71}$$

with

$$c_{1,n}(t) = -i \int_0^t \langle \omega_n(t') \rangle \, \mathrm{d}t', \tag{2.2.72}$$

$$c_{2,n}(t) = -\int_0^t \int_0^\tau \langle \delta\omega_n(\tau) \delta\omega_n(\tau') \rangle \, \mathrm{d}\tau' \, \mathrm{d}\tau. \tag{2.2.73}$$

This allows the correlation function to be expressed in terms of both the spectral density function, and the kernels of fluctuation and dissipation.

2.2.3 Field Interaction Hamiltonian

2.2.3.1 Optical Spectroscopy

Introduction of a laser field into the OQS is achieved via a semi-classical approximation. The external electromagnetic field is described by a time dependent system-field interaction Hamiltonian [37,40],

$$\mathrm{H}_{\mathrm{SF}}(t) = -\boldsymbol{\mu} \cdot \boldsymbol{\mathcal{E}}_{\mathrm{I}}(\mathbf{r}, t), \tag{2.2.74}$$

which produces a coupling between the incident electric field and the transition dipole moment operator, $\boldsymbol{\mu}$, of the system. The electric field for m pulses is

dependent on space, $\mathbf{r}$, and time, t, through

$$\boldsymbol{\mathcal{E}}_{\mathrm{I}}(\mathbf{r},t) = \sum_m \hat{\mathbf{e}}_m \chi_m E'(t-\tau_m)\Big(\exp(-i\omega_m t + i\mathbf{k}_m\cdot\mathbf{r}) + \exp(i\omega_m t - i\mathbf{k}_m\cdot\mathbf{r})\Big), \tag{2.2.75}$$

with circular frequency, $\omega_m = 2\pi\nu_m$, wavevector, $\mathbf{k}_m$, of magnitude $|\mathbf{k}_m| = \frac{\omega}{c}$, and field strength χ_m, in V m^{-1} [234–236]. The unit vector, $\hat{\mathbf{e}}_m$, defines the polarisation of each pulse [237–239]. The field envelope, $E'(t-\tau_m)$, is assumed to be Gaussian and centred at τ_m,

$$E'(t-\tau_m) = \exp\Big(-\frac{(t-\tau_m)^2}{2\varsigma^2}\Big), \tag{2.2.76}$$

with a full-width-at-half-maximum (FWHM) $\tau_{1/2} = 2\sqrt{2\ln 2}\cdot\varsigma$ in the time domain, which is equivalent to $\tau_{1/2}^{(\nu)} = \frac{4\ln 2}{\pi c \tau_{1/2}}$ in the frequency domain. When the length of the temporal pulse is shorter, the spectrum of frequencies becomes broader. Therefore, in the limit of instantaneous pulses, known as the impulsive limit, the field envelope is a delta function and the laser spectrum is flat, and white, incorporating all frequencies [240,241].

2.2.3.2 Quantum Correlations

In section 4.1, a study of the fundamentals of optical correlation within a molecular environment [3], a simplified form of the field interaction Hamiltonian was chosen in order to restrict excitation to fundamental transitions only. This was achieved by driving with a continuous laser field at a single frequency, i.e. in the limit of infinitesimal laser breadth, denoted (CW),

$$\boldsymbol{\mathcal{E}}_{\mathrm{I}}^{(\mathrm{CW})} = \hat{\mathbf{e}}\Big(\chi E_0' \exp(-i\omega_{eg}t + i\mathbf{k}\cdot\mathbf{r}) + \chi E_0' \exp(i\omega_{eg}t - i\mathbf{k}\cdot\mathbf{r})\Big), \tag{2.2.77}$$

which is resonant with the fundamental electronic transition of the system, ω_{eg}, and where the envelope function, $E'(t-\tau) = E_0'$, is a constant.

2.2.3.3 Dipole Moment Operator

Transitions between electronic states of the system occur due to interaction between the transition dipole moment [242] and the electric field orientation vector. The transition electric dipole moment, which depends on the initial and final separation of the eigenstates, $\hat{\mathbf{d}}_{\mathrm{fi}}$, i and f denote initial and final, and the magnitude, μ, is

$$\boldsymbol{\mu}_{\mathrm{fi}} = \mu_{\mathrm{fi}}\hat{\mathbf{d}}_{\mathrm{fi}}. \tag{2.2.78}$$

The operator form of the dipole moment, μ, is a combination of the vector dipole moment, $\boldsymbol{\mu}_{\mathrm{fi}}$, and a matrix component of the Hilbert space of the system,

which is determined by the selection rules. This operator contains both diagonal and off-diagonal elements which correspond to descriptions of permanent dipoles associated with the system states, caused by an uneven distribution of electron density, and associated transition dipole moments, respectively. In this work we enforce the dipole approximation, which assumes that each dipole is of infinitesimal width: a point dipole, valid when the wavelength of the electromagnetic radiation is larger than the size of the quantum system, such that it is perceived as spatially uniform, subject to an oscillating field[37,243]. The models within this thesis only consider the impact of transition dipoles, there are no permanent dipoles introduced. Considering only electronic states, a monomer with an allowed transition between the ground and excited states has the dipole moment operator,

$$\mu^{\mathrm{S}}_{\mathrm{el,M}} = \boldsymbol{\mu}_{eg}\Big(|g\rangle\langle e| + |e\rangle\langle g| \Big). \tag{2.2.79}$$

For a vibronic monomer, which also contains vibrational levels, this must be expanded using the completeness relation for the vibrational degrees of freedom, $\mathrm{I}_{\mathrm{vib}} = \sum_n |n\rangle\langle n|$, such that, in the site basis[68],

$$\mu^{\mathrm{S}}_{\mathrm{M}} = \boldsymbol{\mu}_{eg}\left(|g\rangle\langle e| \otimes \sum_n |n\rangle\langle n| + |e\rangle\langle g| \otimes \sum_n |n\rangle\langle n| \right), \tag{2.2.80}$$

$$= \boldsymbol{\mu}_{eg} \sum_n \Big(|g,n\rangle\langle e,n| + |e,n\rangle\langle g,n| \Big). \tag{2.2.81}$$

Equivalent vibrational levels of the electronic states are connected through non-zero off-diagonal elements which describe purely electronic transitions.

This operator is transformed into the vibronic basis in a fashion identical to that proposed in section 2.2.1.1, via

$$\mu^{\mathrm{V}}_{\mathrm{M}} = (\mathrm{U}^{\mathrm{VS}}_{\mathrm{M}})^{\dagger} \mu^{\mathrm{S}}_{\mathrm{M}} \mathrm{U}^{\mathrm{VS}}_{\mathrm{M}}. \tag{2.2.82}$$

The vibronic transition dipole moment operator contains an increased number of non-zero off-diagonal elements, the number of which is further increased by larger displacement of the excited state potential energy surface which leads to non-zero wavefunction overlap for a greater range of transitions, including vibronic overtones and hot bands. The dipole moment operator for a vibronic dimer is created by extending the Hilbert space to include two monomer units as,

$$\mu^{\mathrm{S}}_{\mathrm{D}} = \mu^{\mathrm{S}}_{\mathrm{MA}} \otimes \mathrm{I}_{\mathrm{MB}} + \mathrm{I}_{\mathrm{MA}} \otimes \mu^{\mathrm{S}}_{\mathrm{MB}}, \tag{2.2.83}$$

and can subsequently be transformed into the exciton basis via,

$$\mu^{\mathrm{E}}_{\mathrm{D}} = (\mathrm{U}^{\mathrm{ES}}_{\mathrm{D}})^{\dagger} \mu^{\mathrm{S}}_{\mathrm{D}} \mathrm{U}^{\mathrm{ES}}_{\mathrm{D}}. \tag{2.2.84}$$

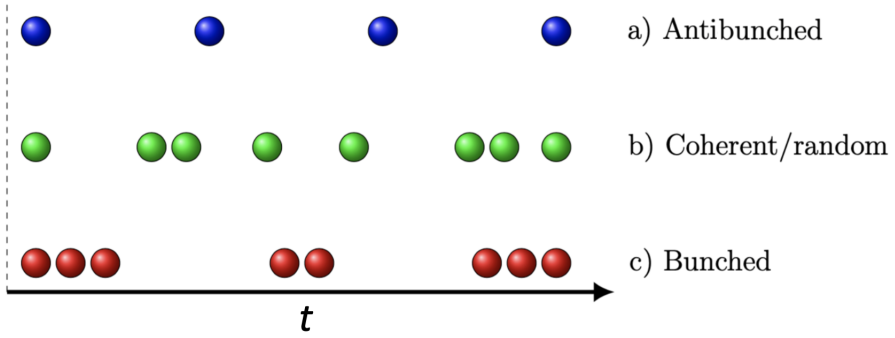

Figure 2.3.1: Schematic depicting, a) A beam of antibunched bosons, b) A coherent/random boson beam, c) A bunched boson beam.

The electronic coupling is determined by a combination of the displacement and relative orientation of the two monomer dipole moments, as discussed in section 2.2.1.2, and can be exploited by application of polarised pulses in order to isolate specific vibronic signatures[244–246]. However, the formation of aggregates discussed in section 4.4 is restricted to a collinear arrangement of monomer dipole moments.

2.3 Two-time Bosonic Correlation Functions

It is possible to construct a measure of the level of mutual similarity between system observables, based on physical system and field parameters, known as correlation. Functions of the correlation for beams of bosons, in analogy with expansions, pertain to physical properties based on their order. First order correlation functions correspond to measurement of bosonic field amplitude, and second order correspond to field intensity. Correlation is of interest in OQSs because it allows quantum effects to be probed dynamically[247,248]. The classical behaviour of boson *bunching* is defined as the detection probability being more closely bunched in time than that of a coherent/random beam. This occurs when thermal effects are dominant, and detection events constructively interfere resulting in an amplified variance and super-Poissonian statistics [249,250]. The quantum behaviour of boson *antibunching* is the contrasting definition where the detection probability is more separated than in a coherent/random beam in time. This behaviour is an expression of sub-Poissonian statistics, and by definition, this process is quantum because sub-Poissonian statistics invalidate the Cauchy-Schwarz inequality - which is possible only for non-classical probability distributions[249,250]. An idealised schematic of this is shown in figure 2.3.1 where the detection probability for a beam of arbitrary particles is presented [10,251].

In this thesis we consider correlating two photon emission events, or pairs of

emission events, at two times. Upon interaction with an incident field of the form, $\boldsymbol{\mathcal{E}}_{\mathrm{I}}$ (2.2.77), the system will scatter the radiation resulting in $\boldsymbol{\mathcal{E}}_{\mathrm{sc}}$ which has left and right moving components[22,252],

$$\boldsymbol{\mathcal{E}}^{\pm} = \frac{a^{\dagger}(t)\exp(\pm i\mathbf{k}\cdot\mathbf{r})}{\epsilon_0}\hat{\mathbf{e}}. \tag{2.3.1}$$

Transition probabilities, such as a ground to excited state transition, can then be described in terms of the field through a braket,

$$P = |\langle g|\boldsymbol{\mathcal{E}}^{+}|e\rangle|^2. \tag{2.3.2}$$

For mixed states, this probability is written in terms of the ensemble via the density matrix,

$$P = \mathrm{Tr}\left[\rho\boldsymbol{\mathcal{E}}^{-}(\mathbf{r},t)\boldsymbol{\mathcal{E}}^{+}(\mathbf{r},t)\right]. \tag{2.3.3}$$

In direct analogy, a similar statistical correlation of operators at different times and positional coordinates can be created in order to obtain the correlations between pairs of amplitudes, or intensities.

$$G^{(1)}(t,\tau) = \langle\boldsymbol{\mathcal{E}}^{-}(t)\boldsymbol{\mathcal{E}}^{+}(t+\tau)\rangle, \tag{2.3.4}$$

$$= I_0\langle \mathrm{c}(t)\mathrm{c}^{\dagger}(t+\tau)\rangle, \tag{2.3.5}$$

$$G^{(2)}(t,\tau) = \langle\boldsymbol{\mathcal{E}}^{-}(t)\boldsymbol{\mathcal{E}}^{-}(t+\tau)\boldsymbol{\mathcal{E}}^{+}(t+\tau)\boldsymbol{\mathcal{E}}^{+}(t)\rangle, \tag{2.3.6}$$

$$= I_0^2\langle \mathrm{c}_1(t)\mathrm{c}_2(t+\tau)\mathrm{c}_2^{\dagger}(t+\tau)\mathrm{c}_1^{\dagger}(t)\rangle, \tag{2.3.7}$$

where I_0 and I_0^2 are the amplitude and intensity of the radiation respectively, and $\mathrm{c}^{(\dagger)}$, $\mathrm{c}_1^{(\dagger)}$, and $\mathrm{c}_2^{(\dagger)}$ are the annihilation(creation) operators for arbitrary bosons. These forms of the correlation are normalised in order to generate conditional probabilities,

$$g^{(1)}(t,\tau) = \frac{\langle \mathrm{c}(t)\mathrm{c}^{\dagger}(t+\tau)\rangle}{\langle \mathrm{c}(t)\mathrm{c}^{\dagger}(t)\rangle}, \tag{2.3.8}$$

$$g^{(2)}(t,\tau) = \frac{\langle \mathrm{c}_1(t)\mathrm{c}_2(t+\tau)\mathrm{c}_2^{\dagger}(t+\tau)\mathrm{c}_1^{\dagger}(t)\rangle}{\langle \mathrm{c}_1(t)\mathrm{c}_2(t)\mathrm{c}_2^{\dagger}(t)\mathrm{c}_1^{\dagger}(t)\rangle}. \tag{2.3.9}$$

When the operators are chosen such that $\mathrm{c}_{1,2} = \mathrm{a} = \mu_{eg}|g\rangle\langle e|$, the photon annihilation operator, we obtain the photon-photon correlation function $g^{(2)}_{\mathrm{aa}}$, which reflects the joint probability of a photon being emitted at time $t+\tau$ given that a photon was emitted at time t. By appropriately choosing $\mathrm{c}_{1,2}$ from the photon and phonon operators a and b, respectively, we can correspondingly construct the phonon-phonon correlation function $g^{(2)}_{\mathrm{bb}}$ and, notably, the photon-phonon and phonon-photon cross-correlation functions $g^{(2)}_{\mathrm{ab}}$ and $g^{(2)}_{\mathrm{ba}}$ in a manner similar to refs. 248,253–256. Hence, the formal definitions of *bunching* and *antibunching* are [257]: $g^{(2)}_{c_1c_2}(t,\tau=0) < g^{(2)}_{c_1c_2}(t,\tau>0)$ and

$g^{(2)}_{c_1c_2}(t,\tau = 0) > g^{(2)}_{c_1c_2}(t,\tau > 0)$, respectively. The former implies that the probability of a second emission event immediately following a first is suppressed. In contrast, the latter occurs when the probability of simultaneous emission is enhanced. Note that this definition encompasses not only photon-photon or phonon-phonon correlation, but is also generalised[253,254] to include cross-correlations where the two emission events consist of one photon and one phonon.

Computational calculation of products of operators at two times is non-trivial and requires the application of the quantum regression theorem. This assumption dictates that a description of evolution as a single-point function can be used to define the evolution of two-point or multi-point correlations[258]. Additionally, a practical physical assumption relating to the magnitude of normalisation is introduced, such that all emitted photons and phonons are detected, regardless of scattering directions, e.g., by imagining the system enclosed by a detector [10,259–262]. Subsequently, correlations are computed as,

$$g^{(1)}_{\mathrm{c}}(t,\tau) = \frac{\mathrm{Tr}\Big(\mathrm{c}\exp(\mathcal{L}\tau)(\mathrm{c}^\dagger)\Big)}{\mathrm{Tr}(\mathrm{c}\rho\mathrm{c}^\dagger)}, \tag{2.3.10}$$

$$g^{(2)}_{\mathrm{c_1c_2}}(t,\tau) = \frac{\mathrm{Tr}\left(\mathrm{c}_1^\dagger\mathrm{c}_1\exp(\mathcal{L}\tau)(\mathrm{c}_2\rho\mathrm{c}_2^\dagger)\right)}{\mathrm{Tr}(\mathrm{c}_1\rho\mathrm{c}_1^\dagger)\mathrm{Tr}(\mathrm{c}_2\rho\mathrm{c}_2^\dagger)}, \tag{2.3.11}$$

where $\rho = \rho(t)$ is the density matrix at time t, $\mathcal{L}$ is the Liouvillian operator for the time evolution of the system and $\mathrm{c} = \{\mathrm{c}_1, \mathrm{c}_2\}$. Care must be taken to preserve continuity of the driving field during this calculation, or a rotating wave approximation (RWA) must be employed so that the frame of reference is tied to the driving field[262]. All the models in this thesis neglect the RWA and continuity of the driving field is maintained manually.

2.3.1 Non-normalised Correlation

In systems with a particularly small mean boson number, the denominator of the mth order correlation function can tend towards zero faster than the numerator. Such a scenario demonstrates that the variance is changing slower than the mean. When this happens normalising the correlation function will lead the amplitude to diverge. Therefore, in cases where the mean boson number is particularly low it can make more sense to present the non-normalised correlation function. The associated second order non-normalised correlation function is defined as

$$G^{(2)}_{\mathrm{c_1c_2}}(t,\tau) = \mathrm{Tr}\Big(\mathrm{c}_1^\dagger\mathrm{c}_2\exp(\mathcal{L}\tau)(\mathrm{c}_1\rho\mathrm{c}_2^\dagger)\Big), \tag{2.3.12}$$

where $\rho = \rho(t)$ and c_1 and c_2 are arbitrary bosonic creation operators.

2.3.1.1 Applications of Correlation

2.3.1.1.1 Interferometry

Intensity, $g^{(2)}$ and amplitude, $g^{(1)}$, measurements are crucial in interferometry devices. The seminal study of optical correlation by Hanbury, Brown and Twiss[6] in which intensity interferometry was employed to measure the radius of a star has lead to a broad interest in statistical correlation. Applications arose in high-precision imaging, calculation of stellar distances, information processing, boson bunching leading to Bose-Einstein condensation, and in open quantum system dynamics, due to its phase sensitivity which allows for measurements across a number of spatial orders of magnitude. All such applications exploit the nature of quantum interference to extract information regarding either the body scattering the coherent sources, or the distance between the sources, from the level of interference of the superimposed waves.

By correlating a pair of beams, which are allowed to interfere, a measure of fringe visibility can be generated. If there is a phase difference between the beams of less than π during the period of observation, then clear fringe patterns emerge as a result of constructive and destructive interference. If this phase difference is greater than the critical value then no interference pattern will be observed upon interaction of these beams. By tuning the distance over which each beam travels, or the distance between slits inducing interference, the phase difference between the two beams can be controlled. This allows for prediction of physical properties based on the disappearance of fringe patterns[28].

A modern example of these principles is present in a Michelson type interferometer. This consists of a single coherent source of photons, a beam splitter, a pair of mirrors and a photoelectric detector. The coherent source is emitted and split into a pair of beams, equivalent to a $g^{(1)}$ correlation at a pair of times t and τ, which are reflected by a pair of mirrors. The reflected beams recombine at the photoelectric detector, behind the splitter, and produce an interference based on their relative phase difference due to the differing path lengths travelled to their respective mirrors. Implementation of different length paths for the light, or intermediate materials to generate light-matter interactions lead to a range of applications. Figure 2.3.2, shows a simple schematic of a Michelson type interferometer which utilises splitting of a single photon beam.

A model of a beam splitting experiment, for application in interferometry, is considered in section 4.3, and the influence of system-bath boundary on these correlations is considered.

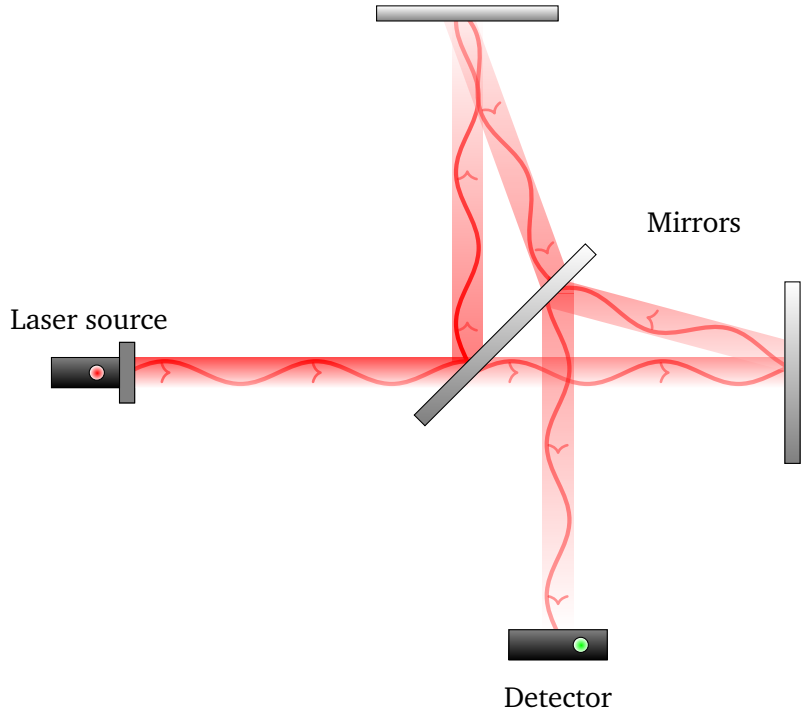

Figure 2.3.2: Schematic of a Michelson Interferometer, containing a laser source, detector, and three mirrors. The arrows show the direction of travel of the laser beam.

2.3.1.1.2 Correlation in Molecular Systems

Molecular systems which continuously emit bosons, for example the emission of photons during fluorescence, demonstrate quantum behaviour in a manner similar to quantum information. In an experiment, or model, this is measured through the probability of bosonic emission whereby antibunching leads to a suppression of secondary emission immediately after a first[257]. As discussed in section 2.3, an mth order correlation function corresponds to the correlation of m bosons at a given time leading to $g^{(1)}$ measures of excited state population, $g^{(2)}$ measures of quantum correlation, and $g^{(m)}$ measures of mth order coherence. Second order correlation functions are a powerful statistical tool which have been applied to a range of bosonic systems including: photons in optical cavities[15–19], photons in quantum emitters which behave as superatoms[22,23], phonons in opto-mechanical[263,264] and spin-mechanical[62,265] systems, and magnons introducing photon-magnon blockade in ferrimagnetic materials[253]. Higher order blockade effects and other complex dynamic behaviours are accessible through higher order correlation functions[26], and can be exploited for high-precision imaging[27], however the work in this thesis focuses on first and second order correlations with $m = \{1, 2\}$.

2.4 Theory of Spectroscopy

In addition to correlation measurements of quantum behaviour, it is possible to create two-dimensional spectra which demonstrate changes related to quantum information which was discussed in section 2.1.5. Starting from a description of the macroscopic polarisation, this section describes the response function formalism for linear and 2D photon echo spectroscopy.

2.4.1 Polarisation

The oscillating electric field of the incident laser, is coupled to the transition dipole moment of the system of interest following the system-field interaction Hamiltonian in equation (2.2.74). During the course of an energy conserving absorption of a photon from the laser field by the system, the molecule is transferred from its ground state to an excited state as the photon is annihilated. For a specific electronic transition, this occurs when the frequency of the oscillating field resonates with the transition frequency between the two quantised levels of the electronic structure which are connected with a non-zero transition moment. When the field is detuned from the resonant frequency the transition-dipole moment tends to zero as the transition becomes forbidden. As the laser spectrum has a finite width, several resonant transitions occur simultaneously across an ensemble, creating a wavepacket involving the superposition of multiple such exited states, each with a distribution of frequencies due to the stochastic bath interactions. When each of the molecules within an ensemble are oscillating there is the possibility for them to be in or out of phase with each other. In-phase oscillations create a non-equilibrium charge distribution which persists even after the laser field is deactivated, which is termed the *macroscopic polarisation*[38]. In contrast, out-of-phase contributions do not generate a charge distribution and correspond to the equilibrium state of the system. The macroscopic polarisation produced during a light-matter interaction is the physical observable which this model aims to replicate[230]. Due to the stochastic interactions with the environment, each molecule within the ensemble experiences a different local environment. The impact of this is that, after interaction with the electric field, the induced polarisation rapidly dephases to the equilibrium distribution[38].

As a consequence of the semi-classical approximation which governs the electric field, the macroscopic polarisation is calculated as the expectation value of the dipole moment operator and density matrix as a reflection of Maxwell's equations[37,38,266],

$$P = \mathrm{Tr}(\mu\rho) = \langle \mu \rangle \,. \tag{2.4.1}$$

This is then expanded as a power series in terms of the field interactions which, after neglecting higher order coupling terms, results in a first order perturbative calculation of the polarisation,

$$P = P^{(1)} + P^{(2)} + P^{(3)} + \dots, \tag{2.4.2}$$

where $P^{(1)}$ is the linear polarisation. In order for this perturbation to be valid, the electric field must be sufficiently strong that it can be assumed to be classical, but simultaneously weak enough that the eigenstates of the system are unaffected by the interaction. This requires that $\mathrm{H_{SF}}(t) \ll \mathrm{H_S}$.

By temporarily neglecting the spatial dependence of the electric field, which additionally transforms each component into a scalar, (where the spatial dependence corresponds to the orientation of the m input fields[267]) the polarisation after the interaction can be written as[40,111,241]

$$\begin{aligned} P^{(m)}(t) = \int_0^\infty \int_0^\infty \dots \int_0^\infty \mathcal{E}_\mathrm{I}(t-t_m)\mathcal{E}_\mathrm{I}(t-t_m-t_{m-1})\cdot\dots \\ \times \mathcal{E}_\mathrm{I}(t-t_m-\dots-t_1)R^{(m)}(t_m,\dots,t_1)\,\mathrm{d}t_1\dots\,\mathrm{d}t_{m-1}\,\mathrm{d}t_m, \end{aligned} \tag{2.4.3}$$

the convolution of each pulse with the *molecular response function*[38]

$$\begin{aligned} &R^{(m)}(t_m,\dots,t_1) = \\ &\quad -\Big(-\frac{i}{\hbar}\Big)^m \langle \mu(t_m+\dots+t_1)[\mu(t_{m-1}+\dots+t_1),\dots[\mu(0),\rho_\mathrm{S}(-\infty)]\dots]\rangle\,, \end{aligned} \tag{2.4.4}$$

which contains information about the system structure and its interaction with the environment. Additionally, $\rho_\mathrm{S}(-\infty)$ corresponds to the reduced density matrix of the system at its equilibrium configuration before interaction with the electric fields and t_m are time intervals between the field interactions. Physically, the molecular response function represents free system evolution in the absence of a field interaction, such as between pulses, which corresponds to a commutator of the interaction picture dipole moment operator,

$$\mu(t) = \mathrm{V}(t,t_0)\mu, \tag{2.4.5}$$

which can be written explicitly as

$$\mu(t) = \exp\Big(\frac{i}{\hbar}\mathrm{H_S}(t-t_0)\Big)\mu\exp\Big(-\frac{i}{\hbar}\mathrm{H_S}(t-t_0)\Big), \tag{2.4.6}$$

when system-bath interactions are negligible. Therefore, the interaction picture dipole moment operator for a vibronic monomer in the site basis, equation

(2.2.80), is,

$$\mu_{\mathrm{M}}^{\mathrm{S}}(t) = \boldsymbol{\mu}_{eg}\Big(\exp(-i\omega_{eg}t)\,|g\rangle\langle e| + \exp(i\omega_{eg}t)\,|e\rangle\langle g| \Big) \otimes \mathrm{I}_{\mathrm{vib}}, \tag{2.4.7}$$

where $\omega_{eg} = (E_e - E_g)/\hbar$ is the transition frequency between the ground and excited electronic state and $\mathrm{I}_{\mathrm{vib}}$ is the identity operator over the nuclear degrees of freedom of the system.

Based on symmetry only odd numbers of interaction, with a corresponding odd power, result in a non-zero polarisation for isotropic media. For $m = 1$, and 3 the result is first and third order response functions corresponding to linear and 2D photon echo spectroscopy[37,38]. Fifth and higher order response functions are presented in the literature, but are not discussed within this thesis[40,138].

2.4.2 First Order Linear Spectroscopy

First order perturbations of the field interactions within the polarisation, when $m = 1$, result in linear spectroscopy. This spectroscopy is the convolution of a single electric field with the first order molecular response function, corresponding to the interaction of the system with a single laser pulse,

$$P^{(1)}(t) = \int_0^\infty \mathcal{E}_{\mathrm{I}}(t - t_1) R^{(1)}(t_1)\, \mathrm{d}t_1, \tag{2.4.8}$$

where

$$R^{(1)}(t_1) = \frac{i}{\hbar} \left\langle \mu(t_1)[\mu(0), \rho_{\mathrm{S}}(-\infty)] \right\rangle, \tag{2.4.9}$$

and $\rho_{\mathrm{S}}(-\infty)$ corresponds to the equilibrium state of the system, accounting for correlated initial conditions. This is one of many simplifying approximations described in section 2.5, in particular this assumes the system is initially factorisable. However, it is important to note that correlation and factorisability are not mutually exclusive because the two are not necessary and sufficient statements. [e] The series of events leading to an emission event can be gleaned from the first order response function by reading it from right to left. First, there is an initial interaction between the system and the electric field at t_0, followed by a waiting period of evolution before emission of light through equation (2.4.1) at t_1 [138]. The single commutator, denoting an interaction, within the first order response function means that it contains two terms

$$R^{(1)}(t) = \frac{i}{\hbar}\Big(\langle \mu(t_1)\mu(0)\rho_{\mathrm{S}}(-\infty)\rangle - \langle \rho_{\mathrm{S}}(-\infty)\mu(0)\mu(t_1)\rangle \Big), \tag{2.4.10}$$

where, in each term, the invariance of the trace results in the two dipole moment operators acting on different sides of the density matrix[38]. Each term

[e] Correlation $\not\Longrightarrow$ not factorisable, but uncorrelated $\Longrightarrow$ factorisable.

corresponds to a *Liouville pathway*, which describes the change in state of the system during the course of the interaction[37]. This pair of orderings correspond to two different possible intermediate coherences, which lead to the same excitation event, during the interaction.

If only the electronic degrees of freedom are considered, in order to simplify considerations, and starting from a purely ground state population, $\rho_{\mathrm{S}}(-\infty) = |g\rangle\langle g|$, then operation of the dipole moment operator with the ket side of the density matrix generates the coherence $\mu(0)\rho_{\mathrm{S}}(-\infty) \propto |e\rangle\langle g|$, whereas operation from the opposite side results in $\rho_{\mathrm{S}}(-\infty)\mu(0) \propto |g\rangle\langle e|$. Each variation corresponds to a superposition of system states which is associated with a particular off-diagonal element within the density matrix. In the absence of any system-bath interactions, if this system is left to relax due to the second operation of the dipole moment, it will return to the ground state following

$$\langle \mu(t_1)\mu(0)\rho_{\mathrm{S}}(-\infty)\rangle = \mu_{eg}^2 \exp(-i\omega_{eg}t_1), \tag{2.4.11}$$

$$\langle \rho_{\mathrm{S}}(-\infty)\mu(0)\mu(t_1)\rangle = \mu_{eg}^2 \exp(i\omega_{eg}t_1). \tag{2.4.12}$$

From equation (2.2.75) we can introduce the electric field as two complex valued components, where we propagate the assumption that the field is spatially independent[f],

$$\mathcal{E}_{\mathrm{I}} = \chi_1 E'(t)\exp(-i\omega_1 t) + \chi_1 E'(t)\exp(i\omega_1 t), \tag{2.4.13}$$

which can be simplified to[38]

$$\mathcal{E}_{\mathrm{I}} = \mathfrak{E}(t) + \mathfrak{E}^*(t), \tag{2.4.14}$$

where $*$ denotes the complex conjugate. Both Liouville pathways interact with each complex part of the field such that the first order polarisation has four terms,

$$P^{(1)}(t) = \int_0^\infty \Big(\mathfrak{E}(t-t_1) + \mathfrak{E}^*(t-t_1)\Big) R^{(1)}(t_1)\,\mathrm{d}t_1, \tag{2.4.15}$$

$$P^{(1)}(t) = \int_0^\infty \frac{i}{\hbar}\Big(\langle \mu(t_1)\mu(0)\rho_{\mathrm{S}}(-\infty)\rangle\, \mathfrak{E}(t-t_1) + \langle \mu(t_1)\mu(0)\rho_{\mathrm{S}}(-\infty)\rangle\, \mathfrak{E}^*(t-t_1)$$
$$- \langle \rho_{\mathrm{S}}(-\infty)\mu(0)\mu(t_1)\rangle\, \mathfrak{E}(t-t_1) - \langle \rho_{\mathrm{S}}(-\infty)\mu(0)\mu(t_1)\rangle\, \mathfrak{E}^*(t-t_1)\Big)\,\mathrm{d}t_1, \tag{2.4.16}$$

[f] Note that the envelope function is now centred on zero.

which upon inserting the trace gives,

$$P^{(1)}(t) = \frac{i}{\hbar}\mu_{eg}^2 \exp(-i\omega_1 t) \int_0^\infty E'(t-t_1)\times \left(\exp\Big(i(\omega_1-\omega_{eg})t_1\Big) - \exp\Big(i(\omega_1+\omega_{eg})t_1\Big)\right) \mathrm{d}t_1 + \frac{i}{\hbar}\mu_{eg}^2 \exp(i\omega_1 t) \int_0^\infty E'(t-t_1)\times \left(\exp\Big(-i(\omega_1-\omega_{eg})t_1\Big) - \exp\Big(-i(\omega_1+\omega_{eg})t_1\Big)\right) \mathrm{d}t_1. \quad (2.4.17)$$

When the laser frequency, ω_1, is set so that it is in resonance with the electronic transition of the system two of the four contributions vanish leaving two highly oscillatory components. Application of the rotating wave approximation, which is discussed further in appendix D, means that these contributions can be neglected on the basis that integrating over highly oscillatory functions largely generates components which cancel[268]. Subsequently, the two remaining resonant pathways result from $\langle \mu(t_1)\mu(0)\rho_{\mathrm{S}}(-\infty)\rangle\, \mathfrak{E}(t-t_1)$ and its complex conjugate, $\langle \rho_{\mathrm{S}}(-\infty)\mu(0)\mu(t_1)\rangle\, \mathfrak{E}^*(t-t_1)$, which correspond to the same physical process[38].

In an equivalent fashion, when the system-bath interaction is not discounted, the first order response function in the Schrödinger picture takes the form

$$R^{(1)}(t_1) = \frac{i}{\hbar}\mathrm{Tr}\Big(\mu \mathrm{V}(t_1,t_0)[\mu,\rho_{\mathrm{S}}(-\infty)]\Big), \quad (2.4.18)$$

where $\mathrm{V}(t_1,t_0)$ is the propagator of an associated EOM which defines the evolution of the system during the period $t \in [t_0,t_1]$.

In order to obtain a spectrum for this system the time-dependent signal of the response function is Fourier transformed into the frequency domain. Such a procedure results in a signal which is phase shifted by $\frac{\pi}{2}{}^{\mathrm{c}}$ when compared to the macroscopic polarisation, and consequently, the signal is found on the imaginary axis, $\propto iP(t)$. [g] This signal is reduced by the action of destructive interference, and as such is termed *absorption*, consistent with the quantum mechanical interpretation[38]. As discussed, the required physical information is contained within the response function, which here is convoluted with the electric field. This signal either needs to be deconvoluted or assumed to be in the *impulsive* limit such that the envelope function is infinitesimally thin. Under such an assumption the envelope function becomes a delta function, such that convolution results purely in the sifting property, and the polarisation is

[g] Angles in radians are denoted $\{\cdot\}^c$.

equivalent to the molecular response function given by

$$\tilde{R}^{(1)}(\omega) = \sigma_{\mathrm{A}}(\omega) = \int_0^\infty \exp(i\omega t) i R^{(1)}(t)\ \mathrm{d}t. \tag{2.4.19}$$

Note that restricting the trace in equation (2.4.18) to the ground electronic state avoids duplication of the spectrum at negative frequencies. All linear spectra in this thesis are calculated in the impulsive limit to show all allowed transitions.

2.4.3 Third Order Photon Echo Spectroscopy

2.4.3.1 Polarisation and Response Function

The next lowest order of polarisation in isotropic media is the third order contribution which corresponds to a series of three laser pulses. In practice this technique is a four-wave-mixing process, with the fourth wave being detection, in which there are three phase-locked ultrafast laser pulses. It is standard for these constituent pules to be presented to the sample in a square BOXCARS geometry with controllable delay times such that the fourth signal is emitted in the phase-matched direction[38,39,111,269]. Detection of the real and imaginary components of the photon echo signal, which correspond to absorptive and dispersive response, is achieved through mixing with a strong oscillating field. This detection method, known as heterodyne detection, introduces phase sensitivity because the product of electric field waveforms results in a pair of new signals at the sum and difference of the waveform frequencies. This additional waveform, which is also propagated in the phase-matched direction, is known as the local oscillator (LO)[241,242,246]. The benefit of this approach over standard homodyne detection, which measures photon echo signals directly, is the vastly improved signal to noise ratio, coupled with the phase sensitivity[37].

The third order polarisation is expressed as the convolution of three electric fields with the third order molecular response function, $R^{(3)}(t_1, t_2, t_3)$, dependent on three waiting times $t_1,\ t_2,$ and t_3[111,270],

$$\begin{aligned} P^{(3)}_{\mathbf{k}_s}(\tau, T, t) = \int_0^\infty \int_0^\infty \int_0^\infty & \mathcal{E}_{\mathrm{I}}(t - t_1 - t_2 - t_3) \\ & \times \mathcal{E}_{\mathrm{I}}(t - t_2 - t_3)\mathcal{E}_{\mathrm{I}}(t - t_3) R^{(3)}(t_1, t_2, t_3)\ \mathrm{d}t_3\ \mathrm{d}t_2\ \mathrm{d}t_1. \end{aligned} \tag{2.4.20}$$

For a set of successive pulses, the polarisation produced is non-zero when each of the waiting times are greater than or equal to zero[111]. Each of the pulses is modelled as having a Gaussian envelope, as in equation (2.2.76), centred on $\tau_m,\ m \in \{1, 2, 3\}$ resulting in a third order polarisation signal. Pulses are separated by: the coherence time, $\propto |e\rangle\langle g|$, for the first and second pulses,

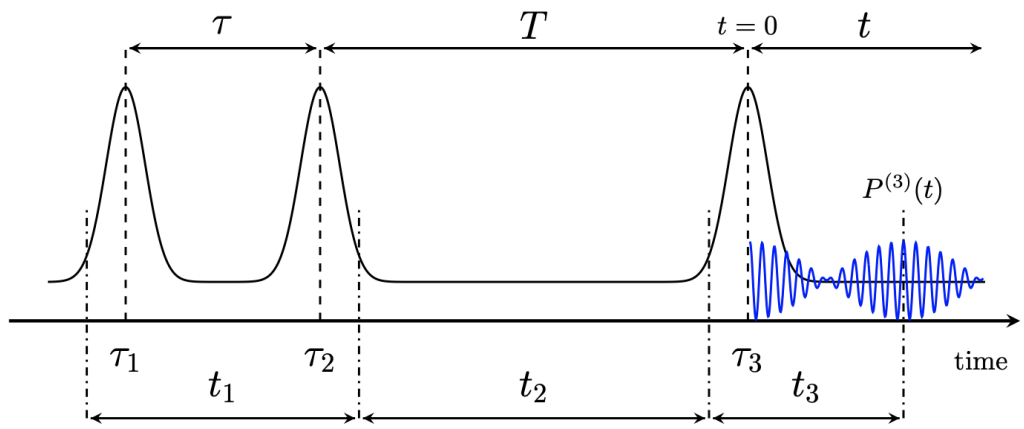

Figure 2.4.1: Schematic depicting the three pulses generating the third order polarisation. The associated waiting times between field envelopes and emission of the third order polarisation, $P^{(3)}(t)$, in the rephasing direction are shown in black and blue respectively.

and the population time $\propto |e\rangle\langle e|$, for the second and third pulses, where an echo signal occurs for $t \geq 0$ where τ_3, the centre of the final pulse, is set to be zero. Due to the breadth of each pulse the order of interaction is not fixed, system-field interaction events can occur at any point within the envelope unless each pulse is infinitesimally thin. In the impulsive limit, as the width of the Gaussian pulses tends towards zero and the peak separation becomes large, the coherence times tend towards the peak centres such that $\tau = t_1$, $T = t_2$ and $t = t_3$. In this limit, the pulse order becomes fixed such that pulses occur in ascending order, $t_1 < t_2 < t_3$. All combinations of pulse interaction orders are possible and consequently, a range of non-linear polarisation vectors are emitted in directions dependent on the constituent wavevectors[38]. Subsequent isolation of the desired component is achieved via heterodyne methods which focus the LO along the phase-matched direction amplifying emissions from the system in an equivalent direction.

A single interaction with each pulse where the order is t_1, followed by t_2 and finally t_3, results in a non-linear polarisation vector in the *rephasing*

$$\mathbf{k}_s = -\mathbf{k}_1 + \mathbf{k}_2 + \mathbf{k}_3, \tag{2.4.21}$$

and *non-rephasing*

$$\mathbf{k}_s = \mathbf{k}_1 - \mathbf{k}_2 + \mathbf{k}_3, \tag{2.4.22}$$

directions[39,93]. Permuting the first two wavevectors in either of the rephasing or non-rephasing wavevectors allows the total waveform to be aligned with the complementary polarisation vector[237,271]. Physically, this corresponds to a negative coherence time, τ, which swaps the arrival order of the pulses, and allows both resultant polarisations to be measured in a single experiment by

simply swapping the pulse order.

The total third order molecular response function[38]

$$R^{(3)}(t_3,t_2,t_1) = -\frac{i}{\hbar^3}\left\langle \mu(t_3+t_2+t_1)[\mu(t_2+t_1),[\mu(t_1),[\mu(t_0),\rho_{\mathrm{S}}(-\infty)]]]\right\rangle, \tag{2.4.23}$$

$$= -\frac{i}{\hbar^3}\left\langle \mu_3[\mu_2,[\mu_1,[\mu_0,\rho_{\mathrm{S}}(-\infty)]]]\right\rangle, \tag{2.4.24}$$

is also read from right to left, just like equation (2.4.9). The corresponding series of interactions are an instantaneous interaction of the first field with the equilibrium state, follow by a period of free evolution, followed by the second and then third pulse interactions and their respective periods of free evolution, before the non-linear polarisation is emitted as the macroscopic polarisation signal following equation (2.4.1). An additional notational shorthand has been employed in (2.4.23) whereby the subscript of each transition dipole moment operator denotes the final interval involved in that pulse interaction: $\mu_3 \implies t_3+t_2+t_1$, etc. Just as for the linear polarisation, the commutator can be expanded to determine Liouville pathway contributions. In this instance the commutators simplify to four complex conjugate pairs,

$$\begin{aligned} R^{(3)}(t_3,t_2,t_1) = -\frac{i}{\hbar^3}\Bigg(&\langle \mu_3\mu_0\rho_{\mathrm{S}}(-\infty)\mu_1\mu_2\rangle - \langle \mu_2\mu_1\rho_{\mathrm{S}}(-\infty)\mu_0\mu_3\rangle \\ &+ \langle \mu_3\mu_1\rho_{\mathrm{S}}(-\infty)\mu_0\mu_2\rangle - \langle \mu_2\mu_0\rho_{\mathrm{S}}(-\infty)\mu_1\mu_3\rangle \\ &+ \langle \mu_3\mu_2\rho_{\mathrm{S}}(-\infty)\mu_0\mu_1\rangle - \langle \mu_1\mu_0\rho_{\mathrm{S}}(-\infty)\mu_2\mu_3\rangle \\ &+ \langle \mu_3\mu_2\mu_1\mu_0\rho_{\mathrm{S}}(-\infty)\rangle - \langle \rho_{\mathrm{S}}(-\infty)\rangle\, \mu_0\mu_1\mu_2\mu_3 \Bigg), \end{aligned} \tag{2.4.25}$$

Under the assumption that the final pulse, μ_3, operates on the ket (left) side of the density matrix, this process corresponds to four Liouville pathways which, when labelled with 2DES convention, are

$$R^{(3)}(t_3,t_2,t_1) = R_1 + R_1^* + R_2 + R_2^* + R_3 + R_3^* + R_4 + R_4^*, \tag{2.4.26}$$

where

$$R_1 = \langle \mu_3\mu_0\rho_{\mathrm{S}}(-\infty)\mu_1\mu_2\rangle, \quad R_1^* = \langle \mu_2\mu_1\rho_{\mathrm{S}}(-\infty)\mu_0\mu_3\rangle, \tag{2.4.27}$$

$$R_2 = \langle \mu_3\mu_1\rho_{\mathrm{S}}(-\infty)\mu_0\mu_2\rangle, \quad R_2^* = \langle \mu_2\mu_0\rho_{\mathrm{S}}(-\infty)\mu_1\mu_3\rangle, \tag{2.4.28}$$

$$R_3 = \langle \mu_3\mu_2\rho_{\mathrm{S}}(-\infty)\mu_0\mu_1\rangle, \quad R_3^* = \langle \mu_1\mu_0\rho_{\mathrm{S}}(-\infty)\mu_2\mu_3\rangle, \tag{2.4.29}$$

$$R_4 = \langle \mu_3\mu_2\mu_1\mu_0\rho_{\mathrm{S}}(-\infty)\rangle, \quad R_4^* = \langle \rho_{\mathrm{S}}(-\infty)\mu_0\mu_1\mu_2\mu_3\rangle. \tag{2.4.30}$$

Analogously the total electric field, after factorisation of the vector and spatial components, can be expanded into three complex pairs of the time dependent

envelope function from equation (2.4.14), resulting in

$$\mathcal{E}_{\mathrm{I}} = \mathfrak{E}_1(t) + \mathfrak{E}_1^*(t) + \mathfrak{E}_2(t) + \mathfrak{E}_2^*(t) + \mathfrak{E}_3(t) + \mathfrak{E}_3^*(t). \tag{2.4.31}$$

There are $N_{\mathcal{E}}^m N_{\mathrm{LP}}$ possible permutations of Feynman diagrams which depict these Liouville pathways, where $N_{\mathcal{E}}$ is the number of electric field contributions, m the number of pulses, and N_{LP} is the number of Liouville pathways. With six components contained within the electric field and four Liouville pathways, $N_{\mathcal{E}} = 6$, $m = 3$, $N_{\mathrm{LP}} = 4$, such that the total number of permutations is 864. This number can be reduced by assuming non-overlapping pulses such that the time-ordering is fixed with interactions occurring in ascending order: μ_0 due to $\mathfrak{E}_1$, μ_1 due to $\mathfrak{E}_2$, and μ_2 due to $\mathfrak{E}_3$. This reduces $N_{\mathcal{E}}$ to 2 and the total number of permutations to 32[272]. Additionally, the rotating wave approximation can be applied to the highly oscillatory components which further reduces the total number of pathways to four. Each pathway describes resonant interactions due to one component, R_x with $x \in \{1, 2, \ldots, N_{\mathrm{LP}}\}$, of the total response function, $R^{(3)}$ [37,38].

Each of the Liouville pathways can be classified as rephasing or non-rephasing, subject to equations (2.4.21) and (2.4.22), based on the sequence of field interactions. The order of the pulses, and whether the intermediate state at time t_2 before emission of the final signal is a ground or excited state population, dictates the physical process each Feynman pathway depicts. Ground state populations are present during the waiting time t_2 and correspond to a *ground state bleach*. Excited state populations present at t_2, correspond to *stimulated emission*.

Pathways which are termed rephasing exist in oppposite coherence states during the first and final waiting times such that an inhomogeneous distribution of frequencies which becomes out of phase over some period in the coherence, will return to being in phase when placed into the opposite coherence for the same duration. This results in a revival of the polarisation at $\tau = t$ due to a photon echo, and is hence named rephasing. Those pathways which are labelled as non-rephasing exist in the same, $|e\rangle\langle g|$, coherence during both t_1 and t_3 waiting times such that the inhomogeneous distribution moves further out of phase.

Systems which have additional excited states, beyond those of a simple two level electronic system, introduce extra terms which survive the rotating wave approximation. These extra states, due to a second excited state $|f\rangle$, are regularly utilised in 2D infrared spectroscopy (2DIR) because they are able to induce transitions between vibrational levels with infrared frequencies rather than between electronic states with UV/visible frequencies. These processes, termed *excited state absorption*, start from the first excited state population

during the t_2 waiting time, but then enter a coherence in the t_1 waiting time. The rephasing pathway exists as $|g\rangle\langle e|$ at t_1 followed by double excitation to the coherence $|f\rangle\langle e|$ in the waiting time t_3. In contrast, the non-rephasing pathway exists in the coherence $|e\rangle\langle g|$ at t_1 and is impacted by a pair of excitation events resulting in $|f\rangle\langle e|$ at t_3. Importantly, vibrational states always have an accessible f state, whereas electronic states do not, so ESA is essential in 2DIR. A full description of the Liouville pathways and their corresponding Feynman diagrams can be found in the work of D. Green[173], but is beyond the scope of this thesis.

The current classifications exist in closed and open quantum systems, but the system-bath interaction plays an important role during each interaction. When the system is placed into a coherence, such that an excited state wavepacket exists within the system PES, thermal jostling by the environment degrees of freedom leads the wavepacket to dephase and the polarisation to decay. During waiting times when the system is evolving freely, dissipation of energy to the environment corresponding to vibrational relaxation and luminescence, leads to additional decay of the polarisation. Resolution of these processes, in a dynamic fashion, is one of the crucial measurements applied within this thesis through changes to 2DES spectra.

In the Schrödinger picture, the third order response function can be written in terms of the propagator of an EOM, as[138,273]

$$R^{(3)}(t_3,t_2,t_1) = -\frac{i}{\hbar^3}\mathrm{Tr}\Big(\mu \mathrm{V}(t^{(3)},t^{(2)})\mu^{\times}\mathrm{V}(t^{(2)},t^{(1)})\mu^{\times}\mathrm{V}(t^{(1)},t_0)\mu^{\times}\rho_{\mathrm{S}}(-\infty)\Big), \tag{2.4.32}$$

with $t^{(m)} = \sum_{i=1}^{m} t_i$.

If the transition dipole moment operator is instead split into absorption and emission components due to raising and lowering operators, μ_+ and μ_-, respectively, then rephasing and non-rephasing contributions of the response function can be expressed as[155,159]

$$R^{(3)}_{\mathrm{R}}(t_3,t_2,t_1) = -\mathrm{Tr}\Big(\mu \mathrm{V}(t^{(3)},t^{(2)})\frac{i}{\hbar}\mu_+^{\times}\mathrm{V}(t^{(2)},t^{(1)})\frac{i}{\hbar}\mu_+^{\times}\mathrm{V}(t^{(1)},t_0)\frac{i}{\hbar}\mu_-^{\times}\rho_{\mathrm{S}}(-\infty)\Big), \tag{2.4.33}$$

and

$$R^{(3)}_{\mathrm{NR}}(t_3,t_2,t_1) = -\mathrm{Tr}\Big(\mu \mathrm{V}(t^{(3)},t^{(2)})\frac{i}{\hbar}\mu_+^{\times}\mathrm{V}(t^{(2)},t^{(1)})\frac{i}{\hbar}\mu_-^{\times}\mathrm{V}(t^{(1)},t_0)\frac{i}{\hbar}\mu_+^{\times}\rho_{\mathrm{S}}(-\infty)\Big), \tag{2.4.34}$$

respectively. All 2DES in this thesis is calculated in the impulsive limit and produced from solutions of the response function when the EOM propagator is chosen to use HEOM dynamics, described in sections 2.5.4.1 and 2.5.6.

System-field interactions are accounted for by applying the commutators to every auxiliary within the hierarchy, to allow uniform interaction across all HEOM auxiliary density operators, equation (2.5.40), before propagation is continued. The impact of this is that system-bath correlations are maintained throughout the calculation such that all necessary non-Markovian memory effects are present in the resultant spectra[150,155,157].

When the crucial feature of interest is the system-bath coupling, as in 3.1, 4.3, and, 3.3, the 2D spectra are calculated in the impulsive limit, which focuses on these effects. However, finite pulse effects significantly impact spectral features, including through distortion of the lineshape due to significant overlap of pulses at early times. This is mitigated by moving away from the perturbative expansion of the polarisation as employed in equation (2.4.3) and instead using the equation-of-motion phase-matching approach.

2.4.3.2 2D Spectra

2DES are calculated as the double Fourier transform of the third order polarisation with respect to τ and t as

$$\tilde{P}^{(3)}_{\mathrm{R}} = S_{\mathrm{R}}(\omega_\tau, T, \omega_t) = \int_0^\infty \int_0^\infty \exp(-i\omega_\tau \tau) \exp(i\omega_t t) i P^{(3)}_{\mathrm{R}}(\tau, T, t)\ \mathrm{d}\tau\ \mathrm{d}t, \tag{2.4.35}$$

for the rephasing and

$$\tilde{P}^{(3)}_{\mathrm{NR}} = S_{\mathrm{NR}}(\omega_\tau, T, \omega_t) = \int_0^\infty \int_0^\infty \exp(i\omega_\tau \tau) \exp(i\omega_t t) i P^{(3)}_{\mathrm{R}}(\tau, T, t)\ \mathrm{d}\tau\ \mathrm{d}t, \tag{2.4.36}$$

for the non-rephasing contributions[36,84,238,274]. The different signs within each of the Fourier transforms reflect the change in time orderings of the pulses when generating a rephasing versus non-rephasing signal. Performing a forward transform of the third order polarisation in both the τ and t axes, results in signal in the $(\mp\omega_\tau, \pm\omega_t)$ quadrants, whereas the non-rephasing is found in the $(\pm\omega_\tau, \pm\omega_t)$ quadrants[38,242]. The Jones group follows the convention of an inverse transform performed in τ in order to generate rephasing and non-rephasing signals in the same quadrant[173].

These Fourier transformed variables correspond to the excitation and detection frequencies in 2DES experiments, presented for a fixed population time T. The excitation ω_τ is the frequency associated with the first system-field interaction event, and ω_t is the frequency associated with the final emitted signal. The rephasing and non-rephasing spectra each contain absorptive and dispersive components, which are real and imaginary contributions respectively, which are typically summed to generate the total, purely absorptive,

spectrum[38,155,157,238]

$$S_{\mathrm{A}} = \mathcal{R}(S_{\mathrm{R}} + S_{\mathrm{NR}}). \tag{2.4.37}$$

The resultant 2D spectra contain a mix of both diagonal and off-diagonal peaks corresponding to transitions which would be identified by linear absorption spectroscopy, and those which are a result of coherences, respectively. Off-diagonal peaks have unequal excitation and emission frequencies due to changes in the state of the system caused by intermediate field interactions. The expression of populations within a spectrum, which is equivalent to states that have the same ket and bra constituents, are known as population pathways and decay exponentially as a consequence of dephasing and relaxation. In contrast, the expression of coherences during the population time T is through oscillations at the frequency of the energy gap between the respective states within the coherence[275] as a consequence of a coherent superposition. This is the spectral manifestation of quantum beating[236,276].

The location and oscillation of peaks provides information of the structure of the system, whilst the lineshape gives details of the bath, in terms of homogeneous and inhomogeneous broadening[269,277]. In contrast to linear spectroscopy, in which both types of broadening are projected onto their underlying axis, in 2D spectroscopy, homogeneous and inhomogeneous contributions are separated onto their own axes. The anti-diagonal broadening, which contains exclusively homogeneous contributions, are the result of a decay in the excited state which introduces uncertainty regarding the exact transition frequency of the system[110,242]. This kind of lifetime broadening results in a Lorentzian lineshape[230,278]. Consequently homogeneous broadening affects all system molecules equally. In contrast, a combination of homogeneous and inhomogeneous broadening is found on the diagonal[h], and is a result of ensemble effects. An example of one such environmental effect is diagonal elongation due to a Gaussian distribution of different transition frequencies within an ensemble resulting from conformational freedom or differing solvent environments[138,268]. The degree of elongation along the diagonal due to environmental effects is exploited in conjunction with measures of quantum information in section 3.1 to quantify non-Markovian effects.

The aforementioned differences, in section 2.4.3.1, between rephasing and non-rephasing Liouville pathways are further differentiated through the spectral lineshape. Rephasing pathways, which initially dephase before being encouraged to re-phase by a change to the complementary coherence state at $\tau = t$, present elongated peaks due to an inhomogeneous distributions which persists into the absorptive spectrum[274]. This elongation persists into the purely absorptive spectrum after summation of the non-rephasing and rephasing

[h] This is the reason for asymmetry for 2DES with low spectral diffusion as in appendix F.

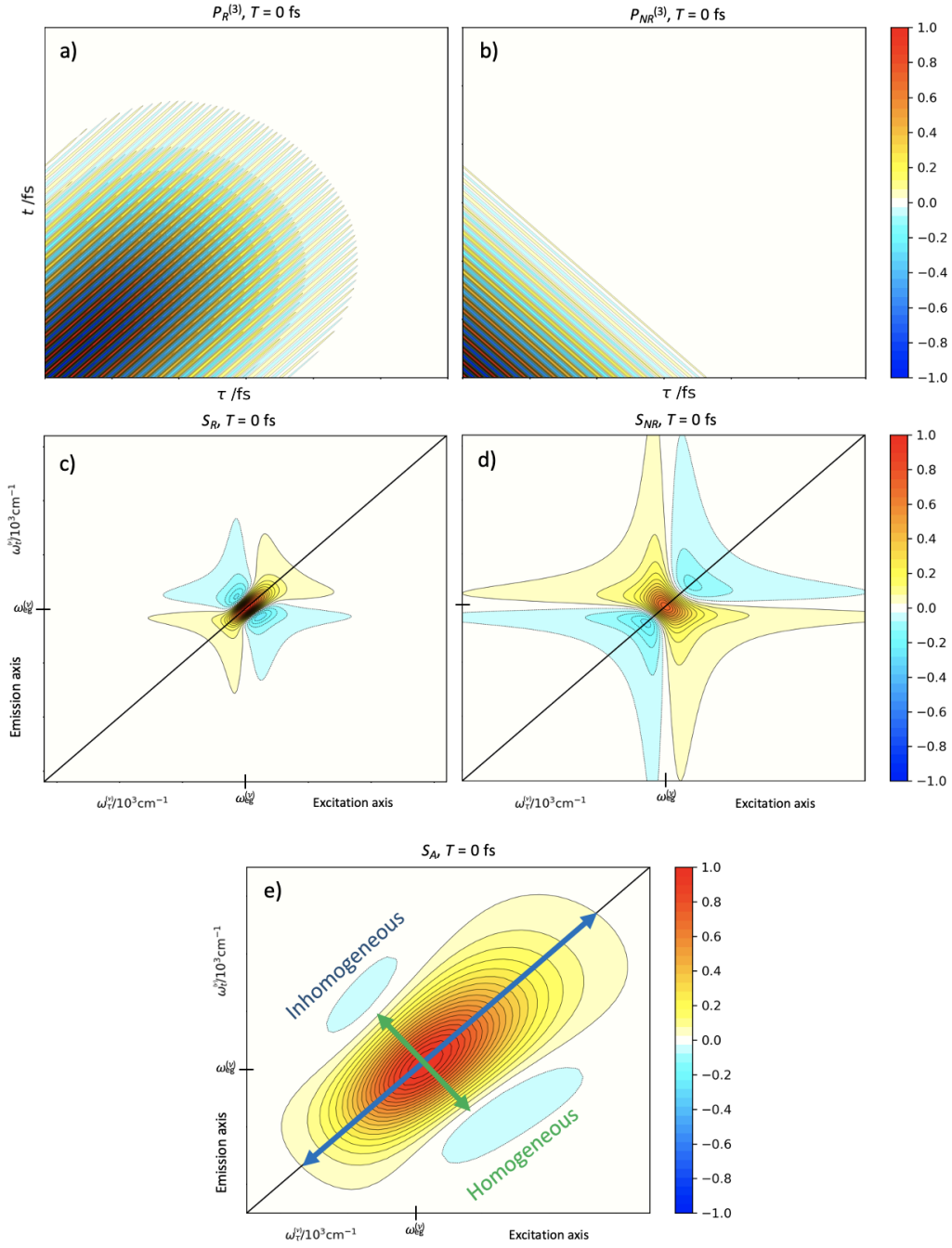

Figure 2.4.2: The third order polarisation and 2D spectra in the impulsive limit for a two-level-system with significant inhomogeneous broadening. The non-rephasing polarisation and spectrum are normalised to the maximum of the equivalent rephasing signal to demonstrate how the elongation of the rephasing spectrum persists when the components are summed producing the absorptive spectrum. a) rephasing polarisation, b) the non-rephasing polarisation, c) the rephasing spectrum, d) the non-rephasing spectrum, and e) the absorptive spectrum, all at $T = 0$ fs.

components. An example two-level system with significant inhomogeneous broadening, calculated in the impulsive limit, is presented in figure 2.4.2. The inhomogeneous and homogeneous broadening is labelled on this figure along with a demonstration of the rephasing and non-rephasing contributions. However, this elongation along the diagonal is not significant for all population times, T. When T is close to zero the elongation is large, but as the population time increases, spectral diffusion as a consequence of the decay of system-bath correlations diminishes the revival of polarisation leading to rephasing and non-rephasing signals of almost equal intensity[38,279,280]. This is evident in the purely absorptive spectrum too, as the population time is increased the level of diagonal elongation decreases until the peak is symmetrical and rounded. This process is discussed in detail in section 3.1.

2.5 Equations of Motion

As discussed in chapter 1, an equation of motion is the fundamental method of describing a physical system, and can be exact or approximate. If a closed form solution cannot be generated then an approximate solution can be generated through perturbative or non-perturbative means. Derivations from first principles are contained in appendix D, increasing in complexity and with a range of simplifying approximations, as a way of intimately understanding the behaviour of dynamics associated with each model.

2.5.1 Exact Approaches

Under certain conditions, which are usually restrictive (examples being closed, factorisable dynamics, or the Markovian approximation), an EOM may generate a closed-form, analytical, solution for the dynamics of an OQS. However, many of these approximations prohibit the appearance of memory effects, and an increase in the number of degrees of freedom is necessary in order to introduce non-Markovian memory effects. Exact and approximate approaches are often unable to model systems with very large numbers of degrees of freedom, or with large system molecules, because an increase in the total degrees of freedom increases the complexity of the system-bath interactions, and the size of the composite Hilbert space. This can be rationalised by considering the Markovianity of the EOMs: numerically explicit equations which are fully time local can be easily solved and may have analytic solutions. In contrast, strongly non-Markovian dynamics entangle[i] the system and bath dynamics in a strongly time dependent fashion resulting in time non-local dynamics which are not

[i] Entanglement of system and bath states through interaction. This is later referred to as bathentanglement.

numerically explicit. The only way to generate solutions from such systems is to employ approximations regarding the nature of the system-bath interaction.

The list of exact EOMs is very limited based on the stringent requirements for dynamics to produce analytical solutions. A number of closed-form solutions exist for the time-dependent non-relativistic Schrödinger equation including for a two-state quantum system, quantum harmonic oscillator, and Morse potential[281]. The Schrödinger equation with a non-zero trapping potential, V, is shown below

$$i\hbar\frac{\partial}{\partial t}\psi(\mathbf{r},t) = \Big(-\frac{\hbar^2}{2m}\nabla^2 + V(\mathbf{r})\Big)\psi(\mathbf{r},t). \tag{2.5.1}$$

It is clear from this equation, further details can be found in appendix D.1.1.2, that we are considering a single non-relativistic particle, in microscopic continuous coordinates. In addition, since the energy is conserved we are dealing with a system of conservation laws for a closed system. In order to model dissipative open systems many of these assumptions need to be relaxed.

2.5.2 Perturbative Approaches

Perturbative theories involve generating approximate solutions to non-trivial problems through relation to solutions of a simpler, or more tractable, problem. One way to achieve this is by addressing the source of system complexity as a power series in a small parameter, ϵ, and then neglecting terms within the EOM which are of higher order than $\mathcal{O}(\epsilon)$. This approach is effective when the true dynamics of the system can be expressed in terms of some small deviation from the solution, an example being a particle trajectory. This method of generating solutions will fail when problems are ill-conditioned, meaning that a small error in data will produce a large error in solution, or when small perturbations may fundamentally alter the nature of the dynamics, such as in some quantum phenomena. The benefit of this is that it increases the number of applicable systems which can be modelled, while also keeping the method of modelling simplistic and easily solvable. One such approach is the Bloch-Redfield Master Equation (BRME)[121],

$$\frac{\partial}{\partial t}\rho_{\mathrm{S}}(t) = -i\epsilon[\mathrm{H},\rho_{\mathrm{S}}(t)] - \epsilon^2\sum_m[\mathrm{S}_m, \varpi_m\rho_{\mathrm{S}}(t) - \rho_{\mathrm{S}}(t)\varpi_m^\dagger], \tag{2.5.2}$$

where ϖ_m is the bath correlation function written as a power spectrum (discussed further in appendix D.1.5), which simplifies full dynamics through the Born-approximation, the weak coupling limit, and through a Markovian assumption about the system-bath interaction. The Born-approximation stipulates that there is never any bathentanglement resulting in factorisable system-bath states. The weak coupling limit requires that the strength of

interactions is small relative to the scale of intrinsic system modes, and the Markovian approximation simplifies the system-bath interaction so that the bath has no time-dependence resulting in phonons dissipating without recurrence, resulting in time locality of the EOM. This approach has been used in models of weakly driven open, and multi-level systems[122,123]. However, the BRME does not necessarily need to be Markovian as demonstrated by non-Markovian corrections to the standard Redfield equation[126,282].

A similar perturbative approach to the BRME is the Lindblad Master Equation (LME) in which the dynamics are are assumed to be Markovian, and in the weak-coupling limit, along with the Born-approximation to separate bathentanglement. In addition, the rotating wave approximation, which separates oscillations based on their scale is applied and neglects fast scales.

$$\frac{\partial}{\partial t}\rho_{\mathrm{S}}(t) = -i[\mathrm{H}+\mathrm{H}_{\mathrm{L}},\rho_{\mathrm{S}}(t)] + \sum_{\omega,l}\Big(\mathfrak{L}_l(\omega)\rho_{\mathrm{S}}(t)\mathfrak{L}_l^{\dagger}(\omega) - \frac{1}{2}\Big\{\mathfrak{L}_l^{\dagger}\mathfrak{L}_l(\omega),\rho_{\mathrm{S}}(t)\Big\}\Big), \tag{2.5.3}$$

where $\mathfrak{L}$ is the Lindbladian (jump) operator, and S is the component of the interaction Hamiltonian which acts purely on system degrees of freedom. This can be related to the BRME directly through application of the secular approximation which restricts the environment to resonant frequencies, valid for long times. Applications include electronic TLSs coupled weakly to an environment, and qubits[124,125,127,282].

Finally, the general Markovian Master equation is considered. As discussed in section 2.1.2, the evolution of the reduced density operator can be generated from the propagator of the dynamics, $\mathrm{V}(t,t_0)$, which accounts for the interaction with the bath through the generator $\mathcal{L}_{\mathrm{g}}(t)$, (2.1.17). The master equation of the reduced system has the general form[115,283]

$$\frac{\partial\rho_{\mathrm{S}}}{\partial t} = \mathcal{L}_{\mathrm{g}}(t)\rho_{\mathrm{S}}(t) = -\frac{i}{\hbar}[\mathrm{H}_{\mathrm{S}}+\mathrm{H}_{\mathrm{SF}}(t),\rho_{\mathrm{S}}] + \mathrm{D}[\rho_{\mathrm{S}}(t)], \tag{2.5.4}$$

where the first square brackets denote the commutator, and $\mathrm{D}[\rho_{\mathrm{S}}(t)]$ is an arbitrary relaxation superoperator defining the interaction with the bath. This EOM is generated from a second order perturbation of the Liouville Von-Neumann equation with a time dependent Hamiltonian:

$$i\hbar\frac{\partial\rho_{\mathrm{S}}}{\partial t} = [\mathrm{H}(t),\rho_{\mathrm{S}}], \tag{2.5.5}$$

$$= [\mathrm{H}_0+\epsilon\mathrm{H}_1(t),\rho_{\mathrm{S}}], \tag{2.5.6}$$

such that the equation can be rewritten as[284]

$$\frac{\partial\rho_{\mathrm{S}}}{\partial t} = -\frac{i}{\hbar}[\mathrm{H}_0,\rho_{\mathrm{S}}] + \Gamma_{\mathrm{g}}\Big(\rho_{\mathrm{S}}(t)-\rho_{\mathrm{S}}(0)\Big), \tag{2.5.7}$$

where Γ_{g} is a, less general, form of the relaxation superoperator due to the generator $\mathcal{L}_{\mathrm{g}}$. If the time independent component of the total Hamiltonian is written as the system contribution, $\mathrm{H_S}$, and the relaxation superoperator is written in its most general form, $\mathrm{D}[\rho_{\mathrm{S}}(t)]$, this is equivalent to the most general master equation (ME). When the Markovian approximation is applied to this EOM the relaxation superoperator can be converted to either

$$\mathrm{D}[\rho_{\mathrm{S}}(t)] = -\epsilon^2 \sum_m [\mathrm{S}_m, \varpi_m \rho_{\mathrm{S}}(t) - \rho_{\mathrm{S}}(t)\varpi_m^\dagger], \text{ or} \tag{2.5.8}$$

$$\mathrm{D}[\rho_{\mathrm{S}}(t)] = \sum_{\omega,l} \Big(\mathfrak{L}_l(\omega)\rho_{\mathrm{S}}(t)\mathfrak{L}_l^\dagger(\omega) - \frac{1}{2}\Big\{ \mathfrak{L}_l^\dagger \mathfrak{L}_l(\omega), \rho_{\mathrm{S}}(t) \Big\} \Big), \tag{2.5.9}$$

generating the aforementioned BRME and LME.

2.5.3 Non-Perturbative Approaches

In contrast, functions or variables which cannot be expanded as a power series through a perturbative theory are known as *non-perturbative*. The cost of removing the perturbation is that additional complexity is returned to the system and EOMs being solvable is not guaranteed, often leading to complex high order partial differential equations (PDEs). The purpose of this is to introduce strongly non-Markovian, quantum characteristics to OQS. This generally manifests itself as time non-locality in the equations of motion, meaning that the Markov approximation is invalidated. One approach to reaching solvable equations of motion is, in a manner analogous to the Born approximation, splitting the dynamics into fast and slow 'irrelevant' and 'relevant' parts respectively. The Nakajima-Zwanzig equation (NZE) [130,131],

$$\frac{\partial}{\partial t}\rho_{\mathrm{S}} = \epsilon \mathcal{P}\mathcal{L}(t)\rho_{\mathrm{S}} + \epsilon^2 \int_{t_0}^{t} \mathcal{K}\rho_{\mathrm{S}}\, \mathrm{d}t', \tag{2.5.10}$$

$$\mathcal{K}(t,t') = \mathcal{P}\mathcal{L}(t)\mathcal{G}(t,t')\mathcal{Q}\mathcal{L}(t'), \tag{2.5.11}$$

splits the dynamics into a relevant, ρ_{S}, and irrelevant ρ_{B}, contribution based on the scale of oscillations within each component. This is achieved through the Zwanzig projection operators $\mathcal{P}$ and $\mathcal{Q}$ which result in the non-Markovian propagator for the dynamics, $\mathcal{K}(t,t')$, and transform the density matrix $\mathcal{P}\rho = \rho_{\mathrm{S}}$, $\mathcal{Q}\rho = \rho_{\mathrm{B}}$. This equation is still completely exact, but is often no easier to solve than the full problem because of the inseparable, time non-local integral over the kernel $\mathcal{K}$. An ideal EOM would have almost completely exact dynamics while also reducing complexity. Through an introduction of the superoperator

$$\mathrm{D}[\rho_{\mathrm{S}}(t)] = -\epsilon^2 \int_{t_0}^{t} [\mathrm{H_I}(t), [\mathrm{H_I}(t'), \rho_{\mathrm{S}}(t)]]\, \mathrm{d}t', \tag{2.5.12}$$

a general quantum Master equation of the form equation (2.5.4) can be transformed into the Nakajima-Zwanzig equation. This is because the integral form of the superoperator introduces explicit time non-locality and high orders of the interaction Hamiltonian coupling through the double commutator.

An alternative is to employ stochastic variables and Itô calculus which introduces random variables and forcing. This allows the influence of Brownian oscillator environments to be introduced into the EOM statistically. The quantum Langevin equation (QLE)[285],

$$m\frac{\mathrm{d}^2\mathrm{x}}{\mathrm{d}t^2}+\zeta\frac{\mathrm{dx}}{\mathrm{d}t}+\frac{\mathrm{d}V(\mathrm{x})}{\mathrm{dx}}=F(t), \tag{2.5.13}$$

contains ζ, a friction constant associated with the random forcing applied by the environment ensemble, where the forcing operator is defined by its symmetric correlation and commutator relation:

$$\frac{1}{2}\left\langle F(t)F(0)+F(0)F(t)\right\rangle=\frac{\zeta}{\pi}\int_0^\infty \hbar\omega\coth(\hbar\omega\tilde{\beta}^{-1})\cos(\omega t)\,\mathrm{d}\omega, \tag{2.5.14}$$

$$[F(t),F(0)]=-\frac{2i\hbar\zeta}{\pi}\int_0^\infty \omega\sin(\omega t)=2i\hbar\zeta\delta'(t). \tag{2.5.15}$$

This equation is simpler to solve than the NZE, in general, but additionally requires assumptions about the nature of the environment distribution such as the approximation of canonical distribution. Stochastic Gaussian processes with a direct forcing and a friction term introduce white noise[j], fluctuations (often characterised by successive weak interaction) which influences the system probability distribution resulting in Brownian motion and non-Markovianity. This model has been used in models of condensed phase spectroscopic experiments and for modelling molecular polaritons[134,135].

Many non-perturbative equations of motion can also be generated through path integral approaches based on work by both Calderia and Leggett, and Feynman and Vernon[4,143,144,214]. The path integral generalises classical action and proposes that the most probable trajectory is a sum over an infinite number of quantum trajectories resulting in a quantum amplitude. This process takes a set of temperature dependent variables and performs a Wick rotation onto the complex plane where they become imaginary times, as discussed in section E.1. A quantum particle moving within a potential is subsequently described by a path integral as a superposition of paths, each with an associated phase, expressed as the exponential of an action, and follows a trajectory between the initial and final states of the integral. Each trajectory varies based on quantum uncertainty, which manifests as paths which are less or more likely, where the

[j]While white noise is often associated with Markovianity, in this context, as a consequence of the pair of time dependent commutators in the kernel, this is equivalent to a time-locality assumption rather than strict Markovianity. This is similar to the simplification used in NZE.

-	NLS	LVN	BRME	LME	NZE	QLE	KSLE	SSE	FPE	HEOM
Closed	✔	✔	✘	✘	✘	✘	✘	✘	✘	✘
Open	✘	✘	✔	✔	✔	✔	✔	✔	✔	✔
Stochastic	✘	✘	✘	✘	✘	✔	✔	✔	✔	✢
Projection	✘	✘	✘	✘	✔	✘	✘	✘	✘	✘
Weak-Coupling	✢	✢	✔	✔	✢	✢	✢	✢	✢	✢
Rotating-wave	✢	✢	✘	✘	✘	✘	✘	✢	✘	✘
Secular	✢	✢	✢	✔	✘	✢	✘	✢	✢	✢
Born	✢	✢	✔	✔	✢	✢	✢	✢	✘	✘
Markovian	✢	✢	✔	✔	✘	✘	✘	✘	✘	✘
Factorisable	✢	✢	✔	✔	✔	✘	✢	✔	✢	✢
Infinite Bath	✘	✘	✘	✘	✘	✔	✘	✔	✘	✘
Canonical Dist.	✢	✢	✢	✢	✢	✔	✘	✢	✢	✢
High Temp	✘	✘	✢	✢	✢	✘	✢	✘	✢	✢
Cond. Moment	✢	✢	✢	✢	✢	✘	✢	✢	✔	✢

Table 2.1: ✔ denotes essential approximations. ✘ denotes incompatible approximations. ✢ is a weaker statement, it is used to denote approximations which could be applied (but may result in excessive simplification) i.e. those approximations which are not inconsistent with essential approximations. Full acronyms can be found in appendix K.

classical action defines the most likely trajectory. This is analogous to the statistical equivalent: an ensemble of particles, which varies as a consequence of temperature, leading to a state corresponding to the least energy. In the interest of brevity, full relationships between non-perturbative approaches are discussed only in appendix D. Additionally, a full calculation of a path integral (for a simple free particle) is presented in appendix C.

Figure 2.5.1 and table 2.1 summarise the full set of approximations and assumptions which are used to generate all the EOMs discussed, and those which are discussed in appendix D. In addition, the flow chart, figure 2.5.1, depicts the interrelation of different forms of exact, perturbative, and non-perturbative models, demonstrating the advancement of models to more complex non-Markovian EOMs.

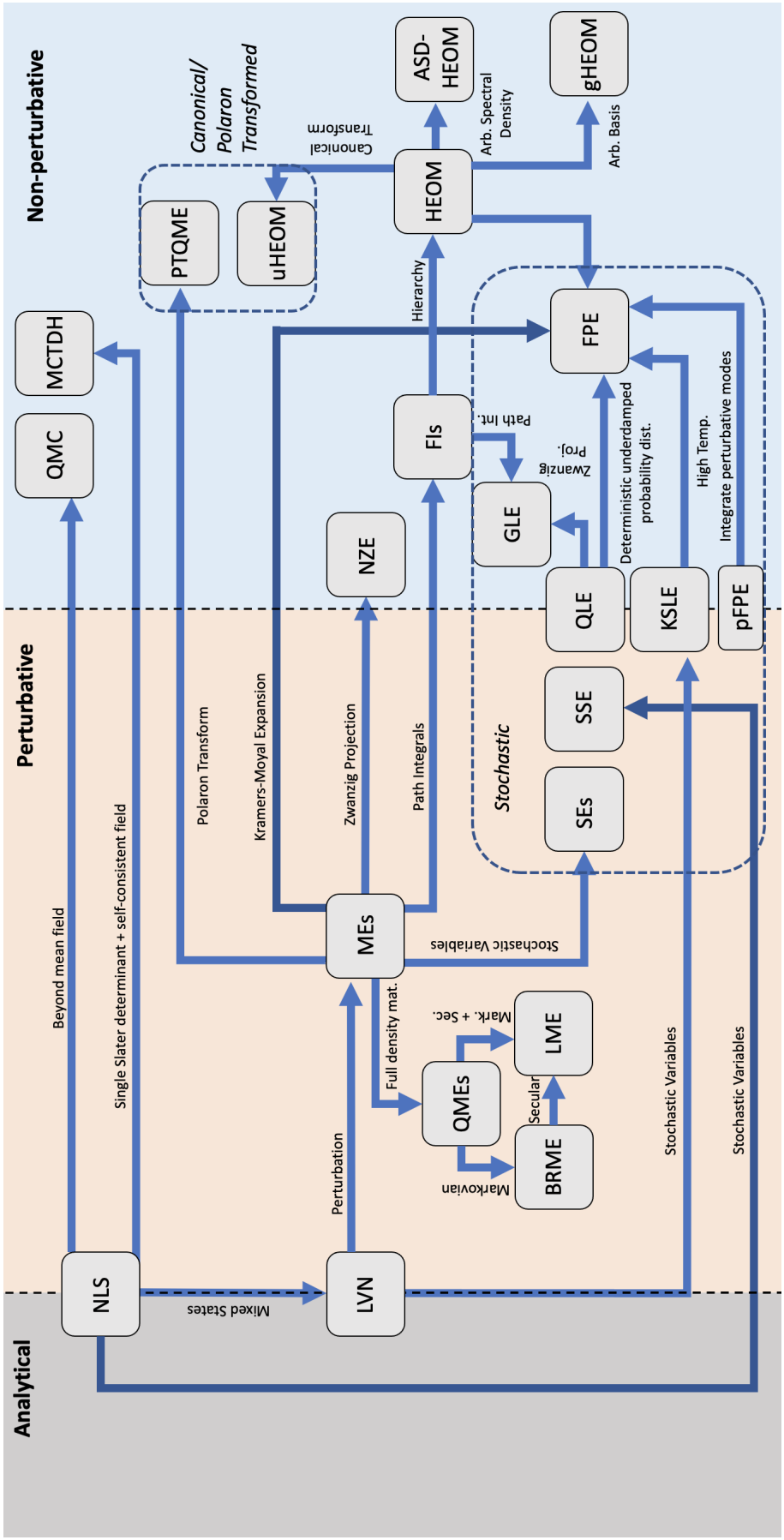

Figure 2.5.1: A flow chart depicting the relationship between a range of equations of motion which are either exact, perturbative, or non-perturbative. These equations are discussed in detail in appendix D. Full acronyms can be found in appendix K.

2.5.4 Hierarchical Equations of Motion

2.5.4.1 Overdamped HEOM

It is clear from these assumptions and approximations that the hierarchical equations of motion are one of the most general techniques which can be employed to model OQSs. Additionally, it is particularly suited to the aim of this project as it facilitates movement of the system-bath boundary in two essential ways. The first is that the Born approximation is unnecessary for HEOM construction: the nature of bathentanglement is crucial to the dynamics upon movement of the system-bath boundary and needs to be accounted for. Secondly, it is not necessary to employ a Markovian approximation which means a full range of non-Markovian feedback can occur during the movement of the system-bath boundary, allowing quantum behaviours dependent on non-Markovianity to emerge. As a result of this, a simplified derivation of the HEOM is performed, with full details in section D, starting from overdamped environments.

The key component of each HEOM derivation is its constituent spectral density and the expansion used to decompose this into individual contributions. The full derivation is considered for the overdamped case and the differences are highlighted in other cases but their full derivation will be omitted and their original source noted. The overdamped hierarchy is derived from an exponential expansion of an overdamped spectral density,

$$J_n^{(\mathrm{O})}(\omega) = \frac{2\eta_n \omega \Lambda_n}{\Lambda_n^2 + \omega^2}, \tag{2.5.16}$$

which is computed through a contour integral.

2.5.4.1.1 System-bath Model

We consider a one-dimensional system coupled to a single bath, with $n = 1$. Consequently, B operators, and η, Λ parameters in the following derivation have no subscript. Any other n subscripts denote Matsubara dimensions. The system of interest is defined by a potential $V_{\mathrm{S}}(\mathrm{q})$ - where q is the position operator as in the non-linear Schrödinger equation - and its mass m. The oscillators in the ensemble have masses $\{m_j\}$, frequencies $\{\omega_j\}$ and coupling constants $\{c_j\}$. The total Hamiltonian,

$$\mathrm{H}_{\mathrm{tot}} = \mathrm{H}_{\mathrm{S}} + \mathrm{H}_{\mathrm{B}} + \mathrm{H}_{\mathrm{SB}}, \tag{2.5.17}$$

where,

$$\mathrm{H}_{\mathrm{S}} = \frac{\mathrm{p}^2}{2m} + V(\mathrm{q}), \tag{2.5.18}$$

$$\mathrm{H_B} = \sum_j \left(\frac{\mathrm{p}_j^2}{2m_j} + \frac{m_j \omega_j \mathrm{x}_j^2}{2} \right), \tag{2.5.19}$$

$$\mathrm{H_{SB}} = -\sum_j c_j \mathrm{x}_j \mathrm{q}, \tag{2.5.20}$$

and $\mathrm{p}, \mathrm{q}, \{\mathrm{p}_j\}, \{\mathrm{x}_j\}$ are the respective momentum and position operators for the system and the bath.

Given this description of the system and bath we can construct the density matrix. For a set of states $\{|\mathrm{q}_i, \mathrm{x}_i\rangle\}$ with corresponding transition probabilities $\{P_i\}$ the density matrix is equivalent to the outer product,

$$\rho(\mathrm{q}, \mathrm{x}) = \sum_i P_i \left|\mathrm{q}_i, \mathrm{x}_i\right\rangle \left\langle \mathrm{q}_i, \mathrm{x}_i\right|. \tag{2.5.21}$$

2.5.4.1.2 Feynman and Vernon Influence Functional

To derive the equations of motion we define the evolution of the density matrix from time zero to a time t using the path integral formalism[4,143]. Introducing the time propagation operators we can find the density matrix at an arbitrary, time, t given the form of the density matrix at time zero,

$$\rho_t(\mathrm{q}, \mathrm{x}) = \exp\left(\frac{i\mathrm{H}(\mathrm{q}, \mathrm{x})t}{\hbar}\right) \rho_0(\mathrm{q}, \mathrm{x}) \exp\left(\frac{-i\mathrm{H}(\mathrm{q}, \mathrm{x})t}{\hbar}\right). \tag{2.5.22}$$

Next we apply the initial condition assumption that the system is, initially, in a factorisable state and that the bath is in thermal equilibrium - but not in equilibrium with the system of interest.

$$\rho_0(\mathrm{q}, \mathrm{x}) = \rho_\mathrm{S}(\mathrm{q}) \rho_\mathrm{B}(\mathrm{x}). \tag{2.5.23}$$

Additionally, we transform into a coherent state basis which is dependent on the creation and annihilation operators for the system modes, $\mathrm{a}_i^\dagger$ and a_i, rather than operators x_j and p_j for environment modes $\{j\}$. This transforms $\mathrm{q}_{\{\cdot\}} \rightarrow \mathrm{Q}_{\{\cdot\}}(\phi, \phi^*)$, where

$$\left|\phi\right\rangle = \exp\left(\sum_i \phi_i \mathrm{a}^\dagger\right) \left|0\right\rangle, \tag{2.5.24}$$

with $|0\rangle$ the system vacuum sate, ϕ_i are complex numbers, and ϕ_i^* their complex conjugates such that

$$\mathrm{a}_i \left|\phi\right\rangle = \phi_i \left|\phi\right\rangle, \tag{2.5.25}$$

$$\left\langle\phi\right| \mathrm{a}_i^\dagger = \left\langle\phi\right| \phi_i^*. \tag{2.5.26}$$

Given this, the reduced density matrix element in path integral form is[143]

$$\rho(\mathrm{Q}_t, \mathrm{Q}'_t, t) = \iint \int_{\mathrm{Q}_0}^{\mathrm{Q}_t} \int_{\mathrm{Q}'_0}^{\mathrm{Q}'_t} \exp(i\mathrm{S}_\mathrm{S}[\mathrm{Q}_t]/\hbar) \exp(-i\mathrm{S}_\mathrm{S}[\mathrm{Q}'_t]/\hbar)\mathcal{F}[\mathrm{Q}_t, \mathrm{Q}'_t]\times \rho_\mathrm{S}(\mathrm{Q}_0, \mathrm{Q}'_0, 0)\ \mathcal{D}[\mathrm{Q}_t]\mathcal{D}[\mathrm{Q}'_t]\mathrm{d}\mathrm{Q}_0\mathrm{d}\mathrm{Q}'_0, \quad (2.5.27)$$

where $\int \mathcal{D}[\mathrm{Q}]$ denotes a Feynman path integral. Here the classical action - in terms of the Lagrangian - for an isolated system is used. Bath effects are contained within the Feynman and Vernon influence functional, $\mathcal{F}$, which is dependent on the overdamped spectral density, (2.2.59). When the influence functional is cast in terms of the thermal fluctuation and dissipation of energy of the system it can be written as,

$$\mathcal{F} = \exp\Bigg(-\frac{i}{\hbar}\int_0^t \int_0^\tau \mathrm{B}^\times(\mathrm{Q}_t, \mathrm{Q}'_t; \tau) \times \Big\{ iL_\mathcal{I}^{(\alpha)}(\tau - \tau')\mathrm{B}^\circ(\mathrm{Q}_t, \mathrm{Q}'_t; \tau) + L_\mathcal{R}^{(\alpha)}(\tau - \tau')\mathrm{B}^\times(\mathrm{Q}_t, \mathrm{Q}'_t; \tau) \Big\}\ \mathrm{d}\tau'\ \mathrm{d}\tau \Bigg), \quad (2.5.28)$$

where

$$\mathrm{B}^\times(\mathrm{Q}_t, \mathrm{Q}'_t; \tau) = \mathrm{B}(\mathrm{Q}_t; \tau) - \mathrm{B}(\mathrm{Q}'_t; \tau), \text{ and} \quad (2.5.29)$$

$$\mathrm{B}^\circ(\mathrm{Q}_t, \mathrm{Q}'_t; \tau) = \mathrm{B}(\mathrm{Q}_t; \tau) + \mathrm{B}(\mathrm{Q}'_t; \tau). \quad (2.5.30)$$

These kernels, $L_\mathcal{R}^{(\alpha)}(t)$ and $L_\mathcal{I}^{(\alpha)}(t)$, which correspond to fluctuations and dissipation respectively, can be expressed in terms of the spectral distribution as,

$$L_\mathcal{R}^{(\alpha)}(t) = \int_0^\infty J(\omega)\cos(\omega t)\mathrm{coth}\left(\frac{\beta\hbar\omega}{2}\right)\mathrm{d}\omega, \quad (2.5.31)$$

$$L_\mathcal{I}^{(\alpha)}(t) = -\int_0^\infty J(\omega)\sin(\omega t)\ \mathrm{d}\omega. \quad (2.5.32)$$

Substitution of the overdamped spectral density generates an integral which can be solved through contour integration. A semicircle in the upper-half plane is chosen and the residue is calculated through the application of Jordan's lemma

$$\oint f(z)\ \mathrm{d}z = 2\pi i \sum \mathrm{Res} = \int_{-\infty}^{\infty} f(z)e^{izT}\ \mathrm{d}z + 0$$

Where Res are the residues of the poles inside the semi-circle C_Γ.

For the complex plane $\omega + i\sigma$ a semicircular contour in the upper half plane $C_\Gamma = \Gamma_1 + \Gamma_2$ is used such that the integral along the real axis can be computed

$$\int_{\Gamma_1} f(\omega)e^{i\omega t}\mathrm{d}\omega = 2\pi i \sum_j \mathrm{Res}(j).$$

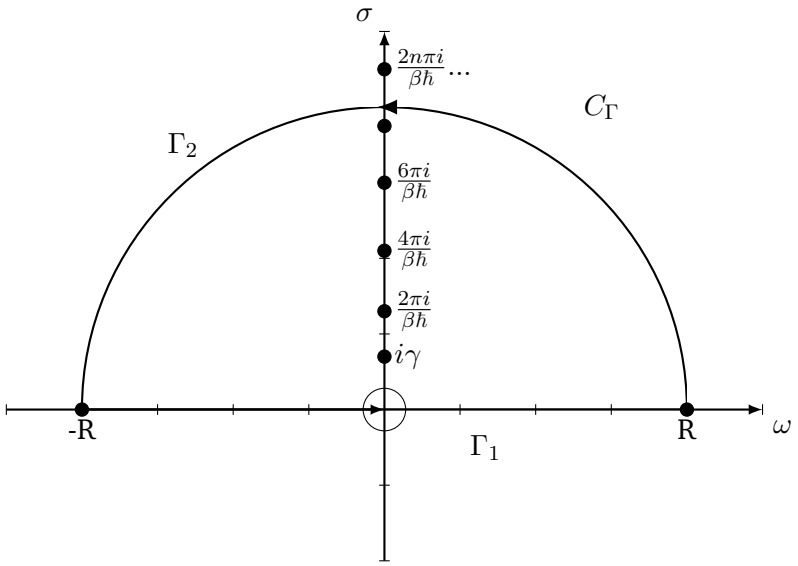

Figure 2.5.2: Complex Semicircle, C_Γ, with an imaginary, temperature independent, pole at $i\gamma$ and then poles at integer multiples of $\frac{2\pi}{\beta\hbar}$ on the imaginary axis which correspond to Matsubara (thermal) frequencies.

This results in the Matsubara decomposition of the spectral density in terms of an exponential basis[k]:

$$d_0 = \eta\Lambda(\cot\left(\frac{\beta\hbar\Lambda}{2}\right) - i), \quad \nu_0 = \Lambda, \tag{2.5.33}$$

$$d_n = \frac{4\eta\Lambda\nu_n\beta\hbar}{(\nu_n\beta\hbar)^2 - (\Lambda\beta\hbar)^2}, \quad \nu_n = \frac{2n\pi}{\beta\hbar}, \tag{2.5.34}$$

such that

$$L^{(\alpha)}_{\text{corr}}(t) = \sum_{n=0}^{\infty} d_n \exp(-\nu_n t). \tag{2.5.35}$$

The resulting form of the correlation function represents a memory-frequency decomposition of the bath correlation. The exponential expansion of bath correlation function dictates the structure of the HEOM being derived[286–288]. These forms of the correlation functions, under the assumption that

$$\nu_n \exp(-\nu_n(\tau - \tau')) \approx \delta(\tau - \tau') \quad \text{when} \quad n \geq K + 1, \tag{2.5.36}$$

[k]For overdamped baths with $n = 1$, Λ_1 is simplified to Λ.

allow the influence functional to be written as

$$\mathcal{F}[\mathrm{Q}_t,\mathrm{Q}'_t] \approx \exp\left(\frac{1}{\hbar^2}\int_0^t \mathrm{B}^\times \exp(-\Lambda\tau')\int_0^{\tau'} \Lambda\theta_{(\mathrm{O})}\exp(\Lambda\tau)\,\mathrm{d}\tau\,\mathrm{d}\tau'\right)\times \prod_{n=1}^{K}\exp\left(+\frac{1}{\hbar^2}\int_0^t \mathrm{B}^\times\exp(-\nu_n\tau')\int_0^{\tau'}\nu_n\psi_n^{(\mathrm{O})}\exp(\nu_n\tau)\,\mathrm{d}\tau\,\mathrm{d}\tau'\right)\times \prod_{n=K+1}^{\infty}\exp\left(\int_0^t\frac{1}{\hbar^2}\mathrm{B}^\times\psi_n^{(\mathrm{O})}\,\mathrm{d}\tau\right), \quad (2.5.37)$$

where

$$\theta_{(\mathrm{O})} = \left(\eta\Lambda\cot\left(\frac{\beta\hbar\Lambda}{2}\right)\mathrm{B}^\times - i\eta\Lambda\mathrm{B}^\circ\right), \quad (2.5.38)$$

$$\psi_n^{(\mathrm{O})} = \mathrm{B}^\times\frac{4\eta\Lambda\nu_n\beta\hbar}{(\nu_n\beta\hbar)^2-(\Lambda\beta\hbar)^2}. \quad (2.5.39)$$

In order to derive the equation of motion, we additionally introduce the equation for the auxiliary density operators (ADOs) as,

$$\rho_{\mathbf{j}}(\phi,\phi^*;t) = \iint\left\{\left(-\frac{i}{\hbar}\int_0^t\exp(-\Lambda(t-\tau))\theta_{(\mathrm{O})}\,\mathrm{d}\tau\right)\right\}^{j_0}\times \prod_{n=1}^{K}\left\{\left(-\frac{i}{\hbar}\int_0^t\exp(-\nu_n(t-\tau))\psi_n^{(\mathrm{O})}\,\mathrm{d}\tau\right)\right\}^{j_n}\times \exp\left(\frac{i\mathrm{S}_{\mathrm{S}}[\mathrm{Q}_t]}{\hbar}\right)\mathcal{F}[\mathrm{Q}_t,\mathrm{Q}'_t]\exp\left(\frac{-i\mathrm{S}_{\mathrm{S}}[\mathrm{Q}'_t]}{\hbar}\right)\mathcal{D}[\mathrm{Q}'_t]\,\mathcal{D}[\mathrm{Q}_t], \quad (2.5.40)$$

then we can construct the equation of motion by differentiating this equation and substituting for the influence functional. This can be extended to a general case of N_{B} baths, as shown for underdamped hierarchies. [l]

$$\frac{\partial\rho_{\mathbf{j}}}{\partial t} = -\left\{\frac{i}{\hbar}\mathrm{H}^\times + \sum_{n=0}^{K}j_n\nu_n - \frac{1}{\hbar^2}\sum_{n=K+1}^{\infty}\exp\left(\mathrm{B}^\times\psi_n^{(\mathrm{O})}\right) - \frac{\Xi_{(\mathrm{O})}}{\hbar^2}\right\}\rho_{\mathbf{j}} - \frac{i}{\hbar}\left\{d_n\mathrm{B}\rho_{j_n}^- - d_n^*\mathrm{B}\rho_{j_n}^-\right\} - \frac{i}{\hbar}\mathrm{B}^\times\rho_{j_n}^+, \quad (2.5.41)$$

where

$$\Xi_{(\mathrm{O})} = \frac{\eta}{\beta}\left\{1-\beta\Lambda\cot\left(\frac{\beta\hbar\Lambda}{2}\right)\right\}\mathrm{B}^\times\mathrm{B}^\times, \quad (2.5.42)$$

and the associated terminator is

$$\frac{\partial\rho_{\mathbf{j}}}{\partial t} \approx -\left\{\frac{i}{\hbar}\mathrm{H}^\times - \frac{1}{\hbar^2}\sum_{n=K+1}^{\infty}\exp\left(\mathrm{B}^\times\psi_n^{(\mathrm{O})}\right) - \frac{\Xi_{(\mathrm{O})}}{\hbar^2}\right\}\rho_{\mathbf{j}}, \quad (2.5.43)$$

[l] Reintroduction of the number of baths means subscripts n denote bath number and Matsubara dimensions move to l. Additionally, each term will be additionally summed from 1 to N_{B} meaning that the bounds for the termination criterion becomes $\frac{\max(w_{n0})}{\min(\nu_{nl})}$.

valid for integers $\mathbf{j} = (j_0, \ldots, j_K)$, with

$$\sum_{n=0}^{K} j_n \gg \frac{\omega_0}{\min(\nu_n)}, \quad \Longrightarrow \quad \Gamma_{\max} = 10\ \Lambda. \tag{2.5.44}$$

This criterion terminates each Matsubara axis in an identical manner resulting in hierarchies of self-similar volumes. These volumes are discussed further in section 3.3. Dependent on the necessary level of termination this equation can be simplified down to purely the Markovian free propagation of the system (red), but here is shown in full generality. Throughout this thesis, unless stated otherwise, the convergence criterion is set to $\Gamma_{\max} = 10\ \max(\Lambda)$, which in this instance with $n = 1$ is 10Λ. The first term (red) within the generated HEOM, equation (2.5.41), describes the Markovian free propagation of the system, and the second term (blue) introduces the impact on this propagation of integer multiples of Matsubara frequencies corresponding to interaction with bath phonons. The final two terms (blue) proportional to $\rho_{\mathbf{j}}$ are the low temperature correction of the free propagation and a double commutator of the bath operator which introduce higher order bath interactions, a square coupling, to account for the introduction of the cutoff K. This term was derived by Ishizaki and Tanimura in order to reduce the number of Matsubara frequencies required under strong coupling to reach convergence[150]. By propagating a series of ADOs, representing different arrangements of bath phonons, the HEOM accounts for a history of interactions such that non-Markovian effects are automatically included. The ADOs are interconnected via ADO raising and lowering terms which are denoted by $\mathbf{j}^{\pm} = (j_0, \ldots, j_k \pm 1, \ldots, j_K)$ vectors. The first $\rho^{-}_{\{\cdot\}}$ dependent term (term five - cyan) in the HEOM, equation (2.5.41), is the first raising term. The action of $\frac{i}{\hbar} d_n \mathrm{B}$, and its conjugate, is to destroy bath phonons, of coupling amplitude d_n, as they are absorbed by the system. This corresponds to an increase of ADO tier resulting in a 'raising' of the ADO. Subsequently, this process is associated with thermal fluctuations and the real part of the correlation function because of its temperature dependence. The final term (orange), dependent on $\rho^{+}_{\{\cdot\}}$, is the corresponding lowering term. The action of $\frac{i}{\hbar}\mathrm{B}^{\times}$ is to demolish the system states corresponding to the creation of bath phonons as they are emitted from the system into the bath. Destruction of system states in this manner are a consequence of the imaginary part of the correlation function associated with system dissipation.

An example overdamped hierarchy is presented in figure 2.5.3, where ADOs are depicted as spheres in a lattice structure, with each Matsubara frequency given its own dimension. The full structure of such hierarchies is discussed further in section 2.5.5.1. The first ADO beyond $\Gamma_{\max}$ in each axis is assigned as a terminator such that the overall hierarchy defines a sealed volume, within which non-Markovian memory effects are fully accounted for. Each information

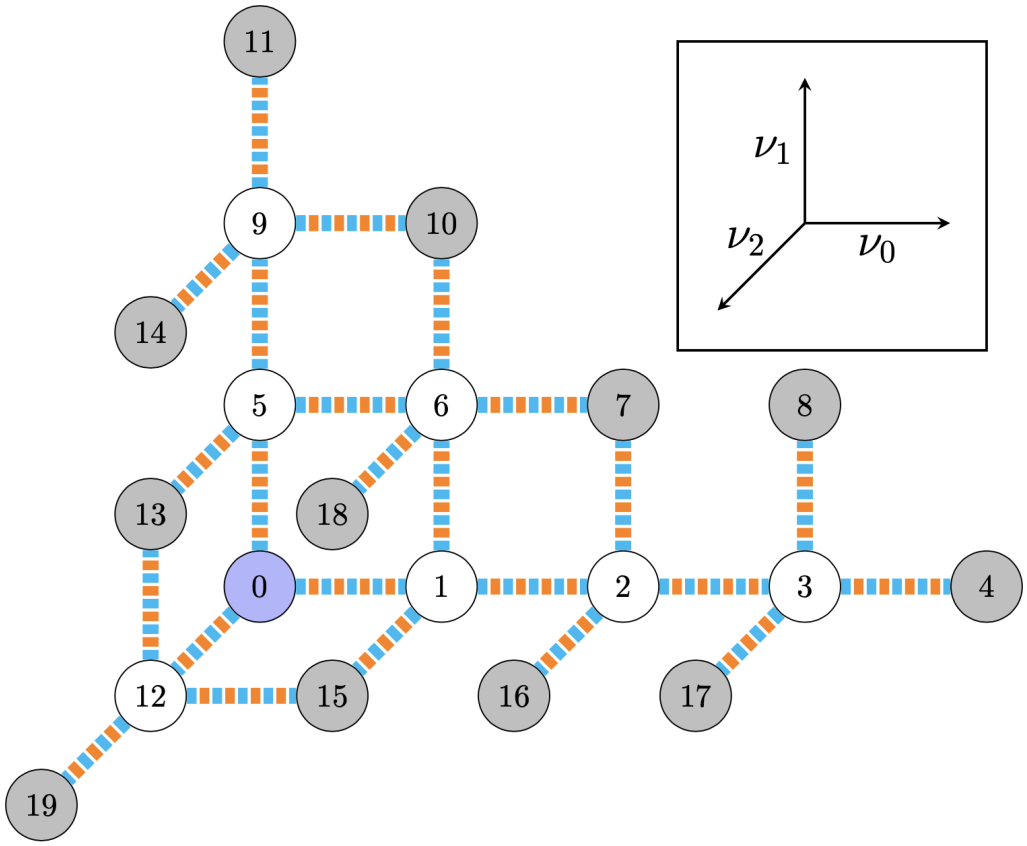

Figure 2.5.3: Hierarchy diagram for a single overdamped bath, such that there are three Matsubara dimensions. The longest axis is the temperature independent Matsubara frequency associated with an overdamped bath. Each sphere represents a density operator where the reduced density matrix of the system is blue, normal ADOs are white and terminating ADOs are grey. Each ADO is connected by a coloured line which matches terms in equation (2.5.41) corresponding to their origin.

channel, or raising/lowering event, is colour coded to match the terms in the overdamped HEOM, (2.5.41), to depict bath phonon creation and annihilation.

2.5.4.2 Underdamped HEOM

Similarly it is possible to generate an EOM from underdamped spectral densities

$$J_n^{(\mathrm{U})}(\omega) = \frac{2\eta_n\gamma_n\omega_{0n}^2\omega}{(\omega_{0n}^2-\omega^2)^2-(\gamma_n\omega)^2}. \tag{2.5.45}$$

The exponential expansion for this spectral density can be constructed in a manner analogous to the method performed for the overdamped spectral density, with the caveat that the Matsubara poles are now complex rather than purely imaginary. This results in a translation of the contour. In addition, this form of spectral density is associated with the canonical transform, discussed in detail in section 2.2.2.2, resulting in the system mode, ω_{0n}, being subsumed into

the environment degrees of freedom. As discussed, this is the primary method of moving the system-bath boundary which is discussed in detail in this thesis, and it involves obscuring the distinction between the bath and system degrees of freedom. This has a profound impact on quantum information and correlations, discussed in chapters 3, and 4.

The associated underdamped fluctuation and dissipation kernels are,

$$L^{(\alpha)}_{\mathcal{R},n} = \frac{\hbar\eta_n\omega_{0n}^2}{2i\zeta_n}\Bigg\{\exp\Big(-\Big(\frac{\gamma}{2}-i\zeta_n\Big)t\Big)-\exp\Big(-\Big(\frac{\gamma}{2}+i\zeta_n\Big)t\Big)\Bigg\}, \tag{2.5.46}$$

$$\begin{aligned} L^{(\alpha)}_{\mathcal{I},n} = &\frac{\hbar\eta_n\omega_{0n}^2}{2\zeta_n}\exp\Big(-\Big(\frac{\gamma}{2}-i\zeta_n\Big)t\Big)\coth\left(\frac{\hbar\beta}{2}\Big(\zeta_n+i\frac{\gamma_n}{2}\Big)\right)\\ &-\frac{\hbar\eta_n\omega_{0n}^2}{2\zeta_n}\exp\Big(-\Big(\frac{\gamma}{2}+i\zeta_n\Big)t\Big)\coth\left(\frac{\hbar\beta}{2}\Big(-\zeta_n+i\frac{\gamma_n}{2}\Big)\right)\\ &-\frac{4\eta_n\gamma_n\omega_{0n}^2}{\hbar\beta}\sum_{k=1}^{\infty}\frac{\nu_k\exp(-\nu_k t)}{(\omega_{0n}^2+\nu_k^2)^2-(\gamma_n\nu_k)^2}, \end{aligned} \tag{2.5.47}$$

where $\zeta_n = \sqrt{\omega_{n0}^2-\left(\frac{\gamma_n}{2}\right)^2}$ when $\gamma_n < 2\omega_{0n}$ and $\nu_k = \frac{2\pi k}{\hbar\beta}$ are the Matsubara frequencies. The derivation for the underdamped kernels is equivalent to that of the overdamped spectral density, however, introduction of the system mode splits the single temperature independent Matsubara frequency into two: positive and negative combinations of the intrinsic damping parameter, $\frac{\gamma_n}{2}$, and $i\zeta_n$. This means that following the same derivation leads to two terms in $L^{(\alpha)}_{\mathcal{R},n}$ rather than one, and three in $L^{(\alpha)}_{\mathcal{I},n}$ rather than two, due to the split temperature independent cases.

This is then written as an expansion in the exponential basis with Matsubara

frequencies and coefficients, ν_{nl} and d_{nl},

$$\nu_{n0} = \frac{\gamma_n}{2} - i\zeta_n, \tag{2.5.48}$$

$$\nu_{n1} = \frac{\gamma_n}{2} + i\zeta_n, \tag{2.5.49}$$

$$\nu_{nl} = \frac{2\pi(l-1)}{\hbar\beta}, \tag{2.5.50}$$

$$d_{n0} = \frac{\hbar\eta_n\omega_{0n}^2}{2\zeta_n}\left\{\coth\left(\frac{\hbar\beta}{2}\left(\zeta_n + i\frac{\gamma_n}{2}\right)\right) - 1\right\}, \tag{2.5.51}$$

$$d_{n1} = -\frac{\hbar\eta_n\omega_{0n}^2}{2\zeta_n}\left\{\coth\left(\frac{\hbar\beta}{2}\left(-\zeta_n + i\frac{\gamma_n}{2}\right)\right) - 1\right\}, \tag{2.5.52}$$

$$d_{nl} = -\frac{4\eta_n\gamma_n\omega_{0n}^2}{\hbar\beta}\frac{\nu_{nl}}{(\omega_{0n}^2 + \nu_{nl}^2)^2 - (\gamma_n\nu_{nl})^2}, \tag{2.5.53}$$

such that

$$L^{(\alpha)}_{\mathrm{corr},n}(t) = \sum_{l=0}^{\infty} d_{nl}\exp(-\nu_{nl}t). \tag{2.5.54}$$

The EOM for the ADOs of this expansion is then[1],

$$\begin{aligned}\frac{\partial\rho_{\mathbf{j}}}{\partial t} = -\Bigg(&\frac{i}{\hbar}\mathrm{H}^{\times} + \sum_{n=1}^{N_\mathrm{B}}\sum_{l=0}^{K} j_{nl}\nu_{nl} - \sum_{n=1}^{N_\mathrm{B}}\sum_{l=K+1}^{\infty}\mathrm{B}_n^{\times}\psi_{nl}^{(\mathrm{U})}\Bigg)\rho_{\mathbf{j}} \\ &+ \sum_{n=1}^{N_\mathrm{B}}\sum_{l=0}^{K}\mathrm{B}_n^{\times}\rho^{+}_{j_{nl}} + \sum_{n=1}^{N_\mathrm{B}} j_{n0}\Theta_n^{-}\rho^{-}_{j_{n0}} + \sum_{n=1}^{N_\mathrm{B}} j_{n1}\Theta_n^{+}\rho^{-}_{j_{n1}} \\ &+ \sum_{n=1}^{N_\mathrm{B}}\sum_{l=2}^{K} j_{nl}\nu_{nl}\psi_{nl}^{(\mathrm{U})}\rho^{-}_{j_{nl}},\end{aligned} \tag{2.5.55}$$

where

$$\psi_{nl}^{(\mathrm{U})} = \frac{4\eta_n}{\hbar\beta}\frac{\gamma_n\omega_{0n}^2}{(\omega_{0n}^2 + \nu_{nl}^2)^2 - (\gamma_n\nu_{nl})^2}\mathrm{B}_n^{\times}, \tag{2.5.56}$$

$$\Theta_n^{\pm} = \frac{\eta_n\omega_{0n}^2}{2\zeta_n}\left\{\mp\mathrm{B}_n^{\circ} \pm \coth\left(\frac{\hbar\beta}{2}\left(\mp\zeta_n + i\frac{\gamma_n}{2}\right)\right)\mathrm{B}_n\right\}, \tag{2.5.57}$$

and $\mathrm{B}_n^{\times}\rho = [\mathrm{B}_n, \rho]$ denotes the commutator of the bath coupling operator and the density matrix and $\mathrm{B}_n^{\circ}\rho = \{\mathrm{B}_n, \rho\}$ the corresponding anti-commutator. The associated terminator for this hierarchy is[164]

$$\frac{\partial\rho_{\mathbf{j}}}{\partial t} \approx -\left(\frac{i}{\hbar}\mathrm{H}^{\times} + i\sum_{n=1}^{N_\mathrm{B}}(j_{n0} - j_{n1})\zeta_n - \sum_{n=1}^{N_\mathrm{B}}\sum_{l=K+1}^{\infty}\mathrm{B}_n^{\times}\psi_{nl}^{(\mathrm{U})}\right)\rho_{\mathbf{j}}, \tag{2.5.58}$$

valid for integers $\mathbf{j} = (j_{n0}, \ldots, j_{N_\mathrm{B}K})$, with

$$\sum_{n=1}^{N_\mathrm{B}}\sum_{l=0}^{M} j_{nl} > \frac{\max(\omega_{n0})}{\mathcal{R}(\min(\nu_{nl}))}, \quad \Longrightarrow \quad \Gamma_{\max} = 10\,\max(\gamma_n). \tag{2.5.59}$$

In addition, computationally the sum to infinity is truncated with a sufficiently high value with respect to the criterion $\Gamma_{\max}$.

Equivalent to the overdamped hierarchy, the ADOs are characterised by the $N_{\mathrm{B}}(K+1)$-dimensional vectors $\mathbf{j}$ and $\mathbf{j}^{\pm}$, with the terms of equation (2.5.55) interpreted in terms of the creation and annihilation of bath phonons, but where the complex Matsubara frequencies have split the temperature independent term in two such that there are now additional terms involving $\Theta_n^{\pm}$.

An example underdamped hierarchy is presented in figure 2.5.4, again demonstrating a sealed volume and showing annihilation and creation with colours matching equation (2.5.55). The full structure of such hierarchies is discussed further in section 2.5.5.1. It is worth noting, the splitting of the temperature independent Matsubara frequency into ν_{n0} and ν_{n1} results in the first two axes having equal depth, such that the underdamped HEOM involves many more ADOs than the overdamped case, increasing computational complexity.

The underdamped spectral density, equation (2.5.45), reproduces the Drude form on increasing the damping to the overdamped limit, when $\gamma_n \gg \omega_{0n}$, also requiring $\zeta_n = i\sqrt{\left(\frac{\gamma_n}{2}\right)^2 - \omega_{0n}^2}$. However, due to a singularity in the exponential basis which is the foundation of these derivations, $\omega_{0n} \approx \gamma_n$, this HEOM is insufficiently stable and the additional computational requirements of the underdamped HEOM means the overdamped HEOM, equation (2.5.41), is preferable for overdamped environments. This weakness in basis is most evident from the divergent limit of vanishing ζ_n in the temperature independent Matsubara terms, $\lim_{\zeta_n \to 0} d_{n0} = \lim_{\zeta_n \to 0} d_{n1} = \infty$. This flaw is addressed by Ikeda and Scholes[139] through the generalised HEOM discussed in section 2.5.4.4.

2.5.4.3 Arbitrary Spectral Density (ASD) HEOM

As discussed in section 2.2.2.2, the power of structured spectral densities is that they can be used to model processes which are strongly non-Markovian, or which have had system modes subsumed into them by the canonical transform. Therefore, it stands to reason that a hierarchy which is derived from a purely general spectral density would allow for modelling a broad range of physical regimes. Tanimura considers this possibility is one of his original articles[149], where the HEOM becomes a more general integro-differential equation of

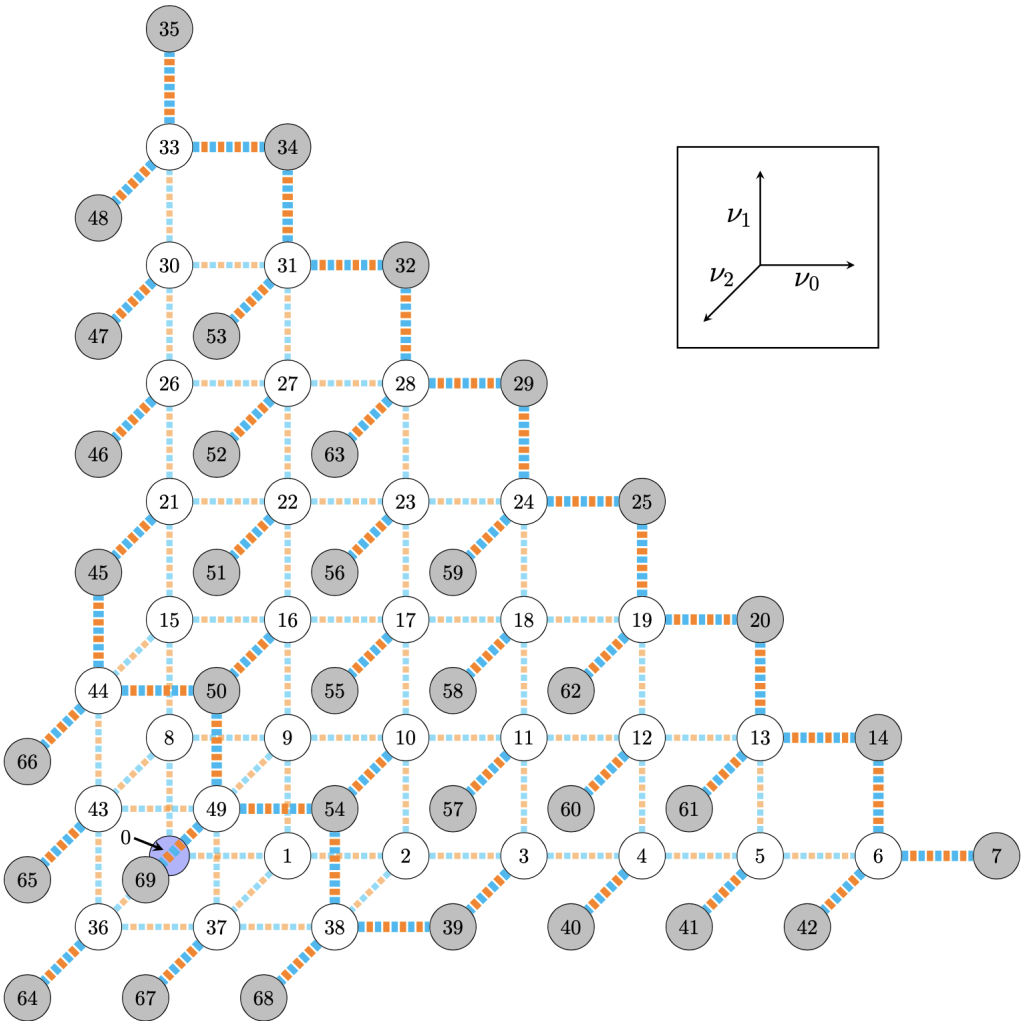

Figure 2.5.4: Hierarchy diagram for a single underdamped bath, such that there are three Matsubara dimensions. The longest two axes ($\nu_0,\ \nu_1$) are the temperature independent Matsubara frequency associated with an underdamped bath. Each sphere represents a density operator where the reduced density matrix of the system is blue, normal ADOs are white and terminating ADOs are grey. Each ADO is connected by a coloured line which matches terms in equation (2.5.55) corresponding to their origin.

motion,

$$\begin{aligned}\frac{\partial}{\partial t}\rho_{\mathrm{S}}(t;\omega_1,\omega_2,\ldots,\omega_m) = &-\left(\frac{i}{\hbar}\mathrm{H}^{\times} + i\sum_{j=1}^{M}\omega_j\right)\rho_{\mathrm{S}}(t;\omega_1,\omega_2,\ldots,\omega_m)\\ &- i\int_{-\infty}^{\infty}\mathrm{B}^{\times}\rho_{\mathrm{S}}(t;\omega_1,\omega_2,\ldots,\omega_{m+1})\,\mathrm{d}\omega_{m+1}\\ &- i\sum_{k=1}^{m-1}\Theta(\omega_k)\rho_{\mathrm{S}}(t;\omega_1,\omega_2,\ldots,\omega_{k-1},\omega_{k+1},\ldots,\omega_m)\\ &- i\Theta(\omega_m)\rho_{\mathrm{S}}(t;\omega_1,\omega_2,\ldots,\omega_{m-1}),\end{aligned} \tag{2.5.60}$$

where,

$$\Theta(\omega) = J(\omega)\left(\coth\Big(\frac{\beta\hbar\omega}{2}\Big)\mathrm{B}^{\times} + \mathrm{B}^{\circ}\right), \tag{2.5.61}$$

written in terms of the total spectral density, $J(\omega) = \sum_{n=1}^{N_\mathrm{B}} J_n(\omega)$, and bath coupling operator, $\mathrm{B} = \sum_{n=1}^{N_\mathrm{B}} \mathrm{B}_n$. The auxiliary equations for $\rho_\mathrm{S}(t;\omega_1,\omega_2,\ldots,\omega_m)$ represent simultaneous evolution of the system in the presence of m bath phonons with associated frequencies ω_m. Just as in the previous HEOMs there are cyan lowering terms, and an orange ADO raising term, but here because of the generality of the spectral density the raising term involves an integral over the phonon frequency ω_{m+1}.

While it is possible to reach this equation using a derivation analogous to the method presented in appendix D.1.10, the general spectral density makes it impossible to calculate a specific contour integral to expand the Matsubara components. For this reason Tanimura[149] presents an elegant alternative involving multiplication of continued fraction forms of the Laplace transform. The Laplace transform, discussed in appendix A, is very similar to the Fourier transform and the equation used for the contour integration. It takes a function of time and moves it into the complex frequency domain with the added effect of transforming ordinary differential equations into algebraic equations and convolutions of functions into products. Within the ASD-HEOM this allows the system-bath entanglement, due to the arbitrary spectral density, to be expressed in resolvent form through products of operators as part of a continued fraction:

$$\rho_\mathrm{S}[s] = \frac{1}{s + \frac{i}{\hbar}\mathrm{H}^{\times} + \int \mathrm{B}^{\times} \frac{\Theta(\nu_1)}{s+i\nu_1+\frac{i}{\hbar}\mathrm{H}^{\times}+\int \mathrm{B}^{\times}\frac{\Theta(\nu_2)}{s+i\nu_2+\ldots}\,\mathrm{d}\nu_2}\,\mathrm{d}\nu_1}\rho_\mathrm{S}(t_0), \tag{2.5.62}$$

where $\mathcal{L}_\mathrm{Lap}\{t\} = s$, is the Laplace (Lap) transform of t.

This generalisation of spectral influence on the HEOM evolution nicely demonstrates the incorporation of non-Markovian effects. Interaction of the system and bath, through $i\int_{-\infty}^{\infty}\mathrm{B}^{\times}\{\cdot\}\mathrm{d}\omega_{m+1}$, creates bath phonons which are propagated alongside the reduced system within the ADOs. This accounts for the transfer of information, along a quantum channel, from the system to the bath where it is stored within the environment degrees of freedom. Then, dependent on the timescales of bath relaxation relative to the system, the behaviour is either a local or global evolution. When the environment relaxation timescale is rapid compared to the system, the phonons will dissipate throughout the bath degrees of freedom and will not influence the system dynamics again, resulting in local, Markovian, evolution. Alternatively, if the timescales are commensurate, the phonons can be reabsorbed by the system, through the action of $i\Theta(\omega)$, creating a feedback of information and linking the current state with past auxiliaries. This produces a global, non-Markovian,

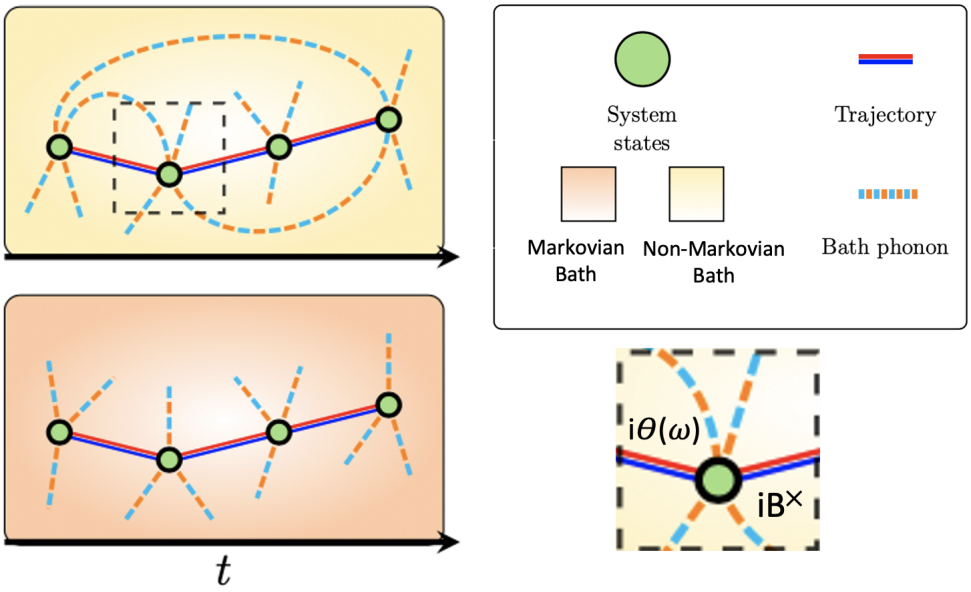

Figure 2.5.5: Non-Markovian vs. Markovian evolution demonstrating global or local behaviour for the ASD-HEOM. The colours in the figure match those in the EOMs.

evolution. Both Markovian and non-Markovian evolutions are depicted in figure 2.5.5. In this way, the HEOM accounts for all possible sequences of interactions and the creation and annihilation of bath phonons of any frequency in any order, accurately modelling the dynamics of the system in a broad range of conditions.

However, despite the power of being able to create models which require highly structured, non-Markovian, environments this method suffers a pair of drawbacks. The first is that it is incredibly costly to implement computationally because of the large dependence on phonon frequencies. Discretising the spectral density to W frequencies, the mth layer involves W^m auxiliaries, each with dimensions of the reduced density operator, which itself is large in the case of the vibronic dimers discussed in section 2.2.1.3. The other drawback is that, despite the increased number of physical regimes accessible with an arbitrary spectral density, it does not circumvent flaws in the basis functions. As discussed in the section on the underdamped HEOM, 2.5.4.2, the exponential basis is highly sensitive to the bath damping strength relative to the system mode frequency especially in the region of critical damping. The divergence of the Matsubara frequencies in these cases have not been addressed by the arbitrary choice of spectral density which means that it addresses niche, highly structured, regimes within the strongly underdamped limit. This is demonstrated in the work in appendix F, where the ASD-HEOM is employed, and this flaw is rectified by Ikeda and Scholes[139].

2.5.4.4 Generalised HEOM

The generalised HEOM, denoted gHEOM[139], addresses the flaw with the basis functions, crucial to previous HEOM derivations, by including treatment of non-exponential correlation functions. This addition means that a full range of damping strengths, including critical damping, can be modelled. This derivation makes use of the cumulant expansion technique, which was discussed in section 2.2.2.2.1, and as such does not directly follow the steps discussed in appendix D.1.10. A full description of the current derivation is beyond the scope of this thesis, but it is summarised for completeness.

A set of K time dependent basis functions $\phi^{(\mathrm{g})}$ are generated in order to produce symmetrised and anti-symmetrised correlation functions from linear combinations of this basis and the delta function:

$$\mathcal{S}(t) = \sum_{lk} \sigma_l s_{lk} \phi_k^{(\mathrm{g})}(t) + S_\delta \cdot 2\delta(t), \tag{2.5.63}$$

$$\mathcal{A}(t) = \sum_{lk} \sigma_l a_{jk} \phi_k^{(\mathrm{g})}(t), \tag{2.5.64}$$

where σ_l, s_{lk}, and a_{lk} are constants dependent on the system parameters. These correlation functions are equivalent to the fluctuation and dissipation kernels, $\mathcal{S}(t) = L_{\mathcal{R}}^{(\alpha)}(t)$, and $\mathcal{A}(t) = L_{\mathcal{I}}^{(\alpha)}(t)$, equation (2.2.53). With these substitutions the influence functional, equivalent to (D.1.206), can be expressed in terms of cumulants as,

$$\mathcal{F} = \exp\left(\int_{t_0}^{t} i\mathrm{B}^{\times} \int_{t_0}^{s} \left(\frac{i}{\hbar}\mathcal{S}(s-u)\mathrm{B}^{\times}(u) - \frac{1}{\hbar}\mathcal{A}(s-u)\mathrm{B}^{\circ}(u) \right) \mathrm{d}u \, \mathrm{d}s \right), \tag{2.5.65}$$

$$= \exp\left(\int_{t_0}^{t} -\Xi^{(\mathrm{g})}(s) + \sum_j \phi_l^{(\mathrm{g})}(s \int_{t_0}^{s} \Theta_l^{(\mathrm{g})})(s,u) \, \mathrm{d}u \, \mathrm{d}s \right), \tag{2.5.66}$$

where

$$\Xi^{(\mathrm{g})}(s) = -S_\delta \left(\frac{i\sigma_l}{\hbar}\mathrm{B}^{\times}(s) \right)^2, \tag{2.5.67}$$

$$\Theta_l^{(\mathrm{g})}(t,s) = \sum_k \frac{i}{\hbar}\sigma_l s_{lk} \phi_k^{(\mathrm{g})}(t-s)\mathrm{B}^{\times}(s) - \frac{1}{\hbar} a_{lk} \phi_k^{(\mathrm{g})}(t-s)\mathrm{B}^{\circ}(s). \tag{2.5.68}$$

Introduction of additional terms into $\Theta_l^{(\mathrm{g})}(t,s)$, which act as the ADO lowering operator, correspond to additional non-Markovian corrections which link auxiliaries with the same number of phonon interactions. Differentiation of the subsequent equation for the auxiliary density matrix elements results in,

$$\frac{\partial \rho_{\mathbf{j}}}{\partial t} = -\left(\frac{i}{\hbar}\mathrm{H}^{\times} + \Xi^{(\mathrm{g})} \right) \rho_{\mathbf{j}} - \sum_{l,k} n_l \gamma_{lk} \rho_{j_{l-1,k+1}} - \sum_k \frac{i\sigma_k}{\hbar}\mathrm{B}_k^{\times} \rho_{j_{k+1}} - \sum_k n_k \Theta_k^{(\mathrm{g})} \rho_{j_{k-1}}, \tag{2.5.69}$$

in the Schrödinger picture. This equation is terminated in a similar fashion to previous EOMs through,

$$\frac{\partial \rho_{\mathbf{j}}}{\partial t} \approx -\Big(\frac{i}{\hbar}\mathrm{H}^{\times} + \Xi^{(\mathrm{g})}\Big)\rho_{\mathbf{j}}, \tag{2.5.70}$$

but with a considerably simplified Markovianity criterion[139]

$$\sum_{k} n_k > \Gamma_{\max}. \tag{2.5.71}$$

As before, the red term is the Markovian free propagation of the system, the first blue term is a Markovian correction containing a double commutator, the second blue term is the introduction of bath phonons as a consequence of the basis set $\phi^{(\mathrm{g})}$, the orange term is the associated ADO raising, and the cyan term is the associated ADO lowering term.

As mentioned, because of the extension of the basis to include a full range of damping strengths, the coupling between the ADOs is more complex than for previous cases. There are additional links between processes involving one phonon from different Matsubara dimensions, referred to as *tier* one in each axis which is discussed in section 3.3, which accounts for all sources of non-Markovian feedback. This is shown in figure 2.5.6 with a general gHEOM hierarchy diagram, the structure of which is discussed further in section 2.5.5.1.

2.5.4.5 Lorentz-Drude Undamped Oscillator (LDUO) HEOM

Finally, a new derivation specific to the aims of this thesis is considered. In order to demonstrate the changes to the open quantum system during the movement of the system-bath boundary a hierarchy with two components must be generated in a manner equivalent to the work of Tanimura[157]. Here, as discussed in Humphries et al.[2], the addition of the overdamped and underdamped spectral densities as part of the canonical transform results in intrinsic canonical damping from the underdamped modes which are not present in the vibration when in positional coordinates. This originates from the canonical transform which moves a pure vibrational system mode into the environment degrees of freedom as an underdamped mode.

As outlined in chapter 5, we consider a one-dimensional system coupled to a bath of N_{B} harmonic oscillators, with microscopic continuous position coordinate operator q with particle mass m, ensemble oscillator operator x, masses $\{m_j\}$, frequencies $\{\omega_j\}$ and coupling constants $\{c_j\}$, in a manner equivalent to the overdamped HEOM. We also continue by applying the approximation that the system is initially uncorrelated, however, from here the

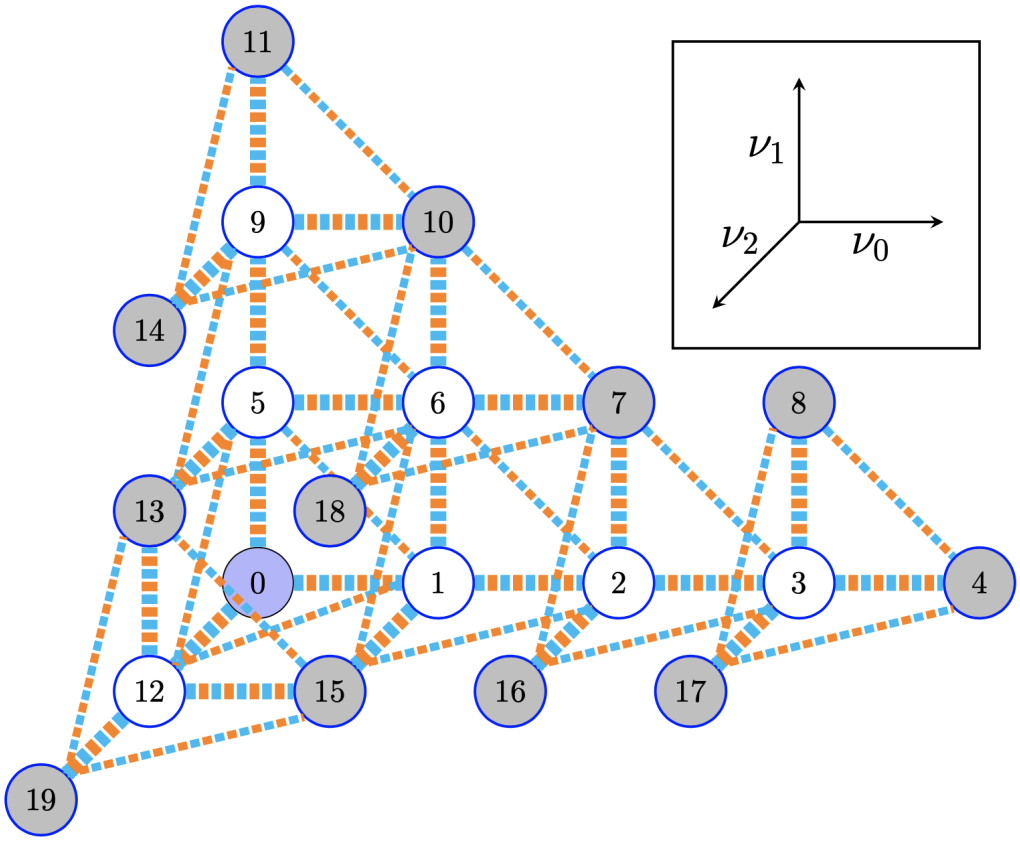

Figure 2.5.6: Hierarchy diagram for the gHEOM. Each sphere represents a density operator where the reduced density matrix of the system is blue, normal ADOs are white and terminating ADOs are grey. Each ADO is connected by a coloured line which matches terms in equation (2.5.69) corresponding to their origin.

treatments diverge. The reduced density matrix element expressed in path integral form, for an EOM which has multiple baths and multiple spectral densities[143] such that the total spectral density takes the form J_n. The environment modes are treated as overdamped through the Lorentz-Drude spectral density,

$$J_{\mathrm{LD}}(\omega) = \frac{2\eta_{\mathrm{LD}}\omega\Lambda_{\mathrm{LD}}}{\omega^2 + \Lambda_{\mathrm{LD}}^2}, \tag{2.5.72}$$

and the subsumed intramolecular vibration is treated as a pure, undamped oscillation through

$$J_{\mathrm{UO}} = \frac{1}{2}S_{\mathrm{UO}}^{\mathrm{HR}}\omega\left(\delta(\omega-\omega_{\mathrm{UO}}) + \delta(\omega+\omega_{\mathrm{UO}})\right), \text{ or } \quad J_{\mathrm{UO}} = S_{\mathrm{UO}}^{\mathrm{HR}}\omega_{\mathrm{UO}}\delta(\omega-\omega_{\mathrm{UO}}), \tag{2.5.73}$$

with $S_{\mathrm{UO}}^{\mathrm{HR}} = \lambda_{\mathrm{UO}}/\omega_{\mathrm{UO}}$, and the Huang-Rhys factor which is a measure of the strength of the electronic and vibrational coupling[289]. The omission of the factor ω_{UO} relative to Seibt and Mancal ensures that the spectral density is coupled to the system with a magnitude equivalent to only the undamped coupling strength rather than being simultaneously dependent on the magnitude of vibrational mode. The individual bath contributions are

decomposed through contour integration which leads to poles at the Matsubara frequencies, discussed in section 2.5.5.1. The process of deriving this hierarchy is summarised graphically in figure 2.5.7, and shown in full in appendix D.

Following the process outlined in figure 2.5.7 results in the LDUO-HEOM, equation (5.1.27) which is repeated here,

$$\begin{aligned}\frac{\partial}{\partial t}\rho^{(m,l_k)}_{j_1\ldots j_K} = &\left(-\frac{i}{\hbar}\mathrm{H}^{\times}_{\mathrm{S}} - \sum_k (l_k\gamma_k + m\Lambda_{\mathrm{LD}}) - \sum_{n=1}^{K} j_n\nu_n + \sum_{n=K+1}^{\infty}\mathrm{B}^{\times}\Psi_n\right)\rho^{(m,l_k)}_{j_1\ldots j_K} - \\ &\sum_k l_k\Theta_k\rho^{(m,l_k-1)}_{j_1\ldots j_K} - m\Lambda_{\mathrm{LD}}\vartheta\rho^{(m-1,l_k)}_{j_1\ldots j_K} - \sum_{n=1}^{K} j_n\nu_n\Psi_n\rho^{(m,l_k)}_{j_1\ldots j_{n-1}\ldots j_K} - \\ &\left(\mathrm{B}^{\times}\rho^{(m+1,l_k)}_{j_1\ldots j_K} + \sum_k \mathrm{B}^{\times}_k\rho^{(m,l_k+1)}_{j_1\ldots j_K}\right) - \sum_{n=1}^{K}\mathrm{B}^{\times}\rho^{(m,l_k)}_{j_1\ldots j_{n+1}\ldots j_K}. \quad (2.5.74)\end{aligned}$$

This HEOM, by the nature of the undamped mode, is capable of generating vibronic progressions from a pure vibrational mode interacting with an overdamped environment. Consequently, canonical damping of the BVM will be avoided.

2.5.5 Matsubara Frequencies and Hierarchy Dimensions

Matsubara frequencies arise from poles in the spectral distribution function in the complex plane, and therefore are closely related to imaginary time. Imaginary times, which often are used in EOMs to minimise energy, are discussed in further detail in appendix E before being used to describe hierarchy dimensions.

2.5.5.1 Dimensions

As discussed in detail within the HEOM derivation, 2.5.4, the hierarchical equations of motion is comprised of a number of terms, each of which operates on an order of auxiliary density operator (ADO). These auxiliaries are sub-equations which define contributions to the full density matrix at different positions within the infinite hierarchy structure. The first term operates on ADOs of order n and contains Markovian dynamics for the free propagation of the system and also the dynamics of integer multiples of phonons corresponding to non-Markovian free propagation of the environment. Then there are non-Markovian and low temperature correction terms (depending on the hierarchy variant) which are at orders n^+, and n^- and correspond to raising and lowering between different auxiliary density operators. This creates a hierarchy structure where each level couples above and below. In this way, non-Markovian

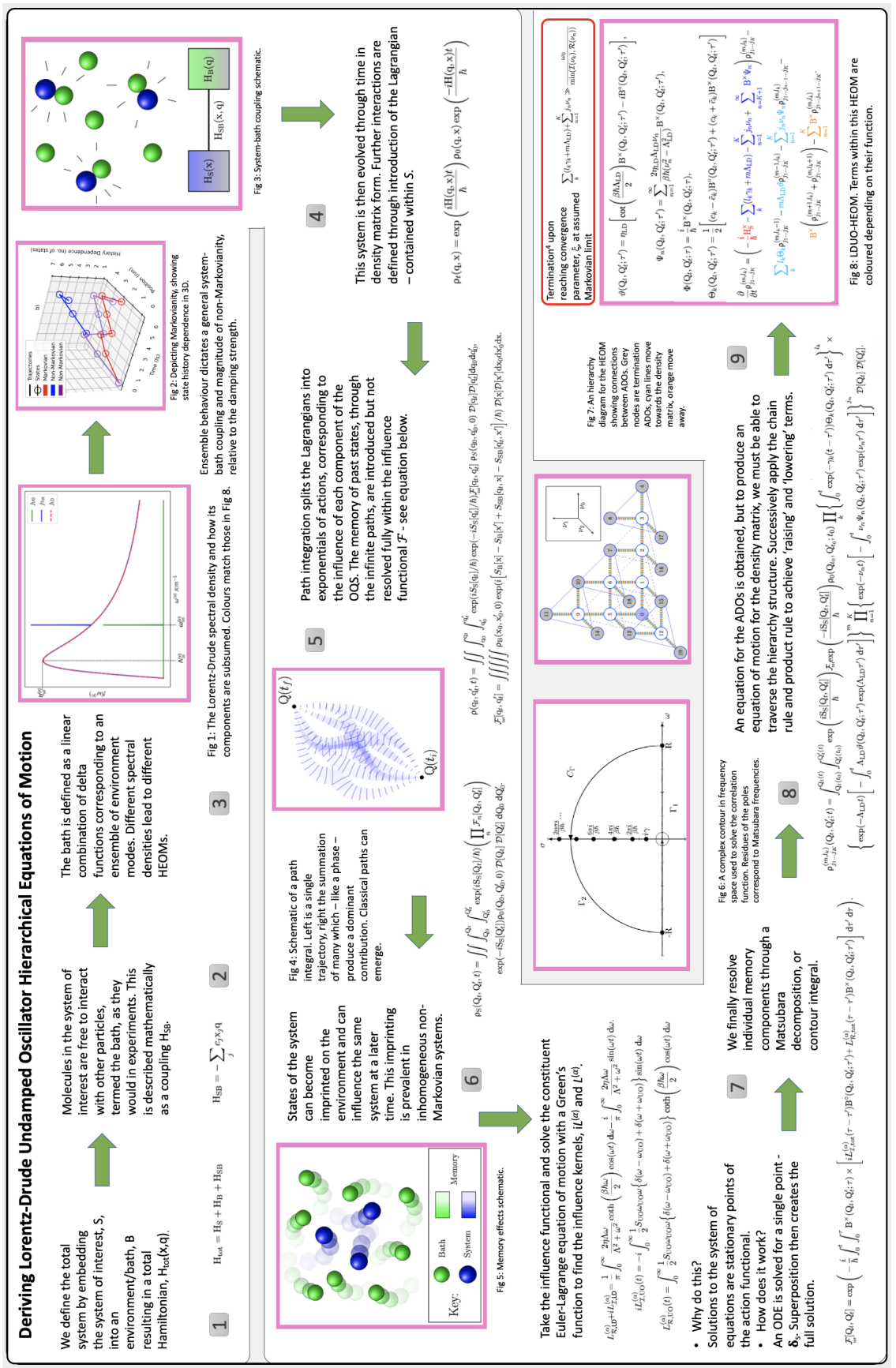

Figure 2.5.7: A flow diagram showing the general concepts behind the derivation of the LDUO hierarchical equations of motion, starting from the OQS Hamiltonian, and incorporating memory effects and direct particle couplings.

feedback can occur throughout the system and bath stemming from different ADOs. Finally, the infinite volume of ADOs created is terminated through a constraint which is determined by physical system characteristics such as the frequency, strength of bath coupling, or Markovianity. This constraint is enforced at every level of the hierarchy through an inequality which results either in the full equations of motion, or a terminator variant being applied which seals the hierarchy volume. It is the entire hierarchy structure that defines the nature of the system-bath interaction, but *only* one level of the hierarchy has physical meaning: the zeroth layer - density matrix.

The aforementioned hierarchy structure of auxiliary density operators exists within a coordinate space dependent on the number of Matsubara frequencies. The Matsubara dimension space is a purely mathematical construction, but each dimension relates to both the physical system properties and the magnitude of the Markovian constraint applied. In an overdamped hierarchy we require the sum of an infinite number of Matsubara frequencies in order to write the spectral density, and we decompose in this fashion in order to resolve time dependent bath contributions. In such a hierarchy this results in the first frequency being real and related to the bath speed, and subsequent integer multiples of $\frac{2\pi}{\beta\hbar}$ are thermal frequencies arising as a consequence of poles in the spectral function.

$$\nu_0 = \Lambda, \tag{2.5.75}$$

$$\nu_k = \frac{2\pi k}{\beta\hbar}. \tag{2.5.76}$$

As such, the Markovian constraint, Γ_{max}, applied on each ADO determines the number of auxiliaries and the total number of Matsubara dimensions where each frequency becomes its own independent axis.

$$\#_{\text{axes}} = K, \tag{2.5.77}$$

$$\frac{2\pi K}{\beta\hbar} > \Gamma_{\text{max}}. \tag{2.5.78}$$

Along each axis will exist auxiliaries which contain interactions with integer multiples of the Matsubara frequency of the given dimension. This corresponds to the interaction of multiples of thermal phonons within the total system, leading to non-Markovian feedback. At some point, the interactions are deemed to be sufficiently small and fast relative to the system of interest, that they can be neglected as Markovian dynamics by the action of Γ_{max}. The full dimensions of each HEOM depend on the number of Matsubara terms that are included in the hierarchy. For example, the overdamped HEOM has a single temperature independent contribution, at Λ, whereas the underdamped HEOM has two, dependent on the sign of ζ_n. This depends on the type of spectral density used to generate the full EOM, and is discussed alongside each respective HEOM

along with an example of a sealed hierarchy.

2.5.6 Computational Implementation

From these EOMs, termination conditions, and hierarchy structures, python functions which call efficient FORTRAN algorithms to step in a numerically explicit fashion through the hierarchy have been developed. In particular, a new FORTRAN script for the LDUO-HEOM has been generated and added to the wider suite of over and underdamped codes which have been developed from foundations established by D. Green[173]. Integration of the EOMs is achieved by application of Fourth Order Runge-Kutta (RK4), detailed in appendix B, with a step size of fifty attoseconds. This quadrature has been chosen for its sophisticated weighted average of increments, when compared to other simpler quadratures, which result in an improved numerical accuracy.

2.5.6.1 Computational Initial Conditions

Taking system Hamiltonian and bath coupling operators defined in the fashion of section 2.2, it is possible to prepare the initial density matrix for a molecular system, for example a vibronic dimer in the exciton basis,

$$\rho_{\mathrm{D}}^{\mathrm{E}} = \sum_{k} P_k \left|\psi_{\mathrm{D},k}^{\mathrm{S}}\right\rangle \left\langle\psi_{\mathrm{D},k}^{\mathrm{S}}\right|, \tag{2.5.79}$$

where the initial population of each state is Boltzmann weighted,

$$P_k = \frac{\exp\left(-\frac{\epsilon_k}{k_{\mathrm{B}}T}\right)}{Z}, \tag{2.5.80}$$

and the canonical partition function, Z, is

$$Z = \sum_{k} \exp\left(-\frac{\epsilon_k}{k_{\mathrm{B}}T}\right) = \mathrm{Tr}\left(\exp\left(-\frac{\mathrm{H}_{\mathrm{D}}^{\mathrm{E}}}{k_{\mathrm{B}}T}\right)\right). \tag{2.5.81}$$

Construction in this manner corresponds to employing an uncorrelated initial conditions approximation, which is discussed in detail in section 2.5 and appendix D, such that the initial state of the system and bath can be factorised. As described by Tanimura the initial system-bath correlations, regardless of whether they are factorised or correlated, must be established by propagation of the HEOM for a few picoseconds prior to main simulations to allow introduction and evolution of bathentanglement[151]. Simulations can be performed in the site, vibronic, or exciton bases as long as this choice is consistent across all operators.

2.5.6.2 Hamming Apodisation Function

When the system-bath interaction is probed closely through the canonical transform it can be easy to generate strongly underdamped signals which are not conducive to application in the theories of spectroscopy and quantum correlations. Overdamped hierarchies which exhibit particularly static environments or underdamped hierarchies which contain very strong system vibrational modes are examples of such systems. In these circumstances the third order polarisation, discussed in section 2.4, persists indefinitely as a result of strongly oscillating correlations between the system and bath. When this is Fourier transformed to produce a 2DES spectrum, the strong oscillations are translated into a poorly resolved peak with additional satellite peaks. Satellite peaks of this kind can also be generated in experimental setups as a result of a poor signal to noise ratio, and subsequently are typically removed through an apodisation function. These functions are applied to the third order polarisation to introduce a stronger level of, artificial, damping which reduces noise in experimental signals and increases peak definition in models[290–294]. Within this thesis, this is achieved by implementation of a Hamming function to force decay. The Hamming apodisation function,

$$w_{\mathrm{Ham}}(n) = a_0\left(1 - \cos\left(\frac{2\pi n}{N}\right)\right), \tag{2.5.82}$$

for a domain $[0, N]$ and where $a_0 = 0.54$, limits the oscillating component of the system-bath correlation. Figure 2.5.8 shows the Hamming window, and an underdamped third order polarisation signal and 2DES spectrum before and after apodisation with a Hamming function.

As demonstrated in the polarisation signal in a), b) figure 2.5.8, the Hamming function is similar to a two dimensional Gaussian in t and τ, acting to diminish the rephasing signal within the 200 square femtosecond window of the computation. a) results in a poorly defined 2DES peak, c), with artefact, satellite peaks, emerging horizontally and vertically from the central peak as a result of Fourier transforming a polarisation signal which has not sufficiently decayed within the time window. b) corresponds to the more sharply defined 2DES peak in d), which is equivalent to the peak in c) but when the oscillating polarisation signal is made to decay within the time window.

The following chapters contain results derived from computational implementation of the EOMs from section 2.5.4 and appendix D, as well as the systems described in section 2.2, to measure the impact of a thermal bath and moving the system-bath boundary on quantum information and quantum correlations.

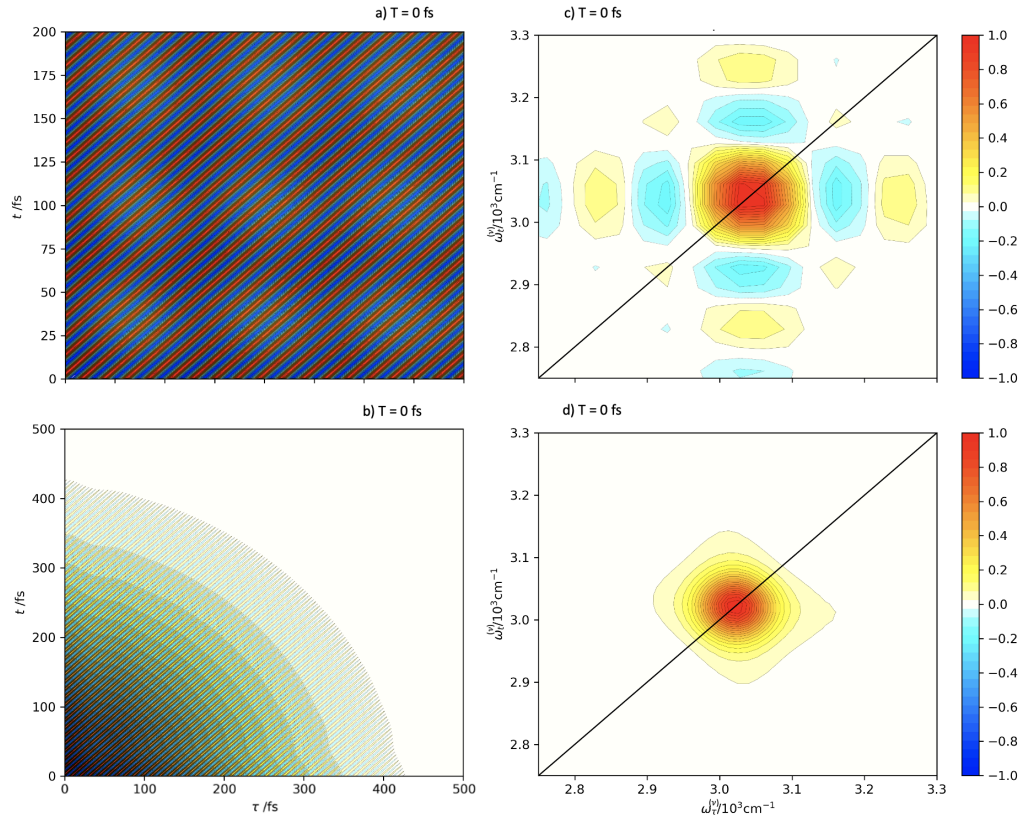

Figure 2.5.8: a) Rephasing third order polarisation signal before application of the Hamming window, and b) rephasing third order polarisation signal after application of the Hamming window. c) 2DES spectrum of a single peak at $\omega_{eg}^{(\nu)} = 3\,000$ cm^{-1} for a vibronic monomer, before apodisation, demonstrating artifact satellite peaks, and d) 2DES spectrum of a single peak at $\omega_{eg}^{(\nu)} = 3\,000$ cm^{-1} for a vibronic monomer after apodisation.

3 Measuring Quantum Information

3.1 Analysis of Quantum Information and Spectral Lineshape

Based on the theory outlined in section 2.2, it is possible to generate models for a range of vibronic molecules which can then be evolved through EOMs constructed in section 2.5.4 in the presence of a thermal bath with a range of possible damping strengths. To begin addressing Hypothesis 2[a], we consider the broad range of possible scenarios and how these are impacted by the location of different degrees of freedom within the system. The differences in location of the vibrational mode relative to the system-bath boundary for the undamped, overdamped and underdamped scenarios are shown in figure 3.1.1.

The first of these cases, figure 3.1.1 a), is when the total system is undamped. This corresponds to a model where the electronic degrees of freedom of the system are coupled purely to a single vibrational mode, which can then be evolved in the absence of a bath. When the system is undamped, oscillations within the correlation functions persist indefinitely and subsequently the macroscopic polarisation decays very slowly due to dephasing, over a period of nanoseconds, as the electronic excited state relaxes. This leads to spectral lineshapes which are dominated by the slow dephasing interaction, with a vibronic progression of sharp Lorentzian peaks with breadths proportional to the electronic excited state lifetime. This collection of peaks in the linear spectrum are generated as the result of the Franck-Condon principle, whereby electronic transitions occur without changes to the nuclear degrees of freedom. The intensity of each of the peaks within the progression are determined by the overlap integrals of the respective quantum harmonic oscillator bound eigenstates, described by Franck-Condon factors as discussed in section 2.2.1.1[295–297].

When this model is opened through the addition of an overdamped bath, capable of inducing electronic dephasing, the correlation function begins to decay rather than purely oscillating. This results in a more rapid decay of the

[a] *Are genuine quantum effects strongly impacted by system-bath boundary placement, and can these impacts be controlled by approximations and advanced formalisms?*

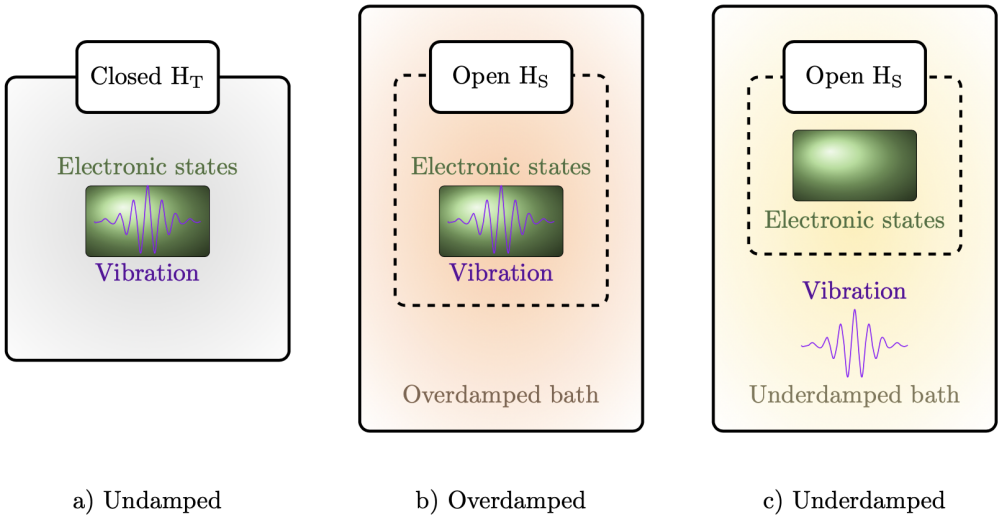

Figure 3.1.1: The limits of damping in terms of the system-bath boundary in what later becomes known as the Hamiltonian versus Spectral vibration models. a) The absence of any bath interaction results in a closed system which is undamped. In b), the vibrational levels are contained within the system Hamiltonian, and then coupled to an overdamped bath with a Lorentz-Drude spectral density. In c), a canonical transformation moves the vibrational mode into the bath degrees of freedom such that the system Hamiltonian contains the electronic states only. Bath interaction with this system is then modelled as an underdamped Brownian Oscillator.

macroscopic polarisation, of the order of hundreds of femtoseconds, which leads to considerable peak broadening. This scenario, known as the Hamiltonian vibration model in section 3.2, is depicted in figure 3.1.1 b). Additionally, the vibration is introduced through hot vibrational states in the Hamiltonian. In such a model, the broadening is applied uniformly to each vibronic peak, rather than peak specific broadening which is applied by structured spectral densities. In contrast, as in c), the fundamental system vibration can be subsumed into the bath through the canonical transform, leaving only electronic states coupled to a bath modelled by an underdamped Brownian oscillator. This construction, known as the bath (or spectral) vibration model in section 3.2, has only explicit electronic levels within the Hamiltonian and the interaction with an external laser field is only able to induce electronic transitions. However, as a consequence of the mathematical equivalence between canonically transformed models and those models without a canonical transform, a vibronic progression may still emerge in the linear spectrum as a consequence of the oscillations within the system-bath correlation function caused by strong coupling to the underdamped mode. Through combinations of these scenarios it is possible to construct models which consist of electronic states coupled to multiple vibrational modes, which each could be damped by separate under or overdamped baths[154,157]. A detailed analysis of these additional scenarios is considered throughout sections 3.2, 4.3, and 5.

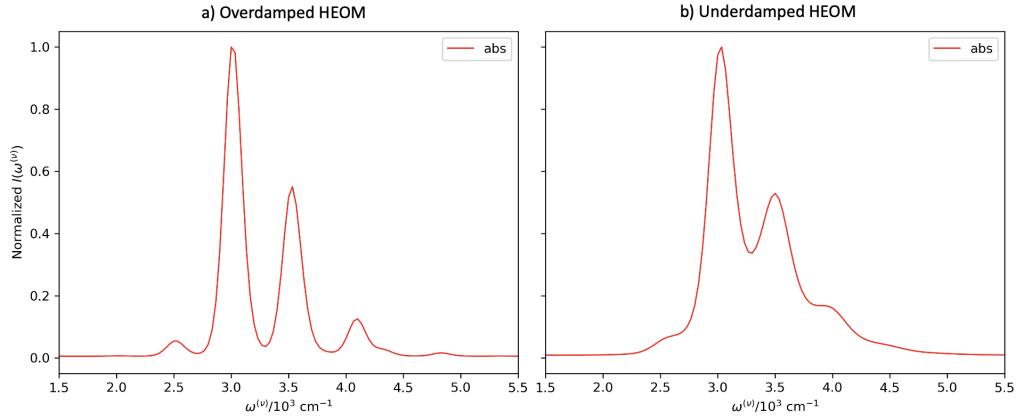

Figure 3.1.2: Linear absorption spectra for a vibronic monomer where a) Hamiltonian vibrational degrees of freedom result in peaks broadened by an overdamped bath and b) system vibrational structure within the bath degrees of freedom generate a vibronic progression which is broadened by an underdamped bath.

A comparison of linear absorption spectra for the HVM and BVM systems is considered for a vibronic monomer. The vibronic monomer system, defined in 2.2.1.1, has a fundamental electronic transition of $\omega_{eg}^{(\nu)} = 3\,000$ cm^{-1}, a mode frequency of $\omega_0^{(\nu)} = 500$ cm^{-1}, and a dimensionless excited state displacement $\tilde{d}_0 = 1$ such that the system reorganisation energy is $\lambda_0^{(\nu)} = 300$ cm^{-1}. Here, the superscript (ν) is applied to computational parameters which have been converted to the units of wavenumbers via the multiplication by $(2\pi c)^{-1}$ for angular frequencies or c^{-1} for linear frequencies. This is in contrast to the notation traditionally adopted in the Jones group, such as in Green[173], of $\{\tilde{\cdot}\}$ which in this thesis is reserved for transformations of mathematical functions and variables such as through the Fourier transform.

Figure 3.1.2 presents this spectrum where, in a), the system vibrational degrees of freedom for a single strongly coupled mode are contained within the Hamiltonian, versus vibrational structure contained purely within the bath as in b). The vibrational structure contained within the Hamiltonian, in a), is generated through a truncation at $\nu_0 = 5$, where ν_0 is the vibrational quantum number for the 0th mode. Additionally, $\tilde{d}_0$ results in a sufficiently small Huang-Rhys factor for the most intense peak, which corresponds to the fundamental transition, without loss of additional peaks within the vibronic progression. Hot band transitions, at frequencies lower than the fundamental, are due to the minimum in vibrationally excited states of the ground electronic state. Additionally, each peak within the vibronic progression is uniformly broadened by the action of coupling to the single overdamped bath. This is achieved through the dephasing operator $\mathrm{B}_{1,\mathrm{M}}$, from (2.2.47), which has an associated bath reorganisation energy of $\eta_1^{(\nu)} = 20$ cm^{-1} and a bath speed of $\Lambda^{(\nu)} = 40$ cm^{-1} at $300K$. The Markovian truncation criterion for the HEOM is

set at $\Gamma_{\max}^{(\nu)} = 2\,000$ cm^{-1} such that there are 187 ADOs within the overdamped hierarchy.

In contrast, when explicit vibrational structure is canonically transformed out of the Hamiltonian as in figure 3.1.2 b), the remaining system structure is an electronic two-level system with ground and excited states, $|g\rangle$ and $|e\rangle$. The resulting Hamiltonian is of the form

$$\mathrm{H_S} = -\frac{\hbar\omega_{eg}}{2}\sigma_z = \hbar\omega_{eg}\,|e\rangle\langle e|\,, \tag{3.1.1}$$

where ω_{eg} is the fundamental electronic transition frequency, and σ_z is the diagonal Pauli matrix capable of inducing pure dephasing. The bath is defined as an underdamped Brownian oscillator with an equivalent coupling operator to that which is used in a), $\mathrm{B}_1 = |e\rangle\langle e|$. In addition the mode frequency and temperature also remain the same at $\omega_{0,1}^{(\nu)} = 500$ cm^{-1} and 300 K, respectively. In contrast, the bath damping parameter, Λ, is replaced by the underdamped equivalent as discussed in section 2.2.2.2, $\gamma_1 = 100$ cm^{-1}, and the bath reorganisation energy, which in the course of a canonical transformation tends towards the system reorganisation energy λ_0, is slightly increased to $\eta_1^{(\nu)} = 500$ cm^{-1} in order to generate a vibronic progression of equivalent intensity. The hierarchy is terminated with a Markovian criterion of $\Gamma_{\max}^{(\nu)} = 2\,000$ cm^{-1} resulting in an underdamped hierarchy containing $95\,658$ ADOs. The two spectra are generated from correlated initial conditions, discussed in section 2.4.2, where the monomer dipole moment μ_{M} from equation (2.2.80) is used in figure 3.1.2 a) and $\mu = \boldsymbol{\mu}_{eg}\sigma_x$ for b), with a magnitude $\mu_{eg} = 11$ D. Here σ_x is the off-diagonal Pauli matrix. As a consequence of the canonical transform, generation of the similar vibronic progression to that of figure 3.1.2 a) is a direct consequence of bath interactions and each peak is individually broadened by the damping parameter γ_1. Overall, this highlights how an undamped vibronic progression is broadened uniformly by the bath in figure 3.1.2 a), but that in figure 3.1.2 b) the vibronic progression emerges from the spectral vibration and its interaction with the bath degrees of freedom, in competition with the damping.

The differences between these two approaches become more apparent in the 2D spectra where the homogeneous and inhomogeneous broadening can be observed as a function of the population time, T. 2DES corresponding to the linear spectra in 3.1.2 are shown in figure 3.1.3 for population times $T = 0$, 80, and 200 fs, calculated from the response function in the impulsive limit, as in section 2.4.3.1. The peaks present within these spectra are each separated by the system mode frequency, and each peak has dynamical intensity proportional to the broadening, dependent on the population time T, which is controlled by the level of coupling to the vibrational mode and its location. In figure 3.1.3 a),

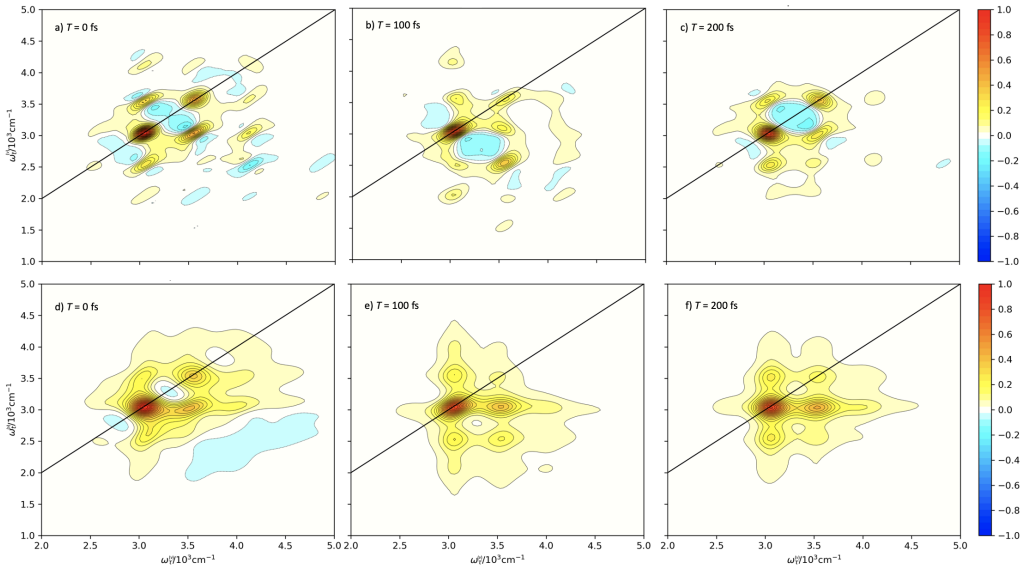

Figure 3.1.3: 2D electronic spectra for a vibronic monomer where, in a) – c), Hamiltonian vibrational degrees of freedom result in peaks broadened by an overdamped bath and, in d) – f), system vibrational structure within the bath degrees of freedom generate a vibronic progression which is broadened by an underdamped bath.

the vibration is contained within the Hamiltonian, and as a result the peaks are elongated along the diagonal. For early population times there is considerable inhomogeneous broadening as a consequence of the strong overdamping which is applied uniformly to the peaks. As the population time increases the correlation between the excitation and emission frequencies decays resulting in equivalent levels of homogeneous and inhomogeneous broadening and rounded peaks: spectral diffusion. In direct contrast, spectra in figure 3.1.3 b) are generated with system vibrations subsumed into the bath degrees of freedom. The immediately complementary lineshape is characterised by its Lorentzian shape which is as a consequence of the peak specific broadening induced by γ_1. Despite this, the peak locations, and emergence of any vibronic structure, are as a direct consequence of bath interaction highlighting the difference in information transfer between the system and bath. This is discussed further in sections 3.2 and 3.3. It is worth noting that the regions of negative intensity in the spectra, particularly for population times close to zero, are an artefact due to the unequal intensities of the rephasing and non-rephasing components, and is mentioned in section 2.4.3.2.

For systems which have more vibrational structure than a vibronic monomer, such as dimers or lattices which are discussed further in section 2.2.1.2, a far larger Hamiltonian is required and therefore a greater number of auxiliaries are necessary for propagation. The dimensions of the Hamiltonian can be reduced by truncating the required number of explicit energy levels, either by introducing a hard limit to the α and n degrees of freedom, or by canonically

extracting the vibrational component entirely. The number of auxiliary density operators is dependent on the bath complexity and level of damping. Underdamped environments introduce more Matsubara frequencies, and non-Markovian dynamics induce larger integer multiples of phonon interactions within the bath which requires many more ADOs to propagate. Both areas of complexity have advantages and disadvantages such as issues concerning truncation of energy levels and number of explicit modes, which are addressed in sections 3.2, 3.3, and 4.3.

3.1.1 Limits of the Lineshape

As a first step in understanding the nature of the canonical transform we consider the limits of lineshape under a range of physical and model conditions, as first presented in Green[173]. A full range of damping strengths from over to underdamped, excluding only critical damping, is performed and the linear spectra are analysed. First, a set of linear absorption spectra are generated using the same parameters as those for figure 3.1.2 and in turn, the temperature, bath dissipation rate/homogeneity, are varied holding all other parameters fixed. This is performed for both the overdamped and underdamped baths so that the dependence of lineshape on all of the parameters involved in the simulations is ascertained.

In a) and b) of figure 3.1.4 there is a clear vibronic progression with peaks at integer multiples of the system mode frequency above the fundamental transition. All peaks within these panels demonstrate a Lorentzian shape as a consequence of the mode frequency being much greater than the bath damping which limits the FWHM. In b) the vibronic progression is sharply defined due to the decreased temperature for many of the runs. At lower temperatures bath motion is reduced and the environment ensemble is limited to a small number of frequencies, narrowing the Lorentzian peaks towards delta functions. In the limit of zero temperature, with the exception of finite widths from the quantum uncertainty principle, the correlation function for this model would become a pure oscillation as the ensemble becomes a single frequency. In a), with a fixed temperature of 300 K the peaks are less well defined due to increased broadening. Peak area is preserved such that, as bath speed increases the peaks broaden and decrease in intensity. This is as a consequence of the increased dephasing associated with larger bath damping. Due to dephasing the indistinguishable states of the system becomes increasingly distinguishable as separate frequencies, which corresponds to a recurrence of information as the distinguishability increases.

In e) and f) of figure 3.1.4, when the system is coupled to an overdamped

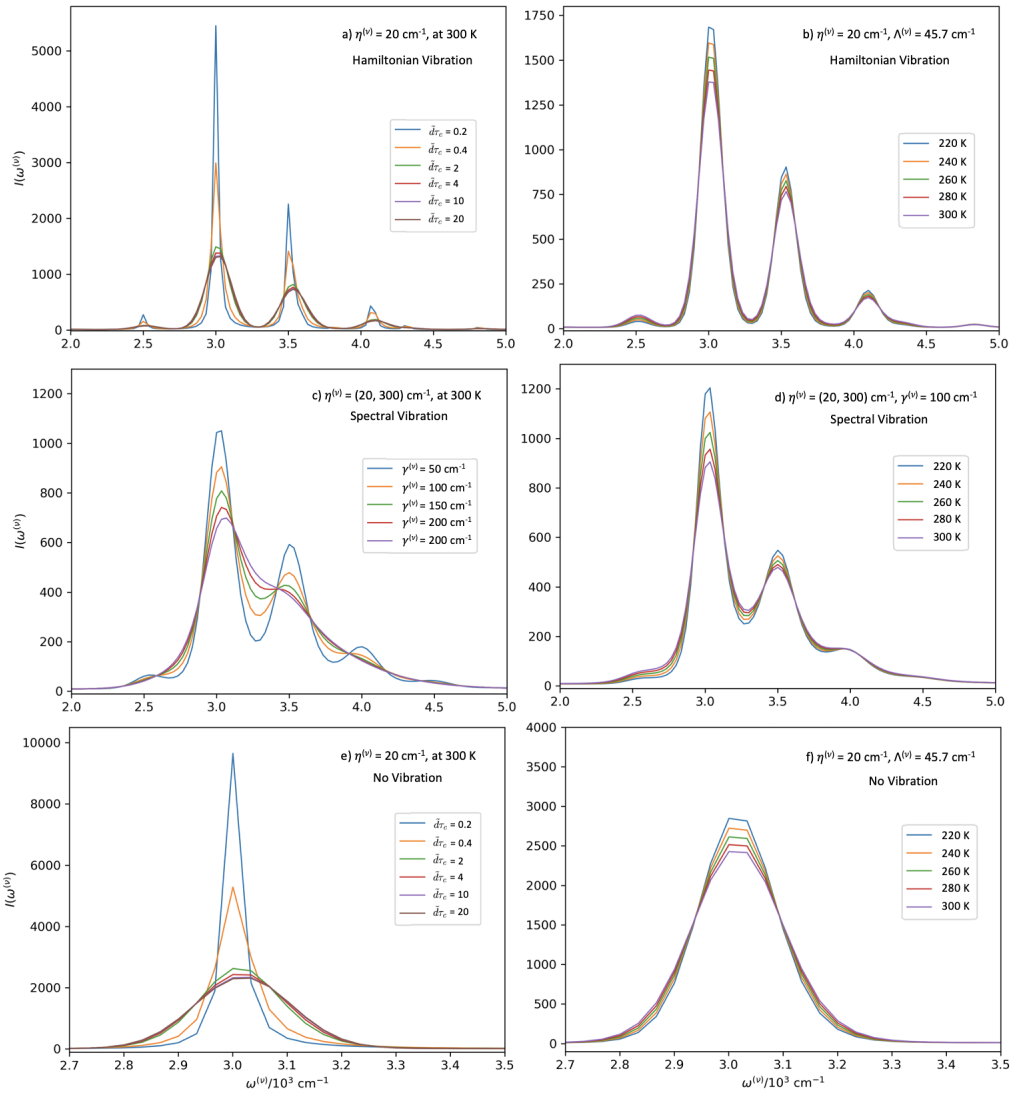

Figure 3.1.4: a) For an overdamped bath, $\eta^{(\nu)} = 20$ cm^{-1}, $T = 300$ K are held fixed while the homogeneity is varied and measured by $\tilde{d}\tau_c$. Values include: 0.2, 0.4, 2, 4, 10 and 20. b) For an overdamped bath, $\eta^{(\nu)} = 20$ cm^{-1}, and $\Lambda^{(\nu)} = 45.7$ cm^{-1} are held fixed while the temperature is varied. Values include: 220, 240, 260, 280, and 300K. This is considered a Hamiltonian vibration. c) For an underdamped bath, $\eta^{(\nu)} = 500$ cm^{-1}, $\omega_0^{(\nu)} = 500$ cm^{-1}, and $T = 300$ K are held fixed while the bath dissipation rate, $\gamma^{(\nu)}$ is varied. Values include: 50, 100, 150, 200, and 250 cm^{-1}. d) For an underdamped bath, $\eta^{(\nu)} = 500$ cm^{-1}, $\omega_0^{(\nu)} = 500$ cm^{-1}, and $\gamma^{(\nu)} = 100$ cm^{-1} are held fixed while the temperature is varied. Values include: 220, 240, 260, 280 and 300 K. This is considered a spectral vibration. e) For an overdamped bath, $\eta^{(\nu)} = 20$ cm^{-1}, $T = 300$ K are held fixed while the homogeneity is varied and measured by $\tilde{d}\tau_c$. Values include: 0.2, 0.4, 2, 4, 10 and 20. f) For an overdamped bath, $\eta^{(\nu)} = 20$ cm^{-1}, and $\Lambda^{(\nu)} = 45.7$ cm^{-1} are held fixed while the temperature is varied. Values include: 220, 240, 260, 280, and 300 K. In this instance vibrational structure is removed.

bath, the bath dephasing rate $\Lambda^{(\nu)}$ leads to a range of environment homogeneities. Physically, homogeneity is a description of how rapidly the environment returns to equilibrium after perturbation. When the response time is very slow the environment will separate into distinct sub-environments with different properties, however when the response time is fast the bath will act as a thermal reservoir, averaging out any perturbations. The homogeneity is measured through the dimensionless quantity $\tilde{d}\tau_c$, where $\tilde{d}$ is description of the spread of transition frequencies across the ensemble due to stochastic modulation, and τ_c is the lifetime of correlations within the system before it returns to equilibrium. For fast correlation response times, relative to the amplitude of the fluctuation, the environment is characterised as white noise. This is the homogeneous limit which is defined as $\tilde{d}\tau_c \ll 1$. The bath response is rapid enough that all perturbation of the excited state due to dephasing is thermally averaged, producing a uniform interaction across the ensemble and a sharply defined Lorentzian peak[138]. Contra-thermal narrowing is the spectrum produced in the inhomogeneous limit, defined as $\tilde{d}\tau_c \gg 1$. In such a scenario the distinct sub-environments lead to a Gaussian spread of frequencies, and a range of different bath interactions, which decreases the intensity at the fundamental frequency and broadens the peaks. This corresponds to a range of correlation response times for the rate of return to equilibrium, characteristic of a static environment ensemble. Subsequently, figure 3.1.4 e) demonstrates the full range of homogeneities from sharp Lorentzian peaks when $\tilde{d}\tau_c \ll 1$ in the thermally averaged regime, which broadens into a shallow Gaussian as the homogeneity tends towards $\tilde{d}\tau_c \gg 1$ and the static limit. When in the inhomogeneous limit there is also a Stokes Raman shift corresponding to an increased emission wavelength as a photon is excited, but upon relaxation it returns to a hot vibrational state[37,120]. Figure 3.1.4 f) demonstrates an equivalent decrease of the FWHM of the Gaussian lineshape of an inhomogeneous overdamped system, equivalent to that which is presented in b). This change is linked directly the changing value of $\tilde{d}$ with temperature and is a consequence of the spread of transition frequencies within the ensemble. Finally, c) and d) show results in agreement with those in a), b) and e), f) but with additional spectral broadening. This highlights the difference of moving the system-boundary.

Distinguishable transition frequencies which lead to Gaussian peaks, versus indistinguishable thermally averaged transitions which have motionally narrowed peaks, indicate that quantum information is the mediator of the additional damping. Non-Markovian recurrence of information along quantum channels, discussed in 2.1.4, lead to changes in the information content of the system of interest which manifests as measurable lineshape changes. We quantify these changes and the relationship between non-Markovianity and lineshape through 2DES in the next section.

3.1.2 Quantifying Non-Markovianity and Its Effect on Spectral Lineshape

Quantification of the impact of non-Markovianity on the spectral lineshape is achieved through implementation of the BLP measure of quantum information, detailed in section 2.1.5, on a model system under a range of bath conditions spanning all damping limits, first presented in Green et. al.[1]. The degree of Markovianity is then compared with linear and 2DES lineshape, calculated with the same model and parameters as those use to generate 1DES in figure 3.1.4, to link memory-effects and spectral features directly. This model is constructed as an electronic two-level-system with a fundamental frequency of $\omega_{eg}^{(\nu)} = 3\,000$ cm^{-1}, associated dipole operator $\mu = \sigma_x$, and with all vibrational degrees of freedom canonically transferred to the bath. The bath is constructed as having a single vibrational mode, $\omega_0^{(\nu)} = 500$ cm^{-1} so that the system is coupled to an underdamped Brownian oscillator when $\gamma \ll \omega_0$, or an overdamped bath when $\gamma \gg \omega_0$. The HEOM is used to compute the dynamics of the system evolution through equations (2.5.55), or (2.5.41) in the under and overdamped limits, respectively. Within this work, a single environment bath is necessary such that $n = 1$ for EOMs in section 2.5. The bath is coupled to the system through a pair of summed operators accounting for both dephasing and dissipation,

$$\mathrm{B} = \sigma_x + \frac{\sigma_z}{2}, \tag{3.1.2}$$

where $\sigma_{\{.\}}$ are Pauli matrices. In addition, the bath reorganisation energy is fixed at $\eta^{(\nu)} = 20$ cm^{-1} with an excited state displacement of $d^{(\nu)} = 91.33$ cm^{-1} at a temperature of 300 K. The resulting Huang-Rhys parameter of $S_{\mathrm{HR}} = \frac{\eta}{\omega_0} = 0.04$ corresponding to a small mean phonon modulation[198]. A full spectrum of damping strengths are considered, presented in table 3.1 along with the associated dissipation rates, Λ, correlation times, τ_c, and $\tilde{d}\tau_c$ for overdamped baths. This range of values were chosen to facilitate observation of the underdamped and overdamped limits, as well as homogeneous and inhomogeneous limits in the latter case, through scanning only the selected damping strengths.

The BLP metric of non-Markovianity, $\mathcal{N}$, is generated for each set of parameters through comparing the dynamics of the system from two different initial conditions: after interaction with a single Gaussian laser pulse, and without interaction. The initial condition for this system is the electronic ground state,

$$\rho_{\mathrm{S}}(t=0) = |g\rangle\langle g| = \begin{pmatrix} 1 & 0 \\ 0 & 0 \end{pmatrix}. \tag{3.1.3}$$

The system is then propagated for 2.05 ps to introduce bathentanglement, with the Markovian truncation criterion set to $\Gamma_{\mathrm{max}}^{(\nu)} = 5\,000$ cm^{-1}. Through

$\gamma^{(\nu)}/\text{cm}^{-1}$	$\Lambda(2\pi)^{-1}/\text{fs}^{-1}$	τ_c/fs	$\tilde{d}\tau_c$
50	0.1500	7	-
275	0.0273	37	-
500	0.0150	67	-
950	0.0079	127	0.35
1 500	0.0050	200	0.55
3 000	0.0035	400	1.10
9 000	0.0008	1 200	3.29

Table 3.1: Damping strengths, dissipation rates and correlation times used, for $\eta^{(\nu)} = 20$ cm^{-1} such that $d^{(\nu)} = 91.33$ cm^{-1} at 300 K. $\tilde{d}\tau_c$ are given for overdamped environments only. Results in red are those which are very close to the critical damping value, $1\,000$ cm^{-1}, and demonstrate a failure of this EOM. Based on the study in Green et. al.[1].

application of the semi-classical theory of system-field interactions, introduced in section 2.2.3, the system-field interaction is added to the Hamiltonian and evolved. The incident field has a Gaussian envelope centred at $\tau_m = 2$ ps. After the pulse has decayed, corresponding to a complete interaction, the ADOs are propagated for an additional 2 ps, resulting in the states which are used for the calculation of the BLP. Each of the lasers, applied to the sets of parameters, are identical with a strength $\chi = 10^3$ Vm^{-1}, and a frequency chosen to be exactly on resonance with the fundamental transition of the system, $\omega_{eg}^{(\nu)}$. The system which is propagated without interaction, denoted ρ_1, is achieved by setting the FWHM of the pulse to 0 fs, whereas the secondary setup (for ρ_2) is generated from a pulse with FWHM of 20 fs.

The following results, in a) and b) of figure 3.1.5, present the trace distance $D(\rho_1, \rho_2)$ and the cumulative integrated positive flux $\int \sigma > 0 \, \mathrm{d}t$ respectively, for each of the sets of parameter sets listed in table 3.1. In particular, these results demonstrate the effect described in figure 2.1.2, whereby a loss of distinguishability of states ρ_1 and ρ_2 is mediated by losses of information and energy to the bath resulting in a decreased trace distance. It is clear that, if the minor oscillatory mode is temporarily discounted, the global trend is a monotonic decrease of the trace distance synonymous with globally Markovian dynamics. However, the minor oscillations within each curve demonstrate that, particularly at early times, there are periodic recurrences of information due to the positive flux. Figure 3.1.5 b) demonstrates that in all cases there is a positive flux, $\sigma > 0$, of information which is a consequence of non-Markovian recurrence of information from historic states imprinted on the bath. The maximum of each

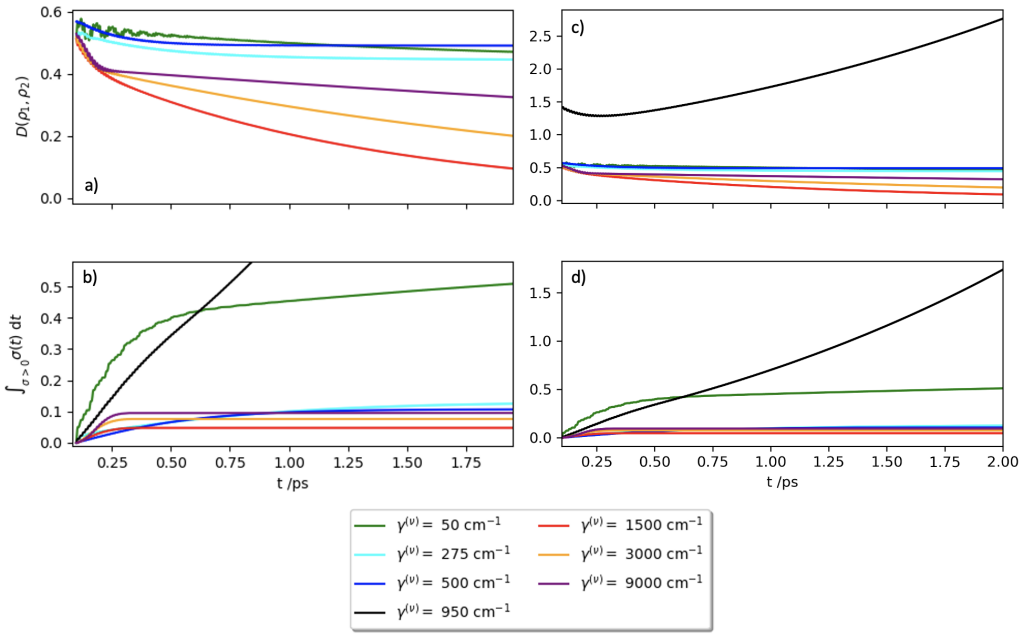

Figure 3.1.5: a) Trace distance, $D(\rho_1, \rho_2)$. b) Cumulative integration of the positive flux, with maximum equal to $\mathcal{N}$, for each of the damping strengths in table 3.1. c) and d) depict the trace distance and cumulative flux, respectively, for a greater range demonstrating the divergence at close to critical damping. These results are based on similar considerations in Green et. al.[1].

line is the associated degree of non-Markovianity $\mathcal{N}$.

One of the major trends from figure 3.1.5 is that baths with a lower damping rate show a more prolonged increase in the integrated total flux. This is further exemplified by figure 3.1.6 in which, for $\gamma^{(\nu)} = 50$ cm^{-1}, $\gamma^{(\nu)} = 275$ cm^{-1}, and $\gamma^{(\nu)} = 500$ cm^{-1}, the positive flux is characterised by low amplitude, long lived, oscillations which provide a continuous recurrence of information from the bath to the system. In b) of figure 3.1.5 the underdamped parameter regimes also exhibit a much more gradual increase in integrated flux, as a consequence of the continual feedback of information. Additionally, it is clear that after approximately 2 ps the integrated flux for $\gamma^{(\nu)} = 500$ cm^{-1} is beginning to plateau, similar to overdamped baths, but after the same time the flux for $\gamma^{(\nu)} = 50$ cm^{-1} is still increasing. This suggests that the maximum measurable non-Markovianity is achieved more gradually in baths with weaker damping. In contrast to the persistent oscillations within the underdamped flux, overdamped baths exhibit a rapid decay of all oscillations. When the bath damping strength is increased into the overdamped limit, $\gamma^{(\nu)} = 1\,500,\ 3\,000,$ and $9\,000$ cm^{-1}, oscillations decay within the first hundred femtoseconds corresponding to an immediate intense recurrence of information from the bath followed by irreversible Markovian transfer of energy and information to the bath. This profile of a small period of non-Markovianity followed by strong Markovianity is equivalent to intense, short-lived, environment interaction inducing memory

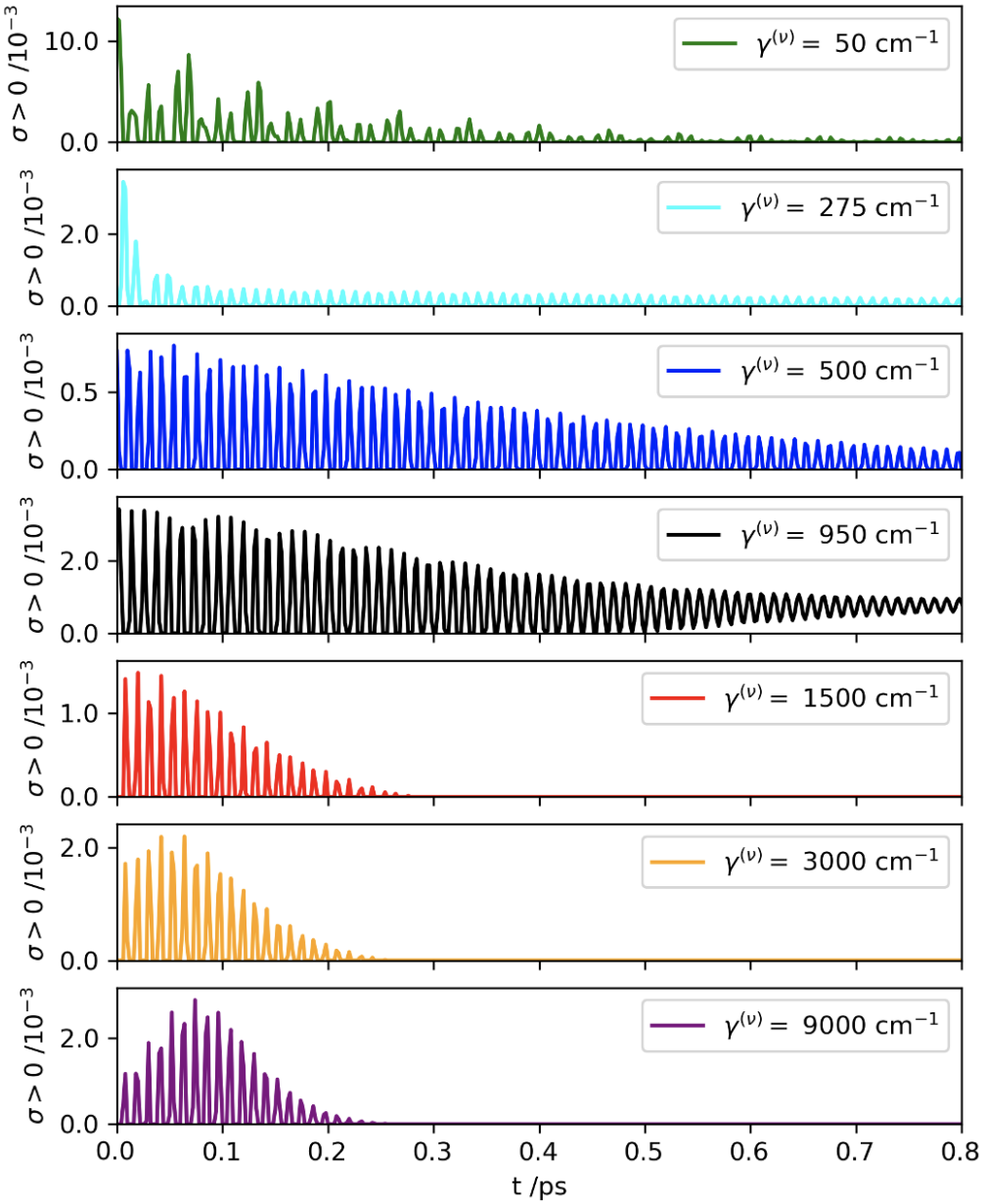

Figure 3.1.6: Positive flux of the trace distance shown in figure 3.1.5, for each of the damping strengths in table 3.1, demonstrating the periodic recurrence. These results are based on similar considerations in Green et. al.[1].

effects, shortly followed by a Markovian process. This description is consistent with a rapid reorganisation of solvent molecules upon system excitation, followed by relaxation of the excited state, generating the globally Markovian profile expected for a TLS. Furthermore, as the damping strength increases from $\gamma^{(\nu)} = 1\,500$, to $9\,000$ cm^{-1}, both the rate of reaching the maximum non-Markovianity and the maximum non-Markovianity increase. This suggests that inhomogeneous overdamped baths, which have more static environments, present greater non-Markovian feedback than those which are homogeneous. This highlights the importance of non-Markovian feedback in static, inhomogeneous, environments but that underdamping is an even greater source

$\gamma^{(\nu)}/\text{cm}^{-1}$	$\tilde{d}\tau_c$	$\mathcal{N}$	FWHM $(\pm 1)/\text{cm}^{-1}$
50	-	0.512	7
275	-	0.107	19
500	-	0.124	32
950	0.35	1.74	51
1 500	0.55	0.048	99
3 000	1.10	0.076	150
9 000	3.29	0.096	198

Table 3.2: Measured $\mathcal{N}$ and linear absorption spectrum FWHM for each damping strength in table 3.1, for $\eta^{(\nu)} = 20$ cm^{-1} such that $d^{(\nu)} = 91.33$ cm^{-1} at 300 K. $\tilde{d}\tau_c$ are given for overdamped environments only. Data in red is close to the critical damping value, $1\,000$ cm^{-1}. Based on the study in Green et. al.[1].

of non-Markovianity despite it taking longer to develop. In addition this presents the possibility that a minimum of non-Markovianity may exist in the homogeneous thermally averaged, overdamped limit. The measured maximum non-Markovianity after 2 ps is presented in table 3.2.

The patterns which emerge from the non-Markovianities are comparable to those found within the spectral lineshape of the linear and 2D spectra. For each set of parameters within table 3.1 the linear and 2D spectra were calculated from the molecular response function in the impulsive limit, with correlated initial conditions, as described in section 2.4. The expected behaviour, of Lorentzian and Gaussian lineshapes, are presented in the linear spectra, figure 3.1.7. The sharpest peak is observed at the smallest damping rate, $\gamma^{(\nu)} = 50$ cm^{-1}, with an intense Lorentzian peak at the electronic transition frequency, with a secondary vibronic peak at $\omega_{eg}^{(\nu)} + \omega_0^{(\nu)}$. The vibronic peak has a dramatically lower intensity as a consequence of low mean phonon deviation, even in the underdamped limit with $S_{\text{HR}} = 0.04$. As the damping is increased, signifying an increase in quantum information returned to the system, through $\gamma^{(\nu)} = 275$ cm^{-1}, to $\gamma^{(\nu)} = 500$ cm^{-1}, the intensity of the peak at the fundamental decreases and the broadening increases resulting in the vibronic peak being obscured. However, the secondary peak is not just hidden by increased broadening, but vanishes as the model moves from the underdamped to the overdamped limit. This peak results from prolonged non-Markovianity, which is synonymous with persistent oscillatory correlation such as in figure 3.1.6. This oscillation is able to exist beyond 2 ps because the vibrational mode has been subsumed into the environment degrees of freedom by the canonical transform which intrinsically links the system and bath degrees of freedom.

Subsequently, spectroscopic measurements in underdamped models can probe the combined canonically transformed environment degrees of freedom which include both system and bath modes. Therefore, in the limit of weak damping, reversible information exchange between the system and bath occurs which leads to the secondary vibronic peak, but this peak vanishes in other damping regimes.

In the overdamped limit the intensity of the fundamental continues to decrease as the lineshape profile changes, dependent on the temperature and environment. The FWHM of the fundamental peak for each of the parameter regimes is listed is table 3.2. If the model is at high temperature, such that the high temperature approximation $k_{\mathrm{B}}T \gg \hbar\Lambda$ is valid, then the absorption spectrum in the thermally averaged (homogeneous) limit has a Lorentzian structure described by

$$I(\omega) = \frac{\Gamma}{(\omega - \omega_{eg})^2 + \Gamma^2}, \tag{3.1.4}$$

where the FWHM is defined as $2\Gamma = 2\tilde{d}^2\tau_c$ [37,120]. This formula for the FWHM predicts that, for a relatively overdamped bath $\gamma^{(\nu)} = 1\,500$ cm^{-1} with homogeneity $\tilde{d}\tau_c = 0.55$, the FWHM should be 100 cm^{-1}. The predicted value is in good agreement with the measured value, in table 3.2, where the difference in the two values arises from $\tilde{d}\tau_c = 0.55$ being too large with respect to that of the perfectly thermally averaged limit, $\tilde{d}\tau_c \ll 1$. Similarly, a fully static bath in the inhomogeneous limit, $\tilde{d}\tau_c \gg 1$, has a linear spectrum described by a Gaussian profile,

$$I(\omega) = \sqrt{2\pi\tilde{d}^2}\exp\left(-\frac{(\omega - \omega_{eg})^2}{2\tilde{d}^2}\right), \tag{3.1.5}$$

with a predicted FWHM of $2\sqrt{2\ln 2}\cdot\tilde{d}$, which is directly proportional to the amplitude of fluctuations[37,120,298]. Similar to the Lorentzian profile, the predicted value of 215 cm^{-1} is close to the measured value in table 3.2 when in the inhomogeneous regime, $\gamma^{(\nu)} = 9\,000$ cm^{-1}. Again, the discrepancy between the two values highlights that $\tilde{d}\tau_c = 3.29$ does not represent a perfectly static environment, but does highlight that 3.29 is sufficiently greater than 1 to produce a closer approximation than its homogeneous counterpart.

As discussed, when in the inhomogeneous limit, the long response time to perturbations causes bath motion to be effectively static with respect to the timescale of system relaxation, leading to a Gaussian, normal, distribution of all transition frequencies within the ensemble. This process demonstrates the concept depicted in figure 2.1.2, whereby, in the static limit when localised inhomogenities contribute to the lineshape, there is maximum distinguishability and information within the system. Similarly, when in the homogeneous thermally averaged limit, short correlation times result in an identical system-bath interaction across the entire ensemble corresponding to a narrowed

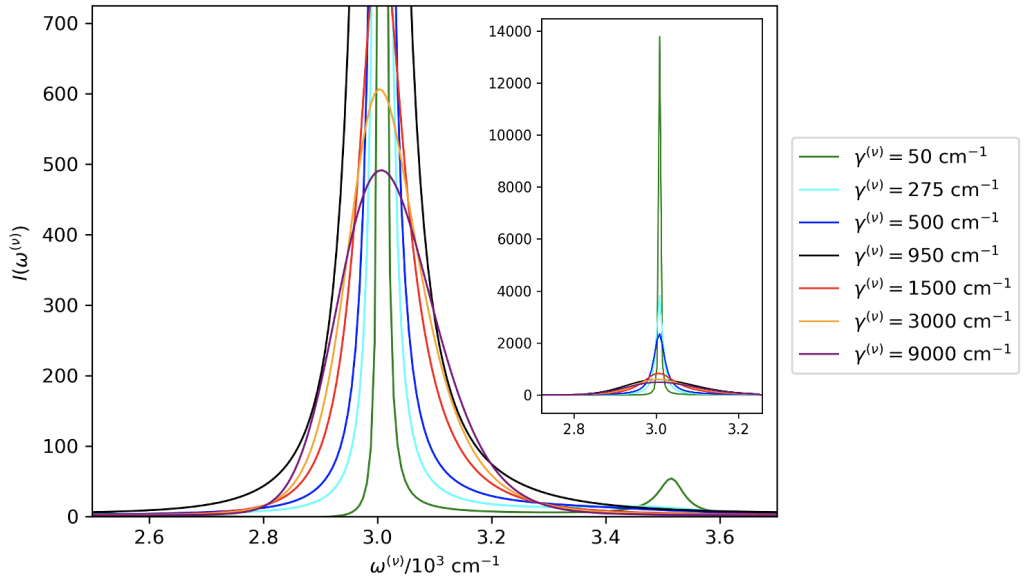

Figure 3.1.7: Calculated linear absorption spectra for each of the damping strengths in table 3.1. The black data shows an unnatural broadening away from the mutual intersection of other spectra due to the EOM failure at critical damping. These results are based on similar considerations in Green et. al.[1].

lineshape, and a minimum of information and distinguishability[138]. This is in agreement with the results observed in the overdamped limit in figures 3.1.5 and 3.1.6 where the maximum $\mathcal{N}$ is larger and obtained through a large initial information flux. As is demonstrated in figure 3.1.6 by the maximum flux localised around the origin, in inhomogeneous systems non-Markovian feedback is almost instantaneous. Whereas, in the homogeneous limit the indistinguishable, constant, system-bath interaction leads to a delta function correlation function after Fourier transform resulting in completely numerically explicit, Markovian, dynamics[138]. This behaviour is the source of the dip in maximum integrated flux in figure 3.1.5 on increasing the damping strength: $\mathcal{N}$ decreases on moving from the underdamped limit to the homogeneous overdamped limit, through the critical region, and then increases again as the overdamped environment becomes more static. These observations demonstrate how effective HEOM methods are at correctly accounting for non-Markovian dynamics induced by coloured and structured spectral densities[150,155].

The 2DES for each set of parameters are computed for population times $T = 0 - 300$ fs for the $\gamma^{(\nu)} = 275$ cm^{-1} underdamped bath and for the three overdamped baths and are presented in figure 3.1.8. Each of the four cases is labelled with its homogeneity, $\tilde{d}\tau_c$, with the exception of the underdamped bath which is denoted $\gamma < \omega_0$. In the underdamped limit the spectra, irrespective of the population time, exhibit a very intense narrow Lorentzian peak which does not decay or oscillate. The overdamped spectra are significantly less intense, and broader, demonstrating a loss of inhomogeneous elongation proportional to

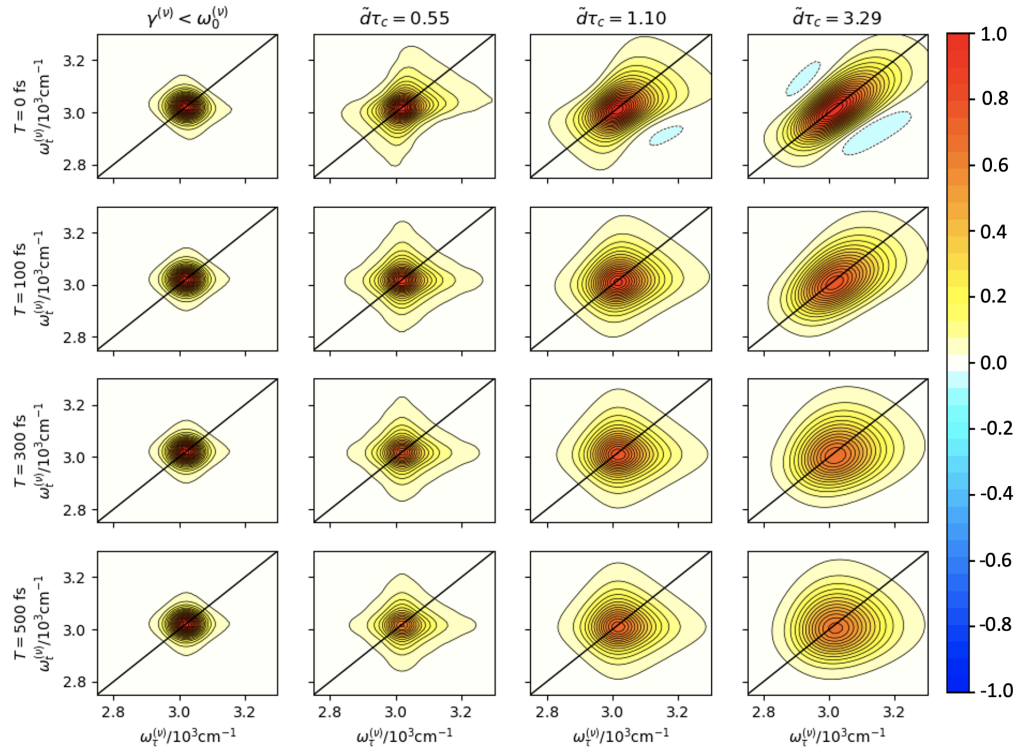

Figure 3.1.8: Absorptive 2D spectra for population times $T = 0 - 500$ fs for the $\gamma^{(\nu)} = 275$ cm^{-1} underdamped bath, labelled $\gamma^{(\nu)} < \omega_0^{(\nu)}$, and the three overdamped baths, identified by their $\tilde{d}\tau_c$ values from table 3.1, normalised to the maximum of $\tilde{d}\tau_c = 0.55$ at $T = 0$ fs. These results are based on similar considerations in Green et. al.[1].

the decay of the system-bath correlation. This process, termed *spectral diffusion*, transforms peaks which are elongated along the diagonal for early population times into evenly rounded peaks with equivalent diagonal and anti-diagonal broadening. The ellipticity, denoted E_ω, is a quantification of the level of broadening along the diagonal, ς_D, and the anti-diagonal, ς_A, through an analytical, fitted, Gaussian. This allows for the direct measurement of the system-bath correlation function, and the quantification of 'how elliptical' a peak in a 2D spectrum is[280,299,300],

$$E_\omega = \frac{\varsigma_\text{D}^2 - \varsigma_\text{A}^2}{\varsigma_\text{D}^2 + \varsigma_\text{A}^2}. \tag{3.1.6}$$

Alongside the 2DES, the ellipticities of the peaks at each population time are considered and plotted in figure 3.1.10.

At zero population time, spectra generate peaks which are Lorentzian in the underdamped limit, through to a strongly diagonally elongated Gaussian in the case of $\tilde{d}\tau_c = 3.29$. This is a consequence of the increased damping upon movement from the homogenenous bath, $\tilde{d}\tau_c = 0.55$, to the static limit, and correctly generates a Lorentzian to Gaussian transition as was observed in the linear spectra of figure 3.1.7. Additionally, the degree of diagonal elongation

relative to the anti-diagonal homogeneous broadening suggests that, even in the most homgeneous of the overdamped baths, the environment is not fully thermally averaged. However, in contrast to the overdamped spectra, disparity between the homogeneous and inhomogenenous broadening is entirely absent in the underdamped spectra[b]. Inhomogeneous elongation is present within all spectra with $T < \tau_c$, as it is dependent on the decay of correlation between the system and bath.

The ellipticity, in figure 3.1.10 further highlights the fact that there is an exponential decay in the inhomogeneous broadening, but additionally that the slower decay for static environments is accompanied by a corresponding increase in the total non-Markovianity, $\mathcal{N}$. Short correlation times, associated with homogeneous conditions, produce the most rapid decrease in ellipticity as demonstrated by the data for $\tilde{d}\tau_c = 0.55$. Consequently, elongation present within the 2DES, figure 3.1.8, for this parameter regime has decayed within 300 fs, however, elongation still persists in the most inhomogeneous $\tilde{d}\tau_c = 3.29$ case. In addition, increased correlation times result in significantly more spectral diffusion which produces round peaks, with Gaussian diagonal and anti-diagonal slices, for long times, whereas shorter correlation times produce Lorentizan slices. This is further discussed in appendix F. The trends present within figures 3.1.8, 3.1.5, and 3.1.7 confirm that 2D lineshape can be treated in an equivalent fashion to one dimensional lineshape, and conclusions regarding the broadening and total non-Markovianity will be consistent. In the inhomogeneous limit when there is slow diffusion, and correlations induced by stochastic perturbation persist, there will be considerably more non-Markovian feedback leading to diagonal elongation of peaks, representing the increased information which the system possesses about the distribution of ensemble frequencies. As the damping is decreased, shifting the regime towards the homogeneous limit, shorter correlation times prevent the same degree of peak diagonal elongation. This corresponds to a reduced level of non-Markovian feedback, in comparison with the inhomogenenous limit, increased diffusion speed, and an increase in irreversible dissipation. The increased degree of non-Markovianity in the case of $\tilde{d}\tau_c = 3.29$ at zero population time is also attributed to the greater elongation of the peak in the 2DES when compared to that of the homogeneous parameters.

The black flux data-set in figures 3.1.5 – 3.1.10, which corresponds to the red data within tables 3.2 and 3.1, with particular emphasis on 3.1.7, demonstrates that the underdamped HEOM is insufficiently stable between the homogeneous overdamped regime and the underdamped limit to further explore non-Markovianity in this region. This is as a consequence of the basis failure

[b] Underdamped spectra employ a Hamming apodisation function, in agreement with experimental procedures, discussed in section 2.5.6.2.

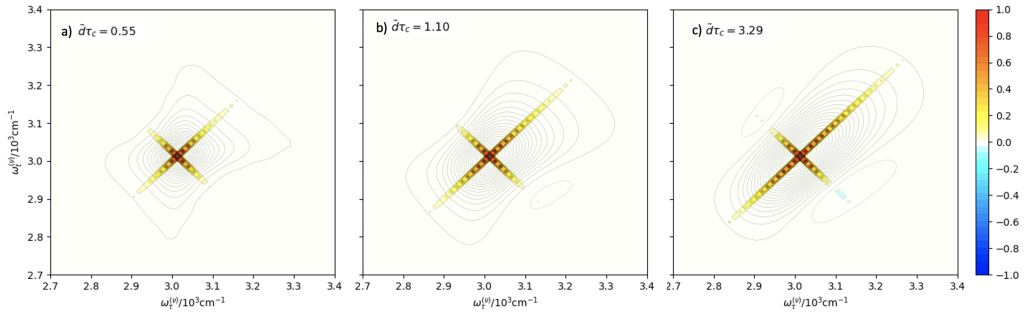

Figure 3.1.9: Spectral slices of the absorptive 2D spectra at a population time of $T = 0$ fs shown for each of the overdamped homogeneities, $\tilde{d}\tau_c$ values shown in table 3.1, which are used to generate the ellipticity in figure 3.1.10.

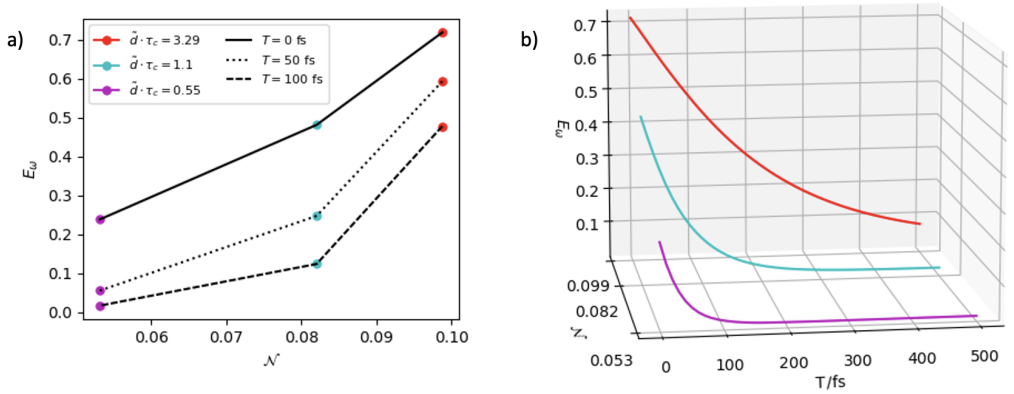

Figure 3.1.10: Ellipticity, E_ω, of the absorptive 2DES against the measured maximum non-Markovianity, $\mathcal{N}$, for the three overdamped baths, identified by their $\tilde{d}\tau_c$ values, for a) $T = 0, 50$ and 100 fs and b) $T = 0 - 500$ fs, sampled at 10 fs intervals. These results are generated from the spectral slices in figure 3.1.9. These results are based on similar considerations in Green et. al[1].

present in the over, under, ASD-, and LDUO- HEOMs described in section 2.5 when in the region of critical damping. This failure is most obvious in the fluxes in c) and d) of figure 3.1.5 in which there is a divergence. This divergence results in a lifting of the positive flux away from the time axis for long time, observed in figure 3.1.6, corresponding to Markovian dynamics vanishing. The result of this is that there is significantly more relative non-Markovian recurrence, and damping, which leads the one dimensional lineshape of figure 3.1.7 for $\gamma^{(\nu)} = 500$ cm^{-1} to broaden away from the shared intersection at $\omega^{(\nu)} \sim 2\,800$ and $3\,300$ cm^{-1}. Further parameter regimes in the under and overdamped limits, and a study involving the gHEOM, (2.5.69), would help rectify this problem. However, a full analysis of damping strengths is beyond the scope of this thesis, and is left as future work, dependent on the implementation of the gHEOM.

In summary, this study has shown that a decrease in the damping strength for a Brownian oscillator of fixed mode frequency and reorganisation energy results in the maximum non-Markovianity being reached at a slower rate. Additionally

it has been demonstrated that the largest values of $\mathcal{N}$ are generated for underdamped baths in which there are persistent oscillations in the correlation function as a consequence of static environments, leading to prolonged feedback of information from the bath to the system. In contrast, as the damping is increased and the system moves into the homogeneous overdamped regime the total non-Markovianity reduces due to the shorter correlation times and increased Markovian dissipation. These features have been corroborated by the ellipticity of the 2D spectra for equivalent parameter regimes such that the intrinsic link between non-Markovianity and inhomogeneous broadening is confirmed. Any increase in non-Markovianity, $\mathcal{N}$, leads to inhomogeneous broadening which is proportional to the information gained by the system from the bath, and in canonically transformed systems this impacts the bath and system components of the total environment degrees of freedom.

Now that we have quantified the non-Markovianity within OQS and have linked this to spectral lineshape it is possible to use this to address the remaining question: *what is the impact of canonically transforming a system vibration into the bath, and are the two resulting models still completely equivalent?*

3.2 Hamiltonian versus Bath/Spectral Vibration for a Homodimer

Through the canonical transform the complexity of a model OQS can be shifted from the Hamiltonian to the spectral density leading to mathematically equivalent descriptions of the total system. A system containing a fundamental intramolecular vibration can be constructed with vibrational degrees of freedom expressed as explicit energy levels within the Hamiltonian, up to a point of truncation in ν, or with vibrational degrees of freedom canonically subsumed into the bath. The model with Hamiltonian vibrational structure is denoted the *Hamiltonian vibration model* (HVM), whereas when the intramolecular vibration is a component of the environment degrees of freedom the model is termed the *bath/spectral vibration model* (BVM)[2]. In order to elucidate the impact on 2DES lineshape of this system-bath boundary placement, a pair of mathematically equivalent models are generated and their spectra calculated and compared. The generated spectra are suitable for comparison as they correspond to physical observables. The two schemes, which are equivalent to cases b) and c) from figure 3.1.1, are considered in the context of a vibronic monomer and a homodimer constructed following the theory in sections 2.2.1.1 and 2.2.1.3 which is better depicted in figure 3.2.1. However, computational application of theory relies on assumptions, approximations, and truncations which will lead to a breakdown of mathematical equivalence, the impact of which, we aim to

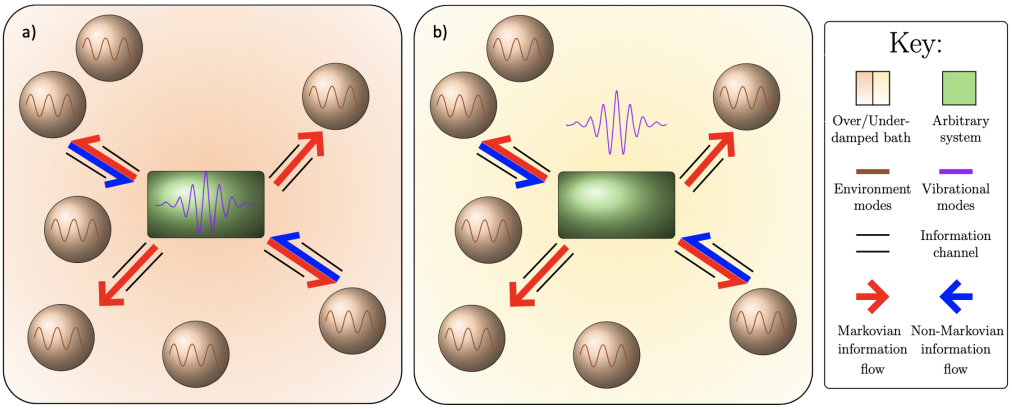

Figure 3.2.1: A schematic of the HVM and BVM schemes, equivalent to cases b) and c) from figure 3.1.1. An arbitrary system of interest is highlighted in green, with or without its fundamental intramolecular vibration, and the bath is either over, a), or underdamped, b), dependent on whether the system vibration has been canonically subsumed. Quantum information channels, depicted as tubes, transfer information between the system and bath which impacts the spectral lineshape, quantified in section 3.1. Reproduced from ref. 2, with the permission of AIP Publishing.

elucidate.

Within the following simulations, the ground and excited electronic states of the monomer are separated by $\omega_{eg}^{(\nu)} = 10\,000$ cm^{-1}, which is coupled to a vibrational mode of frequency $\omega_0^{(\nu)} = 500$ cm^{-1}, with a dimensionless excited state displacement of $\tilde{d} = 1.09$ inducing a system reorganisation energy of $\lambda^{(\nu)} = 300$ cm^{-1}. Formation of the corresponding J-aggregate homodimer involves coupling the transition dipole moments for a pair of monomers through equation (2.2.27), with a strength of $J^{(\nu)} = -400$ cm^{-1}, in the strong coupling limit. In the HVM models, explicit vibrational energy levels are present within the Hamiltonian, but after diagonalisation following a unitary transformation, equation (2.2.25), these levels are truncated leaving only $\nu_{\mathrm{M}} = \{0, 1, 2\}$.

The environment is constructed as an infinite ensemble of harmonic oscillators, reduced to a spectral density function of the form (2.2.63), with $n = 1$ for the HVM and $n = 2$ for the BVM. The open system is constructed by coupling the system of interest to a phononic reservoir which is described by an overdamped spectral density that is weakly inhomogeneous. This component, which is the sole bath for the HVM and the first component of the BVM total bath, is denoted

$$J_{\mathrm{O}}(\omega) = \frac{2\eta_{\mathrm{O}}\omega\Lambda_{\mathrm{O}}}{\omega^2 + \Lambda_{\mathrm{O}}^2}. \tag{3.2.1}$$

This is equivalent to the Lorentz-Drude spectral density discussed in 2.2.2.2, which is often referred to as an overdamped spectral density, and is depicted in figure 3.2.2. The overdamped bath reorganisation energy is chosen to be

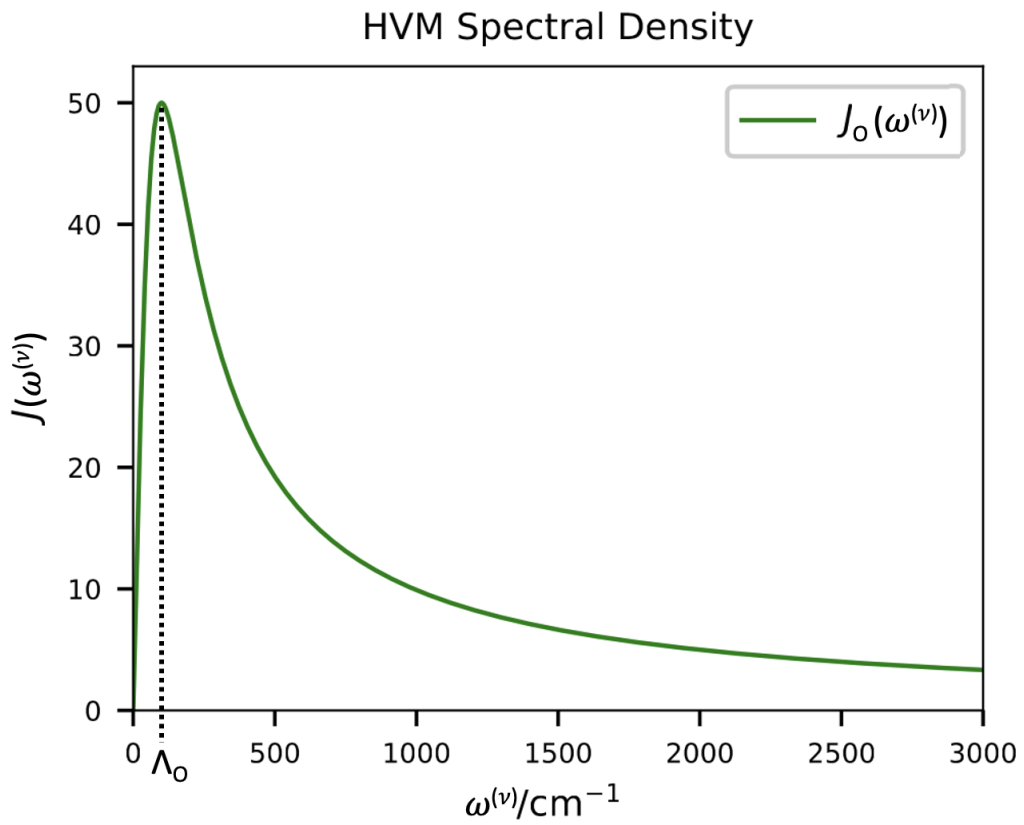

Figure 3.2.2: The total HVM spectral density, J_{O}. The environmental contributions are a redshifted Gaussian profile of low frequency modes with an intensity equal to the bath reorganisation energy, $\eta_{\mathrm{O}}^{(\nu)} = 50$ cm^{-1}. Reproduced from ref. 2, with the permission of AIP Publishing.

$\eta_{\mathrm{O}}^{(\nu)} = 50$ cm^{-1}, and damping rate $\Lambda_{\mathrm{O}}^{(\nu)} = 100$ cm^{-1} so that the environment is dominated by moderately intense low frequency modes, as is typical for condensed phase spectroscopy at 300 K. The damping rate is large, so that the environment is classed as overdamped, with $\gamma_1^{(\nu)} = 2\,500$ cm^{-1} which is equivalent to $\Lambda_{\mathrm{O}}^{(\nu)} = 100$ cm^{-1}. Consequently the rate of decay of system-bath correlation, $\tau_c = \Lambda_{\mathrm{O}}^{-1}$, is sufficiently slow to introduce visible inhomogeneous broadening to the resultant 2DES.

In the BVM, the intramolecular vibrational mode is subsumed into the bath degrees of freedom through a canonical transformation resulting in an $n = 2$ component. This reduces the size of the system Hamiltonian to the electronic states only, which are then coupled to an underdamped Brownian oscillator. The spectral density for the BVM has two components[157],

$$J_{\mathrm{U}}(\omega) = \frac{2\eta_1\omega_1^2\omega}{(\omega_1^2-\omega^2)^2+(\gamma_1\omega)^2} + \frac{2\eta_2\omega_2^2\omega}{(\omega_2^2-\omega^2)^2+(\gamma_2\omega)^2}, \tag{3.2.2}$$

where the second component corresponds to the intramolecular vibrational mode in the underdamped limit[231], $\omega_2 \gg \gamma_2$, such that $\omega_2 = \omega_0$ the vibrational mode frequency, and $\eta_2 = \lambda$ from equation (2.2.8). The first component corresponds to

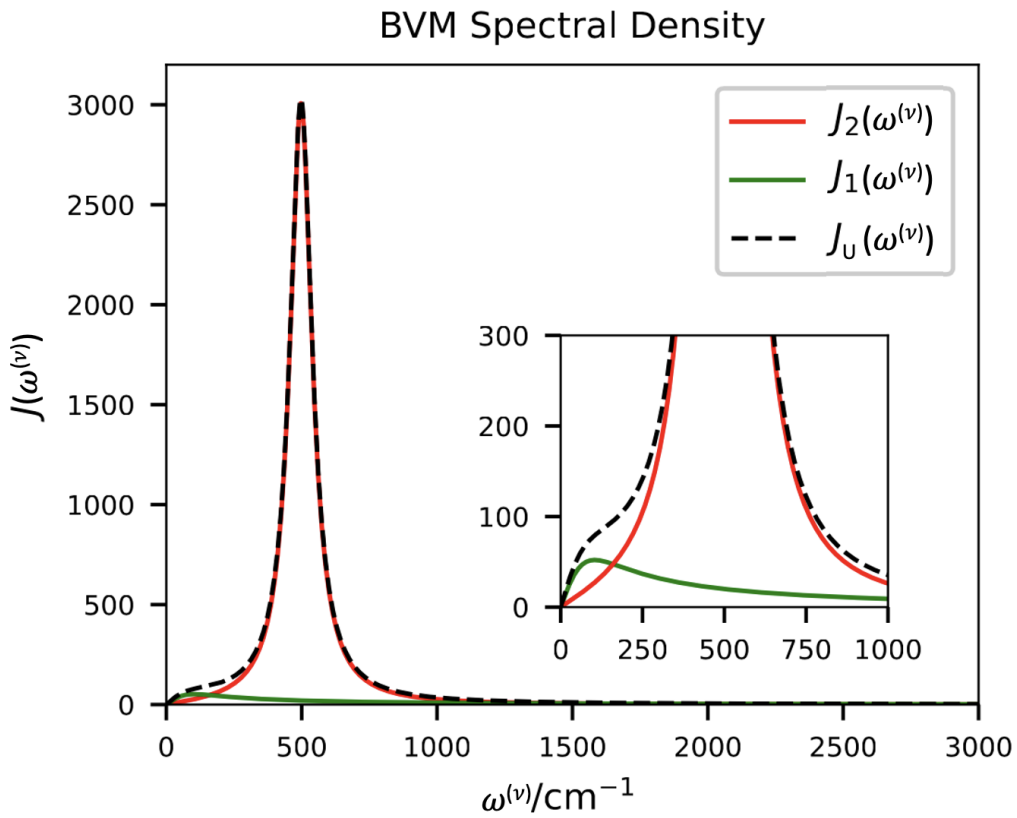

Figure 3.2.3: The total BVM spectral density, J_{U}, the purely environmental component, J_2, and the intramolecular vibration component, $J_1 = J_{\mathrm{O}}$. The intense Lorentzian peak at the vibrational mode frequency, ω_0, is shown alongside the weakly intense redshifted Gaussian of environment modes with a reorganisation energy of 50 cm^{-1}. Reproduced from ref. 2, with the permission of AIP Publishing.

the purely environmental degrees of freedom from the HVM model. As a result of $\omega_1 \ll \gamma_1$ this reduces to the Debye form

$$J_{\mathrm{U}}(\omega) = \frac{2\eta_{\mathrm{O}}\omega\Lambda_{\mathrm{O}}}{\omega^2 + \Lambda_{\mathrm{O}}^2} + \frac{2\eta_2\omega_2^2\omega}{(\omega_2^2 - \omega^2)^2 + (\gamma_2\omega)^2}. \tag{3.2.3}$$

The total spectral density for the BVM is shown in figure 3.2.3 as well as the separate underdamped, and overdamped, components. In contrast to the broad overdamped spectral density for the low frequency bath modes, the underdamped spectral density features a sharp Lorentzian peak at the intramolecular mode frequency with width determined by the damping parameter γ_2.

In the HVM model, the bath is coupled to the electronic excited states through the coupling operators (2.2.47) which undergo the same unitary transformation as the diagonalisation of the Hamiltonian. This operation induces a fluctuation in the transition frequency of the excited state, due to stochastic motion, leading to dephasing of excited state wavepackets and spectral broadening. The HVM

model is simplified by assuming that vibrational relaxation and any associated modulation of the electronic coupling are much slower processes than the electronic dephasing, with negligible effect on the 2DES spectra at very early population times $T \leq 100$ fs such that dissipation processes are neglected. Similarly, in the BVM model, the purely electronic system states couple to the bath through the pure dephasing operators

$$\mathrm{B}_{\mathrm{M}}^{\mathrm{S}} = |e\rangle\langle e|\,, \tag{3.2.4}$$

for the monomer and

$$\mathrm{B}_{\mathrm{D}}^{\mathrm{S}} = |e^{+}\rangle\langle e^{+}| + |e^{-}\rangle\langle e^{-}| + 2\,|f\rangle\langle f|\,, \tag{3.2.5}$$

for the dimer. In both cases the system Hamiltonians are renormalised to counter the energy shift induced by the system-bath coupling. γ_2 introduces additional damping of the intramolecular mode in the BVM, absent in the HVM. Approaching the limit $\gamma_2 \to 0$, the BVM becomes equivalent to the undamped intramolecular vibrational mode in the HVM. However, zero damping invalidates the HEOM termination criterion[1] for this EOM construction, resulting in an infinite hierarchy. By canonically subsuming a pure intramolecular vibrational mode as an underamped vibration, additional damping is added to the model. This is referred to as *canonically derived damping* or *canonical damping*.

Figure 3.2.4, as shown below, presents 2DES for the vibronic monomer, obtained using the HVM and BVM models, used to determine the efficacy of these methods. Based on the theory of the canonical transform we expect a strong agreement between the two models, but contrasting levels of broadening as a consequence of the unavoidable canonical damping in the BVM. Figure 3.2.4 presents distinct peaks at the system fundamental transition frequency, ω_{eg}, and vibronic pathways at plus and minus integer multiples of the vibrational mode frequency, ω_0, in agreement with the theory outlined in 2.2.1.3. Peak positional information is explicit within the HVM as a consequence of having three vibrational levels per electronic state, resulting in a Hilbert space $|\alpha\rangle \otimes |n\rangle$ of $\dim(\mathcal{H}) = 6$, such that peaks are particularly distinct. In contrast, the BVM has a Hilbert space with $\dim(\mathcal{H}) = 2$, which accounts for explicit electronic states only. Despite this, there is clear evidence of cross peaks demonstrating that the system vibration is manifested through system interaction with the bath degrees of freedom. Furthermore, oscillation of vibrational coherence pathways[272] over the waiting time, T, results in peak amplitude changes within both spectra in figure 3.2.4. The similarity between these peak intensities suggests that both models are able to capture all the essential features for the monomer.

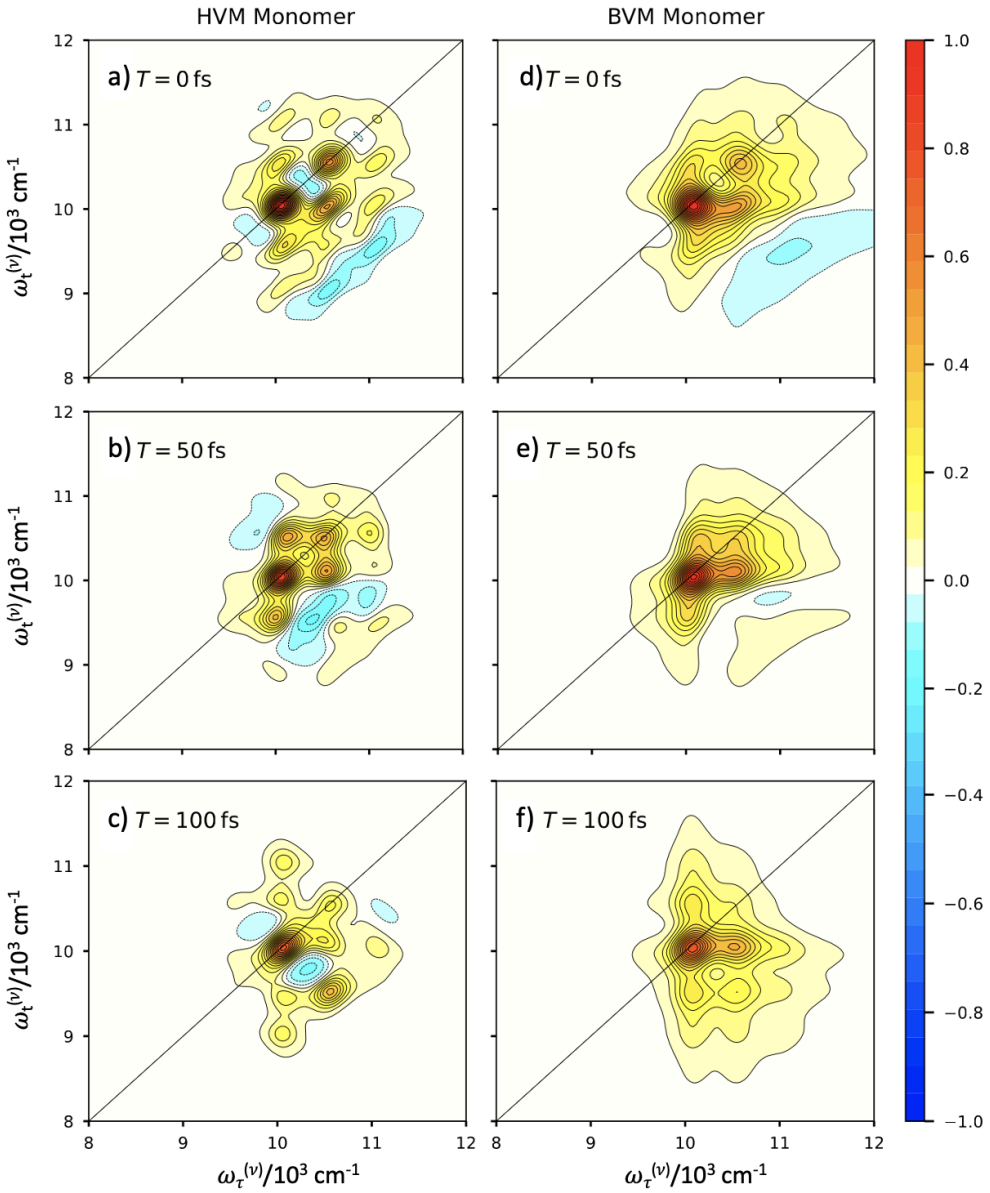

Figure 3.2.4: Absorptive 2D spectra for the HVM monomer a) – c) and BVM monomer d) – f) at $T = 0, 50$ and $100\,\mathrm{fs}$, normalised to the maximum at $T = 0\,\mathrm{fs}$. Reproduced from ref. 2, with the permission of AIP Publishing.

In contrast to these similarities, there are also a number of noteworthy differences between the two models. At early waiting times within the HVM, $T < 50$ fs, the uniform action of the overdamped bath elongates the vibronic peaks along the diagonal, generating peak definition, however as the waiting time increases this is lost. Additionally, the diagonal elongation, due to the inhomogeneity introduced by the environment, causes a loss of definition due to spectral diffusion. In contrast, the BVM is not restricted to three system vibrational levels, canonically subsuming the vibrations introduces the full continuum of vibrational levels into the bath. This allows expression of additional vibronic peaks which are truncated as part of the HVM. The cost of this additional vibronic detail is a greater degree of broadening, as a

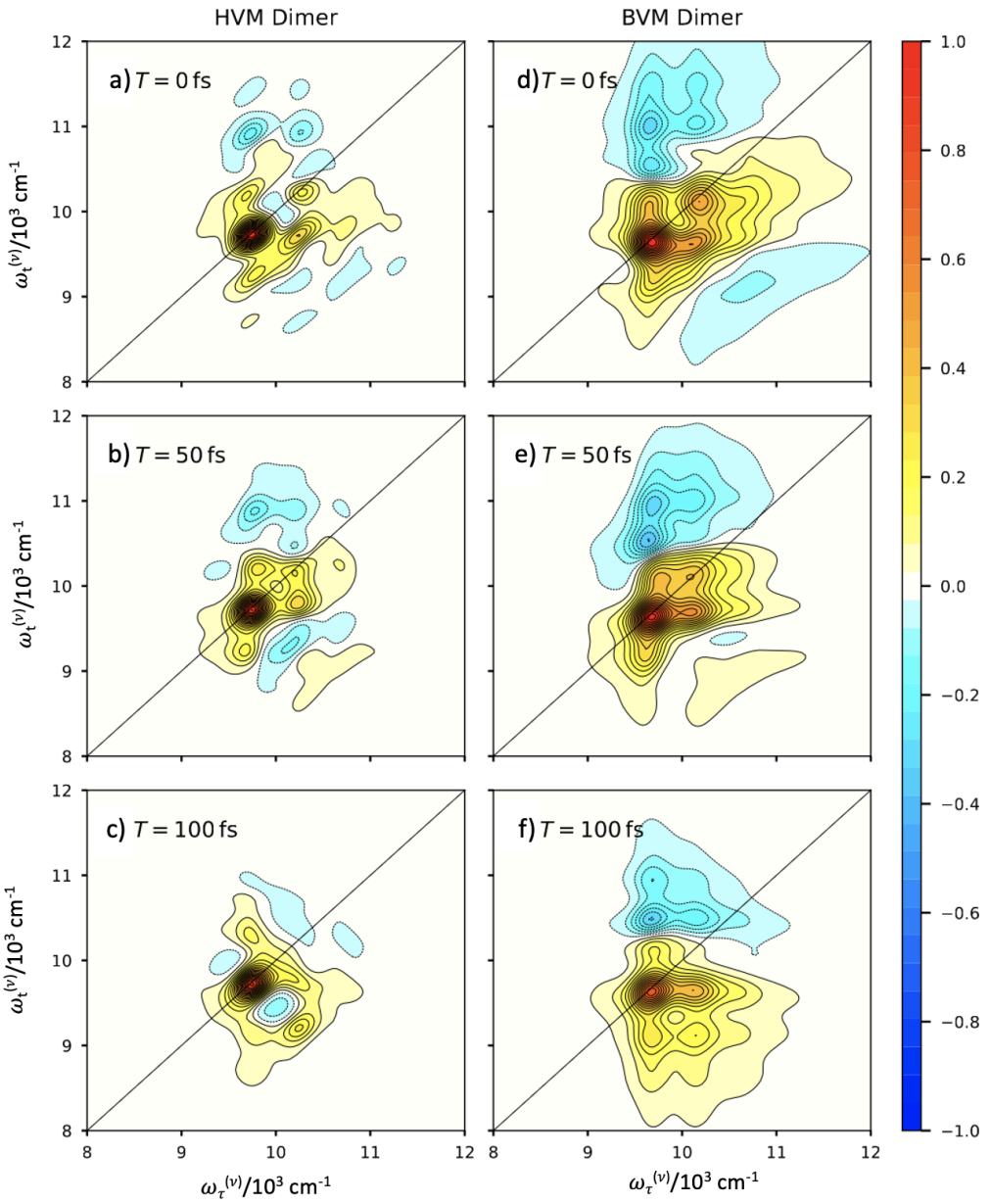

Figure 3.2.5: Absorptive 2D spectra for the HVM dimer a) – c) and BVM dimer d) – f) at $T = 0, 50$ and 100 fs, normalised to the maximum at $T = 0$ fs. Reproduced from ref. 2, with the permission of AIP Publishing.

consequence of the secondary bath, which obscures spectral diffusion and leads to poor peak definition, and positional precision.

In all spectra in figure 3.2.4 there are significant regions of negative intensity below the diagonal at $T = 0$ fs, which should not be mistaken for excited state absorption peaks. The monomer has a single excited state, or pair of electronic states, making excited state absorption impossible. These regions on the spectra are the result of rephasing vibrational coherence pathways which oscillate with opposite phase above and below the diagonal[210,231]. However, in the dimers the any blue regions above the diagonal are excited state absorption peaks.

The results for the strongly coupled J-aggregate homodimer are presented in figures 3.2.5 and 3.2.5, and are in strong agreement with the analysis of the monomer spectra. In both the HVM and BVM models, peak positions and intensities are comparable, and the expected redshift by J of the fundamental peak from ω_{eg} to ω_{e^+g} is observed. Additionally, the theoretically predicted hot band peaks resulting from vibrationally excited states[69] are clearly present. Since a secondary excited state is present within dimer systems, excited state absorption (ESA) pathways become possible. Both models clearly depict this region of strong ESA above the diagonal, corresponding to transitions from the bright exciton state, $|e^+\rangle$ to the doubly excited state, $|f\rangle$. The demonstration of commensurate peak amplitudes in HVM and BVM spectra, for all waiting times, is a clear indication that both models are able to generate vibronic pathways for the extended excited state structure of a dimer. This is a consequence of the oscillation of the vibrational coherence pathways[82] present within the model. In addition, the fundamental peak in each spectrum has an increased amplitude relative to the associated vibronic peaks[301] which is indicative of a J-aggregate.

Despite these similarities, just as for the monomer spectra, there are also a number of differences between the two models. In agreement with the monomer spectra, there is a uniform broadening along the diagonal as a consequence of inhomogeneity introduced by the overdamped bath in the HVM which is obscured by additional broadening in the BVM. The most fundamental difference in these results, which was not relevant in the monomer case, is whether the expected J-aggregate redshift is present. Based on the theory for J-aggregates there will be a redshift of $J^{(\nu)} = -400$ cm^{-1} which is quenched[75–77] by the vibronic coupling of the system to a reduced magnitude. The quenched dimer redshift is directly observable in the HVM spectra in figure 3.2.5 and matches the decrease in transition frequency relative to the monomer shown by the Hamiltonian eigenvalues for the system of -316 cm^{-1}. In striking contrast, in both the eigenvalues and spectra in figure 3.2.5, there is a full redshift of $J^{(\nu)} = -400$ cm^{-1} with a complete absence of vibronic quenching. This demonstrates a fundamental difference between the two models: *canonical transformation of system vibrations into the bath results in the loss of vibronic quenching within dimer models*.

One of the most striking and fundamental differences between the HVM and BVM models, predicted during construction and evident in the spectra, is the significant change in broadening. In order to correctly attribute these differences in spectral lineshape to the system-bath boundary placement, a series of spectra are generated for a sequence of decreasing damping strengths towards the limit of vanishing γ_2. In the limit, $\gamma_2 \to 0$ the FWHM of the spectral density describing the intramolecular vibration will also vanish, resulting in an entirely undamped mode. Since the canonical transform maps an *undamped*,

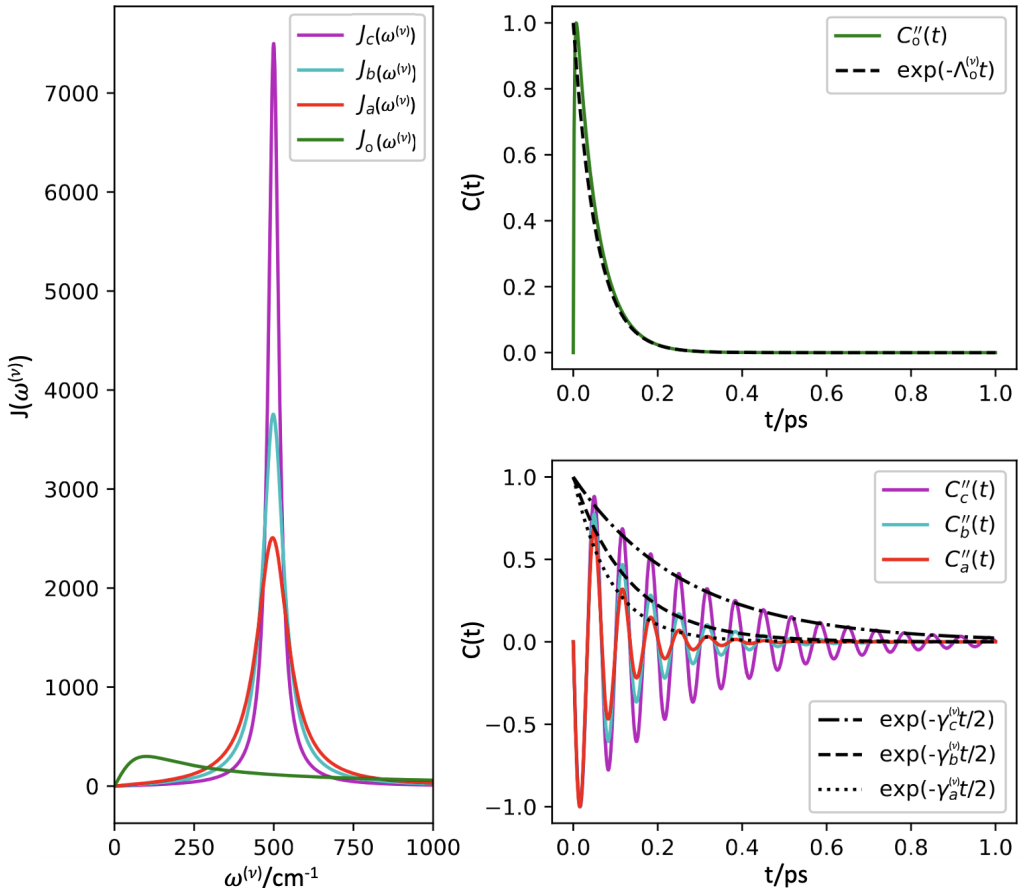

Figure 3.2.6: Spectral densities and correlation functions, with exponential fits, for an overdamped, $\Lambda_{\mathrm{O}}^{(\nu)} = 100$, and three underdamped spectral densities with damping strengths $\gamma_{\mathrm{a}}^{(\nu)} = 120$ cm^{-1}, $\gamma_{\mathrm{b}}^{(\nu)} = 80$ cm^{-1}, and $\gamma_{\mathrm{c}}^{(\nu)} = 40$ cm^{-1}. Reproduced from ref. 2, with the permission of AIP Publishing.

pure, intramolecular vibrational mode onto harmonic modes of the environment, it will have introduce a secondary source of quantum information and damping. Subsequently, progressing to lower damping rates minimises the decaying component of the correlation function, for the system vibration, which reduces the additional electronic dephasing which is added to the total system, and limits the additional lineshape broadening. With this choice of HEOM reaching the limit of zero canonical damping is impossible, as it will invalidate the termination criterion, so an entirely new EOM construction would be necessary to confirm that the BVM and HVM become formally equivalent. A new HEOM, for exactly this purpose, is considered in chapter 5.

It is clear from these results that canonical transformation of a system intramolecular vibration, while theoretically equivalent, is not practically equivalent to the explicit Hamiltonian models when applied to standard over and underdamped HEOMs. Subsuming this fundamental vibration leads to qualitatively similar 2DES lineshape but the change in Hamiltonian structure has a considerable impact on the total dynamics. When the HVM is applied to a

vibronic dimer the three vibrational levels per electronic state result in a Hilbert space $\dim(\mathcal{H}) = 36$, whereas the corresponding BVM model has a Hilbert space of $\dim(\mathcal{H}) = 4$ [166]. Consequently the HVM contains all relevant couplings between the truncated set of explicit energy levels, giving rise to sharply defined peaks. The broadening of these peaks is applied uniformly as a result of the overdamped spectral density of environment modes leading to Lorentzian peaks with precise positional information. In contrast, peak information and energy transfer in the BVM occurs as a result of non-Markovian feedback from energy fluctuations within the bath, and vibronic peaks arise naturally as a consequence of the system-bath interaction. This means that broadening is peak specific, and enhanced by the secondary source of damping, resulting in less positional precision but broadening which is closer to that which would be observed in experiments. In addition, canonical transformation of the system vibrational mode into the environment degrees of freedom removes vibrational truncation, which is present in the HVM, leading to vibronic peaks forming due to the full vibrational continuum of states.

These features have implications for the computational cost of each model. The truncation of the Hilbert space by removal of explicit vibrational states reduces the computational cost of diagonalisation when compared to the HVM. However, the increased computational cost of the BVM comes from the increased complexity of the spectral density, and resulting HEOM, which will have many more ADOs in order to generate the full dynamics. A balance should be reached between the level of explicit Hamiltonian structure necessary, versus the level of bath structure required in order to generate approximate dynamics with a minimum of computational effort.

3.2.1 The Canonical Transform, Examined Close to the Zero Canonical Damping Limit

In this model some degree of canonical damping is unavoidable, so a demonstration of the minimisation of this added broadening in considered through the correlation function. This is achieved by introducing three different damping parameters which progress towards the limit of vanishing canonical damping: $\gamma_{\mathrm{a}}^{(\nu)} = 120$ cm^{-1}, $\gamma_{\mathrm{b}}^{(\nu)} = 80$ cm^{-1}, and $\gamma_{\mathrm{c}}^{(\nu)} = 40$ cm^{-1}. A formal solution of the correlation function is computed from the fluctuation-dissipation theorem, discussed in appendix 2.2.53, under the substitution of the underdamped spectral density and with $n = 1$. The forms of the solution are the aforementioned kernels of dissipation and thermal fluctuations (2.5.31):

$$L_{\mathrm{U,corr}}^{(\alpha)}(t) = L_{\mathrm{U},\mathcal{R}}^{(\alpha)}(t) + iL_{\mathrm{U},\mathcal{I}}^{(\alpha)}(t). \tag{3.2.6}$$

As previously discussed, in the overdamped regime the correlation function has no imaginary component and reduces to an exponential decay, $\exp(-\frac{t}{\tau_c})$. This results in shallow, broadened, 2DES peaks. Figure 3.2.6 shows the spectral density for the HVM, its calculated correlation function, and a fitted exponential decay.

In contrast, all three of the additional underdamped regimes have correlation functions which consist of both oscillations and decays as a consequence of the highly specific frequency (peak) present within the structured spectral density, when compared to the overdamped contribution. When correlations take this form we expect the decaying component to have a rate proportional to the associated damping rate $\frac{\gamma_{\{\cdot\}}^{(\nu)}}{2}$ attributed to the added mode. This follows from the simplification of the imaginary part of the correlation function[37]:

$$L_{\mathrm{u},\mathcal{I}}^{(\alpha)}(t) = \frac{\hbar\eta_2\omega_0^2}{2\zeta}\sin(\zeta t)\exp\Big(-\frac{\gamma_{\{\cdot\}}^{(\nu)}}{2}|t|\Big), \tag{3.2.7}$$

where $\zeta = \sqrt{\omega_0^2 - \left(\frac{\gamma_{\{\cdot\}}^{(\nu)}}{2}\right)}$. Figure 3.2.6, in addition to the overdamped correlation, shows the negative exponential dephasing rates, calculated using $\frac{\gamma_{\{\cdot\}}^{(\nu)}}{2}$, for all three underdamped spectral densities. This demonstrates that decreasing the damping and increasing the dephasing time results in a sharpening of the spectral mode, and an increase in the amplitude of oscillations in the correlation function.

These alterations to the underdamped spectral density are then applied to the BVM monomer evolution, presented in 3.2.7. The successive reduction of γ_2 shows a clear trend towards the lineshape of the HVM, in figure 3.2.4 a), with peaks becoming more well defined and broadening diminishing. However, there are computational implications to this. The number of ADOs increases exponentially as the damping strength is reduced such that, for a reduction of 40 cm^{-1} as in $\gamma_{\mathrm{b}}^{(\nu)}$ to $\gamma_{\mathrm{c}}^{(\nu)}$, an additional $115\,620$ auxiliaries are required. Consequently, this is not a computationally tractable approach, and the limit of vanishing damping must be reached with an alternate method. Furthermore, the current termination scheme $\Gamma_{\max}^{(\nu)} = 10\gamma_{\{\cdot\}}^{(\nu)}$ which is generated due to $\max\left(\frac{\max(\omega_0)}{\mathcal{R}(\min(\nu_{\{\cdot\}}))}\right)$ from equation (2.5.59), is clearly singular in the limit:

$$\lim_{\gamma_{\{\cdot\}}\to 0}\min(\nu_{\{\cdot\}}) = \lim_{\gamma_{\{\cdot\}}\to 0}\frac{\gamma_{\{\cdot\}}}{2} - i\zeta_n, \tag{3.2.8}$$

$$= \lim_{\gamma_{\{\cdot\}}\to 0}\frac{\gamma_{\{\cdot\}}}{2} - i\sqrt{\omega_0^2 - \left(\frac{\gamma_{\{\cdot\}}^{(\nu)}}{2}\right)} = \mp i\omega_0, \tag{3.2.9}$$

as there is no real contribution. This would require an infinite number of auxiliaries due to the singularity in the termination criterion, which invalidates

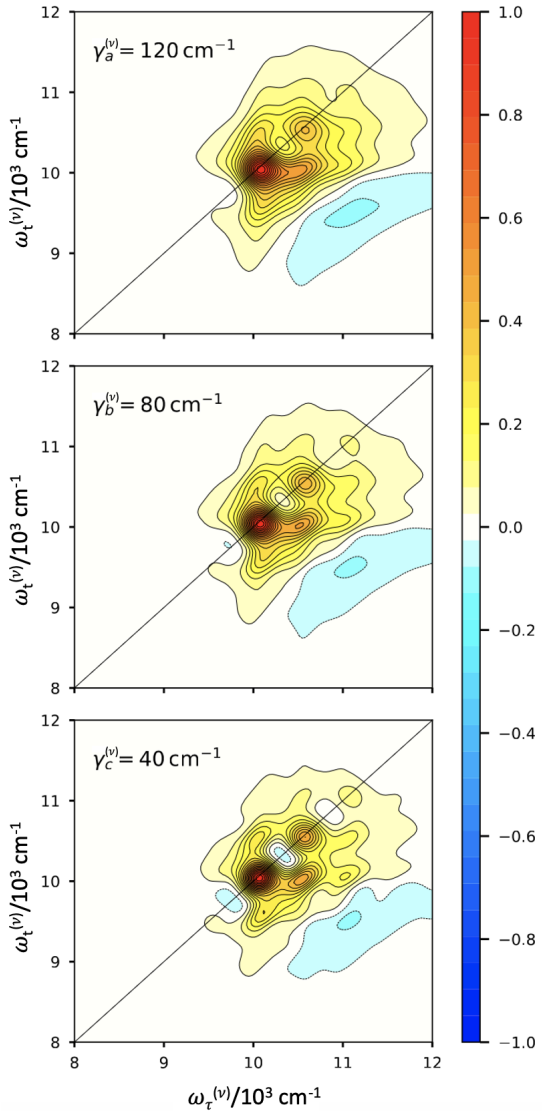

Figure 3.2.7: Absorptive 2D spectra for the BVM monomer at $T = 0\,\mathrm{fs}$, normalised to the maximum at $T = 0\,\mathrm{fs}$, with damping strengths $\gamma_{\mathrm{a}}^{(\nu)} = 120\ \mathrm{cm}^{-1}$, $\gamma_{\mathrm{b}}^{(\nu)} = 80\ \mathrm{cm}^{-1}$, $\gamma_{\mathrm{c}}^{(\nu)} = 40\ \mathrm{cm}^{-1}$. Reproduced from ref. 2, with the permission of AIP Publishing.

this termination scheme. Therefore, this model is sufficient as an approximation of the true lineshape, but it is not equivalent to the HVM unless a new EOM is constructed which is capable of reaching the limit of vanishing canonical damping.

In summary, this study has shown that HVM and BVM models of vibronic monomers and homodimers are qualitatively similar, based on the 2D spectral lineshape, and would become formally equivalent in the limit of vanishing canonical damping, $\gamma_2^{(\nu)} \to 0$. Both sets of results, for the monomer and dimer, successfully reproduce the expected spectral features, but the broadening varies dependent on the structure of the spectral density. The HVM has uniform broadening across all peaks as a result of system-bath interaction with the

overdamped bath. However, due to the construction of the BVM, the uniform broadening applied to each peak from the Hamiltonian is obscured as a consequence of the unavoidable additional damping from the underdamped mode. This means that there is a choice when attempting to model OQSs between an HVM or BVM approach. The system-bath boundary placement in these approaches alters the vibronic coupling effects, as is evidenced by the lack of vibronic quenching relative to the Hamiltonian eigenvalues for the BVM. Clearly, HVM versus BVM is a choice between energetic informational precision (peak position) and greater dynamic broadening, respectively. This represents a shift in focus from an accurate system Hamiltonian to a model that efficiently includes a more complete system-bath interaction. Finally, we comment on the relative computational effort of each approach. An HVM approach specifically includes vibronic states in the Hamiltonian, capturing vibronic quenching of dimers, but it is expensive because of the diagonalisation. In this case the computational bottleneck is the system choice and the corresponding Hilbert space dimension. In contrast, the BVM contains all vibrational detail within the bath, as an underdamped spectral density, allowing the Hilbert space dimension to be significantly reduced. Application of the BVM shifts the computational bottleneck to the bath dynamics, exponentially increasing the number of auxiliaries as a function of decreasing damping strength. However, this introduces the risk of neglected vibronic quenching in electronically coupled systems, and additional damping which results in greater peak broadening across the spectrum.

The first two studies in this section have left three, major, open questions: 'Can the limit of vanishing canonical damping be reached?', 'Can highly structured spectral densities, similar to the underdamped canonically transformed mode, be leveraged to attain greater control over the system-bath boundary and canonical damping?', and finally, 'Can explicit measurement of subsumed vibrational levels still be observed after canonical transformation, with similar qualitative meaning as physical observables?'. Chapter 5, appendix F, and section 3.3 each address these respective problems.

While it is clear from the discussion of HEOM methods in section 2.5, and appendix D, that the ASD-HEOM is a powerful tool for modelling non-Markovian systems. The ability to introduce highly structured spectral densities means that strongly non-Markovian system-bath interactions can be generated allowing for considerable memory effects. However, as outlined in appendix F, this EOM requires considerable computational effort and introduces a number of computational artefacts as a consequence of the strongly non-Markovian dynamics. For these reasons the ASD-HEOM is intractable and unsuitable for generating spectra in the limit of vanishing canonical damping. Consequently, a new form of HEOM, the LDUO-HEOM is generated for this

purpose in chapter 5.

3.3 Auxiliary Density Operators and Virtual Quantum Information

To investigate the canonically subsumed vibrations within the spectral density, a set of models with similar parameters to those of the BVM in section 3.2 are constructed. In these variations of the BVM model the direction of information flow within the hierarchy is examined as well as the contents of the auxiliary density operators. Within the hierarchy of the HEOM, only the density matrix contains physical information about the system of interest. However, as established in the theory of an underdamped spectral density section 2.2.2.2, it is possible to subsume a system intramolecular vibrational mode into the environment degrees of freedom. In this way the system-bath boundary placement results in a spectral density containing a mixture of system and bath degrees of freedom, meaning that bath operators no longer contain purely environmental physical parameters. The nature of the auxiliaries, and their intrinsic relation to the system parameters, are discussed within the work of Fay et. al.[302], and Yan et. al.[303], but the level of insight that can be gained from the auxiliaries is not discussed. In the absence of a quantitative interpretation of the behaviours from the ADOs, the impact of the vibrational structure lost through subsuming information into the spectral density is analysed through application of the BLP metric, equation (2.1.27).

In all simulated 2D spectra we use a ground and excited state separation of $\omega_{eg}^{(\nu)} = 10\,000$ cm^{-1}. The vibrational mode of the system is $\omega_0^{(\nu)} = 500$ cm^{-1}, where the non-dimensional displacement of the excited state potential is $\tilde{d} = 1.09$ in order to generate a physical system reorganisation energy of $\lambda^{(\nu)} = 300$ cm^{-1}. Computationally, after diagonalisation the Hamiltonians are truncated to include only the $\nu_{\mathrm{M}} = \{0, 1, 2\}$ vibrational levels. In this study three BVM monomer regimes are chosen which span the limits of homogeneity denoted as fast dissipation, standard dissipation, and slow dissipation models based on the structure of the second (underdamped) bath contribution in equation (3.2.2). This is compared to a single HVM monomer. The associated bath coupling and vibrational mode frequency are $\eta_2^{(\nu)} = \lambda^{(\nu)}$, $\omega_2^{(\nu)} = \omega_0^{(\nu)}$, $\eta_1^{(\nu)} = 50$ cm^{-1}, and $\omega_1^{(\nu)} = 500$ cm^{-1}. The corresponding bath damping parameters are $\gamma_2^{(\nu)} = 1\,750$ cm^{-1}, and $\gamma_1^{(\nu)} = 2\,500$ cm^{-1} such that $\Lambda^{(\nu)} = 100$ cm^{-1} for the fast dissipation model. The standard dissipation model has $\gamma_2^{(\nu)} = 100$ cm^{-1}, and $\gamma_1^{(\nu)} = 2\,500$ cm^{-1} such that $\Lambda^{(\nu)} = 100$ cm^{-1} in agreement with the BVM results from section 3.2. The slow dissipation model has $\gamma_2^{(\nu)} = 100$ cm^{-1}, and $\gamma_1^{(\nu)} = 300$ cm^{-1}. The simulations are performed at

300 K, within the bounds of the high temperature approximation, and the Markovian limit is set to $\Gamma^{(\nu)}_{\text{max}} = 2\,000$ cm^{-1}. As in the BVM model, this system is coupled to the bath through a purely diagonal operator, $\mathrm{B} = \sigma_z$. The fast, standard, and slow dissipation models are propagated using the HEOM and contain $1\,264$, $39\,149$, and $98\,513$ ADOs respectively. 2D spectra are generated with a coherence time up to $\tau = 200$ fs in steps of 0.5 fs, for population times of $T = 0,\ 50,$ and 100 fs. Along with the 2DES, the BLP measure of non-Markovianity is calculated for the density matrix and for the ADOs through application of equation (2.1.27), upon substitution of an auxiliary state in place of the density operator. In order to sufficiently distinguish physical quantum information and that which is contained by ADOs, this is termed *virtual information*.

The hierarchy structure associated with the BVM dynamics, discussed in section 2.5.5.1, is considered in detail and the direction of virtual information flow is analysed. Each auxiliary has an associated vector which describes its location within the Matsubara dimensions. For example, a three dimensional hierarchy would have ADOs and associated vectors, $\mathbf{j}$. An example being, $\mathbf{j} = (1, 0, 0)$, which is the first ADO in the first Matsubara axis. Generally, writing out the full Matsubara coordinate vector is feasible, however when the number of dimensions increases beyond three, as is common for strongly non-Markovian dynamics, and when the ADO number increases it becomes a hindrance. In order to discuss individual ADOs ($\rho_{\mathbf{j}}$) and axes, each Matsubara dimension is termed $M\{\cdot\}$ such that the full vector can be simplified to $n_{\{\cdot\}}$, where n is the position along the respective axis, or *tier*[304–306], corresponding to the number of phonons involved in the process. From this definition we could write an ADO which is tier 3 in $M1$ and tier 2 in $M5$ with a total of 8 Matsubara dimensions as $(3, 0, 0, 0, 2, 0, 0, 0) = 3_1 2_5$. In this notation zeros in any position are omitted, with the exception of the density matrix which is denoted 0_0. In addition, the total distance of a given Matsubara vector from the density matrix can be calculated as $\sum n$.

The direction of virtual information flow within the hierarchy can be considered through a two dimensional hierarchy diagram, in contrast to three dimensional node diagrams shown with each EOM derivation, which is coloured to denote flux direction. In figure 3.3.1 each auxiliary has six quantum channels, although some HEOMs have more, (which are depicted as faces/sides of the cube/square) and their colour determines whether information is free to flow through the respective channel. An example of this is ADO $\rho_{1,1,0}$ which is connected in every direction to another ADO. In the figure 3.3.1 a) information moves upwards, increasing in tier, from 0_0. The blue faces indicate information cannot move into the $M1M2$ plane at $M3$ tier 0 because a -1^{th} tier does not exist. Similarly, information cannot move out of 2_3 as within this idealisation it is a terminator. In figure 3.3.1 b) information moves downwards, decreasing in

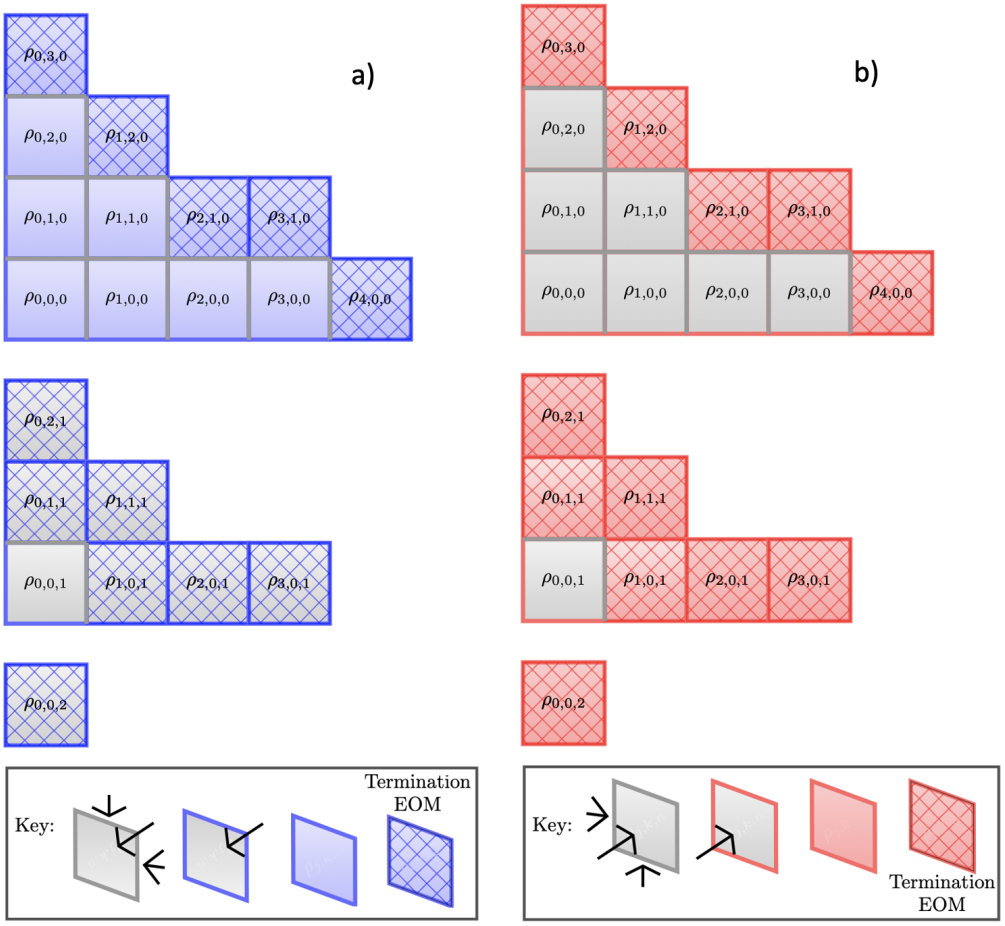

Figure 3.3.1: An idealised underdamped hierarchy structure. The freedom of information to flow away from the density matrix a) (increasing tier) or towards the density matrix b) (decreasing tier) is depicted in blue and red, respectively. The auxiliaries are labelled based on their Matsubara vector, **j**. In contrast to the hierarchy diagrams in section 2.5, these diagrams show that virtual information content in the ADOs on each edge is different to other ADOs. This is because it is a strictly Markovian information based on the termination criterion. Such Markovian information is governed by termination EOMs which are marked with cross-hatching.

tier, towards 0_0. The red face in 2_3 denotes that it is a terminator and information cannot move down from higher tiers, and the red plane $M1M2$ at $M3$ tier 0 indicates information cannot move down beyond $M3$ tier 0.

The following figures show the resulting flux and BLP measures from the BVM dynamics where each ADO is generated through a hierarchy generation algorithm and given an associated index based on when it was generated, between 0 (the density matrix) and N_{ADO} the total number of ADOs. The trace distance, flux, positive flux, BLP measure, and 2DES are generated for each set of results along with a contour in BLP, time, ADO number space, allowing for analysis of the sequence of ADOs that are created (the order of auxiliary generation). The trace distance, flux, positive flux, and BLP are additionally

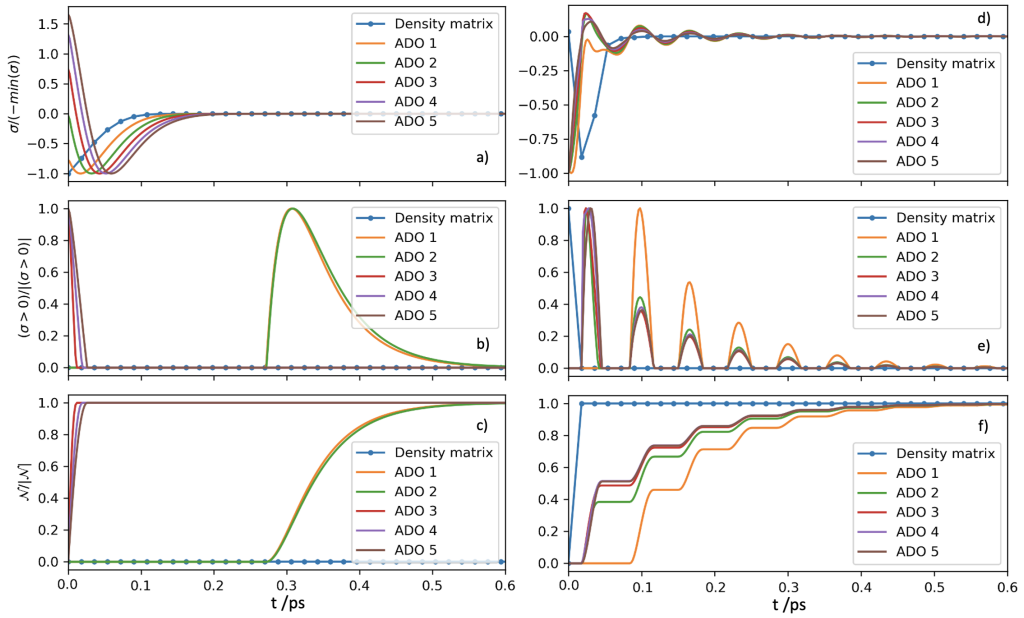

Figure 3.3.2: Total normalised flux, positive flux, and BLP for the HVM model, a) – c), and the equivalent standard dissipation rate BVM model, d) – f).

normalised based on their maximum absolute value. This is achieved through $\frac{\sigma}{-\min(\sigma)}$ where σ is the flux and $\min(\sigma)$ is the maximum Markovian flux. Dividing the flux by $-\min(\sigma)$ ensures that both non-Markovian and Markovian fluxes retain their original sign (positive and negative respectively) while also being normalised relative to the maximum Markovian flux, which is usually the larger flux. Hence, $\frac{\sigma}{-\min(\sigma)} > 0$ is non-Markovian. The reason for this is so that all ADOs can be compared directly to each other, and to distinguish the relative scale of both Markovian and non-Markvoian dynamics within the system. Some authors decide to introduce a scaling factor into the ADOs, of $\rho_n = \prod_k \prod_l (|d_{kl}|^{n_{lk}} n_{lk}!)^{-\frac{1}{2}} \rho_n$ [289,307], to improve convergence, such that each ADO shrinks proportional to the exponent of the matrix element $n_{lk}^{\pm}$, however in this thesis no such convention is applied.

3.3.1 Virtual Information in the HVM and BVM

The models of the HVM, fast dissipation BVM, the standard dissipation BVM, and slow dissipation BVM for monomers are compared against one another in order to demonstrate the intrinsic difference in virtual information flow when the system-bath boundary is shifted from the Hamiltonian and moved into the bath. Additionally, the range of damping strengths in the BVM should present a range of broadenings which demonstrate the difference in how broadening is applied in BVM versus HVM models.

Figure 3.3.2 shows the normalised flux, positive flux, and BLP for the HVM mononmer in a) – c), and the standard dissipation BVM in d) – f). a)

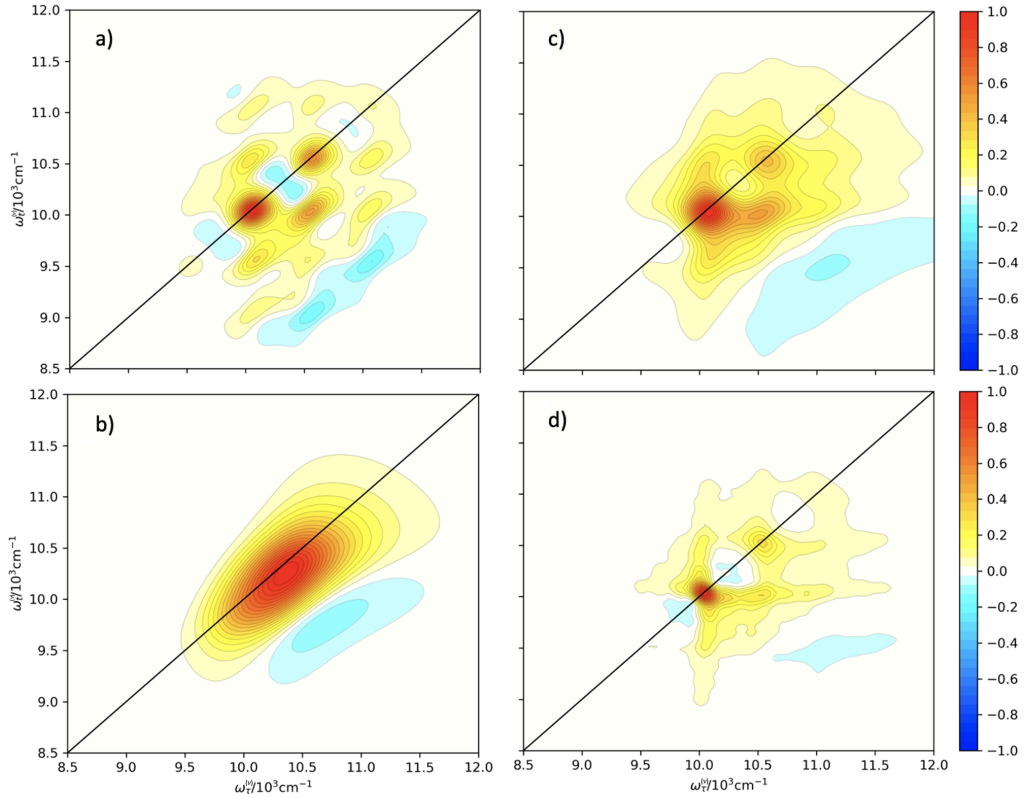

Figure 3.3.3: 2DES spectra for each of the four models at $T = 0$ fs. a) HVM, b) fast dissipation rate BVM, c) standard dissipation rate BVM, and d) slow dissipation rate BVM. Specific parameters are discussed in section 3.3.

demonstrates a clean progression of flux through the first Matsubara dimension, $M1$, where each ADO has the same flux profile but that is gradually translated so that the maximum Markovian feedback occurs later in the evolution. As discussed in section 2.5.5, higher tier ADOs involve larger integer multiples of phonon interactions, and subsequently have a much shorter timescale of information flow. This manifests as an instantaneous non-Markovian feedback, equivalent to a solvent reorganisation, before the globally Markovian dynamics of excited state relaxation occurs at a later time. Translation of the flux profile, for ADOs 1 to 5 in a), is a consequence of this behaviour and results in a larger maximum of instantaneous non-Markovian feedback. The data for ADOs 1 and 2 in a) – c) are consistent with this understanding, as it is strictly zero or negative. This means these ADOs are purely Markovian, information moves strictly away from the density matrix, and correspond to smaller numbers of phonons (lower in the Matsubara axis) with longer timescales. This is the cause of the apparently large non-Markovian feedback at ~ 0.35 ps. As is evident in a) this feedback is less than 1% of the magnitude of the Markovian feedback, but due to normalisation has been amplified.

d) – f) of figure 3.3.2 show the associated BVM results in a) – c). In agreement with the results in section 3.2 the global behaviour of the systems are

similar, however there are a number of differences in virtual information flow which lead to the differences in 2DES lineshape. Both models show strongly Markovian dynamics, during the process of excited state relaxation, with some non-Markovian feedback in deeper ADOs. This demonstrates that the bath is capable of producing larger multiples of phonon interactions due to system modes. However, the magnitude of non-Markovianity and the recurrence of information from the bath are markedly different. The magnitude of initial positive flux in d) is less than 1% of Markovian flux, whereas a) shows that high tier ADOs have a positive flux that is 1.5 times the size of the equivalent Markovian flux. Additionally, the incredibly small amount of non-Markovian flux which is present is returning to the system in a non-monotonic, gradual process, rather than in a sharp instantaneous feedback. This suggests that blurring the distinction between system and bath degrees of freedom results in oscillations as a consequence of system vibrational modes in the virtual information flux. Subsequently, the BVM model presents a gradual increase up to a maximum BLP in the density matrix, which is not present in the HVM. This is a further demonstration of the canonical intrinsic damping in the BVM which adds damping as a consequence of broadening the sharp underdamped vibration within the spectral density. Since the broadening occurs on the vibrational mode, and its impact on the overdamped contribution is minimal, this damping leads to broadening of the 2DES lineshape, particularly through inhomogeneous broadening.

These features of additional broadening are particularly evident when each of the four models are compared against each other, as in figure 3.3.3. This figure shows the 2DES spectra, at population time $T = 0$ fs, for a) the HVM monomer, b) the fast dissipation BVM monomer, c) the standard dissipation BVM monomer, and d) the slow dissipation BVM model. In agreement with 3.2, all of these spectra are qualitatively similar, and successfully depict the monomer system. In a) the peaks are uniformly broadened by a single overdamped bath with peak position defined by explicit energy levels, which leads to positional precision. When a BVM scenario is employed, in the overdamped limit, there are two baths and both add additional virtual information. This leads to a spectrum where peak locations have been obscured by the significant broadening associated with the larger virtual information content. Finally, c) and d) demonstrate a movement towards the limit of vanishing canonical damping, discussed partially in section F.2. The peaks become more Lorentzian in shape with broadening applied in a peak specific fashion from the spectral density.

Figure 3.3.4 demonstrates the change in broadening of the 2DES spectra for the HVM model as the population time T is increased up to 100 fs, and a contour depicting the changes in virtual information over the course of the evolution. It is clear from the contour plot in figure 3.3.4 that, the virtual information content

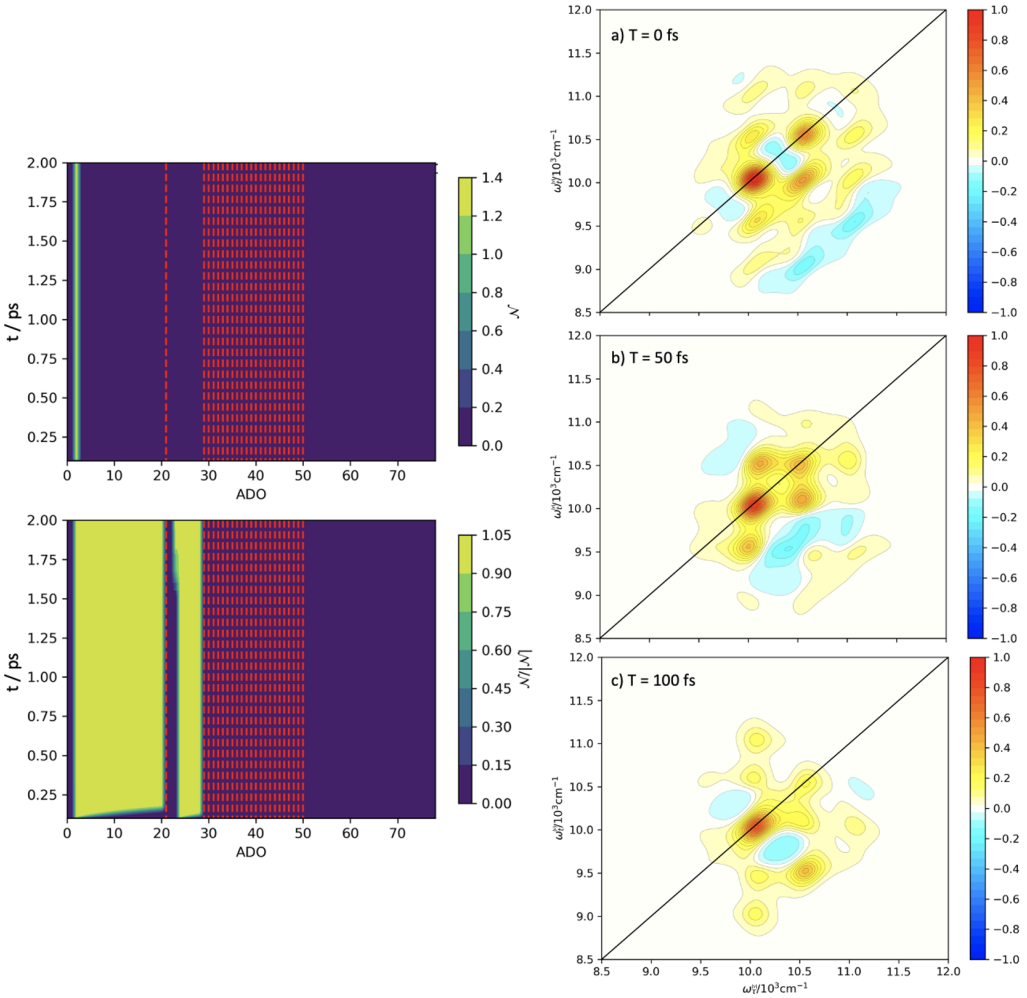

Figure 3.3.4: Contour plot for the HVM where red dashed lines denote terminators, and 2D electronic spectra for population times $T = 0$, 50, 100 fs.

has a very small magnitude when the ADO number is greater than 5, equivalent to the dynamics being dominated by ADOs close to the density matrix, but when this is normalised auxiliaries up to ADO number 30 have significant contributions. As a consequence of the Hamiltonian complexity and relative simplicity of the bath, this hierarchy contains only 79 ADOs and $\sim \frac{1}{3}$ of them are terminators. However, there are clearly some ADOs which contain virtual information that is of relatively low importance, based on its normalised magnitude, that are not terminated. Additional truncation of these auxiliaries could be used to improve computation times for the HVM model.

3.3.2 Integer Phonon Contributions to Virtual Information in the BVM

The previous results, in particular figure 3.3.2 e), show the increase in oscillatory structure in the BVM as a consequence of the canonical transform. This is analysed systematically by considering integer multiples of Matsubara

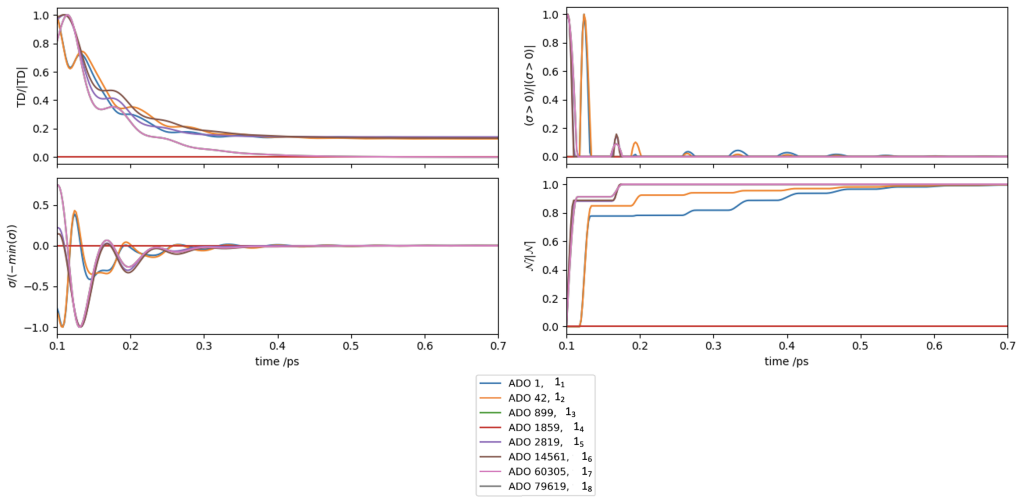

Figure 3.3.5: Slow dissipation BVM model with $\gamma_1^{(\nu)} = 100$ cm^{-1}, and $\gamma_1^{(\nu)} = 300$ cm^{-1} showing normalised trace distance, flux, positive flux, and BLP measure for $1_{\{\cdot\}}$ showing relative size of Markovian and non-Markovian feedback. The ADO number and associated Matsubara shorthand are shown.

frequencies and how they add to the total hierarchy.

Figure 3.3.5 presents a consideration of all the one phonon, tier-1 auxiliaries within the underdamped hierarchy, for the slow dissipation BVM model. This model contains eight Matsubara dimensions with ADOs from 1 up to $79\,619$ and those which are the first ADO in each of these Matsubara axes are considered. As the phonons associated with different axes have different Matsubara frequencies, the associated virtual information content is similarly different, resulting in dissimilar oscillating behaviour. The lower ADOs, 1_1 and 1_2 initially have a maximum Markovian feedback of virtual information followed by a recurrence of virtual information of approximately 40% the initial magnitude. Whereas the ADOs in higher Matsubara dimensions, 1_7 and 1_8, have an initial non-Markovian feedback before the Markovian virtual information flux occurs. The fact that the total information flux, positive information flux, and resultant BLP metric are so different for each case suggests that phonon contributions from different Matsubara axes behave differently.

In direct contrast to this, figure 3.3.6 presents all the phonon and virtual information contributions from a single Matsubara axis, $M1$. All four sections of the figure show very uniform oscillating patterns with small changes in amplitude based on the number of phonons. There is a linear decrease in the equilibrium value of the trace distance and consequently an increase in relative peak amplitude in the normalised positive virtual information flux. Based on the uniformity of oscillations and peak locations in the positive flux it is clear that phonons in the same axis behave very similarly to each other and have less in common with ADOs of the same tier in different Matsubara axes. This can be attributed to the different Matsubara frequencies, which themselves are a

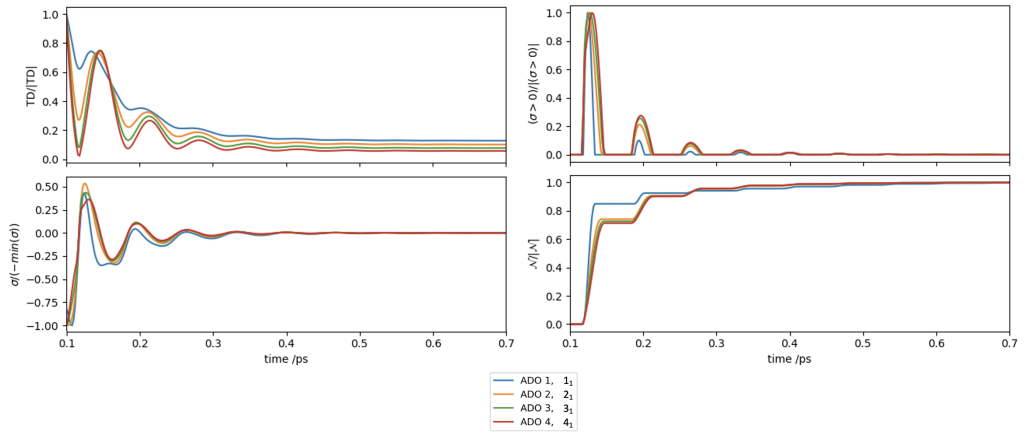

Figure 3.3.6: Slow dissipation BVM model with $\gamma_2^{(\nu)} = 100$ cm^{-1}, and $\gamma_1^{(\nu)} = 300$ cm^{-1} showing normalised trace distance, flux, positive flux, and BLP measure for n_1, $n = \{1, 2, 3, 4\}$, showing relative size of Markovian and non-Markovian feedback. The ADO number and associated Matsubara shorthand are shown.

consequence of periodic oscillations in imaginary time arising from the thermal ensemble distribution. The linear increase in relative peak amplitude also highlights that an increasing phonon number is accompanied by a corresponding increase in relative virtual information recurrence. As a consequence of the chosen normalisation this does not mean that higher tier ADOs contribute more virtual information, but that relative to their size, each peak contributes a larger proportion of the maximum virtual BLP.

From these findings, along with the discussion of multi-tier ADOs, and independence of each temperature dependent Matsubara dimension, discussed within Appendix G, we can conclude that multi-tier auxiliaries are most similar to their constituent dimensions and most strongly resemble those of the highest tier. Temperature dependent effects, which control the level of thermal narrowing in 2DES, are strongly independent based on their differing timescales unlike temperature independent poles.

These results, in addition to the supplemental analysis in appendix G, show that ADOs which contain similar phonons (the same Matsubara frequency) are more similar than compared to those with different phonons (different Matsubara frequencies). This includes ADOs which have integer numbers of specific phonons greater than one, $n > 1$, and these are most closely related to those ADOs with single phonons, $n = 1$, at the same Matsubara frequency. Finally, ADOs which are composites of multiple Matsubara frequencies behave most like their constituent phonons, where they are most similar to other ADOs which depend on their constituent Matsubara frequency with the lowest integer number of phonons. For example, $1_1 3_2$ would be expected to behave most like $M1$ phonons. The only exception to these conclusions is the temperature independent ADOs, two frequencies for underdamped and one for overdamped

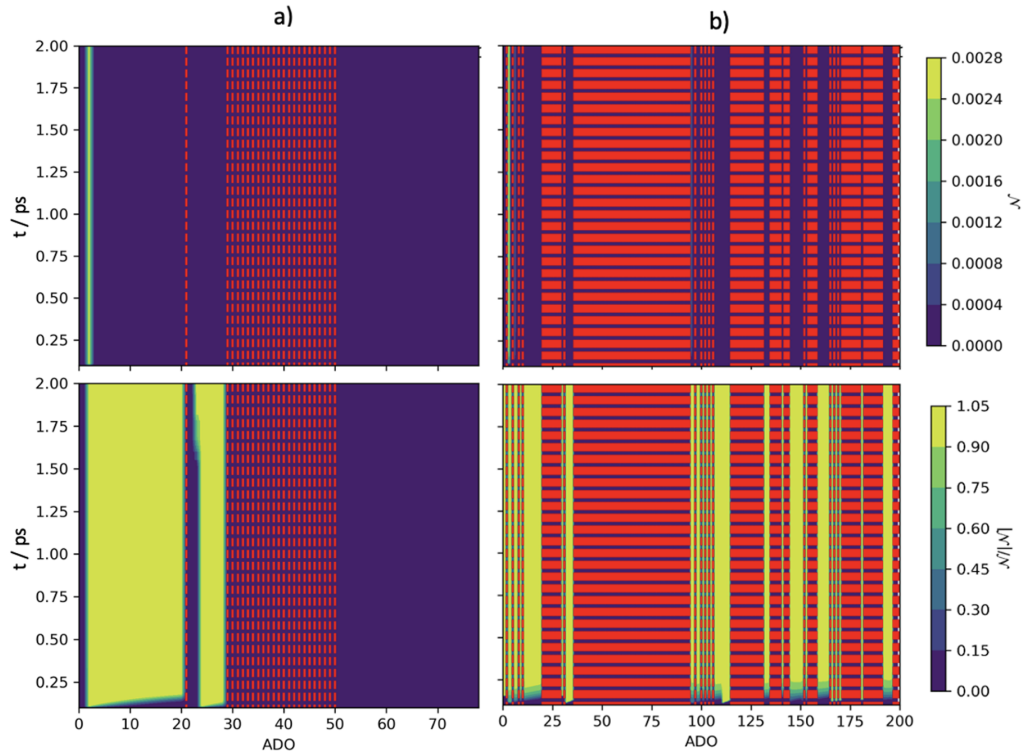

Figure 3.3.7: Normalised and non-normalised contour plots for the HVM, column a), and fast dissipation BVM model, column b) for ADO number against time and BLP measure. These figures are the corresponding contours for 2DES in equivalently named panels of figure 3.3.3.

hierarchies, discussed in section 2.5, which behave similarly to each other because they do not depend on temperature.

Figure 3.3.7 shows contour plots of the BLP metric, ADO number, and time for, column a) the HVM model, and column b) the fast dissipation rate BVM model. Column a) has a maximum ADO number of 79 as it is overdamped, whereas column b) has $98\,513$ ADOs, as it is underdamped, so the first 200 are shown. Figure 3.3.8 shows contour plots of the BLP metric, ADO number, and time for, column a) the standard dissipation BVM model, and column b) the slow dissipation rate BVM model. In both figures red dashed lines indicate terminating ADOs and correspond to the end of a Matsubara dimension within the hierarchy. This highlights that in strongly underdamped calculations the termination criterion is effective at minimising the virtual information that is evolved. Additionally, each of the Matsubara axes depicted show a region of depleting virtual information towards the density matrix, ADO 0. Those ADOs which are lower tier, and closer to the density matrix, contribute a smaller percentage of non-Markovian information flux and fewer of the phonon interactions within this dimension are non-Markovian. This is supported by the increasing breadth of the BLP depletion in successively more damped models and suggests that as irreversible Markovian processes grow, due to overdamping, the non-Markovianity is most prevalent closest to the density

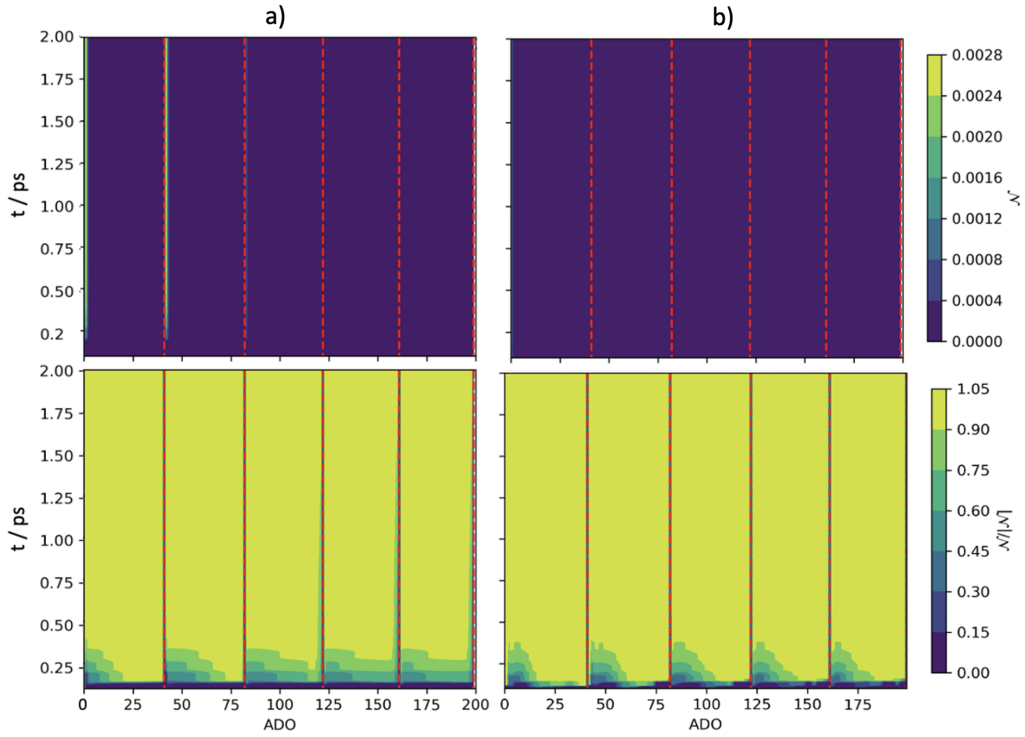

Figure 3.3.8: Normalised and non-normalised contour plots for the standard dissipation BVM model, column a), and slow dissipation BVM model, column b) for ADO number against time and BLP measure. Vertical red dashed lines indicate a terminating auxiliary. These figures are the corresponding contours for 2DES in equivalently named panels of figure 3.3.3.

matrix where the non-Markovian signatures of low integer Matsubara phonons are present at frequencies below the Markovian criterion. Similarly, this region is in agreement with the results in figure 3.1.5, section 3.1, where the area of BLP depletion is equivalent to the sharp increase and plateau of cumulative integrated flux. When the system is overdamped there is a sharp BLP increase up to the maximum as a consequence of instantaneous non-Markovian feedback from solvent reorganisation, whereas in underdamped environments with a smaller proportion of temperature independent Matsubara axes, BLP builds up gradually. Therefore, in the overdamped model, low tier ADOs present a sharp increase in non-Markovianty up to the maximum, at which point no further BLP is added leading to a depletion in successive ADOs. These findings confirm that increasingly underdamped environments will have a Markovian cutoff criterion which is found significantly deeper (at higher tier) within the hierarchy. The results in figure 3.3.7 column a) are in agreement with these conclusions. The overdamped environment, in the homogeneous limit, has fewer phonon modes at high tier and subsequently has few ADOs, with some containing zero virtual information and not being terminators. Larger hierarchies necessarily have a larger number of terminators, but additionally have a much smaller number of empty non-terminators.

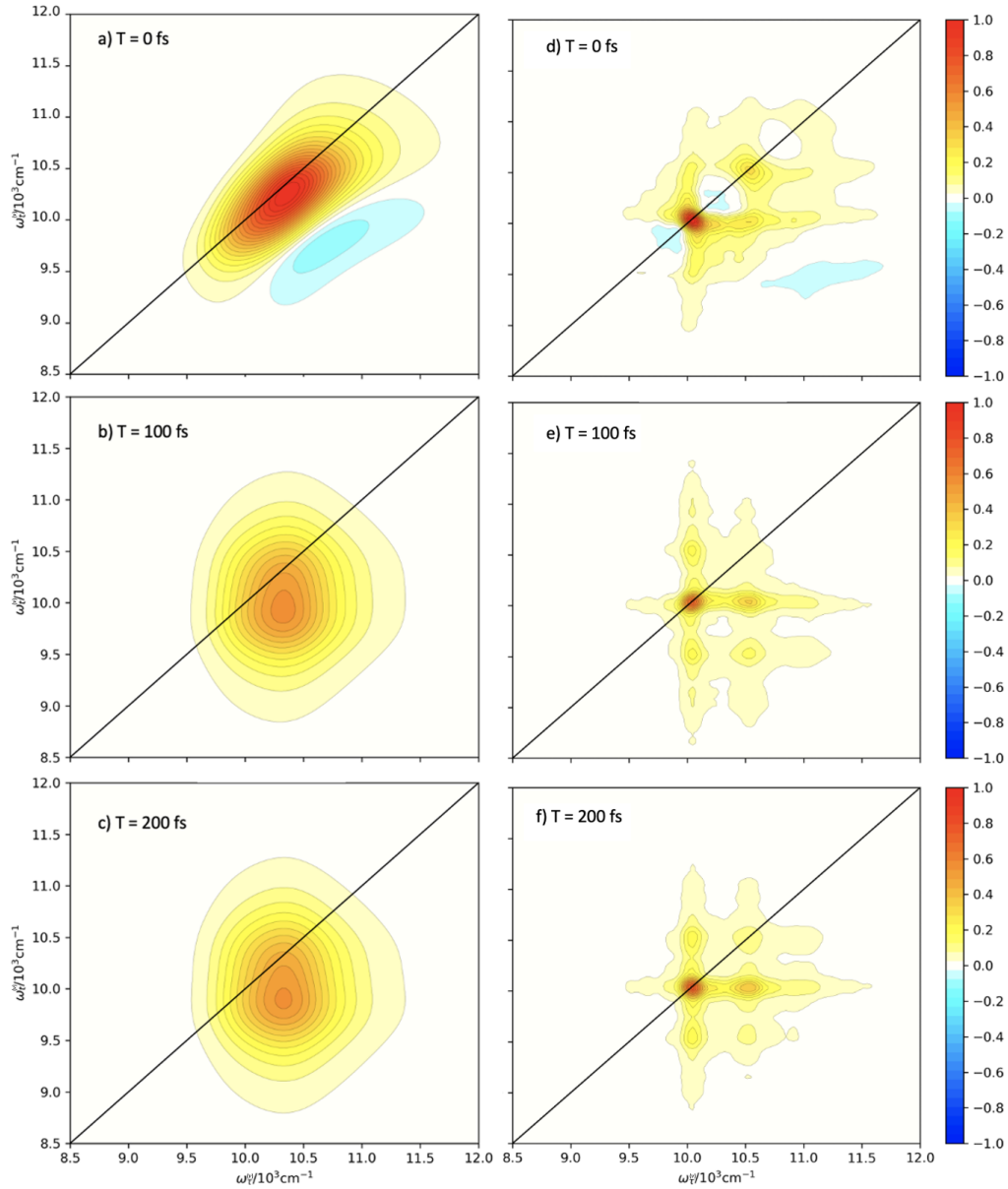

Figure 3.3.9: 2D electronic spectra for the fast and slow dissipation rate limits of the BVM model system at $T = 0$, 100 and 200 fs.

Figure 3.3.9 presents the 2DES for the two limiting cases of the model: a), b), and c) present the overdamped model in 100 fs increments up to 200 fs, and d), e), and f) present the equivalent underdamped spectra. As anticipated from the conclusions of section 3.2, peak position is obscured by the very large inhomogeneous broadening introduced by the strongly overdamped vibrational mode subsumed into the environment. This broadening results in what appears to be a single large peak, although the intensity differences at $\sim 10\ 300$ cm^{-1} along the excitation axis suggest that there is vibrational character and population is relaxing into lower vibrational states up to two vibrational mode frequencies below the fundamental. Clearly a large number of terminators relative to the total ADO number results in a significant increase in inhomogeneous broadening as a result of the limited non-Markovian phonon

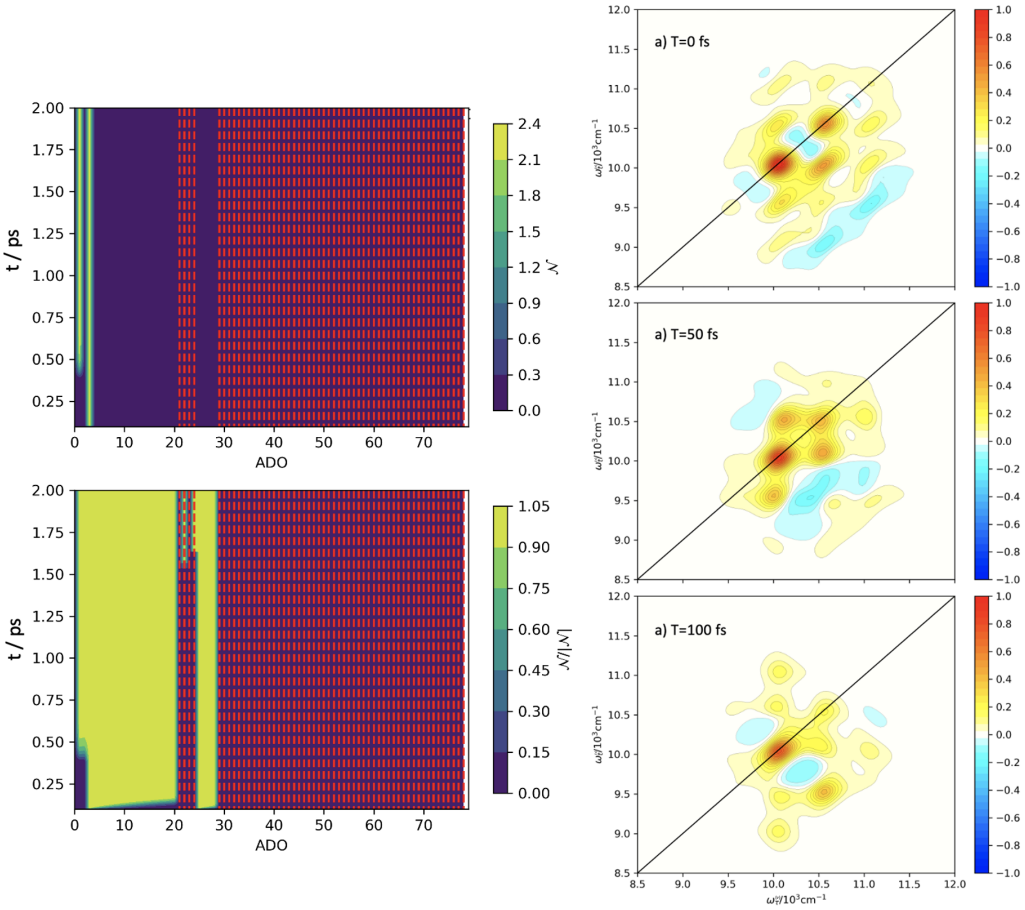

Figure 3.3.10: Contour plot for the HVM showing the additional termination of auxiliaries 21-24, and 2D electronic spectra for the HVM including the volume reducing terminator. $T = 0$, 50, 100 fs.

contributions. In contrast, in the underdamped limit, figure 3.3.9 d), e) and f) the spectra have very precise positions and many cross-peaks are present. Even at low time the peaks are Lorentzian in shape, reflecting a reduced intrinsic canonical damping from section 3.2, with a balance between the inhomogeneous and homogeneous broadening as a consequence of the underdamping of the modes subsumed into the spectral density. This results in high positional precision, low broadening accuracy, a low (relative) number of terminators, and a more uniform spread of relative virtual BLP over all of the ADOs. This supports the idea that underdamped systems require larger hierarchies where each ADO contributes to the total non-Markovianity.

3.3.3 Impact of Additional, Volume Reducing, Termination

A new type of termination of the HVM model, in section 3.3.1, is considered where those ADOs with a low virtual information content are additionally terminated through a new, additional, criterion. This is used to reduce the volume of the total hierarchy and is consequently termed *volume reducing*

termination. Figure 3.3.10 shows an updated version of figure 3.3.4, after volume reducing termination. The contour plot shows that the additional termination has occurred for ADOs $21 - 24$ which have negligible virtual information, and the empty ADOs for ADO number greater than 50 are also truncated. The spectra show the associated 2DES after both termination schemes have been applied, and they show no change in broadening or peak position relative to figure 3.3.4. This highlights that volume reducing termination in this way has had minimal impact on the dynamics while increasing computational efficiency. This is achieved through demonstration that qualitatively equivalent spectra can be generated even when a proportion of the total generated ADOs ($\sim 40\%$ of HVM ADOs) are additionally terminated. By generating an algorithm to cut these dimensions from the hierarchy, the dynamics will be considerably quicker. Such computations are of interest for future studies.

Next a volume reducing termination scheme is considered for the more complex BVM scenarios. This is propsed through discussion of the phonons present within each ADO which was developed in the previous analysis in section 3.3.2.

Based on the efficiency of the current termination criterion in the BVM contours there is no saving to be made with empty ADOs, in contrast to the result for the HVM. However, the behaviour of individual auxiliaries along a specific Matsubara axis is being repeated. For example in figure 3.3.6, we observe that n_1 behave in an almost identical fashion such that this characteristic is being replicated four times within the hierarchy. We propose an additional, new, termination which reduces the number of auxiliaries based on the number of repetitions of behaviour that are present. If multiple 'copies' of a behaviour are present within any Matsubara vectors (multiply-tiered or otherwise) then we can additionally terminate those with the smallest magnitude, which corresponds to truncating the most Markovian ADOs. Continuing the example of n_1 for $n = \{1, 2, 3, 4\}$, the volume reducing termination scheme would reduce this to n_1 for $n = \{1, 2\}$ where $n = \{3, 4\}$ become terminators. Additionally, we could consider altering the volume reducing termination scheme to An_1 for $n = \{1, 2\}$ where $n = \{3, 4\}$ become terminators, and A is a constant addition to account for any repeated character.

Figure 3.3.11 shows a contour plot of the standard dissipation BVM model before, a), and after, b), volume reduced termination, where the volume reduced termination involves removal of repeated behaviour of integer multiples of phonon modes. Here, repeated behaviour is ADOs which correspond to greater than two phonon processes, and these auxiliaries are forced to become terminators. This will not remove these sections from the total

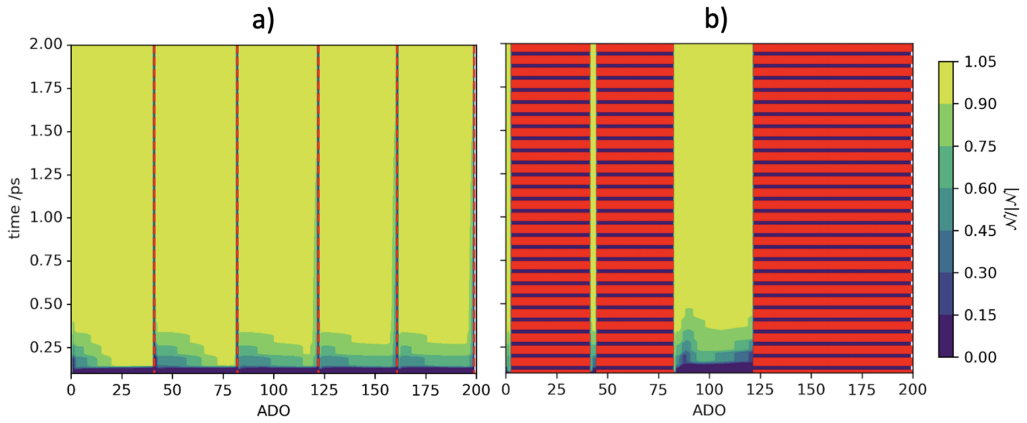

Figure 3.3.11: Contour plot of time, ADO number, and BLP metric for the standard dissipation rate BVM model, a) before and b) after volume reducing termination. Red dashed lines denote terminators.

hierarchy volume, but it will prevent virtual information from being contributed by these sections. a) of figure 3.3.11 is in agreement with the results in figures 3.3.7 and 3.3.8, demonstrating the increasing breadth of the BLP depletion for a greater damping strength. The spectra are similar to the underdamped regime, however the virtual information recurrence at early time is more pronounced based on the reduced damping in the subsumed vibration. Additionally, b) highlights the non-linear progression which the hierarchy algorithm takes during generation of the model. The first 75 ADOs progress linearly along the first two Matsubara dimensions, generating two signals followed by terminated multiple phonon modes, and then the third block moves non-linearly through the hierarchy. The next ~ 50 ADOs are multi-tier, and therefore not terminated by the second criterion, and contribute significantly to the new dynamics. It is clear that many more ADOs are terminated, in a manner similar to the overdamped regime, and exhibit reduced broadening due to the secondary source of damping leading to greater peak positional precision. Consequently, this could serve as a method of artificially correcting the canonical damping.

The spectra in figure 3.3.12 show the corresponding 2DES associated with the respective ADO, time, BLP contours in figure 3.3.11. Both sets of spectra are in increments of 50 fs, up to 100 fs. a) – c) are exactly those in section 3.2, and are for the standard dissipation rate BVM model[2]. They show a reasonable level of inhomogeneous broadening as a consequence of the subsumed vibrational mode, but vibronic peaks are still clearly distinguishable. All peaks, including the cross-peaks, are broadened individually by the coupling to the bath resulting in more broadening than in the fully underdamped model, but significantly more peak precision than in the overdamped regime.

In comparison, the spectra in figure 3.3.12 d) – f) show qualitatively similar peak profiles. Despite all ADOs containing virtual information pertaining to

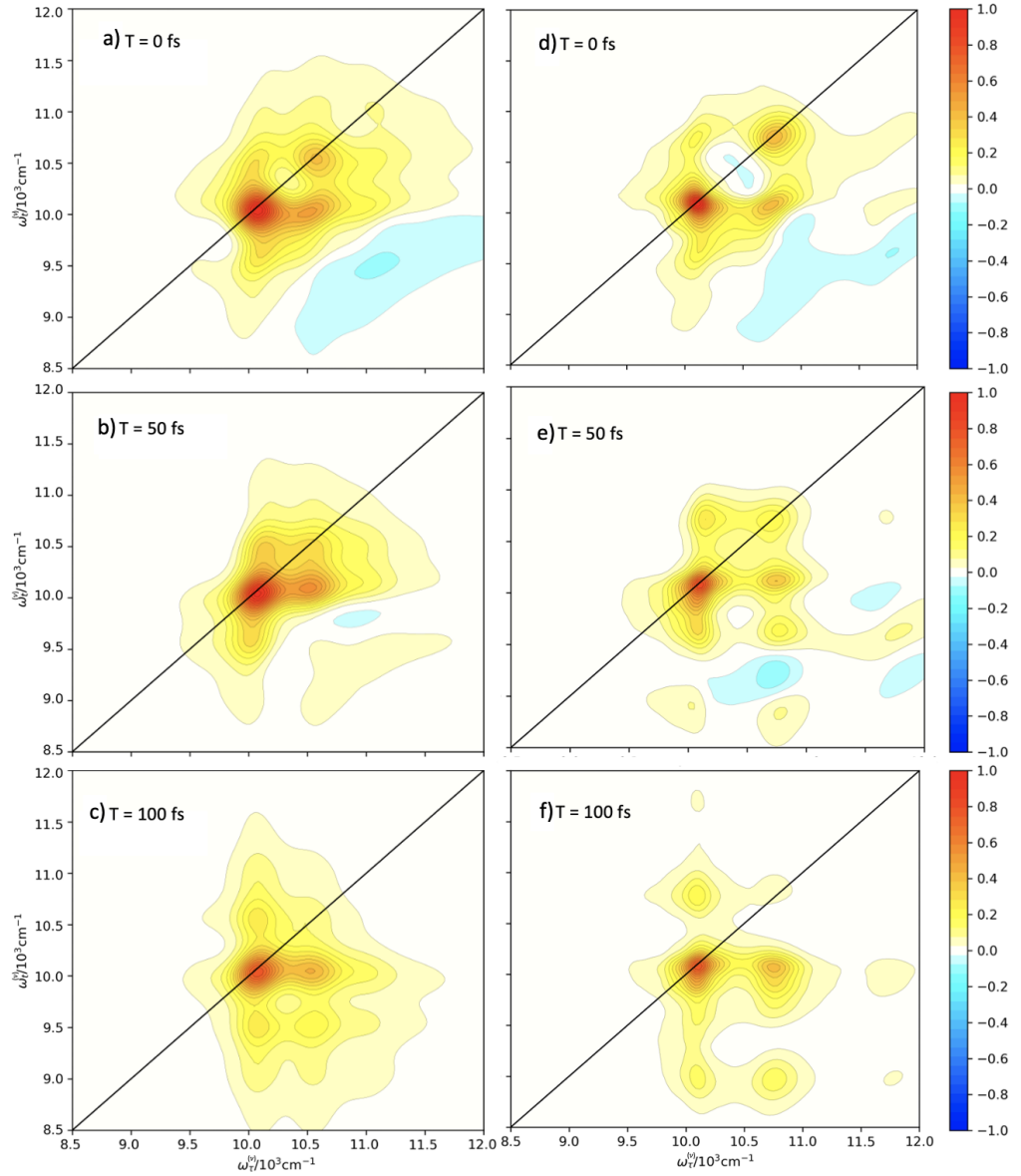

Figure 3.3.12: 2D electronic spectra for the standard dissipation BVM model system before, a) – c), and after, d) – f), volume reducing termination at $T = 0$, 50, and 100 fs.

greater than 2 phonon processes and a significantly increased percentage of the total hierarchy being terminated, the individual peaks have well resolved positions and have not been overbroadened. As demonstrated by 3.3.9 d) – f) regimes which are far into the overdamped limit tend to produce hugely broad peaks with very minimal positional resolution - but this is not evident after volume reducing termination. In contrast, the peaks are fairly Lorentzian and additional peaks have become apparent, examples being at approximately $(10\,000,\ 11\,750)$, $(11\,750,\ 10\,000)$ and $(11\,750,\ 9\,000)$ wavenumbers in figure 3.3.12 f), showing agreement with the HVM results in figure 3.2.4 of section 3.2. This demonstrates that high energy, multi-phonon processes contribute to the overall broadening of the 2D spectra, and obscure weak overtone peaks.

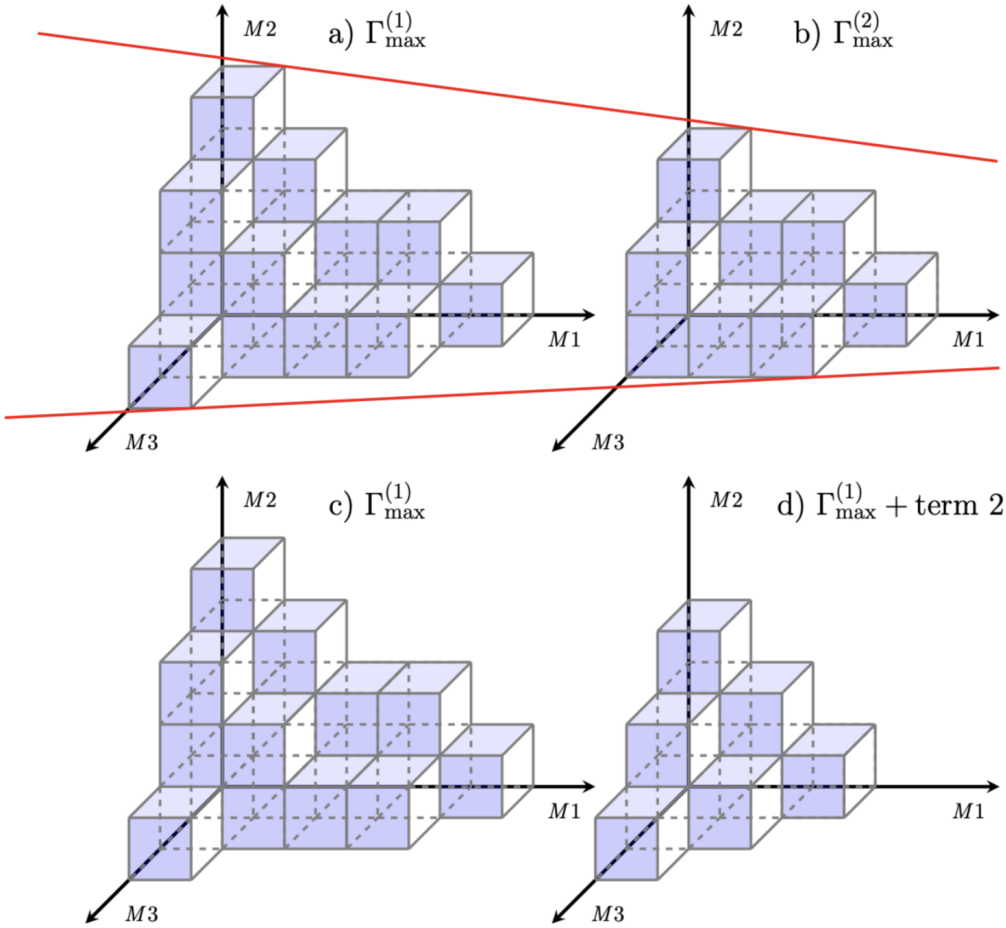

Figure 3.3.13: Schematic showing the closed hierarchy volume. a) and c) An arbitrary value of $\Gamma^{(1)}_{\max}$. b) For $\Gamma^{(2)}_{\max} < \Gamma^{(1)}_{\max}$. d) First $\Gamma^{(1)}_{\max}$, and then the volume reducing termination scheme. Movement from a) to b) demonstrates a self-similar volume, whereas c) to d) demonstrates a regime without this restriction.

Therefore, the most significant virtual information is stored within the lowest tier ADOs with the lowest phonon numbers. This confirms that it would be feasible, and useful, to truncate the hierarchy volume by different amounts along different axes. Currently, the hierarchy is a sealed volume which can only be reduced by decreasing $\Gamma_{\max}$ resulting is a self-similar shaped hierarchy of smaller volume. However, it would be more efficient to reduce each axis to a certain number of multiples of phonon interaction, corresponding to different lengths for each Matsubara axis. This maximises the accuracy relative to the experimental spectra of the model, while reducing the hierarchy volume significantly by changing the volume to a different, non-self-similar shape. This is demonstrated pictorially in figure 3.3.13.

In summary, these results show that the auxiliary density operators contain virtual information which, while not completely physical, allows insight into subsumed physical vibrations within the system of interest after canonical

transformation. Qualitative understanding about the nature of the system-bath interaction and the level of non-Markovian feedback this induces, mediated by integer multiples of phonons in each Matsubara dimension, can be obtained directly from the virtual information BLP metric when it is applied to the ADOs. It is shown that, except for temperature independent axes, Matsubara axes are independent of each other and the resulting integer multiples of phonons behave more like each other than those from other axes, as a consequence of their relative timescale. The 2DES spectra are in agreement with those in sections 3.1, and 3.2, demonstrating increased inhomogeneous broadening in systems with greater damping, which is directly related to non-Markovian feedback of phonons. This study also introduces a, new, volume reducing termination scheme based on the physical understanding afforded by analysis of phonons within the auxiliary density operators. This scheme proposes a method of reducing computational cost in large calculations by reducing the size of the sealed hierarchy volume by allowing non-self-similar volumes.

4 Measuring Quantum Correlations

Quantum measurements in the context of information have been considered in the previous chapter and linked to 2DES, but a second source of quantum behaviour is considered: quantum correlations. The theory of vibronic monomers and dimers, in sections 2.2.1.1 and 2.2.1.3, are combined with the bosonic two-time correlation functions, section 2.3, to generate a measure of quantum antibunching, and classical bunching, in systems continually driven by a laser field.

4.1 Phonon Signatures in Photon Correlations

It is evident from the previous studies that environmental conditions have a profound impact on the dynamics of an open quantum system. When the environment is particularly thermally active an averaging effect occurs over the ensemble system-bath interactions which leads to a narrowing of 2DES. Additionally, in more static environments, when system and bath timescales are closer, the system-bath interactions broaden into a normal distribution of distinct frequencies leading to recurrence of information. The emergence of quantum behaviour as a consequence of system-bath interaction is ubiquitous in a broad range of phenomena. The following sections consider the impact of a movable system-bath boundary on the bosonic two-time correlation function which can model the purely quantum effect of antibunching, discussed in detail in section 2.3.

Here an OQS model for a vibronic molecule, following section 2.2.1.1, is generated and is continuously driven by a monochromatic laser field, as described in section 2.2.3. As in the previous studies, this model incorporates vibrational and electronic degrees of freedom and a coupling to a thermal environment, the impact of which on the bosonic correlation functions is of particular interest. Bosonic second-order correlation functions, following section 2.3, are generated for photons and phonons, with $\mathrm{c}_1 = \mathrm{c}_2 = \mathrm{a}$ or $\mathrm{c}_1 = \mathrm{c}_2 = \mathrm{b}$, and cross-correlations[248,253–256], with $\mathrm{c}_1 \neq \mathrm{c}_2$. The impact of this is that electronic and vibrational modulation of the mutually dependent phonon and photon dynamics and emission of light from the system of interest occurs. This

system of interest is depicted within the total, open, system in figure 4.1.1.

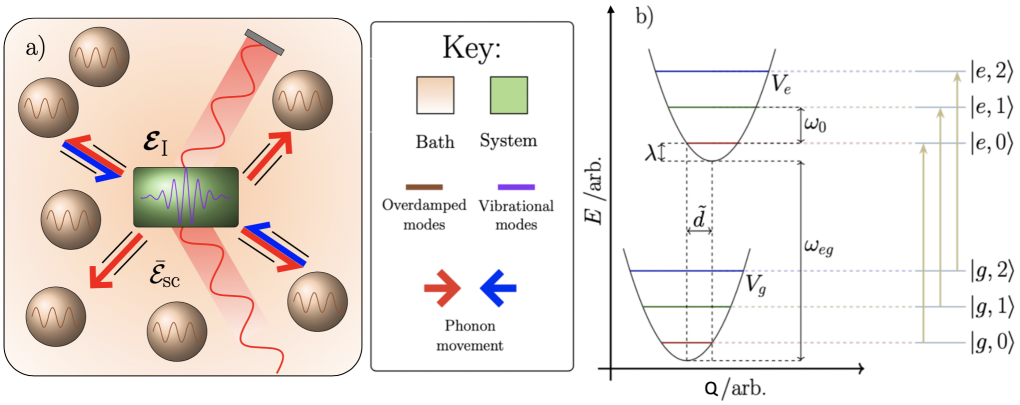

Figure 4.1.1: a) Schematic of the molecule coupled to bath modes and driven by laser field $\boldsymbol{\mathcal{E}}_{\mathrm{I}}$, resulting in the scattered field $\bar{\mathcal{E}}_{\mathrm{sc}}$. Phonon movement between system and environment indicated by arrows. b) Diabatic energy levels, with excited state displacement $\tilde{d}$, system reorganization energy λ, fundamental transition frequency ω_{eg}, and system mode frequency ω_0. Corresponding adiabatic levels on the far right. Reproduced from ref. 3, with the permission of APS Publishing.

It is worth noting that the incident and scattered laser fields are treated as a vector and an operator[a] respectively. The reason for this is that the incident field is a semi-classical vector whereas all explicit use of the scattered field is in the quantised operator form.

As discussed in section 2.3 the rotating wave approximation is not applied in this model, and the driving field remains continuous throughout the evolution. Similarly, it is assumed that the incident field is not detected as part of the scattered field during the evolution. This can be achieved experimentally through the addition of a thin wire as in the dark-ground imaging technique employed by Andrews et. al.[308]. Additionally, all dynamics are generated from models constructed in the adiabatic basis. This means that the energy levels exist in a hybridised state of mixed character, this is depicted in figure 4.1.1 b). Vibrational relaxation within this system occurs as a result of phonon dissipation from the system to the environment which is modelled as an infinite ensemble of harmonic oscillator modes, section 2.2.2.2, with an associated coupling, section 2.2.2.1. The spectral distribution function is an overdamped Brownian oscillator such that stochastic Gaussian fluctuations are introduced into the nuclear dynamics, which correspond to low frequency interactions with the solvent. System-bath coupling in this fashion leads to vibrational dephasing and dissipation within the system[38,155]. As demonstrated in the previous chapter, there are many different approaches for generating a computational solution to the EOM for OQSs[12,18,309–312]. In this chapter the hierarchical equations of

[a] In the absence of roman font for this operator with a calligraphic 'E' it is explicitly labelled as $\{\bar{\cdot}\}$ to accentuate the difference with respect to the incident field. All other instances of operators remain labelled with roman font.

motion (HEOM) method[118,147] is employed in the overdamped limit, equivalent to the HVM for a vibronic monomer in section 3.2.

Each of the model systems considered have, unless otherwise specified, $\eta^{(\nu)} = 5\,\mathrm{cm}^{-1}$, $\Lambda^{(\nu)} = 200\,\mathrm{cm}^{-1}$, $\omega_0^{(\nu)} = 500\,\mathrm{cm}^{-1}$, $\tilde{d} = 1.2$ such that $\lambda^{(\nu)} \approx 360\,\mathrm{cm}^{-1}$, $\omega_{eg}^{(\nu)} = 10^4\,\mathrm{cm}^{-1}$, $E_0 = 10^7\,\mathrm{NC}^{-1}$, and $T = 298\,\mathrm{K}$. Such parameters guarantee that the system can be simplified via the weak coupling approximation and that resultant dynamics are sufficiently Markovian. As is standard for the HVM, Hamiltonian vibration structure is truncated at $N = 10$, chosen to be large enough so that system evolution is not impacted by the level of truncation. These conditions are equivalent to molecules with electronic and vibrational transition frequencies of $\sim 10^4$ cm^{-1} and $\sim 10^2$ cm^{-1}, respectively[313,314] and environments equivalent to standard experimental non-polar solvents[1,2] with weak system-bath coupling. As discussed in section 2.5.6 the system is initialised in a Boltzmann distribution before further propagation occurs.

4.1.1 Simultaneous Time Correlation

Figure 4.1.2 presents the normalised first order correlations of photons and phonons at simultaneous time, $\tau = 0$. a) – c), the photon $g_a^{(1)}$, show the population of the monomer excited state for three different bath reorganisation energies: 0, 5 cm^{-1}, and 10 cm^{-1}. The impact of phonon dissipation and energy dissipation into the bath from the system is demonstrated by the damping of the Rabi oscillations when the excited state displacement is non-zero. If the excited state displacement is zero, and subsequently the system reorganisation energy is zero, the ground state Boltzmann distribution is able to project perfectly to an equivalent Boltzmann distribution in the excited state due to maximum Franck-Condon overlap leading to a persistent Rabi oscillation for all bath reorganisation energies. For displacements greater than zero the Rabi oscillation is damped to a steady state which is formed in a time proportional to $\tilde{d}$.

Similarly, d) – f) in figure 4.1.2 show the corresponding phonon detection probabilities. As a direct consequence of the zero excited state displacement, and system reorganisation energy, there is a minimum detection probability when no additional phonon movement is introduced. This corresponds to the background level of phonon transfer within the system in the absence of excited state displacement when the Franck-Condon overlap integral is maximised. An increase in the system reorganisation energy, which pushes the system away from equilibrium, results in increased vibrational relaxation and a linear increase in the $g_b^{(1)}$. When $\lambda > 0$ the phonon detection probability exhibits a beating pattern consistent with the electronic Rabi oscillation demonstrating the

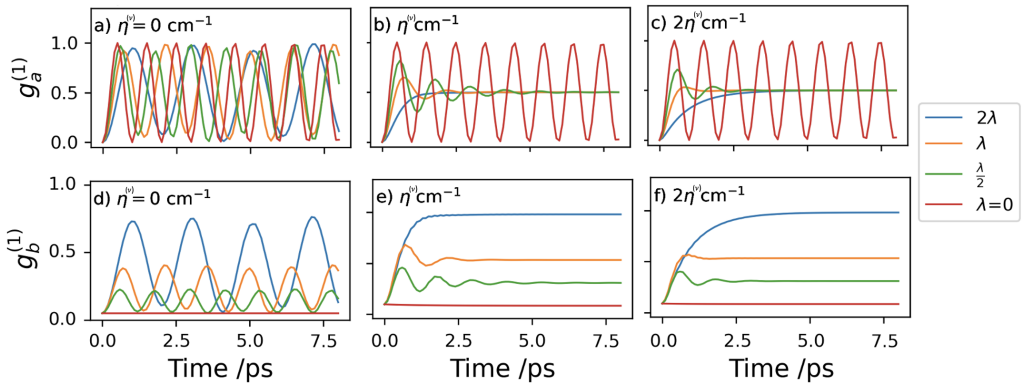

Figure 4.1.2: a), b), c): $g_a^{(1)}(t, \tau = 0)$ correlation function corresponding to photon detection probability. d), e), f): $g_b^{(1)}(t, \tau = 0)$ correlation function corresponding to phonon detection probability. Both include scanning over bath and system reorganization energies η and λ. Reproduced from ref. 3, with the permission of APS Publishing.

increased probability of phonon movement after electronic excitation. Equivalent to a) – c), introduction of a non-zero bath reorganisation energy leads to a dramatic reduction in the formation time of the steady state probabilities.

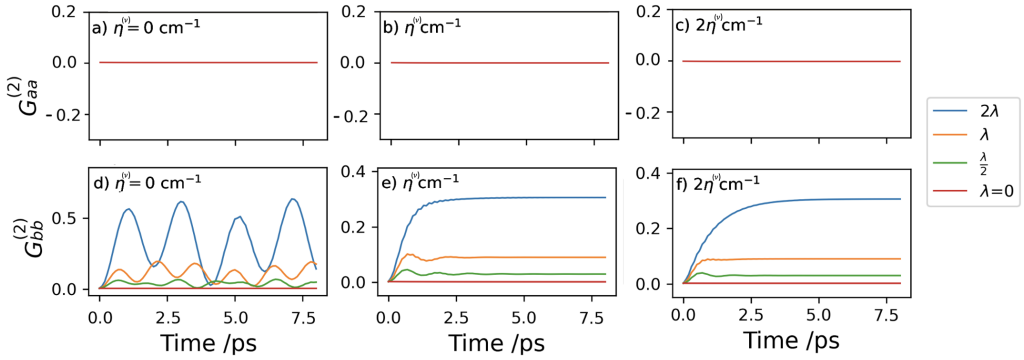

Figure 4.1.3: a), b), c): $G_{aa}^{(2)}(t, \tau = 0)$ second order non-normalised correlation function. d), e), f): $G_{bb}^{(2)}(t, \tau = 0)$ second order non-normalised correlation function. Both include scanning over bath and system reorganization energies η and λ. Reproduced from ref. 3, with the permission of APS Publishing.

Figure 4.1.3 presents a set of non-normalised second-order, simultaneous time, correlation functions for photons and phonons. Based on the chosen vibronic monomer structure of the system, when $\tau = 0$ it is impossible to have a second excitation and emission, as there is no electronic doubly excited state in this TLS. Therefore, the photon correlation is zero for all values of time, t. In contrast, the HVM system has a number of accessible vibrational levels, and a bath of phonons which allow for vibrational dissipation. Subsequently, simultaneous detection of two phonons is possible and, in a fashion similar to figure 4.1.2, the double phonon correlation is modulated by the electronic Rabi oscillation.

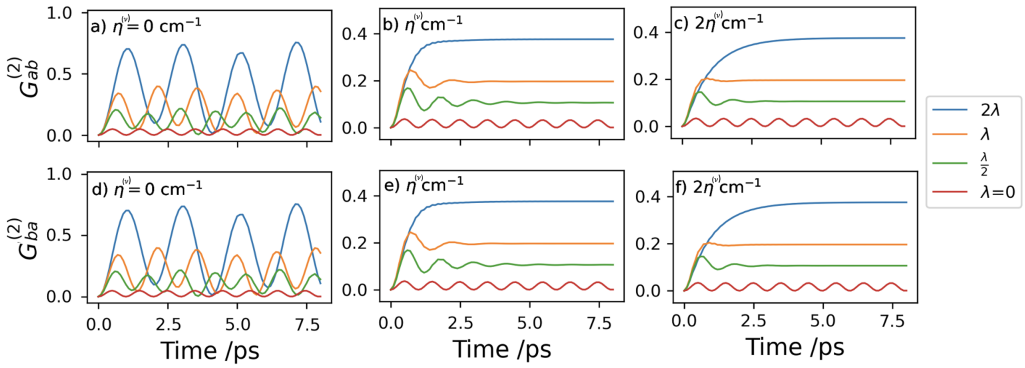

Figure 4.1.4: a), b), c): $G^{(2)}_{ab}(t, \tau = 0)$ non-normalised cross-correlation function at simultaneous time. d), e), f): $G^{(2)}_{ba}(t, \tau = 0)$ non-normalised cross-correlation function at simultaneous time. Both include scanning over bath and system reorganization energies, η and λ, respectively. Reproduced from ref. 3, with the permission of APS Publishing.

Similarly, figure 4.1.4 a) – f), presents the cross-correlations for this system, which are strongly dependent on the number of accessible electronic and vibrational levels. When $\tau = 0$ the order of detection events is indistinguishable and therefore $g^{(2)}_{ab} = g^{(2)}_{ba}$. Additionally, these correlations exhibit a superimposition of photon Rabi oscillations on to the phonon correlations which are linearly dependent on excited state displacement. Subsequently, when the bath reorganisation energy is greater than zero, there is an increase (vertical translation) of the correlation as a result of increased VR, and when $\lambda^{(\nu)} = 0$ cm^{-1} the probability of second detection is strongly tied to the electronic beating.

4.1.2 Two-time Second-Order Correlation

Second-order correlations are generated by evolving the total system again, for another period of time τ after emission of the first boson, but in an independent time coordinate. As depicted in figure 4.1.5, the first order correlations are generated at simultaneous time at the end of the first cycle of evolution. Correlation which reach the equilibrium within 8 ps will have a starting amplitude that is independent of the time, however those which do not reach equilibrium have variable amplitudes. The Rabi cycle within the correlation can be at a maximum, a minimum, or somewhere in between, and this amplitude is the starting point for the successive evolution. As the second evolution is in an independent time axis, τ the time after the first bosonic emission, the starting value of correlation will have a considerable impact on the probability of secondary emission.

Figure 4.1.6 presents the two-time, second-order, normalised correlation function for photons and phonons where t_{end} has been chosen uniquely for each

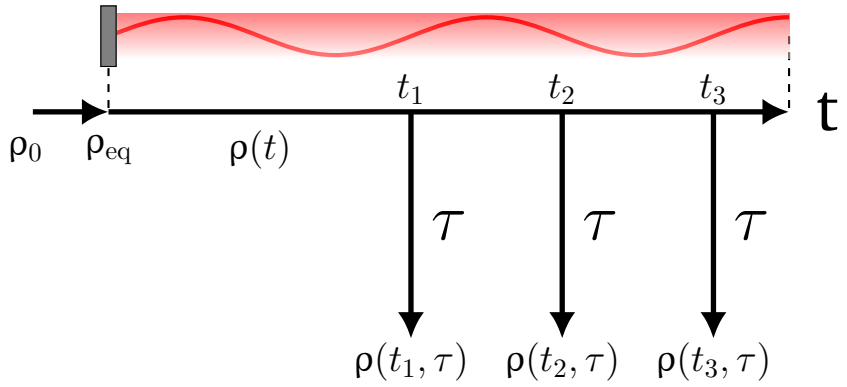

Figure 4.1.5: Schematic depicting the order of evolution for a two-time correlation measurement. The initial density matrix, ρ_0, is equilibrated in time to ρ_{eq}. The continuous laser field is then activated and the system is evolved through time, t, up to $t = t_{end}$, where $t_{end} = \{t_1, t_2, t_3\}$. Subsequent propagation starts at t_{end} and evolves the system through τ to the end state $\rho(t_{end}, \tau)$.

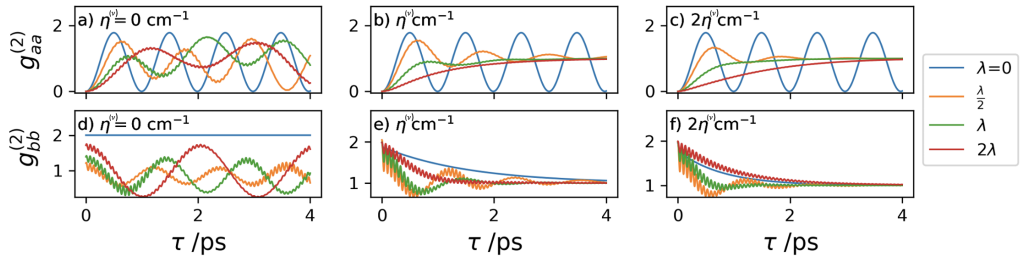

Figure 4.1.6: a), b), c): $g^{(2)}_{aa}(\tau)$ second-order correlation function, d), e), f): $g^{(2)}_{bb}(\tau)$ second-order correlation function, scanning over bath (η) and system (λ) reorganization energies. Reproduced from ref. 3, with the permission of APS Publishing.

reorganisation energy to maximise correlation in all cases. The endpoint of the t evolution, denoted $g^{(1/2)}(t = t_{end})$, is considered in three cases: the correlation $g^{(1/2)}(t = t_{end})$ is maximised for each value of $\lambda^{(\nu)}$ resulting in unique values of t_{end}. Consequently, values are selected so that each oscillation is at a comparable amplitude. Within further sections, $t_{end} = 4.7$ is chosen for $\lambda = 0$ correlations, $t_{end} = 3.5$ ps is chosen for $\lambda/2$ correlations, $t_{end} = 4.3$ is chosen for λ correlations, and $t_{end} = 4.0$ ps is chosen for the 2λ correlations. Unless specified otherwise, the former case is the default setup for this HVM system. Due to the initial Boltzmann distribution in the ground state, after excitation a wavepacket moves within the harmonic potential[75,85,196]. If the system reorganisation energy and excited state displacement are zero then the continual driving by the laser field results in a Rabi oscillation. This beating is a consequence of transitions $|g,0\rangle \rightarrow |e,0\rangle, |g,1\rangle \rightarrow |e,1\rangle, ...$, when the Franck-Condon overlap is maximised, and is evident in the major oscillation in figure 4.1.6 a) – c), leading to antibunching. In contrast, when the system reorganisation energy is greater than zero, the system is able to undergo VR leading to a change in the excited state wavepacket population distribution. This leads to modulation of the

detection probability at the system vibrational mode frequency, demonstrated in figure 4.1.6 as the minor oscillation. This implies that the experimentally measurable second-order photon correlation function contains a measurable phonon signature despite the fact that phonons are not directly detected. This behaviour emerges as a direct consequence of the change in overlap of the quantum harmonic bound eigenstates of the excited and ground states[315]. As the system reorganisation energy increases, the Franck-Condon overlap integral decreases proportionally, resulting in an increased Rabi oscillation period where more population enters the vibronic $|e,0\rangle$ state via VR.

Figure 4.1.6 d) – f) present the second order phonon correlation, $g_{bb}^{(2)}(\tau)$, for the same parameters. In the absence of a system reorganisation energy, population is free to move resonantly between the ground and excited electronic states with no VR[316], resulting in the background phonon transfer rate observed in figure 4.1.2 a) with $\lambda = 0$. For system reorganisation energies (λ) which are greater than zero, there is a non-stationary population out of thermal equilibrium for all values of bath reorganisation energy. Similar to the photonic correlations, the $g_{bb}^{(2)}(\tau)$ is strongly dependent on the electronic excited state population, and tracks the electronic Rabi oscillation leading to a more classical phonon bunching phenomenon. Introduction of a system-bath coupling which is non-zero results in a rapid decay of correlation in τ to a steady state as a consequence of the strong phonon dissipation.

b), c) and e), f), of figure 4.1.6 consider non-zero bath reorganisation energies. Increasing $\eta^{(\nu)}$ proportionally increases the rate of phonon dissipation into the bath and the resultant damping of the Rabi oscillation forms a steady state.

Alternatively, a value of t_{end} could be chosen which maximises a specific contribution within the correltaion function. Figures 4.1.7 and 4.1.8 present results which are analogous to figure 4.1.6 but with different choices of t_{end}. The chosen endpoints of the first evolution, t, differ by $0.5\,\text{ps}$ which corresponds to one half of the period of the non-displaced Rabi oscillation cycle. Subsequently, moving from $t_{\text{end}} = 3.5$ ps to $t_{\text{end}} = 4.0$ ps shifts the final amplitude of the correlations from a trough to a maximum. The other values of non-zero system reorganisation energy will therefore be similarly translated but at a starting point which is not perfectly at a trough. The choice of t_{end} is crucial for τ dependent results, as the starting point of the evolution dictates the starting amplitudes for all of the subsequent correlations, which can tend to favour or disfavour certain modes. Similar considerations would also be necessary in experimental realisations of these experiments.

Through comparison with figure 4.1.2 panel a), it is clear that in figure 4.1.7, with $t_{\text{end}} = 3.5$ ps, $\frac{\lambda}{2}$, and λ are the closest to their maximum value, whereas, 2λ, and $\lambda = 0$ are closest to their minimum. As a consequence of this, the modulation

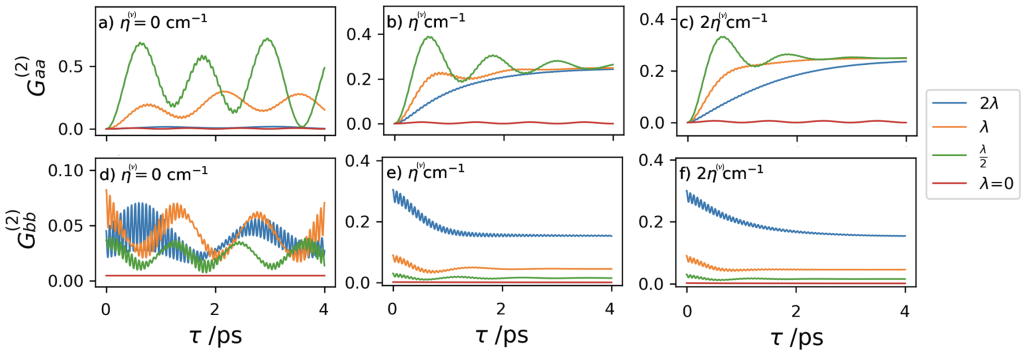

Figure 4.1.7: a), b), c): $G^{(2)}_{aa}(t = 3.5, \tau)$ non-normalised second order correlation function. d), e), f): $G^{(2)}_{bb}(t = 3.5, \tau)$ non-normalised second order correlation function. Both include scanning over the bath and system reorganization energies η and λ, and both start the τ evolution from $t = 3.5$ ps. Reproduced from ref. 3, with the permission of APS Publishing.

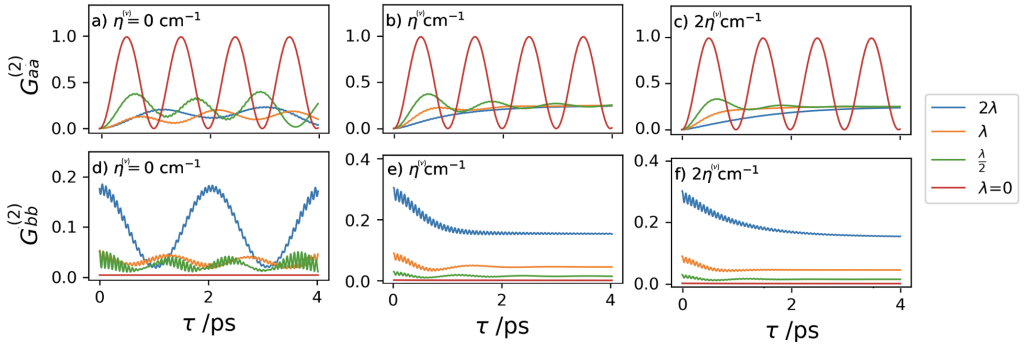

Figure 4.1.8: a), b), c): $G^{(2)}_{ab}(t = 4.0, \tau)$ non-normalised second order correlation function. d), e), f): $G^{(2)}_{ba}(t = 4.0, \tau)$ non-normalised second order correlation function. Both include scanning over the bath and system reorganization energies η and λ, and both start the τ evolution from $t = 4.0$ ps. Reproduced from ref. 3, with the permission of APS Publishing.

due to electronic transitions is minimised for 2λ, and $\lambda = 0$ which improves the resolution of the smaller vibrational contributions. This is particularly well demonstrated through the minor oscillation in figure 4.1.7 panel d). In contrast, vibrational contributions are obscured by an amplification of the electronic Rabi oscillations within figure 4.1.8 with $t_{\text{end}} = 4.0$ ps.

Despite changes in the amplitude of the correlations, all of these results share the fact that there are two fundamental oscillatory modes: major electronic Rabi oscillations, and minor vibrational contributions at the system mode frequency. The major mode represents modulations in the detection probability dependent on the excited state population. Minor oscillatory modes are a consequence of changes in the excited state wavepacket population with respect to the ground state Boltzmann distribution, corresponding to phonon transitions.

Both the $g^{(2)}_{aa}$ and $g^{(2)}_{bb}$, by definition, have no dependence on the order of detection events since τ separates the detection of identical particles. In both

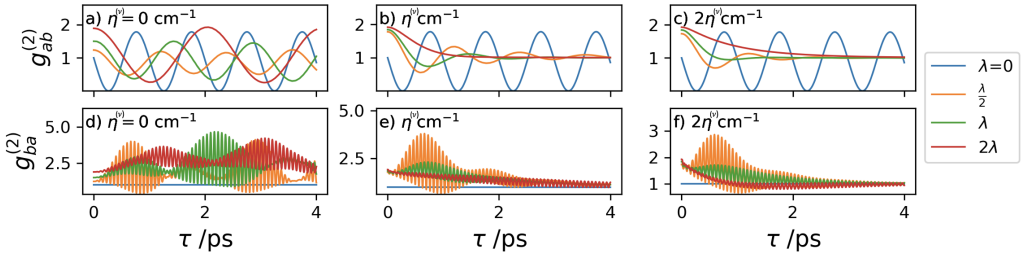

Figure 4.1.9: a), b), c): $g^{(2)}_{ab}(\tau)$ cross-correlation function, d), e), f): $g^{(2)}_{ba}(\tau)$ cross-correlation function, scanning over bath (η) and system (λ) reorganization energies. Reproduced from ref. 3, with the permission of APS Publishing.

cases there is a single source of vibrational character. For the $g^{(2)}_{aa}$ this is indirect, from the strong dependence of photons on the vibrational populations, whilst for $g^{(2)}_{bb}$ this is from direct measurement of the phonon number. In both cases, vibrational character is observed as oscillations at the vibrational mode frequency ω_0. Cross-correlations, which do depend on detection order, can be used to better illuminate these sources of vibrational character.

Figure 4.1.9 shows the two-time cross correlation of photons and phonons, where the order of detection is altered between photon first, $g^{(2)}_{ab}$, to phonon first, $g^{(2)}_{ba}$. This demonstrates that the second detection event determines the dominant character of the cross-correlation as a function of τ. In a) – c) the phonon detection is second, which defines the predominant character of this cross-correlation, and onto this we observe a superimposition of photon correlation. The first detection event is an instantaneous measurement of the photon number and contains no vibrational information, imparting no minor oscillation to the correlation. Similarly, phonon detection which occurs τ later, also does not incur a minor oscillatory mode. This is because, despite the fact that vibrational transitions occur during the period of time τ, the fast phonon signatures are very small with respect to the electronic contributions and their impact on the excited-state adiabatic population is minimal. Consequently, neither detection event incurs vibrational character, as demonstrated in panels a) – c). Additionally, these correlations demonstrate bunching whereby a photon detection is likely to be immediately followed by a phonon which reflects the non-equilibrium population distribution following photon emission.

In striking contrast to this is the phonon-photon cross-correlation function, $g^{(2)}_{ba}$, which exhibits significant vibrational character. As the secondary boson detection is a photon, the characteristics of the $g^{(2)}_{aa}$ figure 4.1.6, dominate, with phonon characteristics superimposed. The first boson detection event is of a phonon and therefore is associated with intrinsic vibrational character at the system mode frequency. However, unlike the $g^{(2)}_{ab}$, the second detection event also introduces vibrational character. The secondary detection probability, of a photon, is modulated by vibrational transitions due to the differing wavepacket

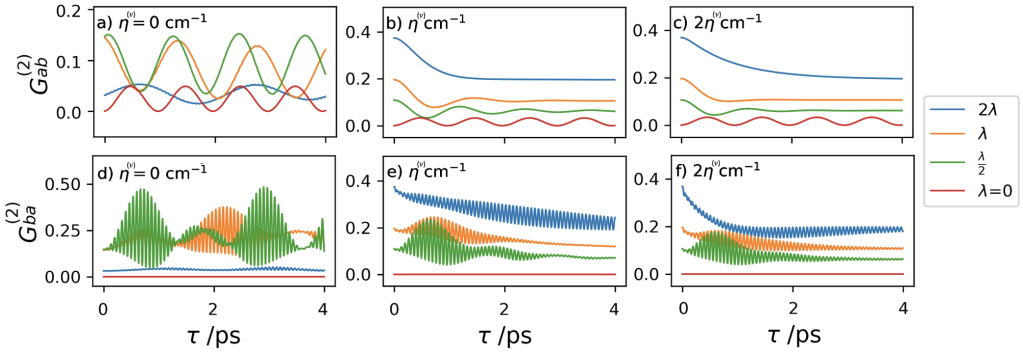

Figure 4.1.10: a), b), c): $G^{(2)}_{ab}(t = 3.5, \tau)$ non-normalised cross-correlation function. d), e), f): $G^{(2)}_{ba}(t = 3.5, \tau)$ non-normalised cross-correlation function. Both include scanning over the bath and system reorganization energies η and λ, and both start the τ evolution from $t = 3.5$ps. Reproduced from ref. 3, with the permission of APS Publishing.

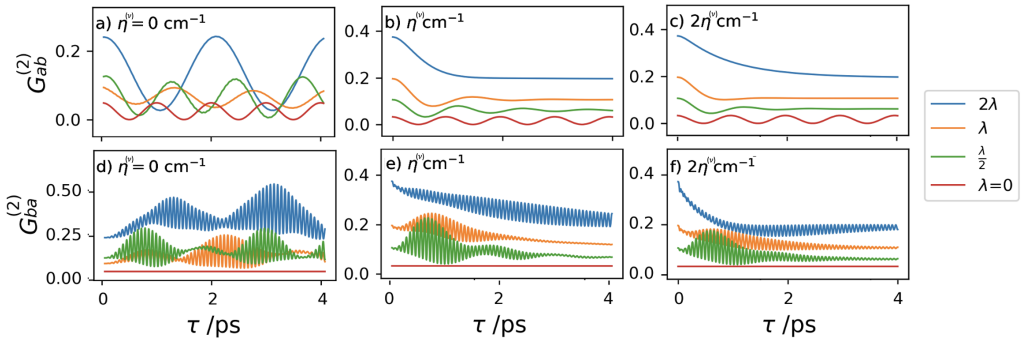

Figure 4.1.11: a), b), c): $G^{(2)}_{ab}(t = 4.0, \tau)$ non-normalised cross-correlation function. d), e), f): $G^{(2)}_{ba}(t = 4.0, \tau)$ non-normalised cross-correlation function. Both include scanning over the bath and system reorganization energies η and λ, and both start the τ evolution from $t = 4.0$ps. Reproduced from ref. 3, with the permission of APS Publishing.

populations. Consequently, there are two sources of vibrational character: 1) intrinsically from the first detection event, and 2) from the phonon effects during the optical beating of the photonic correlation.

These cross-correlations 4.1.9 are, like their $g^{(2)}_{bb}$ counterpart, strongly dependent on the system reorganisation energy and excited state displacement. When there is no displacement, and ground state populations are projected completely into the equivalent excited state distribution, there is a constant minimum of phonon transfer. Upon increasing $\lambda^{(\nu)}$ the two sources of vibrational character introduce significant variation in the detection probability leading to probabilities suppressed below the zero displacement value. This corresponds to a large proportion of the excited state wavepacket undergoing vibrational transitions within the excited state which moves population into vibrational states which disfavour relaxation to the electronic ground state. Even in the presence of phonon dissipation this effect persists at early τ, but

additional damping prevents a reduction of probability below the probability of $\lambda^{(\nu)} = 0$ cm^{-1} at later times. In agreement with the results in figure 4.1.3 a) – c), these correlations exhibit antibunching behaviour as a consequence of poorer Franck-Condon overlap of the bound quantum harmonic oscillator eigenstates, suppressing transitions at ω_{eg} as system reorganisation energy increases. This means that phonon emission tends to inhibit subsequent photon emission when $\tau \approx 0$.

Similar to figures 4.1.7 and 4.1.8, figures 4.1.10 and 4.1.11 present cross-correlations for different values of t_{end} which correspond to maxima and minima in the initial correlation amplitudes. As a consequence of this, the detection probabilities vary due to electronic transitions, minimising these contributions for 2λ, and $\lambda = 0$ which improves the resolution of the smaller vibrational contributions in 4.1.10. In contrast, vibrational contributions are obscured by an amplification of the electronic Rabi oscillations within figure 4.1.11 with $t_{\text{end}} = 4.0$ ps. This is demonstrated particularly well in figures 4.1.10 and 4.1.11 for the case of 2λ reorganisation energy, where almost all vibrational contributions are removed for $t_{\text{end}} = 3.5$ ps, but are maximised when $t_{\text{end}} = 4$ ps. Additionally, these figures demonstrate that the impact of changing t_{end} is reduced significantly when the environment reorganisation energy is greater than zero as a consequence of all values being pushed heavily towards the steady state.

In this section, we have demonstrated theoretically photon antibunching in the fluorescence of a vibronic molecule under continuous laser drive and a thermal environment and that the photon-photon correlations exhibit signatures of the phonon interaction with the bath, suggesting that these are experimentally directly measurable. These appear as oscillations at the system-mode frequency on top of slower modulations associated with the electronic Rabi-like oscillations. Theoretically also considering phonon detection and photon-phonon cross-correlation functions, we have shown how vibrational contributions are understood as arising either directly, through phonon detection, or indirectly, through photon detection subsequent to phonon emission. As such, the order of particle detection can dramatically impact the behaviour of the correlation functions, which could in principle be exploited to investigate the phonon impact on photon emission. More immediately, these correlation functions present an opportunity to investigate phonon dynamics indirectly using existing quantum-optical techniques to understand the impact on quantum versus classical processes in molecular systems.

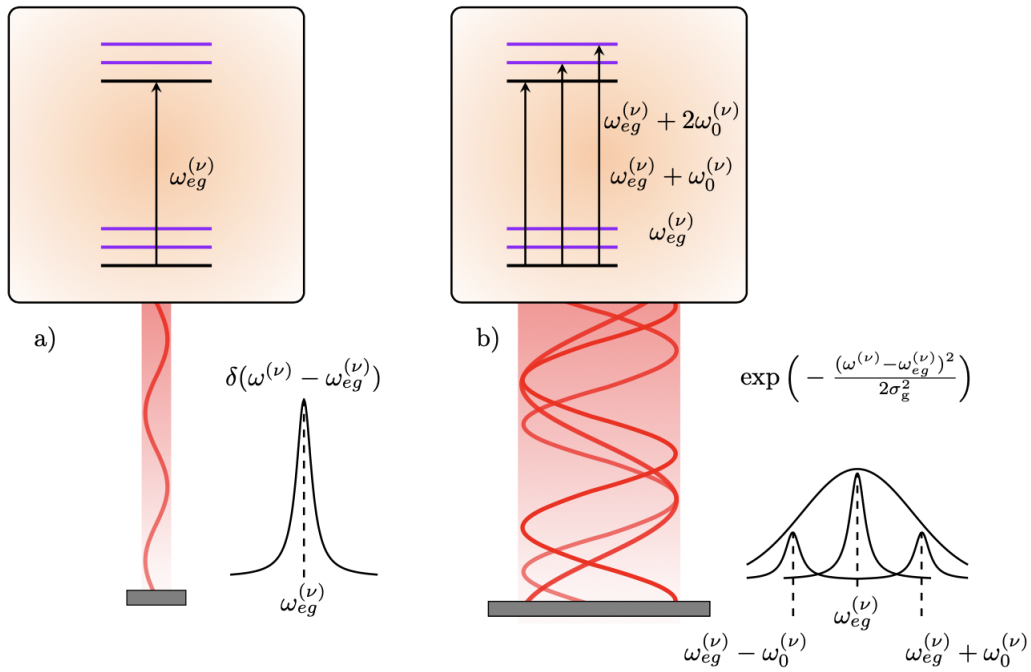

Figure 4.2.1: Schematic of a two-level electronic system interacting with a pair of continuous laser fields. a) a delta function pulse width which stimulates excitation at only the fundamental electronic transition frequency. b) Gaussian finite pulse width which stimulates excitation at the fundamental electronic frequency and $\pm$ integer multiples of the vibrational mode frequency.

4.2 Correlations Induced by a Laser with a Gaussian Width

In the previous section, an HVM system was considered under the influence of continuous driving by a laser field and a phononic bath. However, experimental setups generate finite pulse widths, discussed in part in section 2.4, resulting in more accessible transitions than purely the fundamental electronic transition. This HVM vibronic monomer model is extended by broadening the laser pulse from a delta function to a narrow Gaussian with a range of FWHMs of 50, 250, and 500 cm^{-1}. This is depicted in figure 4.2.1.

4.2.1 Continuous or Pulse-like Driving Fields

The broader range of frequencies present within the finite width pulse results in allowed transitions that are at integer multiples of the vibrational mode frequency above and below the fundamental electronic transition frequency. Subsequently, Stokes and anti-Stokes Raman scattering processes will be accessible transitions[317]. The three choices of FWHM used accessible transitions above and below the fundamental electronic transition frequency of one or two

vibrational levels, and the lowest FWHM of $50\ \mathrm{cm}^{-1}$ represents a model of an experimentally accurate finite laser width as an approximation of a delta function.

Each of the model systems considered have parameters equivalent to those in section 4.1 such that, unless otherwise specified, $\eta^{(\nu)} = 5\,\mathrm{cm}^{-1}$, $\Lambda^{(\nu)} = 200\,\mathrm{cm}^{-1}$, $\omega_0^{(\nu)} = 500\,\mathrm{cm}^{-1}$, $\tilde{d} = 1.2$ such that $\lambda^{(\nu)} \approx 360\,\mathrm{cm}^{-1}$, $\omega_{eg}^{(\nu)} = 10^4\,\mathrm{cm}^{-1}$, $E_0 = 10^7\,\mathrm{NC}^{-1}$, and $T = 298\,\mathrm{K}$. Such parameters guarantee that the system can be simplified via the weak coupling approximation and that resultant dynamics are sufficiently Markovian. In contrast to the previous models the laser field which drives the system is given a finite width defined as a Gaussian envelope similar to that which is defined in section 2.2.3.1. The laser field, equation (2.2.75) in section 2.2.3, can be expressed explicitly as a temporal and spatial superposition of waveforms such that,

$$\boldsymbol{\mathcal{E}}_{\mathrm{I}}(\mathbf{r},t) = \sum_m \hat{\mathbf{e}}_m \chi_m \Big(\mathcal{E}(\mathbf{r},\omega_m,t) + \mathcal{E}(\mathbf{r},\omega_m,t)^* \Big) E'(\omega_m). \tag{4.2.1}$$

Here, instead of a temporal field envelope function, $E'(t)$, the envelope is a spatial function, $E'(\omega)$, describing the spectral bandwidth of the laser beam applied to the system. If all field components are assumed to be parallel and reflected contributions negligible then this can be written as

$$\mathcal{E}_{\mathrm{I}}(t) = \sum_m \chi_m \mathcal{E}(\omega_m,t) E'(\omega_m), \tag{4.2.2}$$

where

$$\mathcal{E}(\omega_m,t) = \exp(-i\omega_m t), \quad E'(\omega_m) = \exp\Big(-\frac{(\omega_m - \omega_{eg})^2}{2\sigma_{\mathrm{g}}^2} \Big). \tag{4.2.3}$$

In the limit $m \to \infty$ the range of frequencies contained in the spectrum of the laser becomes a continuous frequency variable, and in the limit $\sigma_{\mathrm{g}} \to 0$ the envelope function becomes a delta function centred on the fundamental electronic transition frequency, equivalent to that which is used in section 4.1. Each FWHM is calculated from the width parameter, σ_{g}, of the Gaussian profile through $\mathrm{FWHM} = 2\sqrt{2\ln 2} \cdot \sigma_{\mathrm{g}}$. In addition to the three values of FWHM, $50,\ 250,\ 500$ cm^{-1}, three values of m are also considered: 41, 101, and 401. These values demonstrate a range of frequencies within the continuous wave resulting in a continuous oscillation when $m = 41$, but destructive interference from the broad range of phases leads to a spatial wavepacket[b] when $m = \{101,\ 401\}$. Figure 4.2.2 shows each of these waveforms as a function of both time and space. Additionally, figure 4.2.3 depicts the resolution of the spectral bandwidth which results in $m = \{41,\ 101,\ 401\}$ discrete frequencies

[b] Strictly a spatial superposition of frequency modes, rather than the 2DES wavpacket of eigenmodes within the PES.

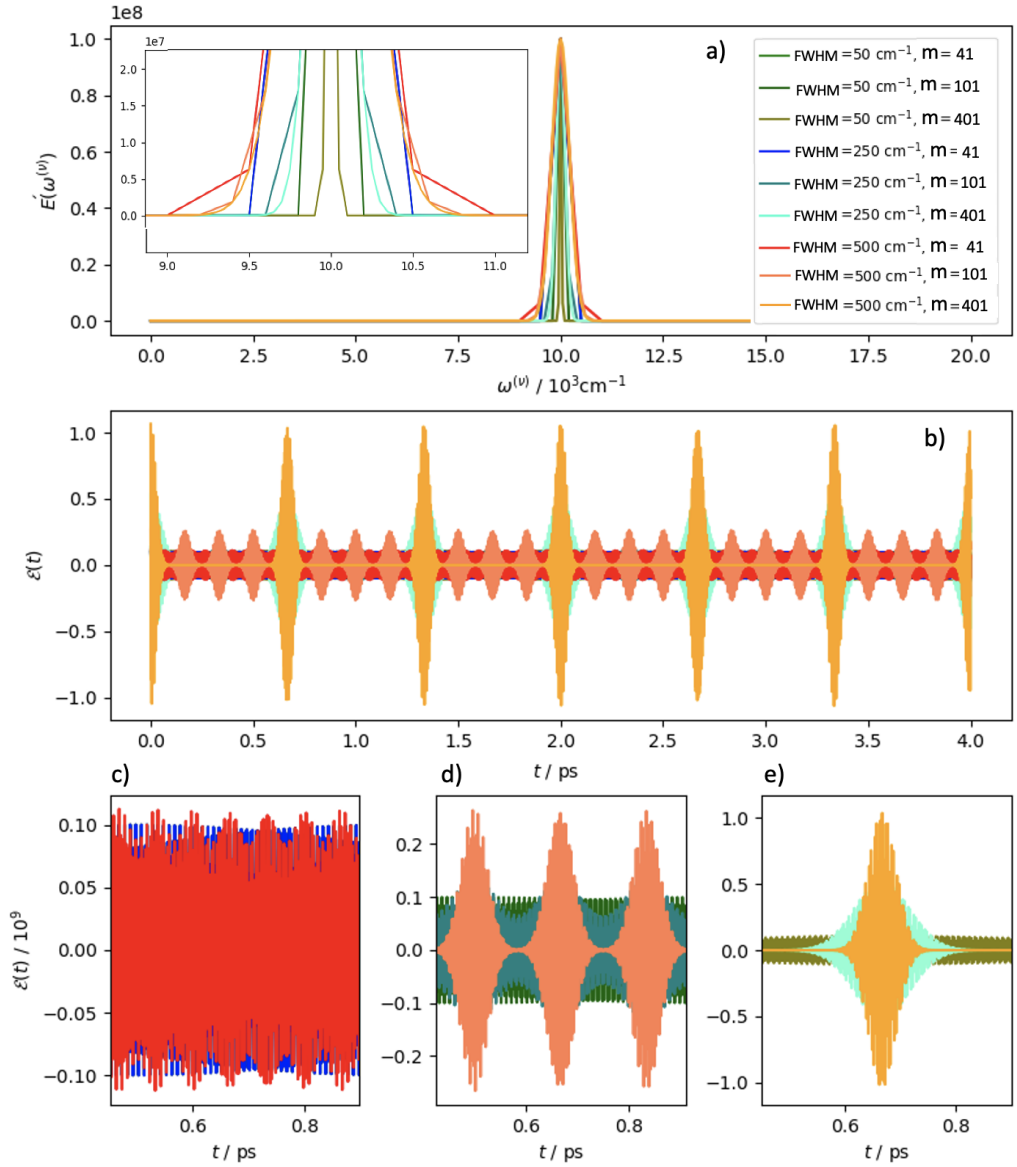

Figure 4.2.2: The envelope function for the continuous driving laser field. When m is large, considerable destructive interference occurs between the constituent waves leading to a spatial wavepacket of varying period. a) The spacial Gaussian breadth of the laser for varying σ_{g}. b) The time domain incident field for each value of σ_{g} and m resulting in a range of forms from a continuous wave for low m to discrete wavepackets in time for large m. c) Plot of all FWHMs with $m = 40$ demonstrating the range of continuous waves for differing numbers of accessible vibrational excited states. d) Plot of all FWHMs with $m = 100$ demonstrating the transition to a set of discrete wavepackets when σ_{g} is large, such as $500\ \mathrm{cm}^{-1}$. e) Plot of all FWHMs with $m = 400$ demonstrating that for the largest number of discrete frequencies within the laser the field only remains a continuous wave for the smallest value of $\mathrm{FWHM} = 50\ \mathrm{cm}^{-1}$.

within the spatial superposition.

It is clear from figure 4.2.2 that increasing the number of discrete frequencies present within the incident field results in a greater amount of destructive interference and a temporal wavepacket with a greater time between pulse

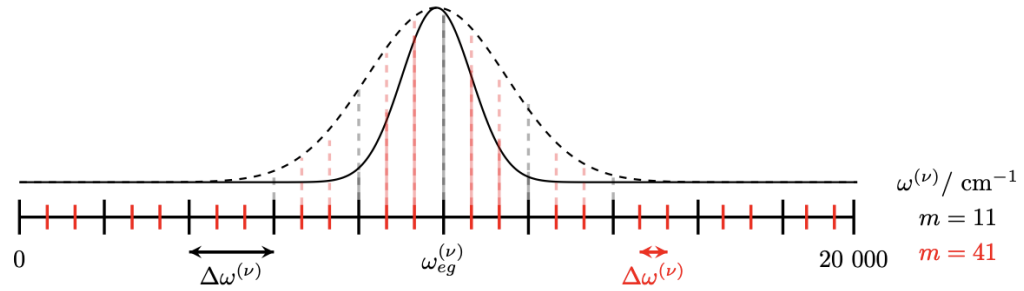

Figure 4.2.3: A schematic of the spectral bandwidth, showing how m frequencies are contained within the spatial wavepacket. Within this schematic m is 11 and m is 41. This demonstrates the change in frequency resolution, $\Delta\omega^{(\nu)}$, from 2 000 to 500 cm^{-1}. Simultaneously the spatial FWHM of the pulse changes, with two examples shown in dashed and solid lines.

center. c) demonstrates that when the number of discrete frequencies within the interval is low the incident field remains a continuous oscillation. The magnitude of σ_{g} dictates whether there is any envelope, such as is evident for $\mathrm{FWHM} = 500$ cm^{-1}. When at the vibrational mode frequency, despite the low number of discrete constituent frequencies, transitions to low energy excited vibrational levels are also possible resulting in a sinusoidal envelope. e) depicts the opposite extreme: very large m such that the frequency is almost continuous. This results in almost entirely temporal wavepacket (a single pulse) behaviour with the exception of very small values of FWHM, such as 50 cm^{-1}. This is because low integer multiples of this FWHM are not sufficient to reach any of the vibrational excited states within the system. d) depicts behaviour between these two extremes, when $m = 101$, leading to a transition from a continuous wave to wavepackets dependent on the FWHM.

4.2.2 First and Second Order Correlations

Figure 4.2.4 presents both orders of two-time photon correlation for $\sigma_{\mathrm{g}} = 500$ cm^{-1}. Here the FWHM of the incident laser is set resonant with the system mode which results in many of the transition frequencies having a significant amplitude within the superposition. When $m = 41$ the discrete energies are also at intervals ($\Delta\omega^{(\nu)}$) of the vibrational mode frequency, and as a consequence of the small sample of frequencies, the incident field is still a continuous oscillation in time with minimal destructive interference. This case is shown in c) of figure 4.2.2 where the large FWHM has made the oscillation pulse-like with a sinusoidal envelope function. However, even with the largest FWHM, the amplitudes of multiply excited vibrational states are still negligible resulting in correlation which is qualitatively similar to the continuous wave results in section 4.1. The results in column 1 show the same trend as for the continuous wave: dissipation of phonons to the bath damps the electronic Rabi

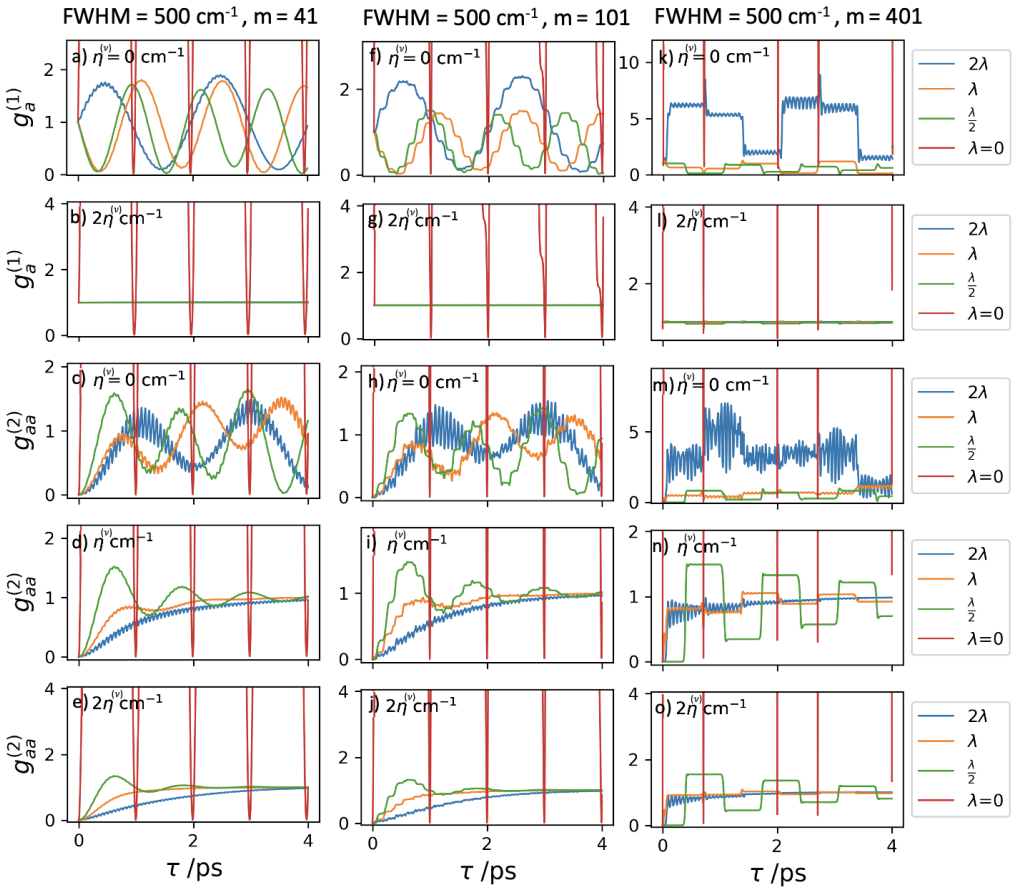

Figure 4.2.4: Order one and two photon correlations with a spatial pulse width of $\mathrm{FWHM} = 500\ \mathrm{cm}^{-1}$ for a range of frequency distributions dictated by m. Column 1, a) – e), $m = 41$. Column 2, f) – j), $m = 101$. Column 3, k) – o), $m = 401$. Each results in a different temporal structure of the incident field, depicted in figure 4.2.2.

cycle, and minor modes present the impact of phonons due to the formation of excited state wavepackets[c]. However, there are two contrasting features with respect to the system driven by a continuous laser. The first is the amplitude of correlations with $\lambda = 0$. Introduction of any finite width to the laser pulse results in allowed transitions not at the fundamental electronic frequency which act as a perturbation of the excited state Boltzmann distribution. Subsequently, there will be an infinitesimal wavepacket population in the excited state when $\lambda = 0$ leading to a divergence in the correlation signifying that the variance of this photon distribution is becoming vanishingly small slower than the mean. Consequently, the magnitude of correlation is massive when normalised. Secondly, the increased amplitude of phonon oscillations, particularly evident in c) for 2λ, as a consequence of excitation of hot states resulting in an excited state wavepacket.

Column 2 presents equivalent results where the number of discrete

[c] A system wavepacket rather than a wavepacket in the field.

frequencies within the temporal superposition is increased to $m = 101$. The spatial FWHM remains at $500\ \mathrm{cm}^{-1}$ but the accessible transitions (due to the spectral resolution $\Delta\omega^{(\nu)}$) are shifted to integer multiples of $200\ \mathrm{cm}^{-1}$. When this number of frequencies exist within the temporal superposition the phase difference is significant enough that the continuous field is reduced to a series of pulses. Each pulse is separated from neighbouring peaks by $\sim 0.1\ \mathrm{ps}$ and the laser field can no longer be considered continuous, demonstrated by the coral data in d) of figure 4.2.2. Subsequently, there are sudden drops and spikes in probability within the correlations corresponding to the pulsing of the laser field. Additionally, because the spacing does not result in levels which are exactly at additions of the vibrational mode frequency to the fundamental electronic transition correlation due to these vibrational excited states cannot occur. This results in correlations f) – j), in figure 4.2.4, which are globally in agreement with the results for driving by a continuous laser field, but exhibit an additional sinusoidal modulation due to temporal nodes in the laser frequency from destructive interference. The lack of an increased minor oscillation amplitude with respect to column 1, due to phonon modes, reflects the fact that these contributions are not at the system vibrational mode frequency.

Column 3 presents the data for correlations with both the largest spatial FWHM and number of discrete frequencies within the temporal superposition, $m = 400$. These results, panels k) to o), are similar to those in the second column. The large number of discrete frequencies in the temporal superposition results in significant destructive interference and a pulse pattern with a separation of $\sim 0.6\ \mathrm{ps}$. This dramatic increase in pulse separation is accompanied by an increase in pulse amplitude reflecting the larger number of constituent frequencies within the superposition. Subsequently, the field is no longer continuous and exists as a series of 6 pulses shown in b) and e) of figure 4.2.2. This means that there are significant time periods when there is no driving field influencing the system of interest followed by regions of intense stimulation by a broad range of different frequencies. This leads to the step pattern in the electronic Rabi cycles in panels k) – o). Additionally, and in contrast to column 2, because the number of discrete frequencies is 401 the accessible transitions are at integer multiples of $\Delta\omega^{(\nu)} = 50\ \mathrm{cm}^{-1}$ allowing stimulation of vibrational excited states which are integer multiples of $500\ \mathrm{cm}^{-1}$. It is for this reason that k), m), n) and o) exhibit a significantly larger amplitude of the minor oscillation: more phonon modes at different frequencies are excited simultaneously by the pulse. This is equivalent to the formation of a complex wavepacket in the excited state which is further altered by the pulses of driving. Despite this, the global behaviour is in agreement with the results in section 4.1 with a continuous driving field.

Figure 4.2.5 presents the corresponding first and second order phonon

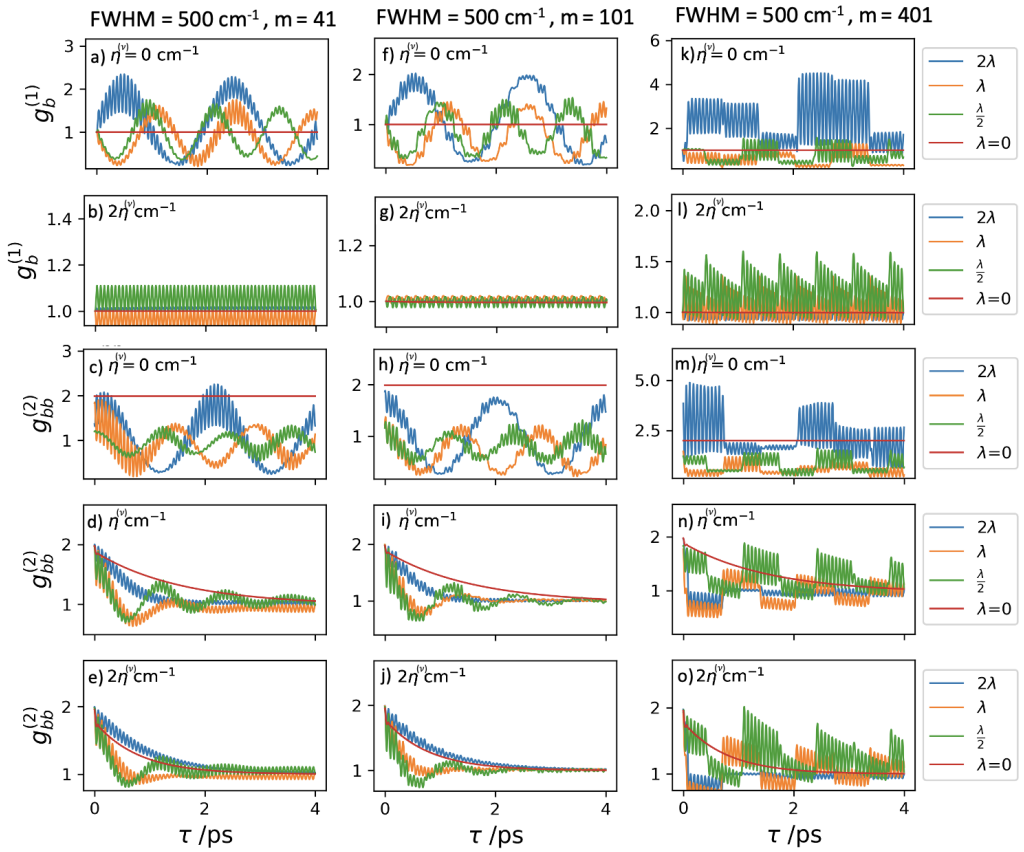

Figure 4.2.5: Order one and two phonon correlations with a spatial pulse width of $\sigma_g = 500\ \mathrm{cm}^{-1}$ for a range of frequency distributions dictated by m. Column 1, a) - e), $m = 41$. Column 2, f) – j), $m = 101$. Column 3, k) – o), $m = 401$. Each results in a different temporal structure of the incident field, depicted in figure 4.2.2.

correlations for this model system under the influence of each kind of driving field. These results are in agreement with both figure 4.2.4, and the results in section 4.1. Similar to the first column of the previous figure, column 1 of figure 4.2.5 depicts phonon correlations equivalent to those present during driving by a continuous wave, however the minor oscillation amplitude is increased. This demonstrates the increase in accessible vibrational levels even for the smallest value of m. In contrast to figure 4.2.4, when the system reorganisation energy is zero there is no divergence of the correlation. This is because, due to the large number of phonons within the system, there will never be a vanishingly small mean or variance. Similarly, integer multiples of the vibrational mode frequency on either side of the fundamental electronic transition frequency, $\omega_{eg}^{(\nu)} \pm \omega_0^{(\nu)} = 10\ 000 \pm 500\ \mathrm{cm}^{-1}$ (Stokes and anti-Stokes Raman transitions), will have non-zero amplitudes. This means that modulation of electronic correlation will be present due to the scale of the driving field's spatial superposition. However, for phonons, when the system reorganisation energy is zero there can be no vibrational relaxation (VR), as equilibrium is maintained, meaning that correlation will be equivalent to the mean number of phonons.

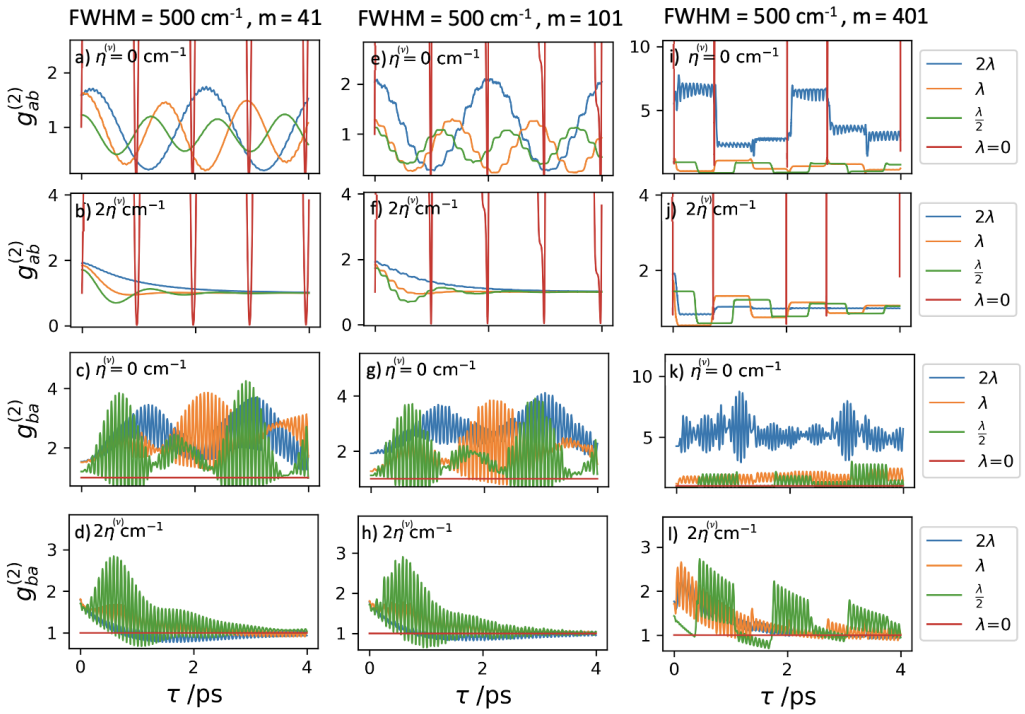

Figure 4.2.6: Order two crossed photon and phonon correlations with a spatial pulse width of $500\ \mathrm{cm}^{-1}$ for a range of frequency distributions dictated by m. Column 1, a) – e), $m = 41$. Column 2, f) – j), $m = 101$. Column 3, k) – o), $m = 401$. Each results in a different temporal structure of the incident field, depicted in figure 4.2.2.

Since there are many vibrational levels the mean is not vanishingly small, and subsequently, there is no divergence.

Column 2 of figure 4.2.5 is also in agreement with the previous results. The global behaviour is equivalent and depicts major oscillations due to electronic transitions with minor oscillations modulating these correlations further based on the specific vibrational levels involved in the excitation. Similarly, the damping of all the oscillatory modes within the correlation upon increasing the bath reorganisation is also demonstrated. As discussed for the previous results, when the number of discrete frequencies is increased to $m = 101$ the superposition consists of integer multiples of $200\ \mathrm{cm}^{-1}$ rather than the vibrational mode frequency. In phonon correlations this results in a reduction in the minor oscillation, which is particularly evident for λ and $\lambda/2$, in contrast to the minor oscillation in photon correlations. This is because the fundamental electronic transition is a multiple of the vibrational spacing, but singly vibrational excited states are not. The action of the laser field is to drive the ground vibronic state population into the equivalent excited electronic state or $\omega_{eg}^{(\nu)} + 2\omega_0^{(\nu)}$, which is also a multiple of $200\ \mathrm{cm}^{-1}$. However, in contrast to the electronic transitions, excitation to the first vibrational state is not promoted as the spectral resolution is $200\ \mathrm{cm}^{-1}$, and $|g,0\rangle \rightarrow |e,1\rangle$ is not sampled. Therefore

the relative amplitude of the minor oscillation is reduced for phonon correlations.

Figure 4.2.5 k) – o) depict phonon correlations with the largest spatial FWHM and for the largest number of discrete frequencies within the temporal superposition. This data is also in agreement with the previous findings. The large number of frequencies results in a laser field which is no longer continuous and behaves as a series of pulses with a separation depicted in b) of figure 4.2.2. Consequently the correlation exhibits sharp steps due to the nodes followed by jumps consistent with electronic transitions and minor oscillations with a large amplitude. This minor oscillation signature is due to the large number of accessible hot states resulting in many phonon signatures consistent with a number of phonon modes within the excited state wavepacket. Consequently, dissipation of phonons into the bath leads to a minimal reduction of these oscillations.

Figure 4.2.6 contains the corresponding crossed-correlations associated with each of the driving fields. Equivalent to the results in section 4.1, these correlations exhibit a superimposition of the nature of the former particle onto the probability distribution of the latter. For example, the $g_{\mathrm{ab}}^{(2)}$ in a), e), and i), present major oscillations due to the electronic Rabi beating and a minor oscillation due to phonon contributions to the excited state wavepacket. Similarly, a step-function mode is introduced which modulates the correlation based on the time between pulses when the laser field is no longer continuous and the minor mode oscillations increase significantly when the discrete frequencies are integer multiples of the vibrational mode frequency. In agreement with the previous results, and most evident in c), g), and k), as the laser field transitions into a pulse definition of the electronic Rabi oscillations is obscured by periods of zero field interaction. Additionally, in column 3 the phonon signatures are amplified due to instantaneous excitation of a range of frequencies upon interaction with the laser pulse.

These results are supplemented by a full analysis of each different spatial FWHM, in appendix H. These results show that for smaller spatial FWHMs, such as $50\ \mathrm{cm}^{-1}$, the weighting of allowed transitions is highly focused on the fundamental electronic frequency and vibrational modulation away from the results of driving by a continuous wave are largely absent. This is supported by c) of figure 4.2.2 in which the field never becomes entirely separated pulses, no matter the choice of m. Intermediate FWHMs, such as $250\ \mathrm{cm}^{-1}$, demonstrate a subtle movement from continuous to pulse-like field structure, with small modulations of the correlation arising due to temporal nodes in the laser field for only the largest number of discrete frequencies.

To summarise, it has been shown that moving from a laser field which is a

delta function spectrum to a field of finite width can modify both the electronic and vibrational beatings within the correlation of photons and phonons. When the spatial FWHM is small the driving field remains continuous for any number of discrete constituent frequencies, up to $m = 401$, resulting in only minor alterations to the correlation. However, when intermediate or larger FWHMs are employed the driving field can move from being a continuous wave to a pulse with a separation time proportional to the number of discrete frequencies. In such a scenario the electronic Rabi oscillations tend towards step functions where there are regions of constant correlation in the absence of the field. Upon interaction with this pulse a number of transitions at different frequencies occur. If the spacing of these frequencies is at the vibrational mode frequency of the system, the resulting excited state wavepacket will contain a greater contribution from higher levels and therefore has an increased amplitude of the minor oscillation. However, if the spectral resolution ($\Delta\omega^{(\nu)}$) is not at the vibrational mode frequency, or does not generate frequencies which are multiples of $\omega_0^{(\nu)}$, then the minor oscillation amplitude can be tuned. In figure 4.2.5 f), the resolution is set to $200\ \mathrm{cm}^{-1}$ resulting in transitions to the first electronic excited state being accessible, but the first vibrational levels being forbidden. Subsequently there is a reduction of the phonon contributions in the excited state wavepacket relative to those in photon correlations.

This study demonstrates the efficacy of the HVM method for quantum correlations in an equivalent fashion to that which has been shown for quantum information in section 3.1. It remains to be seen whether the BVM is equally suitable for correlation studies, and what qualitative correlation measures can be obtained from the system after canonically subsuming the fundamental system vibration. This is addressed in the next section, in analogy with sections 3.2 and 3.3.

4.3 Enhanced Phonon Signatures within the Virtual Correlation Functions of Auxiliary Density Operators

It has been demonstrated that the HVM OQS model is effective at modelling quantum correlations and, in a manner equivalent to section 3.1, the impact of these correlation functions has been analysed for a test system. Now the system-bath boundary location is moved into the spectral density through the canonical transform, resulting in a familiar BVM model, in order to ascertain the impact of such a movement on quantum correlations.

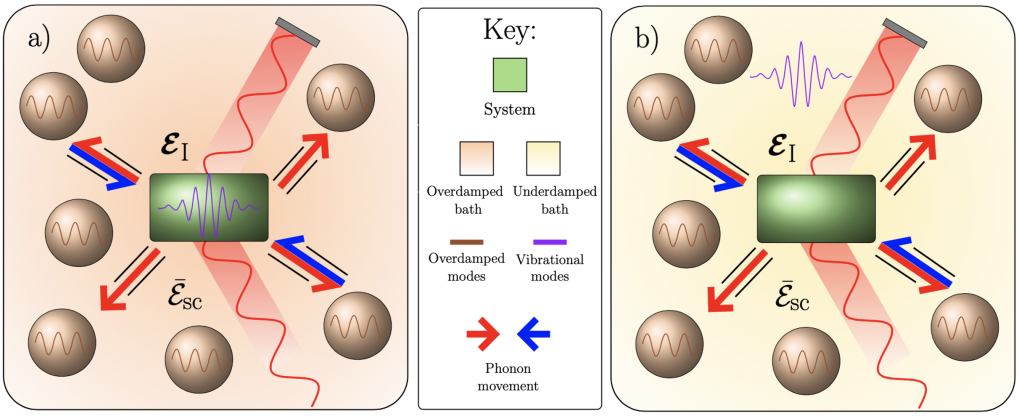

Figure 4.3.1: a) The HVM model with an overdamped environment and an intramolecular vibrational mode contained in the system Hamiltonian. b) The BVM model with an underdamped environment consisting of overdamped bath modes and the canonically subsumed intramolecular vibrational mode. In both cases the system of interest is continuously driven by a continuous laser field, with a spatial delta function distribution of frequencies, shown by $\boldsymbol{\mathcal{E}}_{\mathrm{I}}$. This field is scattered resulting in the quantised operator, $\bar{\mathcal{E}}_{\mathrm{sc}}$. System-bath interaction allows dissipation and recurrence of information and phonons through quantum information channels.

4.3.1 Hamiltonian Versus Spectral Model

Based on the theory discussed in section 3.2 and the structure of a vibronic monomer from section 2.2.1.1, a pair of models are generated which differ only in system-bath boundary placement. These models are depicted in a) and b) of figure 4.3.1.

In both cases the ground and excited electronic states are separated by $\omega_{eg}^{(\nu)} = 10\,000$ cm^{-1}, which is then coupled to a vibrational mode of frequency $\omega_0^{(\nu)} = 500$ cm^{-1}. The excited state potential energy surface is displaced from the ground state along the molecular coordinate by $\tilde{d}$, a dimensionless parameter, of magnitude 1.09 resulting in a system reorganisation energy of $\lambda^{(\nu)} = 300$ cm^{-1}. In the HVM model vibrational degrees of freedom are contained by the Hamiltonian explicitly as energy levels. Following numerical diagonalisation of these levels through a unitary transformation (2.2.25) the remaining levels are a truncated subset, $\nu_{\mathrm{M}} = \{0,\ 1,\ 2\}$. In contrast, the BVM has no explicit vibrational energy levels but has a secondary bath to compensate for this loss.

For the HVM there is a single weakly inhomogeneous bath, with $n = 1$, constructed as an infinite ensemble of harmonic oscillators and reduced to the Lorentz-Drude spectral density function, as in equation (2.2.45). The BVM model has $n = 2$ and is constructed with a pair of spectral distributions: an overdamped component equivalent to the HVM, and an underdamped

contribution arising from the canonical transform of the vibrational degrees of freedom. The overdamped spectral density takes the form, equation (4.3.1), and the underdamped equation (4.3.2), which are equivalent to those discussed in section 2.2.2.2.

$$J_{\mathrm{O}}(\omega) = \frac{2\eta_{\mathrm{O}}\omega\Lambda_{\mathrm{O}}}{\omega^2 + \Lambda_{\mathrm{O}}^2}, \tag{4.3.1}$$

$$J_{\mathrm{U}}(\omega) = \frac{2\eta_{\mathrm{O}}\omega\Lambda_{\mathrm{O}}}{\omega^2 + \Lambda_{\mathrm{O}}^2} + \frac{2\eta_2\omega_2^2\omega}{(\omega_2^2 - \omega^2)^2 + (\gamma_2\omega)^2}. \tag{4.3.2}$$

The coupling of the overdamped bath, determined by the associated reorganisation energy, is $\eta_{\mathrm{O}}^{(\nu)} = 50$ cm^{-1}, and the bath dissipation rate is $\Lambda_{\mathrm{O}}^{(\nu)} = 100\ \mathrm{cm}^{-1}$ so that the environment is dominated by low frequency modes, as is typical for solution phase photochemistry at 300 K. In order to induce a slow decay of the system-bath correlation, leading to weak inhomogeneity, the damping rate is chosen to be $\gamma_1^{(\nu)} = 2\,500$ cm^{-1} which is equivalent to $\Lambda_{\mathrm{O}}^{(\nu)} = 100$ cm^{-1}.

The two components in the BVM spectral density, equation (4.3.2), corresponds to the purely environmental degrees of freedom from the HVM model and the intramolecular vibrational mode in the underdamped limit[231], respectively. In addition, $\omega_2 \gg \gamma_2$, such that $\omega_2 = \omega_0$ the vibrational mode frequency, and $\eta_2 = \lambda$ from equation 2.2.8. Rather than being dominated by low frequency modes, this bath features a sharp Lorentzian peak at the vibrational mode frequency. This peak has an unavoidable canonical damping, outlined in sections 3.2 and F.2, with breadth proportional to γ_2.

The bath is coupled to the explicit Hamiltonian states through the coupling operators (2.2.47) which have been transformed through the same unitary transformation as the Hamiltonian. In the HVM this coupling induces a modulation of the excited state transition frequency, which as a consequence of stochastic motion, leads to dephasing of the associated wavepacket. In the HVM the vibrational contributions to this wavepacket, which are absent in the BVM, are neglected by assuming that the vibrational relaxation, and any associated modulation of the electronic coupling, are much slower processes than the electronic dephasing. Similarly, the BVM which has only explicit electronic states, is coupled to the bath through a pure dephasing operator equivalent to that used for the HVM. For this vibronic monomer system the coupling operator takes the form,

$$\mathrm{B}_{\mathrm{M}}^{\mathrm{S}} = |e\rangle\langle e|\,. \tag{4.3.3}$$

In both models the system Hamiltonians are renormalised in order to account for the shift in energy due to the system-bath coupling[1].

4.3.2 Virtual Correlation

From these models, correlation functions are generated following section 2.3 but, in a manner similar to section 3.3, this metric is also applied to the ADOs. Unlike virtual information the auxiliary density operators vary by orders of magnitude in scale based on the exponent of $j_{\{\cdot\}}$ in the equation for the auxiliary density matrix element, equation (2.5.40). Therefore an additional normalisation is employed to allow comparison between ADOs,

$$\bar{g}^{(1)}_{\mathrm{c}}(t,\tau) = \frac{g^{(1)}_{\mathrm{c}}(t,\tau)}{\max\Big(|g^{(1)}_{\mathrm{c}}(t,\tau)|\Big)}, \tag{4.3.4}$$

$$\bar{g}^{(2)}_{\mathrm{c_1c_2}}(t,\tau) = \frac{g^{(2)}_{\mathrm{c_1c_2}}(t,\tau)}{\max\Big(|g^{(2)}_{\mathrm{c_1c_2}}(t,\tau)|\Big)}, \tag{4.3.5}$$

where $\mathrm{c} = \{\mathrm{c}_1, \mathrm{c}_2\}$, and either $\mathrm{c}_1 = \mathrm{c}_2$ or $\mathrm{c}_1 \neq \mathrm{c}_2$, for auto- or crossed-correlations respectively. Similar to the virtual information discussed in section 3.3, application of standard metrics to the ADOs does not usually result in physically meaningful information as only the density matrix is physical. This is true for the HVM, however, the BVM mixes the system and environment degrees of freedom through the canonical transform as the system-bath boundary is moved into the spectral density. If there are mixed degrees of freedom within the spectral density then qualitative physical insights can be drawn from the ADOs about the system vibrations.

4.3.3 HVM and BVM Virtual Correlation

Figure 4.3.2 shows the virtual correlation of photons and phonons of order one and two for the density matrix, and first eight auxiliaries, of a BVM model. a) and b) which depict the first and second order correlation of photons clearly demonstrate that the coupling of the system and bath vibrational structure which is able to arise in 2DES through vibronic cross-peaks is unable to emerge in correlations. This is because during the canonical transform the concept of vibrational levels is extracted from the Hamiltonian and moved into the bath degrees of freedom. Therefore, it no longer makes sense to consider vibrational creation operations within the system. This manifests as a pure Rabi oscillation highlighting that the photon correlation is only dependent on the electronic degrees of freedom and is independent of phonon modes. Additionally, after normalisation, there is no difference between any of the auxiliaries with each being a replica of the density matrix.

In contrast, the following figures present results for the HVM model. Figure

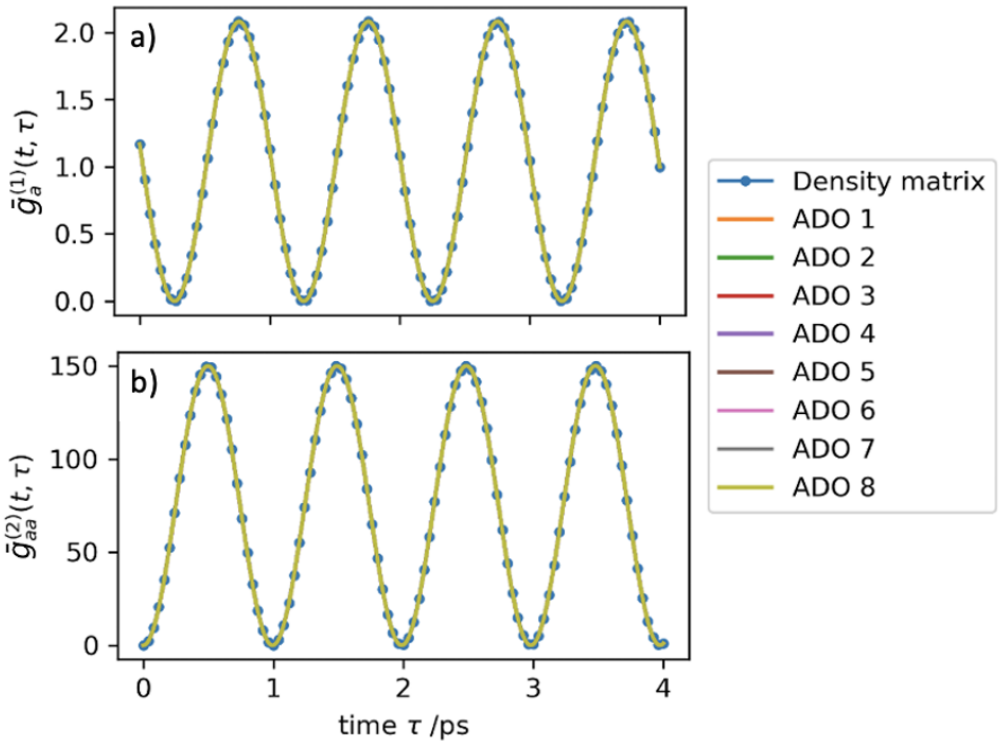

Figure 4.3.2: First and second order photon correlations for the BVM, normalised following equations (4.3.4) and (4.3.5), are shown in a) and b) respectively.

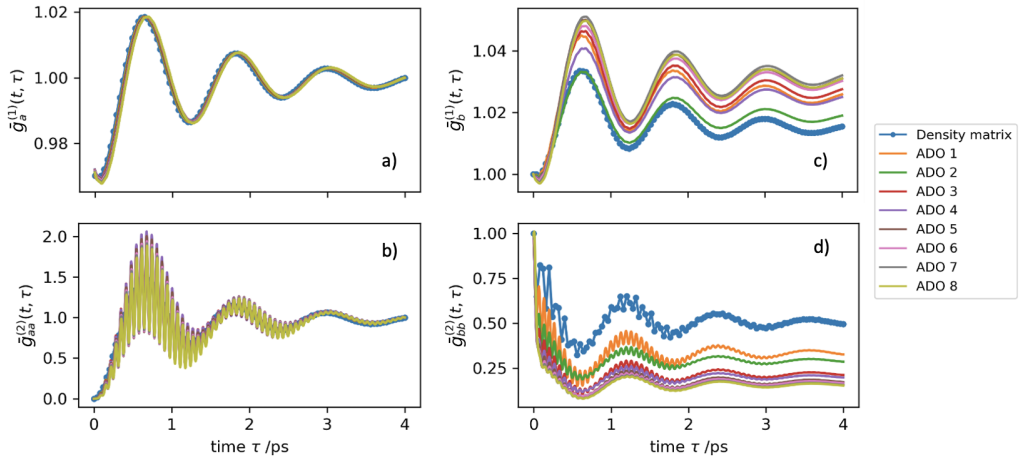

Figure 4.3.3: First order photon and phonon correlations for the HVM, normalised following equation (4.3.4), shown in a) and c) respectively. b) and d) show the associated second order correlations normalised following (4.3.5). The bath reorganisation energy is set at $\eta_{\mathrm{O}}^{(\nu)}$.

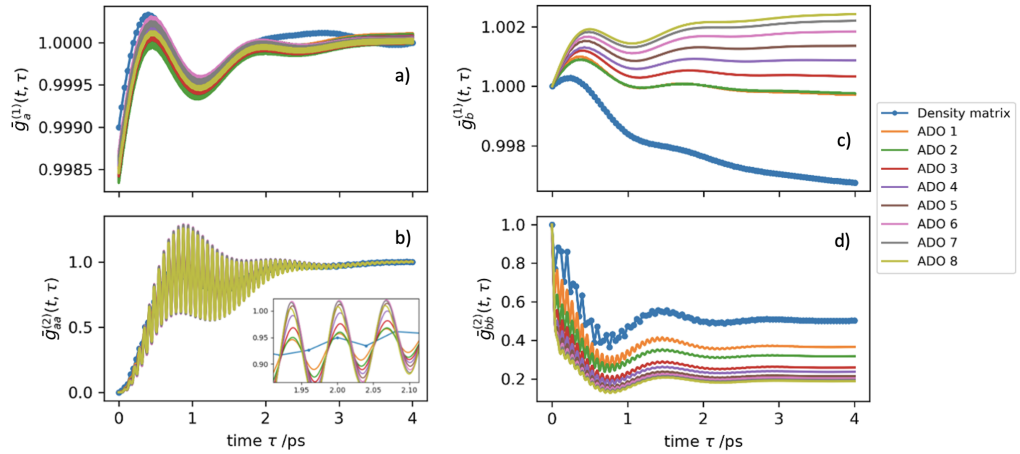

Figure 4.3.4: First order photon and phonon correlations for the HVM, normalised following equation (4.3.4), shown in a) and c) respectively. b) and d) show the associated second order correlations normalised following (4.3.5). The bath reorganisation energy is set at $2\eta_{\mathrm{O}}^{(\nu)}$.

4.3.3 shows the virtual correlations, which are now *strictly* non-physical as they have not been canonically transformed, for the HVM. a) and b) show the photon correlation of first and second order and c) and d) are the associated phonon contributions. These results produce the familiar result associated with continuous driving by a laser field of a vibronic monomer, shown in section 4.1, including both electronic and vibrational modes. In the photon correlations there is an electronic Rabi oscillation damped by the loss of phonons and, for the second-order correlation, a minor oscillation associated with phonon modes. In analogy with other phonon correlations, c) and d), present a vertical translation for each ADO. The reversed order of vertical translation in first order versus second order phonon correlations demonstrates an intrinsic difference in behaviour of a single split beam of phonons (such as in interferometry), which tends to antibunch, and a pair of sources which leads to bunching. This poses an interesting consideration for models of interferometry.

Figures 4.3.3, 4.3.4, and 4.3.5 demonstrate electronic Rabi oscillations in the correlation which are damped as phonons are lost to the bath through the system-environment coupling. In all of the photon correlations there is the anticipated minor oscillation as a consequence of phonon modes within the excited state wavepacket which occur when $\lambda^{(\nu)} > 0$. In each case the system demonstrates quantum antibunching. Similarly, the phonon correlations exhibit a more classical bunching, along with an electronic Rabi oscillation which is damped upon increasing the bath reorganisation energy.

In addition to the agreement with results in section 4.1, and a fundamental difference with the BVM method, these results demonstrate the difference of vibrational characteristics exhibited by each auxiliary. The phonon correlations

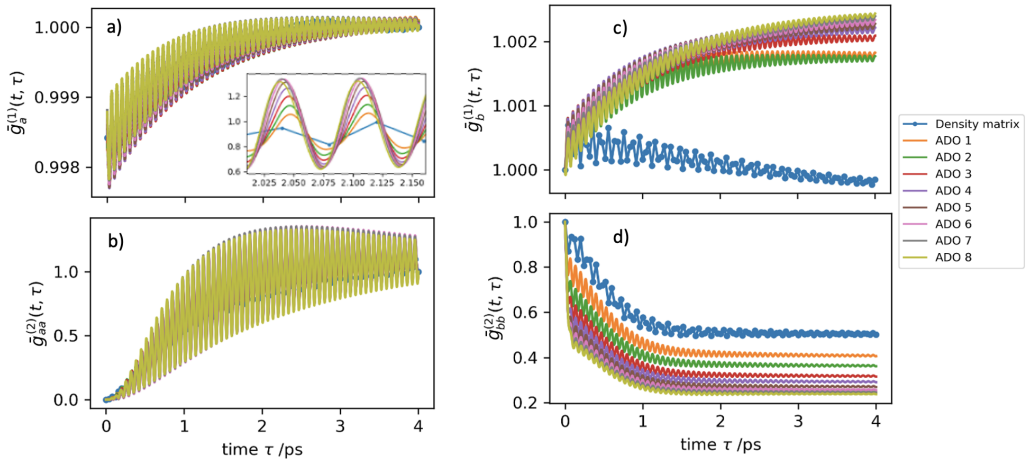

Figure 4.3.5: First order photon and phonon correlations for the HVM, normalised following equation 4.3.4, shown in a) and c) respectively. b) and d) show the associated second order correlations normalised following (4.3.5). The bath reorganisation energy is set at $3\eta_{\mathrm{O}}^{(\nu)}$.

in figures 4.3.3, 4.3.4, and 4.3.5, all demonstrate the aforementioned vertical translation with increasing ADO tier as a result of constituent Matsubara frequencies. Similarly, the amplitude of the minor oscillation in the photon correlations increase in amplitude in proportion to the auxiliary tier.

4.3.4 Zero Environment Reorganisation Energy

The nature of each auxiliary operator is further considered by producing correlations for an HVM vibronic monomer and in the limit of the bath reorganisation energy is zero. Under these conditions the dynamics are controlled by only the Markovian free propagation terms in the HEOM, discussed in section 2.5.4.

Figure 4.3.6 depicts all kinds of second order virtual correlation for photons and phonons for the first three ADOs and for two bath reorganisation energies: $0\ \mathrm{cm}^{-1}$ and $\eta_{\mathrm{O}}^{(\nu)}\ \mathrm{cm}^{-1}$. Each column of this figure shows results for a different ADO, and every two rows depict a different type of correlation. Each type of correlation is considered first with zero bath reorganisation energy, and then with $\eta_{\mathrm{O}}^{(\nu)}$ reorganisation energy. Odd rows, a) – c), h) – j), n) – p), and t) – v), clearly show that all of the auxiliaries contain no virtual correlation when the bath is not coupled to the system. This confirms the vibrational nature of auxiliaries, which are dependent on their Matsubara dimensions, and how they relate to integer multiples of phonon interactions from the EOM. This is true even for the non-thermal Matsubara dimensions, which for the overdamped hierarchy is dimension one, which is shown in the first column. Even rows, d) – f), k) – m), q) – s), and w) – y), show the correlation when the bath is coupled to the system

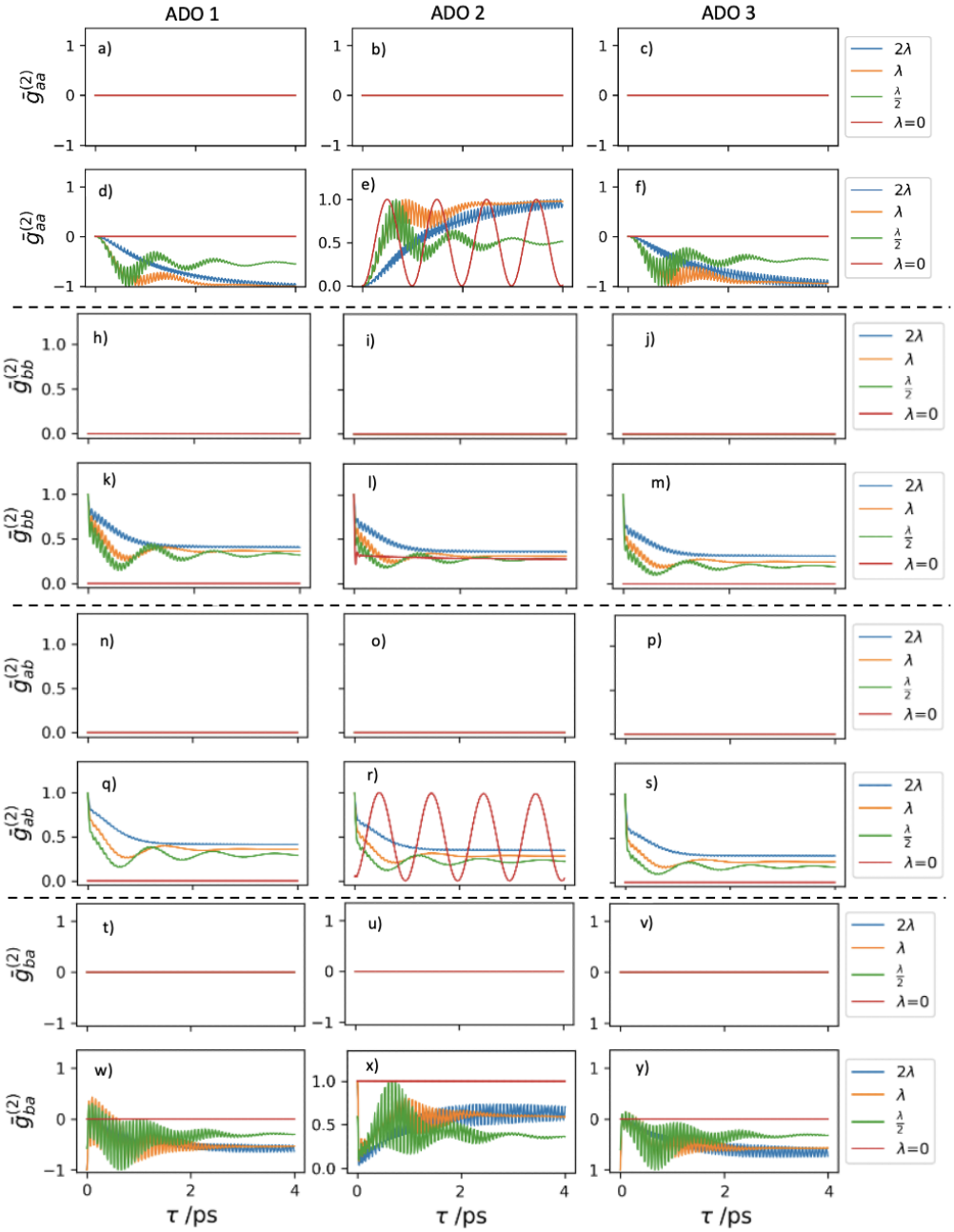

Figure 4.3.6: Columns one two and three depict quantum correlations for an HVM vibronic monomer in ADOs 1, 2, and 3 , respectively. Row 1, a) – c), shows the normalised $\bar{g}^{(2)}_{\mathrm{aa}}$ with zero bath reorganisation energy, and row 2, d) – f), with $\eta^{(\nu)}_{\mathrm{O}}$. Row 3, h) – j), shows the normalised $\bar{g}^{(2)}_{\mathrm{bb}}$ with zero bath reorganisation energy and row 4, k) – m), with $\eta^{(\nu)}_{\mathrm{O}}$. Row 5, n) – p), shows the normalised $\bar{g}^{(2)}_{\mathrm{ab}}$ with zero bath reorganisation energy and row 6, q) – s), with zero bath reorganisation energy. Row 7, t) – v), shows the normalised $\bar{g}^{(2)}_{\mathrm{ba}}$ with zero bath reorganisation energy and row 8, w) – y), with $\eta^{(\nu)}_{\mathrm{O}}$. Correlations for each ADO are shown at 0, $\frac{\lambda}{2}$, λ, and 2λ system reorganisation energies.

and is in agreement with figures 4.3.3, 4.3.4, and 4.3.5.

In summary, this work has shown that the BVM model structure, despite being effective for 2DES models, is incompatible with this metric of quantum correlation. The only signal which can be resolved is that of the electronic Rabi cycle due to electronic transitions at the fundamental frequency. Additionally, alongside consideration of virtual correlation in the HVM, this has elucidated the intrinsic vibrational nature of the ADOs. Each auxiliary is dependent on a Matsubara frequency, from the dimensions of the hierarchy, and these correspond to integer multiples of phonon modes. Interaction of these phonon modes and dissipation from the system to the bath results in non-Markovian dynamics leading to virtual correlation in ADOs and correlation in the density matrix.

4.4 Phonon Signatures in Photon Correlations of Electronically Coupled Molecules

The ubiquitous power of statistical measures of classical bunching, and quantum antibunching have resulted in a plethora of physical applications. The original experiments of Hanbury and Twiss[6] have led to a range of interferometers able to measure cosmic distances according to the loss of fringe interference patterns, as well as microscopic measurements in ultracold conditions of strongly bunched bosons which exhibit Bose-Einstein Condensation[318]. The original experiments were performed with blue light from a mercury-vapor lamp[6,319], but in recent years there has been considerable interest in generating other kinds of reliable photon sources ranging from Alkali metal atoms, quantum dots[320], and nanotubes[318,321] for the generation of sub-poissonian statistics, to emission of circularly polarised light resulting from excitonic fine structure[322].

Tunable photon sources allow dynamical analysis of the non-radiative decay of singlet-singlet or singlet-triplet annihilation in excitons[320,323], as well improved analysis of 2DES through improved spectral filtering of Liouville pathways[7]. These processes are achieved through scattering from excitonic states, and therefore the study of electronically coupled molecules such as J- and H-aggregates, which are discussed in section 2.2.1.2, is imperative. To this end, this section considers the second order photon and phonon correlations of a range of electronically coupled molecules. Based on the results of section 4.3 these models are constructed in the HVM regime, as the BVM is incompatible with this type of correlation metric, and the impact of this choice of system-bath boundary placement is considered.

4.4.1 HVM Model of Electronically Coupled Species

Each of the model systems are created as HVM, such that they can be visualised in the same way as in figure 4.3.1 a). Within this framework the structure of the (green) system component can be varied to generate HVM open quantum models for a range of molecules. When there is no electronic coupling the system depicts a monomer, and when the electronic coupling is zero the model describes a *monomer lattice*. This is a spatially fixed, uncoupled dimer containing two constituent monomers which can either be the same (homo) or different (hetero) species. Such species physically represent molecules in the limit of vanishing coupling strength, equivalent to molecules becoming increasingly separated ($J \propto \mathrm{r}^{-3}$). In addition, this could be used for molecules which have TDMs that are orthogonal and a laser field which is capable of driving both constituents. Alternatively, if $|J| > 0$ equivalent homo- and hetero-dimers are generated. The homo- and heterodimer models are constructed with a range of J values, summarised in table 4.1, such that both J- and H-aggregate systems, described in section 2.2.1.2, are analysed. Figure 4.4.1 depicts each of the proposed systems, based on theory in sections 2.2.1.1 and 2.2.1.3, which result in a full range of electronic coupling strengths. The excited state potential energy surface for each of the systems is displaced by increasing amounts leading to a decreasing Franck-Condon overlap integral of the ground electronic bound eigenstates. The smallest displacement induces a system reorganisation energy $\lambda^{(\nu)} \approx 360\ \mathrm{cm}^{-1}$. Correspondent with the parameter regimes in sections 4.1 and 4.3, these systems are coupled to an overdamped phonon bath with damping $\eta^{(\nu)} = 5\ \mathrm{cm}^{-1}$ and bath speed $\Lambda^{(\nu)} = 200\ \mathrm{cm}^{-1}$ at $T = 298$ K. Similarly, the driving field is assumed to be a delta function in the frequency domain such that excitations are induced only at the fundamental transition frequency. This laser has strength $E_0 = 10^7$ NC^{-1} and frequencies $\omega_{\mathrm{Res}}^{(\nu)}$ and $\omega_{\mathrm{Det}}^{(\nu)}$ in order to be resonant with the fundamental transition of the system, or detuned from it, respectively. Specific values of the laser frequency, dependent on the system type, are summarised in table 4.1. For a hetero-monomer lattice the resonant frequency is at the fundamental transition frequency of monomer A whereas the detuned frequency is at that of monomer B to demonstrate transitioning the spectrum from one monomer to the other over the course of the detuning. In the excitonic systems, the range of system reorganisation energies chosen lead to demonstrations of both weak and strong coupling. When $\tilde{d} \to 0$, corresponding to strong electronic coupling outlined in section 2.2.1.3.1, bright and dark exciton states become grouped resulting in a band structure and full Davydov splitting of $2J$. In contrast, when $\tilde{d} > 0$, corresponding to weak electronic coupling outlined in section 2.2.1.3.2, bands are not sufficiently separated, leading to a mixture of levels, and each exciton pair is split by a reduced $2J_{\mathrm{vib}}$. This change to the energy levels of molecules with non-zero coupling are

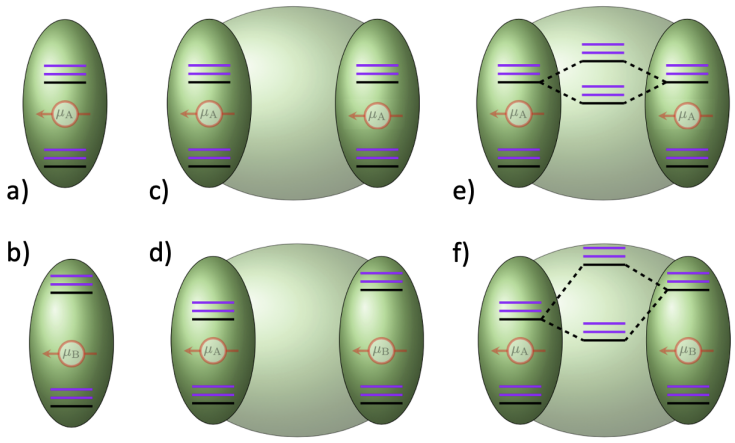

Figure 4.4.1: a) Monomer A with fundamental transition frequency and transition dipole moment, $\omega_{eg\mathrm{A}}^{(\nu)}$ and μ_{A}. b) Monomer B with fundamental transition frequency and transition dipole moment, $\omega_{eg\mathrm{B}}^{(\nu)}$ and μ_{B}. c) Homo-monomer lattice, consisting of two uncoupled but spatially fixed A monomer units. d) Hetero-monomer lattice, consisting of one monomer A and one monomer B which are spatially fixed but uncoupled. e) Homodimer, consisting of a pair of coupled A monomers which results in a pair of excitonic states split by $2J$. f) Heterodimer, consisting of one monomer A and one monomer B which are coupled resulting in a pair of excitonic states. Black energy levels vibrational ground states, purple electronic states are vibrational excited states, which are included explicitly in the Hamiltonian, separated by the vibrational mode frequency $\omega_0^{(\nu)} = 500\ \mathrm{cm}^{-1}$.

Species	J/cm^{-1}	$\omega_{\mathrm{Res}}^{(\nu)}\ /\ \mathrm{cm}^{-1}$	$\omega_{\mathrm{Det}}^{(\nu)}\ /\ \mathrm{cm}^{-1}$
Monomer (Type A)	0	$\omega_{eg\mathrm{A}}^{(\nu)}$	$\omega_{eg\mathrm{B}}^{(\nu)}$
Monomer (Type B)	0	$\omega_{eg\mathrm{B}}^{(\nu)}$	$\omega_{eg\mathrm{A}}^{(\nu)}$
Homo-monomer lattice (Type A)	0	$\omega_{eg\mathrm{A}}^{(\nu)}$	$\omega_{eg\mathrm{B}}^{(\nu)}$
Hetero-monomer lattice	0	$\omega_{eg\mathrm{A}}^{(\nu)}$	$\omega_{eg\mathrm{B}}^{(\nu)}$
J aggregate, homodimer (Type A)	$-500, -250, -50$	$\lvert\psi_{\mathrm{A}}^{+}\rangle$	$\lvert\psi_{\mathrm{A}}^{+}\rangle + \lvert\omega_{eg\mathrm{B}}^{(\nu)} - \omega_{eg\mathrm{A}}^{(\nu)}\rvert$
H aggregate, homodimer (Type A)	50, 250, 500	$\lvert\psi_{\mathrm{A}}^{+}\rangle$	$\lvert\psi_{\mathrm{A}}^{+}\rangle + \lvert\omega_{eg\mathrm{B}}^{(\nu)} - \omega_{eg\mathrm{A}}^{(\nu)}\rvert$
J aggregate, heterodimer	$-500, -250, -50$	$\lvert\psi_{\mathrm{A}}^{+}\rangle$	$\lvert\psi_{\mathrm{A}}^{+}\rangle + \lvert\omega_{eg\mathrm{B}}^{(\nu)} - \omega_{eg\mathrm{A}}^{(\nu)}\rvert$
H aggregate, heterodimer	50, 250, 500	$\lvert\psi_{\mathrm{A}}^{+}\rangle$	$\lvert\psi_{\mathrm{A}}^{+}\rangle + \lvert\omega_{eg\mathrm{B}}^{(\nu)} - \omega_{eg\mathrm{A}}^{(\nu)}\rvert$

Table 4.1: Parameters for each of the HVM electronically coupled species. The associated electronic transition frequencies are $\omega_{eg\mathrm{A}}^{(\nu)} = 15\,000\ \mathrm{cm}^{-1}$, $\omega_{eg\mathrm{B}}^{(\nu)} = 18\,000\ \mathrm{cm}^{-1}$, and the vibrational mode frequency is $\omega_0^{(\nu)} = 500\ \mathrm{cm}^{-1}$.

accounted for in the resonant frequencies chosen, as shown in table 4.1.

4.4.2 First and Second Order Correlations

4.4.2.1 Limits of Electronic Coupling

Figure 4.4.2 shows the second order photon correlations for a range of electronic coupling strengths. Column 1 shows the correlation of a monomer A which has no electronic coupling. Columns 3 and 4 are the two kinds of monomer lattice, homo- (monomer A) and hetero-, which also both have zero electronic coupling. Columns 4 and 5 are the two kinds of excitonic dimer, homo- (monomer A) and hetero-, with a J coupling of $-50\ \mathrm{cm}^{-1}$ resulting in J-aggregates. The top half of the figure, a) – l), presents results which are driven by a laser field frequency that is resonant with the fundamental electronic transition of the system, as shown in table 4.1. The bottom half of the figure, m) – x), shows the associated models when driven at a frequency detuned from the fundamental electronic transition, $\omega_{\mathrm{Det}}^{(\nu)}$. a) – f), and m) – r), of of the figure have an environment reorganisation energy of $0\ \mathrm{cm}^{-1}$, and g) – l), and n) – x), have $\eta^{(\nu)}\ \mathrm{cm}^{-1}$. In all cases the system reorganisation energy is varied through 0, $\frac{\lambda}{2}$, λ, up to 2λ.

a) and g) in column 1 of figure 4.4.2, for the vibronic monomer A, is in agreement with the results in section 4.1. The ground state Boltzmann population of vibronic levels are promoted into their corresponding excited state upon interaction with the driving field which, with the exception of the zero system reorganisation models, results in an excited state wavepacket. When $\lambda = 0$ there will be maximum Franck-Condon overlap between the ground and excited state bound eigenstates such that electronic Rabi cycles at the fundamental frequency are established without any phonon contributions. However, when $\lambda > 0$ and the excited state potential energy surface is displaced from the ground state, leading to a wavepacket upon projection of the ground state population into the excited state. Within this wavepacket phonon signatures at the vibrational mode frequency are induced through VR to the ground vibrational state. The amplitude of the minor oscillatory mode increases proportionally with the system reorganisation energy as a larger displacement results in a lower Franck-Condon overlap with the ground state but better overlap for higher vibrational excited states. The contrast between a) and m) demonstrates the difference of detuning: the electronic Rabi oscillation is entirely absent at the detuned frequency, and phonon effects cause the only modulation of probability. When the system is driven at $\omega_{\mathrm{Res}}^{(\nu)}$ the familiar vibrational signals and electronic Rabi oscillations arise, but when the system is detuned by $3\,000\ \mathrm{cm}^{-1}$ no transitions at the fundamental frequency are stimulated - not even a small percentage. This leads to a flat $g_{\mathrm{aa}}^{(2)}$ profile which is

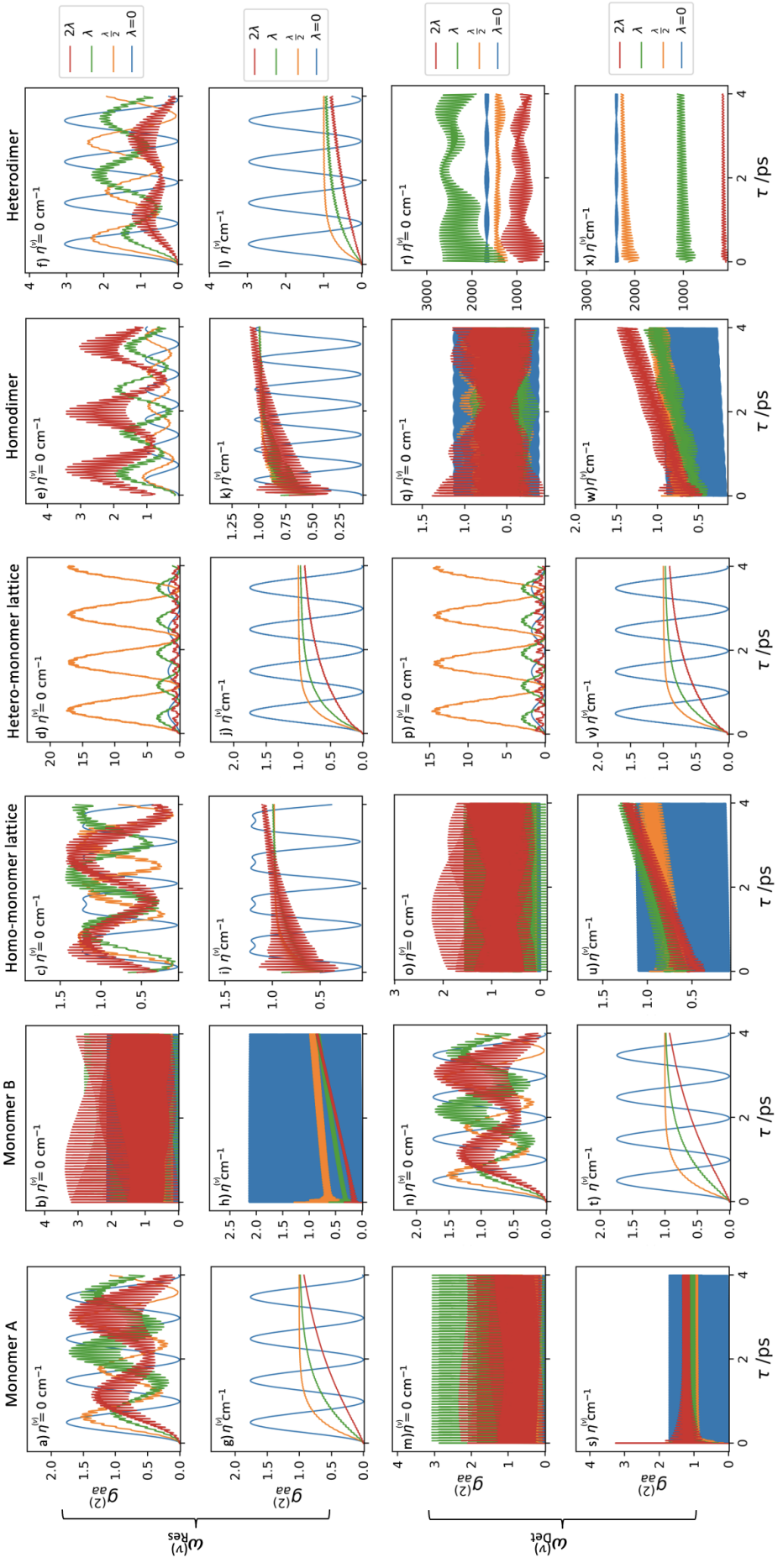

Figure 4.4.2: Second order photon correlations for a range of electronically coupled species. (Top) at the resonant frequency $\omega^{(\nu)}_{\mathrm{Res}}$ in table 4.1 (Bottom) at a frequency detuned from the fundamental transition of the system $\omega^{(\nu)}_{\mathrm{Det}}$, also shown in table 4.1. Column 1 and 2 show results from a monomer A and B, column 3 for a homo-monomer lattice of A monomers, column 4 for a hetero-monomer lattice, column 5 for a homodimer J-aggregate, and column 6 for a heterodimer J-aggregate, both with a coupling of $-50\ \mathrm{cm}^{-1}$. a) – f), m) – r), are for a bath reorganisation energy of zero, whereas g) – l), s) – x), have a bath reorganisation of η.

dominated by the background movement of phonons. Detuning is particularly highlighted by the appearance of phononic signatures in cases when the excited state potential is not displaced, $\lambda = 0$, signifying that no electronic Rabi frequencies are able to occur.

Column 2 shows equivalent results to those in figure 4.4.2 column 1, but with a monomer B, with a higher fundamental transition frequency. This swaps the behaviour from the b) and h) signifying that the system is now detuned by $3\,000\ \mathrm{cm}^{-1}$ as in table 4.1. Even though the transitions are at significantly higher frequencies the correlations generated in n) are equivalent to those in a). In subtle contrast, b) and h) show a major oscillation, and gentle increase in correlation, respectively, which signifies that a very small proportion of higher vibrational states are able to transition at the fundamental transition frequency, $|g,0\rangle \rightarrow |e,6\rangle$. This is likely due, in part, to the divergence of higher energy levels of the quantum harmonic oscillator potential, and also demonstrates that the resonance is not binary: even when the driving field is a continuous wave that a small proportion of forbidden transitions occur. This is as a consequence of the semi-classical approximation.

Column 3 of figure 4.4.2 presents the results for the homo-monomer lattice with zero $J = 0$. This model consists of a pair of identical monomers, each with associated vibrational levels, which are spatially fixed. This behaves like a three level system with the 'doubly' excited state corresponding to simultaneous excitation of both monomers, the singly excited state corresponding to one of the two monomers being excited, and the ground state being the doubly ground. Subsequently, there is a competition between the transition from the doubly ground state to the first excited state and the transition between the singly and doubly excited states, producing a double peak in the photon correlations (most evident for $\lambda = 0$). One other noticeable feature is that, for $\lambda = 0$ at early τ times, the observed behaviour for photons is bunching rather than antibunching. This is because both excited states (or the 'doubly' excited state) tend to relax at the same time when in equilibrium with the driving field. Apart from this, the results are qualitatively similar to those of a monomer and are in agreement with the first column. In contrast to panel g) for an isolated monomer A, u) shows a large amplitude vibrational oscillation at the system mode frequency when the system is coupled to the bath. This is a consequence of doubling the number of monomers within the system, which allows an equilibrium to be established with the laser whereby the system exists more predominantly in vibrationally excited states, leading to greater VR and a larger minor oscillation, because of the two competing excited states. Subsequently, phononic vibrations within the wavepacket persist for longer even when coupled to the bath. o) and u) present results in agreement with those in both a), g) and b), h) showing strong phonon signatures in the absence of the

electronic Rabi cycle. In addition, the increase in population which increases vibrations in i) also occurs here, and results in higher vibrational states having enough population for a minor increase in correlation to occur while detuned.

Column 4 shows the other type of monomer lattice: the hetero-monomer case. These results also include a change to the dimensions of the truncation of the Hamiltonian, as in order to access both the lowest vibrational levels of $\omega_{\mathrm{egA}}^{(\nu)}$ and $\omega_{\mathrm{egB}}^{(\nu)}$, requires a broad Hamiltonian truncation window. This is discussed in detail in appendix I. Subsequently, the broad truncation has limited the number of accessible vibrational levels and the majority of the phonon signatures are lost from the correlations along with a change in the period of the electronic Rabi cycles. This highlights how important vibrational contributions are to these systems, even in the absence of electronic coupling, and that full vibrational and electronic complexity is necessary to observe the correct correlations. This would be achieved by allowing full vibrational and electronic complexity with a broad truncation window, at significant computational cost, but in this thesis such an approach is not possible because of the associated cost.

This system also has a pair of electronic energy levels and associated vibrational energy levels, but they are not degenerate. The energy levels of monomer A are at a lower energy to those of monomer B so that when the system is driven by the field $\omega_{\mathrm{Det}}^{(\nu)}$ only one of the monomers is able to reach the excited state. Subsequently, the correlation for this system behaves like a single monomer B, demonstrating the effect of moving between resonant and detuned driving frequencies. This means d), j) and p), v) present equivalent correlations, just as in a), g) and n), t), depicting movement from one monomer to the other. As shown in appendix I, the profiles of column 4 are equivalent to those of a monomer when the same restrictive truncation window is applied.

Column 5 of figure 4.4.2 shows the photon correlations for a homodimer of A monomers with an electronic coupling of $J = -50\ \mathrm{cm}^{-1}$. The system is now delocalised into a single system, but with an increased total phonon number, as such there is an equivalence between these results and column 3. The importance difference is, as a consequence of state delocalisation, that there is no competition between the two individual monomers and double peaks are absent in the correlations. Instead the system acts as a single homodimer with the electronic Rabi period doubling as a consequence, but the phononic signatures having a similar magnitude to the lattice, most evident in e), k). This means that the early time bunching of phonons in the lattice, due to the two TLSs, is absent in these correlations and the homodimer presents early time antibunching. Comparison of column 6, e), k), q), w) and column 1, a), g), m), s), shows a clear similarity between the monomer A species correlations and those of a monomer A homodimer. Both columns have minor and major

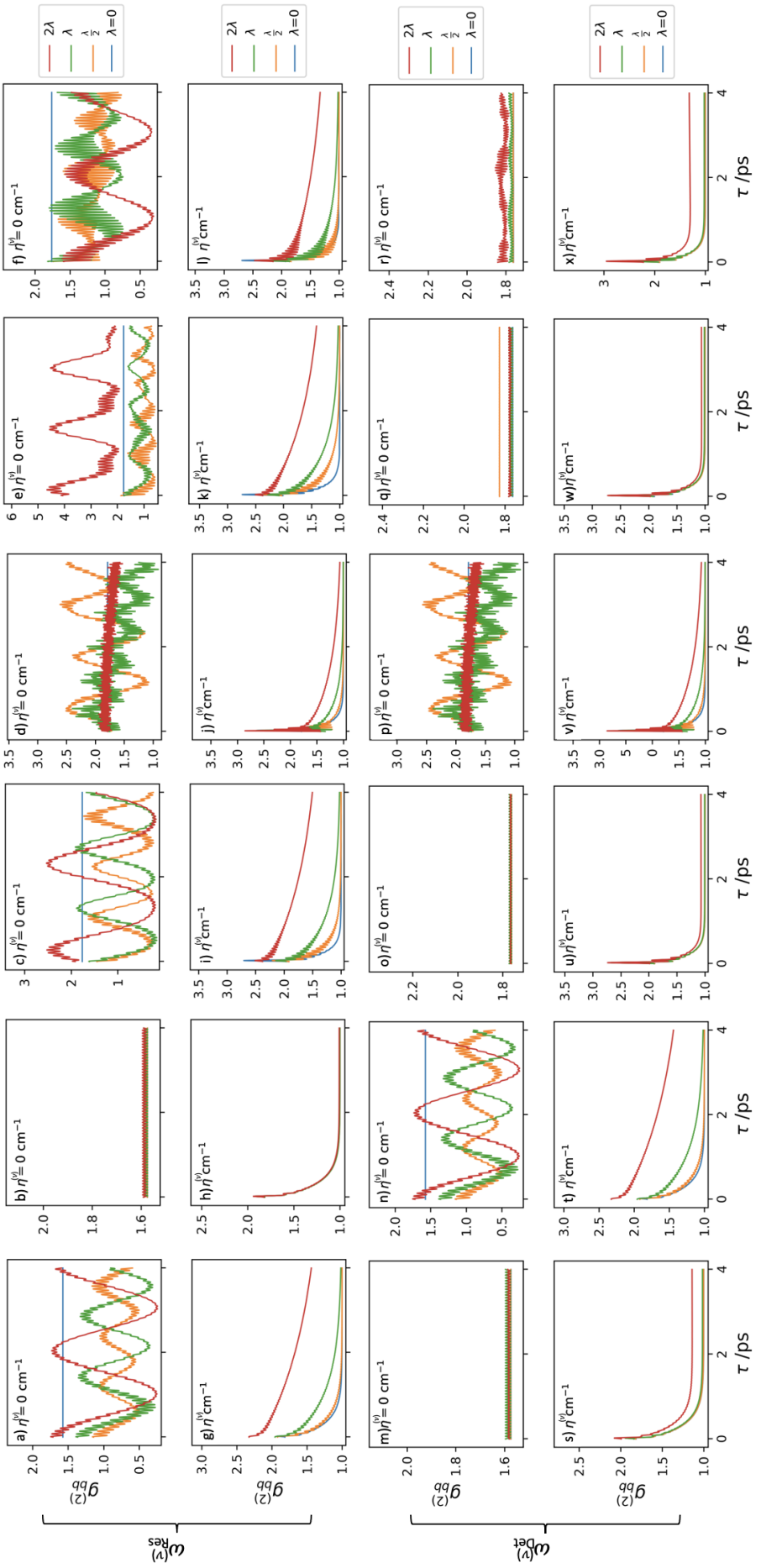

Figure 4.4.3: Second order phonon correlations for a range of electronically coupled species. (Top) at the resonant frequency $\omega^{(\nu)}_{\mathrm{Res}}$ in table 4.1 (Bottom) at a frequency detuned from the fundamental transition of the system $\omega^{(\nu)}_{\mathrm{Det}}$, also shown in table 4.1. Column 1 and 2 show results from a monomer A and B, column 3 for a homo-monomer lattice of A monomers, column 4 for a hetero-monomer lattice, column 5 for a homodimer J-aggregate, and column 6 for a heterodimer J-aggregate, both with a coupling of $-50\ \mathrm{cm}^{-1}$. a) – f), m) – r), are for a bath reorganisation energy of zero, whereas g) – l), s) – x), have a bath reorganisation of η.

oscillations of equivalent amplitude and reach similar states at equilibrium (long τ). Similar to column 3, the homodimer has a shorter period than the monomer consistent with the change in energy of the split exciton levels. Additionally, similar to u) and in contrast to s), the gradual increase in correlation at higher system reorganisation energies suggests that there is an energy transfer process from dark to bright exciton states increasing correlations as a consequence of the electronic coupling. The difference in behaviour between q), w) and p), v) also highlights the significance of different constituent species: molecules with more than one constituent monomer can exhibit correlations that are not dominated by phonons at resonant and detuned frequencies.

Column 6 of figure 4.4.2 shows the photon correlations for a heterodimer of A and B monomers also with an electronic coupling of $J = -50\ \mathrm{cm}^{-1}$. Similar to the homodimer in column 5, the system is delocalised into exciton states resulting in photon correlations which are similar to the monomer from column 1, but with double the probability reflecting the increase in photon number. r) and x) present the detuned correlations, and show almost constant values with a very large probability, but in contrast to the other detuned correlations, the phonon signatures do not dominate. This suggests that the system is detuned from the fundamental transition but that the electronic coupling has brought the electronic Rabi frequency closer to the value of the laser field such that a small percentage is able to transfer. This means that the major oscillation is still present, and is most evident for the reorganisation energy of λ. The very large probability is a sign that the mean photon number is vanishing more quickly than the variance of the photons, and subsequently the correlation diverges when normalised. This highlights that the phonon number is vanishingly small and correlations are very unlikely: suggesting the driving field is significantly detuned from the transition frequency. The small relative amplitude of the phonon signatures within r), x) suggest that not all of the vibrational levels of necessary higher frequency transitions are being included in the model, as a consequence a broader truncation window could be used similar to column 4. Ideally, with much greater computational power, the full Hamiltonian could be considered to further elucidate these signatures when far from resonance. Another interesting open question is whether a double peak could be introduced into the system if the laser was moved from being continuous, to a Gaussian width which covers both the fundamental transitions of monomer A and B. Again, this would require significantly more computational power in order to process much larger proportions of the full Hamiltonian.

Figure 4.4.3 presents the second order phonon correlations for each of the electronically coupled systems. These results are in agreement with both figure 4.4.2 and the results in section 4.1 and demonstrates the intrinsic difference in vibrational signatures within systems that have and do not have electronic

coupling.

Column 1 shows the correlation of phonons in a monomer (species A), and highlights that, as a consequence of the independence from the order of detection events, there is only a single source of vibrational character. The phonon modes, at $\omega_0^{(\nu)}$, arise from direct measurement of the phonon number resulting in a low amplitude minor oscillation. In those systems with an excited state displacement, the resulting wavepacket will contain a superposition of vibrational states. However, when there is no system reorganisation energy there will be maximum Franck-Condon overlap of the ground and excited state and no wavepacket forms resulting in no minor mode. In agreement with figure 4.4.2, both columns 1 and 2 demonstrate very similar correlations in their respective resonant regimes. The only difference is that in t), with 2λ, the increased energy of the detuning field promotes a greater probability of detecting phonons than in s). In particular, g) and t) demonstrate the linear proportionality between the excited state displacement and the magnitude of vibrational correlation signifying that as the Franck-Condon overlap integral with higher vibrational states increases so too does the amount of VR. In all cases, both monomer A and B demonstrate bunching of phonons for early τ.

The correlations for the homo-monomer lattice are shown in column 3 of figure 4.4.3 and show very similar trends to those in the third column of figure 4.4.2. While the double peak introduced by the competition between the 'doubly' excited state and singly excited states is less pronounced due to the large mean phonon number relative to photons, it is still evident from the change in period of the major Rabi oscillations (most evident for 2λ). The early τ behaviour is inverted for this reorganisation energy to depict antibunching of phonons and the period is stretched so that fewer full oscillations can occur over 4 ps. This is a consequence of the equilibrium established with the driving field which promotes simultaneous emission of photons from the singly and doubly excited states at early τ, and the lag time from this emission reduces the probability of instantaneous phonon emission. However, the vibrational signatures in the phonon correlations are in strong contrast with figure 4.4.2. In all panels of column 3, figure 4.4.3, the amplitude of the minor oscillation is far smaller, as a consequence of mean phonon number relative to the photons. In the photon correlations, indirect phonon contributions to the excited state wavepackets were amplified by doubling the number of photons within the system, however, because the system already had many more phonons than photons doubling does not have the same impact on phonon correlations. Despite this, the increase in phonon number leads to a greater magnitude of overall two phonon correlation for all system reorganisations energies reflecting the increase in VR in the system containing multiple monomer units.

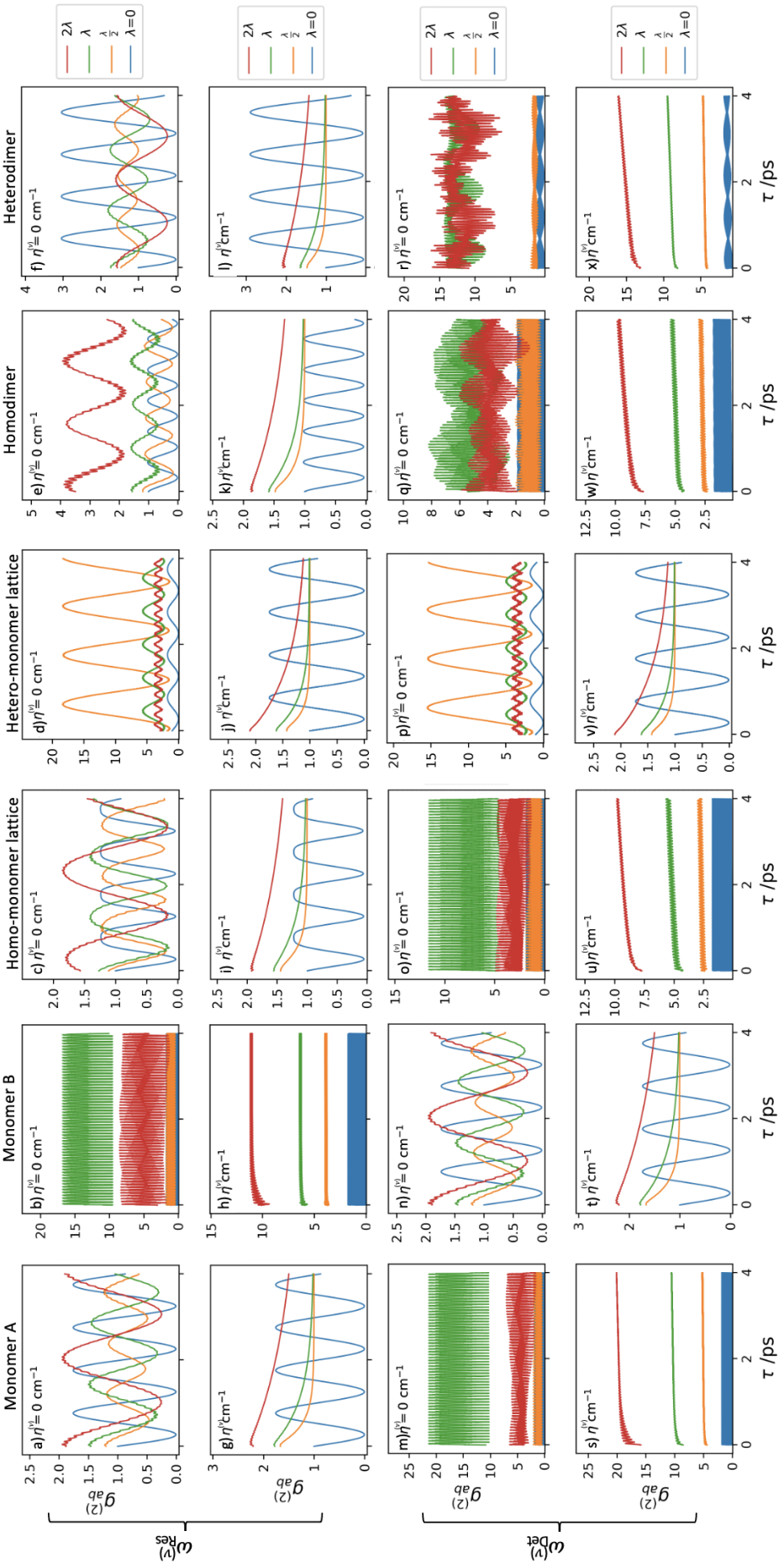

Figure 4.4.4: Second order crossed correlations, $g_{\mathrm{ab}}^{(2)}$, for a range of electronically coupled species. (Top) at the resonant frequency $\omega_{\mathrm{Res}}^{(\nu)}$ in table 4.1 (Bottom) at a frequency detuned from the fundamental transition of the system $\omega_{\mathrm{Det}}^{(\nu)}$, also shown in table 4.1. Column 1 and 2 show results from a monomer A and B, column 3 for a homo-monomer lattice of A monomers, column 4 for a hetero-monomer lattice, column 5 for a homodimer J-aggregate, and column 6 for a heterodimer J-aggregate, both with a coupling of $-50\ \mathrm{cm}^{-1}$. a) – f), m) – r), are for a bath reorganisation energy of zero, whereas g) – l), s) – x), have a bath reorganisation of η.

Column 4 of figure 4.4.3 shows equivalent trends to those in figure 4.4.2, with both the resonant and detuned frequencies presenting correlations commensurate with individual monomers A and B under the influence of a restrictive truncation. When the bath is coupled to the system, phonons are rapidly dissipated into the bath resulting in an equilibrium correlation being established, demonstrated by g) – l) and s) – x).

Column 5 of figure 4.4.3 shows the phonon correlations for a homodimer of A monomers. Equivalent to figure 4.4.2 the delocalisation of the states results in the loss of double peaks, and a doubling of the period of the electronic Rabi oscillations. However, in contrast to the photon correlations, for the largest value of excited state displacement, the dimer correlation of phonons antibunch for early τ.

Column 6 of figure 4.4.3 shows the phonon correlations for a heterodimer of A and B monomers with an electronic coupling of $J = -50\ \mathrm{cm}^{-1}$. The trends are similar to those shown in column 1 but with a significantly larger minor oscillation due to the increased number of phonons within the delocalised system.

In contrast to the photon correlations, the signal of detuning in the phonon correlations is a return to the equilibrium value of phonon transfer. Additionally, as the number of phonons greatly outweighs the number of phonons, vibrational correlations are insensitive to the movement of other phonons and detuned correlations do not modulate. From the phonon correlations, in particular for the homo-monomer lattice and homodimer, it is clear that highly displaced excited states which induce wavepackets with a large vibrational component can alter whether the system exhibits phonon bunching or antibunching at early τ.

In a manner equivalent to the discussion in section 4.1 it is possible to understand the appearance of phonon signatures in the photon correlations from the cross-correlation functions where the order of detection does matter. Figure 4.4.4 shows the second order cross-correlation, $g^{(2)}_{\mathrm{ab}}$, when the first detection event is a photon and the second, τ later, is a phonon. In agreement with section 4.1 the minor oscillation due to phonon contributions has a very small amplitude, with notable exceptions being the homo-monomer lattice driven off resonance, o), and the homodimer driven at resonance, e), with 2λ reorganisation energy. In all other resonant panels, the minor oscillation amplitude is minimised. This is because the primary behaviour of the cross-correlation is of electronic Rabi cycles due to the photons. The first detection is an instantaneous measurement of the photon number within the system, and subsequently, does not induce any phonon signatures. The second detection event, the τ dependent detection, is modulated by the population of vibrational excited states throughout the time domain leading to signatures at the vibrational mode frequency. However, because the phonon signatures are

very small with respect to the electronic contributions their impact on the excited state adiabatic population is minimal. In agreement with the previous results, and because the primary character of these correlations is photonic, when driven by a field detuned from resonance, the electronic Rabi cycle is minimised or eradicated. In contrast, e) and p) have a larger vibrational component for 2λ reorganisation energies. For the hetero-monomer lattice this is because the broad truncation is not capturing sufficient vibrational levels, and those which are caught are subtly diverging which increases the oscillation amplitude. In the homodimer, e), this is a consequence of the delocalisation of degenerate monomer A states. The increased population coupled with better Franck-Condon overlap for higher vibrational excited states leads to an excited state wavepacket with a more prominent vibrational contribution.

Similar to figure 4.4.4 a deeper understanding of the phonon signatures in photon correlations can be gleaned from the cross-correlation functions where the order of detection does matter. Figure 4.4.5 shows the second order cross-correlation when the first detection event is a phonon and the second, τ later, is a photon. In agreement with section 4.1 the minor oscillation due to phonon contributions has a much larger amplitude, becoming a major component of the probability. This is because the first and second detection event both introduce vibrational character to the correlation. The detection of the phonon at $\tau = 0$ is an instantaneous measurement of phonon number with intrinsic vibrational character at the system mode frequency. Similarly, the detection of the photon at a time τ later introduces further vibrational character due to vibrational transitions occurring between the detections. This means that there is a direct and indirect source of vibrational character which combine to produce a large amplitude minor oscillation at the vibrational mode frequency. In all columns, when the system reorganisation energy is zero, the correlation remains at a constant non-zero value, corresponding to the phonon movement in the absence of excited state displacement. In addition, all resonant panels exhibit a reduction in the probability below this phonon detection probability in the absence of displacement as a direct result of the vibrational contributions. This is attributed to a large proportion of the wavepacket undergoing vibrational transitions such that further correlations are hindered. This effect is most prominent when there is no electronic coupling, columns 1 and 2. This effect persists for small values of τ and with strong bath dissipation. This is because photon emission at $\omega_{eg}^{(\nu)}$ from higher vibrational levels is increasingly suppressed for larger λ due to decreasing Franck-Condon overlap. When system-bath interaction occurs, g) – l) and s) – x), the dissipation of phonons to the bath leads to a reduction in the correlation with photons such that all columns exhibit a reduction below the phonon movement in the absence of a bath. Notably, in all models with the exception of the homo-monomer lattice and homodimer i), k), the cross-correlation tends towards the value of phonon

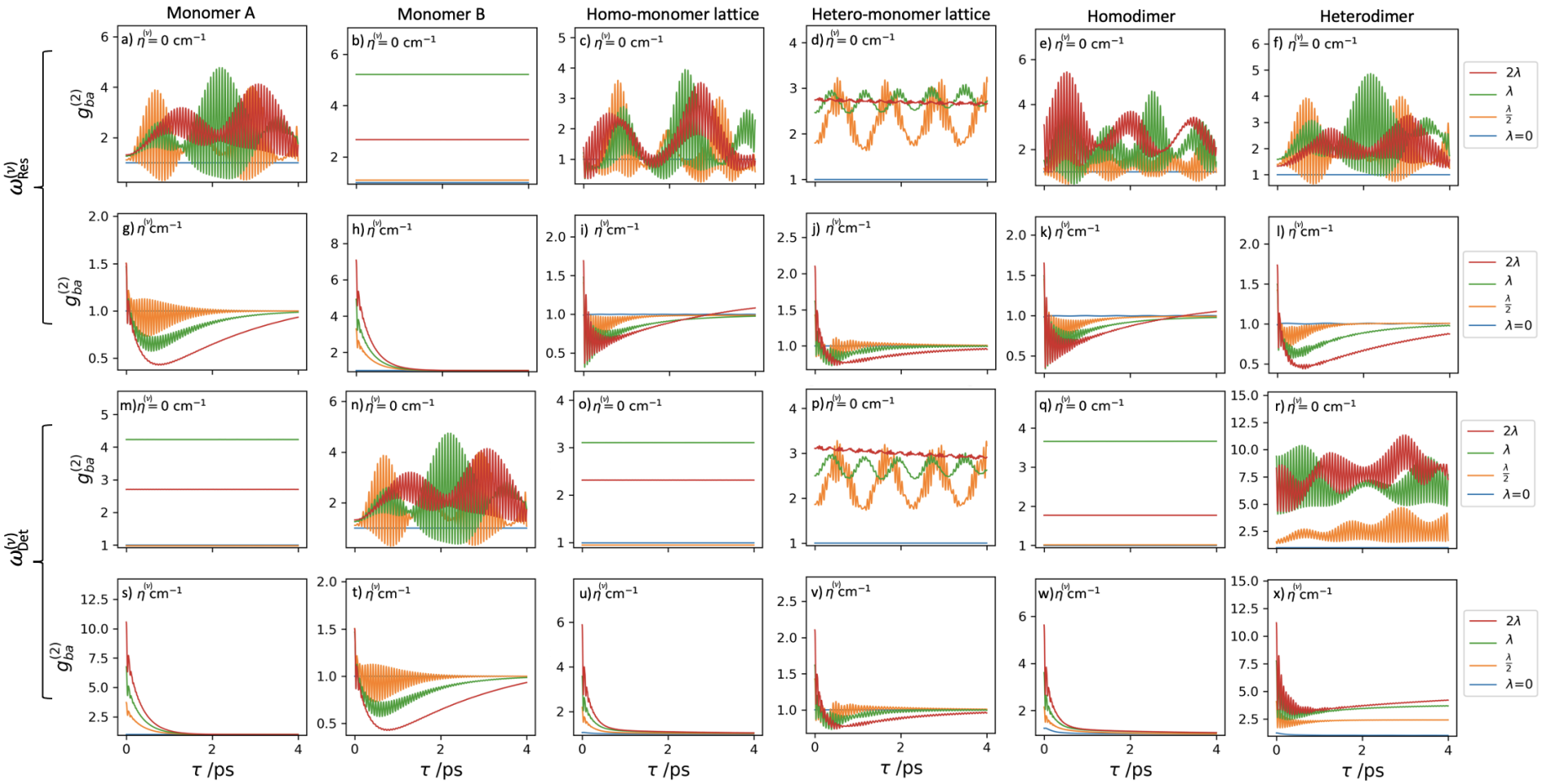

Figure 4.4.5: Second order crossed correlations, $g_{\mathrm{ba}}^{(2)}$, for a range of electronically coupled species. (Top) at the resonant frequency $\omega_{\mathrm{Res}}^{(\nu)}$ in table 4.1 (Bottom) at a frequency detuned from the fundamental transition of the system $\omega_{\mathrm{Det}}^{(\nu)}$, also shown in table 4.1. Column 1 and 2 show results from a monomer A and B, column 3 for a homo-monomer lattice of A monomers, column 4 for a hetero-monomer lattice, column 5 for a homodimer J-aggregate, and column 6 for a heterodimer J-aggregate, both with a coupling of $-50\ \mathrm{cm}^{-1}$. a) – f), m) – r), are for a bath reorganisation energy of zero, whereas g) – l), s) – x), have a bath reorganisation of η.

movement in the absence of a bath. In the homo-monomer lattice and homodimer species the gradient of the correlation, and the correlation for 2λ, suggest that they will exceed this value in the limit of large τ. This is a consequence of the reduced energy of the bright exciton state, specifically in the homodimer, and the competition between the singly and 'doubly' excited states in the homo-monomer lattice which promote the wavepacket to have larger phononic contributions. All of the columns in figure 4.4.5 present a quantum antibunching, as phonon emission tends to inhibit subsequent photon emission, particularly for small values of τ.

In summary, these results demonstrate the limits of electronic coupling in coupled species, through to uncoupled and monomer systems. When there is no electronic coupling it is shown that equivalent correlations are generated in monomers, independent of their fundamental electronic transition frequency and the frequency of the driving field. Additionally, in spatially fixed monomer-lattices there is a competition between the constituent monomers when their energy levels are degenerate. Consequently, homo-monomer lattices exhibit double peaks due to the competition of the two TLSs. An equilibrium is established between the system and the driving field such that the energetic minimum, 'doubly ground', state can be reached which leads to a bunching of the emitted photons from the two monomer units. In contrast, when the monomer units are different (hetero-monomer lattice) either correlations consistent with monomer A or monomer B appear, dependent on the driving field frequency. In dimer species, as a result of the delocalisation due to electronic coupling, there is a doubling of the period of electronic Rabi oscillations rather than a doubling of the number of peaks. This highlights that the system is now delocalised allowing for energy and phonon transfer between different localised sites in the molecule.

4.4.2.2 Analysis of Electronic Coupling in Dimer Species

Given the analysis in the previous section, 4.4.2.1, different strengths of electronic coupling are considered for both homodimers and heterodimers when they are driven resonantly. Following figure 2.2.4, both J- and H-aggregates are considered, however, due to the method of computational truncation of the diagonalised matrices, the results for H-aggregates are less precise. When the electronic coupling is negative the monomer excited state energy levels are split by $2J$ into a pair of exciton states with the lower energy exciton state being the allowed, bright, state. As a result of this, the lowest energies contained in the Hamiltonian above the ground state correspond to the desired exciton states allowing the large dimensions to be truncated saving computational effort. However, when the electronic coupling is positive, the allowed, bright, exciton

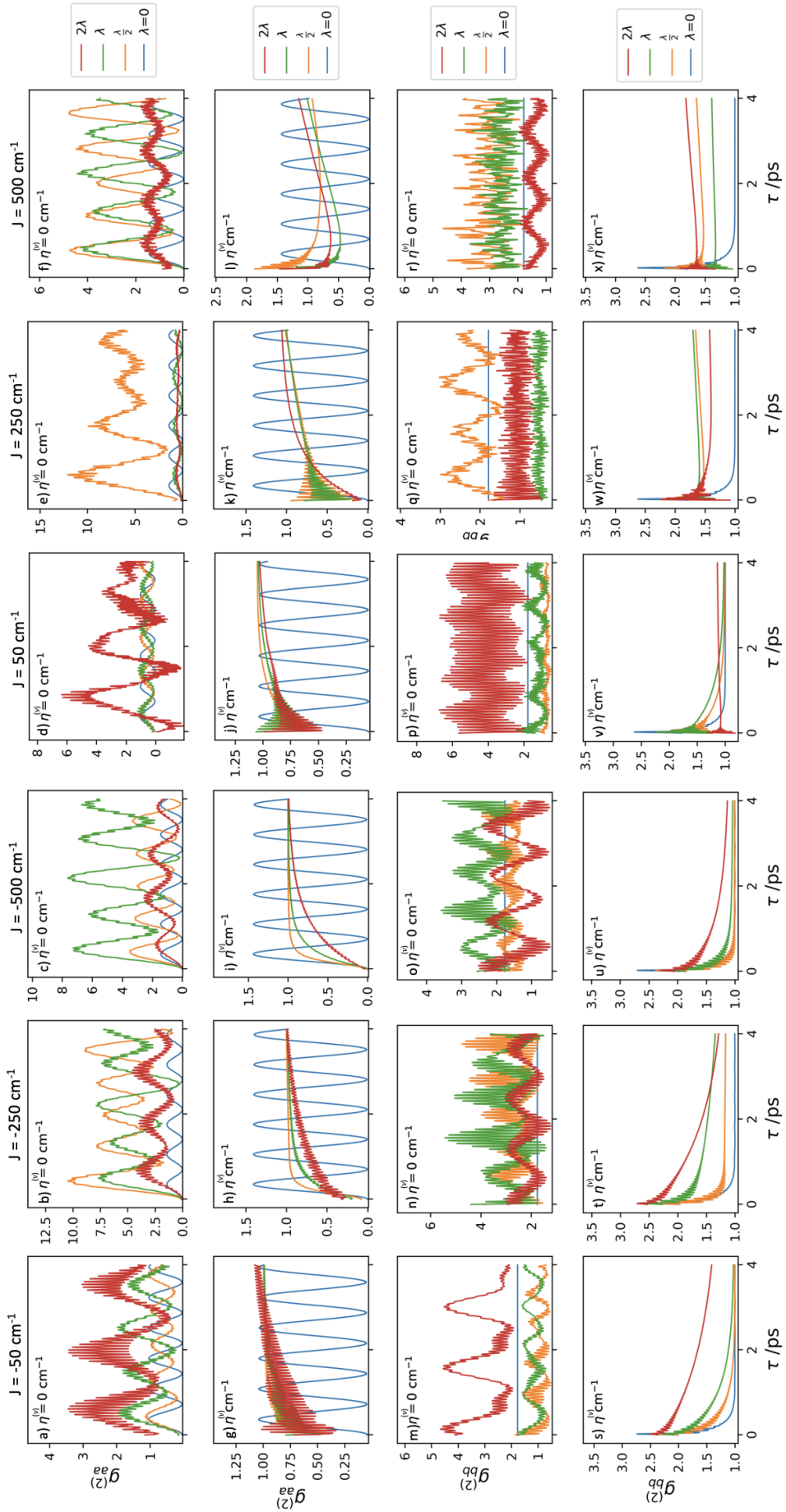

Figure 4.4.6: Second order photon, a) – l), and phonon m) – x), correlations for a range of electronic coupling strengths in a homodimer. Columns 1 - 6 show $J = -50\ \mathrm{cm}^{-1}$, $-250\ \mathrm{cm}^{-1}$, $-500\ \mathrm{cm}^{-1}$, $50\ \mathrm{cm}^{-1}$, $250\ \mathrm{cm}^{-1}$, and $500\ \mathrm{cm}^{-1}$, respectively. a) – f), m) – r), have bath reorganisation energies of $0\ \mathrm{cm}^{-1}$, and g) – l), s) – x), have bath reorganisation energies of $\eta^{(\nu)}\ \mathrm{cm}^{-1}$.

state is at higher energy. Subsequently, the exciton of interest is contained within a number of vibrational excited state energies dependent on the system parameters. There is no simple solution for finding the exact location of each desired H-aggregate state, so in order to propagate for the same time period, the dimensions of the composite Hilbert space are reduced sufficiently so that the full matrix can be propagated. This results in a much poorer resolution of the vibrational mode frequency, as higher energy levels begin to diverge, but global, electronic oscillations will be resolved sufficiently well. This is discussed further in appendix I.

Figure 4.4.6 shows the result of resonantly driving a series of homodimers for a full range of electronic coupling, resulting in a series of J-aggregates in a) – c), g) – i), m) – o), s) – u), and H-aggregates in d) – f), j) – l), p) – r), v) – x). Row one shows that electronic coupling strengths closest to zero have the largest phonon signatures in the photon correlation. This is because larger coupling strengths split the levels into significantly higher energies for H-aggregates, or lower energies for J-aggregates, resulting in poorer Franck-Condon overlap of the ground state with vibrational excited states and the subsequent wavepacket will have a smaller vibrational contribution. When the coupling is closest to zero, the splitting of $2J$ will still be much less than the vibrational mode frequency resulting in the best Franck-Condon overlap. Increasing the coupling to $250\ \mathrm{cm}^{-1}$ or $500\ \mathrm{cm}^{-1}$ results in coupling at the magnitude of the vibrations, or greater, which dramatically reduces the overlap integral. Additionally, upon increasing the coupling strength of the J- or H-aggregate regimes, the starting amplitude due to the choice of t_{end} changes. When $|J| = 50\ \mathrm{cm}^{-1}$ each of the reorganisation energies has been given a tailored value of t_{end} which maximises the starting amplitude for the τ evolution. However, when the coupling is increased to $|J|$ is $250\ \mathrm{cm}^{-1}$ or $500\ \mathrm{cm}^{-1}$ the electronic Rabi cycles are increased in period proportional to the excitonic splitting. Each Rabi cycle is effectively independent as, in the first row, the bath is not coupled to the system which means that the different increases in period move the contributions for different reorganisation energies out of phase. Subsequently, contributions from $\frac{\lambda}{2}$ are maximised when $|J| = 250\ \mathrm{cm}^{-1}$ as this is half of the vibrational mode frequency, and then λ is maximised for $|J| = 500\ \mathrm{cm}^{-1}$.

When the bath is activated, in row 2, the oscillations are rapidly damped towards an equilibrium with the driving field. In all cases, the phonon signatures decrease with increasing coupling in agreement with the results in row 1, and g) – j), s) – u), converge towards an equilibrium correlation of 1. In contrast to this, the H-aggregates show an increase in the equilibrium position of the photon correlation proportional to the strength of the electronic coupling. This is evident in k) from the gradient (particularly for $\frac{\lambda}{2}$, and λ), l), and in the higher equilibrium position in w), x). When $J = 50\ \mathrm{cm}^{-1}$ the splitting of the

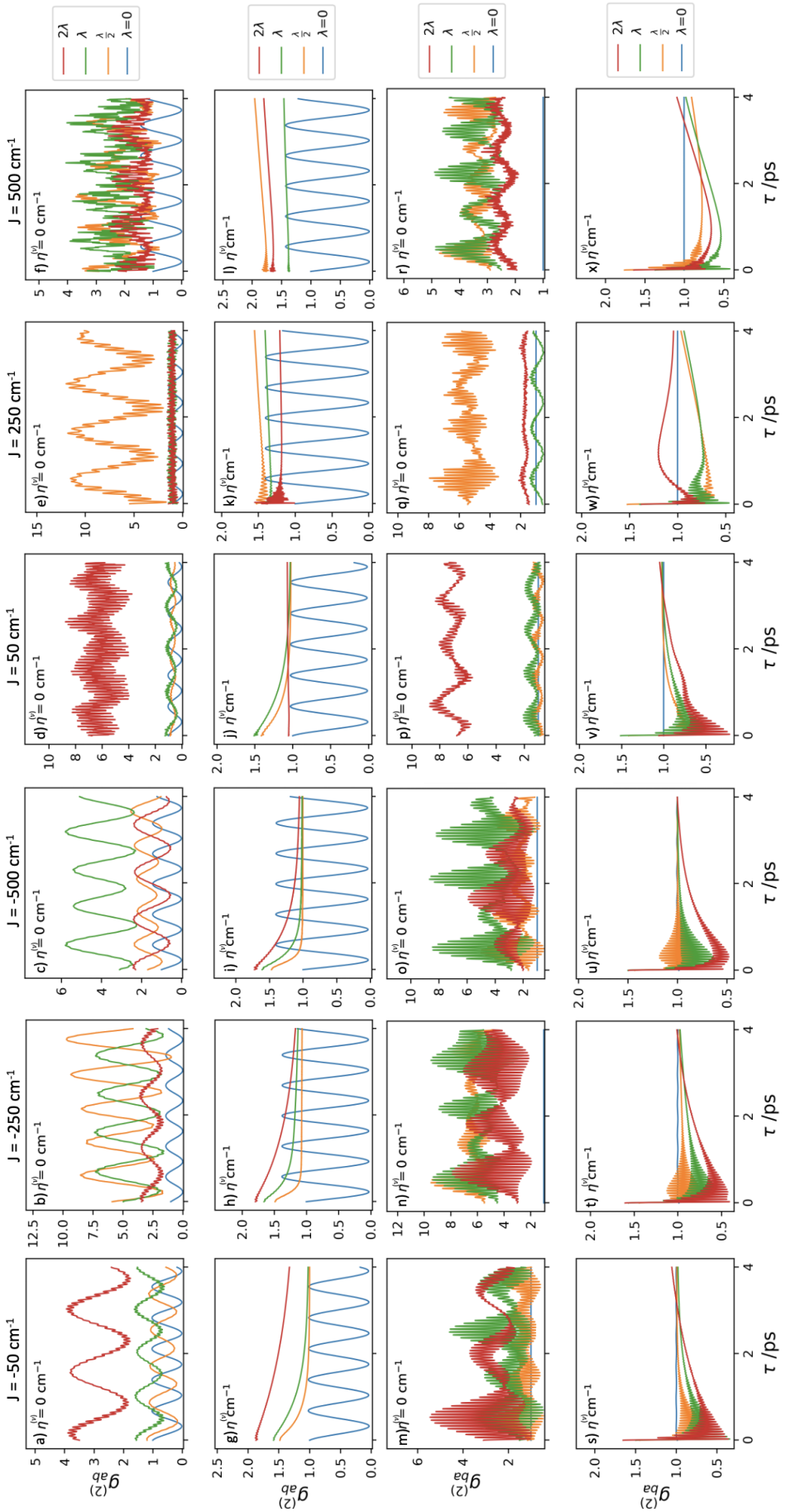

Figure 4.4.7: Second order crossed-correlations, $g^{(2)}_{\mathrm{ab}}$, a) – l), and $g^{(2)}_{\mathrm{ba}}$, m) – x), for a range of electronic coupling strengths in a homodimer. Columns 1 - 6 show $J = -50\ \mathrm{cm}^{-1}$, $-250\ \mathrm{cm}^{-1}$, $-500\ \mathrm{cm}^{-1}$, $50\ \mathrm{cm}^{-1}$, $250\ \mathrm{cm}^{-1}$, and $500\ \mathrm{cm}^{-1}$, respectively. a) – f), m) – r), have bath reorganisation energies of $0\ \mathrm{cm}^{-1}$, and g) – l), s) – x), have bath reorganisation energies of $\eta^{(\nu)}\ \mathrm{cm}^{-1}$.

exciton states is not close enough to the vibrational transition frequency of $500\ \mathrm{cm}^{-1}$ to induce any resonance energy transfer effects. However, when the electronic coupling is increased, in k) and l) the equilibrium correlation diverges away from 1 in the systems with the largest excited state displacement. This suggests that higher vibrational levels are able to induce transfer of photons between donor and acceptor sites of the system, leading to large τ antibunching. In all cases, except a small τ region for the first H-aggregate with reorganisation energy of 2λ which is attributed to the truncation error, all photon correlations exhibit early τ antibunching, with the strongest coupled H-aggregates also showing this at large τ.

The phonon correlations show similar trends to those of the photon correlations, but rather than exhibiting primarily antibunching, they demonstrate bunching. All of the third row, m) – r), shows good agreement with the findings in the previous rows, with a noticeable increase in the period of the electronic Rabi oscillations with increasing electronic coupling, and a shift in the starting τ evolution amplitude due to t_{end}. However, in these correlations, the vibrational mode frequency becomes more prominent as the electronic coupling increases in the absence of a bath. In agreement with the previous results, the equilibrium value of phonon correlation tends to 1 in J-aggregates, but for highly coupled H-aggregates it diverges and demonstrating the first instance of phonon antibunching, for long τ when coupled to a bath, due to transfer between the system.

Similar to the results in figures 4.4.4 and 4.4.5, the crossed correlations in 4.4.7 allow the sources of vibrational and electronic character to be further analysed by changing the order of detection events. In agreement with the results in section 4.1 the $g^{(2)}_{\mathrm{ab}}$ correlations display a minimisation of the vibrational signatures, with the exclusion of H-aggregate correlations at high excited state displacement. This exclusion is again because these results will be most impacted by the harsher truncation of the Hamiltonian and divergence of the energy levels necessary to compute the correlations. In agreement with the previous findings, the already minimal phonon signatures decrease as $|J|$ increases due to the relative size of the splitting and system vibrations. Additionally, the increase in period of the Rabi oscillations leading to maximisation of correlation for different reorganisation energies. In addition to this, the correlation of photons and phonons leads to a bunching for early τ, where photons tend to be followed immediately by phonon emission. These correlations also exhibit a divergence of probability when coupled to a bath for strongly coupled H-aggregates, signifying that resonance energy transfer is occurring.

Similarly, the $g^{(2)}_{\mathrm{ba}}$ correlations, in which the phonon is detected first, exhibit a

strong amplification of the phonon signatures due to two sources of vibrational character, as in section 4.1. The strong dependence on phonons results in a relatively constant minor oscillation amplitude with increasing coupling in both J- and H-aggregates, however the amplitude is larger for J-aggregates. When coupled to the bath, these correlations exhibit a number of different behaviours.

In J-aggregates, the correlations tend to the equilibrium value for long τ times, however at early τ and coupling strengths $|J| \geq 250\ \mathrm{cm}^{-1}$ (most evident in t), u)) a peak of probability occurs. When there is no bath reorganisation energy, or in the long τ limit, antibunching suppresses photon emission due to mixing of high vibrational states with higher (dark) excitons. However, there is an additional small region of enhanced antibunching due to vibrations promoting further photon emission when the exciton splitting is close to the vibrational frequency such that vibrational excited states and lower exciton states have degenerate energies.

In H-aggregates the weaker two coupling regimes have a similar increase in probability above the non-displaced value, but only for the largest excited state displacements. This region of antibunching is not tied directly to the vibrational modes, as is the case for J-aggregates, but, because of the large increase in correlation magnitude, are attributed to transfer within the molecule. Finally, for the largest coupling there is an inversion of this profile leading to a bunching at early times, followed by antibunching for large τ as the correlation diverges away from the equilibrium value.

Finally, the second order photon and phonon correlations for a heterodimer are considered for a range of electronic coupling strengths. The non-degenerate monomer levels lead to a number of differences in the delocalised exciton states which persist into the correlations, however, many of the trends previously discussed are still present.

Row one, a) – f), of figure 4.4.8 shows very similar trends to those in row one of figure 4.4.6, however the difference in energy of the constituent monomer levels leads to differences in maximised reorganisation energies. In b), c), the λ reorganisation energy is maximised whereas, in d) – f) the maximised energies are $\frac{\lambda}{2}$, 2λ and λ respectively. However, this still reflects the changing period of the isolated transitions within the system. In all cases, the photon correlation presents (unambiguously) antibunching for early τ.

In agreement with the results for the homodimer, when coupled to the bath almost all of the systems exhibit antibunching and tend towards an equilibrium value of the correlation. However, in contrast to the previous results, there is a dip in the mean photon number for J- and H-aggregates with a coupling of $|J| = 250\ \mathrm{cm}^{-1}$, signified by the diverging probability. This suggests that the

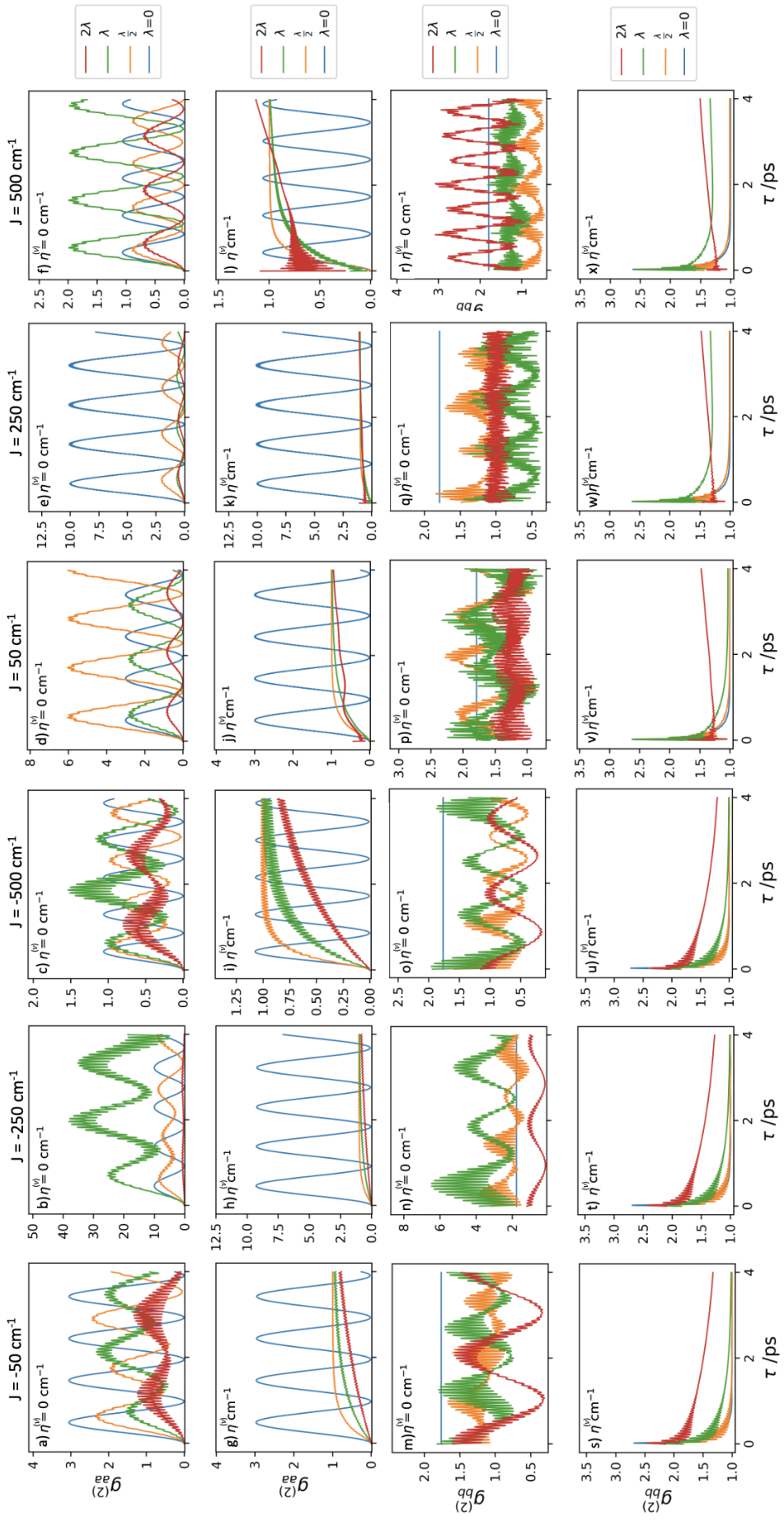

Figure 4.4.8: Second order photon, a) – l), and phonon, m) – x), correlations for a range of electronic coupling strengths in a heterodimer. Columns 1 - 6 show $J = -50\ \mathrm{cm}^{-1}$, $-250\ \mathrm{cm}^{-1}$, $-500\ \mathrm{cm}^{-1}$, $50\ \mathrm{cm}^{-1}$, $250\ \mathrm{cm}^{-1}$, and $500\ \mathrm{cm}^{-1}$, respectively. a) – f), m) – r) have bath reorganisation energies of $0\ \mathrm{cm}^{-1}$, and g) – l), s) – x), have bath reorganisation energies of $\eta^{(\nu)}\ \mathrm{cm}^{-1}$.

splitting is moving the transitions partially out of resonance with driving field.

The H-aggregate results are also in agreement with the homodimer results, and demonstrate a divergence of the correlation away from the equilibrium value at large τ times. However, a noticeable difference is that the bath has not fully damped the electronic signatures out of the correlation for the strongest excited state displacements which is able to manifest as a result of the asymmetric exciton states. The large vibrational signature for $J = 500\ \mathrm{cm}^{-1}$ is discounted as being due to the divergence of the highest energy levels and harsh truncation as it only impacts the highest vibrational levels.

The phonon correlations are also directly comparable to the results for homodimers. The only noticeable difference in the aforementioned trends is for H-aggregates, where in the case of heterodimers, the divergence from the equilibrium value of correlation occurs also for the weakly coupled ($J = 50\ \mathrm{cm}^{-1}$) H-aggregate in v).

Finally the cross correlations are considered. The vast majority of trends are equivalent to those present in the previous homodimer figure, 4.4.7, however, the H-aggregates show further new behaviour. Notably, all $g^{(2)}_{\mathrm{ab}}$ correlations present minimal phonon signatures, in equivalence with section 4.1, with the exception of f) for a reorganisation energy of 2λ. d), j), f), r), cases also exhibit a more classical bunching effect, except for 2λ reorganisation energy, and again this is attributed, in part, to systematic errors due to the computational cost. However, based on j), k), v), w) this antibunching is not purely due to truncation, and emerges because of strong electronic dependence which is also noticeable in the $g^{(2)}_{\mathrm{ba}}$.

Additionally, when the system is coupled to the bath, the behaviour of the $g^{(2)}_{\mathrm{ba}}$ correlations are strikingly different. They exhibit both a vibrational enhancement of the probability above the equilibrium value, similar to the J-aggregate homodimers in figure 4.4.7, and simultaneously exhibit the long τ time enhancement of antibunching present in all other H-aggregates. This is attributed to strongly vibrational, high energy, wavepackets which are not completely dissipated upon interaction with the bath, leading to early time bunching, before a resonance energy transfer, or recurrence from the bath, produces antibunching in the long τ limit. Necessarily, any recurrence that does occur must have a very small magnitude so as to not invalidate the Markovian approximation and the quantum regression theorem. Such small recurrences were demonstrated in Markovian dynamics within section 3.1.

In summary, this work demonstrates that not only do changes in quantum antibunching and bunching effects occur due to the strength of electronic coupling within a molecule, but that energy transfer can be observed within

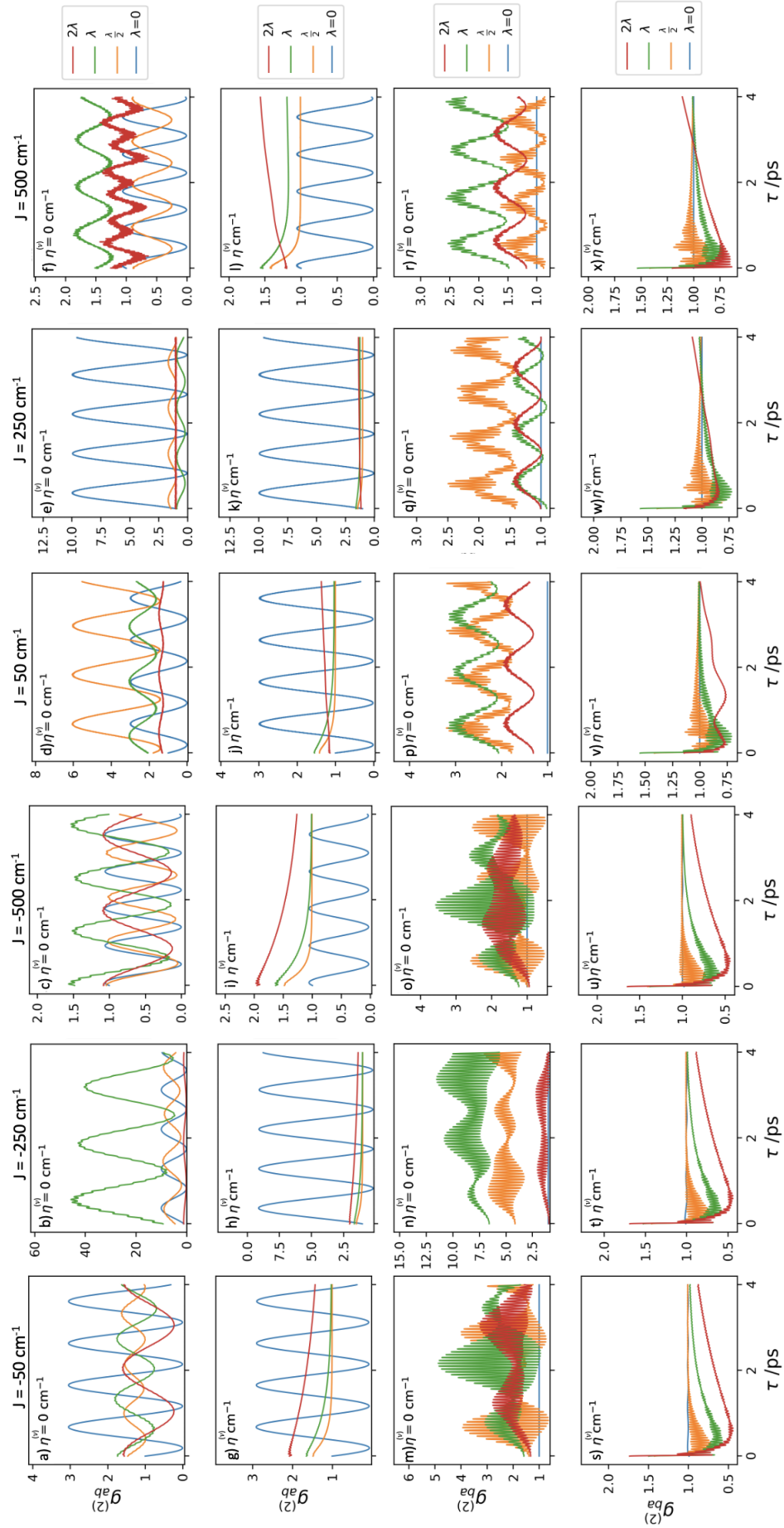

Figure 4.4.9: Second order crossed-correlations, $g^{(2)}_{\mathrm{ab}}$, a) – l), and $g^{(2)}_{\mathrm{ba}}$, m) – x), for a range of electronic coupling strengths in a heterodimer. Columns 1 - 6 show $J = -50\ \mathrm{cm}^{-1}$, $-250\ \mathrm{cm}^{-1}$, $-500\ \mathrm{cm}^{-1}$, $50\ \mathrm{cm}^{-1}$, $250\ \mathrm{cm}^{-1}$, and $500\ \mathrm{cm}^{-1}$, respectively. a) – f), m) – r), have bath reorganisation energies of $0\ \mathrm{cm}^{-1}$, and g) – l), s) – x), have bath reorganisation energies of $\eta^{(\nu)}\ \mathrm{cm}^{-1}$.

these systems via correlation function in complement to observations in experimental 2DES. This can give rise to new insights about the quantum nature of energy transfer. In J-aggregates coupled to a bath the correlations tend towards an equilibrium state, whereas in H-aggregates vibrational contributions to the wavepacket enhance correlations above the equilibrium value for small τ, and in the long τ limit resonance energy transfer from acceptor to donor sites in the system, or recurrence from the bath, cause antibunching independent of phonon signatures. Changes in the level of Franck-Condon overlap of higher vibrational states, in all species, is shown to increase the proportion of VR and subsequently phonon effects in the excited state wavepacket are presented through a larger amplitude of the minor vibrational oscillation. In addition, by setting the driving laser field to be either resonant with the fundamental transition of the system, or detuned from it, it has been demonstrated that individual components of the correlation can be amplified, or minimised, including the constituent phonon signatures.

5 Spectral Vibrations in the Limit of Zero Canonical Damping

5.1 Realising Equivalence of the HVM and BVM

The location of the system-bath boundary has been demonstrated to have a profound impact of the dynamics of the OQS model, as discussed in appendix D, and sections 3.2, 4.3. In the HVM and BVM models, which differ only in boundary placement, it has been shown that 2DES spectral features and lineshape are in qualitative agreement between the two models, however the same is not true for quantum correlations. Based on their construction, the HVM and BVM should become mathematically equivalent models in the limit of vanishing secondary damping but, as discussed in section 2.5, this is not possible in conventional HEOMs. It is possible to use the ASD-HEOM to overcome this, but at considerable computational expense. In this chapter a new HEOM construction is considered which explicitly removes the secondary intrinsic damping allowing the HVM and BVM to become equivalent, without the computational expense of the ASD-HEOM. This is achieved through a HEOM with two spectral density components, one of overdamped Lorentz-Drude form, and the other an entirely undamped mode describing the pure intramolecular vibration.

Finally, a new derivation which specifically addresses the limit of vanishing canonical damping and hypotheses 1 and 3. In order to demonstrate the changes to the open quantum system during the movement of the system-bath boundary a hierarchy with two components must be generated in a manner equivalent to the work of Tanimura[157]. Here, as discussed in Humphries et. al.[2], the addition of the overdamped and underdamped spectral densities as part of the canonical transform results in intrinsic canonical damping from the underdamped modes which are not present in the vibration when in positional coordinates. This originates from the canonical transform which moves a pure vibrational system mode into the environment degrees of freedom as an underdamped mode. By creating a hierarchy which contains an overdamped component, which is redefined as LD for Lorentz-Drude[a], and an undamped contribution we aim to demonstrate the effect of vanishing canonical damping. This requires some

[a] This choice is to adequately distinguish the undamped oscillator (UO) mode, from the overdamped mode. Subsequently the overdamped bath speed, Λ, is recast as Λ_{LD}.

subtle alterations to the theory used in the overdamped derivation 2.5.4.1, which are outlined below. The full details of this can be found in appendix D.

5.1.1 Deriving the Lorentz-Drude Undamped Oscillator HEOM

We consider a one-dimensional system coupled to a bath of N harmonic oscillators, with microscopic continuous operator q with particle mass m, ensemble oscillator operator x, masses $\{m_j\}$, frequencies $\{\omega_j\}$ and coupling constants $\{c_j\}$, in a manner equivalent to the overdamped HEOM. We also continue by applying the approximation that the system is initially uncorrelated with the bath, however, from here the treatments diverge. The reduced density matrix element expressed in path integral form, for an EOM which has n baths, is[143]:

$$\begin{aligned}\rho(\mathrm{q}_t, \mathrm{q}'_t, t) = \iint \int_{\mathrm{q}_0}^{\mathrm{q}_t} \int_{\mathrm{q}'_0}^{\mathrm{q}'_t} \exp\left(\frac{i\mathrm{S}_\mathrm{S}[\mathrm{q}_t]}{\hbar}\right) \\ \times \exp\left(-\frac{i\mathrm{S}_\mathrm{S}[\mathrm{q}'_t]}{\hbar}\right)\left(\prod_n \mathcal{F}_n[\mathrm{q}_t, \mathrm{q}'_t]\right)\rho_\mathrm{S}(\mathrm{q}_0, \mathrm{q}'_0, 0) \\ \times \mathcal{D}[\mathrm{q}_t]\mathcal{D}[\mathrm{q}'_t]\,\mathrm{d}\mathrm{q}_0\,\mathrm{d}\mathrm{q}'_0, \quad (5.1.1)\end{aligned}$$

where $\int \mathcal{D}[\mathrm{q}_t]$ represents the functional integral. The action corresponding to the system Hamiltonian, H_S, is denoted $\mathrm{S}_\mathrm{S}[\mathrm{q}_t; t]$. The bath effects are contained within the Feynman and Vernon influence functional for the nth bath with spectral density

$$J_n(\omega) = \frac{2\eta_n\gamma_n\omega_{0,n}^2\omega}{(\omega_{0,n}-\omega)^2 + (\gamma_n\omega)^2}, \quad (5.1.2)$$

and they take the form[143]

$$\begin{aligned}\mathcal{F}_n[\mathrm{q}_t, \mathrm{q}'_t] = \iiiint \rho_\mathrm{B}(\mathrm{x}_0, \mathrm{x}'_0, 0) \\ \times \exp\left(\frac{i}{\hbar}\Big[\mathrm{S}_{\mathrm{B},n}[\mathrm{x}] - \mathrm{S}_{\mathrm{B},n}[\mathrm{x}'] + \mathrm{S}_{\mathrm{SB},n}[\mathrm{q}_t, \mathrm{x}] - \mathrm{S}_{\mathrm{SB},n}[\mathrm{q}'_t, \mathrm{x}']\Big]\right) \\ \times \mathcal{D}[\mathrm{x}]\mathcal{D}[\mathrm{x}']\mathrm{d}\mathrm{x}_0\mathrm{d}\mathrm{x}'_0\mathrm{d}\mathrm{x}. \quad (5.1.3)\end{aligned}$$

The influence functional can be recast into a form that contains the kernels corresponding to fluctuation, $L^{(\alpha)}_{\mathcal{R},n}(t)$, and dissipation, $iL^{(\alpha)}_{\mathcal{I},n}(t)$[4,144] and dependent on the system creation and annihilation operators through a coherent state basis, equations (2.5.24) – (2.5.25). In such a basis the system is dependent on the creation and annihilation operators for the system modes, $\mathrm{a}_i^\dagger$ and a_i, rather than operators x_j and p_j for environment modes $\{j\}$.

Subsequently, the influence functional becomes

$$\mathcal{F}_n = \exp\left(-\frac{i}{\hbar}\int_0^t\int_0^\tau \mathrm{B}_n^{\times}(\mathrm{q}_t,\mathrm{q}_t';\tau)\Big[iL_{\mathcal{I},n}^{(\alpha)}(\tau-\tau')\mathrm{B}_n^{\circ}(\mathrm{q}_t,\mathrm{q}_t';\tau') + L_{\mathcal{R},n}^{(\alpha)}(\tau-\tau')\mathrm{B}_n^{\times}(\mathrm{q}_t,\mathrm{q}_t';\tau')\Big]\mathrm{d}\tau'\,\mathrm{d}\tau\right), \quad (5.1.4)$$

where $\mathrm{B}_n^{\times}(\tau) = \mathrm{B}_n(\mathrm{q}_t;\tau) - \mathrm{B}_n(\mathrm{q}_t';\tau)$, and $\mathrm{B}_n^{\circ}(\tau) = \mathrm{B}_n(\mathrm{q}_t;\tau) + \mathrm{B}_n(\mathrm{q}_t';\tau)$. These kernels can be expressed by the spectral distribution as

$$L_{\mathcal{R},n}^{(\alpha)}(t) = \int_0^\infty J_n(\omega)\cos(\omega t)\coth\left(\frac{\beta\hbar\omega}{2}\right)\mathrm{d}\omega, \quad (5.1.5)$$

$$iL_{\mathcal{I},n}^{(\alpha)}(t) = -\int_0^\infty J_n(\omega)\sin(\omega t)\,\mathrm{d}\omega. \quad (5.1.6)$$

These equations are equivalent to equation (2.5.31), from the fluctuation-dissipation theorem, and are restated here to highlight that they hold for n baths. Note that there is a subtlety in the notation of B operators for the LDUO derivation: overdamped contributions have one spectral density so these coupling operators have no subscript, those for the undamped component have two, and a corresponding subscript. We split our environment into two major contributions: an overdamped bath which is appropriate for Gaussian noise and the calculation of further correlation function measures, and an undamped oscillator (UO) mode. The undamped oscillator mode is equivalent to subsuming a fundamental system vibration within the spectral density and then taking the limit to zero of its intrinsic canonical damping, as proposed in Humphries et. al.[2].

$$J(\omega) = J_{\mathrm{LD}}(\omega) + J_{\mathrm{UO}}(\omega), \quad (5.1.7)$$

where

$$J_{\mathrm{LD}}(\omega) = \frac{2\eta_{\mathrm{LD}}\gamma_{\mathrm{LD}}\omega_0^2\omega}{(\omega_0-\omega)^2 + (\gamma_{\mathrm{LD}}\omega)^2},$$

which can be further simplified to the Lorentz-Drude form given that $\gamma_{\mathrm{LD}} \gg \omega_0$ such that $\Lambda_{\mathrm{LD}} = \omega_0^2/\gamma_{\mathrm{LD}}$,

$$J_{\mathrm{LD}}(\omega) = \frac{2\eta_{\mathrm{LD}}\omega\Lambda_{\mathrm{LD}}}{\omega^2 + \Lambda_{\mathrm{LD}}^2}, \quad (5.1.8)$$

and either

$$J_{\mathrm{UO}} = \frac{1}{2}S_{\mathrm{UO}}^{\mathrm{HR}}\omega_{\mathrm{UO}}\omega\left(\delta(\omega-\omega_{\mathrm{UO}}) + \delta(\omega+\omega_{\mathrm{UO}})\right), \quad J_{\mathrm{UO}} = S_{\mathrm{UO}}^{\mathrm{HR}}\omega_{\mathrm{UO}}\delta(\omega-\omega_{\mathrm{UO}}), \quad (5.1.9)$$

with $S_{\mathrm{UO}}^{\mathrm{HR}} = \lambda_{\mathrm{UO}}/\omega_{\mathrm{UO}}$, the Huang-Rhys factor which is a measure of the strength of the electronic and vibrational coupling. The two forms depend on whether the vibration is split into two componenets, as in Seibt[289], or whether there is a single undamped vibrational mode. The next step is to decompose the

respective bath contributions, according to the Matsubara scheme, in order to explicitly incorporate time-dependent - but temperature-independent - Matsubara decomposition coefficients and frequencies[289,324] into the correlation function. We perform this process for each component of the total spectral density piecewise. Starting with the Lorentz-Drude component we decompose the correlation function using complex contour integration, resulting in:

$$L_{\mathrm{LD}}^{(\alpha)}(t) = \eta_{\mathrm{LD}}\Lambda_{\mathrm{LD}}\left(\cot\left(\frac{\beta\hbar\Lambda_{\mathrm{LD}}}{2}\right) - i\right)e^{-\Lambda_{\mathrm{LD}}t} + \sum_{n=1}^{\infty}\frac{2\eta_{\mathrm{LD}}\Lambda_{\mathrm{LD}}\nu_n}{\beta\hbar(\nu_n^2 - \Lambda_{\mathrm{LD}}^2)}e^{-\nu_n t}, \tag{5.1.10}$$

which can be simplified in terms of purely Matsubara frequencies by denoting,

$$d_0 = \eta_{\mathrm{LD}}\Lambda_{\mathrm{LD}}\left(\cot\left(\frac{\beta\hbar\Lambda_{\mathrm{LD}}}{2}\right) - i\right), \quad \nu_0 = \Lambda_{\mathrm{LD}}, \tag{5.1.11}$$

$$d_n = \frac{2\eta_{\mathrm{LD}}\Lambda_{\mathrm{LD}}}{\beta\hbar}\left(\frac{\nu_n}{\nu_n^2 - \Lambda_{\mathrm{LD}}^2}\right), \quad \nu_n = \frac{2n\pi}{\beta\hbar}, \tag{5.1.12}$$

such that

$$L_{\mathrm{LD}}^{(\alpha)}(t) = \sum_{n=0}^{\infty} d_n e^{-\nu_n t}. \tag{5.1.13}$$

Next we decompose the undamped oscillator mode component, proposed by Seibt et. al.[289], through the sifting property of the delta function resulting in:

$$L_{\mathrm{UO}}^{(\alpha)}(t) = \frac{S_{\mathrm{UO}}^{\mathrm{HR}}\omega_{\mathrm{UO}}^2}{2}\Bigg[\exp(-i\omega_{\mathrm{UO}}t)\left(\coth\left(\frac{\beta\hbar\omega_{\mathrm{UO}}}{2}\right) + 1\right) + \exp(i\omega_{\mathrm{UO}}t)\left(\coth\left(\frac{\beta\hbar\omega_{\mathrm{UO}}}{2}\right) - 1\right)\Bigg]. \tag{5.1.14}$$

From this we have generated the Matsubara decomposition coefficients and frequencies for the second bath:

$$c_1 = \tilde{c}_2 = \frac{1}{2}S_{\mathrm{UO}}^{\mathrm{HR}}\omega_{\mathrm{UO}}^2\left(\coth\left(\frac{\beta\hbar\,\omega_{\mathrm{UO}}}{2}\right) + 1\right), \tag{5.1.15}$$

$$c_2 = \tilde{c}_1 = \frac{1}{2}S_{\mathrm{UO}}^{\mathrm{HR}}\omega_{\mathrm{UO}}^2\left(\coth\left(\frac{\beta\hbar\,\omega_{\mathrm{UO}}}{2}\right) - 1\right), \tag{5.1.16}$$

$$\gamma_1 = \tilde{\gamma}_2 = i\omega_{\mathrm{UO}}, \tag{5.1.17}$$

$$\gamma_2 = \tilde{\gamma_1} = -i\omega_{\mathrm{UO}}. \tag{5.1.18}$$

Given these decompositions, and in a manner equivalent to the process in Ishizaki and Tanimura[150], we construct the total influence function as:

$$\prod_n \mathcal{F}_n = \mathcal{F}_{\mathrm{LD}} \times \mathcal{F}_{\mathrm{UO}}, \tag{5.1.19}$$

$$\mathcal{F}_{\mathrm{UO}} = \exp\left(-\frac{1}{\hbar}\int_0^t\int_0^\tau \sum_k \mathrm{B}_k^{\times}(\mathrm{Q}_t,\mathrm{Q}_t';\tau)\exp(-\gamma_k(\tau-\tau'))\Theta_k(\mathrm{Q}_t,\mathrm{Q}_t';\tau')\,\mathrm{d}\tau'\,\mathrm{d}\tau\right). \tag{5.1.20}$$

where,

$$\Theta_k = \frac{1}{2}\left[(c_k-\tilde{c}_k)\mathrm{B}_k^{\circ}(\mathrm{Q}_t,\mathrm{Q}_t';\tau') + (c_k+\tilde{c}_k)\mathrm{B}_k^{\times}(\mathrm{Q}_t,\mathrm{Q}_t';\tau')\right], \tag{5.1.21}$$

and

$$\mathcal{F}_{\mathrm{LD}} = \exp\left(-\frac{1}{\hbar}\int_0^t\int_0^\tau \mathrm{B}^{\times}(\mathrm{Q}_t,\mathrm{Q}_t';\tau)\vartheta(\mathrm{Q}_t,\mathrm{Q}_t';\tau')\Lambda_{\mathrm{LD}}\exp(-\Lambda_{\mathrm{LD}}(\tau-\tau'))\,\mathrm{d}\tau'\,\mathrm{d}\tau\right)$$
$$\times\prod_{n=1}^{\infty}\exp\left(-\frac{1}{\hbar}\int_0^t\int_0^\tau \mathrm{B}^{\times}(\mathrm{Q}_t,\mathrm{Q}_t';\tau)\Psi_n(\mathrm{Q}_t,\mathrm{Q}_t';\tau')\nu_n\exp(-\nu_n(\tau-\tau'))\,\mathrm{d}\tau'\,\mathrm{d}\tau\right). \tag{5.1.22}$$

where,

$$\vartheta = \eta_{\mathrm{LD}}\left[\cot\left(\frac{\beta\hbar\Lambda_{\mathrm{LD}}}{2}\right)\mathrm{B}^{\times}(\mathrm{Q}_t,\mathrm{Q}_t';\tau') - i\mathrm{B}^{\circ}(\mathrm{Q}_t,\mathrm{Q}_t';\tau')\right], \tag{5.1.23}$$

$$\Psi_n = \sum_{n=1}^{\infty}\frac{2\eta_{\mathrm{LD}}\Lambda_{\mathrm{LD}}\nu_n}{\beta\hbar(\nu_n^2-\Lambda_{\mathrm{LD}}^2)}\mathrm{B}^{\times}(\mathrm{Q}_t,\mathrm{Q}_t';\tau'). \tag{5.1.24}$$

For a value of K, which satisfies $\nu_K = 2\pi K/\beta\hbar \gg \omega_0$ - where ω_0 is the fundamental frequency of the system - then $\nu_n\exp(-\nu_n(\tau-\tau')) \approx \delta(\tau-\tau'), \quad n \geq K+1$. This simplifies the influence functional

$$\mathcal{F} \approx \exp\left(-\int_0^t\int_0^\tau \sum_k \mathrm{B}_k^{\times}(\mathrm{Q}_t,\mathrm{Q}_t';\tau)\exp(-\gamma_k(\tau-\tau'))\Theta_k(\mathrm{Q}_t,\mathrm{Q}_t';\tau')\,\mathrm{d}\tau'\,\mathrm{d}\tau\right)\times$$
$$\exp\left(-\int_0^t \mathrm{B}^{\times}(\mathrm{Q}_t,\mathrm{Q}_t';\tau)\exp(-\Lambda_{\mathrm{LD}}\tau)\left[-\int_0^\tau \Lambda_{\mathrm{LD}}\vartheta(\mathrm{Q}_t,\mathrm{Q}_t';\tau')\exp(\Lambda_{\mathrm{LD}}\tau')\,\mathrm{d}\tau'\right]\mathrm{d}\tau\right)\times$$
$$\prod_{n=1}^{K}\exp\left(-\int_0^t \mathrm{B}^{\times}(\mathrm{Q}_t,\mathrm{Q}_t';\tau)\exp(-\nu_n\tau)\left[-\int_0^\tau \nu_n\Psi_n(\mathrm{Q}_t,\mathrm{Q}_t';\tau')\exp(\nu_n\tau')\,\mathrm{d}\tau'\right]\mathrm{d}\tau\right)\times$$
$$\prod_{n=K+1}^{\infty}\exp\left(\int_0^t \mathrm{B}^{\times}(\mathrm{Q}_t,\mathrm{Q}_t';\tau)\Psi_n(\mathrm{Q}_t,\mathrm{Q}_t';\tau)\,\mathrm{d}\tau\right). \tag{5.1.25}$$

In order to derive the equations of motion we additionally introduce the equation for the auxiliary density operators. This equation takes the same form as the influence functional, omitting $-\mathrm{B}^{\times}(\mathrm{Q}_t,\mathrm{Q}_t';\tau)$ as noted in the supplemental material of Seibt and Mancal[325], raised to the power of the ADO number. This creates the hierarchy ADO structure with each order in the hierarchy decreasing by an order of magnitude - as a consequence of the

exponent. We introduce the auxiliary operator, $\rho^{(m,l_k)}_{j_1\ldots j_K}$, by its matrix element as[150]

$$\rho^{(m,l_k)}_{j_1\ldots j_K}(\mathrm{Q}_t,\mathrm{Q}'_t;t)=\int_{\mathrm{Q}_t(t_0)}^{\mathrm{Q}_t(t)}\int_{\mathrm{Q}'_t(t_0)}^{\mathrm{Q}'_t(t)}\exp\left(\frac{i\mathrm{S}_\mathrm{S}[\mathrm{Q}_t,\mathrm{Q}'_t]}{\hbar}\right)\mathcal{F}\exp\left(\frac{-i\mathrm{S}_\mathrm{S}[\mathrm{Q}_t,\mathrm{Q}'_t]}{\hbar}\right)\times$$
$$\rho(\mathrm{Q}_{t_0},\mathrm{Q}'_{t_0};t_0)\prod_k\left\{\int_0^t\exp(-\gamma_k(t-\tau'))\Theta_k(\mathrm{Q}_t,\mathrm{Q}'_t;\tau')\,\mathrm{d}\tau'\right\}^{l_k}\times$$
$$\left\{\exp(-\Lambda_\mathrm{LD}t)\left[-\int_0^t\Lambda_\mathrm{LD}\vartheta(\mathrm{Q}_t,\mathrm{Q}'_t;\tau')\exp(\Lambda_\mathrm{LD}\tau')\,\mathrm{d}\tau'\right]\right\}^m\times$$
$$\prod_{n=1}^K\left\{\exp(-\nu_nt)\left[-\int_0^t\nu_n\Psi_n(\mathrm{Q}_t,\mathrm{Q}'_t;\tau')\exp(\nu_n\tau')\,\mathrm{d}\tau'\right]\right\}^{j_n}\mathcal{D}[\mathrm{Q}_t]\,\mathcal{D}[\mathrm{Q}'_t],\tag{5.1.26}$$

for non-negative integers $l_k,m,j_1,\ldots,j_K$. The reduced density matrix, $\rho^{(0,0)}_{0,\ldots,0}=\rho(t)$ is the only matrix within this hierarchy with physical meaning, and the other auxiliary density operators are introduced for computational purposes. Differentiating equation (5.1.26) with respect to time, and then computing the path integrals, results in the following equations of motion:

$$\frac{\partial}{\partial t}\rho^{(m,l_k)}_{j_1\ldots j_K}=\left(-\frac{i}{\hbar}\mathrm{H}^\times_\mathrm{S}-\sum_k(l_k\gamma_k+m\Lambda_\mathrm{LD})-\sum_{n=1}^K j_n\nu_n+\sum_{n=K+1}^\infty\mathrm{B}^\times\Psi_n\right)\rho^{(m,l_k)}_{j_1\ldots j_K}-$$
$$\sum_k l_k\Theta_k\rho^{(m,l_k-1)}_{j_1\ldots j_K}-m\Lambda_\mathrm{LD}\vartheta\rho^{(m-1,l_k)}_{j_1\ldots j_K}-\sum_{n=1}^K j_n\nu_n\Psi_n\rho^{(m,l_k)}_{j_1\ldots j_n-1\ldots j_K}-$$
$$\left(\mathrm{B}^\times\rho^{(m+1,l_k)}_{j_1\ldots j_K}+\sum_k\mathrm{B}^\times_k\rho^{(m,l_k+1)}_{j_1\ldots j_K}\right)-\sum_{n=1}^K\mathrm{B}^\times\rho^{(m,l_k)}_{j_1\ldots j_n+1\ldots j_K}.\tag{5.1.27}$$

Upon first inspection it may appear that there is an absent factor of γ_k in the creation term from the (l_k-1)th Matsubara axis, however this is not the case. Based on the reduction criteria for the infinite Matsubara components, which for the overdamped contribution is:

$$\nu_K=\frac{2\pi K}{\beta\hbar}\gg\omega_0,\tag{5.1.28}$$

we reduce to a delta function for a sufficient value of K. However, such a reduction cannot be performed for the undamped component. The undamped contribution introduces a pair of Matsubara decomposition coefficients and frequencies, as opposed to an infinite number, and as such a sufficient value of K being chosen is unlikely. This lack of reduction motivates the current derivation and it results in factors of $(c_k\pm\tilde{c}_k)$ in Θ_k, which (based on the form of c_k in equation (5.1.15)) accounts for the apparent missing factor of γ_k.

For the condition

$$\sum_k (l_k\gamma_k + m\Lambda_{\mathrm{LD}}) + \sum_{n=1}^{K} j_n\nu_n \gg \frac{\omega_0}{\min(\mathcal{I}(\nu_k), \mathcal{R}(\nu_n))}, \quad \Longrightarrow \quad \Gamma_{\max} = 10\max\Big(\mathcal{I}(\gamma_k)\Big). \tag{5.1.29}$$

This criterion terminates the over and undamped axes through one condition, leading to self-similar hierarchy volumes, where the overdamped termination is considerably more stringent than necessary. A two step termination process could be introduced as future work which terminates these axes separately.

Subsequently, the infinite hierarchy can be truncated by the terminator:

$$\frac{\partial}{\partial t}\rho^{(m,l_k)}_{j_1\ldots j_K} \approx \left(-\frac{i}{\hbar}\mathrm{H}^{\times}_{\mathrm{S}} - \sum_k l_k\gamma_k + \sum_{n=K+1}^{\infty} \mathrm{B}^{\times}\Psi_n \right)\rho^{(m,l_k)}_{j_1\ldots j_K}. \tag{5.1.30}$$

Here, the phonon contributions from the system characteristic damping rate vanish as they are a purely real decay, whereas the purely imaginary oscillating components persist. This can be rationalised through the limit of infinite time, all contributions with an associated damping will vanish leaving only oscillatory components after the application of the Markovian criterion. This can be rewritten as[164]

$$\frac{\partial}{\partial t}\rho^{(m,l_k)}_{j_1\ldots j_K} \approx \left(-\frac{i}{\hbar}\mathrm{H}^{\times}_{\mathrm{S}} - i(l_0 - l_1)\omega_{\mathrm{UO}} + \sum_{n=K+1}^{\infty} \mathrm{B}^{\times}\Psi_n \right)\rho^{(m,l_k)}_{j_1\ldots j_K}. \tag{5.1.31}$$

Since the undamped oscillator component contributes a pair of Matsubara decomposition frequencies and coefficients, we expect the number of hierarchy elements to be only slightly greater than that of an overdamped EOM.

Equivalent to the overdamped HEOM, the first term (red) within equation (5.1.27) describes the Markovian free propagation of the system. Similarly the first two blue terms describe the impact of the characteristic damping rate of the system, mediated by bath phonons, on the total dynamics. This is split into a purely imaginary oscillation from the undamped modes, and a decay from the overdamped contributions. The final blue term is, again, a product of two bath operator commutator terms which introduce higher order bath interactions, a square coupling, to account for the introduction of the cutoff K[150]. By propagating a series of ADOs, representing different arrangements of bath phonons, the HEOM accounts for a history of interactions such that non-Markovian effects are automatically included. The ADOs are interconnected via ADO raising and lowering terms corresponding to each of the dimensions of the system. The integers l_k refer to the undamped modes, m the temperature independent overdamped modes, and j_n the temperature dependent Matsubara contributions from the overdamped modes. Subsequently raising and lowering

in each of these dimensions are denoted by

$$j_n \pm 1, m \pm 1, l_k \pm 1 \implies \rho^{(m,l_k)}_{j_1 \ldots j_{n\pm1} \ldots j_K}, \rho^{(m\pm1,l_k)}_{j_1 \ldots j_K}, \rho^{(m,l_k\pm1)}_{j_1 \ldots j_K}. \tag{5.1.32}$$

The first cyan term in the LDUO-HEOM is the raising term associated with the undamped modes. The action of Θ_k is to destroy bath phonons and create system states of an equivalent frequency as the phonons are absorbed by the system. This corresponds to an increase of ADO tier resulting in a 'raising' of the ADO. This is a temperature independent, undamped contribution with no intrinsic damping. The second and third cyan terms are the raising terms from the temperature independent frequencies and infinite Matsubara sum of the overdamped modes, respectively. φ and ψ_n have an equivalent purpose to Θ_k but create bath states at frequencies Λ_{LD} and ν_n, respectively. These terms have intrinsic damping due to their overdamped origins. The three orange terms, each with a $\mathrm{B}^{\times}$ operator, are the respective lowering terms for each component. The action of this operator is to demolish the system states, corresponding to the creation of bath phonons, as they are emitted from the system into the bath.

5.1.2 Test Dynamics

Dynamics of the newly generated LDUO-HEOM are analysed through the equilibration period, of 1 ps, to confirm that the undamped modes are correctly introducing coherence into the system. In order to achieve this a test monomer system, generated through a TLS coupled to the undamped mode, is produced. The undamped spectral density contributes purely imaginary poles, with no decaying component, and rather than introducing pure electronic dephasing through a diagonal operator they continually stimulate coherence at the undamped oscillator frequency. This leads to continually growing coherences with time, that do not decay over longer equilibration times. Figure 5.1.1 shows the first ps of dynamics for a vibronic dimer modelled using the LDUO-HEOM hit with a laser pulse at 0.4 ps. The system has a fundamental electronic transition frequency of $3\,000\ \mathrm{cm}^{-1}$ and is initialised into a purely excited state population. The system is evolved for 0.4 ps before being hit by an instantaneous laser field of a single frequency with an infinitesimal spatial width which is resonant with the fundamental electronic transition, before the evolution is continued up to 1 ps.

The system initially exists in the excited state, ρ_{ee}, at $t = 0$ ps with small but non-zero coherences, ρ_{eg} and ρ_{ge}. The settling of the hierarchy after the initialisation in combination with the non-zero coherences establishes an electronic Rabi oscillation within the populations of the system which begins to establish an equilibrium up to 0.4 ps. At this point the system interacts with the

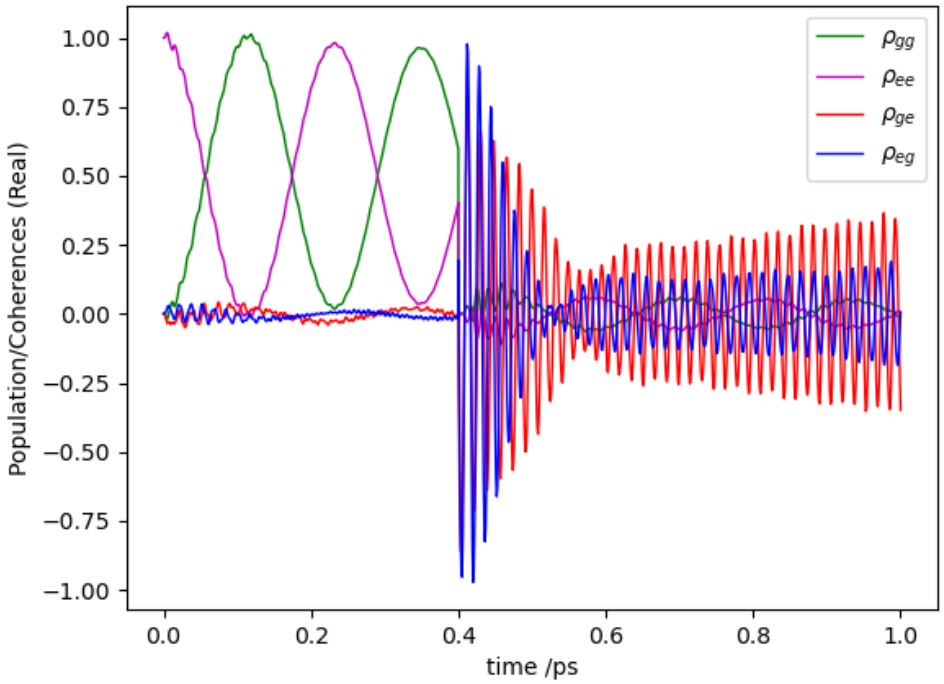

Figure 5.1.1: Populations and coherences for a two-level system evolved for 0.4 ps using the LDUO-HEOM, before being hit by an instantaneous laser field at the fundamental transition frequency, $\omega_{eg}^{(\nu)}$, with an infinitesimal spatial width at 0.4 ps causing a rotation into the coherences, and evolved for the remaining 0.6 ps.

instantaneous laser field at $3\,000$ cm^{-1} which rotates the population states and coherences within the density matrix. This transfers the large population magnitude onto the imaginary axis which is continually increased by the undamped mode within the LDUO hierarchy. The purely imaginary poles add to the coherence leading to a divergent ρ_{eg} and ρ_{ge} dependent on the strength of the undamped mode coupling and the strength of this coupling relative to the overdamped modes. The populations continue to oscillate between fixed values indefinitely and are not divergent. The continual existence of coherences within the density matrix of the LDUO highlights that the system is permanently in a superposition of states throughout the evolution.

5.1.3 LDUO Linear and 2D Nonlinear Optical Spectroscopy

Following the theory of spectroscopy outlined in section 2.4, the evolved density matrix generated from the LDUO-HEOM can be used to produce both linear and non-linear optical spectra. The probability of generating a coherence within the

system is proportional to the corresponding transition dipole moment element[38],

$$\rho_{\mathrm{eg}} \propto i\mu_{ge}\exp(-i\omega_{ge}^{(\nu)}t_1)\exp\Big(-\frac{t_1}{T_2}\Big), \tag{5.1.33}$$

with homogeneous broadening and lifetime dictated by T_2, and can be related to the first order polarisation through $R^{(1)} \propto \mu_{\mathrm{ge}}\rho_{eg}$. The molecular response function, as shown in equation 2.4.3, can be rewritten as

$$P^{(1)}(t) \propto \int_0^\infty R^{(1)}(t_1)\mathcal{E}_{\mathrm{I}}(t-t_1)\exp\Big(-i\omega^{(\nu)}(t-t_1)+i\mathbf{k}_1\cdot\mathbf{r}+i\phi\Big)\,\mathrm{d}t_1, \tag{5.1.34}$$

where ϕ is the associated phase. In the impulsive limit the envelope function is reduced to a delta function and the convolution simplifies to the sifting property. To generate a spectral signal the squared magnitude of the Fourier transformed macroscopic polarisation is calculated[38] yielding, to first order,

$$S(\omega) \approx I_0(\omega) + 2\mathcal{R}\Big(i\tilde{P}^{(1)}(\omega)\Big), \tag{5.1.35}$$

with incident laser field contributions being contained within I_0. The absorption spectrum, which contains only signals from the interference of the incident fields, is generated by subtracting the spectrum of the continuous laser, $S'(\omega^{(\nu)}) = -\log\frac{S(\omega^{(\nu)})}{I_0(\omega^{(\nu)})}$, such that

$$S'(\omega^{(\nu)}) \propto \mathcal{R}\int_0^\infty \mu_{\mathrm{ge}}^2\exp\Big(-i\omega^{(\nu)}(t-t_1)\Big)\,\mathrm{d}t_1 = \mathcal{R}\frac{\mu_{\mathrm{ge}}^2}{i(\omega^{(\nu)}-\omega_{\mathrm{ge}}^{(\nu)})-T_2^{-1}}, \tag{5.1.36}$$

which leads to the *absorptive* component of a Lorentzian spectral contribution (denoted $\tilde{g}_{\{\cdot\}}(\omega^{(\nu)})$))

$$\mathcal{R}(\tilde{g}_{\{\cdot\}}(\omega^{(\nu)})) = A(\omega^{(\nu)}) \propto \frac{\mu_{\mathrm{ge}}^2 T_2^{-1}}{(\omega^{(\nu)}-\omega_{\mathrm{ge}}^{(\nu)})^2+T_2^{-2}}, \tag{5.1.37}$$

and leads to sharp lineshape which decays as $\mathcal{O}\Big((\omega^{(\nu)}-\omega_{\mathrm{ge}}^{(\nu)})^{-2}\Big)$. Similarly, the *dispersive* component of the same Lorentzian spectral contribution is

$$\mathcal{I}(\tilde{g}_{\{\cdot\}}(\omega^{(\nu)})) = D(\omega^{(\nu)}) \propto \frac{-\mu_{\mathrm{ge}}^2(\omega^{(\nu)}-\omega_{\mathrm{ge}}^{(\nu)})}{(\omega^{(\nu)}-\omega_{\mathrm{ge}}^{(\nu)})^2+T_2^{-2}}, \tag{5.1.38}$$

and produces broader spectral lineshapes, if rotated onto the real axis, due to the decay as $\mathcal{O}\Big((\omega^{(\nu)}-\omega_{\mathrm{ge}}^{(\nu)})^{-1}\Big)$. These elements of the total spectrum relate to the behaviour of waves which are travelling as a wavepacket. Contributions to the total superposition with lower frequency will travel slower than those with high frequencies leading to a dispersion, or spreading, of the wavepacket as it propagates. Subsequently, these kinds of waves have a *group velocity* which describes the velocity of the wavepacket envelope, and a *phase velocity* which

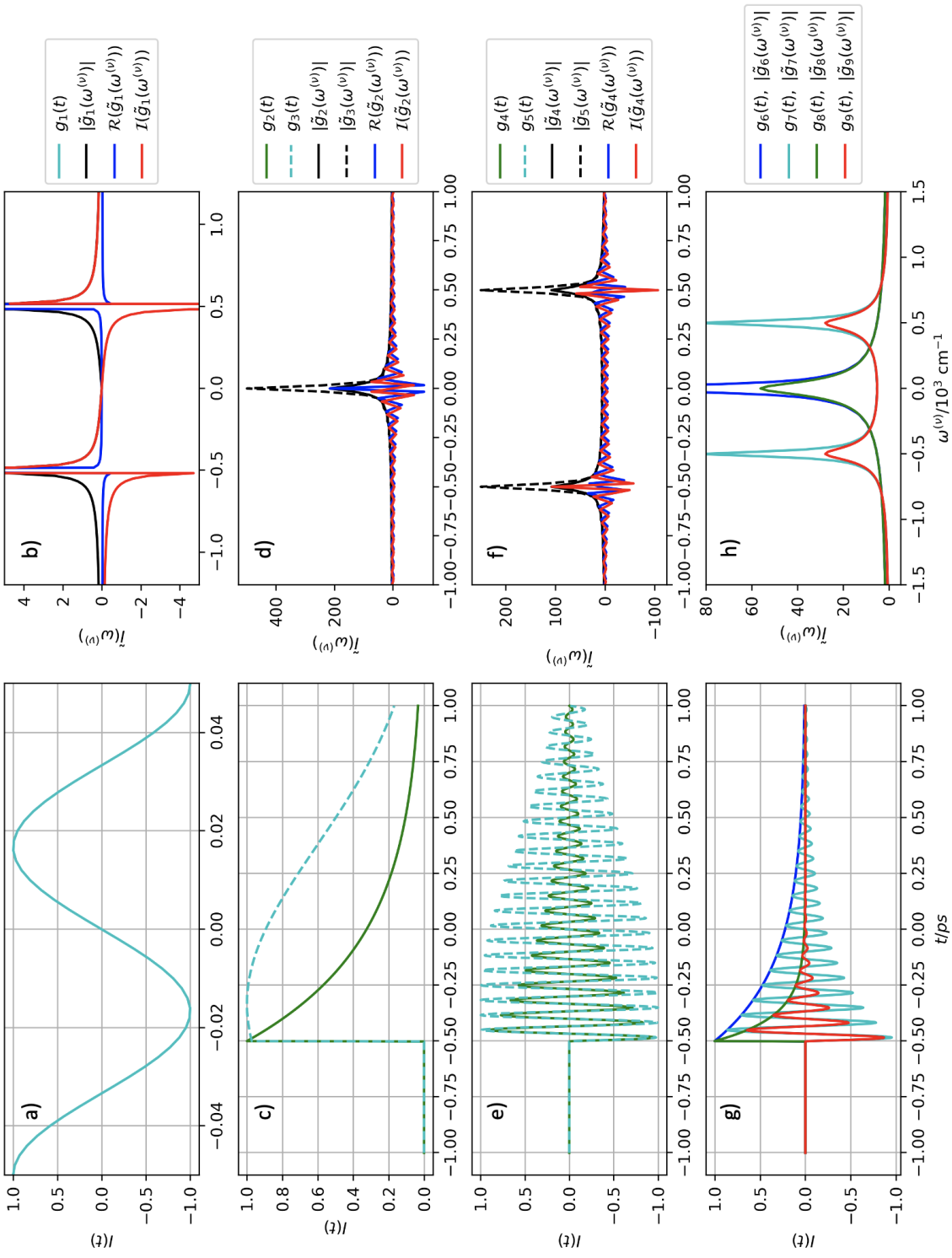

Figure 5.1.2: A series of linear absorptive, dispersive, and absolute linear spectra for a) and b) a pure sinusoidal response function, c) and d) exponential/Gaussian decay response functions, e) and f) sinusoidal decaying response functions, and g) and h) a comparison of exponential decaying envelope response functions and the associated decaying oscillation. Introduction of a step function at -0.5 ps demonstrates that the incomplete periods cause oscillations in the absorptive and dispersive linear signals, but not the absolute.

describes the velocity of each wave contribution within the superposition. In addition, upon interaction of this wave with a medium interface, a proportion of the wave will be transmitted into the material, a fraction will be reflected and a small portion will be absorbed. The energy of the absorbed component relates to the absorptive spectrum, whereas the refracted, transmitted, component is related to the dispersive part. On these grounds, absorptive components are usually positive, as they relate to energy of the constituent modes, but the dispersive component can take negative values dependent on the wave superposition.

Typically, computational calculation of the Fourier transform involves taking the absolute value of the spectrum, resulting in a linear combination of absorptive and dispersive contributions. However, within spectroscopic applications it can be necessary to consider the absorptive and dispersive elements in isolation. In the case of the LDUO-HEOM, the spectral vibration is entirely undamped leading to a pure, single component, oscillation within the response function. The impact of this on the absorptive, dispersive, and absolute spectra are considered in figure 5.1.2.

a) and b) of figure 5.1.2 demonstrate that when there is a single wave component, $g_1(t)$, that the (standard) absolute Fourier spectrum produces a delta function (Lorentzian lineshape), $|\tilde{g}_1(\omega^{(\nu)})|$, with breadth dependent on the domain. In contrast, the absorptive spectrum produces a pair of split Lorentzians which are symmetric about the y-axis and split into quadrants[b] two and four with a node at the fundamental transition frequency, and proportions of negative and positive intensity controlled by the phase ϕ_n. The dispersive spectrum is also a pair of split Lorentzians but with a broader spectrum of order $\mathcal{O}\Big((\omega^{(\nu)} - \omega_{\mathrm{ge}}^{(\nu)})^{-1}\Big)$ in quadrants one and three. The pair of peaks correspond to positive (left moving) and negative (right moving) waves at the undamped oscillator frequency.

In contrast, c) and d) show the resultant Fourier spectra for two kinds of exponential decay which mimic homogeneous broadening or an inhomogenenous distribution with a Gaussian or exponential envelope. In this regime the absolute Fourier spectrum produces a single sharp Gaussian at the origin with amplitude dependent on the rate of decay of the response function, as demonstrated by moving from g_2 to g_3. Additionally, the absorptive and dispersive contributions are oscillatory functions again split into opposite quadrants. The sharp oscillations are a result of the jump discontinuity introduced at $t = 0.5$ ps, resulting in the emergence of the Gibb's phenomenon. This is also demonstrated within decaying oscillations in e) and d).

[b] Standard mathematical quadrants moving anticlockwise from the x, and y positive region in quadrant 1.

Finally the change in breadth and amplitude of the absolute spectra are shown in g) and h) as a function of the decay rate of the response function.

In addition to the differences between absorptive, dispersive, and absolute spectra, differences arise as a consequence of the phase introduced through $\mathcal{E} = \delta(0)\exp(-i\phi_n)$. Figure 5.1.3 depicts the change in response function, and absorptive/dispersive Fourier spectrum components, as the phase is increased from $\phi_1 = 0^{\mathrm{c}}$ to $\phi_4 = \pi^{\mathrm{c}}$. It is clear from column 3 that by increasing the phase, the amplitude and quadrant positions of the split halves of the absorptive and dispersive Fourier spectra can be tuned. When the phase is zero, as in row one, then the absorptive component becomes zero and the split imaginary Lorentzian appears in quadrants two and four. By increasing the phase by $\frac{\pi}{4}^{\mathrm{c}}$ degrees the spectral components are mixed resulting in equal and opposite absorptive and dispersive lineshapes. The imaginary contribution is still found in quadrants two and four, whereas the real absorptive component is in quadrants one and three. The amplitude of these spectra is reduced relative to column one, due to the mixing of dispersive and absorptive contributions. Row 3 depicts a rotation by ninety degrees through application of a phase $\phi_3 = \frac{\pi}{2}^{\mathrm{c}}$, which subsequently takes the imaginary signal from row one and transfers it onto the real axis. As a result, the dispersive element is zero and the absorptive contribution depicts the split Lorentzian with an equivalent amplitude to that shown in row one. This peak is split into quadrants one and three, opposite to those in row one. Finally, row four demonstrates a full inversion of the results in row one through a phase of π radians. This results in a flip of all signals across the y-axis.

The aim of the LDUO-HEOM is to reproduce BVM spectra, with accurate peak broadening, in the limit of vanishing canonical damping. Therefore, the phase is flipped such that the splitting of peaks is removed. This preserves the broadening of the absoprtive and dispersive elements of the Fourier spectrum, and ensures the absorptive components are strictly positive, at the cost of a node appearing within the fundamental peak. In contrast, the absolute spectrum could be used to remove the node and produce purely Lorentzian peaks, but at the cost of increased lineshape broadening which would include both absorptive and dispersive contributions. Figure 5.1.4 a) shows the linear response function for a range of system reorganisation energies and undamped mode coupling strengths with the LDUO-HEOM, and the comparative BVM response functions which have a pair of reorganisation energies for the pair of baths, and no undamped oscillator coupling. Figure 5.1.4 b) shows the associated linear spectrum for each case. A further discussion of spectrum generation and the necessary Hamiltonian truncation can be found in Appendix J.

There is a clear fundamental peak in all spectra, but the LDUO-HEOM peaks closest to the fundamental are split and have a reduction in amplitude towards

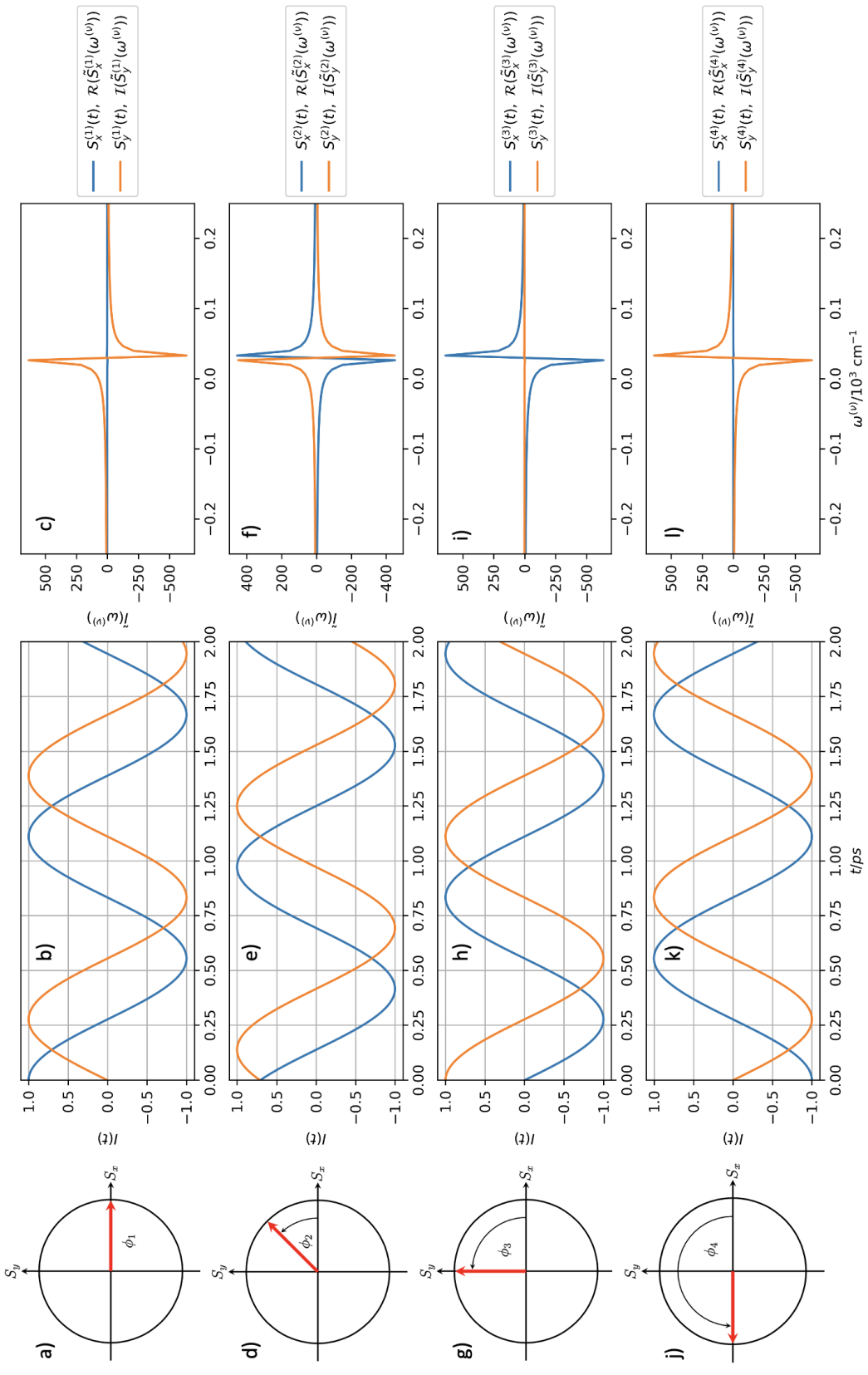

Figure 5.1.3: Columns 1, 2, and 3, depicting the phase, response function, and Fourier spectrum for different phases of a single oscillating component. Panels a) - c) with $\phi_1 = 0^c$, d) - f) with $\phi_2 = 45^\circ$, g) - i) with $\phi_3 = \frac{\pi^c}{2}$, and j) - l) with $\phi_4 = \pi^c$.

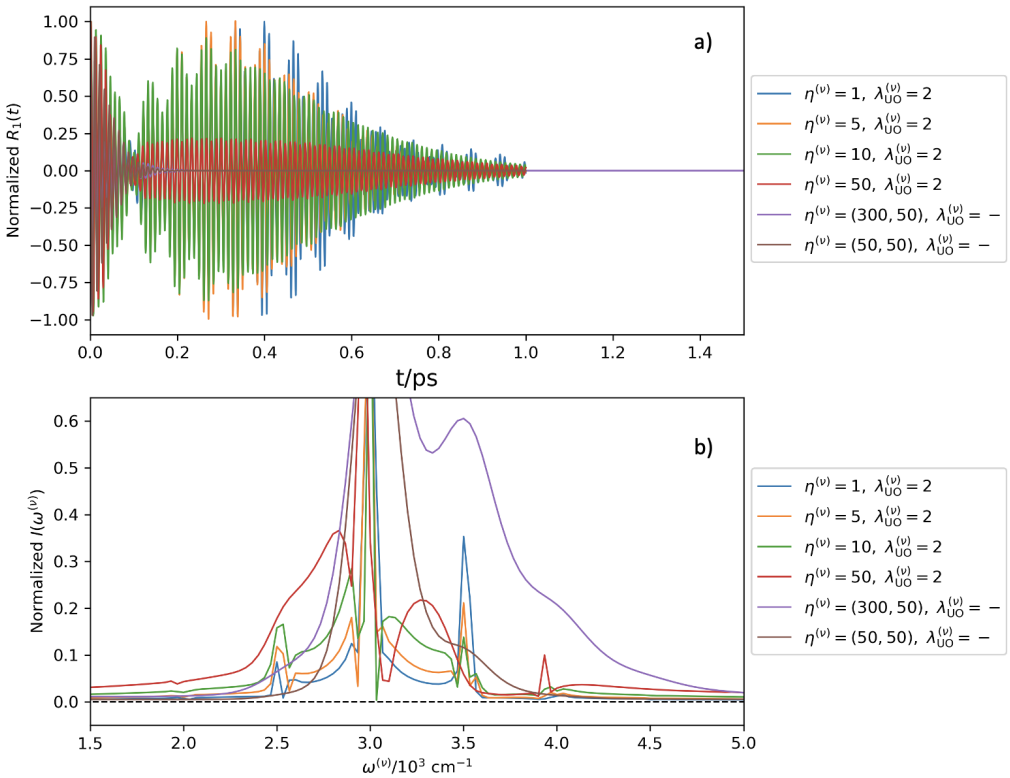

Figure 5.1.4: a) Linear response functions for the LDUO-HEOM and uHEOM, BVM, for a range of bath reorganisation energies, $\eta^{(\nu)}$, and undamped oscillator coupling strengths, $\lambda_{\mathrm{UO}}^{(\nu)}$, between 0.0 and 1.5 ps. b) The associated linear absorption spectra for each response function shown above.

the peak center. This is a consequence of the choice of phase shift, which is chosen to preserve the peak broadening. When the bath reorganisation energies are approximately equivalent, as in the case of $\eta^{(\nu)} = (50, 50)\ \mathrm{cm}^{-1}$ for the BVM and $\eta^{(\nu)} = 50\ \mathrm{cm}^{-1}$, $\lambda_{\mathrm{UO}}^{(\nu)} = 2\ \mathrm{cm}^{-1}$ for the LDUO, the peak broadening and intensity are similar. The clear vibronic progression evident in peaks at integer multiples of $500\ \mathrm{cm}^{-1}$ above and below the fundamental are clear, and arise as a consequence of the envelope of the response function. The sinusoidal envelope is evident in both the LDUO and uHEOM BVM at early times. However, when the balance between overdamped and undamped contributions strays from the ideal regime the envelope function is destroyed as the response function begins to diverge. This is shown by the loss of envelope function in the red data set of panel a) and is shown to increase the broadening erroneously, which signifies that the value of Γ_{max} is limiting the dynamics. Consequently, the response function is constrained with a Hamming window function at 1 ps, ensuring full decay.

Finally, the LDUO-HEOM is applied to nonlinear optical spectroscopy in order to generate 2DES equivalent to the uHEOM BVM in the limit of vanishing secondary damping. Columns one and three of figure 5.1.5 shows the BVM in the weak and strong coupling limits, equivalent to those in figure 5.1.4 with $\eta^{(\nu)} = (50, 50)\ \mathrm{cm}^{-1}$ and $\eta^{(\nu)} = (300, 50)\ \mathrm{cm}^{-1}$. Columns two and four show the

equivalent LDUO-HEOM versions of the weak and strongly coupled BVM, with $\eta^{(\nu)} = 50\ \mathrm{cm}^{-1}$, $\lambda_{\mathrm{UO}}^{(\nu)} = 1\ \mathrm{cm}^{-1}$, and $\eta^{(\nu)} = 50\ \mathrm{cm}^{-1}$, $\lambda_{\mathrm{UO}}^{(\nu)} = 2\ \mathrm{cm}^{-1}$.

All spectra within figure 5.1.5 are qualitatively similar and have very similar peak positions and broadening, demonstrating that the LDUO-HEOM is effective in modelling the BVM in the limit of vanishing canonical damping. Both the uHEOM BVM and LDUO-HEOM spectra present an initial inhomogeneous broadening of the fundamental peak which becomes more rounded for later population times along with clear signs of vibrational relaxation as peaks shift vertically downards. This is especially evident in k) and l) where there is clear movement of population to lower vibrational states within the system. While the LDUO-HEOM is effective at modelling the broadening in this limit, due to the undamped intramolecular vibrational mode in the hierarchy, the fundamental peak in the spectrum is split, with a node close to the fundamental frequency, as a consequence of the choice of phase versus broadening. This results in worse peak positional accuracy in the LDUO-HEOM close to the fundamental, however this is minimal in vibronic peaks further from the fundamental frequency as evidenced by the similarity in peak positional to the uHEOM particularly in i) and l). The other consequence of the undamped mode is a vertical stretching of the peaks. This results from the continually oscillating polarisation and can be attributed, in part, to the response function containing a single, continually oscillating component, rather than a decaying superposition.

One of the most fundamental benefits of this new approach, apart from the simplification of the spectral density is the reduction in computational cost. In order to generate these spectra there is an equilibration step, an evolution, and then an evolution and calculation of 2D spectra. In the uHEOM BVM these steps take 1 hour 29 mins, 3 hours 34 mins, and 16 hours and 19 mins, respectively. However, in the LDUO-HEOM the same steps took ~ 30 seconds, ~ 1 minute, and ~ 3 minutes, respectively for the low coupling case. This means that the LDUO-HEOM took 0.56% of the time the uHEOM did, or better, and represents an improvement of at least 99.4%.

In summary, a new form of hierarchical equations of motion has been generated for the purpose of realising the limit of vanishing canonical damping within the BVM model. This HEOM, after careful phase correction, produces spectra which are qualitatively similar to those of the uHEOM BVM demonstrating effective modelling of the BVM in the limit of zero canonical damping. It is shown that this method dramatically improves the computational time for modelling the BVM model, reducing the time taken by 99.4%, or more, in the weak coupling case.

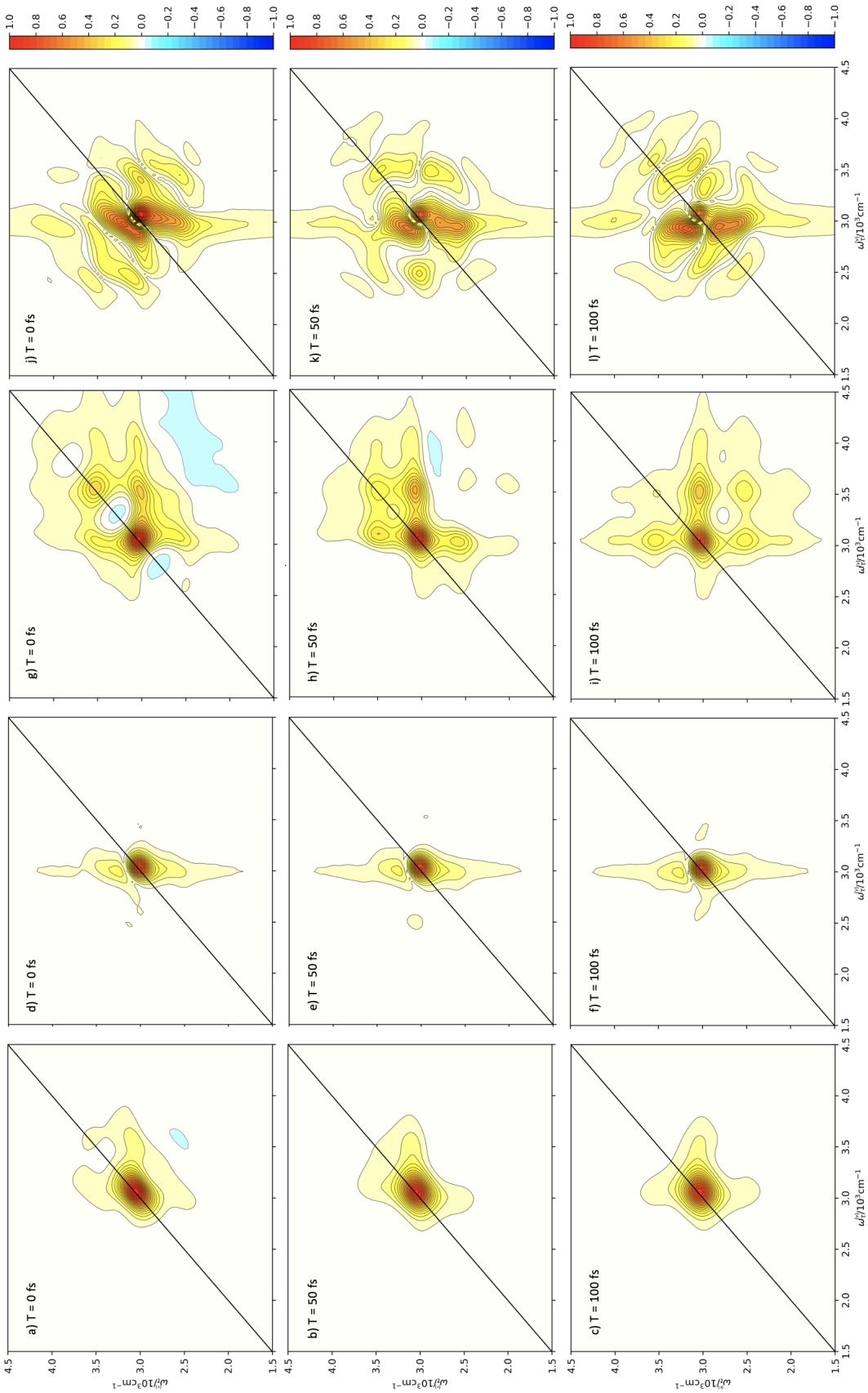

Figure 5.1.5: 2DES for the weakly coupled BVM system, columns 1 and 2, and the strongly coupled BVM, columns 3 and 4, via the LDUO-HEOM and the uHEOM. Columns 2 and 4 are the LDUO-HEOM, whereas columns 1 and 3 are the uHEOM BVM. Each column presents spectra for three population times, $T = 0$, 50, and 100 fs.

6 Conclusions

Perturbative and non-perturbative methods for modelling open quantum systems have been described in detail, with emphasis on the approximations and assumptions necessary to generate a full equation of motion. In each case, a full derivation from first principles has been performed which justifies the advancements leading up to the generation of the hierarchical equations of motion[147] for modelling non-Markovian effects within the bath dynamics of the total system. A formal discussion of each of the damping limits within the oHEOM and uHEOM is considered, as well as the implications this has on the efficiency of termination with the Markovian convergence parameter, $\Gamma_{\max}$. These models have been used to generate 2D electronic spectra in the impulsive limit for vibronic systems, starting with monomers and extending to electronically coupled species, based upon the Kasha model. The efficiency of such models is strongly dependent on the size of the Hamiltonian and total composite Hilbert space of the system, which increases non-linearly with dimer size. Based on the construction of each model, reductions of the full quantum mechanical treatment are considered which simplify the open quantum system dynamics by limiting the total explicit degrees of freedom. The canonical transform is leveraged to subsume vibrational degrees of freedom from the system Hamiltonian into the environment degrees of freedom in order to limit the size of the Hamiltonian. The cost of such an approach is scrutinised in terms of efficacy and computational efficiency through comparison of metrics of quantum behaviour applied to models before and after transformation. The pre-existing suite of HEOM and spectroscopy modules has been expanded to include quantum information and quantum correlation metrics which can be applied to either the density matrix or the auxiliary density operators of the system, as well as the creation of a bespoke equations of motion, the LDUO-HEOM, aimed at elucidating the impact of a movable system-bath boundary.

Chapter 3 presented the impact on quantum information of simplifying hierarchical equations of motion models, with specific emphasis on the 2DES lineshape. It was found that greater non-Markovianity occurs when the system is coupled to an underdamped bath, but that this effect is cumulative over a prolonged period of slow feedback. In contrast, overdamped baths were shown

to exhibit a rapid return of information from the environment to the system. The correlation between the ellipticity of overdamped 2D spectral features and the degree of non-Markovianity highlights that environmental signatures, such as inhomogeneous broadening, are due to a flow of quantum information from the bath to the system which broadens the spectra.

Next, the explicit action of the canonical transform on the 2DES is considered. A pair of models are generated for a vibronic monomer and homodimer, termed the Hamiltonian vibration model (HVM) and bath vibration model (BVM). These approaches differ only in the placement of the system bath boundary, where the HVM has explicit vibrational levels within the Hamiltonian, but the BVM does not. Both models generate clear vibronic structure, in agreement with the previous chapter, but again differ in the level of broadening. It is shown that HVM structure leads to sharp definition of energetic properties (peak position), at the cost of uniform broadening, whereas the BVM has poorer peak positional information but more accurate dynamical broadening when compared to experimental spectra. The BVM broadening is attributed to the intrinsic canonical damping associated with the underdamped intramolecular vibrational mode which is canonically subsumed into the bath. Through analysis of the correlation functions associated with the overdamped and underdamped components of the total environment, it is shown that in the limit of vanishing canonical damping the BVM and HVM are mathematically equivalent. In the more complex homodimer system the 2DES demonstrate that the choice of system-bath boundary placement also alters the vibronic coupling effects. This is demonstrated by the lack of vibronic quenching relative to the the Hamiltonian eigenvalues in BVM system. Application of the BVM shifts the computational bottleneck to the bath dynamics, from the diagonalisation of large Hamiltonians in the HVM, exponentially increasing the number of auxiliary density operators as a function of decreasing damping strength. Therefore a choice of HVM versus BVM is a trade-off between energetic precision, dynamical broadening, and computational expense.

Qualitative physical insights relating to the system-bath interaction and non-Markovianity can be drawn from virtual information flow which is mediated by phonons at integer multiples of each constituent Matsubara frequency within the ADOs. It is shown that, with the exception of temperature independent axes which arise from non-thermal poles of the spectral distribution, Matsubara axes are independent from each other as a consequence of their relative timescale. Subsequently, a new hierarchy termination criterion is considered which simplifies the sealed hierarchy volume by allowing each Matsubara axis to be terminated to a different length rather than requiring self-similar volumes. It is shown through termination contours that the proposed, volume reducing, termination scheme would reduce the

computational cost of large hierarchy volumes. Full implementation of this termination scheme is a computational challenge which is beyond the scope of this thesis, but its efficacy has been demonstrated. Future studies could involve the computational implementation of an algorithm to trim the hierarchy based on this criterion.

Chapter 4 presents an equivalent analysis of the placement of the system-bath boundary, but through the impact on quantum correlations. First, the correlations of a vibronic monomer system, built as HVM, which is continuously driven by a laser field of infinitesimal width are considered. Within the photon correlations, the purely quantum behaviour of antibunching is observed along with phonon signatures, whereas in the phonon correlations bunching is observed. Sources of vibrational character are elucidated through cross-correlations in which the order of boson detection has a considerable impact on the probability. It is shown that sources of vibrational character can be either direct, such as in the number operator for phonons, or indirect, such as in emission of photons modulated by level of vibrational excitation. These sources lead to a strong amplification of phonon signatures in $g^{(2)}_{\mathrm{ba}}$ correlation, and a reduction of such signatures in the $g^{(2)}_{\mathrm{ab}}$. It is noted that, through correlation with photons, these correlation functions present an opportunity to investigate phonon dynamics indirectly using existing quantum-optical techniques to understand the impact on quantum versus classical processes in molecular systems.

Thereafter, the implications of driving fields with Gaussian width are considered. The result of this on the correlation is that the electronic signatures tend towards step functions where there are regions of zero interaction, and zero change in correlation, followed by regions of intense vibrational activity as the system interacts with the field pulse containing many frequencies.

Before moving on to more complex electronically coupled species, an analysis of the movement of vibrational structure through the canonical transform in a vibronic monomer, in the context of quantum correlation, is considered. The second order correlation metric of quantum correlations is applied to the ADOs for the BVM and HVM. It is demonstrated that auxiliary density operators are dependent on a Matsubara frequency, from the dimensions of the hierarchy, and these correspond to integer multiples of phonon modes. Interaction of these phonon modes, and dissipation due to the thermal environment lead to virtual correlations within the ADOs of HVM systems. However, because the canonical transform fundamentally mixes[a] the system vibrations with the environment degrees of freedom, all qualitative physical information about quantum correlations is lost and the BVM is incompatible with current quantum correlation metrics. This poses the possibility of a future study which further

[a] Or 'entagles' the degrees of freedom, similar to bathentanglement.

develops non-Markovian corrections to the theory, such as extensions of the quantum regression theorem, so that the BVM can be extended to these scenarios.

Finally, quantum correlation metrics are applied to complex electronically coupled species, within an HVM framework, in order to elucidate the impact of excitonic coupling on quantum behaviours. In the absence of electronic coupling, such as in the proposed monomer lattice structures, the photon correlations can be amplified due to competition between the doubly and singly excited states, as well as through the relative increase in photon number with respect to a single monomer, which leads to a temporary inversion of correlation statistics from bunching to antibunching. Consequently, photons derived from the driving of a single monomer tend to exhibit antibunching, whereas monomer lattices are able to exhibit both bunching and antibunching dependent on the displacement of the excited state potential energy surface. By detuning the driving field it is shown that the fundamental electronic Rabi cycles can be removed from the correlation leaving modulations purely due to phonon movement. In electronically coupled dimer systems J-aggregates are shown to antibunch at early τ for photons, and bunch for phonons, with both tending towards an equilibrium with the laser when coupled to a bath. In contrast, H-aggregates show more complex correlation character, and tend to diverge away from an equilibrium when coupled to the bath. For low H-aggregate couplings, vibrational contributions to the wavepacket enhance correlations above the equilibrium value for small τ, and in the long τ limit resonance energy transfer from acceptor to donor sites in the system, or recurrence from the bath, cause antibunching independent of phonon signatures.

Chapter 5 presented the realisation of the BVM in the limit of vanishing canonical damping through the LDUO-HEOM. Based on the analysis of necessary approximations and assumptions a new hierarchical equations of motion was generated which incorporated a pure intramolecular vibration coupled to a Lorentz-Drude overdamped environment. This coupling generates a vibronic progression within the linear and 2D electronic spectra, which after correction through a Hamming window and phase flipping, are in agreement with those generated by the uHEOM.

6.1 Response to Proposed Hypotheses

In short, there is an affirmative answer to all of the proposed hypotheses in chapter 1.

Hypothesis 1: Through non-perturbative, modern, formalisms can model

complexity be maximised in conjunction with a minimisation of computational effort? Hypothesis 1 is addressed in chapters 3 and 4 which consider the impact on 2DES and quantum correlations of movement of the system-bath boundary using the HEOM. The volume reducing termination criterion and development of the BVM demonstrate that complexity **can** be maximised in conjunction with a minimisation of computational effort with certain approximations. Additionally the computational savings are demonstrated through a new HEOM, (LDUO) in chapter 5, which represents an improvement of at least 99.4% in computational time.

Hypothesis 2: Are genuine quantum effects strongly impacted by system-bath boundary placement, and can these impacts be controlled by approximations and advanced formalisms? This hypothesis is addressed by implementation of the vibronic Hamiltonian for monomer and dimer systems into quantum dynamical simulations followed by calculation of necessary quantum metrics in chapters 3 and 4. It is shown that quantum behaviours **are** affected by the system-bath boundary placement, examples being vibronic quenching in 2DES and BVM correlations.

Hypothesis 3: Through reduction to an undamped vibrational mode, can models with canonically subsumed vibrations become equivalent to those with explicit vibrational structure? In chapter 5 it was confirmed through a new HEOM that systems modelled with explicit vibrational structure **are** equivalent to models with canonically subsumed vibrations in the limit of zero vibrational mode damping.

6.2 Future Research

Potential future research based on the findings in each chapter are summarised below.

The work in chapter 3, when compared to the systems in chapter 4, suggests that RET could be further considered in H-aggregate systems and the quantum information content of these systems be further analysed. This thesis only went so far as to study homodimers, but did not consider a full range of electronically coupled species. It is clear that H-aggregates with strong coupling exhibit more energy transfer, but the impact this has on the quantum information is unclear. Such studies would require computational improvements to allow for propagation of much larger systems. Additionally, through the analysis of virtual information the impact of subsuming a system vibration could be further explored. Future work could focus on generating an algorithm to reduce the hierarchy, following the proposed volume reducing termination criterion, and

this could be tested on a model molecular system.

Chapter 4 also presents a number of possible future directions for research. It is clear that, currently, the BVM are incompatible with metrics of quantum correlation. This theory could be further developed, potentially through extensions of the quantum regression theorem, to allow the BVM to be utilised in these scenarios. Additionally, the study of electronically coupled species open a number of new avenues. Further exploration of the limit of vanishing coupling, for monomer lattices, through systems which have orthogonal dipole moments for the constituent monomer units could realise this coupling regime without large inter-monomer distances. This would require vectorised systems which do not rely on collinear dipoles, and driving fields capable of stimulating both monomer units. Similarly, this could lead to insights into quantum behaviour when correlations are generated from structured, or circularly polarised light. Finally, RET could be further explored in strong H- and J-aggregates. The current computational limitations could be removed allowing for large values of $\mathrm{N} = \mathrm{ddim}$ so that full vibrational complexity in heterodimers could be achieved. This would remove the limitations involved with harsh truncation.

Finally, chapter 5 presents the new LDUO-HEOM which is applied to a single, simple, test vibronic monomer. Further work could involve further exploring the capabilities and limits of this new hierarchy by modelling vibronic dimers and other electronically coupled species. Currently, the metrics of quantum information and correlation have not been explored deeply for this EOM, and this presents another opportunity for further research.

Appendices

A Mathematical Notation and Physical Interpretation

Notation

Real and Imaginary parts of a number

$$\mathcal{R}, \mathcal{I}. \tag{A.0.1}$$

For example, for an arbitrary complex number $C = a + ib$

$$\mathcal{R}(C) = a, \quad \text{and} \quad \mathcal{I}(C) = b, \tag{A.0.2}$$

where $a, b \in \mathbb{R}$.

Integral

The integral over a variable x between a and b. Here x is strictly a variable, hence the italic font, and is not a functional. For functional integrals see A.0.66.

$$\int_a^b \{\cdot\} \, \mathrm{d}x. \tag{A.0.3}$$

Integral of symmetric integrands

An integral of a function which is symmetric with respect to a defined line or axis C, when integrated along the domain perpendicular to C can be transformed so that the original integral along the entire domain is equal to two lots of the integral over half of the domain. For example, if $f(x)$ is symmetric around C where C is the $y-\text{axis}$ and the domain is $x \in [-\infty, \infty]$ then:

$$2\int_0^\infty f(x) \, \mathrm{d}x = \int_{-\infty}^\infty f(x) \, \mathrm{d}x. \tag{A.0.4}$$

Integral of antisymmetric integrands

Similarly, for an antisymetric function we have:

$$\int_0^a f(x)\,\mathrm{d}x = -\int_{-a}^0 f(x)\,\mathrm{d}x. \tag{A.0.5}$$

Matsubara frequencies

Energy of Matsubara frequencies

The energy associated with the Matsubara frequency ν_n is $\frac{\beta\hbar\nu_n}{2}$.

Spectral Density

A continuous function, $J(\omega)$, which traces the profile of an infinite number of weighted delta functions corresponding to the frequencies of individual modes within an environment ensemble within an open quantum system. The associated dissipation rate of the environment depends on: Λ for overdamped baths, and γ for underdamped baths. This takes the form:

$$J_n(\omega) = \pi \sum_\nu \frac{g_{n,\nu}^2}{2m_{n,\nu}\omega_{n,\nu}} \delta(\omega - \omega_{n,\nu}), \tag{A.0.6}$$

Sine and Cosine functions

$$\sin(\{\cdot\}) = \mathcal{I}\Big(\exp(i\{\cdot\})\Big), \quad \cos(\{\cdot\}) = \mathcal{R}\Big(\exp(i\{\cdot\})\Big). \tag{A.0.7}$$

Hyperbolic Sine and Cosine functions and relations

$$\sinh(\{\cdot\}) = \frac{1}{2}\Big(\exp(\{\cdot\}) - \exp(-\{\cdot\})\Big), \quad \cosh(\{\cdot\}) = \frac{1}{2}\Big(\exp(\{\cdot\}) + \exp(-\{\cdot\})\Big). \tag{A.0.8}$$

$$\sinh(i\{\cdot\}) = i\sin(\{\cdot\}), \quad \cosh(i\{\cdot\}) = \cos(\{\cdot\}). \tag{A.0.9}$$

Laplace Transform

$$\mathcal{L}_{\mathrm{Lap}}\{f\}(s) = \int_0^\infty f(t)\exp(-st)\,\mathrm{d}t, \tag{A.0.10}$$

where Lap denotes the Laplace transform, in order to differentiate it from the Lagrangian, Liouvillian, and Lindbladian operators.

Closed System

A closed system in a single Feynman-Vernon coordinate X is

$$\mathrm{H}(X). \tag{A.0.11}$$

Open System

An open system in a pair of Feynman-Vernon coordinates X and Q is

$$\mathrm{H}(X,Q) = \mathrm{H}(X) + \mathrm{H_I}(X,Q), \tag{A.0.12}$$

with a coupling $\mathrm{H_I}(X,Q)$ in terms of both variables.

Stochastic Forcing

Stochasticity introduced through a random or probabilistic varibale such as forcing $F(t)$.

Scale of Oscillations Approximation

Separation of equations into 'relevant' and 'irrelevant' parts based on the relative speed of the oscillations. This is often achieved through operators, an example being the Zwanzig projection operators.

$$\rho_\mathrm{S} = \mathcal{P}\rho, \quad \rho_\mathrm{B} = \mathcal{Q}\rho. \tag{A.0.13}$$

Similar to the rotating wave approximation, (A.0.15).

Weak coupling Approximation

Simplification based on the scale of interactions, assessed through a small dimensionless quantity, ϵ,

$$\mathrm{H_{I,tot}} = \mathrm{H}_0 + \epsilon \mathrm{H_I}, \tag{A.0.14}$$

where H_0 is the Hamiltonian for the system without interactions, and $\mathrm{H_I}$ links the coordinates of the open system.

Rotating Wave Approximation

Similar to Zwanzig projection operators, (A.0.13). Sufficiently rapid oscillations are neglected such that the system moves into a moving frame of reference.

$$|\omega - \omega'| \gg \epsilon^2, \tag{A.0.15}$$

where ϵ is a small dimensionless quantity.

Secular Approximation

Environmental frequencies are restricted to those at resonance.

$$\omega = \omega'. \tag{A.0.16}$$

Born (Adiabatic) Approximation

The nuclear and electronic contributions to a system evolution are separable such that:

$$|\alpha\rangle \otimes |n\rangle \,. \tag{A.0.17}$$

Markovian Approximation

The system-bath interaction is simpplified through the assumption that bath contributions are not time-dependent (particularly within nested commutators) such that each future evolution step depends solely on the previous time step.

$$\rho_{\mathrm{B}}(t) \approx \rho_{\mathrm{B}}(t_0). \tag{A.0.18}$$

Factorisable Initial Conditions

The system and bath degrees of freedom are initially separable such that,

$$\rho_{\mathrm{tot}} = \rho_{\mathrm{S}}(t)\rho_{\mathrm{B}}(t). \tag{A.0.19}$$

An Infinite Bath

A bath generated from a continuous coordinate rather than discrete environmental modes such that there are an infinite number of distinct

frequencies within the environment ensemble.

$$J(\omega). \tag{A.0.20}$$

Canonical Environment Distribution

A canonically distributed environment approximation requires that the environment represents a thermal equilibrium distribution of molecules.

High Temperature Approximation

High temperature such that,

$$\beta\hbar\gamma \ll 1. \tag{A.0.21}$$

Conditional Moment Exists

An approximation requiring that the conditional moment can be generated as a type of expectation value for the system. In the Schrödinger equation this requires an operator $\mathrm{p} \rightarrow i\hbar\nabla$.

State Vector

A column vector describing the state of a system, $|\psi(t)\rangle$, dependent on the wavefunction.

Unitary Evolution Operator

The operator which evolves a state vector through time, $\mathrm{U}(t, t_0)$,

$$|\psi(t)\rangle = \mathrm{U}(t, t_0)\,|\psi(t_0)\rangle\,. \tag{A.0.22}$$

Chronological Time Ordering Operator

An operator, or path ordering procedure, which generates reorganises constituent operations into a product of time ordered operations, $\mathrm{T}_{\leftarrow}$.

The Trace

For an $n \times n$ matrix, ρ, the trace is defined as

$$\mathrm{Tr}(\rho) = \sum_{i=1}^{n} \rho_{ii}, \tag{A.0.23}$$

where ρ_{ii} are the diagonal entries of the matrix ρ.

Hermitian Conjugate

The Hermitian conjugate of a matrix is the transpose and conjugate. Is the conjugate of a matrix is denoted by a bar, $\bar{\mathrm{A}}$, and the transpose by T, A^{T}, then

$$\mathrm{A}^{\dagger} = (\bar{\mathrm{A}})^{\mathrm{T}} = (\bar{\mathrm{A}^{\mathrm{T}}}). \tag{A.0.24}$$

A matrix is said to be Hermitian if $\mathrm{A}_{ij} = \bar{\mathrm{A}_{ij}}$.

Liouville von Neumann Evolution Superoperator

The superoperator associated with the Liouville von Neumann equation and its dynamics:

$$i\hbar \frac{\partial \rho(t)}{\partial t} = [\mathrm{H}, \rho(t)], \tag{A.0.25}$$

$$= \mathcal{L}_{\mathrm{LVN}} \rho(t). \tag{A.0.26}$$

Tensor Product

A product of two tensors which expands the underlying space of the first tensor by the dimensions of the second, $\mathbb{R}^n \otimes \mathbb{R}^m = \mathbb{R}^{nm}$. For example, a composite Hilbert space which expands the system space to include degrees of freedom from a pair of monomers.

$$|x\rangle \otimes |y\rangle = |x, y\rangle\,, \tag{A.0.27}$$

$$\begin{pmatrix} x_1 & x_2 \\ x_3 & x_4 \end{pmatrix} \otimes \begin{pmatrix} y_1 & y_2 \\ y_3 & y_4 \end{pmatrix} = \begin{pmatrix} x_1 \begin{pmatrix} y_1 & y_2 \\ y_3 & y_4 \end{pmatrix} & x_2 \begin{pmatrix} y_1 & y_2 \\ y_3 & y_4 \end{pmatrix} \\ x_3 \begin{pmatrix} y_1 & y_2 \\ y_3 & y_4 \end{pmatrix} & x_4 \begin{pmatrix} y_1 & y_2 \\ y_3 & y_4 \end{pmatrix} \end{pmatrix} \tag{A.0.28}$$

C^* -algebra

In Quantum Mechanics the state of a physical system, $|\phi(t)\rangle$, is a linear functional which is acting on an abstract C^*-algebra, and physical observables are the hermitian elements of the same algebra. In the context of this thesis the algebra is a closed set of continuous linear operators on a complex Hilbert space.

Dynamical Map

An operator analogous to the unitary evolution operator, A, but which acts solely on the system degrees of freedom is defined as a dynamical map, ϕ_{M}.

A Generator

For a given set of dynamics (examples could be the LVN equation or Lindblad equation) the generator is analogous to the evolution superoperator and takes the form $\mathcal{L}_{\mathrm{g}}$. In this sense, the Liouville von Neumann Evolution Superoperator, A, is a generator.

Propagator

For each generator (evolution superoperator) there is an associated propagator which is the dynamical map, A, for the dynamics of this system. A general time dependent propagator takes the form:

$$\mathrm{V}(t,t_0) = \mathrm{T}_{\leftarrow}\mathrm{exp}\Big(\int_{t_0}^{t}\mathcal{L}_{\{\cdot\}}(s)\,\mathrm{d}s\Big). \tag{A.0.29}$$

If a propagator is entirely divisible, and numerically explicit, then it can be defined as Markovian. This allows dynamical maps to be used as a measure of memory effects.

The Von Neumann Entropy Function

The amount of disorder present within a system:

$$S(\rho) = -k_{\mathrm{B}}\mathrm{Tr}\Big(\rho\ln\rho\Big). \tag{A.0.30}$$

The Helstrom (Bures) Metric

Quantification of the distinguishability of a pair of probability distributions is achieved through a measure of the statistical distance between the two states. When the two probabilities are arbitrary this is known as the Helstrom metric, but when the two probabilities are equal it is known as the trace distance.

$$\Delta_{\mathrm{H}}(\rho_1, \rho_2) = \mathrm{Tr}|p_1\rho_1 - p_2\rho_2|, \tag{A.0.31}$$

when $p_1 = p_2 = \frac{1}{2}$, $\Delta_{\mathrm{H}} = D$.

Information Flux

The amount of information (complement of entropy) moving through quantum channels within an open quantum system is defined as a flux:

$$\sigma = \frac{\mathrm{d}}{\mathrm{d}t} D(\rho_1, \rho_2). \tag{A.0.32}$$

The BLP Metric

The cumulative maximum of the positive information flux is termed the degree of non-Markovianity, or the BLP metric, and is generated through

$$\mathcal{N} = \max_{\rho_{1,2}} \int \sigma(t)\, \mathrm{d}t. \tag{A.0.33}$$

Dimensionless Momentum, Position, and Excited State Displacement Operators

The non-dimensionalised forms of the momentum, position, and excited state displacement operators, from a potential energy surface of a TLS shown in figure 2.2.1. For a potential energy surface of a vibronic monomer where the pair of electronic states are each coupled to the jth vibrational mode, these operators are: $\tilde{\mathrm{p}}_j$, $\tilde{\mathrm{q}}_j$, $\tilde{\mathrm{d}}_j$.

The Kronecker Delta

A function of two variables, dependent on two indices, with either takes the value of 1 or 0, when the indices are equal or not equal, respectively.

$$\delta_{jk} = \begin{cases} 0 & j \neq k, \\ 1 & j = k. \end{cases} \tag{A.0.34}$$

The Creation and Annihilation Operators

Operators, $\mathrm{a}^{(\dagger)}$ and $\mathrm{b}^{(\dagger)}$, which destroy (and generate) a quanta of electronic excitation or vibrational excitation within the system.

$$\mathrm{b}_j^{(\dagger)} = \frac{1}{\sqrt{2}}(\tilde{\mathrm{q}}_j \pm \tilde{\mathrm{p}}_j). \tag{A.0.35}$$

The Huang-Rhys Parameter

Physically this parameter corresponds to the mean number of phonons in a coherent state that has been displaced by the reorganisation energy from that of the vacuum distribution. It is calculated as:

$$S_j^{\mathrm{HR}} = \frac{1}{2}\tilde{d}_j^2. \tag{A.0.36}$$

Electronic Coupling Strength

Whether it be through spatial separation or direct covalent bonding, the electronic coupling of a molecule, J, is given by the Förster coupling equation:

$$J = \frac{\kappa_{\mathrm{AB}}|\boldsymbol{\mu}_{\mathrm{A}}||\boldsymbol{\mu}_{\mathrm{B}}|}{4\pi\varepsilon_r\varepsilon_0 R^3}. \tag{A.0.37}$$

The Molecular Orientation Factor

This factor describes the orientation of the constituent transition dipole moments of a molecule:

$$\kappa_{\mathrm{AB}} = \hat{\boldsymbol{\mu}}_{\mathrm{A}} \cdot \hat{\boldsymbol{\mu}}_{\mathrm{B}} - 3(\hat{\boldsymbol{\mu}}_{\mathrm{A}} \cdot \hat{\mathbf{R}})(\hat{\boldsymbol{\mu}}_{\mathrm{B}} \cdot \hat{\mathbf{R}}), \tag{A.0.38}$$

The Transition Dipole Moment Operator

The magnitude of the transition dipole moment of the system is given by μ, the direction of the vector quantity is given by $\mathbf{d}$, and the operator is given by

$$\mu^{\mathrm{S}}_{\mathrm{el,M}} = \boldsymbol{\mu}_{eg}\Big(|g\rangle\langle e| + |e\rangle\langle g| \Big). \tag{A.0.39}$$

The Identity Operator

Formally, an identity function obeys

$$I_{\mathrm{f}}(X) = X, \tag{A.0.40}$$

such that any input is mapped to itself. For an operator this manifests as a diagonal matrix of ones, where all off-diagonal elements are zero. This takes the form

$$\mathrm{I}^{(n)}, \quad \text{when } n = 2, \tag{A.0.41}$$

$$\mathrm{I}^{(2)} = \begin{pmatrix} 1 & 0 \\ 0 & 1 \end{pmatrix}. \tag{A.0.42}$$

Bath Reorganisation Energy

The strength of coupling of each environmental mode (delta function) within the spectral distribution is given by

$$\eta_n = \frac{1}{\pi}\int_0^\infty \frac{J_n(\omega)}{\omega}\,\mathrm{d}\omega. \tag{A.0.43}$$

Bath Coupling Operators

Explicit forms of the operators (site basis) which couple the system and bath are:

$$\mathrm{B}^{\mathrm{S}}_{1,\mathrm{M}} = \sum_n |e,n\rangle\,\langle e,n|\,, \tag{A.0.44}$$

for a monomer and,

$$\mathrm{B}^{\mathrm{S}}_{1,\mathrm{D}} = \sum_{n_{\mathrm{A}},n_{\mathrm{B}}} \Big(|g,n_{\mathrm{A}},e,n_{\mathrm{B}}\rangle\,\langle g,n_{\mathrm{A}},e,n_{\mathrm{B}}| + |e,n_{\mathrm{A}},g,n_{\mathrm{B}}\rangle\,\langle e,n_{\mathrm{A}},g,n_{\mathrm{B}}| + 2\,|e,n_{\mathrm{A}},e,n_{\mathrm{B}}\rangle\,\langle e,n_{\mathrm{A}},e,n_{\mathrm{B}}| \Big), \tag{A.0.45}$$

for a dimer. These couplings contain no off-diagonal elements and subsequently describe the impact of stochastic bath motion on the transition frequencies between electronic states, which leads to T_2^* pure dephasing.

Correlation Function

The correlation function of system-bath interaction, which is fundamental to the fluctuation-dissipation theorem, models the rate of decay of bath correlations subject to dissipation and thermal fluctuation.

$$L_n^{(\alpha)}(t) = \frac{\hbar}{\pi}\int_0^\infty J_n(\omega)\left(\coth\Big(\frac{\beta\hbar\omega}{2}\Big)\cos\omega t - i\sin\omega t\right)\mathrm{d}\omega. \tag{A.0.46}$$

Different forms of the correlation function, such as autocorrelation, real and imaginary components are labelled as a subscript.

Transition Frequency Fluctuation Magnitude

The magnitude of fluctuations in the excited state energy profile is defined as Δ_n.

Correlation Time

The timescale for the decay of correlations within the excited state energy profile is τ_c. This is equivalent to the time taken for the bath to return to equilibrium after being perturbed.

The Overdamped Bath Dissipation Rate

The overdamped bath dissipation (dephasing) rate is defined as Λ. This relates to the underdamped equivalent through

$$\Lambda = \frac{\omega_0^2}{\gamma} = \frac{1}{\tau_\mathrm{c}}. \tag{A.0.47}$$

The Underdamped Bath Dissipation Rate

The underdamped bath dissipation (damping) rate is defined as γ.

The Vibrational Mode Frequency

The frequency of underdamped vibrational mode in bath is defined as ω_0.

The Electric Field

Via the semi-classical approximation an external electromagnetic field can be introduced where:

$$\boldsymbol{\mathcal{E}}_{\mathrm{I}}(\mathbf{r},t)=\sum_{m}\hat{\mathbf{e}}_{m}\chi_{m}E'(t-\tau_{m})\Bigg(\exp(-i\omega_{m}t+i\mathbf{k}_{m}\cdot\mathbf{r})+\exp(i\omega_{m}t-i\mathbf{k}_{m}\cdot\mathbf{r})\Bigg), \tag{A.0.48}$$

with circular frequency, $\omega_m = 2\pi\nu_m$, wavevector, $\mathbf{k}_m$, of magnitude $|\mathbf{k}_m| = \frac{\omega}{c}$, and field strength χ_m, in V m^{-1}. The unit vector, $\hat{\mathbf{e}}_m$, defines the polarisation of each pulse. Additionally, this can be split into two components, when directional dependence has been removed:

$$\mathcal{E}_{\mathrm{I}}=\mathfrak{E}(t)+\mathfrak{E}^{*}(t). \tag{A.0.49}$$

Field Envelope Function

The field envelope of the laser field is assumed to be Gaussian and centred at τ_m such that

$$E'(t-\tau_{m})=\exp\Big(-\frac{(t-\tau_{m})^{2}}{2\varsigma^{2}}\Big), \tag{A.0.50}$$

with a full-width-at-half-maximum (FWHM) $\tau_{1/2} = 2\varsigma\cdot\sqrt{2\ln 2}$ in the time domain, which is equivalent to $\tau_{1/2}^{(\nu)} = \frac{4\ln 2}{\pi c\tau_{1/2}}$ in the frequency domain. This temporal 'width', ς, is analogous to the spatial width, σ_{g}.

The Electric Field Strength

The electric field strength of the mth pulse is defined as χ_m.

Bosonic Correlation Functions

The correlation of different boson emission events can be produced from the creation and annihilation operators in a normalised, or non-normalised form as:

$$g^{(1)}(t,\tau)=\frac{\langle \mathrm{c}(t)\mathrm{c}^{\dagger}(t+\tau)\rangle}{\langle \mathrm{c}(t)\mathrm{c}^{\dagger}(t)\rangle}, \tag{A.0.51}$$

$$g^{(2)}(t,\tau) = \frac{\langle \mathrm{c}_1(t)\mathrm{c}_2(t+\tau)\mathrm{c}_2^\dagger(t+\tau)\mathrm{c}_1^\dagger(t)\rangle}{\langle \mathrm{c}_1(t)\mathrm{c}_2(t)\mathrm{c}_2^\dagger(t)\mathrm{c}_1^\dagger(t)\rangle}, \tag{A.0.52}$$

and

$$G^{(2)}_{\mathrm{c}_1\mathrm{c}_2}(t,\tau) = \mathrm{Tr}\Big(\mathrm{c}_1^\dagger \mathrm{c}_2 \exp(\mathcal{L}\tau)(\mathrm{c}_1\rho\mathrm{c}_2^\dagger)\Big). \tag{A.0.53}$$

The equation can be extended to an mth order correlation

$$g^{(m)}(t,t_1,\ldots,t_m) = \frac{\langle \boldsymbol{\mathcal{E}}^-(t)\boldsymbol{\mathcal{E}}^-(t^{(1)})\ldots\boldsymbol{\mathcal{E}}^-(t^{(m)})\boldsymbol{\mathcal{E}}^+(t^{(m)})\ldots\boldsymbol{\mathcal{E}}^+(t^{(1)})\boldsymbol{\mathcal{E}}^+(t)\rangle}{\langle|\boldsymbol{\mathcal{E}}(t)|\rangle\,\langle|\boldsymbol{\mathcal{E}}(t^{(1)})|\rangle\ldots\langle|\boldsymbol{\mathcal{E}}(t^{(m)})|\rangle}, \tag{A.0.54}$$

where $t^{(m)} = \sum_{i=1}^{m} t_i$. First order correlations are equivalent to the excited state population (an amplitude), and second order correlations are equivalent to a joint detection probability (an intensity). When $\tau = 0$ these are called simultaneous time correlation functions, and measure an instantaneous correlation, whereas when $\tau > 0$ they are two-time correlations.

The Molecular Response Function

The molecular response function (for an m pulse technique) contains information about the system structure and its interaction with the environment and takes the form:

$$\begin{aligned} &R^{(m)}(t_m,\ldots,t_1) = \\ &\quad -\Big(-\frac{i}{\hbar}\Big)^m \langle \mu(t_m+\ldots+t_1)[\mu(t_{m-1}+\ldots+t_1),\ldots[\mu(0),\rho_{\mathrm{S}}(-\infty)]\ldots]\rangle\,. \end{aligned} \tag{A.0.55}$$

The Polarisation

The polarisation after interaction (with m pulses) can be written as

$$\begin{aligned} P^{(m)}(t) = \int_0^\infty \int_0^\infty \ldots \int_0^\infty &\mathcal{E}_{\mathrm{I}}(t-t_m)\mathcal{E}_{\mathrm{I}}(t-t_m-t_{m-1})\cdot\ldots \\ &\times \mathcal{E}_{\mathrm{I}}(t-t_m-\ldots-t_1)R^{(m)}(t_m,\ldots,t_1)\,\mathrm{d}t_1\ldots\,\mathrm{d}t_{m-1}\,\mathrm{d}t_m. \end{aligned} \tag{A.0.56}$$

The Fourier Transform

The Fourier transform decomposes a waveform, in the time domain, into its constituent frequencies, in the frequency domain, as a Fourier spectrum. This process is denoted by a tilde:

$$\tilde{f}(\omega) = \mathcal{F}_{\mathrm{Fou}}[f(t)] = \frac{1}{\sqrt{2\pi}}\int_{-\infty}^{\infty} \exp(-ik\omega)f(t)\,\mathrm{d}\omega. \tag{A.0.57}$$

Convolution

$$\mathcal{M}(k;\Delta,\Gamma) = \frac{1}{\sqrt{2\pi}} \iint_{-\infty}^{\infty} G(\omega';\Delta) L(\omega-\omega';\Gamma) e^{-ik\omega}\, \mathrm{d}\omega\, \mathrm{d}\omega',$$

is strictly

$$\mathcal{M}(k;\Delta,\Gamma) = \frac{1}{\sqrt{2\pi}} \int_{-\infty}^{\infty} \left(\int_{-\infty}^{\infty} G(\omega';\Delta) L(\omega-\omega';\Gamma)\, \mathrm{d}\omega \right) e^{-ik\omega}\, \mathrm{d}\omega'.$$

Substitute $\eta = \omega - \omega'$ to solve,

$$\mathcal{M}(k;\Delta,\Gamma) = \frac{1}{\sqrt{2\pi}} \iint_{-\infty}^{\infty} G(\omega';\Delta) L(\eta;\Gamma) e^{-ik(\eta+\omega')}\, \mathrm{d}\eta\, \mathrm{d}\omega'.$$

This enables the splitting of the integral into two parts

$$\mathcal{M}(k;\Delta,\Gamma) = \frac{1}{\sqrt{2\pi}} \int_{-\infty}^{\infty} G(\omega';\Delta) e^{-ik\omega'}\, \mathrm{d}\omega' \int_{-\infty}^{\infty} L(\eta;\Gamma) e^{-ik\eta}\, \mathrm{d}\eta.$$

The first half of this equation is exactly the definition of the Fourier transform, the second half is missing a factor of $1/\sqrt{2\pi}$ which we account for, resulting in

$$\mathcal{I}(k;\Delta,\Gamma) = \sqrt{2\pi}\, \mathcal{G}(k;\Delta) \mathcal{L}(k;\Gamma).$$

Translation Property of Fourier Transforms

$$\mathcal{G}(k;\Delta) = \frac{1}{\sqrt{2\pi}} \int_{-\infty}^{\infty} \frac{e^{-((\omega-\omega_{eg})/2\Delta)^2}}{\Delta\sqrt{2\pi}} e^{-ik\omega}\, \mathrm{d}\omega,$$

substitute $\eta = \omega - \omega_{eg}$ such that,

$$\mathcal{G}(k;\Delta) = \frac{1}{\sqrt{2\pi}} \int_{-\infty}^{\infty} \frac{e^{-(\eta/2\Delta)^2}}{\Delta\sqrt{2\pi}} e^{-ik(\eta+\omega_{eg})}\, \mathrm{d}\eta,$$

$$\mathcal{G}(k;\Delta) = \frac{e^{-ik\omega_{eg}}}{\sqrt{2\pi}} \int_{-\infty}^{\infty} \frac{e^{-(\eta/2\Delta)^2}}{\Delta\sqrt{2\pi}} e^{-ik\eta}\, \mathrm{d}\eta,$$

$$\mathcal{G}(k;\Delta) = e^{-ik\omega_{eg}} \mathcal{F}_{\mathrm{Fou}} \left[\frac{e^{-(\eta/2\Delta)^2}}{\Delta\sqrt{2\pi}} \right](k),$$

where Fou denotes the Fourier transform, to differentiate this from the influence functional.

Frequency Shift Property of Fourier Transforms

$$\int_{-\infty}^{\infty} \frac{e^{-ik\omega}}{\omega^2+\Gamma^2}\, \mathrm{d}\omega = \frac{\pi e^{\pm k\Gamma}}{\Gamma}.$$

If this function is denoted $\mathcal{J}(k;\Gamma)$ then,

$$\frac{\pi}{\Gamma}\,\mathcal{J}(k;\Gamma) = \begin{cases} e^{-k\Gamma},\ k>0 \\ e^{k\Gamma},\ k<0 \end{cases}$$

implies

$$\mathcal{J}(k;\Gamma) = \frac{\pi}{\Gamma}e^{-|k|\Gamma}.$$

Now consider

$$Z(\omega;\Gamma) = e^{ik_0\omega}J(\omega;\Gamma).$$

For this function the Fourier transform is

$$\frac{1}{\sqrt{2\pi}}\int_{-\infty}^{\infty}\frac{e^{-ik\omega}e^{ik_0\omega}}{\omega^2+\Gamma^2}\,\mathrm{d}\omega = \frac{1}{\sqrt{2\pi}}\int_{-\infty}^{\infty}\frac{e^{-i(k-k_0)\omega}}{\omega^2+\Gamma^2}\,\mathrm{d}\omega,$$

such that

$$\mathcal{Z}(k;\Gamma) = \frac{\pi}{\Gamma}e^{-|k-k_0|\Gamma}$$

Absorptive, Rephasing, and Non-Rephasing Spectra

The molecular response function and polarisation have rephasing and non-rephasing components equivalent to the absorptive spectrum. Additionally, the absorptive spectrum can be created by:

$$\tilde{P}^{(3)}_{\{\cdot\}} = S_{\{\cdot\}}(\omega_\tau, T, \omega_t), \tag{A.0.58}$$

$$S_{\mathrm{A}} = \mathcal{R}(S_{\mathrm{R}} + S_{\mathrm{NR}}). \tag{A.0.59}$$

The Laplace Operator

The second order derivative of a euclidean space which is the divergence of the gradient:

$$\nabla\cdot\nabla\{\cdot\} = \nabla^2\{\cdot\}, \tag{A.0.60}$$

which in one dimension is equivalent to the second derivative in a spatial coordinate x.

Power Spectrum of the Bath Correlation

The bath correlation function can be written as a noise-power spectrum,

$$\varpi_m = \sum_n \int_0^\infty L_{mn}(\tau)\mathrm{S}_n(-\tau)\,\mathrm{d}\tau. \tag{A.0.61}$$

The Lindbladian Superoperator

The Lindbladian superoperator, or jump operator, is an operator which describes the dissipative component of the dynamics. It is similar to other types of superoperator A. The Lindbladian is denoted $\mathfrak{L}$.

Relaxation Superoperator

$\mathrm{D}[\rho_{\mathrm{S}}(t)]$ is an arbitrary relaxation superoperator defining the interaction with the bath. Γ_{g} is a, less general, form of the relaxation superoperator due to the generator $\mathcal{L}_{\mathrm{g}}$. If the time independent component of the total Hamiltonian is written as the system contribution, H_{S}, and the relaxation superoperator is written in its most general form, $\mathrm{D}[\rho_{\mathrm{S}}(t)]$, this is equivalent to the most general master equation (ME). Depending on the other assumptions and approximations employed within the EOM the relaxation superoperator can take many different forms. Some examples include:

- Markovian approximation $\rightarrow \mathrm{D}[\rho_{\mathrm{S}}(t)] = -\epsilon^2 \sum_m [\mathrm{S}_m, \varpi_m \rho_S(t) - \rho_S(t)\varpi_m^\dagger]$. The Redfield master equation, discussed in section D.1.5
- Markovian approximation $\rightarrow$ $\mathrm{D}[\rho_{\mathrm{S}}(t)] = \sum_{\omega,l} \Big(\mathfrak{L}_l(\omega)\rho_{\mathrm{S}}(t)\mathfrak{L}_l^\dagger(\omega) - \frac{1}{2}\Big\{ \mathfrak{L}_l^\dagger \mathfrak{L}_l(\omega), \rho_{\mathrm{S}}(t) \Big\} \Big)$. The Lindblad master equation, discussed in section D.1.6.
- Non-Markovian $\rightarrow \mathrm{D}[\rho_{\mathrm{S}}(t)] = -\epsilon^2 \int_{t_0}^{t} [\mathrm{H}_{\mathrm{I}}(t), [\mathrm{H}_{\mathrm{I}}(t'), \rho_S(t)]] \ \mathrm{d}t'$. The Nakajima-Zwanzig equation, as discussed in section D.1.3.

Stochastic Friction

The parameter ζ is the associated friction of the random forcing applied by the environment ensemble in a stochastic model.

Coherent State Representation

A coherent state basis which is dependent on the creation and annihilation operators for the system modes, $\mathrm{a}_i^\dagger$ and a_i, rather than operators x_j and p_j for environment modes $\{j\}$. This representation uses

$$|\phi\rangle = \exp\Big(\sum_i \phi_i \mathrm{a}^\dagger \Big) |0\rangle \,, \tag{A.0.62}$$

where $|0\rangle$ is the vacuum sate, ϕ_i are complex numbers, and ϕ_i^* their complex conjugates such that

$$\mathrm{a}_i \left|\phi\right\rangle = \phi_i \left|\phi\right\rangle, \tag{A.0.63}$$

$$\left\langle\phi\right| \mathrm{a}_i^\dagger = \left\langle\phi\right| \phi_i^*. \tag{A.0.64}$$

This is equivalent to considering a movement onto a sphere, analogous to a Bloch sphere, and is similar to the Floquet, and Bogoliubov transforms.

Feynman and Vernon Influence Functional

The Feynman and Vernon influence functional is

$$\mathcal{F}[\mathrm{q}_t, \mathrm{q}'_t] = \iiiint \rho_{\mathrm{B}}(\mathrm{x}_0, \mathrm{x}'_0, 0) \exp(i\Big[\mathrm{S_B}[\mathrm{x}] - S_{\mathrm{B}}[\mathrm{x}'] + \mathrm{S_{SB}}[\mathrm{q}_t, \mathrm{x}] - \mathrm{S_{SB}}[\mathrm{q}'_t, \mathrm{x}']\Big]/\hbar)\ \mathcal{D}[\mathrm{x}]\mathcal{D}[\mathrm{x}']\mathrm{dx}_0\mathrm{dx}'_0\mathrm{dx}, \tag{A.0.65}$$

where $\int \mathcal{D}[\mathrm{x}]$ denotes a Feynman path integral. This contains all of the dependence on the bath coordinates, x, through the bath action and system-bath interaction actions.

Feynman Path Integral

A Feynman path integral over an infinite number of trajectories (histories) which generates the equation for the density matrix elements,

$$\rho_n(\phi, \phi^*; t) = \iint \left\{ \Big(-\frac{i}{\hbar}\Big) \int_0^t \exp(-\Lambda_{\mathrm{O}}(t-\tau)) \eta\Big(\mathrm{B}^\times - i\frac{\beta\hbar\Lambda_{\mathrm{O}}}{2}\mathrm{B}^\circ\Big)\ \mathrm{d}\tau \right\}^n \times \exp\Big(\frac{i\mathrm{S_S}[\mathrm{Q}_t]}{\hbar}\Big) \mathcal{F}[\mathrm{Q}_t, \mathrm{Q}'_t] \exp\Big(\frac{-i\mathrm{S_S}[\mathrm{Q}'_t]}{\hbar}\Big)\ \mathcal{D}[\mathrm{Q}'_t]\ \mathcal{D}[\mathrm{Q}_t], \tag{A.0.66}$$

which is differentiated to form an equation of motion. The $\mathcal{D}$ signifies that this is a path integral, over trajectories, rather than over a variable.

Closed Contour Integral

The integral around a closed curve is denoted $\oint$.

Combined Over- and Under-damped Intrinsic Damping Parameter

$\zeta_n = \sqrt{\omega_{n0}^2 - \left(\frac{\gamma_n}{2}\right)^2}$ contains the intrinsic damping parameter from any baths within the system. This can be purely real, complex, or imaginary depending on the type and number of bath contributions. For the underdamped kernels it is equivalent to that of the overdamped spectral density, however, introduction of the system mode splits the single temperature independent Matsubara frequency into two: positive and negative combinations of the intrinsic damping parameter, $\frac{\gamma_n}{2}$, and $i\zeta_n$.

Matsubara Frequencies

Matsubara frequencies arise from singularities in the spectral distribution function. These singularities become poles in a contour integral which results in Matsubara frequencies at evenly spaced energies. Further discussion of the Matsubara frequencies and dimension can be found in section 2.5.5.

HEOM Raising and Lowering Terms

The different hierarchical equation of motion all have ADO raising and lowering terms dependent on the spectral densities incorporated in their derivation. Each of these terms, which have similar forms, create and destroy phonon modes within the system and bath. Such operators include:

- ϕ_{nl} and $\Theta_n^{\pm}$
- $\Theta_{(\mathrm{O})}$ and $\psi_n^{(\mathrm{O})}$
- $\psi_{nl}^{(\mathrm{U})}$
- $\Xi^{(\mathrm{g})}$ and $\Theta_l^{(\mathrm{g})}$.

Conditional Probability Distribution

The time local equation for a general probability density function is

$$\mathrm{p}^{(\rho)}(\mathrm{x}, t + t') = \int \mathrm{p}^{(\rho)}(\mathrm{x}, t + t'|x', t)\mathrm{p}^{(\rho)}(x', t)\, \mathrm{d}x', \tag{A.0.67}$$

where $\mathrm{p}^{(\rho)}(\mathrm{x}, t + t'|x', t)$ is the conditional probability distribution function, as part of the Kramers-Moyal expansion.

Drift and Diffusion Coefficients

$\mathrm{D}^{(1)}$ is the drift and $\mathrm{D}^{(2)}$ is the diffusion coefficient generated as part of the Kraymers-Moyal expansion of the Fokker-Planck equation.

Bose-Einstein Distribution

A type of spectral distribution function, which here is the expected number of bosons in an energy state i for Bose–Einstein statistics. This is written as

$$n_{\mathrm{B}} = \frac{1}{\exp(\beta\hbar) - 1}. \tag{A.0.68}$$

Generalised Symmetric and Anti-symmetric Correlation Functions

A set of K time dependent basis functions $\phi^{(\mathrm{g})}$ are generated in order to produce symmetric and anti-symmetric correlation functions from linear combinations of this basis and the delta function:

$$\mathcal{S}(t) = \sum_{lk} \sigma_l s_{lk} \phi_k^{(\mathrm{g})}(t) + S_\delta \cdot 2\delta(t), \tag{A.0.69}$$

$$\mathcal{A}(t) = \sum_{lk} \sigma_l a_{jk} \phi_k^{(\mathrm{g})}(t), \tag{A.0.70}$$

where σ_l, s_{lk}, and a_{lk} are constants dependent on the system parameters. These correlation functions are equivalent to the fluctuation and dissipation kernels, $\mathcal{S}(t) = L_{\mathcal{R}}^{(\alpha)}(t)$, and $\mathcal{A}(t) = L_{\mathcal{I}}^{(\alpha)}(t)$, equation (2.2.53).

Canonical Partition Function

The canonical partition function, Z, is

$$Z = \sum_k \exp\Big(-\frac{\epsilon_k}{k_{\mathrm{B}}T}\Big) = \mathrm{Tr}\bigg(\exp\Big(-\frac{\mathrm{H}_{\mathrm{D}}^{\mathrm{E}}}{k_{\mathrm{B}}T}\Big)\bigg). \tag{A.0.71}$$

Hamming Apodisation Function

The Hamming apodisation functions is a method of removing experimental noise or reducing persistent singals within data. This is achieved by

$$w_{\mathrm{Ham}}(n) = a_0\bigg(1 - \cos\Big(\frac{2\pi n}{N}\Big)\bigg), \tag{A.0.72}$$

for a domain $[0, N]$ and where $a_0 = 0.54$, which limits the oscillating component of the system-bath correlation.

The Product Rule

For arbitrary functions $f(x)$, $g(x)$, and $h(x)$, where f is the product of g and h

$$f(x) = g(x)h(x), \tag{A.0.73}$$

the derivative of f can be calculated as

$$\frac{\mathrm{d}f(x)}{\mathrm{d}x} = \frac{\mathrm{d}}{\mathrm{d}x}\Big(g(x)h(x)\Big), \tag{A.0.74}$$

$$\frac{\mathrm{d}f(x)}{\mathrm{d}x} = \frac{\mathrm{d}g(x)}{\mathrm{d}x} \cdot h(x) + g(x) \cdot \frac{\mathrm{d}h(x)}{\mathrm{d}x}. \tag{A.0.75}$$

The Chain Rule

For an arbitrary function $y(x)$ which can be written through a substitution as

$$y(x) = u, \quad \text{where} \quad u = u(x), \tag{A.0.76}$$

in order to simplify further calculations, the derivative of y can be expressed as

$$\frac{\mathrm{d}y}{\mathrm{d}x} = \frac{\mathrm{d}y}{\mathrm{d}u} \cdot \frac{\mathrm{d}u}{\mathrm{d}x}. \tag{A.0.77}$$

This is highly suitable for functions of functions, $y\Big(u(x)\Big)$, an example being $\exp(-x^2)$ where $y(x) = \exp(-u)$ and $u(x) = x^2$.

The Liebniz Integral Rule

For arbitrary functions, $f(x,t)$, $a(x)$, and $b(x)$, the Liebniz rule describes differentiation under integration. For

$$\int_{a(x)}^{b(x)} f(x,t)\ \mathrm{d}t, \tag{A.0.78}$$

with $-\infty < a(x), b(x) < \infty$, then differentiation of equation (A.0.78) yields

$$\frac{\mathrm{d}}{\mathrm{d}x}\left(\int_{a(x)}^{b(x)} f(x,t)\ \mathrm{d}t\right) = f\Big(x, b(x)\Big) \cdot \frac{\mathrm{d}b}{\mathrm{d}x} - f\Big(x, a(x)\Big) \cdot \frac{\mathrm{d}a}{\mathrm{d}x} + \int_{a(x)}^{b(x)} \frac{\partial}{\partial x} f(x,t)\ \mathrm{d}t. \tag{A.0.79}$$

In the specific case of $a(x) = a$ a constant, and $b(x) = x$ this can be simplified to

$$\frac{\mathrm{d}}{\mathrm{d}x}\left(\int_a^x f(x,t)\,\mathrm{d}t\right) = f\Big(x,x\Big)\cdot\frac{\mathrm{d}b}{\mathrm{d}x} + \int_a^x \frac{\partial}{\partial x} f(x,t)\,\mathrm{d}t. \tag{A.0.80}$$

The Pauli Matrices

The Pauli matrices are a set of 2×2 complex, hermitian, unitary matrices which are used in many of the bath coupling operators of OQSs to introduce dephasing and dissipation. They take the form:

$$\sigma_x = \begin{pmatrix} 0 & 1 \\ 1 & 0 \end{pmatrix}, \tag{A.0.81}$$

$$\sigma_y = \begin{pmatrix} 0 & -i \\ i & 0 \end{pmatrix}, \tag{A.0.82}$$

$$\sigma_z = \begin{pmatrix} 1 & 0 \\ 0 & -1 \end{pmatrix}. \tag{A.0.83}$$

B Integration by Numerical Quadrature

B.1 Fourth Order Runge-Kutta

Integration of the EOMs is completed using the Fourth Order Runge-Kutta (RK4) algorithm within the FORTRAN portion of the software[326]. RK4 quadrature, which can be both numerically implicit or explicit, is an extension of the standard forward Euler quadrature for integrating an initial value problem. In the forward Euler method the area below an arbitrary function, $y(t)$, is approximated by its tangent at an initial value and then the trapezoidal area below the tangent is taken as the approximate integral of the function in the specified region. Over many iterations this generates what is known as a polygonal curve.

B.1.1 Forward Euler

The forward Euler method is the simplest of the explicit numerical quadratures and, for an ODE involving the arbitrary function $y(t)$, is expressed as

$$y_{j+1} = y_j + hf(t_j, y_j), \text{ with } t_j = t_0 + jh, \text{ and where} \tag{B.1.1}$$

$$\frac{\mathrm{d}y(t)}{\mathrm{d}t} = f(t, y(t)), \text{ with } y(t_0) = y_0. \tag{B.1.2}$$

Through a Taylor expansion of $y(t)$ is it possible to quantify the local truncation error of forward Euler:

$$y(t_0 + h) = y(t_0) + hy'(t_0) + \tfrac{1}{2}h^2y''(t_0) + \mathcal{O}(h^3), \tag{B.1.3}$$

$$\tau_{j+1} = y(t_0 + h) - y_1 = \tfrac{1}{2}h^2y''(t_0) + \mathcal{O}(h^3), \tag{B.1.4}$$

where primes denote differentiation with respect to t. The local truncation error, τ_{j+1}, is order h^2 when the third derivative is bounded. This local error is the magnitude of difference between the approximate and true solution specifically at a given point within the domain.

Similarly, we can consider the global truncation error which is a measure of convergence of the method over the entire domain. This is constructed from

Lipschitz continuity of y, which has the associated condition

$$|f(t, y_1) - f(t, y_2)| \leq L_{\text{Lip}}|y_1 - y_2|, \tag{B.1.5}$$

where, for $t = [a, b]$, and $y \in \mathbb{R}$,

$$L_{\text{Lip}} = \max\Big(\frac{\partial f}{\partial y}\Big). \tag{B.1.6}$$

By subtracting the definition of the forward Euler method from the local truncation error it is possible to generate the global error. Suppose that $\tilde{y}$ is the solution with Euler's method, then

$$e_{j+1} = e_j + h\Big(f(t_j, y_j) - f(t_j, \tilde{y}_j)\Big) + \tau_{j+1}, \tag{B.1.7}$$

which, if L_{Lip} is bounded, allows introduction of the Lipschitz property

$$|e_{j+1}| \leq (1 + L_{\text{Lip}}h)|e_j| + |\tau_{j+1}|. \tag{B.1.8}$$

This relation for the jth component can be written as a geometric series

$$|e_j| \leq (1 + L_{\text{Lip}}h)^j + \sum_{k=1}^{j}(1 + L_{\text{Lip}}h)^{j-k}|\tau_j|, \tag{B.1.9}$$

which is of the form $\sum_{k=0}^{j-1} ar^k = \frac{r^n-1}{r-1}a$. Subsequently, the global error can be expressed as

$$|e_j| \leq \frac{(1 + L_{\text{Lip}}h)^j - 1}{(1 + L_{\text{Lip}}h) - 1}|\tau_j| = \frac{y''(t_0)h}{2}\Big((1 + L_{\text{Lip}}h)^j - 1\Big). \tag{B.1.10}$$

Noticing that $(1 + L_{\text{Lip}}h) \approx \exp(L_{\text{Lip}}h)$ when h is small, the upper bound can be approximated using $(1 + L_{\text{Lip}}h)^j \leq \exp(L_{\text{Lip}}hj) = \exp(L_{\text{Lip}}(t_j - t_0))$, to

$$|e_j| \leq \frac{y''(t_0)h}{2}\Big(\exp(L_{\text{Lip}}(t_j - t_0)) - 1\Big) \approx \mathcal{O}(h). \tag{B.1.11}$$

As a result of the order h global error, the forward Euler method is considered a first order technique. This means that, in general, an approximation of the global bound can be achieved via $\frac{|\tau_j|}{h}$.

Methods with $\mathcal{O}(h)$ global error are not sufficiently accurate for use as quadrature for the EOMs within this thesis, so a more sophisticated method is applied: namely RK4.

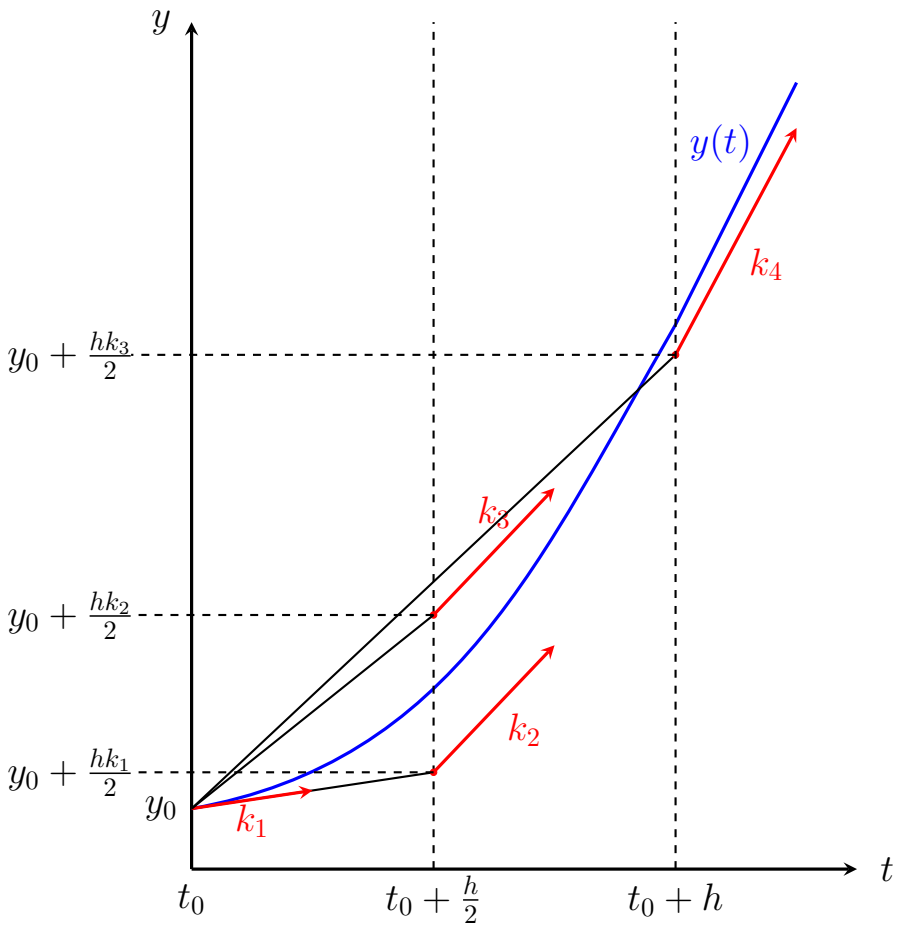

Figure B.1.1: A plot of the arbitrary function y, and the generation of the RK4 constituents, k_1, k_2, and k_3 through forward Euler, and gradients generated from combinations of the midpoint of the subdomain, $\frac{h}{2}$, and $k_{\{\cdot\}}$.

B.1.2 RK4 Quadrature

RK4 is an extension of the Euler method which is generated by improving the 'guess' applied by taking the tangent to the arbitrary curve, y. This is achieved by four steps: the first is an Euler step with a tangential approximation generating k_1. The second is the gradient at the midpoint of the subdomain, $\frac{h}{2}$, using k_1 and y in order to generate k_2. Third is the gradient component at the midpoint of the subdomain using k_2 and y in order to generate k_3. Finally the gradient at the end of the subdomain using k_3 and y is used to create k_4. This process is depicted in figure B.1.1.

The RK4 scheme, depicted in figure B.1.1, is

$$y_{j+1} = y_j + \frac{h}{6}\Big(k_1 + 2k_2 + 2k_3 + k_4\Big), \text{ with } t_{j+1} = t_j + h, \tag{B.1.12}$$

where

$$k_1 = f(t_j, y_j), \quad k_2 = f(t_j + \frac{h}{2}, y_j + \frac{hk_1}{2}), \tag{B.1.13}$$

$$k_3 = f(t_j + \frac{h}{2}, y_j + \frac{hk_2}{2}), \quad k_4 = f(t_j + h, y_j + hk_3). \tag{B.1.14}$$

It is possible to then consider the associated local error of the RK4 scheme. In full generality RK4 can be written as

$$k_1 = f(t_j, y_j), \tag{B.1.15}$$

$$k_2 = f\Big(t_j + \frac{h}{2}, y_j + \frac{h}{2}f(y_j, t_j)\Big), \tag{B.1.16}$$

$$k_3 = f\left(t_j + \frac{h}{2}, y_j + \frac{h}{2}\Big\{f\Big(t_j + \frac{h}{2}, y_j + \frac{h}{2}f(y_j, t_j)\Big)\Big\}\right), \tag{B.1.17}$$

$$k_4 = f\left(t_j + h, y_j + h\left\{f\left(t_j + \frac{h}{2}, y_j + \frac{h}{2}\Big\{f\Big(t_j + \frac{h}{2}, y_j + \frac{h}{2}f(y_j, t_j)\Big)\Big\}\right)\right\}\right). \tag{B.1.18}$$

This can be simplified by considering a test ODE, such as $f(t_j, y_j) = y_j$, which simplifies this scheme to

$$k_1 = y_j, \tag{B.1.19}$$

$$k_2 = y_j + \frac{h}{2}y_j = \Big(1 + \tfrac{h}{2}\Big)y_j, \tag{B.1.20}$$

$$k_3 = y_j + \frac{h}{2}\left(\Big(1 + \tfrac{h}{2}\Big)y_j\right) = \Big(1 + \tfrac{h}{2} + \tfrac{h^2}{4}\Big)y_j, \tag{B.1.21}$$

$$k_4 = y_j + h\left(\Big(1 + \tfrac{h}{2} + \tfrac{h^2}{4}\Big)y_j\right) = \Big(1 + \tfrac{h}{2} + \tfrac{h^2}{4} + \tfrac{h^3}{4}\Big)y_j, \tag{B.1.22}$$

such that the RK4 equation for y_{j+1} becomes

$$y_{j+1} = y_j + \frac{h}{6}\left\{y_j + 2\Big(1 + \tfrac{h}{2}\Big)y_j + 2\Big(1 + \tfrac{h}{2} + \tfrac{h^2}{4}\Big)y_j + \Big(1 + \tfrac{h}{2} + \tfrac{h^2}{4} + \tfrac{h^3}{4}\Big)y_j\right\}, \tag{B.1.23}$$

$$= \Big(1 + h + \tfrac{h^2}{2} + \tfrac{h^3}{6} + \tfrac{h^4}{24}\Big). \tag{B.1.24}$$

Hence, the local error can be found by subtracting this expansion from the Taylor series for $\exp(h)$:

$$\tau_{j+1} = \Big(1 + h + \tfrac{h^2}{2} + \tfrac{h^3}{6} + \tfrac{h^4}{24} + \tfrac{h^5}{120} + \mathcal{O}(h^6)\Big) - \Big(1 + h + \tfrac{h^2}{2} + \tfrac{h^3}{6} + \tfrac{h^4}{24}\Big), \tag{B.1.25}$$

therefore the local error is $\tau_{j+1} = \mathcal{O}(h^5)$ and subsequently the total accumulation of this error across the entire domain, or global error, is $e_{j+1} = \mathcal{O}(h^4)$. The fourth order of global error is what gives RK4 its name.

C Calculation of a Feynman Path Integral

This appendix outlines the process of calculating a Feynman path integral. This is based on the work of Feynman and Vernon[4,144], Caldeira and Leggett[214], Tanimura and Kubo[147], and Mosel[327].

C.1 Free Particle Propagator

Following the work of Mosel[327], a propagator of the form

$$\mathfrak{K}_{\text{free}}(\mathrm{x},t;\mathrm{x}_i,t_i) = N_{\mathrm{T}} \int \exp\left(\frac{i}{\hbar}\mathrm{S}_{\text{free}}\right)\mathcal{D}[\mathrm{x}], \tag{C.1.1}$$

with a normalisation constant, N_{T}, and action of the free particle, S_{free}, can be written as

$$\mathfrak{K}_{\text{free}} = \lim_{n\to\infty}\left(\frac{m}{2\pi\hbar i\eta_t}\right)^{\frac{n+1}{2}} \int_{-\infty}^{\infty} \exp\left(\frac{i}{\hbar}\eta_t \sum_{j=0}^{n}\frac{m}{2}\left(\frac{\mathrm{x}_{j+1}-\mathrm{x}_j}{\eta_t}\right)^2\right) \prod_{k=1}^{n}\mathrm{d}\mathrm{x}_k. \tag{C.1.2}$$

This is a product of Gaussian integrals, which can be computed exactly. A standard Gaussian integral takes the form, $\int_{-\infty}^{\infty}\exp\left(-\frac{1}{2}ax^2\right)\mathrm{d}x = \sqrt{\frac{2\pi}{a}}$, $a>0$ This can easily be extended to a product of n Gaussian integrals

$$\int_{-\infty}^{\infty}\exp\left(-\frac{1}{2}\sum_{k=1}^{n}a_k x_k^2\right)\mathrm{d}x_1\ldots\mathrm{d}x_n = \frac{\sqrt{(2\pi)^n}}{\prod_{k=1}^{n}\sqrt{a_k}}, \quad a_k>0. \tag{C.1.3}$$

Consequently, equation (C.1.2) can be solved by inspection through the application of equation (C.1.3) as

$$\mathfrak{K}_{\text{free}} = \lim_{n\to\infty}\left(\frac{m}{2\pi\hbar i\eta_t}\right)^{\frac{n+1}{2}}\left(\frac{(i\pi)^n}{(n+1)\left(\frac{m}{2\hbar\eta_t}\right)^n}\right)^{\frac{1}{2}}\exp\left(\frac{im}{2\hbar\eta_t(n+1)}(\mathrm{x}-\mathrm{x}_i)^2\right). \tag{C.1.4}$$

When $\mathrm{x}_{n+1}=\mathrm{x}$, $\mathrm{x}_0=\mathrm{x}_i$, and $(\eta_t+1)\eta_t = t-t_i$ this becomes

$$\mathfrak{K}_{\text{free}}(\mathrm{x}-\mathrm{x}_i,t-t_i) = \sqrt{\frac{m}{2\pi\hbar i(t-t_i)}}\exp\left(\frac{i}{\hbar}\frac{m(\mathrm{x}-\mathrm{x}_i)^2}{2(t-t_i)}\right), \quad \text{for } t_i\le t. \tag{C.1.5}$$

D Derivations from first principles

D.1 Equations of Motion

D.1.1 The Schrödinger Equation

The Schrödinger equation is constructed as less of a mathematically rigorous derivation, but rather through physical considerations[113,328,329]. First we consider the similarities to the classical wave equation and then we construct the Schrödinger equation as a quantum equivalent of Newton's second law[330]: *When a body is acted upon by a force, the time rate of change of its momentum equals the force*. This means that, given an initial condition, the energy and momentum can be used to generate a numerically explicit description of future conditions of the system.

D.1.1.1 Particles Like Classical Waves

From Newton's second law, and Hooke's law we can generate the classical wave equation[331]:

$$F_{\text{Newton}} = ma(t), \tag{D.1.1}$$

$$= m\frac{\partial^2 u(x+h,t)}{\partial^2 t}. \tag{D.1.2}$$

If we consider the classical wave equation, then the force exerted on a mass m at $x+h$ is

$$F_{\text{Hooke}} = F_{x+2h} - F_x, \tag{D.1.3}$$

$$= k\{u(x+2h,t) - u(x+h,t)\} - k\{u(x+h,t) - u(x,t)\}. \tag{D.1.4}$$

If we then consider extending this so that there is an array of N weights over a distance $L = Nh$, a total mass $M = Nm$, and a total spring constant $K = k/N$,

and by equating the two forces

$$\frac{\partial^2 u(x+h,t)}{\partial^2 t} = \frac{KL^2}{M}\frac{u(x+2h,t)-2u(x+h,t)+u(x,t)}{h^2}, \tag{D.1.5}$$

$$\tag{D.1.6}$$

then in the limit $N \to \infty$, $h \to 0$ this becomes a full second derivative resulting in the classical wave equation:

$$\frac{\partial^2 u(x,t)}{\partial^2 t} = v^2 \frac{\partial^2 u(x,t)}{\partial^2 x}, \tag{D.1.7}$$

where v is the wave propagation speed.

D.1.1.2 Quantum Mechanics

Intrinsically, the Schrödinger equation is a quantum wave equation which describes matter waves through the wavefunction. The eigenfunction is a superposition of two plane waves, with equal but opposite momenta $\pm p$, forming a standing wave in analogy with a classical string standing wave. In analogy with this classical string we propose a one dimensional wavefunction, which is separable

$$\psi(x,t) = f(x)g(t). \tag{D.1.8}$$

If we propose that the wavefunction, in the x coordinate, is periodic with a period of 2π, takes the form of a simple sinusoid, and moves strictly from left to right then

$$f(x) = \exp\Big(\frac{2\pi i x}{\lambda}\Big). \tag{D.1.9}$$

By substituting this into the classical wave equation we generate a second order homogeneous ordinary differential equation

$$\frac{\mathrm{d}^2 g}{\mathrm{d}t^2} = -\frac{v^2 4\pi^2}{\lambda^2} g, \tag{D.1.10}$$

which when solved using an auxiliary equation with $g = \exp(ct)$, with the substitution $\lambda = v/\omega$

$$g'' + \frac{v^2 4\pi^2}{\lambda^2} g = 0 \tag{D.1.11}$$

$$c^2 + 4\pi^2\omega^2 = 0. \tag{D.1.12}$$

Subsequently the wavefunction takes the form

$$\psi(x,t) = \exp\Big(2\pi i\Big(\frac{x}{\lambda} - \omega t\Big)\Big). \tag{D.1.13}$$

If this is differentiated with respect to time

$$\frac{\mathrm{d}\psi}{\mathrm{d}t} = -2\pi i\omega\psi, \tag{D.1.14}$$

which simplifies via Planck's equation, $E = h\omega$, to

$$\frac{\mathrm{d}\psi}{\mathrm{d}t} = -\frac{iE}{\hbar}\psi. \tag{D.1.15}$$

The derivatives in space of the wavefunction are

$$\frac{\mathrm{d}\psi}{\mathrm{d}x} = \frac{2\pi i}{\lambda}\psi, \tag{D.1.16}$$

$$\frac{\mathrm{d}^2\psi}{\mathrm{d}x^2} = -\frac{4\pi^2}{\lambda^2}\psi, \tag{D.1.17}$$

which simplifies by substitution of the De Broglie formula, $\mathrm{p} = h/\lambda$,

$$\frac{\mathrm{d}^2\psi}{\mathrm{d}x^2} = -\frac{\mathrm{p}^2}{\hbar^2}\psi. \tag{D.1.18}$$

Finally we assume that the particle is nonrelativistic such that the energy and momentum can be related by: $E = (1/2)mv^2 = \mathrm{p}^2/2m$ and substitute the forms of the wavefunction

$$-\frac{\hbar^2}{2m}\frac{\mathrm{d}^2\psi}{\mathrm{d}x^2} = i\hbar\frac{\mathrm{d}\psi}{\mathrm{d}t}. \tag{D.1.19}$$

This is the one-dimensional Schrödinger equation for a free particle. This can be immediately generalised to include trapped particles where there is a non-zero potential energy term, $E = (1/2)mv^2 + V(x)$, and to higher dimensions:

$$i\hbar\frac{\partial}{\partial t}\psi(\mathbf{r},t) = \Big\{ -\frac{\hbar^2}{2m}\nabla^2 + V(\mathbf{r})\Big\}\psi(\mathbf{r},t). \tag{D.1.20}$$

From this derivation it is clear that we are considering a single nonrelativistic particle, which is either trapped or free, in microscopic continuous coordinates. In addition, since the energy is conserved we are dealing with a system of conservation laws for a closed system. In order to model dissipative open systems many of these assumptions need to be relaxed, the first set which we will tackle are the microscopic continuous variables and single particle nature: we will move to quantum states of an ensemble.

D.1.2 The Liouville-von Neumann Equation

The standard, general Schrödinger equation can be written in a form involving operators[113,125] rather than functions of microscopic continuous variables by considering an eigenvector rather than an eigenfunction. The previous form of $\psi(x,t)$ is a sinusoidal function of position and time travelling from left to right.

An exponential solution such as this consists of linear combinations of right and left travelling waves, like in a classical standing wave, and as such lends itself nicely to a vector description. If we consider a Hilbert space, a space of vectors with a well defined inner product distance measure, then a state of the quantum mechanical system can be defined as a colum vector, $|\psi\rangle$. This vector is normalised by the inner product, distance, of the Hilbert space $\langle\psi|\psi\rangle = 1$, and the physical properties of the quantum system can be considered as operators which act on the Hilbert space. Based on this construction, a space-time wavefunction can be written as a time dependent state vector inner product of positional eigenstates: $\psi(x,t) = \langle x|\psi(t)\rangle$. This means that equation (D.1.1.2) can be written as

$$i\hbar\frac{\mathrm{d}}{\mathrm{d}t}|\psi(t)\rangle = \mathrm{H}|\psi(t)\rangle\,, \tag{D.1.21}$$

and it now defines the evolution of a pure state. A pure state is best understood as being a vector which lies on the surface of the Bloch sphere, where the Bloch sphere is a visualisation of the state space for a qubit. As these states lie on the surface of the sphere, they are extreme and independent, and they cannot be written as linear combinations of other pure states. In contrast, a mixed state is a state which can be written as a combination of pure states, and this corresponds to some point within the volume of the Bloch sphere. Pure and mixed states are depicted in figure D.1.1.

As an example consider the red line within figure D.1.1 as a vector $\mathbf{r}$ in spherical coordinates $(\sin\theta\cos\phi, \sin\theta\sin\phi, \cos\theta)$. This vector can be transformed to any point on the surface of the Bloch sphere, or within its volume, with appropriate angles θ and ϕ. If we create an outer product of the resulting state vector $|\varphi\rangle$ and its transpose, then we generate an operator containing the populations and coherences of the system. This is the density operator, or density matrix describing the state $|\varphi\rangle$:

$$|\varphi\rangle\langle\varphi| = \rho, \tag{D.1.22}$$

$$\frac{1}{2}(\mathrm{I} + \mathbf{r}\cdot\boldsymbol{\sigma}) = \rho, \tag{D.1.23}$$

$$= \frac{1}{2}\begin{bmatrix} 1+r_z & r_x - ir_y \\ r_x + ir_y & 1-r_z \end{bmatrix}, \tag{D.1.24}$$

where $\boldsymbol{\sigma}$ are the Pauli matrices. This results in a useful way of differentiating pure and mixed states, as for a pure state

$$\mathrm{Tr}(\rho^2) = 1, \quad \Longrightarrow \quad |\mathbf{r}| = 1. \tag{D.1.25}$$

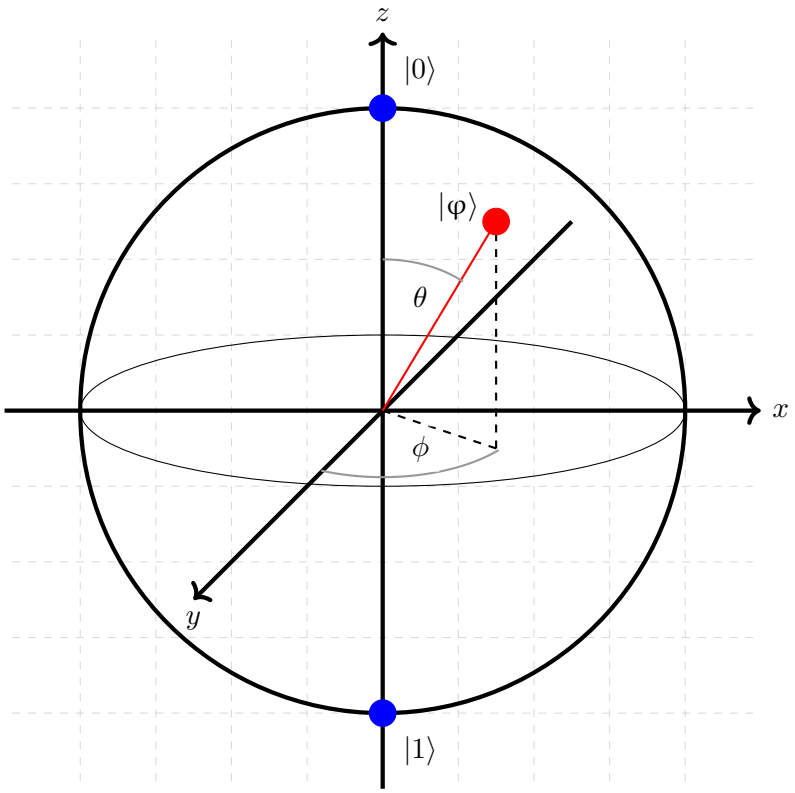

Figure D.1.1: The Bloch sphere for qubit states. Blue nodes are the up and down pure states of an electron (corresponding to basis vectors) and the surface of the sphere produces pure states. The red node is an example of a mixed state at an angle θ and ϕ. Nodes within the sphere volume are mixed states.

Subsequently an example of a pure state is

$$\rho = |\psi\rangle \langle\psi|, \tag{D.1.26}$$

$$= \frac{1}{2}\begin{bmatrix} 1 & 1 \\ 1 & 1 \end{bmatrix}, \tag{D.1.27}$$

which can be written in the $\{|0\rangle, |1\rangle\}$ basis as

$$|\psi\rangle = \frac{|0\rangle + |1\rangle}{\sqrt{2}}, \tag{D.1.28}$$

such that $\mathbf{r} = (1, 0, 0)$. The coherence terms, off diagonal elements, couple the populations together allowing for quantum interference. We can show that the basis vectors for this state are $|0\rangle$ and $|1\rangle$:

$$\det(\rho - \mathrm{I}\lambda) = \begin{bmatrix} \frac{1}{2} - \lambda & \frac{1}{2} \\ \frac{1}{2} & \frac{1}{2} - \lambda \end{bmatrix}, \tag{D.1.29}$$

$$= \lambda^2 - \lambda, \tag{D.1.30}$$

$$= \lambda(\lambda - 1), \tag{D.1.31}$$

therefore $\lambda_1 = 0$ and $\lambda_2 = 1$. This generates a pair of systems of homogeneous

linear equations which can be solved through Gaussian elimination.

$$\left[\begin{array}{cc|c} \frac{1}{2} & \frac{1}{2} & 0 \\ \frac{1}{2} & \frac{1}{2} & 0 \end{array}\right] R_1 \to R_1 \times 2 \quad \sim \quad \left[\begin{array}{cc|c} 1 & 1 & 0 \\ \frac{1}{2} & \frac{1}{2} & 0 \end{array}\right] R_2 \to R_2 - R_1$$

$$\sim \quad \left[\begin{array}{cc|c} 1 & 1 & 0 \\ 0 & 0 & 0 \end{array}\right]$$

$$\mathbf{v}_{\lambda_1} = \begin{bmatrix} 1 \\ 1 \end{bmatrix}, \quad \lambda_1 = 0. \tag{D.1.32}$$

$$\left[\begin{array}{cc|c} -\frac{1}{2} & \frac{1}{2} & 0 \\ \frac{1}{2} & -\frac{1}{2} & 0 \end{array}\right] R_1 \to R_1 \times -2 \quad \sim \quad \left[\begin{array}{cc|c} 1 & -1 & 0 \\ \frac{1}{2} & -\frac{1}{2} & 0 \end{array}\right] R_2 \to R_2 - R_1$$

$$\sim \quad \left[\begin{array}{cc|c} 1 & -1 & 0 \\ 0 & 0 & 0 \end{array}\right]$$

$$\mathbf{v}_{\lambda_2} = \begin{bmatrix} -1 \\ 1 \end{bmatrix}, \quad \lambda_1 = 1. \tag{D.1.33}$$

In contrast a mixed state has $|\mathbf{r}| < 1$, with an example being

$$\rho = |\varphi\rangle \langle\varphi| , \tag{D.1.34}$$

$$= \frac{1}{2} \begin{bmatrix} 1 & 0 \\ 0 & 1 \end{bmatrix}, \tag{D.1.35}$$

Which has basis vectors:

$$\det(\rho - \mathrm{I}\lambda) = \begin{bmatrix} \frac{1}{2} - \lambda & 0 \\ 0 & \frac{1}{2} - \lambda \end{bmatrix}, \tag{D.1.36}$$

$$= \lambda^2 - \lambda + \frac{1}{4}, \tag{D.1.37}$$

$$= \left(\lambda - \frac{1}{2}\right)^2, \tag{D.1.38}$$

therefore $\lambda_1 = \frac{1}{2}$ and $\lambda_2 = \frac{1}{2}$. This generates a pair of systems of homogeneous linear equations which can be solved through Gaussian elimination. $\lambda_{1,2}$ lead to a trivial set of linear equations such that

$$\left[\begin{array}{cc|c} 0 & 0 & 0 \\ 0 & 0 & 0 \end{array}\right]$$

$$\mathbf{v}_{\lambda_1} = \begin{bmatrix} 1 \\ 0 \end{bmatrix}, \tag{D.1.39}$$

$$\mathbf{v}_{\lambda_2} = \begin{bmatrix} 0 \\ 1 \end{bmatrix}, \quad \lambda_1 = \frac{1}{2}. \tag{D.1.40}$$

This particular mixed state has $\mathbf{r} = (0, 0, 0)$ on the interior of the Bloch sphere. Given these definitions we are free to extend the definition of the Schrödinger equation in equation (D.1.2) to evolve the density matrix. If we take the density matrix for an ensemble of particles with p_i the weighting probability[332,333],

$$\rho = \sum_i p_i \left|\psi_i\right\rangle \left\langle\psi_i\right|, \tag{D.1.41}$$

and differentiate it with respect to time to get

$$\frac{\partial \rho}{\partial t} = \left(\frac{\partial}{\partial t}\left|\psi\right\rangle\right)\left\langle\psi\right| + \left|\psi\right\rangle\left(\frac{\partial}{\partial t}\left\langle\psi\right|\right). \tag{D.1.42}$$

Into this we substitute for the quantities contained by parentheses from equation (D.1.2) and its complex conjugate yielding

$$\frac{\partial \rho}{\partial t} = \frac{\mathrm{H}\left|\psi\right\rangle}{i\hbar}\left\langle\psi\right| + \left|\psi\right\rangle\frac{-\left\langle\psi\right|\mathrm{H}}{i\hbar}, \tag{D.1.43}$$

which simplifies to

$$i\hbar\frac{\partial \rho}{\partial t} = \mathrm{H}\rho - \rho\mathrm{H}, \tag{D.1.44}$$

$$i\hbar\frac{\partial \rho}{\partial t} = [\rho, \mathrm{H}], \tag{D.1.45}$$

which is the Liouville-von Neumann equation, or the Schrödinger equation for density matrices. This equation models the Markovian free propagation of an ensemble of particles in terms of states of the system. This equation has the ability to model many particles and ensemble expectation values for the observables can be calculated from the evolved states. However, it still shares a number of the same drawbacks as the general Schrödinger equation: it is a closed system for an ensemble of nonrelativistic particles. The next fundamental difficulty to tackle is the opening of the closed system so that dynamics can be obtained for a dissipative system.

D.1.3 The Nakajima-Zwanzig Equation

The Nakajima-Zwanzig equation is one method of dealing with the extreme complexity of ensembles of interest interacting with environment ensembles. This derivation starts from the Markovian free propagation, equation (D.1.2) - the Liouville-von Neumann equation, and proposes simplification based on the scale of oscillations within the total system[130,131,334]. In a process analogous to the Wentzel–Kramers–Brillouin (WKB) approximation[335] the system is split into a pair of components whose behaviour is dependent on oscillating components with intrinsic lengthscales which differ by orders of magnitude. We term these components $\mathcal{P}$ and $\mathcal{Q}$, which are the reduced density operator and the equilibrium density matrix of the bath respectively. The assumption imposes that $\mathcal{P}$ is the relevant component of the dynamics, with a fundamentally larger timescale, which can be separated from the fast oscillating thermal contribution by projection[130,131],

$$\rho = (\mathcal{P} + \mathcal{Q})\rho, \quad \mathcal{Q} \equiv (1 - \mathcal{P}). \tag{D.1.46}$$

It is this step which is fundamentally non-Markovian[336], and as such, the equation of motion for the reduced density operator will be a non-Markovian equation. In addition we fundamentally, but subtly, alter the Hamiltonian within the governing equation. We propose that

$$\mathrm{H} = \mathrm{H}_0 + \epsilon \mathrm{H}_\mathrm{I}, \tag{D.1.47}$$

where the total Hamiltonian is now written in orders of ϵ. The $\mathcal{O}(\epsilon^0)$ term is the uncoupled evolution of the system and environment, and the $\mathcal{O}(\epsilon)$ term contains the coupling between the system and bath. This is a not yet a perturbative approach[337], as we have not performed a complete expansion, we simply are able to write the Hamiltonian in terms of two orders of the dimensionless expansion parameter (associated with the interaction coupling) ϵ. Consequently, equation (D.1.2) can be written:

$$\frac{\partial \rho}{\partial t} = -\frac{i\epsilon}{\hbar}[\mathrm{H}_\mathrm{I}(t), \rho(t)], \tag{D.1.48}$$

with

$$\mathrm{H}_\mathrm{I} = \exp(i\mathrm{H}_0 t)\mathrm{H}_\mathrm{I} \exp(-i\mathrm{H}_0 t). \tag{D.1.49}$$

From this framework the Liouville-von Neumann equation in equation (D.1.3) can be recast as a pair of simultaneous equations in vector form

$$\frac{\partial}{\partial t}\begin{bmatrix}\mathcal{P}\\ \mathcal{Q}\end{bmatrix}\rho = \epsilon \begin{bmatrix}\mathcal{P}\\ \mathcal{Q}\end{bmatrix}\mathcal{L}\begin{bmatrix}\mathcal{P}\\ \mathcal{Q}\end{bmatrix}\rho + \epsilon \begin{bmatrix}\mathcal{P}\\ \mathcal{Q}\end{bmatrix}\mathcal{L}\begin{bmatrix}\mathcal{Q}\\ \mathcal{P}\end{bmatrix}\rho \tag{D.1.50}$$

where the commutator $i/\hbar[\{\cdot\}, \mathrm{H}]$ is written as the Liouville superoperator $\mathcal{L}\{\cdot\}$. Direct integration of the second equation leads to a formal solution of the form

$$\mathcal{Q}\rho = \mathcal{G}(t, t_0)\mathcal{Q}\rho(t_0) + \epsilon \int_{t_0}^{t} \mathcal{G}(t, t')\mathcal{Q}\mathcal{L}(t')\mathcal{P}\rho(t') \, \mathrm{d}t', \tag{D.1.51}$$

where

$$\mathcal{G}(t, t') \equiv T_{\leftarrow} \exp\Big(\epsilon \int_{t'}^{t} \mathcal{Q}\mathcal{L}(\tau) \, \mathrm{d}\tau\Big), \tag{D.1.52}$$

and $T_{\leftarrow}$ denotes chronological time ordering, such that the time arguments of products of super-operators increase from right to left. This propagator satisfies the following differential equation and appropriate initial condition:

$$\frac{\partial}{\partial t}\mathcal{G}(t, t') = \epsilon\mathcal{Q}\mathcal{L}(t)\mathcal{G}(t, t'), \quad \mathcal{G}(t', t') = \mathrm{I}. \tag{D.1.53}$$

By substitution of the formal solution for the bath contribution to the total density matrix into the equation for the reduced density operator, we arrive at the full Nakajima-Zwanzig equation:

$$\frac{\partial}{\partial t}\mathcal{P}\rho = \epsilon\mathcal{P}\mathcal{L}(t)\mathcal{G}(t, t_0)\mathcal{Q}\rho(t_0) + \epsilon\mathcal{P}\mathcal{L}(t)\mathcal{P}\rho(t) + \epsilon^2 \int_{t_0}^{t} \mathcal{P}\mathcal{L}(t)\mathcal{G}(t, t')\mathcal{Q}\mathcal{L}(t')\mathcal{P}\rho(t') \, \mathrm{d}t'. \tag{D.1.54}$$

This equation is completely exact as currently no expansion has been performed - ϵ is an expansion coefficient for the coupling of the system but no Taylor series has yet been used to reach this. The first term on the right hand side is an inhomogeneous contribution dependent on the initial condition of the system, and the $\mathcal{O}(\epsilon^2)$ term is the fully non-Markovian memory of past states within the interval $[t_0, t]$. Under the assumption[113] that the initial equilibrium configuration of the bath is zero, which occurs when correlations of fluctuations on different sites caused by the thermal bath is zero, or when the initial condition is factorisable - $\rho(t_0) = \rho_{\mathrm{S}}(t_0) \otimes \rho_{\mathrm{B}} \implies \mathcal{P}\rho(t_0) = \rho(t_0), \mathcal{Q}\rho(t_0) = 0$ - inhomogeneous contributions to the dynamics vanish leaving:

$$\frac{\partial}{\partial t}\rho_{\mathrm{S}} = \epsilon\mathcal{P}\mathcal{L}(t)\rho_{\mathrm{S}} + \epsilon^2 \int_{t_0}^{t} \mathcal{K}\rho_{\mathrm{S}} \, \mathrm{d}t', \tag{D.1.55}$$

$$\mathcal{K}(t, t') = \mathcal{P}\mathcal{L}(t)\mathcal{G}(t, t')\mathcal{Q}\mathcal{L}(t'), \tag{D.1.56}$$

where the non-Markovian memory kernel $\mathcal{K}$ and the reduced density operator for the system ρ_{S} have been introduced. Despite the series of transformations performed to reach the Nakajima-Zwanzig equation it is still a considerable challenge to solve this equation for the reduced density operator. This is due to the fact that the memory kernel contains the convolution of a series of superoperators - which is nontrivial to compute. In order to reduce this to a solvable equation we must now consider approximations of equation (D.1.3),

primarily achieved through genuine perturbative expansions of the componenets of the memory kernel. There are two natural choice for perturbations to approximate this equation, namely orders of the interaction Hamiltonian coupling strength or in orders of the memory time. In the latter case, expansions depend on the width of the memory kernel and the purely Markovian contribution is equivalent to a kernel of minimal width, $\mathcal{K}(t,t') \approx \delta(t-t')$. Alternatively take equation (D.1.3) and apply a perturbative expansion in orders of the interaction strength such that equation (D.1.3) can be rewritten in a more explicit form using commutators as,

$$\rho_{\mathrm{B}}(t) = \rho_{\mathrm{B}}(t_0) - i\epsilon \int_{t_0}^{t} [\mathrm{H}_{\mathrm{I}}(t'), \rho_{\mathrm{S}}(t')] \, \mathrm{d}t'. \tag{D.1.57}$$

If we substitute the commutator term into equation (D.1.3) the explicit history dependence in the total density matrix can be expanded into a set of nested commutators corresponding to a change of $t' \to t$. This resulting intermediate equation is very similar to equation (D.1.3),

$$\frac{\partial}{\partial t}\rho_{\mathrm{S}} = -i\epsilon[\mathrm{H}_{\mathrm{I}}(t), \rho_{\mathrm{S}}(t_0)] - \epsilon^2 \int_{t_0}^{t} [\mathrm{H}_{\mathrm{I}}(t), [\mathrm{H}_{\mathrm{I}}(t'), \rho_{\mathrm{S}}(t)]] \, \mathrm{d}t' + \mathcal{O}(\epsilon^3), \tag{D.1.58}$$

and is equivalent to

$$\frac{\partial}{\partial t}\rho_{\mathrm{S}} = \epsilon\mathcal{P}\mathcal{L}(t)\rho_{\mathrm{S}} + \epsilon^2 \int_{t_0}^{t} \mathcal{K}\rho_{\mathrm{S}}(t) \, \mathrm{d}t' + \mathcal{O}(\epsilon^3), \tag{D.1.59}$$

$$\mathcal{K}(t,t') = \mathcal{P}\mathcal{L}(t)\mathcal{Q}\mathcal{L}(t'). \tag{D.1.60}$$

This equation contains a Markovian assumption: if we allow the coupling between the system and environment (interaction strength) to be small, then the density matrix no longer depends on the history of time states t' and is dependent only on t. This also allows us to neglect higher order coupling terms which explicitly contain the non-Markovian contributions of this memory effect resulting in:

$$\frac{\partial}{\partial t}\rho_{\mathrm{S}} = -i\epsilon[\mathrm{H}_{\mathrm{I}}(t), \rho_{\mathrm{S}}(t_0)] - \epsilon^2 \int_{t_0}^{t} [\mathrm{H}_{\mathrm{I}}(t), [\mathrm{H}_{\mathrm{I}}(t'), \rho_{\mathrm{S}}(t)]] \, \mathrm{d}t'. \tag{D.1.61}$$

which is equivalent to

$$\frac{\partial}{\partial t}\rho_{\mathrm{S}} = \epsilon\mathcal{P}\mathcal{L}(t)\rho_{\mathrm{S}} + \epsilon^2 \int_{t_0}^{t} \mathcal{K}\rho_{\mathrm{S}} \, \mathrm{d}t', \tag{D.1.62}$$

$$\mathcal{K}(t,t') = \mathcal{P}\mathcal{L}(t)\mathcal{Q}\mathcal{L}(t'). \tag{D.1.63}$$

This can be further simplified to

$$\frac{\partial}{\partial t}\rho_{\mathrm{S}} = \epsilon^2 \int_{t_0}^{t} \mathcal{P}\mathcal{L}(t)\mathcal{L}(t')\rho_{\mathrm{S}}(t) \, \mathrm{d}t', \tag{D.1.64}$$

under the assumption that $\mathcal{P}\mathcal{L}(t)\mathcal{P} = 0$ which can be written explicitly in terms of the interaction Hamiltonian as

$$\frac{\partial}{\partial t}\rho_{\mathrm{S}} = -\epsilon^2 \int_{t_0}^{t} \mathrm{Tr}_{\mathrm{B}}[\mathrm{H}_{\mathrm{I}}(t), [\mathrm{H}_{\mathrm{I}}(t'), \rho_{\mathrm{S}}(t) \otimes \rho_{\mathrm{B}}]]\, \mathrm{d}t'. \tag{D.1.65}$$

Even this simplified form of the Nakajima-Zwanzing equation, making use of the perturbative expansion in orders of interaction strength, and factorisable initial conditions, is a formidable integro-differential equation. In principle it can be solved approximately, but it often requires significant computational effort. Specifically for this thesis the inability to control the placement of the system-bath boundary and perturbative approach to the dynamics make it a poor choice. Despite this, the equation is powerful because, before perturbation, it is exact and fully non-Markovian[113,336] however due to the difficulty associated with finding solutions it is often impractical. For this reason it is related to a number of similar equations which employ a number of different assumptions or simplifications which make them easier to solve.

D.1.4 Master Equations

As discussed in section 2.1.2, the evolution of the reduced density operator can be generated from the propagator of the dynamics, $\mathrm{V}(t, t_0)$, which accounts for the interaction with the bath through the generator $\mathcal{L}_{\mathrm{g}}(t)$, equation (2.1.17). The master equation of the reduced system has the general form[115,283]

$$\frac{\partial \rho_{\mathrm{S}}}{\partial t} = \mathcal{L}_{\mathrm{g}}(t)\rho_{\mathrm{S}}(t) = -\frac{i}{\hbar}[\mathrm{H}_{\mathrm{S}} + \mathrm{H}_{\mathrm{SF}}(t), \rho_{\mathrm{S}}] + \mathrm{D}[\rho_{\mathrm{S}}(t)], \tag{D.1.66}$$

where $\mathrm{D}[\rho_{\mathrm{S}}(t)]$ is an arbitrary relaxation superoperator defining the interaction with the bath, and where the square brackets denote the commutator. This EOM is generated from a second order perturbation of the Liouville Von-Neumann equation with a time dependent Hamiltonian:

$$i\hbar\frac{\partial \rho_{\mathrm{S}}}{\partial t} = [\mathrm{H}(t), \rho_{\mathrm{S}}], \tag{D.1.67}$$

$$= [\mathrm{H}_0 + \epsilon \mathrm{H}_1(t), \rho_{\mathrm{S}}], \tag{D.1.68}$$

such that the equation can be rewritten as[284]

$$\frac{\partial \rho_{\mathrm{S}}}{\partial t} = -\frac{i}{\hbar}[\mathrm{H}_0, \rho_{\mathrm{S}}] + \Gamma_{\mathrm{g}}\Big(\rho_{\mathrm{S}}(t) - \rho_{\mathrm{S}}(0)\Big), \tag{D.1.69}$$

where Γ_{g} is a, less general, form of the relaxation superoperator due to the generator $\mathcal{L}_{\mathrm{g}}$. If the time independent component of the total Hamiltonian is written as the system contribution, H_{S}, and the relaxation superoperator is written in its most general form, $\mathrm{D}[\rho_{\mathrm{S}}(t)]$, this is equivalent to the most general

master equation (ME).

Depending on the other assumptions and approximations employed within the EOM the relaxation superoperator can take many different forms. Some examples include:

- Markovian approximation $\rightarrow \mathrm{D}[\rho_{\mathrm{S}}(t)] = -\epsilon^2 \sum_m [\mathrm{S}_m, \varpi_m \rho_S(t) - \rho_S(t)\varpi_m^\dagger]$. The Redfield master equation, discussed in section D.1.5
- Markovian approximation $\rightarrow$ $\mathrm{D}[\rho_{\mathrm{S}}(t)] = \sum_{\omega,l} \left(\mathfrak{L}_l(\omega)\rho_{\mathrm{S}}(t)\mathfrak{L}_l^\dagger(\omega) - \frac{1}{2}\left\{ \mathfrak{L}_l^\dagger \mathfrak{L}_l(\omega), \rho_{\mathrm{S}}(t) \right\} \right)$. The Lindblad master equation, discussed in section D.1.6.
- Non-Markovian $\rightarrow \mathrm{D}[\rho_{\mathrm{S}}(t)] = -\epsilon^2 \int_{t_0}^t [\mathrm{H}_{\mathrm{I}}(t), [\mathrm{H}_{\mathrm{I}}(t'), \rho_S(t)]] \ \mathrm{d}t'$. The Nakajima-Zwanzig equation, as discussed in section D.1.3.

D.1.5 The Bloch-Redfield Master Equation

The first alteration to the Nakajima-Zwanzig approach, which is another generalisation of the Liouville-von Neumann equation, is the Bloch-Redfield equation. This is a further generalisation, it is a master equation for quantum applications and it describes the evolution of the density matrix and all off-diagonal elements rather than probabilities of continuous variables[113,121,338]. The Nakajima-Zwanzig equation is a formally exact solution to the quantum master equation but it is very difficult to solve, and as such approximations and simplifying assumptions, as used to generate the Redfield equation, make finding solutions much more manageable. This derivation also considers alterations to the Liouville-von Neumann equation which results in an intermediate form of the Nakajima-Zwanzig equation. Beginning from

$$\frac{\partial}{\partial t}\rho_{\mathrm{S}} = -\epsilon^2 \int_{t_0}^{t} \mathrm{Tr}_{\mathrm{B}}[\mathrm{H}_{\mathrm{I}}(t), [\mathrm{H}_{\mathrm{I}}(t'), \rho_{\mathrm{S}}(t') \otimes \rho_{\mathrm{B}}]] \ \mathrm{d}t', \tag{D.1.70}$$

we simplify further by applying the Born-approximation: there is never any entanglement of the system and environment in such a way that they are fully factorisable. Such an approximation is valid in the weak coupling limit which was used as part of the perturbative approach to simplify the Nakajima-Zwanzig equation. In addition we apply the Markovian approximation which allows the explicit history dependence in the total density matrix to be removed (a change of $t' \rightarrow t$) such that

$$\frac{\partial}{\partial t}\rho_{\mathrm{S}} = -\epsilon^2 \int_{t_0}^{t} \mathrm{Tr}_{\mathrm{B}}[\mathrm{H}_{\mathrm{I}}(t), [\mathrm{H}_{\mathrm{I}}(t'), \rho_{\mathrm{S}}(t) \otimes \rho_{\mathrm{B}}(t_0)]] \ \mathrm{d}t'. \tag{D.1.71}$$

This step takes a time non-local master equation to a time local equation for the density matrix which is much simpler to generate solutions from. However, this equation still contains, implicitly, components which are not fully Markovian from the limit of initial conditions. In order to make the equation fully Markovian[113] we eliminate t_0 through shifting $t_0 \to -\infty$ and $t' \to \tau = t - t'$, which instead introduces the initial equilibrium value of the bath which is assumed to be decoupled from the system

$$\frac{\partial}{\partial t}\rho_{\mathrm{S}} = -\epsilon^2 \int_0^\infty \mathrm{Tr}_{\mathrm{B}}[\mathrm{H}_{\mathrm{I}}(t), [\mathrm{H}_{\mathrm{I}}(t-\tau), \rho_{\mathrm{S}}(t) \otimes \rho_{\mathrm{B}}]]\, \mathrm{d}\tau. \tag{D.1.72}$$

The next assumption additionally splits the bath interaction Hamiltonian into a factorisable form, in an equivalent manner to that of the states of the system,

$$\mathrm{H}_{\mathrm{I}} = \sum_n \mathrm{S}_n \otimes \mathrm{E}_n, \tag{D.1.73}$$

where the operator S_n acts purely on the system degrees of freedom, and the operator E_n acts solely on the bath. Through such a transformation we can introduce the correlation function for the bath influence and system operators:

$$\frac{\partial}{\partial t}\rho_{\mathrm{S}} = -\epsilon^2 \sum_{m,n} \int_0^\infty \Big\{ L_{mn}(\tau)[\mathrm{S}_m(t), \mathrm{S}_n(t-\tau)\rho_{\mathrm{S}}] - L^*_{mn}(\tau)[\mathrm{S}_m(t), \rho_{\mathrm{S}}(t)\mathrm{S}_n(t-\tau)] \Big\}\, \mathrm{d}\tau, \tag{D.1.74}$$

where $L_{mn}(\tau) = \mathrm{Tr}_{\mathrm{B}}(\mathrm{E}_m(t)\mathrm{E}_m(t-\tau)\rho_{\mathrm{B}})$ and the environmental density matrix is at the initial equilibrium value - a steady state. Finally, by writing the bath correlation function as a noise-power spectrum,

$$\varpi_m = \sum_n \int_0^\infty L_{mn}(\tau)\mathrm{S}_n(-\tau)\, \mathrm{d}\tau, \tag{D.1.75}$$

$$\frac{\partial}{\partial t}\rho_{\mathrm{S}}(t) = -i\epsilon[\mathrm{H}, \rho_{\mathrm{S}}(t)] - \epsilon^2 \sum_m [\mathrm{S}_m, \varpi_m \rho_{\mathrm{S}}(t) - \rho_{\mathrm{S}}(t)\varpi_m^\dagger], \tag{D.1.76}$$

which is the general form of the Bloch-Redfield master equation[121]. This master equation is generally much easier to solve than the exact Nakajima-Zwanzig equation because of the series of Markovian assumptions, weak coupling limit and factorisability conditions imposed. However, as a consequence of this the populations within the density matrix for the Redfield equation are no longer strictly positive. One further simplification can be considered: the secular approximation. This restricts the environmental resonant frequencies and is only valid for long timescales. While we do not go into the secular approximation in detail here, it is worth noting that through the secular approximation every Bloch-Redfield master equation can be transformed into a master equation of Lindblad type, which is the next approximation considered.

D.1.6 The Lindblad Master Equation

Next we consider a similar alteration to the Nakajima-Zwanzig approach, which is another generalisation of the Liouville-von Neumann equation[113]. As mentioned this is the Lindblad equation or the Gorini-Kossakowski-Sudarashan-Lindblad equation[339] which relates to the Bloch-Redfield form through the secular approximation. We start from a form of the Redfield equation, but apply the additional rotating wave approximation[125] which discounts extremely rapid oscillations.

$$\frac{\partial}{\partial t}\rho_{\mathrm{S}} = -\epsilon^2 \int_0^{\infty} \mathrm{Tr}_{\mathrm{B}}[\mathrm{H}_{\mathrm{I}}(t), [\mathrm{H}_{\mathrm{I}}(t-\tau), \rho_{\mathrm{S}}(t) \otimes \rho_{\mathrm{B}}]]\, \mathrm{d}\tau, \tag{D.1.77}$$

and again, we assume that the Hamiltonian for the interaction is also factorisable[125] into the form

$$\mathrm{H}_{\mathrm{I}} = \sum_n \mathrm{S}_n \otimes \mathrm{E}_n, \tag{D.1.78}$$

however we also must consider the resonant frequencies. Here S_n generates the eigenvalues of the Hamiltonian when it is applied such that it follows

$$\mathrm{S}_n = \sum_n \mathrm{S}_n(\omega_n), \tag{D.1.79}$$

and

$$[\mathrm{H}, \mathrm{S}_n(\omega)] = -\omega \mathrm{S}_n(\omega), \quad [\mathrm{H}, \mathrm{S}_n^{\dagger}(\omega)] = \omega \mathrm{S}_n^{\dagger}(\omega). \tag{D.1.80}$$

Equation (D.1.6) is an eigen-expansion of the system operator, and in order to apply it we must revert to the Schrödinger picture for the interaction Hamiltonian acting on the system Hilbert space. This is achieved by applying the unitary evolution operators to the eigen-expansion and bath operator

$$\tilde{\mathrm{S}}_j(\omega) = \exp(i\mathrm{H}t)\mathrm{S}_j(\omega)\exp(-i\mathrm{H}t), \quad \tilde{\mathrm{E}}_j = \exp(i\mathrm{H}_{\mathrm{B}}t)\mathrm{E}_j\exp(-i\mathrm{H}_{\mathrm{B}}t), \tag{D.1.81}$$

(note that the environment operators are still in the interaction picture) which after substitution yields

$$\tilde{\mathrm{H}}_k(t) = \sum_{j,\omega} \exp(-i\omega t)\mathrm{S}_j(\omega) \otimes \tilde{\mathrm{E}}_j t, \tag{D.1.82}$$

$$= \sum_{j,\omega} \exp(i\omega t)\mathrm{S}_j^{\dagger}(\omega) \otimes \tilde{\mathrm{E}}_j^{\dagger} t. \tag{D.1.83}$$

Expansion of the commutators in the Redfield equation are required to substitute these expansions

$$\frac{\partial}{\partial t}\rho_{\mathrm{S}}(t) = -\epsilon^2 \mathrm{Tr}_{\mathrm{B}}\Big(\int_0^\infty \mathrm{H}_{\mathrm{I}}(t)\mathrm{H}_{\mathrm{I}}(t-\tau)\rho_{\mathrm{S}}(t)\otimes\rho_{\mathrm{B}}\,\mathrm{d}\tau - \int_0^\infty \mathrm{H}_{\mathrm{I}}(t)\rho_{\mathrm{S}}(t)\otimes\rho_{\mathrm{B}}\mathrm{H}_{\mathrm{I}}(t-\tau)\,\mathrm{d}\tau - \int_0^\infty \mathrm{H}_{\mathrm{I}}(t-\tau)\rho_{\mathrm{S}}(t)\otimes\rho_{\mathrm{B}}\mathrm{H}_{\mathrm{I}}(t)\,\mathrm{d}\tau + \int_0^\infty \rho_{\mathrm{S}}(t)\otimes\rho_{\mathrm{B}}\mathrm{H}_{\mathrm{I}}(t-\tau)\mathrm{H}_{\mathrm{I}}(t)\,\mathrm{d}\tau\Big), \tag{D.1.84}$$

which upon substitution yields an equation very similar to equation (D.1.5) but with τ dependence removed from the system contribution and explicit dependence on the resonant frequencies introduced

$$\frac{\partial}{\partial t}\rho_{\mathrm{S}}(t) = -\epsilon^2 \sum_{\omega,\omega',j,k} \Big(\exp(i(\omega'-\omega)t)L_{jk}(\omega)[\mathrm{S}_k(\omega)\rho_{\mathrm{S}}(t), \mathrm{S}_j^\dagger(\omega')] + \exp(i(\omega-\omega')t)L_{jk}^*(\omega')[\mathrm{S}_k(\omega), \rho_{\mathrm{S}}(t)\mathrm{S}_j^\dagger(\omega')]\Big), \tag{D.1.85}$$

where $L_{jk}(\omega) = \int_0^\infty \exp(i\omega t')\mathrm{Tr}_{\mathrm{B}}(\tilde{\mathrm{E}}_j^\dagger(t)\tilde{\mathrm{E}}_k(t-t')\rho_{\mathrm{B}})\ \mathrm{d}t'$, which is the eigen-expansion of the correlation function of the bath influence. It is now clear how the secular expansion relates the Redfield and Lindblad forms of the master equation based on the explicit frequency dependence. Additionally we can apply the rotating wave equation $|\omega-\omega'| \gg \epsilon^2$, which in the weak coupling limit $\epsilon \to 0$ leaves only contributions at the resonant frequency $\omega = \omega'$. This simplifies the equation for ρ_{S} to

$$\frac{\partial}{\partial t}\rho_{\mathrm{S}}(t) = -\epsilon^2 \sum_{\omega,j,k} \Big(L_{jk}(\omega)[\mathrm{S}_k(\omega)\rho_{\mathrm{S}}(t), \mathrm{S}_j^\dagger(\omega')] + L_{jk}^*(\omega)[\mathrm{S}_k(\omega), \rho_{\mathrm{S}}(t)\mathrm{S}_j^\dagger(\omega)]\Big). \tag{D.1.86}$$

However to reach this equation, we employed an eigen-expansion in the Schrödinger picture for the system components, but in the interaction picture for the bath contributions. In order to reach the full master equation we need to revert solely to the Schrödinger picture. We achieve this by splitting the bath correlation function into Hermitian and non-Hermitian parts

$$L_{jk}(\omega) = \frac{1}{2}(i\mathfrak{G}_{jk}(\omega) + \pi_{jk}(\omega)), \tag{D.1.87}$$

$$\pi_{jk} = L_{jk}(\omega) + L_{jk}^*(\omega), \tag{D.1.88}$$

$$= \int_{-\infty}^\infty \exp(i\omega t')\mathrm{Tr}_{\mathrm{B}}(\tilde{\mathrm{E}}_j^\dagger(t)\mathrm{E}_k\rho_{\mathrm{B}})\,\mathrm{d}t', \tag{D.1.89}$$

$$\mathfrak{G}_{jk}(\omega) = -i(L_{jk}(\omega) - L_{jk}^*(\omega)). \tag{D.1.90}$$

Substitution of these into the master equation results in

$$\frac{\partial}{\partial t}\rho_{\rm S}(t) = -i[{\rm H}+{\rm H}_{\rm L}, \rho_{\rm S}(t)]+\sum_{\omega,j,k}\pi_{jk}(\omega)\Big({\rm S}_k(\omega)\rho_{\rm S}(t){\rm S}_j^\dagger(\omega)-\frac{1}{2}\Big\{{\rm S}_j^\dagger{\rm S}_k(\omega),\rho_{\rm S}(t)\Big\}\Big), \tag{D.1.91}$$

with

$${\rm H}_{\rm L} = \sum_{\omega,j,k}\mathfrak{G}_{jk}(\omega){\rm S}_j(\omega){\rm S}_k(\omega). \tag{D.1.92}$$

Here $\rm H_L$ is the Lamb shift Hamiltonian and it renormalises the energy levels of the system in response to the interaction with the bath. Finally, since π_{jk} are positive Fourier transforms of the environment contributions we can diagonalise this operator with a unitary transformation

$${\rm O}\pi(\omega){\rm O}^\dagger = \begin{bmatrix} d_1(\omega) & 0 & \dots & 0 \\ 0 & d_2(\omega) & \dots & 0 \\ \vdots & \vdots & \ddots & \vdots \\ 0 & 0 & \dots & d_N(\omega) \end{bmatrix}, \tag{D.1.93}$$

leading to the diagonal form of the Lindblad master equation:

$$\frac{\partial}{\partial t}\rho_{\rm S}(t) = -i[{\rm H}+{\rm H}_{\rm L}, \rho_{\rm S}(t)]+\sum_{\omega,l}\Big(\mathfrak{L}_l(\omega)\rho_{\rm S}(t)\mathfrak{L}_l^\dagger(\omega)-\frac{1}{2}\Big\{\mathfrak{L}_l^\dagger\mathfrak{L}_l(\omega),\rho_{\rm S}(t)\Big\}\Big), \tag{D.1.94}$$

where $\mathfrak{L}$ is the Lindbladian (jump) operator.

D.1.7 The Quantum Langevin Equation

While the previously discussed equations are useful for producing approximate solutions, in general they are either exact and difficult to solve or easy to solve and approximate[337,340,341]. Another useful way of constructing an open, dissipative quantum system: by introducing stochastic variables[342]. In previous derivations we have made use of the fact that the Hilbert space can be split into fast and slowly oscillating components with projection operators $\mathcal{P}$ and $\mathcal{Q}$ corresponding to system and bath operators (slow and fast timescales) respectively. This required solution via a pair of coupled equations of motion where simplifying assumptions were made about the dynamics of the bath density matrix. This method proposes solution of this problem by introducing a random forcing term corresponding to a statistically distributed canonical ensemble for the bath. This treatment assumes that the system of interest is a Brownian particle surrounded by independent bath particles, which are also modelled as Brownian[177,343]. The starting point is for the total Hamiltonian consisting of a system Brownian particle in the coordinate $\rm x$ with momentum $\rm p$

and environment particles in the coordinate q_j with momenta p_j:

$$\mathrm{H} = \frac{\mathrm{p}^2}{2m} + V(\mathrm{x}) + \sum_j \Big(\frac{{\mathrm{p_j}}^2}{2m_j} + \frac{1}{2} k_j (\mathrm{q}_j - \mathrm{x})^2 \Big), \tag{D.1.95}$$

with $\{m\}$ and $\{m_j\}$ particle masses, spring constant for the Brownian particles $\{k_j\}$ and terms consisting of a bilinear interaction and an energy renormalisation. $V(\mathrm{x})$ is the potential energy of the external forces on the Brownian particle. These varibales satisfy the standard canonical commutation relations

$$[\mathrm{x}, \mathrm{p}] = i\hbar, \quad [\mathrm{q}_j, \mathrm{p}_k] = i\hbar\delta_{jk}. \tag{D.1.96}$$

The equations of motion for each of the operators in this system are governed by the Heisenberg equation such that

$$\frac{\mathrm{d}\mathrm{x}}{\mathrm{d}t} = \frac{\mathrm{p}}{m}, \quad \frac{\mathrm{d}\mathrm{p}}{\mathrm{d}t} = -\frac{\mathrm{d}V(\mathrm{x})}{\mathrm{d}\mathrm{x}} + \sum_j k_j (\mathrm{q}_j - \mathrm{x}), \tag{D.1.97}$$

and

$$\frac{\mathrm{d}\mathrm{q}_j}{\mathrm{d}t} = \frac{\mathrm{p}_j}{m_j}, \quad \frac{\mathrm{d}\mathrm{p}_j}{\mathrm{d}t} = -k_j (\mathrm{q}_j - \mathrm{x}). \tag{D.1.98}$$

In a manner analogous to the process involved in deriving the Nakajima-Zwanzig equation, we first solve for the bath components in order to generate an equation purely for the system of interest. The equations for the environment result in[344]

$$\mathrm{q}_j(t) = \mathrm{q}_j(0)\cos(\omega_j t) + \frac{\mathrm{p}_j(0)}{m_j\omega_j}\sin(\omega_j t) + \mathrm{x}(t) - \mathrm{x}(0)\cos(\omega_j t) - \int_0^t \cos(\omega_j(t-t'))\frac{\mathrm{d}\mathrm{x}}{\mathrm{d}t'}\,\mathrm{d}t', \tag{D.1.99}$$

where the natural frequency of the oscillators is $\omega_j = \sqrt{k_j/m_j}$. When this is substituted into the equation for the system of interest it becomes

$$m\frac{\mathrm{d}^2\mathrm{x}}{\mathrm{d}t^2} + \int_0^t \mathfrak{B}(t-t')\frac{\mathrm{d}\mathrm{x}}{\mathrm{d}t'} + \frac{\mathrm{d}V}{\mathrm{d}\mathrm{x}} + \mathfrak{B}(t)\mathrm{x}(0) = F_{\mathrm{LE}}(t), \tag{D.1.100}$$

where the forcing operator is

$$F_{\mathrm{LE}}(t) = \sum_j \Big(\mathrm{q}_j(0) k_j \cos(\omega_j t) + \mathrm{p}_j(0)\omega_j \sin(\omega_j t) \Big), \tag{D.1.101}$$

and

$$\mathfrak{B}(t) = \sum_j k_j \cos(\omega_j t). \tag{D.1.102}$$

In this way all of the influence due to the environment particles is contained within the forcing term. To continue we introduce the statistical average of the environment initial conditions. This is achieved by the assumption[344] that the oscillators are canonically distributed with respect to the free oscillator

Hamiltonian:

$$\mathrm{H_O} = \sum_j \frac{\mathrm{p}_j^2}{2m_j} + \frac{k_j \mathrm{q}_j^2}{2}. \tag{D.1.103}$$

Due to this we are able to take the expectation value of the initial conditions with a partial trace over the oscillator coordinates,

$$\langle \mathrm{q}_j(0)\mathrm{q}_k(0)\rangle = \frac{\langle \mathrm{p}_j(0)\mathrm{p}_k(0)\rangle}{(m_j\omega_j)^2} = \delta_{jk}\frac{\hbar\coth(\hbar\omega_j\tilde{\beta}^{-1})}{2m_j\omega_j}, \tag{D.1.104}$$

$$\langle \mathrm{q}_j(0)\mathrm{p}_k(0)\rangle = -\langle \mathrm{p}_k(0)\mathrm{q}_j(0)\rangle = \frac{i\hbar\delta_{jk}}{2}. \tag{D.1.105}$$

with $\tilde{\beta}^{-1} = 1/(2k_\mathrm{B}T)$. It can be shown, through the Gaussian property of the expectation values of the initial conditions, that symmetric correlation of the forcing operator[344–346] is

$$\frac{1}{2}\langle F_\mathrm{LE}(t)F_\mathrm{LE}(t') + F_\mathrm{LE}(t')F_\mathrm{LE}(t)\rangle = \sum_j \frac{1}{2}k_j\hbar\omega_j\coth(\hbar\omega_j\tilde{\beta})\cos(\omega_j(t-t')) \tag{D.1.106}$$

and that

$$[F_\mathrm{LE}(t), F_\mathrm{LE}(t')] = -i\hbar\sum_j k_j\omega_j\sin(\omega_j(t-t')). \tag{D.1.107}$$

Under the assumption that there are an infinite number of bath oscillators which are continuously distributed, we reach the quantum Langevin equation[344,347,348]

$$m\frac{\mathrm{d}^2\mathrm{x}}{\mathrm{d}t^2} + \zeta\frac{\mathrm{dx}}{\mathrm{d}t} + \frac{\mathrm{d}V(\mathrm{x})}{\mathrm{dx}} = F_\mathrm{LE}(t), \tag{D.1.108}$$

where ζ is a friction constant associated with the random forcing applied by the environment ensemble and the forcing operator is defined by its symmetric correlation and commutator relation:

$$\frac{1}{2}\langle F_\mathrm{LE}(t)F_\mathrm{LE}(0) + F_\mathrm{LE}(0)F_\mathrm{LE}(t)\rangle = \frac{\zeta}{\pi}\int_0^\infty \hbar\omega\coth(\hbar\omega\tilde{\beta}^{-1})\cos(\omega t)\,\mathrm{d}\omega, \tag{D.1.109}$$

$$[F_\mathrm{LE}(t), F_\mathrm{LE}(0)] = -\frac{2i\hbar\zeta}{\pi}\int_0^\infty \omega\sin(\omega t) = 2i\hbar\zeta\delta'(t). \tag{D.1.110}$$

D.1.7.1 Kubo's Stochastic Liouville Equation

When considering equations in which there are memory effects introduced by an ensemble of environmental modes it can be easier to consider the formulation through a Feynman and Vernon path integral[178]. In this formalism a sum over an infinite number of trajectories, corresponding to historical states, can be computed to generate the non-Markovian dynamics. Many exact, stochastic methods can be related to formally exact, non-perturbative

treatments of dissipative OQS through a path integral. The quantum Langevin equation is no exception. In order to present the path integral equivalent, first we consider Kubo's Stochastic Liouville equation[349], which is the 'mediator' for the transformation.

Following Kleinert[349] we consider the action generated by:

$$S_{\mathrm{T}}[\mathrm{p_x},\mathrm{p_y},\mathrm{x},\mathrm{y}] = \int_0^t \mathrm{p_x}\frac{\mathrm{dx}}{\mathrm{d}t} + \mathrm{p_y}\frac{\mathrm{dy}}{\mathrm{d}t} - \mathrm{H_T}, \tag{D.1.111}$$

where

$$\mathrm{H_T} = \frac{1}{m}(\mathrm{p_x}+g\mathrm{y})\mathrm{p_y} + V\Big(\mathrm{x}+\frac{\mathrm{y}}{2}\Big) - V\Big(\mathrm{x}-\frac{\mathrm{y}}{2}\Big) - \frac{i}{2\hbar}\mathrm{y}\mathrm{K_T}\mathrm{y}, \tag{D.1.112}$$

where $\mathrm{K_T}(t,t') = \langle F_{\mathrm{KSL}}(t)F_{\mathrm{KSL}}(t')\rangle_{F_{\mathrm{KSL}}}$ is the random noise correlation function, and the analogous noise-dependent effective action $S_{F_{\mathrm{KSL}}}[\mathrm{p_x},\mathrm{p_y},\mathrm{x},\mathrm{y}]$ with Hamiltonian

$$\mathrm{H}_{F_{\mathrm{KSL}}} = \frac{1}{m}(\mathrm{p_x}+g\mathrm{y})\mathrm{p_y} + V\Big(\mathrm{x}+\frac{\mathrm{y}}{2}\Big) - V\Big(\mathrm{x}-\frac{\mathrm{y}}{2}\Big) - \mathrm{y}F_{\mathrm{KSL}}. \tag{D.1.113}$$

Using the path integral and these actions, we can generate an alternative form of the time evolution operator:

$$\mathrm{U_S}(\mathrm{x},\mathrm{y},\mathrm{x}',\mathrm{y}',t) = \mathcal{F}_0 \int \exp\Big(\frac{iS_{\mathrm{T}}[\mathrm{p_x},\mathrm{p_y},\mathrm{x},\mathrm{y}]}{\hbar}\Big)\,\mathcal{D}[\mathrm{p_x}]\mathcal{D}[\mathrm{p_y}]\mathcal{D}[\mathrm{x}]\mathcal{D}[\mathrm{y}], \tag{D.1.114}$$

where $\mathcal{F}_0$ is the initial influence functional $\mathcal{F}_0 = \int \rho_{\mathrm{B}}(0)\mathcal{D}[X]$ for the initial condition X. As such, the noisy density matrix, $\rho_{\mathrm{S}}^{F_{\mathrm{KSL}}}(t)$, obeys the equation

$$i\hbar\rho_{\mathrm{S}}^{F_{\mathrm{KSL}}}(t) = \mathrm{H}_{F_{\mathrm{KSL}}}\rho_{\mathrm{S}}^{F_{\mathrm{KSL}}}(t), \tag{D.1.115}$$

where the reduced density matrix is obtained via

$$\rho_{\mathrm{S}}(\mathrm{x},\mathrm{y},t) = \langle \rho_{\mathrm{S}}^{F_{\mathrm{KSL}}}(t)\rangle_{F_{\mathrm{KSL}}}. \tag{D.1.116}$$

This is Kubo's Stochastic Liouville equation. When the temperature of the system becomes very large, the noise fluctuations become large and local, and the random noise correlation function becomes proportional to a delta function. This is equivalent to thermal averaging effects reducing the noise correlation time. In this limit Kubo's Stochastic Liouville equation can be written purely in terms of the density matrix, and this resulting equation is the Fokker-Planck equation with a finite bath friction.

D.1.7.2 Relation to the Forward-Backward Path Integral

It is possible to define a pair of path integrals which move forwards or backwards in time respectively. This process is useful both for solution of the integral and also for carefully managing the limits of the integration[349,350]. By defining

$$\mathrm{x}_+(0) = \mathrm{x}_1, \quad \mathrm{x}_+(t) = \mathrm{x}, \quad \mathrm{x}_-(0) = \mathrm{x}_1', \quad \mathrm{x}_-(t) = \mathrm{x}', \tag{D.1.117}$$

we can shift the original operators into the forward and backward formalism via

$$\mathrm{x} \equiv \frac{(\mathrm{x}_+ + \mathrm{x}_-)}{2}, \quad \mathrm{y} \equiv \mathrm{x}_+ - \mathrm{x}_-, \tag{D.1.118}$$

as in 349. The forward-backward path integral can then be expressed, through a unitary operator, as

$$\mathrm{U}(\mathrm{x}\mathrm{x}', \mathrm{x}_1\mathrm{x}_1', t) = \int \mathcal{F}[\mathrm{x}_+, \mathrm{x}_-] \exp\left(\frac{i}{\hbar}(\mathrm{S}_\mathrm{S}[\mathrm{x}_+] - \mathrm{S}_\mathrm{S}[\mathrm{x}_-])\right) \mathcal{D}[\mathrm{x}_+]\mathcal{D}[\mathrm{x}_-]. \tag{D.1.119}$$

Writing Kubo's Stochastic Liouville equation in forward-backward variables results in

$$i\hbar\frac{\partial}{\partial t}\rho_\mathrm{S}(t)(\mathrm{x}_+, \mathrm{x}_-, t) = \Big[\mathrm{H}_\mathrm{S}^+ - \mathrm{H}_\mathrm{S}^- + \frac{g}{2m}(\mathrm{x}_+ - \mathrm{x}_-)(\mathrm{p}_+ - \mathrm{p}_-) - (\mathrm{x}_+ - \mathrm{x}_-)\tilde{\eta}_f(t)\Big]\rho_\mathrm{S}(\mathrm{x}_+, \mathrm{x}_-, t), \tag{D.1.120}$$

with

$$\mathrm{p}_\pm = -i\hbar\frac{\partial}{\partial \mathrm{x}_\pm}, \quad \mathrm{H}_\mathrm{S}^\pm = \mathrm{H}_\mathrm{S}(\mathrm{p}_\pm, \mathrm{x}_\pm), \tag{D.1.121}$$

and where $\tilde{F}_\mathrm{KSL}$ is the adjoint operator of the operator-valued Gaussian noise[349]. The rest of this derivation is beyond the intended scope of this thesis, but a summary of the steps from Kleinert[349] is that expansion of the brakets for forward-backward variables along with expansion in terms of noisy Heisenberg operators yields the quantum Langevin equation (D.1.7). This work demonstrates the equivalence between standard projection operator approaches and numerically exact path integral methodologies through the introduction of some ensemble averaged behaviour for the bath - in this instance through a complex valued, forcing term, which takes the form of a Gaussian noise operator.

D.1.8 The Stochastic Schrödinger Equation

As we have seen so far, stochastic interpretations of open quantum systems tend to produce exact solutions or can be directly related to path integral equations which do. The quantum Langevin equation was related to a stochastic form of

the Liouville equation, and subsequently the path-integral formalism, and the same can be achieved for the Schrödinger equation. The benefit of this is that, as we have seen, the Liouville equation is formulated for mixed states, whereas the Schrödinger equation can compute the evolution of a pure state. Following the work of Carballeira[310], we outline the derivation of the Stochastic Schrödinger equation, but there are many other variations[351]. We start from the equation (D.1.2)

$$\frac{\partial}{\partial t}\left|\psi(t)\right\rangle = -\frac{i}{\hbar}\mathrm{H}\left|\psi(t)\right\rangle. \tag{D.1.122}$$

In this case the environment Hamiltonian, which is assumed to consist of an infinite number of bosonic oscillator modes, is written in the Bargmann coherent state basis,

$$\mathrm{H_B} = \sum_n \omega_n \mathrm{b}_n^\dagger \mathrm{b}_n, \tag{D.1.123}$$

where

$$\left|\alpha\right\rangle = \otimes_n \left|\alpha_n\right\rangle, \quad \mathrm{b}_n\left|\alpha\right\rangle = \alpha_n\left|\alpha_n\right\rangle, \tag{D.1.124}$$

is a coherent state. Physically, these coherent states are quantum states which can be expressed as eigenvectors of the lowering (annihilation) operator. Mathematically, they are complex valued and exist in Segal-Bargmann space which has a number of powerful properties for defininining OQS. Segal-Bargmann space is the space of holomorphic functions F^{SB} in n complex variables satisfying the square-integrability condition. Physically this means that it behaves as a type of phase-space such that, a coherent state F_α^{SB} is a probability density for a particle in phase space. In addition to this property, it is very useful to define the OQS in terms of energy, in a creation and annihilation operator basis. With this we can write the state vector for the system in a Bargmann basis

$$\left|\psi(\alpha^*, t)\right\rangle = \left\langle\alpha|\psi(t)\right\rangle, \tag{D.1.125}$$

which in the interaction picture is goverened by

$$\frac{\partial}{\partial t}\left\langle\alpha|\psi(t)\right\rangle = -\frac{i}{\hbar}\left\langle\alpha|\mathrm{H}|\psi(t)\right\rangle. \tag{D.1.126}$$

In a manner very similar to the Nakajima-Zwanzig equation, we introduce the total Hamiltonian (equation (D.1.3) in terms of the interaction Hamiltonian and its associated coupling. In this case however, the system and bath components are explicitly separate, and the interaction is written in terms of the Lindblad coupling operators, $\mathfrak{L}$, and bath mode coupling strengths, g_n:

$$\mathrm{H} = \mathrm{H_S} + \mathrm{H_B} + \epsilon\Big(\mathfrak{L}\sum_n g_n \mathrm{b}_n^\dagger + \mathfrak{L}^\dagger \sum_n g_n^* \mathrm{b}_n\Big). \tag{D.1.127}$$

This means that

$$\hbar\frac{\partial}{\partial t}\left\langle\alpha|\psi(t)\right\rangle = (-i\mathrm{H_S} + \epsilon\mathfrak{L}\alpha(t)^*)\left\langle\alpha|\psi(t)\right\rangle - i\epsilon\mathfrak{L}^\dagger\sum_n g_n^*\exp(-i\omega_n t)\left\langle\alpha|\mathrm{b}_n|\psi(t)\right\rangle, \tag{D.1.128}$$

where the complex Gaussian noise

$$\alpha(t)^* = -i\sum_n g_n\alpha_n^*\exp(i\omega_n t), \tag{D.1.129}$$

has been introduced. In addition, the system-environment evolution operator, $|\psi(t)\rangle = \mathrm{U_{SB}}(t)\,|\psi(0)\rangle$, in the interaction picture is governed by

$$\mathrm{U_{SB}}(t) = \exp(i\mathrm{H_B}t)\exp(-i\mathrm{H}t), \tag{D.1.130}$$

$$\frac{\partial}{\partial t}\mathrm{U_{SB}}(t) = -\frac{i}{\hbar}\Big(\mathrm{H_S} + \epsilon\mathfrak{L}\sum_n g_n\mathrm{b}_n^\dagger\exp(i\omega_n t) + \epsilon\mathfrak{L}^\dagger g_n^*\mathrm{b}_n\exp(-i\omega_n t)\Big)\mathrm{U_{SB}}(t). \tag{D.1.131}$$

In a manner equivalent to that taken in all previous approaches, we assume that the system and environment are initially uncorrelated such that

$$\left\langle\alpha|\mathrm{b}_n|\psi(t)\right\rangle = \left\langle\alpha|\mathrm{b}_n\mathrm{U}_{SB}(0)|\psi(0)\right\rangle, \tag{D.1.132}$$

with the environment in the vacuum state. To proceed, we consider the evolution equation (in the Heisenberg picture) of the annihilation operator, which acts as our coherent state basis,

$$\mathrm{b}_n(t) = \mathrm{U_{SB}^\dagger}(t)\mathrm{b}_n\mathrm{U_{SB}}(t), \tag{D.1.133}$$

$$\frac{\partial}{\partial t}\mathrm{b}_n(t) = \mathrm{U_{SB}}\Big(-\frac{i}{\hbar}\epsilon g_n\exp(i\omega_n t)\mathfrak{L}\Big)\mathrm{U_{SB}}(t), \tag{D.1.134}$$

$$= -\frac{i}{\hbar}\epsilon g_n\exp(i\omega_n t)\mathfrak{L}(t). \tag{D.1.135}$$

This can be solved by direct integration

$$\mathrm{b}_n(t) = \mathrm{b}_n - \frac{i}{\hbar}\epsilon g_n\int_0^t\exp(i\omega_n t')\mathfrak{L}(t')\,\mathrm{d}t', \tag{D.1.136}$$

which we can substitute into the initial condition

$$\left\langle\alpha|\mathrm{U_{SB}}(t)\mathrm{b}_n(t)|0\right\rangle = -\frac{i}{\hbar}\epsilon g_n\int_0^t\exp(i\omega_n t')\left\langle\alpha|\mathrm{U_{SB}}(t)\mathfrak{L}(t')|0\right\rangle\,\mathrm{d}t'. \tag{D.1.137}$$

The initial condition can be introduced into the second term on the right hand side of the equation of motion such that

$$\frac{\partial}{\partial t}\left|\psi(\alpha^*,t)\right\rangle = \frac{1}{\hbar}(-i\mathrm{H_S} + \epsilon\mathfrak{L}\alpha^*(t))\left|\psi(\alpha^*,t)\right\rangle - \frac{\epsilon^2}{\hbar^2}\mathfrak{L}\int_0^t L(t,t')\left\langle\alpha|\mathrm{U_{SB}}(t)\mathfrak{L}(t')|0\right\rangle\left|\psi_S(0)\right\rangle\,\mathrm{d}t', \quad \text{(D.1.138)}$$

where, similar to the previous derivations, we have introduced the zero-temperature environment correlation function $L(t,t') = \sum_n |g_n|^2 \exp(-i\omega_n(t-t'))$. We apply the chain rule of the functional derivative of the Gaussian stochastic process $\alpha^*(t)$ such that

$$\left\langle\alpha|\mathrm{b}_n\mathrm{U_{SB}}(t)|0\right\rangle = \frac{\partial}{\partial\alpha_n^*}\left\langle\alpha|\mathrm{U_{SB}}(t)|0\right\rangle = \int_0^t \frac{\partial\alpha^*(t')}{\partial\alpha_n^*}\frac{\delta}{\delta\alpha_n^*(t')}\left\langle\alpha|\mathrm{U_{SB}}(t)|0\right\rangle\,\mathrm{d}t', \quad \text{(D.1.139)}$$

and the equation of motion for the Stochastic Schrödinger equation becomes

$$\frac{\partial}{\partial t}\left|\psi(\alpha^*,t)\right\rangle = \Big(-\frac{i\mathrm{H_S}}{\hbar} + \frac{\epsilon\mathfrak{L}\alpha_n^*(t)}{\hbar} - \frac{\epsilon^2\mathfrak{L}^\dagger}{\hbar^2}\int_0^t L(t,t')\mathfrak{O}(t,t',\alpha^*)\,\mathrm{d}t'\Big)\left|\psi(\alpha^*,t)\right\rangle, \quad \text{(D.1.140)}$$

where $\mathfrak{O}$ is the ansatz of $\frac{\delta}{\delta\alpha^*(t')}\left|\psi(\alpha^*,t)\right\rangle = \mathfrak{O}(t,t',\alpha^*)\left|\psi(\alpha^*,t)\right\rangle$. This operator is associated with an equation for its evolution:

$$\frac{\partial}{\partial t}\mathfrak{O}(t,t',\alpha^*) = \Big[-\frac{i\mathrm{H_S}}{\hbar} + \frac{\epsilon\mathfrak{L}\alpha^*(t)}{\hbar} - \frac{\epsilon^2\mathfrak{L}^\dagger}{\hbar^2}\tilde{\mathfrak{O}}(t,\alpha^*),\mathfrak{O}(t,t',\alpha^*)\Big] - \frac{\epsilon\mathfrak{L}^\dagger}{\hbar}\frac{\delta\tilde{\mathfrak{O}}(t)}{\delta\alpha^*(t')}, \quad \text{(D.1.141)}$$

where the operator $\tilde{\mathfrak{O}}$ is defined as

$$\tilde{\mathfrak{O}}(t,\alpha^*) = \int_0^t L(t,t')\mathfrak{O}(t,t',\alpha^*)\,\mathrm{d}t', \quad \text{(D.1.142)}$$

with the initial condition

$$\mathfrak{O}(t,t'=t,\alpha^*)\left|\psi(\alpha^*,t)\right\rangle = \mathfrak{L}\left|\psi(\alpha^*,t)\right\rangle. \quad \text{(D.1.143)}$$

The Stochastic Schrödinger equation takes a very similar form to the general Schrödinger equation, apart from the two additional terms on the right hand side which contain two orders of interaction Hamiltonian coupling, and introduce the stochastic Gaussian process for the environment interaction with the system of interest. The additional benefit of this derivation is that it makes use of the coherent state representation, which is a physically convenient basis for this kind of system. This equation is fully non-Markovian, due to the stochastic description of the bath interaction, and does not require approximations such as the secular or rotating wave assumptions of previous EOMs.

D.1.9 The Fokker-Planck Equation

In addition to the previous methods, the quantum Langevin equation can be further generalised to form the Fokker-Planck equation. This equation is also known as the Kolmogorov-forward equation , the Smoluchowski equation in the context of particle diffusion[178], and the Klein-Kramers equation[177] when applied to particle position and momentum. Clearly, based on the large number of applications this equation is particularly powerful. It makes use of stochastic Gaussian processes to introduce a drift and diffusion term, in the Itô sense. Because this equation is non-perturbative, stochastic, and produces exact dynamics there are many ways to derive it[352–356]- and each different form can be related to the others in a similar fashion to the path integral representation of the quantum Langevin equation. As a consequence of this, we will only consider two of the simpler derivations: through the Kramers-Moyal expansion of a general master equation[357], and through functional derivatives resulting in a Kolmogorov-Fokker-Planck equation[355].

D.1.9.1 Kolmogorov-Fokker-Planck Equation

This derivation requires the consideration of Itô calculus[358], an extension of standard calculus to stochastic variables. The fundamental result which we require is Itô's lemma which is a generalisation of the standard chain rule and change of variables. This lemma occurs for a Brownian process as a consequence of a quadratic correction which is not present for variables that are not stochastic.

Lemma D.1.1. *For a twice continuously differentiable function on the reals, f, for an Itô process X, then by Itô's lemma, $f(X)$ is also an Itô process satisfying*

$$\mathrm{d}f[X(t)] = f'[X(t)]\mathrm{d}X(t) + \frac{1}{2}f''[X(t)]\sigma^2(t)\mathrm{d}t. \tag{D.1.144}$$

where primes denote derivatives with respect to the process X.

Following Sharma[355], we then consider a general stochastic differential equation:

$$\frac{\partial \mathrm{x}(t)}{\partial t} = f[\mathrm{x}(t)] + g[\mathrm{x}(t)]\xi(t), \tag{D.1.145}$$

where $\mathrm{x}(t)$ is a non-Markov process and $\xi(t)$ is the Ornstein-Uhlenbeck process - a process governed by a stochastic differential equation of a Wiener process W, for example white noise[358]:

$$\mathrm{d}\xi(t) = -\theta\xi(t)\mathrm{d}t + \sigma\mathrm{d}W(t). \tag{D.1.146}$$

Converting this Wiener term into a white noise function, and converting into

true derivatives ('division' by dt), generates another type of Langevin equation equivalent to (D.1.7). If we consider the Ornstein-Uhlenbeck process to have a zero mean, be stationary and Gaussian then the equation for the probability density functional can be written as

$$\frac{\partial}{\partial t}\mathfrak{p}[\mathrm{x},t] = -\frac{\partial f(\mathrm{x})\mathfrak{p}}{\partial \mathrm{x}} + \frac{\partial}{\partial \mathrm{x}} g(\mathrm{x})\Big(\frac{\partial}{\partial \mathrm{x}}\int_{t_0}^{t} L_{\mathrm{UO}}^{(\alpha)}(t-t')\,\langle \delta(\mathrm{x}(t)-\mathrm{x})\frac{\delta \mathrm{x}(t)}{\delta \xi(t')}\rangle\ \mathrm{d}t'\Big), \tag{D.1.147}$$

where $L_{\mathrm{UO}}^{(\alpha)}(t-t')$ is the autocorrelation function of the Ornstein-Uhlenbeck process and $\frac{\delta \mathrm{x}(t)}{\delta \xi(t')}$ is the functional derivative. We can integrate the general stochastic differential equation to find an exact solution for the non-Markov process $\mathrm{x}(t)$, and then use this within the definition of the functional derivative:

$$\frac{\delta \mathrm{x}(t)}{\delta \xi(t')} = \int_{t'}^{t} f'[\mathrm{x}(\tau)]\frac{\delta \mathrm{x}(\tau)}{\delta \xi(t')} + g'[\mathrm{x}(\tau)]\frac{\delta \mathrm{x}(t)}{\delta \xi(t')}\xi(\tau) + g[\mathrm{x}(\tau)]\frac{\delta \xi(\tau)}{\delta \xi(t')}\,\mathrm{d}\tau, \tag{D.1.148}$$

$$= g[\mathrm{x}(t')] + \int_{t'}^{t} f'[\mathrm{x}(\tau)]\frac{\delta \mathrm{x}(\tau)}{\delta \xi(t')} + g'[\mathrm{x}(\tau)]\frac{\delta \mathrm{x}(\tau)}{\delta \xi(t')}\xi(\tau)\,\mathrm{d}\tau. \tag{D.1.149}$$

In this form we can sequentially introduce the definition of the functional derivative and input the solution for $\mathrm{x}(t)$:

$$\frac{\delta \mathrm{x}(t)}{\delta \xi(t')} = g[\mathrm{x}(t')]\exp\Big(\int_{t'}^{t} f'[\mathrm{x}(\tau)] + g'[\mathrm{x}(\tau)]\xi(\tau)\,\mathrm{d}\tau\Big), \tag{D.1.150}$$

$$= g[\mathrm{x}(t')]\exp\Big(\int_{t'}^{t} \frac{\partial \dot{\mathrm{x}}(\tau)}{\partial \mathrm{x}(\tau)}\,\mathrm{d}\tau\Big), \tag{D.1.151}$$

where $\dot{\mathrm{x}}$ denotes the time derivative of x. The noise coefficient $g[\mathrm{x}(t)]$ can then be expressed in terms of $\dot{\mathrm{x}}$, expanded, and substituted into the previous definition of the functional derivative to yield

$$\frac{\delta \mathrm{x}(t)}{\delta \xi(t')} = g[\mathrm{x}(t')]\exp\Big(\int_{t'}^{t} f'[\mathrm{x}(\tau)] + \frac{g'[\mathrm{x}(\tau)]}{g[\mathrm{x}(\tau)]}f[\mathrm{x}(\tau)]\,\mathrm{d}\tau\Big). \tag{D.1.152}$$

From here we Taylor expand in $t'-t$ up to $\mathcal{O}((t'-t)^2)$,

$$\frac{\delta \mathrm{x}(t)}{\delta \xi(t')} = \frac{\delta \mathrm{x}(t)}{\delta \xi(t)} + (t'-t)\Big(\frac{\partial}{\partial t'}\Big(\frac{\delta \mathrm{x}(t)}{\delta \xi(t')}\Big)|_{t'=t}\Big) + \mathcal{O}((t'-t)^2). \tag{D.1.153}$$

We can use this in combination with the previous definition of the functional derivative to write

$$\frac{\delta \mathrm{x}(t)}{\delta \xi(t)} = g[\mathrm{x}(t)], \tag{D.1.154}$$

$$\frac{\partial}{\partial t'}\Big(\frac{\delta \mathrm{x}(t)}{\delta \xi(t')}\Big)|_{t'=t} = -g[\mathrm{x}(t)]f'[\mathrm{x}(t)] + g'[\mathrm{x}(t)]f[\mathrm{x}(t)]. \tag{D.1.155}$$

This allows us to write every term in the Taylor expansion of the functional

derivative in terms of either f or g

$$\frac{\delta \mathrm{x}(t)}{\delta \xi(t')} = g[\mathrm{x}(t)]\Big(1 + (t-t')\frac{f'[\mathrm{x}(t)]g[\mathrm{x}(t)] - g'[\mathrm{x}(t)]f[\mathrm{x}(t)]}{g[\mathrm{x}(t)]}\Big), \tag{D.1.156}$$

by spotting the quotient rule and applying it in reverse we can write this in terms of the probability distribution from the EOM as

$$\langle \delta(\mathrm{x}(t) - \mathrm{x})\frac{\delta \mathrm{x}(t)}{\delta \xi(t')}\rangle = g[\mathrm{x}](1 + (t-t'))g[\mathrm{x}]\frac{\partial}{\partial \mathrm{x}}\Big(\frac{f[\mathrm{x}]}{g[\mathrm{x}]}\Big)\mathfrak{p}[\mathrm{x}]. \tag{D.1.157}$$

This introduces the particular form of the autocorrelation function

$$L^{(\alpha)}_{\mathrm{UO}}(t-t') = \frac{D}{\tau_{cor}}\exp\Big(-\frac{|t-t'|}{\tau_{cor}}\Big), \tag{D.1.158}$$

where D is the diffusion coefficient and τ_{cor} is the associated correlation time for the correlation of the Ornstein-Uhlenbeck process. The combination of these equations and expansion is the Kolmogorov-Fokker-Planck equation:

$$\frac{\partial \mathfrak{p}[\mathrm{x}]}{\partial t} = -\frac{\partial}{\partial \mathrm{x}}f[\mathrm{x}]\mathfrak{p}[\mathrm{x}] + D\frac{\partial}{\partial \mathrm{x}}\Big(g[\mathrm{x}]\frac{\partial}{\partial \mathrm{x}}\Big(g[\mathrm{x}] + \tau_{cor}g^2[\mathrm{x}]\frac{\partial}{\partial \mathrm{x}}\Big\{\frac{f[\mathrm{x}]}{g[\mathrm{x}]}\Big\}\Big)\mathfrak{p}[\mathrm{x}]\Big). \tag{D.1.159}$$

The benefit of this derivation is the explicit introduction of the diffusion coefficient through standard functional calculus.

D.1.9.2 Kramers-Moyal Expansion

Equivalent to this is the method of the Kramers-Moyal expansion. The benefit of this method is that it does not require any Itô calculus and only one additional assumption. Starting from the time local equation for a general probability density function, we follow the work of Rahimi Tabar et. al. [357] by writing

$$\mathrm{p}^{(\rho)}(\mathrm{x}, t+t') = \int \mathrm{p}^{(\rho)}(\mathrm{x}, t+t'|x', t)\mathrm{p}^{(\rho)}(x', t)\,\mathrm{d}x', \tag{D.1.160}$$

where $\mathrm{p}^{(\rho)}(\mathrm{x}, t+t'|x', t)$ is the conditional probability distribution function. We make the assumption that a conditional moment exists which can be defined in terms of the conditional probability distribution function as

$$\mathrm{K}^{(n)}(\mathrm{x}', t, t') = \langle[\mathrm{x}(t+t') - \mathrm{x}(t)]^n\rangle\,|_{\mathrm{x}(t)=\mathrm{x}'}, \tag{D.1.161}$$

$$= \int (\mathrm{x} - \mathrm{x}')^n \mathrm{p}^{(\rho)}(\mathrm{x}, t+t'|\mathrm{x}', t)\,\mathrm{dx}. \tag{D.1.162}$$

We use the sifting property of the delta function in order to write the conditional probability distribution as

$$\mathrm{p}^{(\rho)}(\mathrm{x}, t+t'|\mathrm{x}', t) = \int \delta(\mathrm{y} - \mathrm{x})\mathrm{p}^{(\rho)}(\mathrm{y}, t+t'|\mathrm{x}', t)\,\mathrm{dy}. \tag{D.1.163}$$

We consider a translation of these coordinates involving x', which is associated with jumps in the probability distribution, and Taylor expand

$$\delta(\mathrm{y}-\mathrm{x}) = \delta(\mathrm{x}'-\mathrm{x}+\mathrm{y}-\mathrm{x}'), \tag{D.1.164}$$

$$= \sum_{n=0}^{\infty}(-1)^n\frac{(\mathrm{y}-\mathrm{x}')^n}{n!}\frac{\partial^n}{\partial \mathrm{x}^n}\delta(\mathrm{x}'-\mathrm{x}). \tag{D.1.165}$$

We can use this to simplify the equation for the conditional probability distribution

$$\mathrm{p}^{(\rho)}(\mathrm{x},t+t'|\mathrm{x}',t) = \sum_{n=0}^{\infty}\frac{(-1)^n}{n!}\frac{\partial^n}{\partial \mathrm{x}^n}\int(\mathrm{y}-\mathrm{x}')^n\delta(\mathrm{x}'-\mathrm{x})\mathrm{p}^{(\rho)}(\mathrm{y},t+t'|\mathrm{x}',t)\,\mathrm{dy}, \tag{D.1.166}$$

which allows the introduction of $\mathrm{K}^{(n)}$

$$\mathrm{p}^{(\rho)}(\mathrm{x},t+t'|\mathrm{x}',t) = \Big[1+\sum_{n=1}^{\infty}\frac{-1^n}{n!}\frac{\partial^n}{\partial \mathrm{x}^n}\mathrm{K}^{(n)}(\mathrm{x}',t,t')\Big]\delta(\mathrm{x}'-\mathrm{x}). \tag{D.1.167}$$

Substituting this solution into the initial equation for the probability distribution of x and $t+t'$ and making use of the sifting property of the delta function gives

$$\mathrm{p}^{(\rho)}(\mathrm{x},t+t') = \int\Big[1+\sum_{n=1}^{\infty}\frac{(-1)^n}{n!}\frac{\partial^n}{\partial \mathrm{x}^n}\mathrm{K}^{(n)}(\mathrm{x}',t,t')\Big]\delta(\mathrm{x}'-\mathrm{x})\mathrm{p}^{(\rho)}(x',t)\,\mathrm{dx}', \tag{D.1.168}$$

$$= \int\mathrm{p}^{(\rho)}(\mathrm{x}',t)\delta(\mathrm{x}'-\mathrm{x})\,\mathrm{dx}' + \sum_{n=1}^{\infty}\frac{(-1)^n}{n!}\frac{\partial^n}{\partial \mathrm{x}^n}\times \tag{D.1.169}$$

$$\int\delta(\mathrm{x}'-\mathrm{x})\mathrm{K}^{(n)}(\mathrm{x}',t,t')\mathrm{p}^{(\rho)}(\mathrm{x}',t)\,\mathrm{dx}'. \tag{D.1.170}$$

Finally, if we reorganise, divide both sides by t' and take the limit of $t'\to 0$ then we produce a full time derivative on the left hand side and obtain the full Kramers-Moyal equation:

$$\frac{\partial\mathrm{p}^{(\rho)}(\mathrm{x},t)}{\partial t} = \sum_{n=1}^{\infty}(-1)^n\frac{\partial^n}{\partial \mathrm{x}^n}\mathrm{D}^{(n)}(\mathrm{x},t)\mathrm{p}^{(\rho)}(\mathrm{x},t), \tag{D.1.171}$$

where

$$\mathrm{D}^{(n)}(\mathrm{x},t) = \lim_{t'\to 0}\frac{\mathrm{K}^{(n)}(\mathrm{x},t,t')}{n!\cdot t'}. \tag{D.1.172}$$

This equation can be simplified by the following theorem, the derivation of which is outside the scope of this thesis:

Pawula's Theorem:

Remark.

1. *The process is deterministic and the expansion contains one term.*

2. *The process is a type of diffusion and the expansion contains only two terms.*
3. *The behaviour is more complex than being deterministic or diffusive and an infinite number of terms is required in order to keep the probability density strictly positive.*

We consider only the second case, and thus form the Fokker-Planck equation: a two term form of the Kramers-Moyal equation

$$\frac{\partial \mathrm{p}^{(\rho)}(\mathrm{x},t)}{\partial t} = \frac{\partial^2}{\partial \mathrm{x}^2}(\mathrm{D}^{(2)}(\mathrm{x},t)\mathrm{p}^{(\rho)}(\mathrm{x},t)) - \frac{\partial}{\partial \mathrm{x}}(\mathrm{D}^{(1)}(\mathrm{x},t)\mathrm{p}^{(\rho)}(\mathrm{x},t)), \qquad \text{(D.1.173)}$$

where $\mathrm{D}^{(1)}$ is the drift and $\mathrm{D}^{(2)}$ is the diffusion coefficient. Based on the fact that there has been a perturbation in time and a previous expansion of the interaction Hamiltonian, this is considered a perturbative method[354].

D.1.10 The Hierarchical Equations of Motion

The final set of derivations aim to be the most free from assumptions and approximations. The hierarchical equations of motion are non-perturbative, and are not limited by orders of interaction coupling strength, do not make use of the Born-approximation, rotating wave-approximation, and can be strongly non-Markovian. The main assumption that this derivation makes is the high temperature approximation as a simplification of the system dissipation kernel $L_{\mathcal{R}}^{(\alpha)}$ to a form which is more amenable to use in combination with an exponential basis. However, there also exist low temperature corrections to the non-Markovian terms which extend the number of temperature regimes out of the high temperature limit. The only other restriction comes from the choice of basis function with which we expand our spectral density and this leads to regimes of applicable homogeneity. As will be shown during the derivation, overdamped and underdamped limits are natural choices and produce hierarchies, but the point of critical damping is an area where the usual method can struggle. This has been addressed recently by Tatsushi Ikeda through a generalisation of the hierarchy scheme using the cumulant expansion which circumvents the difficulty of expanding in an exponential basis[139].

D.1.10.1 Overdamped HEOM

The key component of each HEOM derivation is its constituent spectral density and the expansion used to decompose this into individual contributions. The full derivation is considered for the overdamped case and the differences are highlighted in other cases but their full derivation will be omitted and their original source noted. The overdamped hierarchy is derived from an

exponential expansion of an overdamped spectral density which is computed through a contour integral

$$J_{\mathrm{O}}(\omega) = \frac{2\eta\omega\Lambda}{\Lambda^2 + \omega_2}. \tag{D.1.174}$$

D.1.10.1.1 System-bath Model

We consider a one-dimensional system coupled to a bath of N harmonic oscillators. The system of interest is defined by a potential $V(\mathrm{q})$ - where q is the position operator as in the non-linear Schrödinger equation - and its mass m. The oscillators in the ensemble have masses $\{m_j\}$, frequencies $\{\omega_j\}$ and coupling constants $\{c_j\}$. The total Hamiltonian,

$$\mathrm{H_{tot}} = \mathrm{H_S} + \mathrm{H_B} + \mathrm{H_{SB}}, \tag{D.1.175}$$

where,

$$\mathrm{H_S} = \frac{\mathrm{p}^2}{2m} + V(\mathrm{q}), \tag{D.1.176}$$

$$\mathrm{H_B} = \sum_j \left(\frac{\mathrm{p}_j^2}{2m_j} + \frac{m_j\omega_j\mathrm{x}_j^2}{2} \right), \tag{D.1.177}$$

$$\mathrm{H_{SB}} = -\sum_j c_j \mathrm{x}_j \mathrm{q}, \tag{D.1.178}$$

and $\{\mathrm{p}\}, \{\mathrm{q}\}, \{\mathrm{p}_j\}, \{\mathrm{x}_j\}$ are the respective momentum and position operators for the system and the bath.

Given this description of the system and bath we can construct the density matrix. For a set of states $\{|\mathrm{q}_i, \mathrm{x}_i\rangle\}$ with corresponding transition probabilities $\{P_i\}$ the density matrix is equivalent to the outer product,

$$\rho(\mathrm{q}, \mathrm{x}) = \sum_i P_i \left|\mathrm{q}_i, \mathrm{x}_i\right\rangle \left\langle \mathrm{q}_i, \mathrm{x}_i\right|. \tag{D.1.179}$$

D.1.10.1.2 Feynman and Vernon Influence Functional

To derive the equations of motion we define the evolution of the density matrix at time zero to a time t using the path integral formalism. Introducing the time propagation operators we can find the density matrix at an arbitrary, non-zero time, t given the form of the density matrix at time zero,

$$\rho_t(\mathrm{q}, \mathrm{x}) = \exp\left(\frac{i\mathrm{H}(\mathrm{q}, \mathrm{x})t}{\hbar}\right) \rho_0(\mathrm{q}, \mathrm{x}) \exp\left(\frac{-i\mathrm{H}(\mathrm{q}, \mathrm{x})t}{\hbar}\right). \tag{D.1.180}$$

Next we apply the initial condition assumption that the system is, initially, in a factorisable state and that the bath is in thermal equilibrium - but not in equilibrium with the system of interest.

$$\rho_0(\mathrm{q},\mathrm{x}) = \rho_\mathrm{S}(\mathrm{q})\rho_\mathrm{B}(\mathrm{x}), \tag{D.1.181}$$

$$\rho_\mathrm{S}(\mathrm{q},\mathrm{q}') = \rho_0(\mathrm{q},\mathrm{q}'), \quad \rho_\mathrm{B}(\mathrm{x},\mathrm{x}') = \langle \mathrm{x}| \exp(-\beta \mathrm{H}_\mathrm{B})/Z_\mathrm{B} \, |\mathrm{x}'\rangle \tag{D.1.182}$$

Here β is the inverse temperature $1/(k_\mathrm{B}T)$. We can rewrite the density matrix as,

$$\langle \mathrm{q}_t,\mathrm{x}| \, \rho(t) \, |\mathrm{q}'_t,\mathrm{x}'\rangle = \iiiint \langle \mathrm{q}_t,\mathrm{x}| \exp(i\mathrm{H}t/\hbar) \, |\mathrm{q}_0,\mathrm{x}_0\rangle \, \rho_0(\mathrm{q}_0,\mathrm{q}'_0)\times$$
$$\langle \mathrm{x}_0| \exp(-\beta \mathrm{H}_\mathrm{B})/Z_\mathrm{B} \, |\mathrm{x}'_0\rangle \, \langle \mathrm{q}'_0,\mathrm{x}'_0| \exp(-i\mathrm{H}t/\hbar) \, |\mathrm{q}'_t,\mathrm{x}\rangle \, \mathrm{d}\mathrm{x}_0\mathrm{d}\mathrm{x}'_0\mathrm{d}\mathrm{q}_0\mathrm{d}\mathrm{q}'_0, \tag{D.1.183}$$

equivalent to a probability of transition with time dependent paths q_t, q'_t, x, and x'[4,143,144,214]. The influence of the bath on the system of interest can then be explicitly incorporated, through the action contributions, by application of the path integral formalism and the Feynman and Vernon influence functional:

$$\langle \mathrm{q}_t,\mathrm{x}| \, \rho(t) \, |\mathrm{q}'_t,\mathrm{x}'\rangle = \iiiint \mathfrak{K}(\mathrm{q}_t,\mathrm{x},t,\mathrm{q}_0,\mathrm{x}_0,0)\rho_0(\mathrm{q}_0,\mathrm{q}'_0)\times$$
$$\langle \mathrm{x}_0| \exp(-\beta \mathrm{H}_\mathrm{B})/Z_\mathrm{B} \, |\mathrm{x}'_0\rangle \, \mathfrak{K}^*(\mathrm{q}'_t,\mathrm{x}',t,\mathrm{q}'_0,\mathrm{x}'_0,0) \, \mathrm{d}\mathrm{x}_0\mathrm{d}\mathrm{x}'_0\mathrm{d}\mathrm{q}_0\mathrm{d}\mathrm{q}'_0, \tag{D.1.184}$$

where

$$\langle \mathrm{q}_t,\mathrm{x}| \exp(i\mathrm{H}t/\hbar) \, |\mathrm{q}_0,\mathrm{x}_0\rangle = \mathfrak{K}(\mathrm{q}_t,\mathrm{x},t,\mathrm{q}_0,\mathrm{x}_0,0), \tag{D.1.185}$$
$$= \iint \exp(i\mathrm{S}[\mathrm{q}_t,\mathrm{x}]/\hbar) \, \mathcal{D}[\mathrm{q}_t]\mathcal{D}[\mathrm{x}], \tag{D.1.186}$$

$$\langle \mathrm{q}'_0,\mathrm{x}'_0| \exp(-i\mathrm{H}t/\hbar) \, |\mathrm{q}'_t,\mathrm{x}'\rangle = \mathfrak{K}^*(\mathrm{q}'_t,\mathrm{x}',t,\mathrm{q}'_0,\mathrm{x}'_0,0), \tag{D.1.187}$$
$$= \iint \exp(-i\mathrm{S}[\mathrm{q}_t,\mathrm{x}]/\hbar) \, \mathcal{D}[\mathrm{q}'_t]\mathcal{D}[\mathrm{x}'], \tag{D.1.188}$$

with endpoints: $\mathrm{q}(t) = \mathrm{q}_t$, $\mathrm{q}(0) = \mathrm{q}_0$, $\mathrm{q}'(t) = \mathrm{q}'_t$, $\mathrm{q}'(0) = \mathrm{q}'_0$, $\mathrm{x}(t) = \mathrm{x}$, $\mathrm{x}(0) = \mathrm{x}_0$, $\mathrm{x}'(t) = \mathrm{x}'$, $\mathrm{x}'(0) = \mathrm{x}'_0$, and action $S = \mathrm{S}_\mathrm{S} + \mathrm{S}_\mathrm{B} + \mathrm{S}_\mathrm{SB} = \int_0^t \mathcal{L}_\mathrm{Lag} \, \mathrm{d}\tau$, where $\mathcal{L}_\mathrm{Lag}$ is the Lagrangian. We aim to model physical observables for the system of interest in the coordinate q, so we are free to trace out the bath degrees of freedom:

$$\int \langle \mathrm{q}_t,\mathrm{x}| \, \rho(t) \, |\mathrm{q}'_t,\mathrm{x}'=\mathrm{x}\rangle \, \mathrm{d}\mathrm{x} = \int \Bigg[\iiiint \mathfrak{K}(\mathrm{q}_t,\mathrm{x},t,\mathrm{q}_0,\mathrm{x}_0,0)\rho_0(\mathrm{q}_0,\mathrm{q}'_0)\times$$
$$\langle \mathrm{x}_0| \exp(-\beta \mathrm{H}_\mathrm{B})/Z_\mathrm{B} \, |\mathrm{x}'_0\rangle \, \mathfrak{K}^*(\mathrm{q}'_t,\mathrm{x}'=\mathrm{x},t,\mathrm{q}'_0,\mathrm{x}'_0,0) \, \mathrm{d}\mathrm{x}_0\mathrm{d}\mathrm{x}'_0\mathrm{d}\mathrm{q}_0\mathrm{d}\mathrm{q}'_0 \Bigg] \mathrm{d}\mathrm{x}. \tag{D.1.189}$$

Where we can split the action based on the origin of their respective contributions,

$$\rho(\mathrm{q}_t, \mathrm{q}'_t, t) = \iint \int_{\mathrm{q}_0}^{\mathrm{q}_t} \int_{\mathrm{q}'_0}^{\mathrm{q}'_t} \exp(i\mathrm{S}_\mathrm{S}[\mathrm{q}_t]/\hbar) \exp(-i\mathrm{S}_\mathrm{S}[\mathrm{q}'_t]/\hbar) \mathcal{F}[\mathrm{q}_t, \mathrm{q}'_t] \times \rho_\mathrm{S}(\mathrm{q}_0, \mathrm{q}'_0, 0)\ \mathcal{D}[\mathrm{q}_t]\mathcal{D}[\mathrm{q}'_t]\mathrm{d}\mathrm{q}_0\mathrm{d}\mathrm{q}'_0, \quad \text{(D.1.190)}$$

and the Feynman and Vernon influence functional is

$$\mathcal{F}[\mathrm{q}_t, \mathrm{q}'_t] = \iiiint \rho_\mathrm{B}(\mathrm{x}_0, \mathrm{x}'_0, 0) \exp(i\Big[\mathrm{S}_\mathrm{B}[\mathrm{x}] - \mathrm{S}_\mathrm{B}[\mathrm{x}'] + \mathrm{S}_\mathrm{SB}[\mathrm{q}_t, \mathrm{x}] - \mathrm{S}_\mathrm{SB}[\mathrm{q}'_t, \mathrm{x}']\Big]/\hbar)\ \mathcal{D}[\mathrm{x}]\mathcal{D}[\mathrm{x}']\mathrm{d}\mathrm{x}_0\mathrm{d}\mathrm{x}'_0\mathrm{d}\mathrm{x}. \quad \text{(D.1.191)}$$

where $\int \mathcal{D}[\mathrm{x}]$ denotes a Feynman path integral. Here the classical action - in terms of the Lagrangian - for an isolated system is used,

$$\mathrm{S}_\mathrm{S}[\mathrm{q}_t, t] = \int_0^t \frac{m\Big\{\dot{\mathrm{q}_t(\tau)}\Big\}^2}{2} - V[\mathrm{q}_t(\tau)]\mathrm{d}\tau, \quad \text{(D.1.192)}$$

$$\mathrm{S}_\mathrm{B}[\mathrm{x}, t] = \int_0^t \sum_j \frac{m_j\Big\{\dot{\mathrm{x}_j(\tau)}\Big\}^2}{2} - \frac{m_j\omega_j^2\Big\{\mathrm{x}_j(\tau)\Big\}^2}{2}\mathrm{d}\tau, \quad \text{(D.1.193)}$$

and

$$\mathrm{S}_\mathrm{SB}[\mathrm{q}_t, \mathrm{x}, t] = \int_0^t \sum_j c_j\mathrm{x}_j(\tau)\mathrm{q}_t(\tau)\mathrm{d}\tau. \quad \text{(D.1.194)}$$

The influence functional is then taken in its most general form. This is created by assuming that there is a bilinear coupling between the system and bath such that:

$$L_\mathrm{Lag}^\mathrm{SB} = \mathfrak{g}\mathrm{q}_t\mathrm{x} \quad \text{and} \quad L_\mathrm{Lag}^\mathrm{B}(\dot{\mathrm{x}}, \mathrm{x}, t), \quad \text{(D.1.195)}$$

where,

$$L_\mathrm{Lag}^\mathrm{tot} = L_\mathrm{Lag}^\mathrm{S}(\{\dot{\mathrm{q}_t}\}, \mathrm{q}_t, t) + L_\mathrm{Lag}^\mathrm{B}(\dot{\mathrm{x}}, \mathrm{x}, t) + L_\mathrm{Lag}^\mathrm{SB}(\mathrm{q}_t, \mathrm{x}). \quad \text{(D.1.196)}$$

The influence is considered by studying properties of x - the bath - only, i.e. simply the impact of x on q_t. In Fourier space we define $\tilde{\mathrm{Q}}_t(\omega)$ as the Fourier transform of $\mathfrak{g}(t)\mathrm{q}_t(t)$, from the linear interaction, (where

$$\tilde{a}(\omega) = \int_0^\infty a(t) \exp(-i\omega t)\ \mathrm{d}t, \quad \text{(D.1.197)}$$

$$\tilde{a}^*(\omega) = \int_0^\infty a(t) \exp(i\omega t)\ \mathrm{d}t, \quad \text{(D.1.198)}$$

is defined as the Fourier transform of a general function $a(t)$) and introduce $\tilde{z}$

which is a classical impedence function relating x to an applied force. This function, $\tilde{z}$, is a type of response function dictating the changes and movements in x due to a classical input force. $\tilde{z}$ is calculated by creating a classical system corresponding to x with Lagrangian, $L^{\mathrm{B}}_{\mathrm{Lag}}(\dot{\mathrm{x}}, \mathrm{x}, t)$, and finding the response under the influence of a driving force $f(t)$, derived from the potential $f(t)\mathrm{x}(t)$ - in analogy with $\mathfrak{g}\mathrm{q}_t$. Here, $f(t)$ is applied at $t = 0$ and is subject to the initial conditions: $\dot{\mathrm{x}}(0) = \mathrm{x}(0) = 0$, such that

$$\tilde{z} = \frac{\tilde{f}}{i\omega\tilde{\mathrm{x}}}. \tag{D.1.199}$$

Subsequently, the influence phase is

$$\Phi(\tilde{\mathrm{Q}}_t, \tilde{\mathrm{Q}}'_t) = \frac{1}{2\pi\hbar}\int_0^\infty \left[\frac{\tilde{\mathrm{Q}}'_t(\tilde{\mathrm{Q}}^*_t - \tilde{\mathrm{Q}}'^*_t)}{i\omega\tilde{z}} + \frac{\tilde{\mathrm{Q}}^*_t(\tilde{\mathrm{Q}}_t - \tilde{\mathrm{Q}}'_t)}{-i\omega\tilde{z}}\right] \mathrm{d}\omega, \tag{D.1.200}$$

which in the time domain is

$$i\Phi(\mathrm{q}_t, \mathrm{q}'_t) = -\frac{1}{2\hbar}\int_{-\infty}^{\infty}\int_{-\infty}^{t} \mathfrak{g}(t)\mathfrak{g}(s)(\mathrm{q}_t - \mathrm{q}'_t)\{\mathrm{q}_t(s)F^*(t-s) - \mathrm{q}'_t(s)F(t-s)\}\,\mathrm{d}s\,\mathrm{d}t, \tag{D.1.201}$$

- here F^* is the complex conjugate - where $\mathcal{I}(F(t))$ for $t > 0$ is the classical response of x to a force $f(t) = \delta(t)$. $\mathcal{R}(F(t))$, which is temperature dependent, is the correlation function for the zero point fluctuation of the variable x.

This process is equivalent to substituting the Lagrangian into the influence functional to form a Gaussian functional integral. Rearranging the integrand of this intergal and solving the Euler-Lagrange equation, contained within, generates a solution dependent on the end points of the classically minimised path. This formulates the influence functional into a more useful form containing correlation functions which relate to the fluctuation-dissipation theorem. As such $F(t)$ can be related directly to the correlation functions, which physically represent fluctuation and dissipation,

$$L^{(\alpha)}(\tau - s) = \sum_j \frac{c_j^2}{2m_j\omega_j}\Big(\exp(-i\omega_j(\tau - s)) + \frac{\exp(i\omega_j(\tau - s)) + \exp(-i\omega_j(\tau - s))}{\exp(\beta\hbar\omega_j) - 1}\Big), \tag{D.1.202}$$

where

$$F(t) = L^{(\alpha)}_{\mathcal{R}}(t) + iL^{(\alpha)}_{\mathcal{I}}(t), \tag{D.1.203}$$

$$L^{(\alpha)}_{\mathcal{R}}(t) = -\frac{2}{\pi}\int_0^\infty \mathcal{I}\left(\frac{1}{i\omega\tilde{z}}\right)\cos(\omega t)\,\mathrm{d}\omega, \tag{D.1.204}$$

$$L^{(\alpha)}_{\mathcal{I}}(t) = -\frac{2}{\pi}\int_0^\infty \mathcal{I}\left(\frac{1}{i\omega\tilde{z}}\right)\sin(\omega t)\,\mathrm{d}\omega. \tag{D.1.205}$$

This allows the influence functional to be recast as

$$\mathcal{F}[\mathrm{q}_t, \mathrm{q}'_t] = \exp\Big(-\frac{1}{\hbar}\int_0^t \int_0^{\tau'} (\mathrm{q}_t(\tau) - \mathrm{q}'_t(\tau))\times \\ (L^{(\alpha)}(\tau - s)\mathrm{Q}_t(s) - L^{(\alpha)*}(\tau - s)\mathrm{q}'_t(s))\ \mathrm{d}\tau\ \mathrm{d}s\Big). \quad \text{(D.1.206)}$$

This is now directly related to the spectral density of the harmonic oscillator bath modes, as this is the autocorrelation function of the bath coordinate.

$$F(t) = \int_0^\infty J(\omega)\cos(\omega t)\coth\left(\frac{\beta\hbar\omega}{2}\right)\mathrm{d}\omega - i\int_0^\infty J(\omega)\sin(\omega t)\ \mathrm{d}\omega, \quad \text{(D.1.207)}$$

We can now define the spectral density, $J(\omega)$, which describes the N harmonic oscillators which make up the bath ensemble as

$$J(\omega) = \hbar\sum_j \frac{c_j^2}{2m_j\omega_j}\delta(\omega - \omega_j). \quad \text{(D.1.208)}$$

Introduction of this simplifies the autocorrelation function equation. If we rewrite this, and take the real and imaginary parts - such that we can reduce the exponentials - we get:

$$L_{\mathcal{R}}^{(\alpha)}(t) = \int_0^\infty J(\omega)\cos(\omega t)\coth\left(\frac{\beta\hbar\omega}{2}\right)\mathrm{d}\omega, \quad \text{(D.1.209)}$$

$$L_{\mathcal{I}}^{(\alpha)}(t) = -\int_0^\infty J(\omega)\sin(\omega t)\ \mathrm{d}\omega. \quad \text{(D.1.210)}$$

These forms of $L^{(\alpha)}(t)$ can be combined to produce $L_{\mathrm{corr}}^{(\alpha)}(t)$, which matches the literature[147,149,157]. Next we introduce the Debye spectral density:

$$J(\omega) = \frac{2\eta\Lambda\omega}{\Lambda^2 + \omega^2}.$$

Split the correlation function into two components and solve it with a pair of contour integrals

$$L_{\mathcal{R}}^{(\alpha)} + iL_{\mathcal{I}}^{(\alpha)} = \frac{1}{\pi}\int_0^\infty \frac{2\eta\Lambda\omega}{\Lambda^2+\omega^2}\coth\left(\frac{\beta\hbar\omega}{2}\right)\cos(\omega t)\ \mathrm{d}\omega - \frac{i}{\pi}\int_0^\infty \frac{2\eta\Lambda\omega}{\Lambda^2+\omega^2}\sin(\omega t)\ \mathrm{d}\omega.$$

First consider $L_{\mathcal{R}}^{(\alpha)}$, extend it along the entire real axis and write cosine in exponential form

$$L_{\mathcal{R}}^{(\alpha)}(t) = \frac{1}{2\pi}\mathcal{R}\left[\int_0^\infty \frac{2\eta\Lambda\omega}{\Lambda^2+\omega^2}\coth\left(\frac{\beta\hbar\omega}{2}\right)e^{i\omega t}\ \mathrm{d}\omega\right].$$

In order to compute the contour integral the poles of the integrand are required. In order to achieve this split the $\coth$ function into a fractional form and find the

roots of the denominator

$$(\Lambda^2 + \omega^2)\sinh\left(\frac{\beta\hbar\omega}{2}\right) = 0.$$

The solutions of this equation are

$$\omega = \pm i\Lambda,$$

or when

$$\sinh\left(\frac{\beta\hbar\omega}{2}\right) = 0.$$

Letting ω be complex with real part $\omega_{\mathcal{R}}$ we can solve

$$i\sin\left(\frac{\beta\hbar\omega_{\mathcal{R}}}{2}\right) = 0.$$

Since $\sin(n\pi) = 0 \ \forall \ n \in \mathbb{Z}$ the other solutions are

$$\omega = \frac{2n\pi i}{\beta\hbar}, \ n \in \mathbb{Z} \neq 0.$$

In this case n cannot be zero without the integrand vanishing, and hence this is not a pole. By setting

$$\frac{2\eta\Lambda\omega}{\Lambda^2 + \omega^2}\frac{\cosh\left(\frac{\beta\hbar\omega}{2}\right)}{\sinh\left(\frac{\beta\hbar\omega}{2}\right)} = f(\omega),$$

the general method of integrating a complex function of the form $e^{i\omega z}f(z)$ along the real axis can be considered. In order to do this we apply evaluation of Fourier transforms and solve the problem for a closed semi-circular arc. As such we have an integral of the form[359]

$$I = \int_{-\infty}^{\infty} f(z)e^{imz}\mathrm{d}z.$$

Where if we assume that there are no poles on the real axis, that we have a finite number of poles, and that $f(z) \to 0 \quad \text{as} \quad |z| \to \infty$ then we can apply Cauchy's Residue Theorem and Jordan's Lemma in order to show that:

For $m > 0$ with a contour C_Γ in the upper half of the complex plane

$$\oint f(z)e^{imz}dz = \int_{-R}^{R} f(z)e^{imz}dz + \int_{\Gamma_2} f(z)e^{imz}dz$$

These assumptions come from the proof of Jordan's Lemma using complex analysis. While the proof is not shown here the Lemma is written out explicitly below and the assumptions briefly discussed[359].

Lemma D.1.2. *If C_Γ is the semi-circular arc given by $z = Re^{i\theta}, \ 0 \leq \theta \leq \pi$ then if*

$|f(z)| \to 0$ *as* $|z| \to \infty$ *then:*

$$I_R = \int_{C_\Gamma} f(z)e^{imz}dz \to 0, \quad m > 0 \quad \textit{and real.}$$

The reason for these requirements is that we have to consider which parts of the integrand tend to zero or infinity fastest. When we apply $z = Re^{i\theta}$ then our integrand contains both a small quantity, $f(z)$, and a large quantity, R. Our integrand is $f(Re^{i\theta})e^{imR\cos(\theta)}e^{-mR\sin(\theta)}iRe^{i\theta}$, so if we consider the magnitude of these quantities we find that we must evaluate $\epsilon Re^{-mR\sin(\theta)}$ between 0 and π. Given $\epsilon > 0$, there exists $R_0(\epsilon)$ such that $|z| > R_0 \Rightarrow |f(z)| < \epsilon$. Hence for $R > R_0$:

$$|I_R| \leq \int_0^\pi \epsilon|e^{imR\cos(\theta)}|e^{-mR\sin(\theta)}|iRe^{i\theta}|d\theta \leq \int_0^\pi \epsilon Re^{-mR\sin(\theta)}d\theta$$

We cannot find an analytical solution to this integral easily so we simply approximate it using an underestimate as a pair of straight lines. We apply, $0 \leq \theta \leq \frac{\pi}{2}$, $\sin(\theta) > \frac{2\theta}{\pi}$ so that we have a bound for the magnitude of this decay.

$$|I_R| \leq \epsilon R \cdot \frac{\pi}{mR}[1 - e^{-mR}] < \epsilon R \cdot \frac{\pi}{mR} = \frac{\epsilon\pi}{m}$$

The importance of this result is that the rate of decay of the sine term exactly cancels with the exponentially growing R component meaning that we are left with proportionality to only our small quantity ϵ.

$$\text{Hence,} \quad I_R \to 0, \quad \text{as} \quad R \to \infty \quad \text{for} \quad R > R_0(\epsilon)$$

This means that we can apply Jordan's lemma to the integral along the arc of our semi-circle which simplifies the contour integral to:

$$\oint f(z)dz = 2\pi i \sum \text{Res} = \int_{-\infty}^{\infty} f(z)e^{izT}dz + 0$$

Where Res are the residues of the poles inside the semi-circle C_Γ.

For the complex plane $\omega + i\sigma$ a semicircular contour in the upper half plane $C_\Gamma = \Gamma_1 + \Gamma_2$ is used such that the integral along the real axis can be computed

$$\int_{\Gamma_1} f(\omega)e^{i\omega t}\mathrm{d}\omega = 2\pi i \sum_j \text{Res}(j).$$

Initially take strictly positive poles for the contour in the upper half plane starting with the simple pole $z = i\gamma$.

$$\text{Res}\left(f(z), z = i\gamma\right) = \lim_{z \to i\gamma}\left((z - i\gamma)f(z)\right)$$

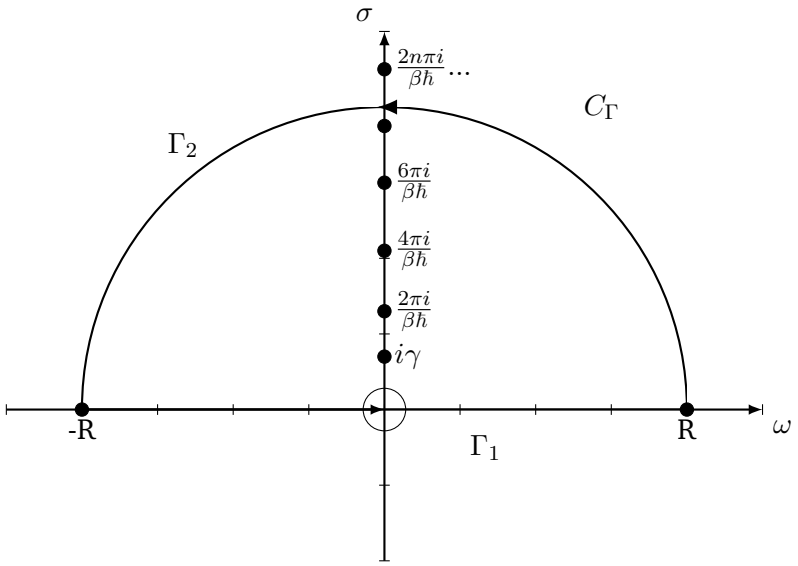

Figure D.1.2: Complex Semicircle, C_Γ, with a, temperature independent, pole at $i\gamma$ and further poles at integer multiples of $\frac{2\pi}{\beta\hbar}$ which correspond to Matsubara (thermal) frequencies.

$$\lim_{z\to i\gamma}\left(2\lambda\gamma\frac{z\gamma}{\gamma^2+z^2}(z-i\gamma)\frac{e^{\beta\hbar z}+1}{e^{\beta\hbar z}-1}e^{izt}\right)=\lambda\gamma^2\frac{e^{i\beta\hbar\gamma}+1}{e^{i\beta\hbar\gamma}-1}e^{-\gamma t}$$

Poles at $z=\frac{2n\pi i}{\beta\hbar}, n\in\mathbb{Z}\geq 1$ have residue

$$\mathrm{Res}\left(f(z), z=\frac{2n\pi i}{\beta\hbar}\right)=\lim_{z\to\frac{2n\pi i}{\beta\hbar}}\left(\frac{2\eta z\Lambda}{z^2+\Lambda^2}\frac{\exp(\beta\hbar z)+1}{\exp(\beta\hbar z)-1}\exp(izt)\right),$$

$$=\sum_{n=1}^{\infty}\left(\frac{2\eta\frac{2n\pi i}{\beta\hbar}\Lambda}{\left(\frac{2n\pi i}{\beta\hbar}\right)^2+\Lambda^2}\frac{\exp(\beta\hbar\frac{2n\pi i}{\beta\hbar})+1}{\exp(\beta\hbar\frac{2n\pi i}{\beta\hbar})-1}\exp(it\frac{2n\pi i}{\beta\hbar})\right), \tag{D.1.211}$$

$$=\sum_{n=1}^{\infty}\frac{4\eta\Lambda n\pi i}{\beta\hbar\left(\Lambda^2-\left(\frac{2n\pi}{\beta\hbar}\right)^2\right)}\frac{\exp(2n\pi i)+1}{\exp(2n\pi i)-1}\exp\Big(-\frac{2n\pi t}{\beta\hbar}\Big), \tag{D.1.212}$$

which, by removing the singularity, yields

$$\sum_{n=1}^{\infty}\frac{4\eta\Lambda n\pi i}{\beta\hbar\left((\Lambda)^2-\left(\frac{2n\pi i}{\beta\hbar}\right)^2\right)}(\exp(2n\pi i)+1)\exp\left(i\left(\frac{2n\pi i}{\beta\hbar}\right)t\right)$$

$$=\sum_{n=1}^{\infty}\frac{8\eta\Lambda n\pi i\beta\hbar}{(\Lambda\beta\hbar)^2-(2n\pi)^2}e^{-\frac{2n\pi t}{\beta\hbar}}. \tag{D.1.213}$$

In order to apply the residue theorem we require

$$|f(z)|\to 0 \quad \text{as} \quad |z|\to\infty, \tag{D.1.214}$$

so in this case

$$\lim_{z\to\infty} \frac{2\eta z\Lambda}{z^2+\Lambda^2}\frac{\cosh\left(\frac{\beta\hbar z}{2}\right)}{\sinh\left(\frac{\beta\hbar z}{2}\right)} \tag{D.1.215}$$

$$= \lim_{z\to\infty} \frac{2\eta\Lambda}{z+\frac{\Lambda^2}{z}}\frac{\exp(-\beta\hbar z)+1}{1-\exp(-\beta\hbar z)}, \tag{D.1.216}$$

where

$$\exp(-\beta\hbar z)\to 0 \quad \text{as} \quad z\to 0, \tag{D.1.217}$$

and

$$\frac{2\eta\Lambda}{z+\frac{\Lambda^2}{z}} \text{ is } \mathcal{O}\left(\frac{1}{z}\right) \quad \text{as} \quad z\to 0, \tag{D.1.218}$$

hence Jordan's lemma is valid. Finally, the overall result of complex integration over the upper half plane is

$$\int_{\Gamma_1} f(\omega)e^{i\omega t}\mathrm{d}\omega = 2\pi i\left[\eta\Lambda\frac{e^{i\beta\hbar\Lambda}+1}{e^{i\beta\hbar\Lambda}-1}e^{-\Lambda t}+\sum_{n=1}^{\infty}\frac{8\eta\Lambda n\pi i\beta\hbar}{(\Lambda\beta\hbar)^2-(2n\pi)^2}e^{-\frac{2n\pi t}{\beta\hbar}}\right].$$

By defining Matsubara frequencies $\nu_0=\Lambda, \nu_n=\frac{2n\pi}{\beta\hbar}$ we can introduce the definition of $\cot$ into our solution. While we can choose any contour which contains any number of poles in order to calculate the integral, physically the choice of strictly positive Matsubara frequencies is another good justification for considering only the upper half plane.

$$L_{\mathcal{R}}^{(\alpha)}(t) = \frac{1}{2\pi}\mathcal{R}\left[\int_{\Gamma_1} f(\omega)e^{i\omega t}\mathrm{d}\omega\right].$$

Hence the result for the first integral is

$$L_{\mathcal{R}}^{(\alpha)}(t) = \eta\Lambda\cot\left(\frac{\beta\hbar\Lambda}{2}\right)e^{-\Lambda t}+\sum_{n=1}^{\infty}\frac{4\eta\Lambda\nu_n\beta\hbar}{(\nu_n\beta\hbar)^2-(\Lambda\beta\hbar)^2}e^{-\nu_n t} \tag{D.1.219}$$

Next the integral for the $L_{\mathcal{I}}^{(\alpha)}(t)$ component,

$$iL_{\mathcal{I}}^{(\alpha)}(t) = \frac{1}{\pi}\int_0^{\infty} -J(\omega)i\sin(\omega t)\ \mathrm{d}\omega.$$

$\sin(\omega t)$ has no poles in the complex plane so the only residue will be from the single Matsubara frequency in the upper half plane.

$$iL_{\mathcal{I}}^{(\alpha)}(t) = -\frac{i}{2\pi}\mathcal{I}\left[\int_{-\infty}^{\infty}\frac{2\eta\Lambda\omega}{\Lambda^2+\omega^2}e^{i\omega t}\mathrm{d}\omega\right].$$

$$\mathrm{Res}(f(z), z=i\Lambda) = \lim_{z\to i\Lambda}((z-i\Lambda)f(z)),$$

$$iL_{\mathcal{I}}^{(\alpha)}(t) = -\frac{i}{2\pi}\mathcal{I}\left[2\pi i\eta\Lambda e^{-\Lambda t}\right],$$

$$L_{\mathcal{I}}^{(\alpha)} = -\eta\Lambda e^{-\Lambda t} \tag{D.1.220}$$

This solution uses the same function $f(z)$ and so Jordan's lemma is still valid. Finally the solution of equation (D.1.10.1.2) can be reconstructed using equations (D.1.10.1.2) and (D.1.10.1.2)

$$L_{\mathrm{corr}}^{(\alpha)}(t) = L_{\mathcal{R}}^{(\alpha)} + iL_{\mathcal{I}}^{(\alpha)}.$$

$$L_{\mathrm{corr}}^{(\alpha)}(t) = \eta\Lambda \cot\left(\frac{\beta\hbar\Lambda}{2}\right) e^{-\Lambda t} + \sum_{n=1}^{\infty} \frac{4\eta\Lambda\nu_n\beta\hbar}{(\nu_n\beta\hbar)^2 - (\Lambda\beta\hbar)^2} e^{-\nu_n t} - i\eta\Lambda e^{-\Lambda t},$$

which can be simplified in terms of purely Matsubara frequencies by denoting,

$$d_0 = \eta\Lambda(\cot\left(\frac{\beta\hbar\Lambda}{2}\right) - i), \quad \nu_0 = \Lambda, \tag{D.1.221}$$

$$d_n = \frac{4\eta\Lambda\nu_n\beta\hbar}{(\nu_n\beta\hbar)^2 - (\Lambda\beta\hbar)^2}, \quad \nu_n = \frac{2n\pi}{\beta\hbar}, \tag{D.1.222}$$

such that

$$L_{\mathrm{corr}}^{(\alpha)}(t) = \sum_{n=0}^{\infty} d_n \exp(-\nu_n t). \tag{D.1.223}$$

The resulting form of the correlation function, in exponential form, represents physically a memory-frequency decomposition of the bath correlation. The exponential expansion of bath correlation function dictates the structure of the HEOM being derived[286–288]. Given this form of the correlation function, we now differentiate the equation for the density matrix, (D.1.10.1.2), in order to reach the HEOM.

$$\frac{\mathrm{d}}{\mathrm{d}t}\rho(t) = \frac{\mathrm{d}}{\mathrm{d}t}\mathcal{U}(t,t_0)\rho_S(t_0), \tag{D.1.224}$$

where the Liouville space evolution superoperator is

$$\mathcal{U}(t,t_0) = \int_{\mathrm{q}_0}^{\mathrm{q}_t}\int_{\mathrm{q}_0'}^{\mathrm{q}_t'} \exp(i\mathrm{S}_{\mathrm{S}}[\mathrm{q}_t]/\hbar)\exp(-i\mathrm{S}_{\mathrm{S}}[\mathrm{q}_t']/\hbar)\mathcal{F}[\mathrm{q}_t,\mathrm{q}_t'] \;\; \mathcal{D}[\mathrm{q}_t]\mathcal{D}[\mathrm{q}_t'] \tag{D.1.225}$$

with

$$\mathcal{F}[\mathrm{q}_t,\mathrm{q}_t'] = \exp\Big(-\frac{1}{\hbar}\int_0^t\int_0^{\tau'} (\mathrm{q}_t(\tau) - \mathrm{q}_t'(\tau))\times (L_{\mathrm{corr}}^{(\alpha)}(\tau-s)\mathrm{q}_t(s) - L_{\mathrm{corr}}^{(\alpha)*}(\tau-s)\mathrm{q}_t'(s))\,\mathrm{d}\tau\,\mathrm{d}s\Big). \tag{D.1.226}$$

The Caldeira-Leggett form of the Feynman path integral[143], in terms of microscopic position and momentum operators in space, can be reformulated into a more useful basis for computation. In a manner similar to the Stochastic Schrödinger equation we move into a coherent state basis which is dependent on the creation and annihilation operators for the system modes, $\mathrm{a}_i^\dagger$ and a_i, rather than operators x_j and p_j for environment modes $\{j\}$. This representation

uses

$$|\phi\rangle = \exp\Big(\sum_i \phi_i \mathrm{a}^\dagger\Big)\,|0\rangle\,, \tag{D.1.227}$$

where $|0\rangle$ is the system vacuum sate, ϕ_i are complex numbers, and ϕ_i^* their complex conjugates such that

$$\mathrm{a}_i\,|\phi\rangle = \phi_i\,|\phi\rangle\,, \tag{D.1.228}$$

$$\langle\phi|\,\mathrm{a}_i^\dagger = \langle\phi|\,\phi_i^*, \tag{D.1.229}$$

as in the original derivation by Tanimura and Kubo[147]. This transformation results in

$$\mathcal{U}(t,t_0) = \int_{\mathrm{Q}_0}^{\mathrm{Q}_t}\int_{\mathrm{Q}_0'}^{\mathrm{Q}_t'} \exp(i\mathrm{S}_\mathrm{S}[\mathrm{Q}_t]/\hbar)\exp(-i\mathrm{S}_\mathrm{S}[\mathrm{Q}_t']/\hbar)\mathcal{F}[\mathrm{Q}_t,\mathrm{Q}_t']\;\;\mathcal{D}[\mathrm{Q}_t]\mathcal{D}[\mathrm{Q}_t'] \tag{D.1.230}$$

and

$$\mathcal{F}[\mathrm{Q}_t,\mathrm{Q}_t'] = \exp\Big(-\frac{1}{\hbar^2}\int_0^t\int_0^{\tau'} \mathrm{B}^\times(\mathrm{Q}_t,\mathrm{Q}_t')\times \Big(L_\mathcal{R}^{(\alpha)}(\tau'-\tau)\mathrm{B}^\times(\mathrm{Q}_t,\mathrm{Q}_t') - iL_\mathcal{I}^{(\alpha)}(\tau'-\tau)\mathrm{B}^\circ(\mathrm{Q}_t,\mathrm{Q}_t')\Big)\,\mathrm{d}\tau\,\mathrm{d}\tau'\Big), \tag{D.1.231}$$

where

$$\mathrm{B}^\times(\mathrm{Q}_t,\mathrm{Q}_t') = \mathrm{B}(\mathrm{Q}_t(\tau)) + \mathrm{B}(\mathrm{Q}_t'(\tau)), \tag{D.1.232}$$

$$\mathrm{B}^\circ(\mathrm{Q}_t,\mathrm{Q}_t') = \mathrm{B}(\mathrm{Q}_t(\tau)) - \mathrm{B}(\mathrm{Q}_t'(\tau)). \tag{D.1.233}$$

This is a movement from trajectories in physical space to trajectories of coherent states: $\mathrm{q}^{(\prime)}$ and $\mathrm{x}^{(\prime)}$ to $\mathrm{Q}_t = (\phi^*(\tau),\phi(\tau))$ and $\mathrm{Q}_t' = (\phi'^*(\tau),\phi'(\tau))$. Into this we can substitute the kernels generated from the spectral density via contour integration and can rearrange the influence functional to

$$\mathcal{F}[\mathrm{Q}_t,\mathrm{Q}_t'] = \exp\Big(-\frac{1}{\hbar^2}\int_0^t\int_0^{\tau'} \mathrm{B}^\times\times\Big(\eta\Lambda\cot\Big(\frac{\beta\hbar\Lambda}{2}\Big)\mathrm{B}^\times - i\eta\Lambda\mathrm{B}^\circ\Big)\exp(-\Lambda(\tau'-\tau)) + \mathrm{B}^\times\mathrm{B}^\times\sum_{n=1}^{\infty}\frac{4\eta\Lambda\nu_n\beta\hbar}{(\nu_n\beta\hbar)^2-(\Lambda\beta\hbar)^2}\exp(-\nu_n(\tau'-\tau))\,\mathrm{d}\tau\,\mathrm{d}\tau'\Big). \tag{D.1.234}$$

Depending on the choice of spectral density, and the complexity of the Matsubara decomposition and frequencies, the difficulty of the following simplification to an equation of motion can vary. In the simplest overdamped scenario where there is not an infinite number of Matsubara contributions, substitution of the kernels is enough simplification[138,149], however in other cases further simplifying assumptions can reduce the expansion complexity.

D.1.10.1.3 High Temperature Hierarchies

This derivation is the simpler of the two temperature cases because it involves two additional approximations: the high temperature approximation, and the assumption that the average thermal energy of the oscillators is large. In this simplified case we have[147,149]

$$J_{\mathrm{O}}(\omega) = \frac{2\eta\omega\Lambda_{\mathrm{O}}}{\Lambda_{\mathrm{O}}^2 + \omega^2}, \tag{D.1.235}$$

where

$$\beta\hbar\Lambda_{\mathrm{O}} \ll 1, \quad \text{and} \quad \coth\Big(\frac{\beta\hbar\Lambda_{\mathrm{O}}}{2}\Big) \sim 1. \tag{D.1.236}$$

The overdamped bath speed, Λ_{O}, is similar to the previous overdamped bath speed, Λ, but the latter does not include any assumption about the scale of the oscillator energy. Consequently the imaginary and real kernels become:

$$L_{\mathcal{I}}^{(\alpha)} = -\eta\frac{\beta\hbar\Lambda_{\mathrm{O}}}{2}\exp(-\Lambda_{\mathrm{O}}t), \quad L_{\mathcal{R}}^{(\alpha)} = \eta\exp(-\Lambda_{\mathrm{O}}t). \tag{D.1.237}$$

These can be directly substituted into the influence functional requiring minimal extra simplification

$$\mathcal{F}[\mathrm{Q}_t, \mathrm{Q}'_t] = \exp\Bigg(\Big(-\frac{i}{\hbar}\Big)^2 \times \int_0^t \mathrm{B}^{\times}\exp(-\Lambda_{\mathrm{O}}\tau')\int_0^{\tau'}\eta\Big(\mathrm{B}^{\times} - i\frac{\beta\hbar\Lambda_{\mathrm{O}}}{2}\mathrm{B}^{\circ}\Big)\exp(\Lambda_{\mathrm{O}}\tau)\,\mathrm{d}\tau\;\,\mathrm{d}\tau'\Bigg). \tag{D.1.238}$$

This can then be introduced into the equation for the density matrix elements,

$$\rho_n(\phi,\phi^*;t) = \iint\Bigg\{\Big(-\frac{i}{\hbar}\Big)\int_0^t \exp(-\Lambda_{\mathrm{O}}(t-\tau))\eta\Big(\mathrm{B}^{\times} - i\frac{\beta\hbar\Lambda_{\mathrm{O}}}{2}\mathrm{B}^{\circ}\Big)\,\mathrm{d}\tau\Bigg\}^n \times \exp\Big(\frac{i\mathrm{S}_{\mathrm{S}}[\mathrm{Q}_t]}{\hbar}\Big)\mathcal{F}[\mathrm{Q}_t,\mathrm{Q}'_t]\exp\Big(\frac{-i\mathrm{S}_{\mathrm{S}}[\mathrm{Q}'_t]}{\hbar}\Big)\,\mathcal{D}[\mathrm{Q}'_t]\,\mathcal{D}[\mathrm{Q}_t], \tag{D.1.239}$$

which is differentiated to form the equation of motion.

D.1.10.1.4 Low Temperature Hierarchies

By relaxing the high temperature and oscillator energy scale approximations results in the most general form of an overdamped hierarchy. This equation will use the standard overdamped spectral density, equation (2.5.4.1), and will have an infinite number of Matsubara frequencies in its expansion. It is possible to relate the individual Matsubara frequency components to each other through a recursion relation, which for low number of Matusbara axes (such as in

undamped hierarchies)[289] can be advantageous, and this is equivalent to applying a cutoff to the Matsubara sum and expanding[138,150,219]. This assumption means that we are simplifying the breadth of certain Matsubara terms to delta functions (rather than having widths dependent on their relative speed) and this is valid for low temperatures as well as for stronger coupling. Subsequently, components beyond the cutoff criterion are assumed to be fully Markovian and have instantaneous correlation times. This allows the influence functional for a more complex overdamped spectral density, equation (D.1.10.1.2), can be written as

$$\begin{aligned}\mathcal{F}[\mathrm{Q}_t,\mathrm{Q}'_t] \approx \exp\Bigg(&-\Big(\frac{i}{\hbar}\Big)^2\int_0^t \mathrm{B}^\times \exp(-\Lambda_\mathrm{O}\tau')\times\\ &\int_0^{\tau'}\Big(\eta\Lambda_\mathrm{O}\cot\Big(\frac{\beta\hbar\Lambda_\mathrm{O}}{2}\Big)\mathrm{B}^\times - i\eta\Lambda_\mathrm{O}\mathrm{B}^\circ\Big)\exp(\Lambda_\mathrm{O}\tau)\,\mathrm{d}\tau\,\mathrm{d}\tau' +\\ \Big(-\frac{i}{\hbar}\Big)^2\sum_{n=1}^{K}\int_0^t \mathrm{B}^\times\exp(-\nu_n\tau')\int_0^{\tau'}\mathrm{B}^\times\frac{4\eta\Lambda_\mathrm{O}\nu_n\beta\hbar}{(\nu_n\beta\hbar)^2-(\Lambda_\mathrm{O}\beta\hbar)^2}\exp(\nu_n\tau)\,\mathrm{d}\tau\,\mathrm{d}\tau' +&\\ \sum_{n=K+1}^{\infty}\int_0^t\mathrm{B}^\times\frac{4\eta\Lambda_\mathrm{O}\nu_n\beta\hbar}{(\nu_n\beta\hbar)^2-(\Lambda_\mathrm{O}\beta\hbar)^2}\,\mathrm{d}\tau\Bigg),\end{aligned}\tag{D.1.240}$$

under the assumption that

$$\nu_n\exp(-\nu_n(\tau-\tau')) \approx \delta(\tau-\tau') \quad \text{when} \quad n \geq K+1.\tag{D.1.241}$$

This can be simplified to

$$\begin{aligned}\mathcal{F}[\mathrm{Q}_t,\mathrm{Q}'_t] \approx \exp\Bigg(&\frac{1}{\hbar^2}\int_0^t\mathrm{B}^\times\exp(-\Lambda_\mathrm{O}\tau')\int_0^{\tau'}\Lambda_\mathrm{O}\theta_{(\mathrm{O})}\exp(\Lambda_\mathrm{O}\tau)\,\mathrm{d}\tau\,\mathrm{d}\tau'\Bigg)\times\\ \prod_{n=1}^{K}\exp\Bigg(&+\frac{1}{\hbar^2}\int_0^t\mathrm{B}^\times\exp(-\nu_n\tau')\int_0^{\tau'}\nu_n\psi_n^{(\mathrm{O})}\exp(\nu_n\tau)\,\mathrm{d}\tau\,\mathrm{d}\tau'\Bigg)\times\\ &\prod_{n=K+1}^{\infty}\exp\Bigg(\int_0^t\frac{1}{\hbar^2}\mathrm{B}^\times\psi_n^{(\mathrm{O})}\,\mathrm{d}\tau\Bigg),\end{aligned}\tag{D.1.242}$$

by defining

$$\theta_{(\mathrm{O})} = \Big(\eta\Lambda_\mathrm{O}\cot\Big(\frac{\beta\hbar\Lambda_\mathrm{O}}{2}\Big)\mathrm{B}^\times - i\eta\Lambda_\mathrm{O}\mathrm{B}^\circ\Big),\tag{D.1.243}$$

$$\psi_n^{(\mathrm{O})} = \mathrm{B}^\times\frac{4\eta\Lambda_\mathrm{O}\nu_n\beta\hbar}{(\nu_n\beta\hbar)^2-(\Lambda_\mathrm{O}\beta\hbar)^2}.\tag{D.1.244}$$

This is equivalent to saying that

$$\nu_K = \frac{2\pi K}{\beta\hbar} \gg \omega_0,\tag{D.1.245}$$

where ω_0 is the fundamental system mode. If we introduce the equation for the density matrix element

$$\begin{aligned}\rho_{\mathbf{j}}(\phi,\phi^*;t) = \iint \left\{ \Big(-\frac{i}{\hbar}\int_0^t \exp(-\Lambda_{\mathrm{O}}(t-\tau))\theta_{(\mathrm{O})}\,\mathrm{d}\tau \Big) \right\}^{j_0} \times \\ \prod_{n=1}^{K} \left\{ \Big(-\frac{i}{\hbar}\int_0^t \exp(-\nu_n(t-\tau))\psi_n^{(\mathrm{O})}\,\mathrm{d}\tau \Big) \right\}^{j_n} \times \\ \exp\Big(\frac{i\mathrm{S}_{\mathrm{S}}[\mathrm{Q}_t]}{\hbar}\Big)\mathcal{F}[\mathrm{Q}_t,\mathrm{Q}'_t]\exp\Big(\frac{-i\mathrm{S}_{\mathrm{S}}[\mathrm{Q}'_t]}{\hbar}\Big)\,\mathcal{D}[\mathrm{Q}'_t]\,\mathcal{D}[\mathrm{Q}_t], \quad \text{(D.1.246)}\end{aligned}$$

then we can construct the equation of motion by differentiating this equation and substituting for influence functional. Notice, that when compared to the high-temperature density matrix element, each ADO is defined by a component of the vector $\mathbf{j} = (j_0,\ldots,j_n,\ldots,j_K)$ as there is now a Matsubara sum component. For simplicity we denote the first two sets of braces (each with exponents) as χ and then successively apply the chain, product, and Liebniz rules.

$$\frac{\partial \rho_n}{\partial t} = \iint \frac{\partial}{\partial t}\Big\{\chi\exp\Big(\frac{i\mathrm{S}_{\mathrm{S}}[\mathrm{Q}_t]}{\hbar}\Big)\mathcal{F}[\mathrm{Q}_t,\mathrm{Q}'_t]\exp\Big(\frac{-i\mathrm{S}_{\mathrm{S}}[\mathrm{Q}'_t]}{\hbar}\Big)\Big\}\,\mathcal{D}[\mathrm{Q}'_t]\,\mathcal{D}[\mathrm{Q}_t], \quad \text{(D.1.247)}$$

First with the product rule this can be expanded to

$$\begin{aligned}\frac{\partial \rho_{\mathbf{j}}}{\partial t} = \iint \frac{\partial \chi}{\partial t}\exp\Big(\frac{i\mathrm{S}_{\mathrm{S}}[\mathrm{Q}_t]}{\hbar}\Big)\mathcal{F}[\mathrm{Q}_t,\mathrm{Q}'_t]\exp\Big(\frac{-i\mathrm{S}_{\mathrm{S}}[\mathrm{Q}'_t]}{\hbar}\Big) \\ + \chi\frac{\partial}{\partial t}\left\{\exp\Big(\frac{i\mathrm{S}_{\mathrm{S}}[\mathrm{Q}_t]}{\hbar}\Big)\right\}\mathcal{F}[\mathrm{Q}_t,\mathrm{Q}'_t]\exp\Big(\frac{-i\mathrm{S}_{\mathrm{S}}[\mathrm{Q}'_t]}{\hbar}\Big) \\ + \chi\exp\Big(\frac{i\mathrm{S}_{\mathrm{S}}[\mathrm{Q}_t]}{\hbar}\Big)\frac{\partial}{\partial t}\left\{\mathcal{F}[\mathrm{Q}_t,\mathrm{Q}'_t]\right\}\exp\Big(\frac{-i\mathrm{S}_{\mathrm{S}}[\mathrm{Q}'_t]}{\hbar}\Big) \\ + \chi\exp\Big(\frac{i\mathrm{S}_{\mathrm{S}}[\mathrm{Q}_t]}{\hbar}\Big)\mathcal{F}[\mathrm{Q}_t,\mathrm{Q}'_t]\frac{\partial}{\partial t}\left\{\exp\Big(\frac{-i\mathrm{S}_{\mathrm{S}}[\mathrm{Q}'_t]}{\hbar}\Big)\right\}\mathcal{D}[\mathrm{Q}'_t]\,\mathcal{D}[\mathrm{Q}_t], \quad \text{(D.1.248)}\end{aligned}$$

which via application of the chain rule becomes

$$\begin{aligned}\frac{\partial \rho_{\mathbf{j}}}{\partial t} = \iint \frac{\partial \chi}{\partial t}\exp\Big(\frac{i\mathrm{S}_{\mathrm{S}}[\mathrm{Q}_t]}{\hbar}\Big)\mathcal{F}[\mathrm{Q}_t,\mathrm{Q}'_t]\exp\Big(\frac{-i\mathrm{S}_{\mathrm{S}}[\mathrm{Q}'_t]}{\hbar}\Big) + \frac{i}{\hbar}\frac{\partial \mathrm{S}_{\mathrm{S}}[\mathrm{Q}_t]}{\partial t}\rho_{\mathbf{j}} \\ + \chi\exp\Big(\frac{i\mathrm{S}_{\mathrm{S}}[\mathrm{Q}_t]}{\hbar}\Big)\frac{\partial}{\partial t}\left\{\mathcal{F}[\mathrm{Q}_t,\mathrm{Q}'_t]\right\}\exp\Big(\frac{-i\mathrm{S}_{\mathrm{S}}[\mathrm{Q}'_t]}{\hbar}\Big) - \frac{i}{\hbar}\frac{\partial \mathrm{S}_{\mathrm{S}}[\mathrm{Q}'_t]}{\partial t}\rho_{\mathbf{j}}\,\mathcal{D}[\mathrm{Q}'_t]\,\mathcal{D}[\mathrm{Q}_t]. \quad \text{(D.1.249)}\end{aligned}$$

Next we consider the differential of χ:

$$\frac{\partial \chi}{\partial t} = \frac{\partial}{\partial t}\Bigg(\bigg\{\Big(-\frac{i}{\hbar}\int_0^t \exp(-\Lambda_{\mathrm{O}}(t-\tau))\theta_{(\mathrm{O})}\,\mathrm{d}\tau\Big)\bigg\}^{j_0}\times \prod_{n=1}^{K}\bigg\{\Big(-\frac{i}{\hbar}\int_0^t \exp(-\nu_n(t-\tau))\psi_n^{(\mathrm{O})}\,\mathrm{d}\tau\Big)\bigg\}^{j_n}\Bigg), \quad \text{(D.1.250)}$$

which through the product and chain rules can be expanded to

$$\begin{aligned}\frac{\partial \chi}{\partial t} = j_0\bigg\{\Big(-\frac{i}{\hbar}\int_0^t \exp(-\Lambda_{\mathrm{O}}(t-\tau))\theta_{(\mathrm{O})}\,\mathrm{d}\tau\Big)\bigg\}^{j_0-1} &\times \frac{\partial}{\partial t}\bigg\{\Big(-\frac{i}{\hbar}\int_0^t \exp(-\Lambda_{\mathrm{O}}(t-\tau))\theta_{(\mathrm{O})}\,\mathrm{d}\tau\Big)\bigg\} \\ \times \prod_{n=1}^{K}\bigg\{\Big(-\frac{i}{\hbar}\int_0^t \exp(-\nu_n(t-\tau))\psi_n^{(\mathrm{O})}\,\mathrm{d}\tau\Big)\bigg\}^{j_n}\Bigg) + &\\ \sum_{n=1}^{K} j_n\bigg\{\Big(-\frac{i}{\hbar}\int_0^t \exp(-\nu_n(t-\tau))\psi_n^{(\mathrm{O})}\,\mathrm{d}\tau\Big)\bigg\}^{j_n-1} &\times \frac{\partial}{\partial t}\bigg\{\Big(-\frac{i}{\hbar}\int_0^t \exp(-\nu_n(t-\tau))\psi_n^{(\mathrm{O})}\,\mathrm{d}\tau\Big)\bigg\} \\ \times \prod_{l=1,\ l\neq n}^{K}\Big(-\frac{i}{\hbar}\int_0^t \exp(-\nu_l(t-\tau))\psi_l^{(\mathrm{O})}\,\mathrm{d}\tau\Big)\times &\\ \bigg\{\Big(-\frac{i}{\hbar}\int_0^t \exp(-\Lambda_{\mathrm{O}}(t-\tau))\theta_{(\mathrm{O})}\,\mathrm{d}\tau\Big)\bigg\}^{j_0}. \quad \text{(D.1.251)}\end{aligned}$$

Take the first term on the right hand side and apply the product rule, followed by the Liebniz rule yielding

$$
\begin{aligned}
j_0\Big\{\Big(-\frac{i}{\hbar}\int_0^t \exp(-\Lambda_{\mathrm{O}}(t-\tau))\theta_{(\mathrm{O})}\,\mathrm{d}\tau\Big)\Big\}^{j_0-1} \\
\times\frac{\partial}{\partial t}\Big\{\Big(-\frac{i}{\hbar}\int_0^t \exp(-\Lambda_{\mathrm{O}}(t-\tau))\theta_{(\mathrm{O})}\,\mathrm{d}\tau\Big)\Big\} \\
\times\prod_{n=1}^{K}\Big\{\Big(-\frac{i}{\hbar}\int_0^t \exp(-\nu_n(t-\tau))\psi_n^{(\mathrm{O})}\,\mathrm{d}\tau\Big)\Big\}^{j_n}\Big) = \\
-j_0\Lambda_{\mathrm{O}}\chi - j_0\Big\{\Big(-\frac{i}{\hbar}\int_0^t \exp(-\Lambda_{\mathrm{O}}(t-\tau))\theta_{(\mathrm{O})}\,\mathrm{d}\tau\Big)\Big\}^{j_0-1}\times-\frac{i\theta_{(\mathrm{O})}}{\hbar} \\
\times\prod_{n=1}^{K}\Big\{\Big(-\frac{i}{\hbar}\int_0^t \exp(-\nu_n(t-\tau))\psi_n^{(\mathrm{O})}\,\mathrm{d}\tau\Big)\Big\}^{j_n}\Big)+ \\
j_0\Big\{\Big(-\frac{i}{\hbar}\int_0^t \exp(-\Lambda_{\mathrm{O}}(t-\tau))\theta_{(\mathrm{O})}\,\mathrm{d}\tau\Big)\Big\}^{j_0-1} \\
\times\Big(-\frac{i}{\hbar}\int_0^t \exp(-\Lambda_{\mathrm{O}}(t-\tau))\frac{\partial\theta_{(\mathrm{O})}}{\partial t}\,\mathrm{d}\tau\Big) \\
\times\prod_{n=1}^{K}\Big\{\Big(-\frac{i}{\hbar}\int_0^t \exp(-\nu_n(t-\tau))\psi_n^{(\mathrm{O})}\,\mathrm{d}\tau\Big)\Big\}^{j_n}\Big). \qquad \text{(D.1.252)}
\end{aligned}
$$

Given the fact that $\mathrm{B}^{\times}$ and B° are not explicitly time dependent, the last term vanishes simplifying this to $-j_0\Lambda_{\mathrm{O}}\chi - \frac{ij_0}{\hbar}\chi_{j_0}^{-}$, where $\chi_{j_0}^{-}$ is shorthand for χ where the exponent j_0 on the first half of the equation contained in parentheses is reduced to an exponent of j_0-1. In an equivalent manner the second terms can be expanded and reduced so that overall

$$
\frac{\partial\chi}{\partial t} = -j_0\Lambda_{\mathrm{O}}\chi - \frac{ij_0}{\hbar}\chi_{j_0}^{-} - \sum_{n=1}^{K} j_n\nu_n\chi - \frac{ij_n}{\hbar}\psi_n^{(\mathrm{O})}\chi_{j_n}^{-}, \qquad \text{(D.1.253)}
$$

where $\chi_{j_n}^{-}$ is shorthand for χ where the exponent j_n on the second half of the equation contained in parentheses is reduced to an exponent of j_n-1. This can be reformulated to match the form generated from a recursion relation:

$$
\frac{\partial\chi}{\partial t} = -\sum_{n=0}^{K} j_n\nu_n\chi - \frac{i}{\hbar}\Big\{d_n\mathrm{B}(\mathrm{Q}_t)\chi_{j_n}^{-} - d_n^{*}\mathrm{B}(\mathrm{Q}_t')\chi_{j_n}^{-}\Big\}, \qquad \text{(D.1.254)}
$$

where d_n are the coefficients from the Matsubara expansion, equation 2.5.4.1.2, $*$ denotes the complex conjugate, and where j_0 and j_n have been combined in a manner equivalent to the poles in the Matsubara expansion. This means that the sum has been expanded to include zero.

The last term to consider is the differential of the influence functional. Taking

equation 2.5.4.1.2 and differentiating it through the chain rule and then application of Liebniz rule results in

$$\frac{\partial \mathcal{F}}{\partial t} \approx \Bigg\{ \left(\frac{1}{\hbar^2} \mathrm{B}^{\times} \exp(-\Lambda_{\mathrm{O}} t) \int_0^{\tau'} \Lambda_{\mathrm{O}} \theta_{(\mathrm{O})} \exp(\Lambda_{\mathrm{O}} \tau) \, \mathrm{d}\tau \right) + \sum_{n=1}^{K} \exp\left(\frac{1}{\hbar^2} \mathrm{B}^{\times} \exp(-\nu_n t) \int_0^{\tau'} \nu_n \psi_n^{(\mathrm{O})} \exp(\nu_n \tau) \, \mathrm{d}\tau \right) + \frac{1}{\hbar^2} \sum_{n=K+1}^{\infty} \exp\left(\mathrm{B}^{\times} \psi_n^{(\mathrm{O})} \right) \Bigg\} \mathcal{F}, \quad \text{(D.1.255)}$$

as none of the integrands are dependent on t. All of these terms can then be resubstituted into the equation for the derivative of the density matrix element:

$$\begin{aligned} \frac{\partial \rho_{\mathbf{j}}}{\partial t} = \iint & \frac{i}{\hbar} \frac{\partial \mathrm{S}_{\mathrm{S}}[\mathrm{Q}_t]}{\partial t} \rho_{\mathbf{j}} - \frac{i}{\hbar} \frac{\partial \mathrm{S}_{\mathrm{S}}[\mathrm{Q}'_t]}{\partial t} \rho_{\mathbf{j}} - \\ & \sum_{n=0}^{K} j_n \nu_n \chi \exp\left(\frac{i \mathrm{S}_{\mathrm{S}}[\mathrm{Q}_t]}{\hbar} \right) \mathcal{F}[\mathrm{Q}_t, \mathrm{Q}'_t] \exp\left(\frac{-i \mathrm{S}_{\mathrm{S}}[\mathrm{Q}'_t]}{\hbar} \right) \\ - \frac{i}{\hbar} & \left\{ d_n \mathrm{B}(\mathrm{Q}_t) \chi_{j_n}^{-} - d_n^{*} \mathrm{B}(\mathrm{Q}'_t) \chi_{j_n}^{-} \right\} \exp\left(\frac{i \mathrm{S}_{\mathrm{S}}[\mathrm{Q}_t]}{\hbar} \right) \mathcal{F}[\mathrm{Q}_t, \mathrm{Q}'_t] \exp\left(\frac{-i \mathrm{S}_{\mathrm{S}}[\mathrm{Q}'_t]}{\hbar} \right) \\ & + \chi \exp\left(\frac{i \mathrm{S}_{\mathrm{S}}[\mathrm{Q}_t]}{\hbar} \right) \Bigg\{ \left(\frac{1}{\hbar^2} \mathrm{B}^{\times} \exp(-\Lambda_{\mathrm{O}} t) \int_0^{\tau'} \Lambda_{\mathrm{O}} \theta_{(\mathrm{O})} \exp(\Lambda_{\mathrm{O}} \tau) \, \mathrm{d}\tau \right) + \\ & \sum_{n=1}^{K} \exp\left(\frac{1}{\hbar^2} \mathrm{B}^{\times} \exp(-\nu_n t) \int_0^{\tau'} \nu_n \psi_n^{(\mathrm{O})} \exp(\nu_n \tau) \, \mathrm{d}\tau \right) + \\ & \frac{1}{\hbar^2} \sum_{n=K+1}^{\infty} \exp\left(\mathrm{B}^{\times} \psi_n^{(\mathrm{O})} \right) \Bigg\} \mathcal{F} \times - \exp\left(\frac{i \mathrm{S}_{\mathrm{S}}[\mathrm{Q}'_t]}{\hbar} \right) \mathcal{D}[\mathrm{Q}'_t] \, \mathcal{D}[\mathrm{Q}_t]. \end{aligned} \quad \text{(D.1.256)}$$

This can be simplified to

$$\begin{aligned} \frac{\partial \rho_{\mathbf{j}}}{\partial t} = \iint & \frac{i}{\hbar} \frac{\partial \mathrm{S}_{\mathrm{S}}[\mathrm{Q}_t]}{\partial t} \rho_{\mathbf{j}} - \\ & \frac{i}{\hbar} \frac{\partial \mathrm{S}_{\mathrm{S}}[\mathrm{Q}'_t]}{\partial t} \rho_{\mathbf{j}} - \sum_{n=0}^{K} j_n \nu_n \rho_{j_n} - \frac{i}{\hbar} \left\{ d_n \mathrm{B}(\mathrm{Q}_t) \rho_{j_n}^{-} - d_n^{*} \mathrm{B}(\mathrm{Q}'_t) \rho_{j_n}^{-} \right\} \\ & - \frac{i}{\hbar} \mathrm{B}^{\times} \rho_{j_n}^{+} + \frac{1}{\hbar^2} \sum_{n=K+1}^{\infty} \exp\left(\mathrm{B}^{\times} \psi_n^{(\mathrm{O})} \right) \rho_{\mathbf{j}} \, \mathcal{D}[\mathrm{Q}'_t] \, \mathcal{D}[\mathrm{Q}_t]. \end{aligned} \quad \text{(D.1.257)}$$

After computing the path integrals this moves from an equation in terms of trajectories and paths back into an equation in terms of energy and creation and annihilation operators in the coherent state basis:

$$\begin{aligned} \frac{\partial \rho_{\mathbf{j}}}{\partial t} = - & \left\{ \frac{i}{\hbar} \mathrm{H}^{\times} + \sum_{n=0}^{K} j_n \nu_n - \frac{1}{\hbar^2} \sum_{n=K+1}^{\infty} \exp\left(\mathrm{B}^{\times} \psi_n^{(\mathrm{O})} \right) \right\} \rho_{\mathbf{j}} - \\ & \frac{i}{\hbar} \left\{ d_n \mathrm{B} \rho_{j_n}^{-} - d_n^{*} \mathrm{B} \rho_{j_n}^{-} \right\} - \frac{i}{\hbar} \mathrm{B}^{\times} \rho_{j_n}^{+}. \end{aligned} \quad \text{(D.1.258)}$$

Termination of this infinite set of equations makes use of a Markovianity criterion which corresponds to the assumption that auxiliary density operators deeper into the hierarchy are significantly smaller than those closer to the density matrix. Under the high temperature approximation this assumption is naturally true, however this is not always true when in the low-temperature and strong-coupling limits. The significance of this is that non-Markovian feedback is much larger and more impactful to the dynamics which means that ADOs deeper into the hierarchy are no longer always smaller, especially when the coupling is strong. The low temperature assumption that there is a cutoff to the ADOs at K, after which Matsubara terms are fully Markovian naturally stabilises the 1 to ∞ components of the expansion through a double B commutator term, but in order to safely suppress the increase in magnitude of deeper elements in the hierarchy the cutoff K must be used in conjunction with a double commutator associated with the first Matsubara frequency[150]:

$$\Xi_{(\mathrm{O})} = \frac{\eta}{\beta}\Big\{1 - \beta\Lambda_{\mathrm{O}}\cot\Big(\frac{\beta\hbar\Lambda_{\mathrm{O}}}{2}\Big)\Big\}\mathrm{B}^{\times}\mathrm{B}^{\times}, \tag{D.1.259}$$

such that the full equation of motion becomes

$$\frac{\partial\rho_{\mathbf{j}}}{\partial t} = -\Bigg\{\frac{i}{\hbar}\mathrm{H}^{\times} + \sum_{n=0}^{K} j_n\nu_n - \frac{1}{\hbar^2}\sum_{n=K+1}^{\infty}\exp\Big(\mathrm{B}^{\times}\psi_n^{(\mathrm{O})}\Big) - \frac{\Xi_{(\mathrm{O})}}{\hbar^2}\Bigg\}\rho_{\mathbf{j}} - \frac{i}{\hbar}\Big\{d_n\mathrm{B}\rho_{j_n}^{-} - d_n^{*}\mathrm{B}\rho_{j_n}^{-}\Big\} - \frac{i}{\hbar}\mathrm{B}^{\times}\rho_{j_n}^{+}. \tag{D.1.260}$$

With the introduction of the necessary stabilisation term the termination of the low-temperature EOM can be generated as

$$\frac{\partial\rho_{\mathbf{j}}}{\partial t} \approx -\Bigg\{\frac{i}{\hbar}\mathrm{H}^{\times} - \frac{1}{\hbar^2}\sum_{n=K+1}^{\infty}\exp\Big(\mathrm{B}^{\times}\psi_n^{(\mathrm{O})}\Big) - \frac{\Xi_{(\mathrm{O})}}{\hbar^2}\Bigg\}\rho_{\mathbf{j}}, \tag{D.1.261}$$

valid for integers $\mathbf{j} = (j_0, \ldots, j_K)$, with

$$\sum_{n=0}^{K} j_n\nu_n >> \frac{\omega_0}{\min(\nu_0, \nu_1)}. \tag{D.1.262}$$

and convergence parameter

$$\frac{2(K+1)\pi}{\hbar\beta} >> \Gamma_{\max}. \tag{D.1.263}$$

This can be further generalised to allow for multiple baths. In this case the derivation is performed in an identical manner, but will require expansions for each component bath, resulting in:

$$d_{n0} = \eta_n\Lambda_n(\cot\left(\frac{\beta\hbar\Lambda_n}{2}\right) - i), \quad \nu_{n0} = \Lambda_n, \tag{D.1.264}$$

$$d_{nl} = \frac{4\eta_n \Lambda_n \nu_{nl} \beta\hbar}{(\nu_{nl}\beta\hbar)^2 - (\Lambda_n \beta\hbar)^2}, \quad \nu_{nl} = \frac{2l\pi}{\beta\hbar}, \tag{D.1.265}$$

with operators

$$\psi_{nl} = \mathrm{B}_n^{\times} \frac{4\eta_n \Lambda_n \nu_{nl} \beta\hbar}{(\nu_{nl}\beta\hbar)^2 - (\Lambda_n \beta\hbar)^2}, \tag{D.1.266}$$

$$\Xi_n = \frac{\eta_n}{\beta}\left\{1 - \beta\Lambda_n \cot\left(\frac{\beta\hbar\Lambda_n}{2}\right)\right\}\mathrm{B}_n^{\times}\mathrm{B}_n^{\times}, \tag{D.1.267}$$

and equation of motion,

$$\begin{aligned}\frac{\partial \rho_{\mathbf{j}}}{\partial t} = -\Bigg\{ \frac{i}{\hbar}\mathrm{H}^{\times} + \sum_{n=0}^{N_\mathrm{B}}\sum_{l=0}^{K} j_{nl}\nu_{nl} - \frac{1}{\hbar^2}\sum_{n=0}^{N_\mathrm{B}}\sum_{l=K+1}^{\infty} \exp\left(\mathrm{B}_n^{\times}\psi_{nl}\right) - \frac{\Xi_n}{\hbar^2}\Bigg\}\rho_{\mathbf{j}} \\ - \frac{i}{\hbar}\left\{ d_{nl}\mathrm{B}_n\rho^{-}_{j_{nl}} - d^{*}_{nl}\mathrm{B}_n\rho^{-}_{j_{nl}}\right\} - \frac{i}{\hbar}\mathrm{B}_n^{\times}\rho^{+}_{j_{nl}},\end{aligned} \tag{D.1.268}$$

and associated terminator

$$\frac{\partial \rho_{\mathbf{j}}}{\partial t} \approx -\left\{ \frac{i}{\hbar}\mathrm{H}^{\times} - \frac{1}{\hbar^2}\sum_{n=0}^{N_\mathrm{B}}\sum_{l=K+1}^{\infty} \exp\left(\mathrm{B}^{\times}\psi_{nl}\right) - \frac{\Xi_n}{\hbar^2}\right\}\rho_{\mathbf{j}}, \tag{D.1.269}$$

valid for integers $\mathbf{j} = (j_{n0}, \ldots, j_{N_\mathrm{B}K})$, with

$$\sum_{n=0}^{N_\mathrm{B}}\sum_{l=0}^{K} j_{nl}\nu_{nl} >> \frac{\max(\omega_{n0})}{\min(\nu_{n0}, \nu_{n1})} = \Gamma_{\max}. \tag{D.1.270}$$

This hierarchy termination criterion terminates each Matsubara axis in an identical manner resulting in hierarchies of self-similar volumes. Dependent on the necessary termination criterion the termination equation can be simplified to contain only the Markovian free propagation of the system (red), but here is shown in full generality. Throughout this thesis, unless stated otherwise, the convergence criterion is set to $\Gamma_{\max} = 10\ \max(\Lambda_n)$.

The first term (red) within the generated HEOM, equation D.1.268, describes the Markovian free propagation of the system, and the second term (blue) introduces the impact on this propagation of integer multiples of Matsubara frequencies corresponding to interaction with bath phonons. The final two terms (blue) proportional to $\rho_{\mathbf{j}}$ are the low temperature correction of the free propagation and a double commutator of the bath operator which introduce higher order bath interactions, a square coupling, to account for the introduction of the cutoff K. This term was derived by Ishizaki and Tanimura in order to reduce the number of Matsubara frequencies required under strong coupling to reach convergence[150]. By propagating a series of ADOs, representing different arrangements of bath phonons, the HEOM accounts for a history of interactions such that non-Markovian effects are automatically included. The ADOs are interconnected via ADO raising and lowering terms which are denoted by $\mathbf{j}^{\pm} = (j_{10}, \ldots, j_{nk} \pm 1, \ldots, j_{N_\mathrm{B}K})$ vectors. The first $\rho^{-}_{\{\cdot\}}$

dependent term (term five - cyan) in the HEOM, equation (D.1.268), is the first raising term. The action of $\frac{i}{\hbar}d_{nl}\mathrm{B}_n$, and its conjugate, is to destroy bath phonons, of coupling amplitude d_{nl}, as they are absorbed by the system. This corresponds to an increase of ADO tier resulting in a 'raising' of the ADO. Subsequently, this process is associated with thermal fluctuations and the real part of the correlation function because of its temperature dependence. The final term (orange), dependent on $\rho^{+}_{\{.\}}$, is the corresponding lowering term. The action of $\frac{i}{\hbar}\mathrm{B}^{\times}_n$ is to demolish the bath states corresponding to the creation of bath phonons as they are emitted from the system into the bath. Destruction of bath states in this manner are a consequence of the imaginary part of the correlation function associated with system dissipation.

An example overdamped hierarchy is presented in figure D.1.3, where ADOs are depicted as spheres in a lattice structure, with each Matsubara frequency given its own dimension. The first ADO beyond $\Gamma_{\max}$ in each axis is assigned as a terminator such that the overall hierarchy defines a sealed volume, within which non-Markovian memory effects are fully accounted for. Each information channel, or raising/lowering event, is colour coded to match the terms in the overdamped HEOM, (D.1.268), to depict bath phonon creation and annihilation.

D.1.10.2 Underdamped HEOM

Similarly it is possible to generate an EOM from an underdamped spectral density

$$J_n^{(\mathrm{U})}(\omega) = \frac{2\eta_n\gamma_n\omega_{0n}^2\omega}{(\omega_{0n}^2-\omega^2)^2-(\gamma_n\omega)^2}. \tag{D.1.271}$$

The exponential expansion for this spectral density can be constructed in a manner analogous to the method performed for the overdamped spectral density, with the caveat that the Matsubara poles are now complex rather than purely imaginary. This results in a translation of the contour. In addition, this form of spectral density is associated with the canonical transform, discussed in detail in section 2.2.2.2, resulting in the system mode, ω_{0n}, being subsumed into the environment degrees of freedom. As discussed, this is the primary method of moving the system-bath boundary which is discussed in detail in this thesis, and it involves obscuring the distinction between the bath and system degrees of freedom. This has a profound impact on quantum information and correlations.

The associated underdamped fluctuation and dissipation kernels are,

$$L^{(\alpha)}_{\mathcal{R},n} = \frac{\hbar\eta_n\omega_{0n}^2}{2i\zeta_n}\left\{\exp\Big(-\Big(\frac{\gamma_n}{2}-i\zeta_n\Big)t\Big)-\exp\Big(-\Big(\frac{\gamma_n}{2}+i\zeta_n\Big)t\Big)\right\}, \tag{D.1.272}$$

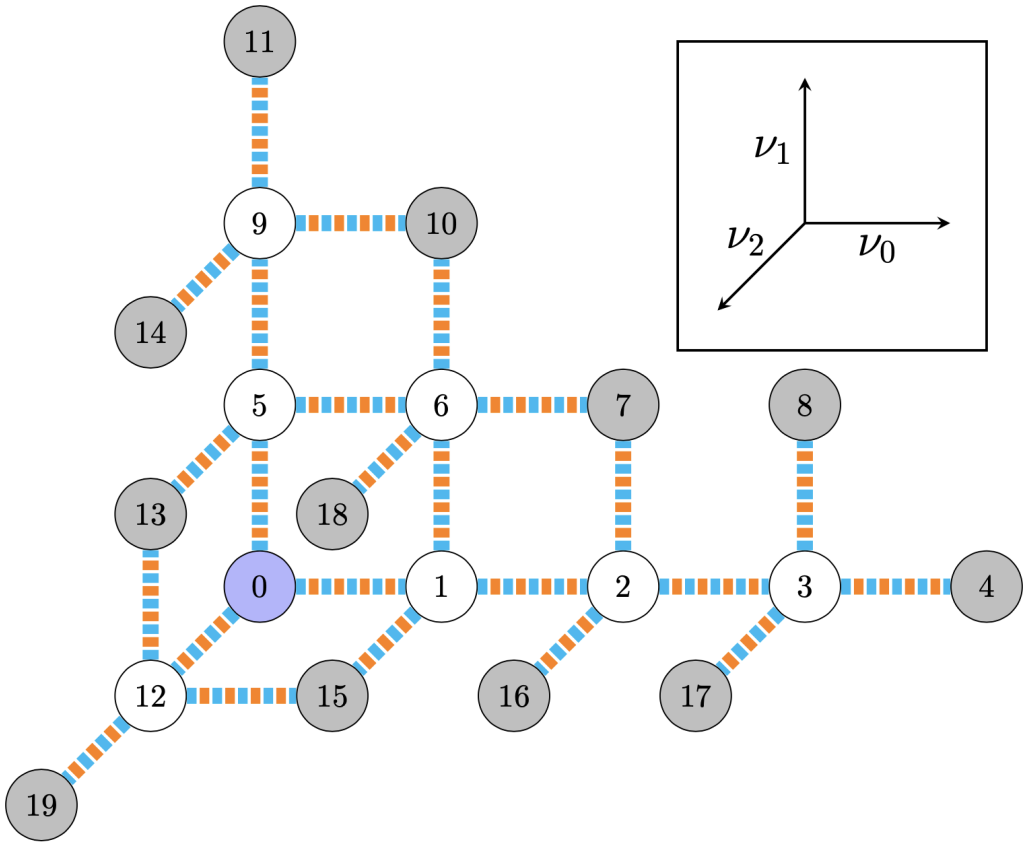

Figure D.1.3: Hierarchy diagram for a single overdamped bath, such that there are three Matsubara dimensions. The longest axis is the temperature independent Matsubara frequency associated with an overdamped bath. Each sphere represents a density operator where the reduced density matrix of the system is blue, normal ADOs are white and terminating ADOs are grey. Each ADO is connected by a coloured line which matches terms in equation (2.5.41) corresponding to their origin.

$$L^{(\alpha)}_{\mathcal{I},n} = \frac{\hbar\eta_n\omega_{0n}^2}{2\zeta_n}\exp\Big(-\Big(\frac{\gamma_n}{2}-i\zeta_n\Big)t\Big)\coth\Big(\frac{\hbar\beta}{2}\Big(\zeta_n+i\frac{\gamma_n}{2}\Big)\Big) - \frac{\hbar\eta_n\omega_{0n}^2}{2\zeta_n}\exp\Big(-\Big(\frac{\gamma_n}{2}+i\zeta_n\Big)t\Big)\coth\Big(\frac{\hbar\beta}{2}\Big(-\zeta_n+i\frac{\gamma_n}{2}\Big)\Big) - \frac{4\eta_n\gamma_n\omega_{0n}^2}{\hbar\beta}\sum_{k=1}^{\infty}\frac{\nu_k\exp(-\nu_k t)}{(\omega_{0n}^2+\nu_k^2)^2-(\gamma_n\nu_k)^2}, \quad \text{(D.1.273)}$$

where $\zeta_n = \sqrt{\omega_{n0}^2 - \left(\frac{\gamma_n}{2}\right)^2}$ when $\gamma_n < 2\omega_{0n}$ and $\nu_k = \frac{2\pi k}{\hbar\beta}$ are the Matsubara frequencies. The derivation for the underdamped kernels is equivalent to that of the overdamped spectral density, however, introduction of the system mode splits the single temperature independent Matsubara frequency into two: positive and negative combinations of the intrinsic damping parameter, $\frac{\gamma_n}{2}$, and $i\zeta_n$. This means that following the same derivation leads to two terms in $L^{(\alpha)}_{\mathcal{R},n}$ rather than one, and three in $L^{(\alpha)}_{\mathcal{I},n}$ rather than two, due to the split temperature independent cases.

This is then written as an expansion in the exponential basis with Matsubara frequencies and coefficients, ν_{nl} and d_{nl},

$$\nu_{n0} = \frac{\gamma_n}{2} - i\zeta_n, \tag{D.1.274}$$

$$\nu_{n1} = \frac{\gamma_n}{2} + i\zeta_n, \tag{D.1.275}$$

$$\nu_{nl} = \frac{2\pi(l-1)}{\hbar\beta}, \tag{D.1.276}$$

$$d_{n0} = \frac{\hbar\eta_n\omega_{0n}^2}{2\zeta_n}\left\{\coth\left(\frac{\hbar\beta}{2}\left(\zeta_n + i\frac{\gamma_n}{2}\right)\right) - 1\right\}, \tag{D.1.277}$$

$$d_{n1} = -\frac{\hbar\eta_n\omega_{0n}^2}{2\zeta_n}\left\{\coth\left(\frac{\hbar\beta}{2}\left(-\zeta_n + i\frac{\gamma_n}{2}\right)\right) - 1\right\}, \tag{D.1.278}$$

$$d_{nl} = -\frac{4\eta_n\gamma_n\omega_{0n}^2}{\hbar\beta}\frac{\nu_{nl}}{(\omega_{0n}^2 + \nu_{nl}^2)^2 - (\gamma_n\nu_{nl})^2}, \tag{D.1.279}$$

such that

$$L^{(\alpha)}_{\mathrm{corr},n}(t) = \sum_{l=0}^{\infty} d_{nl}\exp(-\nu_{nl}t). \tag{D.1.280}$$

The EOM for the ADOs of this expansion is then[1],

$$\begin{aligned}\frac{\partial\rho_{\mathbf{j}}}{\partial t} = -\Bigg(&\frac{i}{\hbar}\mathrm{H}^{\times} + \sum_{n=1}^{N_\mathrm{B}}\sum_{l=0}^{K} j_{nl}\nu_{nl} - \sum_{n=1}^{N_\mathrm{B}}\sum_{l=K+1}^{\infty}\mathrm{B}_n^{\times}\psi_{nl}^{(\mathrm{U})}\Bigg)\rho_{\mathbf{j}} \\ &+ \sum_{n=1}^{N_\mathrm{B}}\sum_{l=0}^{K}\mathrm{B}_n^{\times}\rho^{+}_{j_{nl}} + \sum_{n=1}^{N_\mathrm{B}} j_{n0}\Theta_n^{-}\rho^{-}_{j_{n0}} + \sum_{n=1}^{N_\mathrm{B}} j_{n1}\Theta_n^{+}\rho^{-}_{j_{n1}} \\ &+ \sum_{n=1}^{N_\mathrm{B}}\sum_{l=2}^{K} j_{nl}\nu_{nl}\psi_{nl}^{(\mathrm{U})}\rho^{-}_{j_{nl}},\end{aligned} \tag{D.1.281}$$

where

$$\psi_{nl}^{(\mathrm{U})} = \frac{4\eta_n}{\hbar\beta}\frac{\gamma_n\omega_{0n}^2}{(\omega_{0n}^2 + \nu_{nl}^2)^2 - (\gamma_n\nu_{nl})^2}\mathrm{B}_n^{\times}, \tag{D.1.282}$$

$$\Theta_n^{\pm} = \frac{\eta_n\omega_{0n}^2}{2\zeta_n}\left\{\mp\mathrm{B}_n^{\circ} \pm \coth\left(\frac{\hbar\beta}{2}\left(\mp\zeta_n + i\frac{\gamma_n}{2}\right)\right)\mathrm{B}_n\right\}, \tag{D.1.283}$$

and $\mathrm{B}_n^{\times}\rho = [\mathrm{B}_n, \rho]$ denotes the commutator of the bath coupling operator and the density matrix and $\mathrm{B}_n^{\circ}\rho = \{\mathrm{B}_n, \rho\}$ the corresponding anti-commutator. The associated terminator for this hierarchy is[164]

$$\frac{\partial\rho_{\mathbf{j}}}{\partial t} \approx -\left(\frac{i}{\hbar}\mathrm{H}^{\times} + i\sum_{n=1}^{N_\mathrm{B}}(j_{n0} - j_{n1})\zeta_n - \sum_{n=1}^{N_\mathrm{B}}\sum_{l=K+1}^{\infty}\mathrm{B}_n^{\times}\psi_{nl}^{(\mathrm{U})}\right)\rho_{\mathbf{j}}, \tag{D.1.284}$$

valid for integers $\mathbf{j} = (j_{n0}, \ldots, j_{N_\mathrm{B}K})$, with

$$\sum_{n=1}^{N_\mathrm{B}} \sum_{l=0}^{M} j_{nl} |\mathcal{R}(\nu_{nl})| > \Gamma_{\max}. \tag{D.1.285}$$

In addition, computationally the sum to infinity is truncated with a sufficiently high value with respect to the criterion $\Gamma_{\max}$.

Equivalent to the overdamped hierarchy, the ADOs are characterised by the $N_\mathrm{B}(K+1)$-dimensional vectors $\mathbf{j}$ and $\mathbf{j}^{\pm}$, with the terms of eq. D.1.281 interpreted in terms of the creation and annihilation of bath phonons, but where the complex Matsubara frequencies have split the temperature independent term in two such that there are now additional terms involving $\Theta_n^{\pm}$.

An example underdamped hierarchy is presented in figure D.1.4, again demonstrating a sealed volume and showing annihilation and creation with colours matching equation 2.5.55. It is worth noting, the splitting of the temperature independent Matsubara frequency into ν_{n0} and ν_{n1} results in the first two axes having equal depth, such that the underdamped HEOM involves many more ADOs than the overdamped case, increasing computational complexity.

The underdamped spectral density, equation (D.1.271), reproduces the Drude form on increasing the damping to the overdamped limit, when $\gamma_n \gg \omega_{0n}$, also requiring $\zeta_n = i\sqrt{\left(\frac{\gamma_n}{2}\right)^2 - \omega_{0n}^2}$. However, due to a singularity in the exponential basis which is the foundation of these derivations, $\omega_{0n} \approx \gamma_n$, this HEOM is insufficiently stable and the additional computational requirements of the underdamped HEOM means the overdamped HEOM, equation (2.5.41), is preferable for overdamped environments. This weakness in basis is most evident from the divergent limit of vanishing ζ_n in the temperature independent Matsubara terms, $\lim_{\zeta_n \to 0} d_{n0} = \lim_{\zeta_n \to 0} d_{n1} = \infty$. This flaw is addressed by Ikeda and Scholes[139] through the generalised HEOM discussed in section 2.5.4.4.

D.1.10.3 Arbitrary Spectral Density (ASD) HEOM

As discussed in section 2.2.2.2, the power of structured spectral densities is that they can be used to model processes which are strongly non-Markovian, or which have had system modes subsumed into them by the canonical transform. Therefore, it stands to reason that a hierarchy which is derived from a purely general spectral density would allow for modelling a broad range of physical regimes. Tanimura considers this possibility is one of his original articles[149], where the HEOM becomes a more general integro-differential equation of

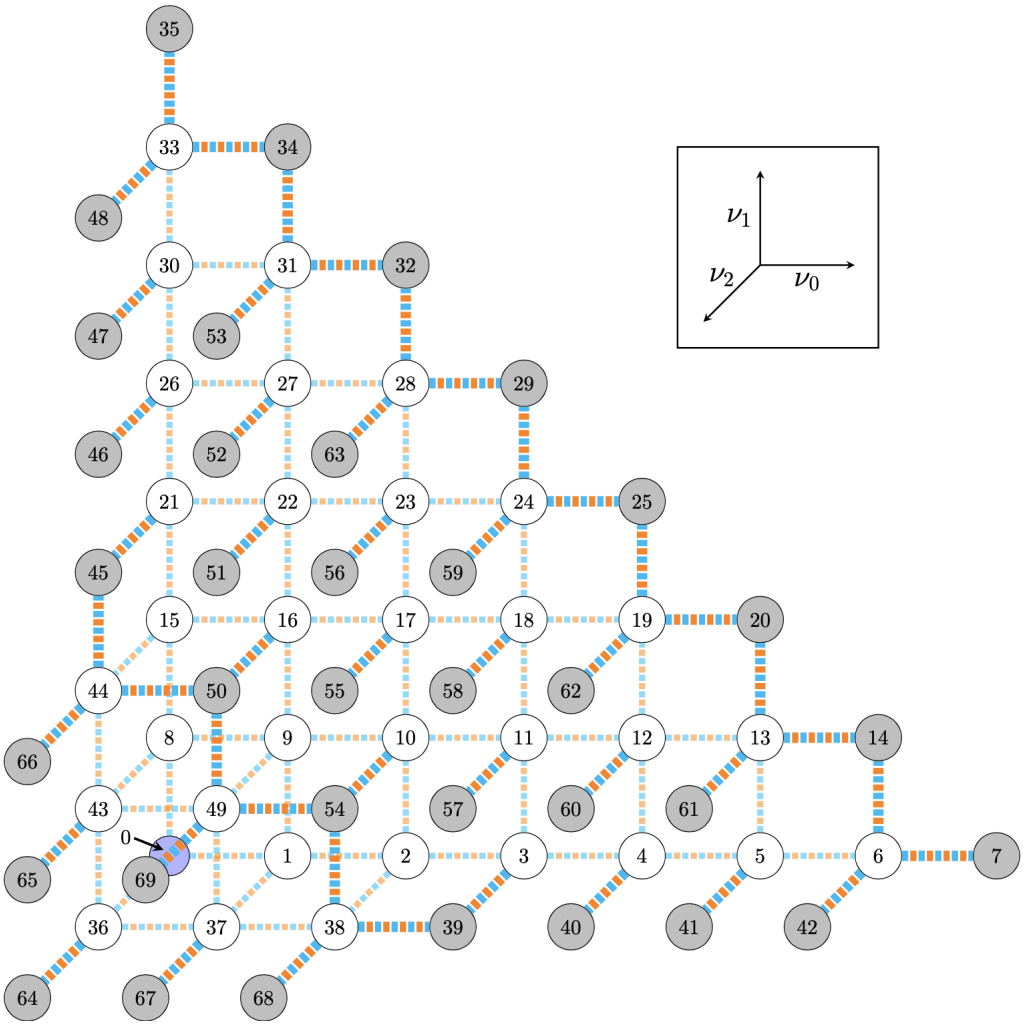

Figure D.1.4: Hierarchy diagram for a single underdamped bath, such that there are three Matsubara dimensions. The longest two axes ($\nu_0,\ \nu_1$) are the temperature independent Matsubara frequency associated with an underdamped bath. Each sphere represents a density operator where the reduced density matrix of the system is blue, normal ADOs are white and terminating ADOs are grey. Each ADO is connected by a coloured line which matches terms in equation (D.1.281) corresponding to their origin.

motion,

$$\begin{aligned}\frac{\partial}{\partial t}\rho_{\mathrm{S}}(t;\omega_1,\omega_2,\ldots,\omega_m) = &-\left(\frac{i}{\hbar}\mathrm{H}^{\times} + i\sum_{j=1}^{M}\omega_j\right)\rho_{\mathrm{S}}(t;\omega_1,\omega_2,\ldots,\omega_m)\\ &- i\int_{-\infty}^{\infty}\mathrm{B}^{\times}\rho_{\mathrm{S}}(t;\omega_1,\omega_2,\ldots,\omega_{m+1})\,\mathrm{d}\omega_{m+1}\\ &- i\sum_{k=1}^{m-1}\Theta(\omega_k)\rho_{\mathrm{S}}(t;\omega_1,\omega_2,\ldots,\omega_{k-1},\omega_{k+1},\ldots,\omega_m)\\ &- i\Theta(\omega_m)\rho_{\mathrm{S}}(t;\omega_1,\omega_2,\ldots,\omega_{m-1}),\end{aligned} \tag{D.1.286}$$

where,

$$\Theta(\omega) = J(\omega)\left(\coth\Big(\frac{\beta\hbar\omega}{2}\Big)\mathrm{B}^{\times} + \mathrm{B}^{\circ}\right), \tag{D.1.287}$$

written in terms of the total spectral density, $J(\omega) = \sum_{n=1}^{N_\mathrm{B}} J_n(\omega)$, and bath coupling operator, $\mathrm{B} = \sum_{n=1}^{N_\mathrm{B}} \mathrm{B}_n$. The auxiliary equations for $\rho_\mathrm{S}(t;\omega_1,\omega_2,\ldots,\omega_m)$ represent simultaneous evolution of the system in the presence of m bath phonons with associated frequencies ω_m. Just as in the previous HEOMs there are cyan lowering terms, and an orange ADO raising term, but here because of the generality of the spectral density the raising term involves an integral over the phonon frequency ω_{m+1}.

While it is possible to reach this equation using a derivation analogous to the method presented in section D.1.10, the general spectral density makes it impossible to calculate a specific contour integral to expand the Matsubara components. For this reason Tanimura[149] presents an elegant alternative involving multiplication of continued fraction forms of the Laplace transform. The Laplace transform, within appendix A, is very similar to the Fourier transform and the equation used for the contour integration. It takes a function of time and moves it into the complex frequency domain with the added effect of transforming ordinary differential equations into algebraic equations and convolutions of functions into products. Within the ASD-HEOM this allows the system-bath entanglement, due to the arbitrary spectral density, to be expressed in resolvent form through products of operators as part of a continued fraction:

$$\rho_\mathrm{S}[s] = \frac{1}{s + \frac{i}{\hbar}\mathrm{H}^{\times} + \int \mathrm{B}^{\times} \frac{\Theta(\nu_1)}{s+i\nu_1+\frac{i}{\hbar}\mathrm{H}^{\times}+\int \mathrm{B}^{\times}\frac{\Theta(\nu_2)}{s+i\nu_2+\ldots}\,\mathrm{d}\nu_2}\,\mathrm{d}\nu_1}\rho_\mathrm{S}(t_0), \tag{D.1.288}$$

where $\mathcal{L}_\mathrm{Lap}\{t\} = s$.

This generalisation of spectral influence on the HEOM evolution nicely demonstrates the incorporation of non-Markovian effects. Interaction of the system and bath, through $i\int_{-\infty}^{\infty}\mathrm{B}^{\times}\{\cdot\}\mathrm{d}\omega_{m+1}$, creates bath phonons which are propagated alongside the reduced system within the ADOs. This accounts for the transfer of information, along a quantum channel, from the system to the bath where it is stored within the environment degrees of freedom. Then, dependent on the timescales of bath relaxation relative to the system, the behaviour is either a local or global evolution. When the environment relaxation timescale is rapid compared to the system, the phonons will dissipate throughout the bath degrees of freedom and will not influence the system dynamics again, resulting in local, Markovian, evolution. Alternatively, if the timescales are commensurate, the phonons can be reabsorbed by the system, through the action of $i\Theta(\omega)$, creating a feedback of information and linking the current state with past auxiliaries. This produces a global, non-Markovian,

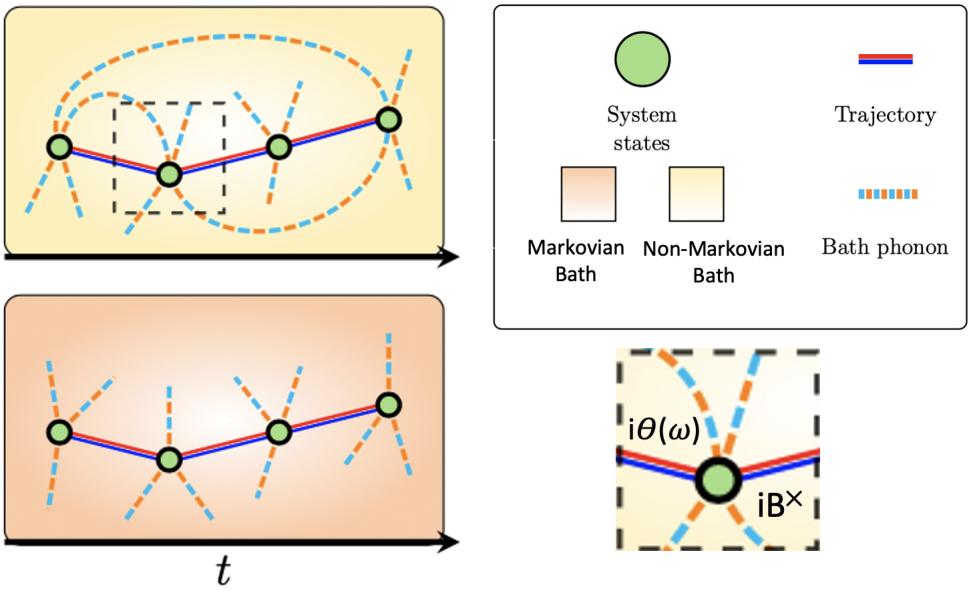

Figure D.1.5: Markovian vs. Non-Markovian evolution demonstrating global or local behaviour for the ASD-HEOM. The colours in the figure match those in the EOMs.

evolution. Both Markovian and non-Markovian evolutions are depicted in figure D.1.5. In this way, the HEOM accounts for all possible sequences of interactions and the creation and annihilation of bath phonons of any frequency in any order, accurately modelling the dynamics of the system in a broad range of conditions.

However, despite the power of being able to create models which require highly structured, non-Markovian, environments this method suffers a pair of drawbacks. The first is that it is incredibly costly to implement computationally because of the large dependence on phonon frequencies. Discretising the spectral density to W frequencies, the mth layer involves W^m auxiliaries, each with dimensions of the reduced density operator, which itself is large in the case of the vibronic dimers discussed in section 2.2.1.3. The other drawback is that, despite the increased number of physical regimes accessible with an arbitrary spectral density, it does not circumvent flaws in the basis functions. As discussed in the section on the underdamped HEOM, D.1.10.2, the exponential basis is highly sensitive to the bath damping strength relative to the system mode frequency especially in the region of critical damping. The divergence of the Matsubara frequencies in these cases have not been addressed by the arbitrary choice of spectral density which means that it addresses niche, highly structured, regimes within the strongly underdamped limit. This is demonstrated in the work of section F, where the ASD-HEOM is employed, and this flaw is rectified by Ikeda and Scholes[139] which is discussed in section D.1.10.4.

D.1.10.4 Generalised HEOM

The generalised HEOM[139], denoted gHEOM, addresses the flaw with the basis functions, crucial to previous HEOM derivations, by including treatment of non-exponential correlation functions. This addition means that a full range of damping strengths, including critical damping, can be modelled. This derivation makes use of the cumulant expansion technique, which was discussed in section 2.2.2.2.1, and as such does not directly follow the steps previously discussed in section D.1.10. A full description of the current derivation is beyond the scope of this thesis, but it is summarised for completeness.

A set of K time dependent basis functions $\phi^{(\mathrm{g})}$ are generated in order to produce symmetrised and anti-symmetrised correlation functions from linear combinations of this basis and the delta function:

$$\mathcal{S}(t) = \sum_{lk} \sigma_l s_{lk} \phi_k^{(\mathrm{g})}(t) + S_\delta \cdot 2\delta(t), \tag{D.1.289}$$

$$\mathcal{A}(t) = \sum_{lk} \sigma_l a_{jk} \phi_k^{(\mathrm{g})}(t), \tag{D.1.290}$$

where σ_l, s_{lk}, and a_{lk} are constants dependent on the system parameters. These correlation functions are equivalent to the fluctuation and dissipation kernels, $\mathcal{S}(t) = L_{\mathcal{R}}^{(\alpha)}(t)$, and $\mathcal{A}(t) = L_{\mathcal{I}}^{(\alpha)}(t)$, equation (2.2.53). With these substitutions the influence functional, equivalent to (D.1.206), can be expressed in terms of cumulants as,

$$\mathcal{F} = \exp\left(\int_{t_0}^{t} i\mathrm{B}^{\times} \int_{t_0}^{s} \left(\frac{i}{\hbar}\mathcal{S}(s-u)\mathrm{B}^{\times}(u) - \frac{1}{\hbar}\mathcal{A}(s-u)\mathrm{B}^{\circ}(u) \right) \mathrm{d}u \, \mathrm{d}s \right), \tag{D.1.291}$$

$$= \exp\left(\int_{t_0}^{t} -\Xi^{(\mathrm{g})}(s) + \sum_j \phi_l^{(\mathrm{g})}(s \int_{t_0}^{s} \Theta_l^{(\mathrm{g})})(s,u) \, \mathrm{d}u \, \mathrm{d}s \right), \tag{D.1.292}$$

where

$$\Xi^{(\mathrm{g})}(s) = -S_\delta \Big(\frac{i\sigma_l}{\hbar} \mathrm{B}^{\times}(s) \Big)^2, \tag{D.1.293}$$

$$\Theta_l^{(\mathrm{g})}(t,s) = \sum_k \frac{i}{\hbar}\sigma_l s_{lk} \phi_k^{(\mathrm{g})}(t-s)\mathrm{B}^{\times}(s) - \frac{1}{\hbar} a_{lk} \phi_k^{(\mathrm{g})}(t-s)\mathrm{B}^{\circ}(s). \tag{D.1.294}$$

Introduction of additional terms into $\Theta_l^{(\mathrm{g})}(t,s)$, acts as the ADO lowering operator, and corresponds to additional non-Markovian corrections which link auxiliaries with the same number of phonon interactions. Differentiation of the

subsequent equation for the auxiliary density matrix elements results in,

$$\frac{\partial \rho_{\mathbf{j}}}{\partial t} = -\Big(\frac{i}{\hbar}\mathrm{H}^{\times} + \Xi^{(\mathrm{g})}\Big)\rho_{\mathbf{j}} - \sum_{l,k} n_l \gamma_{lk} \rho_{j_{l-1,k+1}} - \sum_{k} \frac{i\sigma_k}{\hbar}\mathrm{B}_k^{\times}\rho_{j_{k+1}} - \sum_{k} n_k \Theta_k^{(\mathrm{g})}\rho_{j_{k-1}}, \tag{D.1.295}$$

in the Schrödinger picture. This equation is terminated in a similar fashion to previous EOMs through,

$$\frac{\partial \rho_{\mathbf{j}}}{\partial t} \approx -\Big(\frac{i}{\hbar}\mathrm{H}^{\times} + \Xi^{(\mathrm{g})}\Big)\rho_{\mathbf{j}}, \tag{D.1.296}$$

but with a considerably simplified Markovianity criterion[139]

$$\sum_{k} n_k > \Gamma_{\max}. \tag{D.1.297}$$

As before, the red term is the Markovian free propagation of the system, the first blue term is a Markovian correction containing a double commutator, the second blue term is the introduction of bath phonons as a consequence of the basis set $\phi^{(\mathrm{g})}$, the orange term is the associated ADO raising, and the cyan term is the associated ADO lowering term.

As mentioned, because of the extension of the basis to include a full range of damping strengths, the coupling between the ADOs is more complex than for previous cases. There are additional links between processes involving one phonon from different Matsubara dimensions, referred to as *tier* one in each axis which is discussed in section 3.3, which accounts for all sources of non-Markovian feedback. This is shown in figure D.1.6 with a general gHEOM hierarchy diagram.

D.1.10.5 Lorentz-Drude Undamped Oscillator (LDUO) HEOM

Finally, we consider a new type of HEOM construction, based on the work of Tanimura[157], and Seibt[289,325], in order to directly observe the changes due to the canonical transform of moving the system-bath boundary. The proposed scheme is a combination of a Lorentz-Drude overdamped spectral density with an underdamped spectral density which is denoted LDUO. Such a system should be equivalent to the summation of an overdamped hierarchy and an underdamped hierarchy in the limit of vanishing canonical damping. This name is chosen, where O (overdamped) is replaced with LD (Lorentz-Drude) so that these components are sufficiently different from the UO (undamped) components[a].

In order to generate this EOM the Lorentz-Drude correlation function and the

[a] Subsequently, $\Lambda_{\mathrm{O}} = \Lambda_{\mathrm{LD}}$

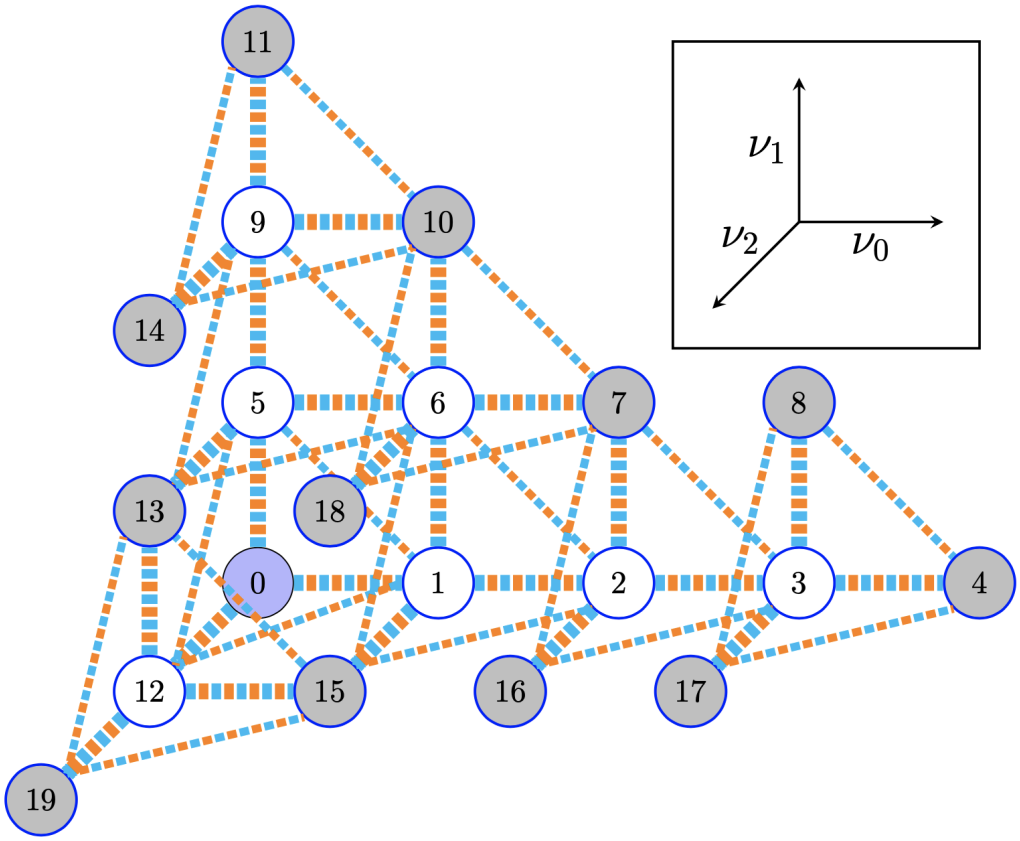

Figure D.1.6: Hierarchy diagram for the gHEOM. Each sphere represents a density operator where the reduced density matrix of the system is blue, normal ADOs are white and terminating ADOs are grey. Each ADO is connected by a coloured line which matches terms in equation (2.5.69) corresponding to their origin.

underdamped oscillator correlation function must be summed to produce a total function describing the fluctuation and dissipation for the system. Equations (2.5.33)–(2.5.35), from the overdamped derivation, are the Lorentz-Drude component.

Undamped oscillator correlation function

Next consider the undamped oscillator component following Seibt and Mancal[289,325]. From either $J_{\mathrm{UO}}(\omega) = 1/2 S^{\mathrm{HR}}_{\mathrm{UO}} \omega_{\mathrm{UO}} \omega \{\delta(\omega - \omega_{\mathrm{UO}}) + \delta(\omega + \omega_{\mathrm{UO}})\}$, or $J_{\mathrm{UO}}(\omega) = S^{\mathrm{HR}}_{\mathrm{UO}} \omega_{\mathrm{UO}} \delta(\omega - \omega_{\mathrm{UO}})$, we generate the kernels required for the undamped oscillator influence functional. The omission of a factor of ω_{UO} in the former spectral density is to ensure that the coupling to the bath has a magnitude of λ_{UO} and is not additionally proportional to the magnitude of vibrational mode frequency. The derivation continues with the split form of the undamped vibration, but this is equivalent to a singular delta function. From the

definition in equation D.1.207

$$iL^{(\alpha)}_{\mathcal{I},\mathrm{UO}}(t) = -i\int_0^\infty \frac{1}{2} S^{\mathrm{HR}}_{\mathrm{UO}}\omega_{\mathrm{UO}}\omega\Big\{\delta(\omega-\omega_{\mathrm{UO}})+\delta(\omega+\omega_{\mathrm{UO}})\Big\}\sin(\omega t)\,\mathrm{d}\omega, \tag{D.1.298}$$

$$= -\frac{iS^{\mathrm{HR}}_{\mathrm{UO}}\omega_{\mathrm{UO}}}{2}\left\{\int_0^\infty \delta(\omega-\omega_{\mathrm{UO}})\omega\sin(\omega t)\,\mathrm{d}\omega + \int_0^\infty \delta(\omega+\omega_{\mathrm{UO}})\omega\sin(\omega t)\,\mathrm{d}\omega\right\}. \tag{D.1.299}$$

Through the sifting property of the delta function this is

$$= -\frac{iS^{\mathrm{HR}}_{\mathrm{UO}}\omega_{\mathrm{UO}}}{2}\Big(\omega_{\mathrm{UO}}\sin(\omega_{\mathrm{UO}}t) + (-\omega_{\mathrm{UO}})\sin(-\omega_{\mathrm{UO}}t)\Big), \tag{D.1.300}$$

$$iL^{(\alpha)}_{\mathcal{I},\mathrm{UD}}(t) = -iS^{\mathrm{HR}}_{\mathrm{UO}}\omega^2_{\mathrm{UO}}\sin(\omega_{\mathrm{UO}}t). \tag{D.1.301}$$

Similarly, the kernel $L^{(\alpha)}_{\mathcal{R},\mathrm{UO}}$ is

$$L^{(\alpha)}_{\mathcal{R},\mathrm{UO}}(t) = \int_0^\infty \frac{1}{2} S^{\mathrm{HR}}_{\mathrm{UO}}\omega_{\mathrm{UO}}\omega\Big\{\delta(\omega-\omega_{\mathrm{UO}})+\delta(\omega+\omega_{\mathrm{UO}})\Big\}\coth\left(\frac{\beta\hbar\omega}{2}\right)\cos(\omega t)\,\mathrm{d}\omega, \tag{D.1.302}$$

$$= \frac{S^{\mathrm{HR}}_{\mathrm{UO}}\omega_{\mathrm{UO}}}{2}\left\{\int_0^\infty \delta(\omega-\omega_{\mathrm{UO}})\,\omega\coth\left(\frac{\beta\hbar\omega}{2}\right)\cos(\omega t)\,\mathrm{d}\omega + \int_0^\infty \delta(\omega+\omega_{\mathrm{UO}})\,\omega\coth\left(\frac{\beta\hbar\omega}{2}\right)\cos(\omega t)\,\mathrm{d}\omega\right\}. \tag{D.1.303}$$

Applying the sifting property and the properties:

$$\cos(-x) = \cos(x), \quad \coth(-x) = -\coth(x), \tag{D.1.304}$$

$$L^{(\alpha)}_{\mathcal{R},\mathrm{UO}}(t) = \frac{S^{\mathrm{HR}}_{\mathrm{UO}}\omega_{\mathrm{UO}}}{2}\left(\omega_{\mathrm{UO}}\coth\left(\frac{\beta\hbar\omega_{\mathrm{UO}}}{2}\right)\cos(\omega_{\mathrm{UO}}t) + (-\omega_{\mathrm{UO}})\coth\left(-\frac{\beta\hbar\omega_{\mathrm{UO}}}{2}\right)\cos(-\omega_{\mathrm{UO}}t)\right), \tag{D.1.305}$$

$$L^{(\alpha)}_{\mathcal{R},\mathrm{UO}}(t) = S^{\mathrm{HR}}_{\mathrm{UO}}\omega^2_{\mathrm{UO}}\coth\left(\frac{\beta\hbar\omega_{\mathrm{UO}}}{2}\right)\cos(\omega_{\mathrm{UO}}t). \tag{D.1.306}$$

The two kernels can be combined to generate the total correlation function, $L^{(\alpha)}_{\mathrm{corr},\mathrm{UO}}(t)$:

$$L^{(\alpha)}_{\mathrm{corr},\mathrm{UO}}(t) = -iS^{\mathrm{HR}}_{\mathrm{UO}}\omega^2_{\mathrm{UO}}\left(\frac{i}{2}\exp(-i\omega_{\mathrm{UO}}t) - \frac{i}{2}\exp(i\omega_{\mathrm{UO}}t)\right) + S^{\mathrm{HR}}_{\mathrm{UO}}\omega^2_{\mathrm{UO}}\coth\left(\frac{\beta\hbar\omega_{\mathrm{UO}}}{2}\right)\left(\frac{\exp(-i\omega_{\mathrm{UO}}t)}{2} + \frac{\exp(i\omega_{\mathrm{UO}}t)}{2}\right), \tag{D.1.307}$$

$$L^{(\alpha)}_{\mathrm{corr,UO}}(t) = \frac{S^{\mathrm{HR}}_{\mathrm{UO}}\omega^2_{\mathrm{UO}}}{2}\Bigg[\exp(-i\omega_{\mathrm{UO}}t)\left(\coth\left(\frac{\beta\hbar\omega_{\mathrm{UO}}}{2}\right)+1\right)+ \exp(i\omega_{\mathrm{UO}}t)\left(\coth\left(\frac{\beta\hbar\omega_{\mathrm{UO}}}{2}\right)-1\right)\Bigg]. \quad \text{(D.1.308)}$$

From this we have generated the Matsubara decomposition coefficients and frequencies for the second bath:

$$c_1 = \tilde{c}_2 = \frac{1}{2}S^{\mathrm{HR}}_{\mathrm{UO}}\omega^2_{\mathrm{UO}}\left(\coth\left(\frac{\beta\hbar\omega_{\mathrm{UO}}}{2}\right)+1\right), \quad \text{(D.1.309)}$$

$$c_2 = \tilde{c}_1 = \frac{1}{2}S^{\mathrm{HR}}_{\mathrm{UO}}\omega^2_{\mathrm{UO}}\left(\coth\left(\frac{\beta\hbar\omega_{\mathrm{UO}}}{2}\right)-1\right), \quad \text{(D.1.310)}$$

$$\gamma_1 = \tilde{\gamma}_2 = i\omega_{\mathrm{UO}}, \quad \text{(D.1.311)}$$

$$\gamma_2 = \tilde{\gamma}_1 = -i\omega_{\mathrm{UO}}. \quad \text{(D.1.312)}$$

Total correlation function

$$L^{(\alpha)}_{\mathrm{corr,tot}}(t) = L^{(\alpha)}_{\mathrm{corr,LD}}(t) + L^{(\alpha)}_{\mathrm{corr,UO}}(t), \quad \text{(D.1.313)}$$

which can additionally be split into the $iL^{(\alpha)}_{\mathcal{I},\mathrm{tot}}(t)$ and $L^{(\alpha)}_{\mathcal{R},\mathrm{tot}}(t)$ components in the same manner as for each constituent part.

$$L^{(\alpha)}_{\mathrm{corr,tot}}(t) = \eta_{\mathrm{LD}}\Lambda_{\mathrm{LD}}\left(\cot\left(\frac{\beta\hbar\Lambda_{\mathrm{LD}}}{2}\right)-i\right)\exp(-\Lambda_{\mathrm{LD}}t)+ \sum_{n=1}^{\infty}\frac{2\eta_{\mathrm{LD}}\Lambda_{\mathrm{LD}}\nu_n}{\beta\hbar(\nu_n^2-\Lambda^2_{\mathrm{LD}})}\exp(-\nu_n t)+ \frac{1}{2}S^{\mathrm{HR}}_{\mathrm{UO}}\omega^2_{\mathrm{UO}}\Bigg[\left(\coth\left(\frac{\beta\omega_{\mathrm{UO}}}{2}\right)+1\right)\exp(-i\omega_{\mathrm{UO}}t)+ \left(\coth\left(\frac{\beta\omega_{\mathrm{UO}}}{2}\right)-1\right)\exp(i\omega_{\mathrm{UO}}t)\Bigg], \quad \text{(D.1.314)}$$

such that:

$$iL^{(\alpha)}_{\mathcal{I},\mathrm{tot}}(t) = \frac{i\eta_{\mathrm{LD}}\Lambda_{\mathrm{LD}}}{2}\exp(-\Lambda_{\mathrm{LD}}t) - iS^{\mathrm{HR}}_{\mathrm{UO}}\omega^2_{\mathrm{UO}}\sin(\omega_{\mathrm{UO}}t), \quad \text{(D.1.315)}$$

$$L^{(\alpha)}_{\mathcal{R},\mathrm{tot}}(t) = \eta_{\mathrm{LD}}\Lambda_{\mathrm{LD}}\cot\left(\frac{\beta\hbar\Lambda_{\mathrm{LD}}}{2}\right)\exp(-\Lambda_{\mathrm{LD}}t)+\sum_{n=1}^{\infty}\frac{2\eta_{\mathrm{LD}}\Lambda_{\mathrm{LD}}\nu_n}{\beta\hbar(\nu_n^2-\Lambda^2_{\mathrm{LD}})}\exp(-\nu_n t)+ S^{\mathrm{HR}}_{\mathrm{UO}}\omega^2_{\mathrm{UO}}\coth\left(\frac{\beta\hbar\omega_{\mathrm{UO}}}{2}\right)\cos(\omega_{\mathrm{UO}}t). \quad \text{(D.1.316)}$$

This form is in agreement with the analogous derivation by Tanimura[157]. It is worth noting that this composite system only contains dissipation terms from the Lorentz-Drude component based on the undamped and temperature independent nature of the Matsubara decomposition of the undamped oscillator. Additionally, this hierarchy will contain two additional Matsubara frequencies in the shared Matsubara axis, when compared to the standard overdamped equations of motion, hence we would expect similar numbers of hierarchy elements and computational performance. The resulting form of the correlation function - in exponential form - represents physically a memory-frequency decomposition of the bath correlation. The exponential expansion of bath correlation function dictates the structure of the HEOM being derived[286–288].

The equations of motion

From our description of the density operator, equation (5.1.1), and the kernel equations (D.1.315), (D.1.316) for $iL^{(\alpha)}_{\mathcal{I},\mathrm{tot}}$ and $L^{(\alpha)}_{\mathcal{R},\mathrm{tot}}$, we can differentiate the density operator to generate an equation for the auxilliary density operators. Introducing our two component baths into equation (5.1.1) results in

$$\rho_{\mathrm{S}}(\mathrm{Q}_t,\mathrm{Q}'_t,t) = \iint\int_{\mathrm{Q}_0}^{\mathrm{Q}_t}\int_{\mathrm{Q}'_0}^{\mathrm{Q}'_t} \exp(i\mathrm{S}_{\mathrm{S}}[\mathrm{Q}_t]/\hbar)\left(\prod_n \mathcal{F}_n[\mathrm{Q}_t,\mathrm{Q}'_t]\right)\times \exp(-i\mathrm{S}_{\mathrm{S}}[\mathrm{Q}'_t])\rho_0(\mathrm{Q}_0,\mathrm{Q}'_0,0)\,\mathcal{D}[\mathrm{Q}_t]\,\mathcal{D}[\mathrm{Q}'_t]\,\mathrm{d}\mathrm{Q}_0\,\mathrm{d}\mathrm{Q}'_0. \quad \text{(D.1.317)}$$

Additionally we take the influence functional from equation (D.1.206) and recast the correlation function using the defined kernels[138,157],

$$\mathcal{F}[\mathrm{Q}_t,\mathrm{Q}'_t] = \exp\left(-\frac{i}{\hbar}\int_0^t\int_0^\tau \mathrm{B}^{\times}(\mathrm{Q}_t,\mathrm{Q}'_t;\tau)\times\left[iL^{(\alpha)}_{\mathcal{I},\mathrm{tot}}(\tau-\tau')\mathrm{B}^{\circ}(\mathrm{Q}_t,\mathrm{Q}'_t;\tau')+ L^{(\alpha)}_{\mathcal{R},\mathrm{tot}}(\tau-\tau')\mathrm{B}^{\times}(\mathrm{Q}_t,\mathrm{Q}'_t;\tau')\right]\mathrm{d}\tau'\,\mathrm{d}\tau\right). \quad \text{(D.1.318)}$$

Following the derivation process outlined in Ishizaki and Tanimura[150], we write out the density matrix and input the kernels in order to simplify:

$$\mathcal{F}[\mathrm{Q}_t,\mathrm{Q}'_t] = \mathcal{F}_{\mathrm{LD}}\times\mathcal{F}_{\mathrm{UO}} \quad \text{(D.1.319)}$$

$$\mathcal{F}_{\mathrm{UO}} = \exp\Bigg(-\frac{i}{\hbar}\int_0^t\int_0^\tau S_{\mathrm{UO}}^{\mathrm{HR}}\omega_{\mathrm{UO}}^2 \mathrm{B}_k^{\times}(\mathrm{Q}_t,\mathrm{Q}_t';\tau)\times \Bigg[-i\sin(\omega_{\mathrm{UO}}(\tau-\tau'))\mathrm{B}_k^{\circ}(\mathrm{Q}_t,\mathrm{Q}_t';\tau') + \coth\left(\frac{\beta\hbar\omega_{\mathrm{UO}}}{2}\right)\cos(\omega_{\mathrm{UO}}(\tau-\tau))\mathrm{B}_k^{\times}(\mathrm{Q}_t,\mathrm{Q}_t';\tau')\Bigg]\,\mathrm{d}\tau'\,\mathrm{d}\tau\Bigg), \quad \text{(D.1.320)}$$

or,

$$\mathcal{F}_{\mathrm{UO}} = \exp\Bigg(-\frac{i}{\hbar}\int_0^t\int_0^\tau \frac{1}{2}S_{\mathrm{UO}}^{\mathrm{HR}}\omega_{\mathrm{UO}}^2 \mathrm{B}_k^{\times}(\mathrm{Q}_t,\mathrm{Q}_t';\tau)\times \Bigg[\exp(-i\omega_{\mathrm{UO}}(\tau-\tau'))\left(\coth\left(\frac{\beta\hbar\omega_{\mathrm{UO}}}{2}\right)\mathrm{B}_k^{\circ}(\mathrm{Q}_t,\mathrm{Q}_t';\tau') + \mathrm{B}_k^{\times}(\mathrm{Q}_t,\mathrm{Q}_t';\tau')\right) + \exp(i\omega_{\mathrm{UO}}(\tau-\tau'))\left(\coth\left(\frac{\beta\hbar\omega_{\mathrm{UO}}}{2}\right)\mathrm{B}_k^{\circ}(\mathrm{Q}_t,\mathrm{Q}_t';\tau') - \mathrm{B}^{\times}(\mathrm{Q}_t,\mathrm{Q}_t';\tau')\right)\Bigg]\,\mathrm{d}\tau'\,\mathrm{d}\tau\Bigg), \quad \text{(D.1.321)}$$

$$\mathcal{F}_{\mathrm{LD}} = \exp\Bigg(-\frac{i}{\hbar}\int_0^t\int_0^\tau \eta_{\mathrm{LD}}\Lambda_{\mathrm{LD}}\mathrm{B}^{\times}(\mathrm{Q}_t,\mathrm{Q}_t';\tau)\times \Bigg[-i\exp(-\Lambda_{\mathrm{LD}}(\tau-\tau'))\mathrm{B}^{\circ}(\mathrm{Q}_t,\mathrm{Q}_t';\tau') + \left\{\cot\left(\frac{\beta\hbar\Lambda_{\mathrm{LD}}}{2}\right)\exp(-\Lambda_{\mathrm{LD}}(\tau-\tau')) + \sum_{n=1}^{\infty}\frac{2\nu_n}{\beta\hbar(\nu_n^2-\Lambda_{\mathrm{LD}}^2)}\exp(-\nu_n(\tau-\tau'))\right\}\times \mathrm{B}^{\times}(\mathrm{Q}_t,\mathrm{Q}_t';\tau')\Bigg]\,\mathrm{d}\tau'\,\mathrm{d}\tau\Bigg). \quad \text{(D.1.322)}$$

From the definition of the Matsubara decomposition coefficients and frequencies for the undamped mode we can introduce

$$\Phi_{\{\cdot\}}(\mathrm{Q}_t,\mathrm{Q}_t';\tau) = \frac{i}{\hbar}\mathrm{B}_{\{\cdot\}}^{\times}(\mathrm{Q}_t,\mathrm{Q}_t';\tau), \quad \text{(D.1.323)}$$

$$\Theta_k(\mathrm{Q}_t,\mathrm{Q}_t';\tau') = \frac{1}{2}\Bigg[(c_k-\tilde{c}_k)\mathrm{B}_k^{\circ}(\mathrm{Q}_t,\mathrm{Q}_t';\tau') + (c_k+\tilde{c}_k)\mathrm{B}_k^{\times}(\mathrm{Q}_t,\mathrm{Q}_t';\tau')\Bigg], \quad \text{(D.1.324)}$$

so that when $\gamma_1 = i\omega_{\mathrm{UO}}$ then

$$\Theta_1(\mathrm{Q}_t,\mathrm{Q}_t';\tau') = \frac{1}{2}S_{\mathrm{UO}}^{\mathrm{HR}}\omega_{\mathrm{UO}}^2\Bigg[\coth\left(\frac{\beta\hbar\omega_{\mathrm{UO}}}{2}\right)\mathrm{B}_1^{\circ}(\mathrm{Q}_t,\mathrm{Q}_t';\tau') + \mathrm{B}_1^{\times}(\mathrm{Q}_t,\mathrm{Q}_t';\tau')\Bigg], \quad \text{(D.1.325)}$$

and when $\gamma_2 = -i\omega_{\mathrm{UO}}$

$$\Theta_2(\mathrm{Q}_t, \mathrm{Q}_t'; \tau') = \frac{1}{2} S_{\mathrm{UO}}^{\mathrm{HR}} \omega_{\mathrm{UO}}^2 \left[\coth\left(\frac{\beta\hbar\omega_{\mathrm{UO}}}{2} \right) \mathrm{B}_2^{\circ}(\mathrm{Q}_t, \mathrm{Q}_t'; \tau') - \mathrm{B}_2^{\times}(\mathrm{Q}_t, \mathrm{Q}_t'; \tau') \right]. \tag{D.1.326}$$

We can now write, based on the definition of γ_k and c_k from equation (5.1.15),

$$\mathcal{F}_{\mathrm{UO}} = \exp\left(- \int_0^t \int_0^\tau \sum_k \Phi_k(\mathrm{Q}_t, \mathrm{Q}_t'; \tau) \exp(-\gamma_k(\tau - \tau')) \Theta_k(\mathrm{Q}_t, \mathrm{Q}_t'; \tau') \, \mathrm{d}\tau' \, \mathrm{d}\tau \right). \tag{D.1.327}$$

We perform a similar set of substitutions to the overdamped component with

$$\vartheta(\mathrm{Q}_t, \mathrm{Q}_t'; \tau') = \eta_{\mathrm{LD}} \left[\cot\left(\frac{\beta\hbar\Lambda_{\mathrm{LD}}}{2} \right) \mathrm{B}^{\times}(\mathrm{Q}_t, \mathrm{Q}_t'; \tau') - i\mathrm{B}^{\circ}(\mathrm{Q}_t, \mathrm{Q}_t'; \tau') \right], \tag{D.1.328}$$

$$\Psi_n(\mathrm{Q}_t, \mathrm{Q}_t'; \tau') = \sum_{n=1}^{\infty} \frac{2\eta_{\mathrm{LD}}\Lambda_{\mathrm{LD}}\nu_n}{\beta\hbar(\nu_n^2 - \Lambda_{\mathrm{LD}}^2)} \mathrm{B}^{\times}(\mathrm{Q}_t, \mathrm{Q}_t'; \tau'), \tag{D.1.329}$$

such that

$$\begin{aligned} \mathcal{F}_{\mathrm{LD}} = \exp\left(- \int_0^t \int_0^\tau \Phi(\mathrm{Q}_t, \mathrm{Q}_t'; \tau) \vartheta(\mathrm{Q}_t, \mathrm{Q}_t'; \tau') \Lambda_{\mathrm{LD}} \exp(-\Lambda_{\mathrm{LD}}(\tau - \tau')) \, \mathrm{d}\tau' \, \mathrm{d}\tau \right) \times \\ \prod_{n=1}^{\infty} \exp\left(- \int_0^t \int_0^\tau \Phi(\mathrm{Q}_t, \mathrm{Q}_t'; \tau) \Psi_n(\mathrm{Q}_t, \mathrm{Q}_t'; \tau') \nu_n \exp(-\nu_n(\tau - \tau')) \, \mathrm{d}\tau' \, \mathrm{d}\tau \right). \end{aligned} \tag{D.1.330}$$

From these substitutions we can write the full influence functional for the composite system as

$$\begin{aligned} \mathcal{F} = \exp\left(- \int_0^t \int_0^\tau \sum_k \Phi_k(\mathrm{Q}_t, \mathrm{Q}_t'; \tau) \exp(-\gamma_k(\tau - \tau')) \Theta_k(\mathrm{Q}_t, \mathrm{Q}_t'; \tau') \, \mathrm{d}\tau' \, \mathrm{d}\tau \right) \times \\ \exp\left(- \int_0^t \int_0^\tau \Phi(\mathrm{Q}_t, \mathrm{Q}_t'; \tau) \vartheta(\mathrm{Q}_t, \mathrm{Q}_t'; \tau') \Lambda_{\mathrm{LD}} \exp(-\Lambda_{\mathrm{LD}}(\tau - \tau')) \, \mathrm{d}\tau' \, \mathrm{d}\tau \right) \times \\ \prod_{n=1}^{\infty} \exp\left(- \int_0^t \int_0^\tau \Phi(\mathrm{Q}_t, \mathrm{Q}_t'; \tau) \Psi_n(\mathrm{Q}_t, \mathrm{Q}_t'; \tau') \nu_n \exp(-\nu_n(\tau - \tau')) \, \mathrm{d}\tau' \, \mathrm{d}\tau \right). \end{aligned} \tag{D.1.331}$$

We now briefly consider the termination of the infinite number of Matsubara frequencies for the overdamped component. For a value of K, which satisfies $\nu_K = 2\pi K/\beta\hbar \gg \omega_0$ - where ω_0 is the fundamental frequency of the system - then $\nu_n \exp(-\nu_n(\tau - \tau')) \approx \delta(\tau - \tau'), \quad n \geq K + 1$. This simplifies the influence

functional

$$\mathcal{F} = \exp\left(-\int_0^t \int_0^\tau \sum_k \Phi_k(\mathrm{Q}_t, \mathrm{Q}'_t; \tau) \exp(-\gamma_k(\tau - \tau'))\Theta_k(\mathrm{Q}_t, \mathrm{Q}'_t; \tau') \, \mathrm{d}\tau' \, \mathrm{d}\tau \right) \times$$
$$\exp\left(-\int_0^t \Phi(\mathrm{Q}_t, \mathrm{Q}'_t; \tau) \exp(-\Lambda_{\mathrm{LD}}\tau) \, \mathrm{d}\tau \left[-\int_0^\tau \Lambda_{\mathrm{LD}} \vartheta(\mathrm{Q}_t, \mathrm{Q}'_t; \tau') \exp(\Lambda_{\mathrm{LD}}\tau') \, \mathrm{d}\tau' \right] \right) \times$$
$$\prod_{n=1}^{K} \exp\left(-\int_0^t \Phi(\mathrm{Q}_t, \mathrm{Q}'_t; \tau) \exp(-\nu_n\tau) \, \mathrm{d}\tau \left[-\int_0^\tau \nu_n \Psi_n(\mathrm{Q}_t, \mathrm{Q}'_t; \tau') \exp(\nu_n\tau') \, \mathrm{d}\tau' \right] \right) \times$$
$$\prod_{n=K+1}^{\infty} \exp\left(\int_0^t \Phi(\mathrm{Q}_t, \mathrm{Q}'_t; \tau) \Psi_n(\mathrm{Q}_t, \mathrm{Q}'_t; \tau) \, \mathrm{d}\tau \right). \quad \text{(D.1.332)}$$

This allows us to terminate the Matsubara axis. In order to derive the equations of motion we additionally introduce the equation for the auxiliary density operators. This equation takes the same form as the influence functional, omitting $-\Phi(\mathrm{Q}_t, \mathrm{Q}'_t; \tau)$ as noted in the supplemental material of Seibt and Mancal[325], raised to the power of the ADO number. This creates the hierarchy ADO structure with each order in the hierarchy decreasing by an order of magnitude - as a consequence of the exponent. We introduce the auxiliary operator, $\rho^{(m,l_k)}_{j_1 \ldots j_K}$, by its matrix element as[150].

$$\rho^{(m,l_k)}_{j_1 \ldots j_K}(\mathrm{Q}_t, \mathrm{Q}'_t; t) = \int_{\mathrm{Q}_t(t_0)}^{\mathrm{Q}_t(t)} \int_{\mathrm{Q}'_t(t_0)}^{\mathrm{Q}'_t(t)} \exp\left(\frac{i\mathrm{S}_{\mathrm{S}}[\mathrm{Q}_t, \mathrm{Q}'_t]}{\hbar} \right) \mathcal{F} \times$$
$$\exp\left(\frac{-i\mathrm{S}_{\mathrm{S}}[\mathrm{Q}_t, \mathrm{Q}'_t]}{\hbar} \right) \rho_0(\mathrm{Q}_{t_0}, \mathrm{Q}'_{t_0}; t_0) \times$$
$$\prod_k \left\{ \int_0^t \exp(-\gamma_k(t - \tau'))\Theta_k(\mathrm{Q}_t, \mathrm{Q}'_t; \tau') \, \mathrm{d}\tau' \right\}^{l_k} \times$$
$$\left\{ \exp(-\Lambda_{\mathrm{LD}} t) \left[-\int_0^t \Lambda_{\mathrm{LD}} \vartheta(\mathrm{Q}_t, \mathrm{Q}'_t; \tau') \exp(\Lambda_{\mathrm{LD}}\tau') \, \mathrm{d}\tau' \right] \right\}^{m} \times$$
$$\prod_{n=1}^{K} \left\{ \exp(-\nu_n t) \left[-\int_0^t \nu_n \Psi_n(\mathrm{Q}_t, \mathrm{Q}'_t; \tau') \exp(\nu_n\tau') \, \mathrm{d}\tau' \right] \right\}^{j_n} \mathcal{D}[\mathrm{Q}_t] \, \mathcal{D}[\mathrm{Q}'_t]. \quad \text{(D.1.333)}$$

In order to differentiate this to form the equations of motion, we successively

apply the product rule. To simplify this process we call

$$\chi[\mathrm{Q}_t,\mathrm{Q}'_t,t]=\rho_0(\mathrm{Q}_{t_0},\mathrm{Q}'_{t_0};t_0)\times\prod_k\left\{\int_0^t\exp(-\gamma_k(t-\tau'))\Theta_k(\mathrm{Q}_t,\mathrm{Q}'_t;\tau')\,\mathrm{d}\tau'\right\}^{l_k}\times$$
$$\left\{\exp(-\Lambda_{\mathrm{LD}}t)\left[-\int_0^t\Lambda_{\mathrm{LD}}\vartheta(\mathrm{Q}_t,\mathrm{Q}'_t;\tau')\exp(\Lambda_{\mathrm{LD}}\tau')\,\mathrm{d}\tau'\right]\right\}^m\times$$
$$\prod_{n=1}^K\left\{\exp(-\nu_nt)\left[-\int_0^t\nu_n\Psi_n(\mathrm{Q}_t,\mathrm{Q}'_t;\tau')\exp(\nu_n\tau')\,\mathrm{d}\tau'\right]\right\}^{j_n},\quad\text{(D.1.334)}$$

so that

$$\rho^{(m,l_k)}_{j_1\ldots j_K}(\mathrm{Q}_t,\mathrm{Q}'_t,t)=\exp\left(\frac{i\mathrm{S}_{\mathrm{S}}[\mathrm{Q}_t,\mathrm{Q}'_t]}{\hbar}\right)\mathcal{F}\exp\left(\frac{-i\mathrm{S}_{\mathrm{S}}[\mathrm{Q}_t,\mathrm{Q}'_t]}{\hbar}\right)\chi[\mathrm{Q}_t,\mathrm{Q}'_t,t].\quad\text{(D.1.335)}$$

Hence,

$$\frac{\partial}{\partial t}\rho^{(m,l_k)}_{j_1\ldots j_K}(\mathrm{Q}_t,\mathrm{Q}'_t,t)=\frac{\partial}{\partial t}\left\{\exp\left(\frac{i\mathrm{S}_{\mathrm{S}}[\mathrm{Q}_t,\mathrm{Q}'_t]}{\hbar}\right)\mathcal{F}\exp\left(\frac{-i\mathrm{S}_{\mathrm{S}}[\mathrm{Q}_t,\mathrm{Q}'_t]}{\hbar}\right)\chi[\mathrm{Q}_t,\mathrm{Q}'_t,t]\right\},\quad\text{(D.1.336)}$$

apply the chain rule, by inspection as we have done previously, on the first instance of the product rule

$$=\frac{i}{\hbar}\frac{\partial\mathrm{S}_S[\mathrm{Q}_t,\mathrm{Q}'_t]}{\partial t}\exp\left(\frac{i\mathrm{S}_{\mathrm{S}}[\mathrm{Q}_t,\mathrm{Q}'_t]}{\hbar}\right)\left\{\mathcal{F}\exp\left(\frac{-i\mathrm{S}_{\mathrm{S}}[\mathrm{Q}_t,\mathrm{Q}'_t]}{\hbar}\right)\chi[\mathrm{Q}_t,\mathrm{Q}'_t,t]\right\}+$$
$$\exp\left(\frac{i\mathrm{S}_{\mathrm{S}}[\mathrm{Q}_t,\mathrm{Q}'_t]}{\hbar}\right)\frac{\partial}{\partial t}\left\{\mathcal{F}\exp\left(\frac{-i\mathrm{S}_{\mathrm{S}}[\mathrm{Q}_t,\mathrm{Q}'_t]}{\hbar}\right)\chi[\mathrm{Q}_t,\mathrm{Q}'_t,t]\right\},\quad\text{(D.1.337)}$$

perform the next of the successive product rules

$$=\frac{i}{\hbar}\frac{\partial\mathrm{S}_{\mathrm{S}}[\mathrm{Q}_t,\mathrm{Q}'_t]}{\partial t}\exp\left(\frac{i\mathrm{S}_{\mathrm{S}}[\mathrm{Q}_t,\mathrm{Q}'_t]}{\hbar}\right)\left\{\mathcal{F}\exp\left(\frac{-i\mathrm{S}_{\mathrm{S}}[\mathrm{Q}_t,\mathrm{Q}'_t]}{\hbar}\right)\chi[\mathrm{Q}_t,\mathrm{Q}'_t,t]\right\}+$$
$$\exp\left(\frac{i\mathrm{S}_{\mathrm{S}}[\mathrm{Q}_t,\mathrm{Q}'_t]}{\hbar}\right)\left[\frac{\partial\mathcal{F}}{\partial t}\left\{\mathcal{F}\exp\left(\frac{-i\mathrm{S}_{\mathrm{S}}[\mathrm{Q}_t,\mathrm{Q}'_t]}{\hbar}\right)\chi[\mathrm{Q}_t,\mathrm{Q}'_t,t]\right\}\right.$$
$$\left.+\mathcal{F}\frac{\partial}{\partial t}\left\{\exp\left(\frac{-i\mathrm{S}_{\mathrm{S}}[\mathrm{Q}_t,\mathrm{Q}'_t]}{\hbar}\right)\chi[\mathrm{Q}_t,\mathrm{Q}'_t,t]\right\}\right],\quad\text{(D.1.338)}$$

perform the last product rule

$$= \frac{i}{\hbar}\frac{\partial \mathrm{S}_{\mathrm{S}}[\mathrm{Q}_t, \mathrm{Q}'_t]}{\partial t} \exp\left(\frac{i\mathrm{S}_{\mathrm{S}}[\mathrm{Q}_t, \mathrm{Q}'_t]}{\hbar}\right)\left\{\mathcal{F}\exp\left(\frac{-i\mathrm{S}_{\mathrm{S}}[\mathrm{Q}_t, \mathrm{Q}'_t]}{\hbar}\right)\chi[\mathrm{Q}_t, \mathrm{Q}'_t, t]\right\}+$$
$$\exp\left(\frac{i\mathrm{S}_{\mathrm{S}}[\mathrm{Q}_t, \mathrm{Q}'_t]}{\hbar}\right)\left[\frac{\partial \mathcal{F}}{\partial t}\left\{\mathcal{F}\exp\left(\frac{-i\mathrm{S}_{\mathrm{S}}[\mathrm{Q}_t, \mathrm{Q}'_t]}{\hbar}\right)\chi[\mathrm{Q}_t, \mathrm{Q}'_t, t]\right\}\right.$$
$$+\mathcal{F}\left\{-\frac{i}{\hbar}\frac{\partial \mathrm{S}_S[\mathrm{Q}_t, \mathrm{Q}'_t]}{\partial t}\exp\left(-\frac{i\mathrm{S}_{\mathrm{S}}[\mathrm{Q}_t, \mathrm{Q}'_t]}{\hbar}\right)\chi[\mathrm{Q}_t, \mathrm{Q}'_t, t]+\right.$$
$$\left.\left.\exp\left(-\frac{i\mathrm{S}_{\mathrm{S}}[\mathrm{Q}_t, \mathrm{Q}'_t]}{\hbar}\right)\frac{\partial \chi[\mathrm{Q}_t, \mathrm{Q}'_t, t]}{\partial t}\right\}\right], \quad \text{(D.1.339)}$$

which we can expand and simplify to

$$\frac{\partial}{\partial t}\rho^{(m,l_k)}_{j_1\ldots j_K} = \frac{i}{\hbar}\frac{\partial \mathrm{S}_{\mathrm{S}}}{\partial t}\rho^{(m,l_k)}_{j_1\ldots j_K} + \frac{\partial \mathcal{F}}{\partial t}\rho^{(m,l_k)}_{j_1\ldots j_K} + \left(-\frac{i}{\hbar}\right)\frac{\partial \mathrm{S}_{\mathrm{S}}}{\partial t}\rho^{(m,l_k)}_{j_1\ldots j_K} + \frac{\partial \chi}{\partial t}\rho^{(m,l_k)}_{j_1\ldots j_K}. \quad \text{(D.1.340)}$$

We now consider the integral of $\mathcal{F}$ and χ, first we take $\mathcal{F}$. By applying the chain rule the first set of products are converted to sums,

$$\frac{\partial \mathcal{F}}{\partial t} = \frac{\partial}{\partial t}\left\{-\int_0^t\int_0^\tau \sum_k \Phi_k(\mathrm{Q}_t, \mathrm{Q}'_t; \tau)\exp(-\gamma_k(\tau-\tau'))\Theta_k(\mathrm{Q}_t, \mathrm{Q}'_t; \tau')\,\mathrm{d}\tau'\,\mathrm{d}\tau+\right.$$
$$\left(\int_0^t \Phi(\mathrm{Q}_t, \mathrm{Q}'_t; \tau)\exp(-\Lambda_{\mathrm{LD}}\tau)\times\left[-\int_0^\tau \Lambda_{\mathrm{LD}}\vartheta(\mathrm{Q}_t, \mathrm{Q}'_t; \tau')\exp(\Lambda_{\mathrm{LD}}\tau')\,\mathrm{d}\tau'\right]\mathrm{d}\tau\right)+$$
$$\sum_{n=1}^K\left(\int_0^t \Phi(\mathrm{Q}_t, \mathrm{Q}'_t; \tau)\exp(-\nu_n\tau)\times\left[-\int_0^\tau \nu_n\Psi_n(\mathrm{Q}_t, \mathrm{Q}'_t; \tau')\exp(\nu_n\tau')\,\mathrm{d}\tau'\right]\mathrm{d}\tau\right)$$
$$\left.+\sum_{n=K+1}^\infty\left(\int_0^t \Phi(\mathrm{Q}_t, \mathrm{Q}'_t; \tau)\Psi_n(\mathrm{Q}_t, \mathrm{Q}'_t; \tau)\,\mathrm{d}\tau\right)\right\}\mathcal{F}. \quad \text{(D.1.341)}$$

To compute this derivative we will have to apply Leibniz' integral rule on each of the three terms.

$$\frac{\partial \mathcal{F}}{\partial t} = -\int_0^t \sum_k \Phi_k(\mathrm{Q}_t, \mathrm{Q}'_t; t)\exp(-\gamma_k(t-\tau'))\Theta_k(\mathrm{Q}_t, \mathrm{Q}'_t; \tau')\,\mathrm{d}\tau'$$
$$+-\int_0^t\int_0^\tau \frac{\partial}{\partial t}\left(\sum_k \Phi_k(\mathrm{Q}_t, \mathrm{Q}'_t; \tau)\exp(-\gamma_k(\tau-\tau'))\Theta_k(\mathrm{Q}_t, \mathrm{Q}'_t; \tau')\right)\mathrm{d}\tau'\,\mathrm{d}\tau+$$
$$\frac{\partial}{\partial t}\left\{\left(\int_0^t \Phi(\mathrm{Q}_t, \mathrm{Q}'_t; \tau)\exp(-\Lambda_{\mathrm{LD}}\tau)\times\left[-\int_0^\tau \Lambda_{\mathrm{LD}}\vartheta(\mathrm{Q}_t, \mathrm{Q}'_t; \tau')\exp(\Lambda_{\mathrm{LD}}\tau')\,\mathrm{d}\tau'\right]\mathrm{d}\tau\right)+\right.$$
$$\sum_{n=1}^K\left(\int_0^t \Phi(\mathrm{Q}_t, \mathrm{Q}'_t; \tau)\exp(-\nu_n\tau)\times\left[-\int_0^\tau \nu_n\Psi_n(\mathrm{Q}_t, \mathrm{Q}'_t; \tau')\exp(\nu_n\tau')\,\mathrm{d}\tau'\right]\mathrm{d}\tau\right)$$
$$\left.+\sum_{n=K+1}^\infty\int_0^t \Phi(\mathrm{Q}_t, \mathrm{Q}'_t; \tau)\Psi_n(\mathrm{Q}_t, \mathrm{Q}'_t; \tau)\,\mathrm{d}\tau\right\}\mathcal{F}, \quad \text{(D.1.342)}$$

During the second application of Leibniz' rule we have to additionally apply the product rule on the integrand,

$$\begin{aligned}
\frac{\partial \mathcal{F}}{\partial t} = &- \int_0^t \sum_k \Phi_k(\mathrm{Q}_t, \mathrm{Q}'_t; t) \exp(-\gamma_k(t-\tau'))\Theta_k(\mathrm{Q}_t, \mathrm{Q}'_t; \tau') \, \mathrm{d}\tau' \\
&- \int_0^t \int_0^\tau \frac{\partial}{\partial t}\left(\sum_k \Phi_k(\mathrm{Q}_t, \mathrm{Q}'_t; \tau) \exp(-\gamma_k(\tau-\tau'))\Theta_k(\mathrm{Q}_t, \mathrm{Q}'_t; \tau') \right) \mathrm{d}\tau' \, \mathrm{d}\tau + \\
&+ \Phi(\mathrm{Q}_t, \mathrm{Q}'_t; t) \exp(-\Lambda_{\mathrm{LD}} t) \left[- \int_0^t \Lambda_{\mathrm{LD}} \vartheta(\mathrm{Q}_t, \mathrm{Q}'_t; \tau') \exp(\Lambda_{\mathrm{LD}} \tau') \, \mathrm{d}\tau' \right] \\
&+ \left\{ \int_0^t \frac{\partial}{\partial t}\left(\Phi(\mathrm{Q}_t, \mathrm{Q}'_t; \tau) \exp(-\Lambda_{\mathrm{LD}} \tau) \right) \times \left[- \int_0^\tau \Lambda_{\mathrm{LD}} \vartheta(\mathrm{Q}_t, \mathrm{Q}'_t; \tau') \exp(\Lambda_{\mathrm{LD}} \tau') \, \mathrm{d}\tau' \right] \mathrm{d}\tau + \right. \\
&\left. \int_0^t \Phi(\mathrm{Q}_t, \mathrm{Q}'_t; \tau) \exp(-\Lambda_{\mathrm{LD}} \tau) \times \left[- \int_0^\tau \frac{\partial}{\partial t}\left(\Lambda_{\mathrm{LD}} \vartheta(\mathrm{Q}_t, \mathrm{Q}'_t; \tau') \exp(\Lambda_{\mathrm{LD}} \tau') \right) \mathrm{d}\tau' \right] \mathrm{d}\tau \right\} + \\
&\frac{\partial}{\partial t} \left\{ \sum_{n=1}^K \left(\int_0^t \Phi(\mathrm{Q}_t, \mathrm{Q}'_t; \tau) \exp(-\nu_n \tau) \times \left[- \int_0^\tau \nu_n \Psi_n(\mathrm{Q}_t, \mathrm{Q}'_t; \tau') \exp(\nu_n \tau') \, \mathrm{d}\tau' \right] \mathrm{d}\tau \right) \right. \\
&\left. + \sum_{n=K+1}^\infty \int_0^t \Phi(\mathrm{Q}_t, \mathrm{Q}'_t; \tau) \Psi_n(\mathrm{Q}_t, \mathrm{Q}'_t; \tau) \, \mathrm{d}\tau \right\} \mathcal{F}, \quad \text{(D.1.343)}
\end{aligned}$$

and the same process is used on the penultimate term

$$\begin{aligned}
\frac{\partial \mathcal{F}}{\partial t} = &\left[- \int_0^t \sum_k \Phi_k(\mathrm{Q}_t, \mathrm{Q}'_t; t) \exp(-\gamma_k(t-\tau'))\Theta_k(\mathrm{Q}_t, \mathrm{Q}'_t; \tau') \, \mathrm{d}\tau' \right. \\
&- \int_0^t \int_0^\tau \frac{\partial}{\partial t}\left(\sum_k \Phi_k(\mathrm{Q}_t, \mathrm{Q}'_t; \tau) \exp(-\gamma_k(\tau-\tau'))\Theta_k(\mathrm{Q}_t, \mathrm{Q}'_t; \tau') \right) \mathrm{d}\tau' \, \mathrm{d}\tau + \\
&\left. + \Phi(\mathrm{Q}_t, \mathrm{Q}'_t; t) \exp(-\Lambda_{\mathrm{LD}} t) \times \left[- \int_0^t \Lambda_{\mathrm{LD}} \vartheta(\mathrm{Q}_t, \mathrm{Q}'_t; \tau') \exp(\Lambda_{\mathrm{LD}} \tau') \, \mathrm{d}\tau' \right] \right. \\
&+ \left\{ \int_0^t \frac{\partial}{\partial t}\left(\Phi(\mathrm{Q}_t, \mathrm{Q}'_t; \tau) \exp(-\Lambda_{\mathrm{LD}} \tau) \right) \times \left[- \int_0^\tau \Lambda_{\mathrm{LD}} \vartheta(\mathrm{Q}_t, \mathrm{Q}'_t; \tau') \exp(\Lambda_{\mathrm{LD}} \tau') \, \mathrm{d}\tau' \right] \mathrm{d}\tau + \right. \\
&\left. \int_0^t \Phi(\mathrm{Q}_t, \mathrm{Q}'_t; \tau) \exp(-\Lambda_{\mathrm{LD}} \tau) \times \left[- \int_0^\tau \frac{\partial}{\partial t}\left(\Lambda_{\mathrm{LD}} \vartheta(\mathrm{Q}_t, \mathrm{Q}'_t; \tau') \exp(\Lambda_{\mathrm{LD}} \tau') \right) \mathrm{d}\tau' \right] \mathrm{d}\tau \right\} + \\
&\left\{ \sum_{n=1}^K \Phi(\mathrm{Q}_t, \mathrm{Q}'_t; t) \exp(-\nu_n t) \times \left[- \int_0^t \nu_n \Psi_n(\mathrm{Q}_t, \mathrm{Q}'_t; \tau') \exp(\nu_n \tau') \, \mathrm{d}\tau' \right] \right. \\
&- \sum_{n=1}^K \left\{ \int_0^t \frac{\partial}{\partial t}\left(\Phi(\mathrm{Q}_t, \mathrm{Q}'_t; \tau) \exp(-\nu_n \tau) \right) \times \left[- \int_0^\tau \nu_n \Psi_n(\mathrm{Q}_t, \mathrm{Q}'_t; \tau') \exp(\nu_n \tau') \, \mathrm{d}\tau' \right] \mathrm{d}\tau + \right. \\
&\left. \sum_{n=1}^K \int_0^t \Phi(\mathrm{Q}_t, \mathrm{Q}'_t; \tau) \exp(-\nu_n \tau) \times \left[- \int_0^\tau \frac{\partial}{\partial t}\left(\nu_n \Psi_n(\mathrm{Q}_t, \mathrm{Q}'_t; \tau') \exp(\nu_n \tau') \right) \mathrm{d}\tau' \right] \mathrm{d}\tau \right\} \\
&\left. + \frac{\partial}{\partial t} \sum_{n=K+1}^\infty \int_0^t \Phi(\mathrm{Q}_t, \mathrm{Q}'_t; \tau) \Psi_n(\mathrm{Q}_t, \mathrm{Q}'_t; \tau) \, \mathrm{d}\tau \right] \mathcal{F}, \quad \text{(D.1.344)}
\end{aligned}$$

and the final application:

$$\begin{aligned}
\frac{\partial \mathcal{F}}{\partial t} = \Bigg[& - \int_0^t \sum_k \Phi_k(\mathrm{Q}_t, \mathrm{Q}'_t; t) \exp(-\gamma_k(t-\tau'))\Theta_k(\mathrm{Q}_t, \mathrm{Q}'_t; \tau') \, \mathrm{d}\tau' \\
& - \int_0^t \int_0^\tau \frac{\partial}{\partial t} \left(\sum_k \Phi_k(\mathrm{Q}_t, \mathrm{Q}'_t; \tau) \exp(-\gamma_k(\tau-\tau'))\Theta_k(\mathrm{Q}_t, \mathrm{Q}'_t; \tau') \right) \mathrm{d}\tau' \, \mathrm{d}\tau + \\
& + \Phi(\mathrm{Q}_t, \mathrm{Q}'_t; t) \exp(-\Lambda_{\mathrm{LD}} t) \times \left[- \int_0^t \Lambda_{\mathrm{LD}} \vartheta(\mathrm{Q}_t, \mathrm{Q}'_t; \tau') \exp(\Lambda_{\mathrm{LD}} \tau') \, \mathrm{d}\tau' \right] \\
+ \Bigg\{ & \int_0^t \frac{\partial}{\partial t} \left(\Phi(\mathrm{Q}_t, \mathrm{Q}'_t; \tau) \exp(-\Lambda_{\mathrm{LD}} \tau) \right) \times \left[- \int_0^\tau \Lambda_{\mathrm{LD}} \vartheta(\mathrm{Q}_t, \mathrm{Q}'_t; \tau') \exp(\Lambda_{\mathrm{LD}} \tau') \, \mathrm{d}\tau' \right] \mathrm{d}\tau + \\
& \int_0^t \Phi(\mathrm{Q}_t, \mathrm{Q}'_t; \tau) \exp(-\Lambda_{\mathrm{LD}} \tau) \times \left[- \int_0^\tau \frac{\partial}{\partial t} \left(\Lambda_{\mathrm{LD}} \vartheta(\mathrm{Q}_t, \mathrm{Q}'_t; \tau') \exp(\Lambda_{\mathrm{LD}} \tau') \right) \mathrm{d}\tau' \right] \mathrm{d}\tau \Bigg\} + \\
& \Bigg\{ \sum_{n=1}^K \Phi(\mathrm{Q}_t, \mathrm{Q}'_t; t) \exp(-\nu_n t) \times \left[- \int_0^t \nu_n \Psi_n(\mathrm{Q}_t, \mathrm{Q}'_t; \tau') \exp(\nu_n \tau') \, \mathrm{d}\tau' \right] \\
+ \sum_{n=1}^K \Bigg\{ & \int_0^t \frac{\partial}{\partial t} \left(\Phi(\mathrm{Q}_t, \mathrm{Q}'_t; \tau) \exp(-\nu_n \tau) \right) \times \left[- \int_0^\tau \nu_n \Psi_n(\mathrm{Q}_t, \mathrm{Q}'_t; \tau') \exp(\nu_n \tau') \, \mathrm{d}\tau' \right] \mathrm{d}\tau + \\
& \sum_{n=1}^K \int_0^t \Phi(\mathrm{Q}_t, \mathrm{Q}'_t; \tau) \exp(-\nu_n \tau) \times \left[- \int_0^\tau \frac{\partial}{\partial t} \left(\nu_n \Psi_n(\mathrm{Q}_t, \mathrm{Q}'_t; \tau') \exp(\nu_n \tau') \right) \mathrm{d}\tau' \right] \mathrm{d}\tau \Bigg\} \\
+ \sum_{n=K+1}^\infty & \Phi(\mathrm{Q}_t, \mathrm{Q}'_t; t) \Psi_n(\mathrm{Q}_t, \mathrm{Q}'_t; t) + \sum_{n=K+1}^\infty \int_0^t \frac{\partial}{\partial t} \left(\Phi(\mathrm{Q}_t, \mathrm{Q}'_t; \tau) \Psi_n(\mathrm{Q}_t, \mathrm{Q}'_t; \tau) \right) \mathrm{d}\tau \Bigg] \mathcal{F}.
\end{aligned} \tag{D.1.345}$$

First, since none of the integrands are explicitly dependent on time, or $\partial \Phi(\mathrm{Q}_t, \mathrm{Q}'_t; \tau)/\partial t = \partial \Theta(\mathrm{Q}_t, \mathrm{Q}'_t; \tau')/\partial t = \partial \vartheta(\mathrm{Q}_t, \mathrm{Q}'_t; \tau')/\partial t = \partial \Psi_n(\mathrm{Q}_t, \mathrm{Q}'_t; \tau')/\partial t = 0$, we can simplify to three terms

$$\begin{aligned}
\frac{\partial \mathcal{F}}{\partial t} = \Bigg\{ & - \int_0^t \sum_k \Phi_k(\mathrm{Q}_t, \mathrm{Q}'_t; t) \exp(-\gamma_k(t-\tau'))\Theta_k(\mathrm{Q}_t, \mathrm{Q}'_t; \tau') \, \mathrm{d}\tau' \\
& + \Phi(\mathrm{Q}_t, \mathrm{Q}'_t; t) \exp(-\Lambda_{\mathrm{LD}} t) \left[- \int_0^t \Lambda_{\mathrm{LD}} \vartheta(\mathrm{Q}_t, \mathrm{Q}'_t; \tau') \exp(\Lambda_{\mathrm{LD}} \tau') \, \mathrm{d}\tau' \right] \\
& + \sum_{n=1}^K \Phi(\mathrm{Q}_t, \mathrm{Q}'_t; t) \exp(-\nu_n t) \left[- \int_0^t \nu_n \Psi_n(\mathrm{Q}_t, \mathrm{Q}'_t; \tau') \exp(\nu_n \tau') \, \mathrm{d}\tau' \right] \\
& + \sum_{n=K+1}^\infty \Phi(\mathrm{Q}_t, \mathrm{Q}'_t; t) \Psi_n(\mathrm{Q}_t, \mathrm{Q}'_t; t) \Bigg\} \mathcal{F},
\end{aligned} \tag{D.1.346}$$

$$\frac{\partial \mathcal{F}}{\partial t} = -\Phi_{\mathrm{tot}}(\mathrm{Q}_t, \mathrm{Q}'_t; t)\Bigg\{ \int_0^t \sum_k \exp(-\gamma_k(t-\tau'))\Theta_k(\mathrm{Q}_t, \mathrm{Q}'_t; \tau')\ \mathrm{d}\tau' + \\ - \exp(-\Lambda_{\mathrm{LD}} t)\Bigg[- \int_0^t \Lambda_{\mathrm{LD}} \vartheta(\mathrm{Q}_t, \mathrm{Q}'_t; \tau') \exp(\Lambda_{\mathrm{LD}}\tau')\ \mathrm{d}\tau' \Bigg] + \\ -\sum_{n=1}^{K} \exp(-\nu_n t)\Bigg[-\int_0^t \nu_n \Psi_n(\mathrm{Q}_t, \mathrm{Q}'_t; \tau') \exp(\nu_n \tau')\ \mathrm{d}\tau' \Bigg] - \sum_{n=K+1}^{\infty} \Psi_n(\mathrm{Q}_t, \mathrm{Q}'_t; t) \Bigg\} \mathcal{F}. \tag{D.1.347}$$

Here we notice that we have generated $-\Phi_{\mathrm{tot}}(\mathrm{Q}_t, \mathrm{Q}'_t; t)$ (which is $-\Phi$ when applied to LD terms and $-\Phi_k$ when applied to UO terms) lots of the product contained within the equation for the ADO matrix element, equation (D.1.333). This can combine with these components to introduce ADO raising terms in each axis in the equations of motion: m, l_k, and j_n. Next considering χ and differentiating we get

$$\frac{\partial}{\partial t}\chi[\mathrm{Q}_t, \mathrm{Q}'_t, t] = \frac{\partial}{\partial t}\Bigg(\rho(q_{t_0}, q'_{t_0}; t_0) \times \prod_k \Bigg\{ \int_0^t \exp(-\gamma_k(t-\tau'))\Theta_k(\mathrm{Q}_t, \mathrm{Q}'_t; \tau')\ \mathrm{d}\tau' \Bigg\}^{l_k} \times \\ \Bigg\{ \exp(-\Lambda_{\mathrm{LD}} t)\Bigg[- \int_0^t \Lambda_{\mathrm{LD}} \vartheta(\mathrm{Q}_t, \mathrm{Q}'_t; \tau') \exp(\Lambda_{\mathrm{LD}}\tau')\ \mathrm{d}\tau' \Bigg] \Bigg\}^{m} \times \\ \prod_{n=1}^{K} \Bigg\{ \exp(-\nu_n t)\Bigg[- \int_0^t \nu_n \Psi_n(\mathrm{Q}_t, \mathrm{Q}'_t; \tau') \exp(\nu_n \tau')\ \mathrm{d}\tau' \Bigg] \Bigg\}^{j_n} \Bigg), \tag{D.1.348}$$

The initial condition can be factorised out of this equation in manner equivalent to Seibt and Mancal[289] such that

$$\frac{\partial}{\partial t}\chi[\mathrm{Q}_t, \mathrm{Q}'_t, t] = \frac{\partial}{\partial t}\Bigg(\prod_k \Bigg\{ \int_0^t \exp(-\gamma_k(t-\tau'))\Theta_k(\mathrm{Q}_t, \mathrm{Q}'_t; \tau')\ \mathrm{d}\tau' \Bigg\}^{l_k} \times \\ \Bigg\{ \exp(-\Lambda_{\mathrm{LD}} t)\Bigg[- \int_0^t \Lambda_{\mathrm{LD}} \vartheta(\mathrm{Q}_t, \mathrm{Q}'_t; \tau') \exp(\Lambda_{\mathrm{LD}}\tau')\ \mathrm{d}\tau' \Bigg] \Bigg\}^{m} \times \\ \prod_{n=1}^{K} \Bigg\{ \exp(-\nu_n t)\Bigg[- \int_0^t \nu_n \Psi_n(\mathrm{Q}_t, \mathrm{Q}'_t; \tau') \exp(\nu_n \tau')\ \mathrm{d}\tau' \Bigg] \Bigg\}^{j_n} \Bigg), \tag{D.1.349}$$

apply the product rule to separate into individual derivatives and then use the

Leibniz' rule to evaluate them.

$$\begin{aligned}\frac{\partial}{\partial t}\chi[\mathrm{Q}_t,\mathrm{Q}'_t,t] = \Bigg(\prod_k \frac{\partial}{\partial t}\Bigg\{\int_0^t \exp(-\gamma_k(t-\tau'))\Theta_k(\mathrm{Q}_t,\mathrm{Q}'_t;\tau')\,\mathrm{d}\tau'\Bigg\}^{l_k}\times \\ \Bigg\{\exp(-\Lambda_{\mathrm{LD}}t)\Bigg[-\int_0^t \Lambda_{\mathrm{LD}}\vartheta(\mathrm{Q}_t,\mathrm{Q}'_t;\tau')\exp(\Lambda_{\mathrm{LD}}\tau')\,\mathrm{d}\tau'\Bigg]\Bigg\}^{m}\times \\ \prod_{n=1}^{K}\Bigg\{\exp(-\nu_n t)\Bigg[-\int_0^t \nu_n\Psi_n(\mathrm{Q}_t,\mathrm{Q}'_t;\tau')\exp(\nu_n\tau')\,\mathrm{d}\tau'\Bigg]\Bigg\}^{j_n}\Bigg)+ \\ \Bigg(\prod_k\Bigg\{\int_0^t \exp(-\gamma_k(t-\tau'))\Theta_k(\mathrm{Q}_t,\mathrm{Q}'_t;\tau')\,\mathrm{d}\tau'\Bigg\}^{l_k}\times \\ \frac{\partial}{\partial t}\Bigg\{\exp(-\Lambda_{\mathrm{LD}}t)\Bigg[-\int_0^t \Lambda_{\mathrm{LD}}\vartheta(\mathrm{Q}_t,\mathrm{Q}'_t;\tau')\exp(\Lambda_{\mathrm{LD}}\tau')\,\mathrm{d}\tau'\Bigg]\Bigg\}^{m}\times \\ \prod_{n=1}^{K}\Bigg\{\exp(-\nu_n t)\Bigg[-\int_0^t \nu_n\Psi_n(\mathrm{Q}_t,\mathrm{Q}'_t;\tau')\exp(\nu_n\tau')\,\mathrm{d}\tau'\Bigg]\Bigg\}^{j_n}\Bigg)+ \\ \Bigg(\prod_k\Bigg\{\int_0^t \exp(-\gamma_k(t-\tau'))\Theta_k(\mathrm{Q}_t,\mathrm{Q}'_t;\tau')\,\mathrm{d}\tau'\Bigg\}^{l_k}\times \\ \Bigg\{\exp(-\Lambda_{\mathrm{LD}}t)\Bigg[-\int_0^t \Lambda_{\mathrm{LD}}\vartheta(\mathrm{Q}_t,\mathrm{Q}'_t;\tau')\exp(\Lambda_{\mathrm{LD}}\tau')\,\mathrm{d}\tau'\Bigg]\Bigg\}^{m}\times \\ \prod_{n=1}^{K}\frac{\partial}{\partial t}\Bigg\{\exp(-\nu_n t)\Bigg[-\int_0^t \nu_n\Psi_n(\mathrm{Q}_t,\mathrm{Q}'_t;\tau')\exp(\nu_n\tau')\,\mathrm{d}\tau'\Bigg]\Bigg\}^{j_n}\Bigg). \quad \text{(D.1.350)}\end{aligned}$$

Take each component in isolation, for ease, and apply the chain rule. Define

$$\begin{aligned}\chi_1 = \prod_k\Bigg\{\int_0^t \exp(-\gamma_k(t-\tau'))\Theta_k(\mathrm{Q}_t,\mathrm{Q}'_t;\tau')\,\mathrm{d}\tau'\Bigg\}^{l_k}\times \\ \Bigg\{\exp(-\Lambda_{\mathrm{LD}}t)\Bigg[-\int_0^t \Lambda_{\mathrm{LD}}\vartheta(\mathrm{Q}_t,\mathrm{Q}'_t;\tau')\exp(\Lambda_{\mathrm{LD}}\tau')\,\mathrm{d}\tau'\Bigg]\Bigg\}^{m}\times \\ \prod_{n=1}^{K}\Bigg\{\exp(-\nu_n t)\Bigg[-\int_0^t \nu_n\Psi_n(\mathrm{Q}_t,\mathrm{Q}'_t;\tau')\exp(\nu_n\tau')\,\mathrm{d}\tau'\Bigg]\Bigg\}^{j_n}, \quad \text{(D.1.351)}\end{aligned}$$

Component (1) becomes

$$\prod_k \frac{\partial}{\partial t}\left\{ \int_0^t \exp(-\gamma_k(t-\tau'))\Theta_k(\mathrm{Q}_t,\mathrm{Q}'_t;\tau')\,\mathrm{d}\tau' \right\}^{l_k} \times \left\{ \exp(-\Lambda_{\mathrm{LD}}t)\left[-\int_0^t \Lambda_{\mathrm{LD}}\vartheta(\mathrm{Q}_t,\mathrm{Q}'_t;\tau')\exp(\Lambda_{\mathrm{LD}}\tau')\,\mathrm{d}\tau' \right] \right\}^{m} \times \prod_{n=1}^{K}\left\{ \exp(-\nu_n t)\left[-\int_0^t \nu_n\Psi_n(\mathrm{Q}_t,\mathrm{Q}'_t;\tau')\exp(\nu_n\tau')\,\mathrm{d}\tau' \right] \right\}^{j_n}$$

$$= l_k \prod_k \frac{\partial}{\partial t}\left\{ \int_0^t \exp(-\gamma_k(t-\tau'))\Theta_k(\mathrm{Q}_t,\mathrm{Q}'_t;\tau')\,\mathrm{d}\tau' \right\} \times \left\{ \exp(-\Lambda_{\mathrm{LD}}t)\left[-\int_0^t \Lambda_{\mathrm{LD}}\vartheta(\mathrm{Q}_t,\mathrm{Q}'_t;\tau')\exp(\Lambda_{\mathrm{LD}}\tau')\,\mathrm{d}\tau' \right] \right\}^{m} \times \prod_{n=1}^{K}\left\{ \exp(-\nu_n t)\left[-\int_0^t \nu_n\Psi_n(\mathrm{Q}_t,\mathrm{Q}'_t;\tau')\exp(\nu_n\tau')\,\mathrm{d}\tau' \right] \right\}^{j_n} \times \chi_1^{l_k^-}, \quad \text{(D.1.352)}$$

where $\chi_1^{l_k^-}$ indicates a reduction by one from l_k in the first component of the derivative of χ. Apply Leibniz' rule

$$= \left(\prod_k l_k\Theta_k(\mathrm{Q}_t,\mathrm{Q}'_t;t) - \prod_k l_k\gamma_k \frac{\partial}{\partial t}\left\{ \int_0^t \exp(-\gamma_k(t-\tau'))\Theta_k(\mathrm{Q}_t,\mathrm{Q}'_t;\tau')\,\mathrm{d}\tau' \right\} + \left\{ \prod_k l_k \int_0^t \exp(-\gamma_k(t-\tau'))\frac{\partial\Theta_k(\mathrm{Q}_t,\mathrm{Q}'_t;\tau')}{\partial t}\,\mathrm{d}\tau' \right\} \right) \times \left\{ \exp(-\Lambda_{\mathrm{LD}}t)\left[-\int_0^t \Lambda_{\mathrm{LD}}\vartheta(\mathrm{Q}_t,\mathrm{Q}'_t;\tau')\exp(\Lambda_{\mathrm{LD}}\tau')\,\mathrm{d}\tau' \right] \right\}^{m} \times \prod_{n=1}^{K}\left\{ \exp(-\nu_n t)\left[-\int_0^t \nu_n\Psi_n(\mathrm{Q}_t,\mathrm{Q}'_t;\tau')\exp(\nu_n\tau')\,\mathrm{d}\tau' \right] \right\}^{j_n} \times \chi_1^{l_k^-}, \quad \text{(D.1.353)}$$

which simplifies to

$$(1) = \left(\prod_k l_k\Theta_k(\mathrm{Q}_t,\mathrm{Q}'_t;t) - l_k\gamma_k \frac{\partial}{\partial t}\left\{ \int_0^t \exp(-\gamma_k(t-\tau'))\Theta_k(\mathrm{Q}_t,\mathrm{Q}'_t;\tau')\,\mathrm{d}\tau' \right\} + \left\{ \exp(-\Lambda_{\mathrm{LD}}t)\left[-\int_0^t \Lambda_{\mathrm{LD}}\vartheta(\mathrm{Q}_t,\mathrm{Q}'_t;\tau')\exp(\Lambda_{\mathrm{LD}}\tau')\,\mathrm{d}\tau' \right] \right\}^{m} \times \prod_{n=1}^{K}\left\{ \exp(-\nu_n t)\left[-\int_0^t \nu_n\Psi_n(\mathrm{Q}_t,\mathrm{Q}'_t;\tau')\exp(\nu_n\tau')\,\mathrm{d}\tau' \right] \right\}^{j_n} \right) \times \chi_1^{l_k^-}. \quad \text{(D.1.354)}$$

We now take the second term in the derivative of χ: (2)

$$\Bigg(\prod_k \Bigg\{ \int_0^t \exp(-\gamma_k(t-\tau'))\Theta_k(\mathrm{Q}_t, \mathrm{Q}'_t; \tau') \, \mathrm{d}\tau' \Bigg\}^{l_k} \times \\ \frac{\partial}{\partial t} \Bigg\{ \exp(-\Lambda_{\mathrm{LD}} t) \Bigg[- \int_0^t \Lambda_{\mathrm{LD}} \vartheta(\mathrm{Q}_t, \mathrm{Q}'_t; \tau') \exp(\Lambda_{\mathrm{LD}} \tau') \, \mathrm{d}\tau' \Bigg] \Bigg\}^{m} \times \\ \prod_{n=1}^{K} \Bigg\{ \exp(-\nu_n t) \Bigg[- \int_0^t \nu_n \Psi_n(\mathrm{Q}_t, \mathrm{Q}'_t; \tau') \exp(\nu_n \tau') \, \mathrm{d}\tau' \Bigg] \Bigg\}^{j_n} \Bigg), \quad \text{(D.1.355)}$$

then apply the chain rule

$$\Bigg(\prod_k \Bigg\{ \int_0^t \exp(-\gamma_k(t-\tau'))\Theta_k(\mathrm{Q}_t, \mathrm{Q}'_t; \tau') \, \mathrm{d}\tau' \Bigg\}^{l_k} \times \\ \frac{\partial}{\partial t} \Bigg\{ \exp(-\Lambda_{\mathrm{LD}} t) \Bigg[- \int_0^t \Lambda_{\mathrm{LD}} \vartheta(\mathrm{Q}_t, \mathrm{Q}'_t; \tau') \exp(\Lambda_{\mathrm{LD}} \tau') \, \mathrm{d}\tau' \Bigg] \Bigg\}^{m} \times \\ \prod_{n=1}^{K} \Bigg\{ \exp(-\nu_n t) \Bigg[- \int_0^t \nu_n \Psi_n(\mathrm{Q}_t, \mathrm{Q}'_t; \tau') \exp(\nu_n \tau') \, \mathrm{d}\tau' \Bigg] \Bigg\}^{j_n} \Bigg) \\ = \\ \Bigg(\prod_k \Bigg\{ \int_0^t \exp(-\gamma_k(t-\tau'))\Theta_k(\mathrm{Q}_t, \mathrm{Q}'_t; \tau') \, \mathrm{d}\tau' \Bigg\}^{l_k} \times \\ m \Bigg\{ \exp(-\Lambda_{\mathrm{LD}} t) \Bigg[- \int_0^t \Lambda_{\mathrm{LD}} \vartheta(\mathrm{Q}_t, \mathrm{Q}'_t; \tau') \exp(\Lambda_{\mathrm{LD}} \tau') \, \mathrm{d}\tau' \Bigg] \Bigg\} \times \\ \prod_{n=1}^{K} \Bigg\{ \exp(-\nu_n t) \Bigg[- \int_0^t \nu_n \Psi_n(\mathrm{Q}_t, \mathrm{Q}'_t; \tau') \exp(\nu_n \tau') \, \mathrm{d}\tau' \Bigg] \Bigg\}^{j_n} \Bigg) \times \chi_1^{m^-}, \quad \text{(D.1.356)}$$

where $\chi_1^{m^-}$ indicates a reduction by one from m in the second component of the

derivative of χ. Now apply Leibniz' rule

$$
\begin{aligned}
= & \left(\prod_k \left\{ \int_0^t \exp(-\gamma_k(t-\tau'))\Theta_k(\mathrm{Q}_t, \mathrm{Q}'_t; \tau') \, \mathrm{d}\tau' \right\}^{l_k} \times \right. \\
& \left\{ -m\Lambda_{\mathrm{LD}} \exp(-\Lambda_{\mathrm{LD}} t) \left[-\int_0^t \Lambda_{\mathrm{LD}} \vartheta(\mathrm{Q}_t, \mathrm{Q}'_t; \tau') \exp(\Lambda_{\mathrm{LD}} \tau') \, \mathrm{d}\tau' \right] + \right. \\
& -m \exp(-\Lambda_{\mathrm{LD}} t) \Lambda_{\mathrm{LD}} \vartheta(\mathrm{Q}_t, \mathrm{Q}'_t; t) \exp(\Lambda_{\mathrm{LD}} t) + \\
& \left. m \exp(-\Lambda_{\mathrm{LD}} t) \left[-\int_0^t \Lambda_{\mathrm{LD}} \frac{\partial \vartheta(\mathrm{Q}_t, \mathrm{Q}'_t; \tau')}{\partial t} \exp(\Lambda_{\mathrm{LD}} \tau') \, \mathrm{d}\tau' \right] \right\} \times \\
& \left. \prod_{n=1}^{K} \left\{ \exp(-\nu_n t) \left[-\int_0^t \nu_n \Psi_n(\mathrm{Q}_t, \mathrm{Q}'_t; \tau') \exp(\nu_n \tau') \, \mathrm{d}\tau' \right] \right\}^{j_n} \right) \times \chi_1^{m^-},
\end{aligned}
\tag{D.1.357}
$$

which simplifies to

$$
\begin{aligned}
\textcircled{2} = & \left(\prod_k \left\{ \int_0^t \exp(-\gamma_k(t-\tau'))\Theta_k(\mathrm{Q}_t, \mathrm{Q}'_t; \tau') \, \mathrm{d}\tau' \right\}^{l_k} \times \right. \\
& \left\{ m\Lambda_{\mathrm{LD}} \exp(-\Lambda_{\mathrm{LD}} t) \left[\int_0^t \Lambda_{\mathrm{LD}} \vartheta(\mathrm{Q}_t, \mathrm{Q}'_t; \tau') \exp(\Lambda_{\mathrm{LD}} \tau') \, \mathrm{d}\tau' \right] - m\Lambda_{\mathrm{LD}} \vartheta(\mathrm{Q}_t, \mathrm{Q}'_t; t) \right] \right\} \times \\
& \left. \prod_{n=1}^{K} \left\{ \exp(-\nu_n t) \left[-\int_0^t \nu_n \Psi_n(\mathrm{Q}_t, \mathrm{Q}'_t; \tau') \exp(\nu_n \tau') \, \mathrm{d}\tau' \right] \right\}^{j_n} \right) \times \chi_1^{m^-},
\end{aligned}
\tag{D.1.358}
$$

Since the third term in the derivative of χ is identical in form to the first term, we can perform this derivative by inspection to yield:

$$
\begin{aligned}
\textcircled{3} = & \left(\prod_k \left\{ \int_0^t \exp(-\gamma_k(t-\tau'))\Theta_k(\mathrm{Q}_t, \mathrm{Q}'_t; \tau') \, \mathrm{d}\tau' \right\}^{l_k} \times \right. \\
& \left\{ \exp(-\Lambda_{\mathrm{LD}} t) \left[-\int_0^t \Lambda_{\mathrm{LD}} \vartheta(\mathrm{Q}_t, \mathrm{Q}'_t; \tau') \exp(\Lambda_{\mathrm{LD}} \tau') \, \mathrm{d}\tau' \right] \right\}^{m} \times \\
& \left. \prod_{n=1}^{K} \left\{ j_n \nu_n \exp(-\nu_n t) \left[\int_0^t \nu_n \Psi_n(\mathrm{Q}_t, \mathrm{Q}'_t; \tau') \exp(\nu_n \tau') \, \mathrm{d}\tau' \right] - \right. \right. \\
& \left. \left. j_n \nu_n \Psi_n(\mathrm{Q}_t, \mathrm{Q}'_t; t) \right] \right\} \times \chi_1^{j_n^-}, \quad \text{(D.1.359)}
\end{aligned}
$$

where $\chi_1^{j_n^-}$ indicates a reduction by one from j_n in the third component of the derivative of χ. If we recombine (1), (2) and (3), then we get:

$$\begin{aligned}
&\frac{\partial}{\partial t}\chi[\mathrm{Q}_t,\mathrm{Q}'_t,t] = \\
&\Bigg[\Bigg(\prod_k l_k\Theta_k(\mathrm{Q}_t,\mathrm{Q}'_t;t) - l_k\gamma_k\frac{\partial}{\partial t}\Bigg\{\int_0^t \exp(-\gamma_k(t-\tau'))\Theta_k(\mathrm{Q}_t,\mathrm{Q}'_t;\tau')\,\mathrm{d}\tau'\Bigg\}+ \\
&\qquad\Bigg\{\exp(-\Lambda_{\mathrm{LD}}t)\Bigg[-\int_0^t \Lambda_{\mathrm{LD}}\vartheta(\mathrm{Q}_t,\mathrm{Q}'_t;\tau')\exp(\Lambda_{\mathrm{LD}}\tau')\,\mathrm{d}\tau'\Bigg]\Bigg\}^m \times \\
&\quad\prod_{n=1}^K\Bigg\{\exp(-\nu_n t)\Bigg[-\int_0^t \nu_n\Psi_n(\mathrm{Q}_t,\mathrm{Q}'_t;\tau')\exp(\nu_n\tau')\,\mathrm{d}\tau'\Bigg]\Bigg\}^{j_n}\Bigg) \times \chi_1^{l_k^-} + \\
&\qquad\Bigg(\prod_k\Bigg\{\int_0^t \exp(-\gamma_k(t-\tau'))\Theta_k(\mathrm{Q}_t,\mathrm{Q}'_t;\tau')\,\mathrm{d}\tau'\Bigg\}^{l_k} \times \\
&\qquad\Bigg\{m\Lambda_{\mathrm{LD}}\exp(-\Lambda_{\mathrm{LD}}t)\Bigg[\int_0^t \Lambda_{\mathrm{LD}}\vartheta(\mathrm{Q}_t,\mathrm{Q}'_t;\tau')\exp(\Lambda_{\mathrm{LD}}\tau')\,\mathrm{d}\tau'\Bigg]- \\
&\qquad\qquad m\Lambda_{\mathrm{LD}}\vartheta(\mathrm{Q}_t,\mathrm{Q}'_t;t)\Bigg]\Bigg\}\times \\
&\quad\prod_{n=1}^K\Bigg\{\exp(-\nu_n t)\Bigg[-\int_0^t \nu_n\Psi_n(\mathrm{Q}_t,\mathrm{Q}'_t;\tau')\exp(\nu_n\tau')\,\mathrm{d}\tau'\Bigg]\Bigg\}^{j_n}\Bigg) \times \chi_1^{m^-} + \\
&\qquad\Bigg(\prod_k\Bigg\{\int_0^t \exp(-\gamma_k(t-\tau'))\Theta_k(\mathrm{Q}_t,\mathrm{Q}'_t;\tau')\,\mathrm{d}\tau'\Bigg\}^{l_k} \times \\
&\qquad\Bigg\{\exp(-\Lambda_{\mathrm{LD}}t)\Bigg[-\int_0^t \Lambda_{\mathrm{LD}}\vartheta(\mathrm{Q}_t,\mathrm{Q}'_t;\tau')\exp(\Lambda_{\mathrm{LD}}\tau')\,\mathrm{d}\tau'\Bigg]\Bigg\}^m \times \\
&\qquad\prod_{n=1}^K\Bigg\{j_n\nu_n\exp(-\nu_n t)\Bigg[\int_0^t \nu_n\Psi_n(\mathrm{Q}_t,\mathrm{Q}'_t;\tau')\exp(\nu_n\tau')\,\mathrm{d}\tau'\Bigg]- \\
&\qquad\qquad j_n\nu_n\Psi_n(\mathrm{Q}_t,\mathrm{Q}'_t;t)\Bigg]\Bigg\} \times \chi_1^{j_n^-}\Bigg]. \qquad \text{(D.1.360)}
\end{aligned}$$

By looking at the form of χ, in equation (D.1.334), it is clear that we have regenerated the original components in each of (1), (2) and (3) allowing us to return $\chi_1^{l_k^-}$, $\chi_1^{m^-}$, and $\chi_1^{j_n^-}$ to χ while additionally introducing ADO lowering terms.

$$\begin{aligned}
\frac{\partial}{\partial t}\chi[\mathrm{Q}_t,\mathrm{Q}'_t,t] = &\prod_k l_k\Theta(\mathrm{Q}_t,\mathrm{Q}'_t;t)\chi_1^{l_k^-} - m\Lambda_{\mathrm{LD}}\vartheta(\mathrm{Q}_t,\mathrm{Q}'_t;t)\chi_1^{m^-} - \\
&\prod_{n=1}^K j_n\nu_n\Psi_n(\mathrm{Q}_t,\mathrm{Q}'_t;t)\chi_1^{j_n^-} - \prod_k(l_k\gamma_k + m\Lambda_{\mathrm{LD}})\chi - \prod_{n=1}^K j_n\nu_n\chi. \qquad \text{(D.1.361)}
\end{aligned}$$

where

$$\chi = \prod_k \left\{ \int_0^t \exp(-\gamma_k(t-\tau'))\Theta_k(\mathrm{Q}_t, \mathrm{Q}'_t; \tau')\, \mathrm{d}\tau' \right\}^{l_k} \times \left\{ \exp(-\Lambda_{\mathrm{LD}} t) \left[- \int_0^t \Lambda_{\mathrm{LD}} \vartheta(\mathrm{Q}_t, \mathrm{Q}'_t; \tau') \exp(\Lambda_{\mathrm{LD}} \tau')\, \mathrm{d}\tau' \right] \right\}^{m} \times \prod_{n=1}^{K} \left\{ \exp(-\nu_n t) \left[- \int_0^t \nu_n \Psi_n(\mathrm{Q}_t, \mathrm{Q}'_t; \tau') \exp(\nu_n \tau')\, \mathrm{d}\tau' \right] \right\}^{j_n} \quad \text{(D.1.362)}$$

We can now recombine these components into equation D.1.340, which takes the form:

$$\frac{\partial}{\partial t} \rho^{(m,l_k)}_{j_1 \ldots j_K} = \frac{i}{\hbar} \frac{\partial \mathrm{S}_{\mathrm{S}}}{\partial t} \rho^{(m,l_k)}_{j_1 \ldots j_K} + \frac{\partial \mathcal{F}}{\partial t} \rho^{(m,l_k)}_{j_1 \ldots j_K} + \left(- \frac{i}{\hbar} \right) \frac{\partial \mathrm{S}_{\mathrm{S}}}{\partial t} \rho^{(m,l_k)}_{j_1 \ldots j_K} + \frac{\partial \chi}{\partial t} \rho^{(m,l_k)}_{j_1 \ldots j_K}. \quad \text{(D.1.363)}$$

$$\begin{aligned} \frac{\partial}{\partial t} \rho^{(m,l_k)}_{j_1 \ldots j_K} = {} & \frac{i}{\hbar} \frac{\partial \mathrm{S}_{\mathrm{S}}[\mathrm{Q}_t]}{\partial t} \rho^{(m,l_k)}_{j_1 \ldots j_K} + \left(- \frac{i}{\hbar} \right) \frac{\partial \mathrm{S}_{\mathrm{S}}[\mathrm{Q}'_t]}{\partial t} \rho^{(m,l_k)}_{j_1 \ldots j_K} + \\ & \left(- \Phi_{\mathrm{tot}}(\mathrm{Q}_t, \mathrm{Q}'_t; t) \left\{ \int_0^t \sum_k \exp(-\gamma_k(t-\tau'))\Theta_k(\mathrm{Q}_t, \mathrm{Q}'_t; \tau')\, \mathrm{d}\tau' + \right. \right. \\ & \exp(-\Lambda_{\mathrm{LD}} t) \left[- \int_0^t \Lambda_{\mathrm{LD}} \vartheta(\mathrm{Q}_t, \mathrm{Q}'_t; \tau') \exp(\Lambda_{\mathrm{LD}} \tau')\, \mathrm{d}\tau' \right] + \\ & \sum_{n=1}^{K} \exp(-\nu_n t) \left[- \int_0^t \nu_n \Psi_n(\mathrm{Q}_t, \mathrm{Q}'_t; \tau') \exp(\nu_n \tau')\, \mathrm{d}\tau' \right] - \\ & \left. \left. \sum_{n=K+1}^{\infty} \Psi_n(\mathrm{Q}_t, \mathrm{Q}'_t; t) \right\} \mathcal{F} \right) \rho^{(m,l_k)}_{j_1 \ldots j_K} + \\ & \left(\prod_k l_k \Theta(\mathrm{Q}_t, \mathrm{Q}'_t; t) \chi_1^{l_k^-} - m \Lambda_{\mathrm{LD}} \vartheta(\mathrm{Q}_t, \mathrm{Q}'_t; t) \chi_1^{m^-} - \right. \\ & \left. \prod_{n=1}^{K} j_n \nu_n \Psi_n(\mathrm{Q}_t, \mathrm{Q}'_t; t) \chi_1^{j_n^-} - \prod_k (l_k \gamma_k + m \Lambda_{\mathrm{LD}}) \chi - \prod_{n=1}^{K} j_n \nu_n \chi \right) \rho^{(m,l_k)}_{j_1 \ldots j_K}, \end{aligned} \quad \text{(D.1.364)}$$

which given the form of the ADO matrix element, in equation (D.1.333), allows

us to reduce this equation to

$$\frac{\partial}{\partial t}\rho^{(m,l_k)}_{j_1\ldots j_K} = \left(\frac{i}{\hbar}\frac{\partial \mathrm{S_S}[\mathrm{Q}_t]}{\partial t} - \frac{i}{\hbar}\frac{\partial \mathrm{S_S}[\mathrm{Q}'_t]}{\partial t} + \sum_{n=K+1}^{\infty}\Phi(\mathrm{Q}_t,\mathrm{Q}'_t;t)\Psi_n(\mathrm{Q}_t,\mathrm{Q}'_t;t)\right)\rho^{(l_k,m)}_{j_1\ldots j_K} - \left(\Phi\rho^{(m+1,l_k)}_{j_1\ldots j_K} + \sum_k \Phi_k\rho^{(m,l_k+1)}_{j_1\ldots j_K}\right) - \sum_k\sum_{n=1}^{K}\Phi_k(\mathrm{Q}_t,\mathrm{Q}'_t;t)\rho^{(m,l_k)}_{j_1\ldots j_{n+1}\ldots j_K} - \sum_k l_k\Theta_k(\mathrm{Q}_t,\mathrm{Q}'_t;t)\rho^{(m,l_k-1)}_{j_1\ldots j_K} - \sum_k m\Lambda_{\mathrm{LD}}\vartheta(\mathrm{Q}_t,\mathrm{Q}'_t;t)\rho^{(m-1,l_k)}_{j_1\ldots j_K} - \sum_{n=1}^{K} j_n\nu_n\Psi_n(\mathrm{Q}_t,\mathrm{Q}'_t;t)\rho^{(m,l_k)}_{j_1\ldots j_{n-1}\ldots j_K} - \sum_k(l_k\gamma_k + m\Lambda_{\mathrm{LD}})\rho^{(m,l_k)}_{j_1\ldots j_K} - \sum_{n=1}^{K} j_n\nu_n\rho^{(m,l_k)}_{j_1\ldots j_K}. \tag{D.1.365}$$

This simplifies to:

$$\frac{\partial}{\partial t}\rho^{(m,l_k)}_{j_1\ldots j_K} = \left(-\frac{i}{\hbar}\mathrm{H}^{\times}_{\mathrm{S}} - \sum_k(l_k\gamma_k + m\Lambda_{\mathrm{LD}}) - \sum_{n=1}^{K} j_n\nu_n + \sum_{n=K+1}^{\infty}\mathrm{B}^{\times}\Psi_n\right)\rho^{(m,l_k)}_{j_1\ldots j_K} - \sum_k l_k\Theta_k\rho^{(m,l_k-1)}_{j_1\ldots j_K} - m\Lambda_{\mathrm{LD}}\vartheta\rho^{(m-1,l_k)}_{j_1\ldots j_K} - \sum_{n=1}^{K} j_n\nu_n\Psi_n\rho^{(m,l_k)}_{j_1\ldots j_{n-1}\ldots j_K} - \left(\mathrm{B}^{\times}\rho^{(m+1,l_k)}_{j_1\ldots j_K} + \sum_k \mathrm{B}^{\times}_k\rho^{(m,l_k+1)}_{j_1\ldots j_K}\right) - \sum_{n=1}^{K}\mathrm{B}^{\times}\rho^{(m,l_k)}_{j_1\ldots j_{n+1}\ldots j_K}. \tag{D.1.366}$$

Upon first inspection it may appear that there is an absent factor of γ_k in the creation term from the (l_k-1)th Matsubara axis, however this is not the case. Based on the reduction criteria for the infinite Matsubara components, which for the overdamped contribution is:

$$\nu_K = \frac{2\pi K}{\beta\hbar} \gg \omega_0, \tag{D.1.367}$$

we reduce to a delta function for a sufficient value of K. However, such a reduction cannot be performed for the undamped component. The undamped contribution introduces a pair of Matsubara decomposition coefficients and frequencies, as opposed to an infinite number, and as such a sufficient value of K being chosen is unlikely. This lack of reduction motivates the current derivation and it results in factors of $(c_k \pm \tilde{c_k})$ in Θ_k, which (based on the form of c_k in equation (5.1.15)) accounts for the apparent missing factor of γ_k.

For the condition

$$\sum_k (l_k\gamma_k + m\Lambda_{\mathrm{LD}}) + \sum_{n=1}^{K} j_n\nu_n \gg \frac{\omega_0}{\min(\mathcal{I}(\nu_k), \mathcal{R}(\nu_n))}, \quad \Longrightarrow \quad \Gamma_{\max} = 10\max\Big(\mathcal{I}(\gamma_k)\Big). \tag{D.1.368}$$

This criterion terminates the over and undamped axes through one condition, leading to self-similar hierarchy volumes, where the overdamped termination is considerably more stringent than necessary. A two step termination process could be introduced as future work which terminates these axes separately.

Subsequently, the infinite hierarchy can be truncated by the terminator:

$$\frac{\partial}{\partial t}\rho^{(m,l_k)}_{j_1\ldots j_K} \approx \left(-\frac{i}{\hbar}\mathrm{H}^{\times}_{\mathrm{S}} - \sum_k l_k\gamma_k + \sum_{n=K+1}^{\infty} \mathrm{B}^{\times}\Psi_n \right)\rho^{(m,l_k)}_{j_1\ldots j_K}. \tag{D.1.369}$$

Here, the phonon contributions from the system characteristic damping rate vanish as they are a purely real decay, whereas the purely imaginary oscillating components persist. This can be rationalised through the limit of infinite time, all contributions with an associated damping will vanish leaving only oscillatory components after the application of the Markovian criterion. This can be rewritten as[164]

$$\frac{\partial}{\partial t}\rho^{(m,l_k)}_{j_1\ldots j_K} \approx \left(-\frac{i}{\hbar}\mathrm{H}^{\times}_{\mathrm{S}} - i(l_0 - l_1)\omega_{\mathrm{UO}} + \sum_{n=K+1}^{\infty} \mathrm{B}^{\times}\Psi_n \right)\rho^{(m,l_k)}_{j_1\ldots j_K}. \tag{D.1.370}$$

Since the undamped oscillator component contributes a pair of Matsubara decomposition frequencies and coefficients, we expect the number of hierarchy elements to be only slightly greater than that of an overdamped EOM.

E Imaginary Time and Resultant Frequencies

E.1 Imaginary Time

The density matrix permits calculation of all static and dynamic properties of an OQS at thermal equilibrium[360,361]. From this statistical description expectation values can be constructed which generate equilibrium values, associated with the density matrix, for any given operator. Therefore, the expectation of an operator $\mathfrak{N}$ within a thermal ensemble of harmonic oscillators at temperature T can be written as

$$\langle \mathfrak{N} \rangle = \sum_j \mathfrak{N}_j \exp(-\beta E_j), \tag{E.1.1}$$

where E_j is the energy of the jth state. This description involves the inverse temperature β and the associated energy of the states. This can be related to the evolution of a superposition of basis states through time, t, via the familiar unitary evolution operation discussed in section 2.1, equation (2.2.25). This results in

$$\left\langle \mathfrak{N} \middle| \exp\Big(-\frac{i\mathrm{H}t}{\hbar}\Big) \middle| \psi \right\rangle = \sum_j \mathfrak{N}_j \exp\Big(-\frac{itE_j}{\hbar}\Big). \tag{E.1.2}$$

It is clear from these two forms that moving from statistical mechanics and the description of the partition function, to a quantum field theoretic approach results in $\beta = \frac{1}{k_{\mathrm{B}}T} = \frac{it}{\hbar}$. This corresponds to a Wick rotation of the temperature dependent terms onto the imaginary axis in the complex plane, and is used as a means of solving mathematical problems through movement from Lorentzian (Minkowski) to Euclidean space.

This concept seamlessly links to the concept of discretised Euclidean path integrals, which are a simplification of full path integrals which are discussed in appendix C. An evolution between a state Q'_t and Q_t can be expressed in terms of a discretised partition function,

$$\left\langle \mathrm{Q}_t \middle| \exp\Big(-\frac{i\mathrm{H}t}{\hbar}\Big) \middle| \mathrm{Q}'_t \right\rangle = \int_{\omega_{\mathrm{FV}}(0)=\mathrm{Q}'_t}^{\omega_{\mathrm{FV}}(t)=\mathrm{Q}_t} \exp\Big(-\frac{S_{\mathrm{Euc}}[\omega_{\mathrm{FV}}]}{\hbar}\Big)\, \mathcal{D}[\omega_{\mathrm{FV}}], \tag{E.1.3}$$

where ω_{FV} is a molecular coordinate variable (similar to X and Q in chapter 1) and FV denotes Feynman-Vernon. In this description an integral is performed

over all trajectories which start at Q'_t and end at Q_t, and therefore is a superposition of Euclidean action[362].

E.2 Frequencies Arising from Imaginary Time

Solutions of EOMs in systems with many degrees of freedom can be achieved through a Matsubara Green's function, which is named for its similarity to standard Green's functions which solve ordinary differential equations. The evolution of an arbitrary wavefunction can be expressed in terms of a Green's function[362,363], which is the propagator of the associated dynamics, as

$$\mathrm{V}(jt, j't') = -i\theta_{\mathrm{G}}(t-t')\left\langle \psi_j \middle| \exp\Big(-\frac{i\mathrm{H}t}{\hbar}\Big) \middle| \psi'_j \right\rangle. \tag{E.2.1}$$

The propagator depends on imaginary time, or Wick transformed temperature, and contains system states $|\psi'_j\rangle$ and $\langle\psi_j|$ corresponding to initial and final conditions of the evolution. In this form θ_{G}, denoted G for Green's function, is the step function. When the imaginary time is restricted so that it is greater than zero but less than the inverse temperature[364] this can be Fourier transformed resulting in

$$\tilde{\mathrm{V}}(\mathbf{k}, \nu_n) = \frac{1}{\zeta_k - i\nu_n}, \tag{E.2.2}$$

where ν_n is defined as the Matsubara frequency,

$$\nu_n = \frac{2\pi n}{\beta\hbar}. \tag{E.2.3}$$

These frequencies emerge as a consequence of integration of periodic signals in imaginary time, with period $\hbar\beta$, which result in singularities in Fourier space. This form of frequency arises in the context of correlation functions and canonical partition functions as poles of the distribution function. Examples of such distribution functions include the Bose-Einstein distribution $n_{\mathrm{B}} = (\exp(\beta\hbar) - 1)^{-1}$ and spectral densities, such as those considered in section 2.2.2.2. The spectral density is expanded in a series of these fundamental frequencies, generated from a contour integral which is discussed in appendix D, during generation of a HEOM. Subsequently, these frequencies are used to generate a set of dimensions which house the auxiliary density operators of the HEOM.

F Application of Highly Structured Spectral Densities

F.1 Intermediate Homogeneities as a Voigt Profile

As discussed in the previous studies, the 2DES lineshape can range from an elliptical peak, due to inhomogeneous broadening, to rounded and symmetrical when homogeneous components dominate the spectrum. If the 2D peaks are projected onto anti-diagonal and diagonal axes, similar to a 1D linear spectrum, then it is clear that this structure arises from the limits of Gaussian and Lorentzian 1D lineshape. As discussed in section 2.4.3.2, spectral lineshape is a manifestation of the system-bath interaction where homogenenous broadening is a result of uncertainty regarding the transition frequency during stochastic perturbation and subsequently is proportional to T_2^* pure dephasing[110,242]. In contrast, the inhomogenenous broadening is directly impacted by the homogeneity of the environment ensemble, where diagonal peak elongation can result from a Gaussian distribution of ensemble transition frequencies in the static limit[138,268]. This is depicted in figure 2.2.11. These features lead the 1D spectrum of the diagonal and anti-diagonal to range from a Lorentzian, such as in the thermally averaged limit of an overdamped spectral density, to a Gaussian, such as in the static limit of an inhomogenenous overdamped environment[365]. Intermediate character which is neither a perfect Guassian or Lorentzian exists between the limiting cases resulting in 2DES peaks which are neither circular or elliptical, depicted in figure F.1.1.

This intermediate character can be described by a Voigt profile, which is a convolution of a Gaussian and a Lorentzian,

$$J_{\mathrm{Voigt}}(\omega;\Delta_{\mathrm{G}},\Gamma_{\mathrm{L}}) = \int_{-\infty}^{\infty} G(\omega';\Delta_{\mathrm{G}})L(\omega-\omega';\Gamma_{\mathrm{L}})\,\mathrm{d}\omega', \tag{F.1.1}$$

where[37]

$$G(\omega;\sigma_{\mathrm{g}}) = \frac{1}{\sigma_{\mathrm{g}}\sqrt{2\pi}}\exp\left(-\frac{(\omega-\omega_{eg})^2}{2\sigma_{\mathrm{g}}^2}\right), \tag{F.1.2}$$

and

$$L(\omega;\Gamma_{\mathrm{L}}) = \frac{1}{\pi}\frac{\Gamma_{\mathrm{L}}}{(\omega-\omega_{eg})^2+\Gamma_{\mathrm{L}}^2}, \tag{F.1.3}$$

Where G and L are Guassian and Lorentzian functions, respectively. This

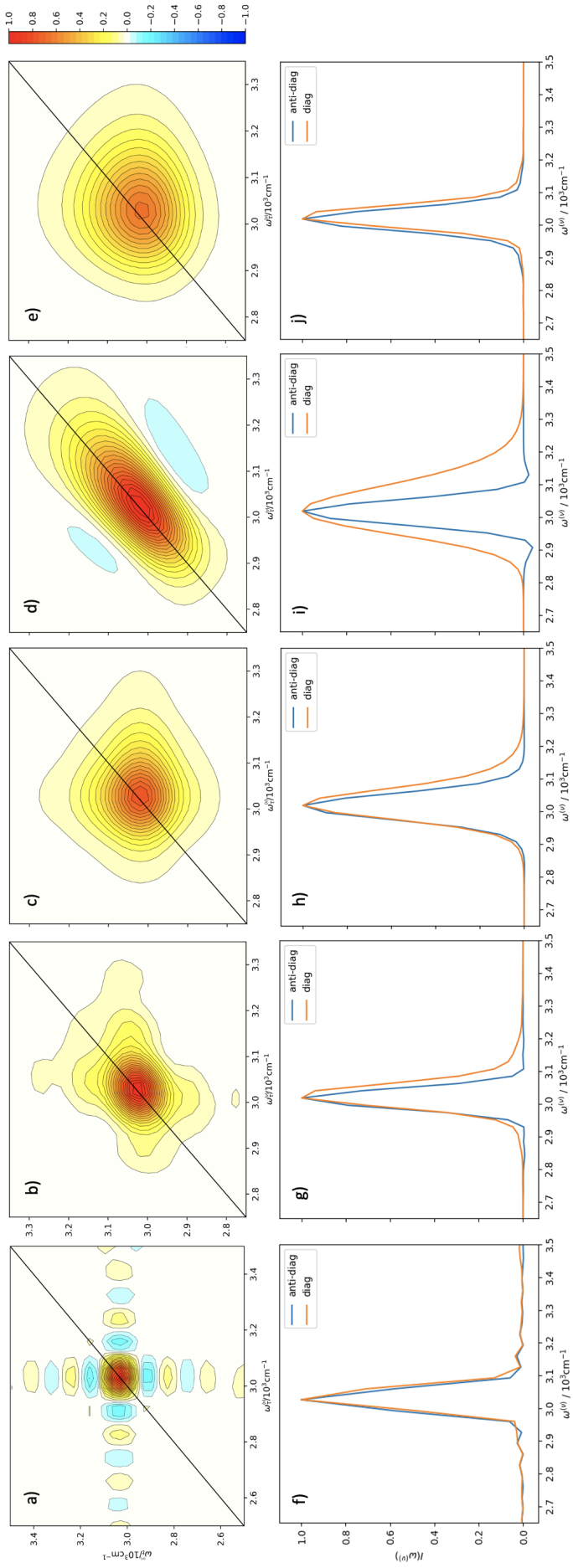

Figure F.1.1: A schematic of 2DES for a range of homogeneous and inhomogeneous broadenings resulting in peaks which are Lorentzian in both axes, and star shaped, through to Gaussian in both axes, and rounded, a) – d). The corresponding 1D diagonal and anti-diagonal projections, e) – h). Parameters are for a), b), c), and d).

function, which presents a hybrid of Lorentzian and Gaussian behaviour can be used to describe intermediate 1D lineshape broadenings such as those in figure F.1.1 f).

Similarly, underdamped modes are described with a Lorentzian spectral density, and strongly overdamped environments with red-shifted Gaussian profiles. In a multi-bath OQS, with $n > 1$, such as the model proposed by Tanimura in ref. 157 and the model in section 3.2 a combined over and underdamped spectral density could take the form of a Voigt profile. This would correspond to a single strong mode with damping from a Gaussian distribution of inhomogeneous molecules. Such an approach would be possible through application of the ASD-HEOM, (2.5.4.3) derived in D.1.10.3, allowing for a range of homogeneities contained within a single spectral density.

However, this approach still suffers from a number of the drawbacks associated with other HEOMs. As this requires the ASD-HEOM for evolution of the density matrix, it will still suffer from basis failure at critical values of damping discussed in section D.1.10, and demonstrated in the results of section 3.1 in the data where the damping strength and subsumed vibrational mode are approximately equivalent in size. Additionally, while this offers options for additional combinations of homogeneity in the environment, it does not address the source of intrinsic canonical damping as a consequence of canonically subsuming a vibrational mode, and therefore will suffer the same broadening problems as the results in section 3.2.

F.2 Delta Function Spectral Densities

In contrast, application of the ASD-HEOM with a delta function spectral density will entirely remove the canonical damping due to the broadening of the peak, due to its infinitesimal width. This is equivalent to taking the limit of vanishing width of a Lorentzian spectral density, but by-passes the associated failure of the truncation criterion as a consequence of the more complex dynamics associated with solving an integro-differential equation. The following spectral density,

$$J_{\mathrm{del}}(\omega) = \delta(\omega - \omega_0), \tag{F.2.1}$$

results in an undamped hierarchy, when applied to equation (2.5.4.3), with a continually oscillating correlation function associated with an entirely static environment in which each ensemble mode interacts with the system uniquely. The spectral density is centred at the vibrational mode frequency of the system of interest, ω_0, so that this construction is equivalent to the canonical transformation of an intramolecular vibration when there is zero added

damping. Based on the construction of the ASD-HEOM, discussed in appendix D, this EOM is equivalent to undamped hierarchies discussed by Tanimura et. al.[118,149].

A model vibronic monomer is generated with a fundamental transition frequency, $\omega_{eg}^{(\nu)} = 10\,000$ cm^{-1}, a dimensionless excited state displacement factor, $\tilde{d} = 1.09$ resulting in a system reorganisation energy of $\lambda^{(\nu)} = 300$ cm^{-1}, and a vibrational mode frequency of $\omega_0^{(\nu)} = 500$ cm^{-1}. This system is coupled to a delta function spectral density with a bath reorganisation energy of $\eta^{(\nu)} = 20$ cm^{-1} through a purely dephasing operator, as applied in section 3.2, $\mathrm{B} = \sigma_z$. As expected of an infinitesimally thin spectral density, system-bath interaction occurs through the filtering property of the delta function, and correlation will persist indefinitely within the system resulting in a continuous polarisation. In order to generate a 2D spectrum, and linear spectrum with readable peaks it is necessary to force the polarisation to partially decay during calculation. This is achieved by implementation of a Hamming function to force decay, discussed in detail in section 2.5.6.2. The Hamming apodisation function,

$$w_{\mathrm{Ham}}(n) = a_0\left(1 - \cos\left(\frac{2\pi n}{N}\right)\right), \tag{F.2.2}$$

for a domain $[0, N]$ and where $a_0 = 0.54$, limits the oscillating component in a fashion equivalent to the process of noise elimination applied in experimental set-ups, discussed in section 2.5.6.2, so that a 2D spectrum can be generated. Figure F.2.1 shows the resultant 2DES and BLP measure associated with the delta function spectral density for a vibronic monomer.

Due to computational restraints the 2DES spectra must be calculated for a similar strongly undamped mode, rather than pure undamped mode, using the uHEOM, but the BLP metric is found from the ASD-HEOM. This is because of the increased computational demand for arbitrary spectral densities, coupled to the increased computational demand for pure vibrational modes. The resultant 2D spectrum contains a sharp Lorentzian peak at the fundamental transition and is surrounded by many equally broad peaks as a consequence of the static environment. These are found at integer multiples of the vibrational mode frequency away from the fundamental in all directions and are especially present in the spectrum as a result of the non-decaying correlation which is expected for an unerdamped mode. Each of these peaks is sharp and Lorentzian, with the only broadening introduced via the sharp Lorentzian spectral density function, which leads to minimal (but non-zero) canonical damping and range of system-environment interactions at every different frequency within the ensemble.

In addition, the BLP metric is shown for the comparable ASD-HEOM model of

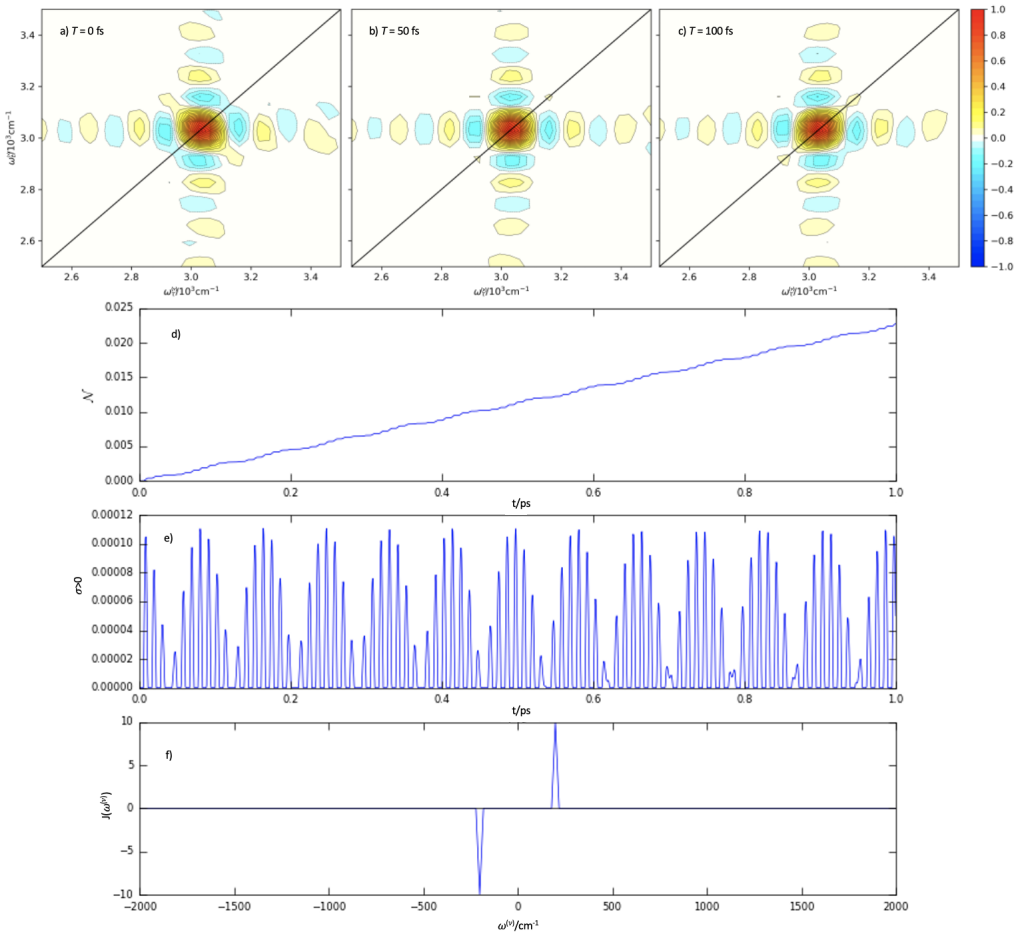

Figure F.2.1: a) – c) 2DES for a vibronic monomer at $T = 0$, 50, and 100 fs generated from a strongly undamped uHEOM (with similar computational limits as the ASD-HEOM). Spectra shown do not include application of the Hamming window to demonstrate the difficulty of calculation with pure undamped/underdamped modes. d) – f) the associated cumulative non-Markovianity, the positive flux, and the form of the spectral density, calculated from the ASD-HEOM.

an undamped mode. There are clear parallels with the results from section 3.1, with a consistent feedback of information as a result of non-Markovian feedback from the environment. Since this mode is entirely undamped, this is the purest form of non-Markovian feedback corresponding to the impact of a single mode in isolation. There is a continuous, regular, sinusoidal feedback of information from the bath to the system of interest. Building up an ensemble of modes, as is performed when generating a spectral density from delta functions, creates a superposition of oscillating recurrence signatures which focus the information flux into a more structured profile. When the global system behaviour is Markovian, such as for a vibronic monomer which is discussed in section 4.1, this leads to a red-shifted Guassian profile corresponding to an instantaneous reaction to the environment at $t = 0$ reflecting, for example, a rapid reorganisation of solvent molecules upon excitation of the solute. Similarly if

this collection of delta functions leads to an underdamped distribution then a sharp Lorentzian peak, mimicking a delta function but with associated breadth, is generated. This generates a continual non-Markovian feedback, as shown in figure 3.1.6, much like the delta function mode, but with an additional instantaneous solvent reorganisation contribution. Summation of contributions at specific transition frequencies, equivalent to the delta function result in figure F.2.1, is capable of generating a full spectrum of behaviour. One such spectral density is shown in appendix F.

However, while the ASD-HEOM has been able to generate undamped hierarchies equivalent to those in work by Tanimura et. al.[149,157,164], it too suffers from problems which relate to its construction. Equivalent to all other HEOM methods, excluding the gHEOM, this method is constructed with an expansion of Matsubara frequencies as an exponential basis. This formulation, while effective for certain spectral densities, fails in the critical damping limit when $\gamma_{\{\cdot\}} \approx \omega_0$. This is due to a singularity in the necessary expansion when at the critical damping value. Despite its breadth of acceptable homogeneities and environments, due to accepting highly structured spectral densities, it is still fundamentally restricted by the basis and its constituent expansion. The additional structured spectral densities are extremes of the current range of damping. Methods which expand this through an arbitrary choice of basis, such as the gHEOM, represent a much broader range of accessible environments, including critical damping.

As a consequence of the arbitrary spectral density, the ASD-HEOM dynamics are more complex than for other simpler HEOMs for specific spectral densities. The EOM is split into specific layers corresponding to the interaction with integer multiples of phonons within the system, analogous to the structure of Matsubara dimensions discussed in section 2.5.5. Subsequently, each additional layer constitutes a significant increase in computational complexity as many additional multiples of phonons, dependent on the system, must be considered. This scales exponentially, based on the order n exponent of the auxiliary density matrix element. Therefore, generation of fully accurate spectra will require a sufficiently large number of layers to incorporate all necessary phonon interactions. As a consequence of the increased size of Matsubara dimenion vectors, corresponding to ADO number, extending beyond the second layer of the ASD-HEOM is infeasible as discussed in sections 2.5.5 and 2.5.4. With appropriate scaling, and sufficiently more computational power, the ASD-HEOM could be a very powerful tool for probing the system-bath boundary as it is tractable in the limit of vanishing canonical damping. However, in this thesis, a less computationally expensive alternative is proposed in section 5.

G Supplement to Quantum Information

G.1 Analysis of Virtual Information Flux

As a supplement to the analysis in section 3.3, an analysis of the virtual information movement within ADOs is considered for a two-level-system, analogous to the model in section 3.1, which corresponds to the HVM, and an in depth analysis of phonon contributions to the hierarchy.

G.1.1 HVM Vibronic Monomers

Figure G.1.1 shows the normalised trace distance, flux, positive flux, and BLP for a TLS subject to three differing Markovianity constraints. The cutoff is set to an incredibly low value, corresponding to a very restrictive Markovian regime, in order to isolate a minimum of ADOs. This constraint is then increased in increments of 50 cm^{-1} so that the number of auxiliaries increases by one with each increment. In this way, the impact of successively adding a single ADO can be examined, and the virtual information that an ADO contains can be analysed. Figure G.1.1 shows the BLP with three of the Markovianity constraints:

$$\begin{aligned}
\text{gammamax} = 1 &\implies \Gamma^{(\nu)}_{\max} = 50 \text{ cm}^{-1}, \\
\text{gammamax} = 2 &\implies \Gamma^{(\nu)}_{\max} = 100 \text{ cm}^{-1}, \text{ and} \\
\text{gammamax} = 3 &\implies \Gamma^{(\nu)}_{\max} = 150 \text{ cm}^{-1}.
\end{aligned}$$

Column a) contains the results when only the density matrix evolution is within the hierarchy. Column b) introduces a single ADO leading to an immediate increase in the total BLP as a consequence of phonons and virtual information being free to recur from the environment. The addition of a single ADO does not just impact the hierarchy locally, but globally, as is demonstrated by the fact the flux of the density matrix is altered by interactions with an additional auxiliary, leading to a non-Markovian feedback which is not present when $\Gamma^{(\nu)}_{\max} = 50$ cm^{-1}. Column c) introduces another single ADO to the total hierarchy. These results show that each successive ADO has a more rapidly decaying trace distance, and a sharper initial peak of non-Markovianity. This is in agreement with the results from section 3.1 and is due to instantaneous

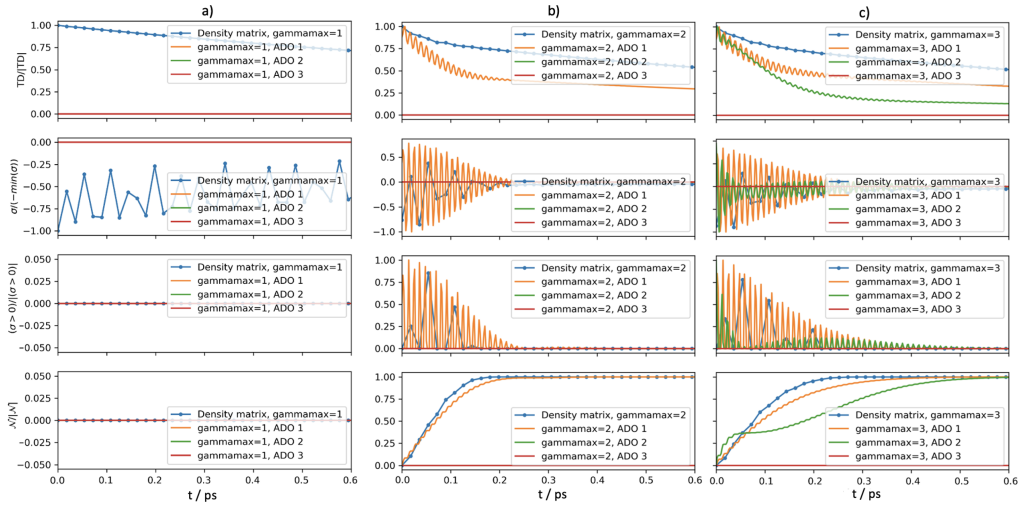

Figure G.1.1: TLS model system showing an ADO by ADO increase along the first Matsubara axis. Normalised, flux, and BLP against time in ps. Column a): $\Gamma^{(\nu)}_{\text{max}} = 50$ cm^{-1}, column b): $\Gamma^{(\nu)}_{\text{max}} = 100$ cm^{-1}, column c): $\Gamma^{(\nu)}_{\text{max}} = 150$ cm^{-1}.

solvent reorganisation. As the tier increases the contributions are due to larger multiples of phonons, reducing the interaction timescale, and shifting closer to the Markovian limit.

G.1.2 Multiple Phonon Contributions to the Hierarchy

In addition to the analysis of the primary Matsubara axes and one phonon contributions to the hierarchy in section 3.3.2, this appendix systematically considers multiple phonon contributions, which have tier greater than 0 in a number of axes, and a consideration about whether contributions from each Matsubara dimension are independent.

Figures G.1.2, and G.1.3 present the contributions from single phonons within the fast dissipation rate BVM model. These are in agreement with the underdamped equivalents in 3.3.2 but with a significantly smaller hierarchy size. This leads to multiple phonon contributions being minimal. This is as a consequence of non-Markovian behaviour arising from structured spectral densities, which induce virtual information recurrence in a large number of ADOs at high tiers. Consequently, the fast dissipation rate BVM model has a small number of multiple phonon contributions, as shown by $n = \{1, 2\}$ for n_1 in figure G.1.3. Therefore, conclusions are drawn from the slow dissipation rate BVM model parameters, due to the increased hierarchy size, but these findings extend naturally to all forms of the BVM.

Figures G.1.4 and G.1.5 present fluxes and BLP for the first and second Matsubara axes, $M1$ and $M2$ of the slow dissipation rate BVM model. The comparison of these two figures are in subtle contrast to the results presented in

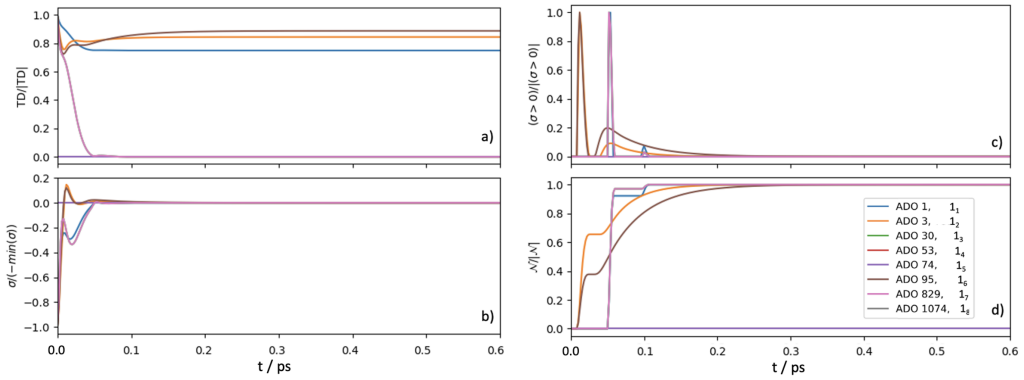

Figure G.1.2: Fast dissipation rate BVM model with $\gamma_2^{(\nu)} = 1\,750$ cm^{-1}, and $\gamma_1^{(\nu)} = 2\,500$ cm^{-1} showing normalised trace distance, flux, positive flux, and BLP measure for 1_n, $n = \{1, 2, 3, 4, 5, 6, 7, 8\}$.

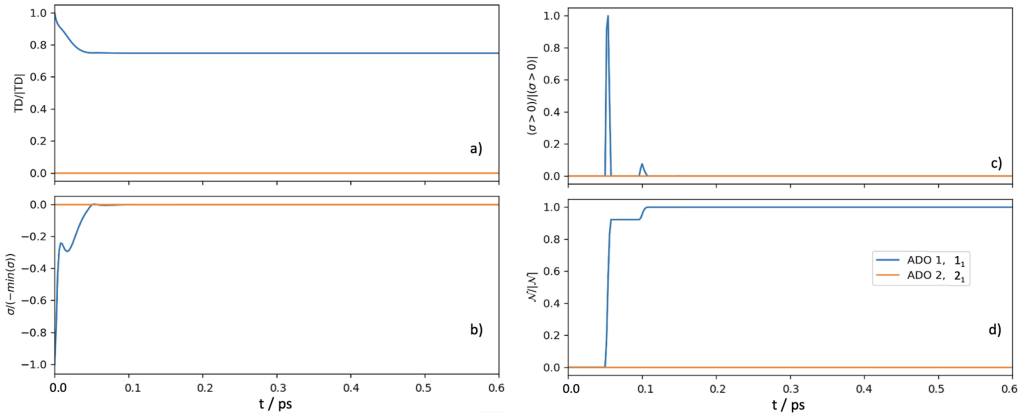

Figure G.1.3: Fast dissipation rate BVM model with $\gamma_2^{(\nu)} = 1\,750$ cm^{-1}, and $\gamma_1^{(\nu)} = 2\,500$ cm^{-1} showing normalised trace distance, flux, positive flux, and BLP measure for n_1, $n = \{1, 2\}$.

section 3.3.2, where it was concluded that (in general) phonons from each Matsubara axis are more similar to those from the same axis than others. However, in contrast to this, in these figures the oscillations of virtual information are regular and similar with a non-Markovian feedback of $\sim 50\%$ of the magnitude of Markovian feedback. This is as a consequence of the structure of the underdamped HEOM, which contains a pair of temperature independent Matsubara frequencies with differing signs of ζ_n. These results demonstrate that, unlike all other temperature dependent axes, the temperature independent axes are similar and have a qualitatively similar movement of virtual information. Temperature dependent effects, which control the level of thermal narrowing in 2DES, are strongly independent based on their differing timescales unlike these poles. This effect is EOM specific, and will change dependent on the construction and damping of the HEOM, being absent in regimes with a faster dissipation rate.

The next consideration is of a combination of two Matsubara axes in order to

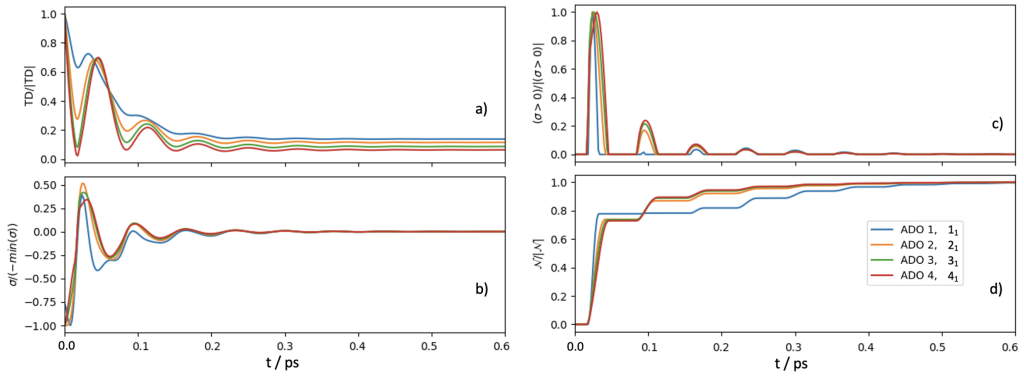

Figure G.1.4: Slow dissipation rate BVM model with $\gamma_2^{(\nu)} = 100$ cm^{-1}, and $\gamma_1^{(\nu)} = 300$ cm^{-1} showing normalised trace distance, flux, positive flux, and BLP measure for n_1, $n = \{1, 2, 3, 4\}$.

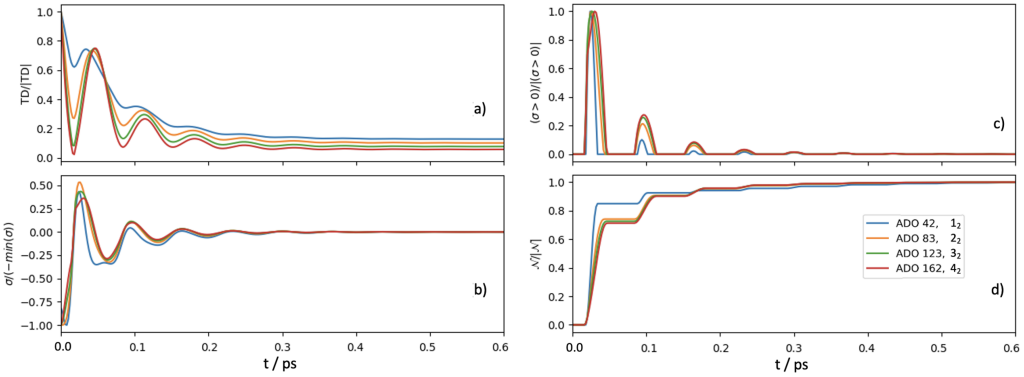

Figure G.1.5: Slow dissipation rate BVM model with $\gamma_2^{(\nu)} = 100$ cm^{-1}, and $\gamma_1^{(\nu)} = 300$ cm^{-1} showing normalised trace distance, flux, positive flux, and BLP measure for n_2, $n = \{1, 2, 3, 4\}$.

generate an ADO which has equal integer multiples of phonons in two dimensions. Based on the previous analysis which demonstrated the similarity between the temperature independent axes, but independence of thermal axes, this is considered through $n_1 n_2$, figure G.1.6, and $n_1 n_3$, figure G.1.7. Figure G.1.6 is in agreement with the findings in the previous figures: the non-thermal dimensions behave similarly. However, the fact that this is now a multi-tiered ADO has an impact on the non-Markovian flux, which manifests as a vertical translation of the trace distance with low tier auxiliaries being more indistinguishable and a larger oscillation amplitude of the positive flux. The loss of state distinguishability resulting in more significant non-Markovian feedback over a longer timescale, coupled with the fact that these multi-tier ADOs have very low auxiliary numbers of less than 200, suggests that they are significant sources of non-Markvoian dynamics for the system. Similarly, figure G.1.7 presents the two multi-tiered contributions from $n_1 n_3$. The small number of ADOs despite the low auxiliary number relative to the maximum of $\sim 90\,000$ suggests that combinations of tiers with a mixture of thermal and non-thermal frequencies are not common and that the timescale of such processes are very

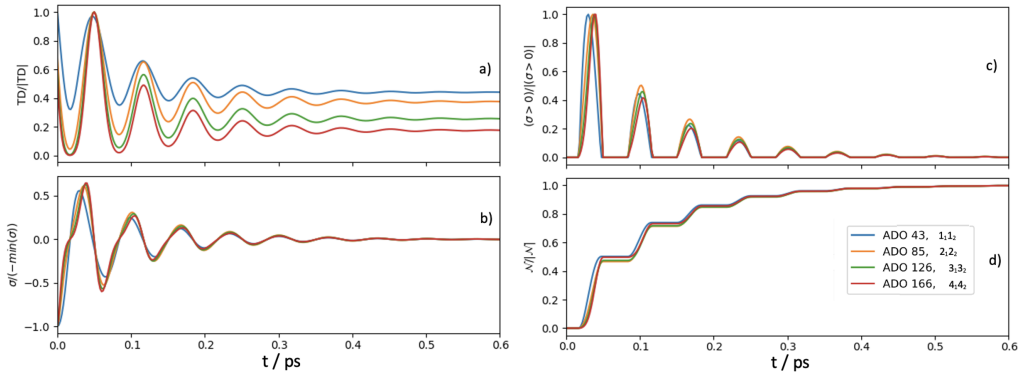

Figure G.1.6: Slow dissipation rate BVM model with $\gamma_2^{(\nu)} = 100$ cm^{-1}, and $\gamma_1^{(\nu)} = 300$ cm^{-1} showing normalised trace distance, flux, positive flux, and BLP measure for $n_1 n_2$, $n = \{1, 2, 3, 4\}$.

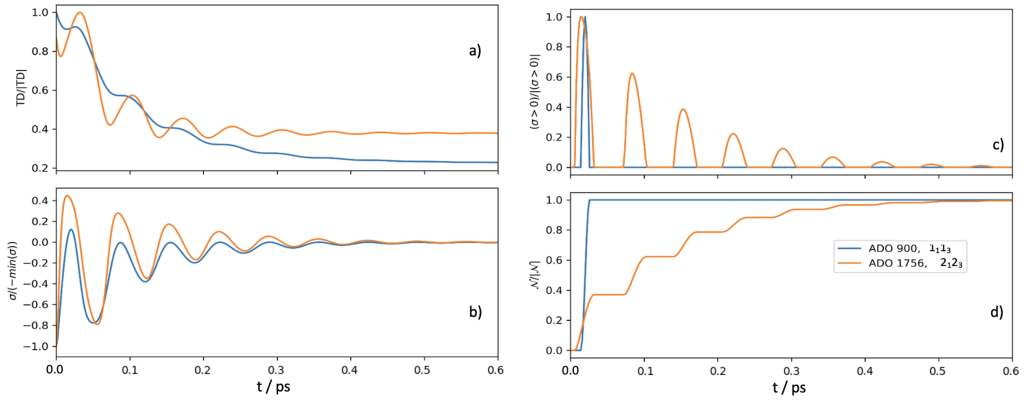

Figure G.1.7: Slow dissipation rate BVM model with $\gamma_2^{(\nu)} = 100$ cm^{-1}, and $\gamma_1^{(\nu)} = 300$ cm^{-1} showing normalised trace distance, flux, positive flux, and BLP measure for $n_1 n_3$, $n = \{1, 2\}$.

fast. Despite this, the same conclusions, as in section 3.3.2, can be drawn: multi-tier contributions seem to be most similar to their constituent axes.

The next set of results, in figures G.1.8 and G.1.9, are for ADOs which are tier-1 in a pair of different Matsubara axes ranging from 1 to 8. These considerations fix the number of phonons to one in each axis, to guarantee a relatively large timescale, and consider each possible axis. These results, in agreement with previous findings, demonstrate that multi-tiered ADOs involving two one phonon interactions from each dimension are most similar to their constituent axes, and share little behaviour with other axes. This is shown by the range of oscillatory periods, amplitudes and percentages of Markovianity presented in a) – d) of figure G.1.8. In addition to pairs of interactions in neighbouring axes, this also extends to axes which are separated as demonstrated in figure G.1.9, where the same findings are observed for $1_n 1_{(n+2)}$ as were found for $1_n 1_{(n+1)}$.

The final set of considerations is the scenario when the tier of the multi-tiered ADOs are not equal in both dimensions, signifying that a number of integer

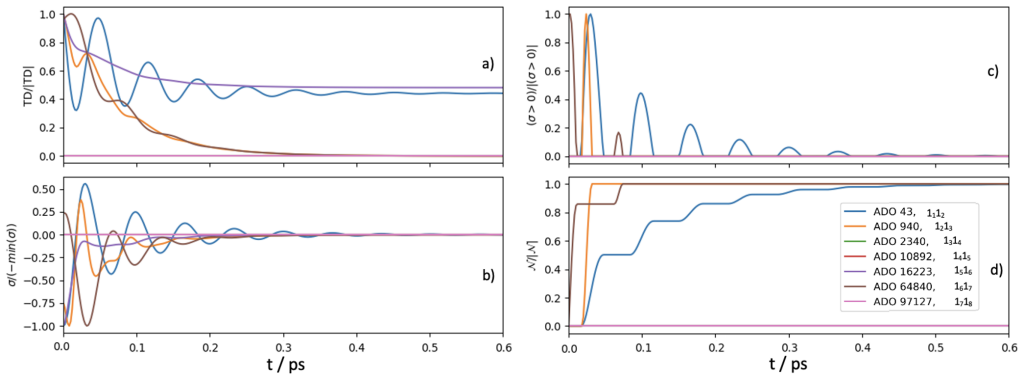

Figure G.1.8: Underdamped BVM model with $\gamma_2^{(\nu)} = 100$ cm^{-1}, and $\gamma_1^{(\nu)} = 300$ cm^{-1} showing normalised trace distance, flux, positive flux, and BLP measure for $1_n 1_{(n+1)}$, $n = \{1, 2, 3, 4, 5, 6, 7\}$.

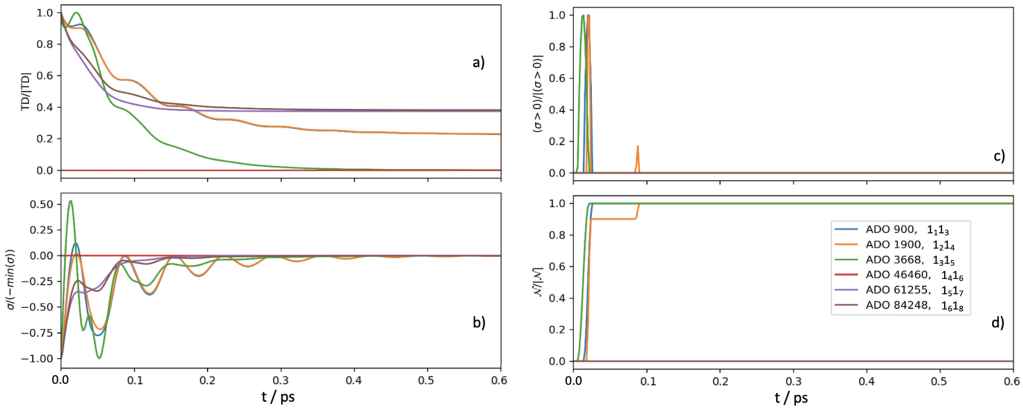

Figure G.1.9: Underdamped BVM model with $\gamma_2^{(\nu)} = 100$ cm^{-1}, and $\gamma_1^{(\nu)} = 300$ cm^{-1} showing normalised trace distance, flux, positive flux, and BLP measure for $1_n 1_{(n+2)}$, $n = \{1, 2, 3, 4, 5, 6\}$.

multiples of phonons are involved from one axis along with a different number of phonons from another axis. Figure G.1.10 is in agreement with the results from figure G.1.8 which both show the striking difference between processes on neighbouring axes. Even when the phonon contributions from the two axes are not equal, as in figure G.1.10 where there are contributions from $2_{(n+1)}$ the dissimilarity between differing axes persists. However, in contrast to figure G.1.8 the magnitude of non-Markovianity has dropped from flux that is $\sim 50\%$ of the Markovian contributions to $\sim 10\%$. This is a consequence of the shorter relative timescale due to the increased number of phonons from one of the axes which pushes these ADOs deeper into the hierarchy and closer to the Markovian cutoff. Subsequently, these ADOs are less significant to the total non-Markovianity of the full dynamics. Similarly, the results from figure G.1.11 are in agreement with those in figure G.1.5 where integer multiples of phonons from the same axis share much more character than with those from different axes. By plotting all of the $n_1 1_2$ for $n = \{2, 3, 4\}$ it is clear that there are only three multi-tier ADOs of this type. Despite the low auxiliary number, this

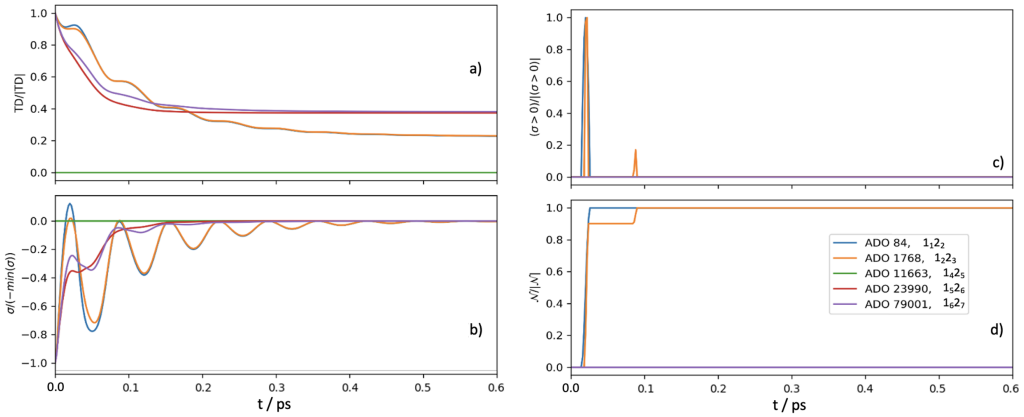

Figure G.1.10: Underdamped BVM model with $\gamma_2^{(\nu)} = 100$ cm^{-1}, and $\gamma_1^{(\nu)} = 300$ cm^{-1} showing normalised trace distance, flux, positive flux, and BLP measure for $1_n2_{(n+1)}$, $n = \{1, 2, 4, 5, 6\}$.

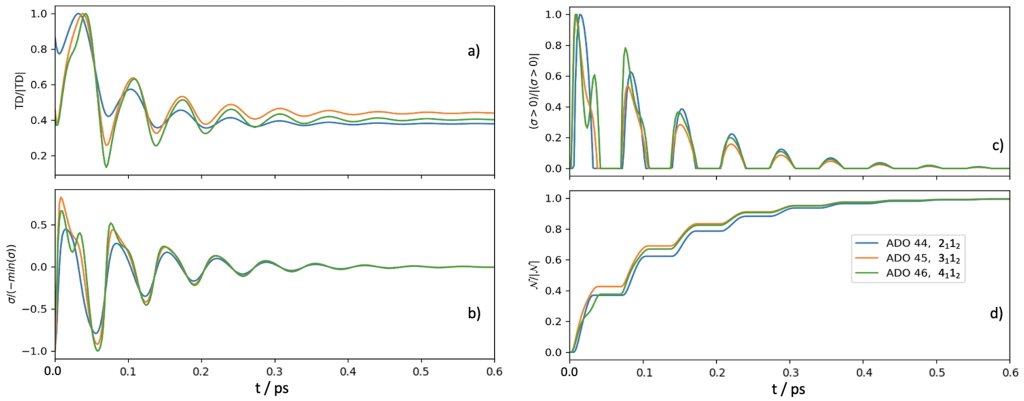

Figure G.1.11: Underdamped BVM model with $\gamma_2^{(\nu)} = 100$ cm^{-1}, and $\gamma_1^{(\nu)} = 300$ cm^{-1} showing normalised trace distance, flux, positive flux, and BLP measure for n_11_2, $n = \{2, 3, 4\}$.

suggests that temperature independent axes contribute fewer high tiered auxiliaries, in agreement with figure G.1.7.

H Supplement to Lasers with a Gaussian Width

H.1 Analysis of Pulse Widths

This appendix contains supplementary analysis from section 4.3 for spatial FWHMs of $50\ \mathrm{cm}^{-1}$ and $250\ \mathrm{cm}^{-1}$. Figures H.1.1 shows the first and second order photon correlations with a spatial FWHM of $50\ \mathrm{cm}^{-1}$. All panels and columns exhibit the same divergence in correlation as for figure 4.2.4 and the first two rows of figure 4.2.6, demonstrating that the mean photon number becomes vanishingly small faster than the variance. It is also clear that changing the magnitude of m from 41 through to 401 has minimal impact on the correlations. This is because, as depicted in c) of figure 4.2.2, changing the number of discrete frequencies when the spatial FWHM is small does not result in a pulse-like structure: the laser remains continuous. When the spatial FWHM is low, only frequencies very close to the electronic fundamental transition will have amplitudes $\sim\ 1$ resulting in a negligible phase difference between constituent waves, and therefore minimal destructive interference. Subsequently, there are no nodes within the laser field and the field intensity, $\omega_{eg}^{(\nu)} \pm 50\ \mathrm{cm}^{-1}$, result in oscillations with an evident minor oscillation for 2λ but in agreement with results for the continuous driving field.

Figure H.1.2 presents the associated first and second order phonon correlations when the spatial FWHM is set at $50\ \mathrm{cm}^{-1}$. In agreement with both the results from sections 4.3 and 4.1 there are electronic Rabi oscillations due to the varying probability of emission as a consequence of electronic excited state population and a minor phonon mode oscillation. The vibrational oscillation has a slightly larger amplitude than those in the model of driving by a continuous wave as a direct result of the FWHM of $50\ \mathrm{cm}^{-1}$ including additional accessible transitions as a consequence of the broader spectrum. In agreement with figure H.1.1, increasing thee number of discrete frequencies within the superposition of waves has minimal impact on the correlation as a result of the small amplitudes imparted by the spatial breadth.

Figure H.1.3 shows the second order crossed correlations for photons and phonons when the spatial FWHM is set at $50\ \mathrm{cm}^{-1}$ and is in agreement with the analysis of the previous figures. The global trend is that in the presence of a

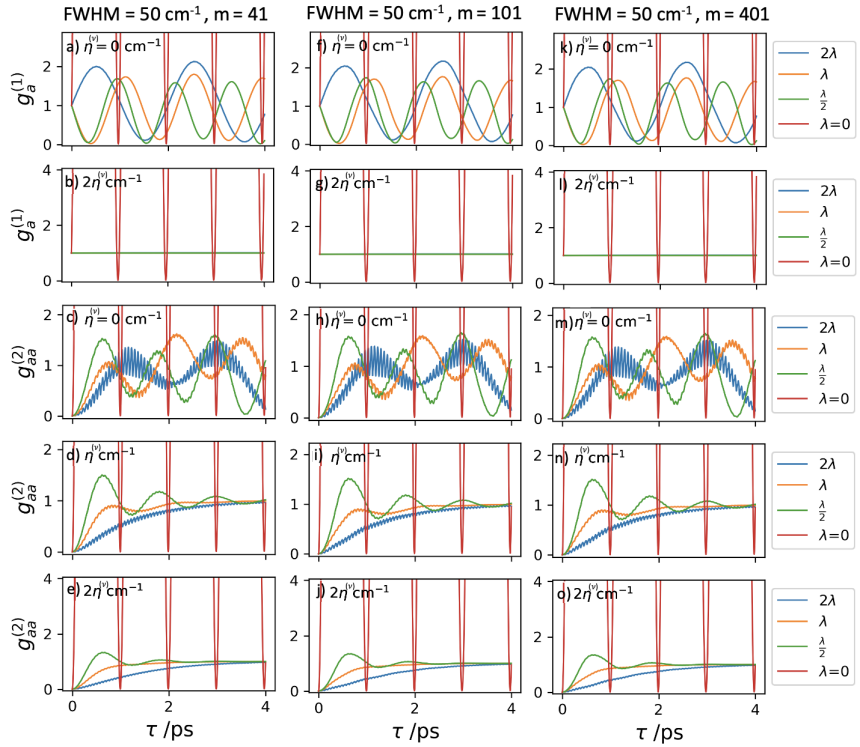

Figure H.1.1: Order one and two photon correlations with a spatial pulse width of $\mathrm{FWHM} = 50\ \mathrm{cm}^{-1}$ for a range of frequency distributions dictated by m. Column 1, a) – e), $m = 41$. Column 2, f) – j), $m = 101$. Column 3, k) – o), $m = 401$. Each results in a different temporal structure of the incident field, depicted in figure 4.2.2.

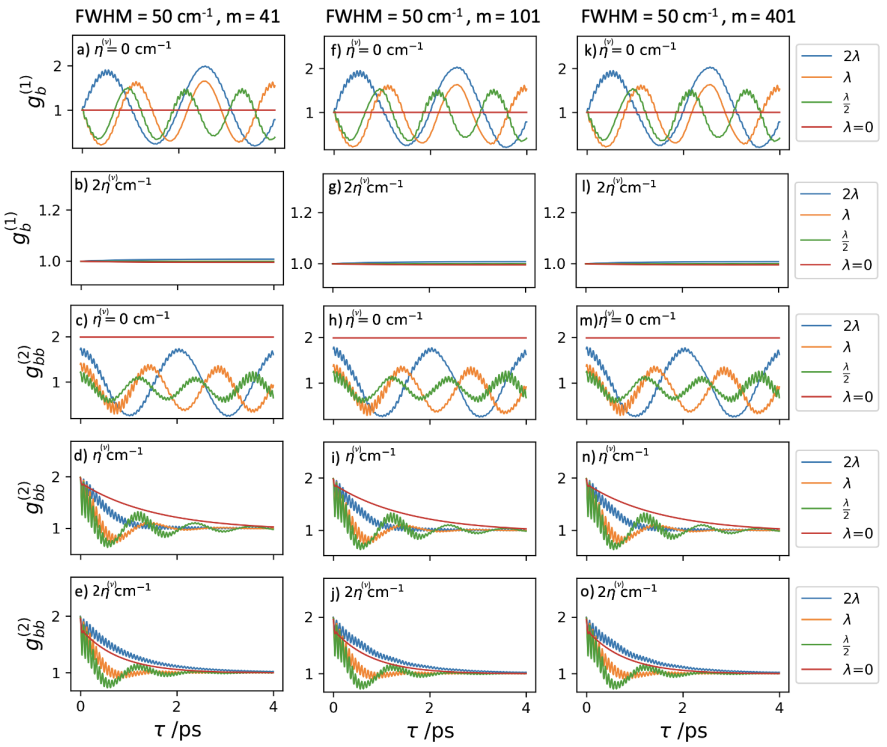

Figure H.1.2: Order one and two phonon correlations with a spatial pulse width of $\mathrm{FWHM} = 50\ \mathrm{cm}^{-1}$ for a range of frequency distributions dictated by m. Column 1, a) – e), $m = 41$. Column 2, f) – j), $m = 101$. Column 3, k) – o), $m = 401$. Each results in a different temporal structure of the incident field, depicted in figure 4.2.2.

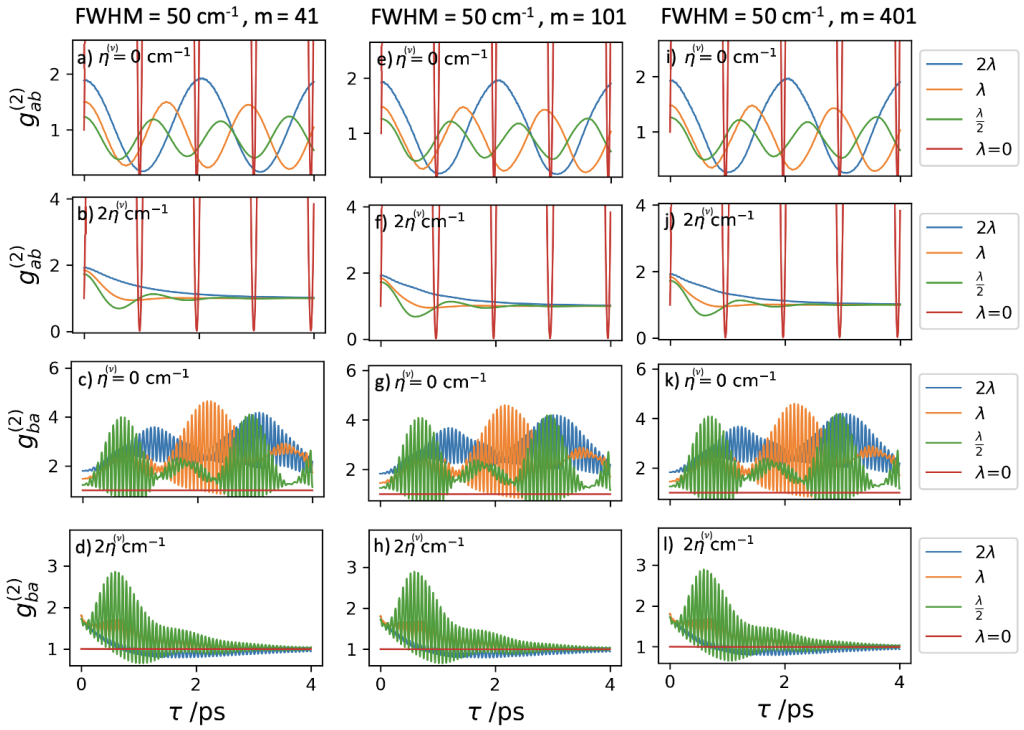

Figure H.1.3: Order two crossed photon and phonon correlations with a spatial pulse width of $\mathrm{FWHM} = 50\ \mathrm{cm}^{-1}$ for a range of frequency distributions dictated by m. Column 1, a) – e), $m = 41$. Column 2, f) – j), $m = 101$. Column 3, k) – o), $m = 401$. Each results in a different temporal structure of the incident field, depicted in figure 4.2.2.

bath the system dissipates phonons and electronic Rabi oscillations are damped. Additionally, the nature of cross correlations is to superimpose the characteristics of the former particle onto the behaviour of the latter. For the $g^{(2)}_{\mathrm{ab}}$, the instantaneous measurement of the photon number does not impart vibrational dependency and the subsequent correlation with phonons presents a limited increase in minor oscillation amplitude because of the larger number of accessible transitions. The reason for this is that the fast phonon signatures are very small with respect to the electronic contributions, hence their impact on the excited-state adiabatic population is minimal. In contrast, $g^{(2)}_{\mathrm{ba}}$ has two sources of vibrational character: vibrations intrinsic to the phonons in the first detection event, and from phonon effects during the optical cycles leading to the photon emission. Subsequently these correlations contain large minor oscillations due to phonons, but the spatial FWHM is a very minor addition to these, so noticeable differences in amplitude are minimal.

In direct contrast to this, are the results showing correlations when the spatial FWHM is increased to $250\ \mathrm{cm}^{-1}$. As depicted in figure 4.2.2 d), with an increase in the FWHM to $\frac{\omega_0^{(\nu)}}{2}$ the driving field profile changes from completely continuous, through sinusoidal envelope, to temporally separated pulses, dependent on the choice of m. This means that a full range of characteristics, from driving by a

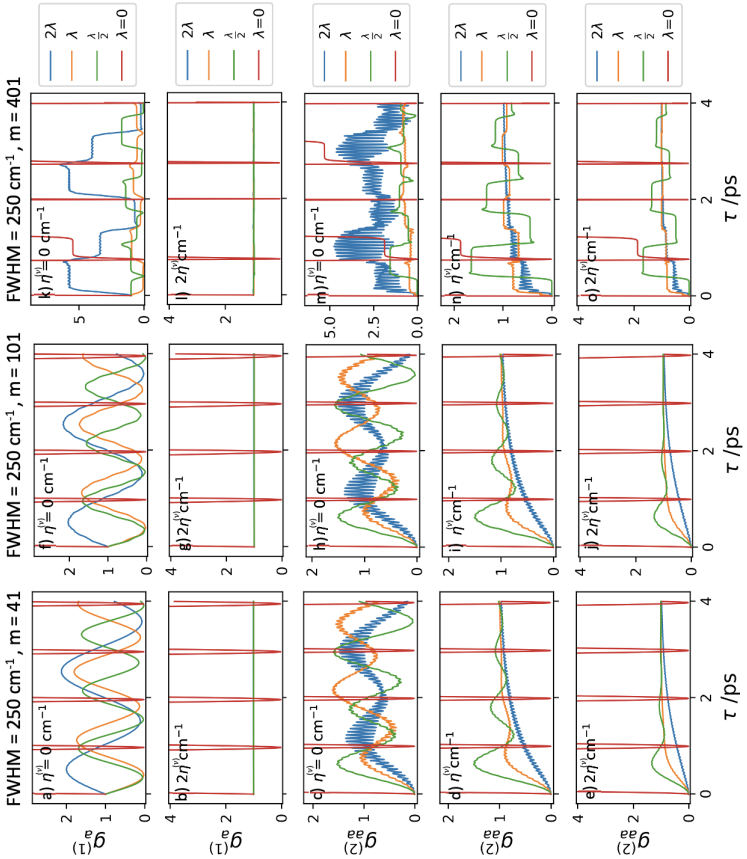

Figure H.1.4: Order one and two photon correlations with a spatial pulse width of FWHM $= 250\ \mathrm{cm}^{-1}$ for a range of frequency distributions dictated by m. Column 1, a) – e), $m = 41$. Column 2, f) – j), $m = 101$. Column 3, k) – o), $m = 401$. Each results in a different temporal structure of the incident field, depicted in figure 4.2.2.

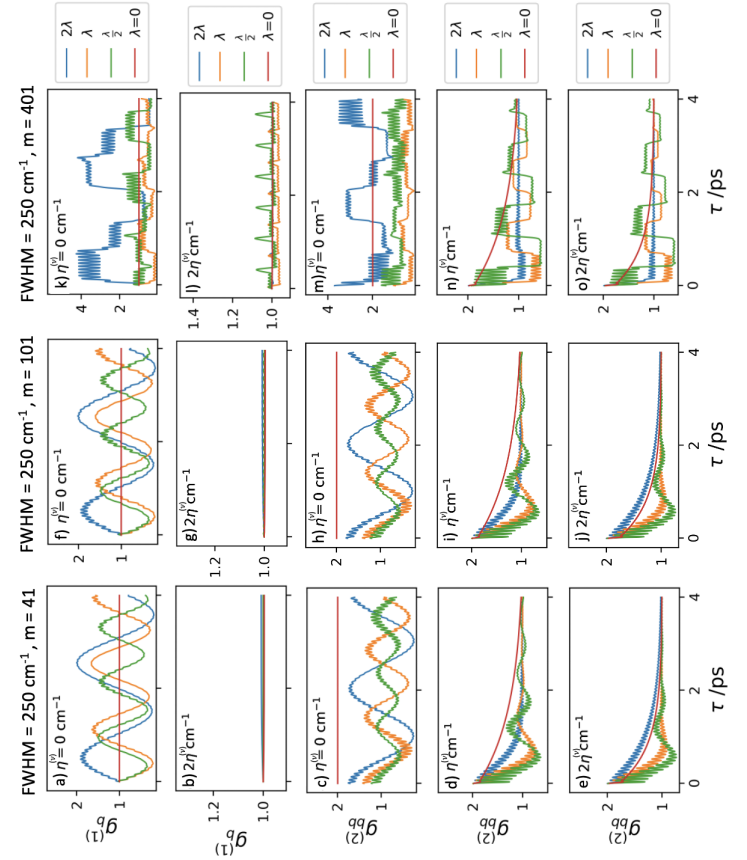

Figure H.1.5: Order one and two phonon correlations with a spatial pulse width of FWHM $= 250\ \mathrm{cm}^{-1}$ for a range of frequency distributions dictated by m. Column 1, a) – e), $m = 41$. Column 2, f) – j), $m = 101$. Column 3, k) – o), $m = 401$. Each results in a different temporal structure of the incident field, depicted in figure 4.2.2.

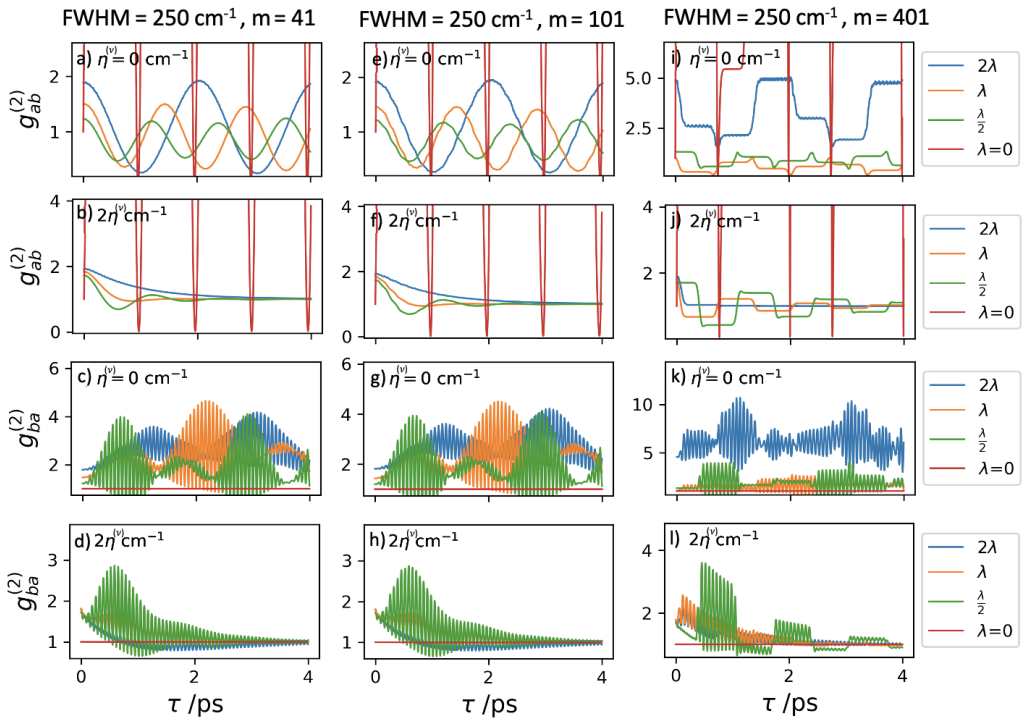

Figure H.1.6: Order two crossed photon and phonon correlations with a spatial pulse width of $\mathrm{FWHM} = 250\ \mathrm{cm}^{-1}$ for a range of frequency distributions dictated by m. Column 1, a) – e), $m = 41$. Column 2, f) – j), $m = 101$. Column 3, k) – o), $m = 401$. Each results in a different temporal structure of the incident field, depicted in figure 4.2.2.

continuous wave through to pulses, will be exhibited by these correlations.

Figure H.1.4 shows the photon correlations of both orders upon increasing the FWHM to $250\ \mathrm{cm}^{-1}$, and is in strong agreement with figure 4.2.4. Column one shows identical correlation to figure H.1.1 because 41 discrete frequencies result in a continuous laser field. In column 2 the combination of the increased spatial FWHM and 101 discrete frequencies lead to a laser envelope function which is beginning to separate into pulses. However, these pulses are not entirely temporally separated, which means that there are regions of reduced correlation, but not zero driving as in figure 4.2.4. Subsequently there is a subtle modulation of the correlations which will tend towards a step function as the driving field is pinched into distinct temporal pulses upon further increasing the FWHM or m. These steps are not more pronounced for the same reason that is discussed in section 4.3: 101 distinct frequencies, at integer multiples of $200\ \mathrm{cm}^{-1}$ ($\Delta\omega^{(\nu)}$), result in a separation which favours the electronic excited state, but only the ground and second excited vibrational states.

Figure H.1.5 presents the phonon correlations, of first and second order, for this model system. These results are in agreement with the discussion of results for figure H.1.4, but particularly nicely demonstrate the effect of the largest value of m. When there are 401 discrete frequencies within the superposition of waves

in the driving field it ceases to be a continuous field, and becomes a series of temporally separated pulses as depicted in e) of figure 4.2.2. For this number of frequencies, the spacing between each constituent increases in multiples ($\Delta\omega^{(\nu)}$) which are factors of the vibrational mode frequency, so upon interaction with the pulse a range of Stokes and anti-Stokes Raman processes will be excited alongside the fundamental electronic transition. Additionally, the separation of the pulses results in regions of zero field interaction which is reflected in the correlation function as a step function profile in agreement with the results in figure 4.2.5.

Finally, figure H.1.6 depicts the crossed correlations of photons and phonons for the intermediate value of spatial FWHM. These results are also in agreement with the previous analysis and nicely demonstrate the intermediate character of this driving field. g), when compared to c), demonstrates a subtle increase in the minor mode amplitude (most evident in the 2λ peak at $\sim$ 3 ps) as a consequence of the sinusoidal envelope function. In addition, column 3 shows the intermediate changes to the electronic beating. The period of the major oscillation is unchanged by the pulse separation but the sinusoidal curve is sharpened into a series of steps. Similarly the $g_{\mathrm{ba}}^{(2)}$ correlation with a system reorganisation of 2λ demonstrates that the correlations do not becomes entirely stepped until higher FWHMs are reached, and that many different phonon modes contribute to the excited state wavepacket.

In summary, these results show that for smaller spatial FWHMs, such as $50\ \mathrm{cm}^{-1}$, the weighting of allowed transitions is highly focused on the fundamental electronic frequency and vibrational modulation away from the results of driving by a continuous wave are largely absent. This is supported by c) of figure 4.2.2 in which the field never becomes entirely separated pulses, no matter the choice of m. Intermediate FWHMs, such as $250\ \mathrm{cm}^{-1}$, demonstrate a subtle movement from continuous to pulse-like field structure, with small modulations of the correlation arising due to temporal nodes in the laser field for only the largest number of discrete frequencies.

I Supplement to Quantum Correlations

I.1 Additional Analysis of Quantum Correlations in Electronically Coupled Molecules

This appendix serves as a supplement to the results in section 4.4 discussing the method of truncating large dimer Hamiltonians, developed as part of 'Spec Suite' by Dr Dale Green[173], and presenting a set of correlations which demonstrate the impact of such truncation.

I.1.1 Truncation of Dimer Hamiltonians

Within a vibronic monomer, as outlined in section 2.2.1.1, the tensor product of electronic and vibrational degrees of freedom is used to generate a composite Hilbert space $|\alpha, n\rangle$. Hamiltonians for such a system will contain n vibrations and α electronic states, which within the computational models and 'Spec Suite' modules corresponds to ddim vibrations and 2 electronic states for the vibronic monomer. Subsequently, the Hamiltonian has x and y dimensions of $2\mathrm{ddim}$ resulting in $(2\mathrm{ddim})^2$ Hamiltonian matrix elements.

Upon moving to the vibronic dimers, outlined in section 2.2.1.3, the tensor product of electronic and vibrational degrees of freedom is extended to $|\alpha_\mathrm{A}, n_\mathrm{A}\rangle \otimes |\alpha_\mathrm{B}, n_\mathrm{B}\rangle$. This means that the total Hamiltonian has x and y dimensions of $(2\mathrm{ddim})^2$, resulting in $(2\mathrm{ddim})^4$ Hamiltonian matrix elements. When this diabatic Hamiltonian is diagonalised into the adiabatic basis, the states of the total system are rearranged in size order such that the doubly ground, gg, single exciton manifold, eg/ge, and doubly excited, ee, states have calculable locations. This Hamiltonian structure is shown schematically in figure I.1.1. In the diabatic basis the location of individual levels and constituent monomer contributions are mixed throughout the Hamiltonian, whereas in the adiabatic basis, after diagonalisation, the location of individual contributions can usually be ascertained. This is possible because the levels lie along the diagonal and increase in energy. The doubly ground is found in the top left, doubly excited in the bottom right, and a mixture of eg and ge states are contained within the central square known as the single exciton manifold. This

Hamiltonian is then truncated, up to an integer dimension N, and a new smaller matrix is constructed from the specific system contributions which are deemed necessary. This new matrix is not renormalised and has no specific orthonormality requirement as this would result in the dynamics being altered to suit the truncated dimension. Figure I.1.1 depicts the generation of the truncated submatrix from the total Hamiltonian.

Within the total Hamiltonian, depicted in figure I.1.1, the singly coloured squares of dimension N^2 contain the levels chosen for truncation. These are the lowest energy levels from the doubly ground state (red), the lowest N^2 and second lowest N^2 energy levels associated with the ge and eg exciton states (mauve and purple), and the lowest energy levels from the doubly excited state (blue). The doubly excited and ground state levels are easily distinguishable in the adiabatic basis by their energies, whereas the single exciton manifold contains a mixture of vibrational and electronic states from the excitons and due to the degenerate nature of many of these levels, they are not necessarily distinguishable. Subsequently, an uneven number of energy levels are taken from the A and B monomers of a heterodimer due to the non-degenerate energies. The lowest energy $2\mathrm{N}^2$ are chosen from the single exciton manifold resulting in greater A contributions unless $\mathrm{ddim} = \mathrm{N}$. In such a situation there is no truncation, but propagation of a full system requires a reduction in the size of ddim. When $\mathrm{ddim} = \mathrm{N}$ the vibrational levels used for evolution, ddim, are reduced significantly allowing the full Hamiltonian to be propagated and equal numbers of A and B dependent states are chosen. The off-diagonal portions of the total Hamiltonian are truncated in an identical fashion for use in the truncated transition dipole moment operator and bath coupling operators. Off-diagonal squares of dimension N^2 have two colours, one for each of the two pure coloured states which they couple. For example, the second square in row one, which is mauve and red, couples the pure red doubly ground state levels and the lowest N^2 energy levels of the single exciton manifold in mauve. The work in this thesis typically uses $\mathrm{N} = \{1, 3, 5\}$ and $\mathrm{ddim} = \{3, 10\}$. The three N values correspond to the standard BVM and other dissipation rate BVM models, with $\mathrm{N} = \{3, 5\}$ being chosen for differing numbers of vibrational levels in the HVM. The two ddim values correspond to such HVM regimes, where the harsh and default truncation limits for the HVM models of monomer-lattices, and dimers have $\mathrm{ddim} = \mathrm{N} = 3$, and $\mathrm{ddim} = 10$, $\mathrm{N} = 3$, respectively. Larger values are possible, but would require more computational power than is currently available.

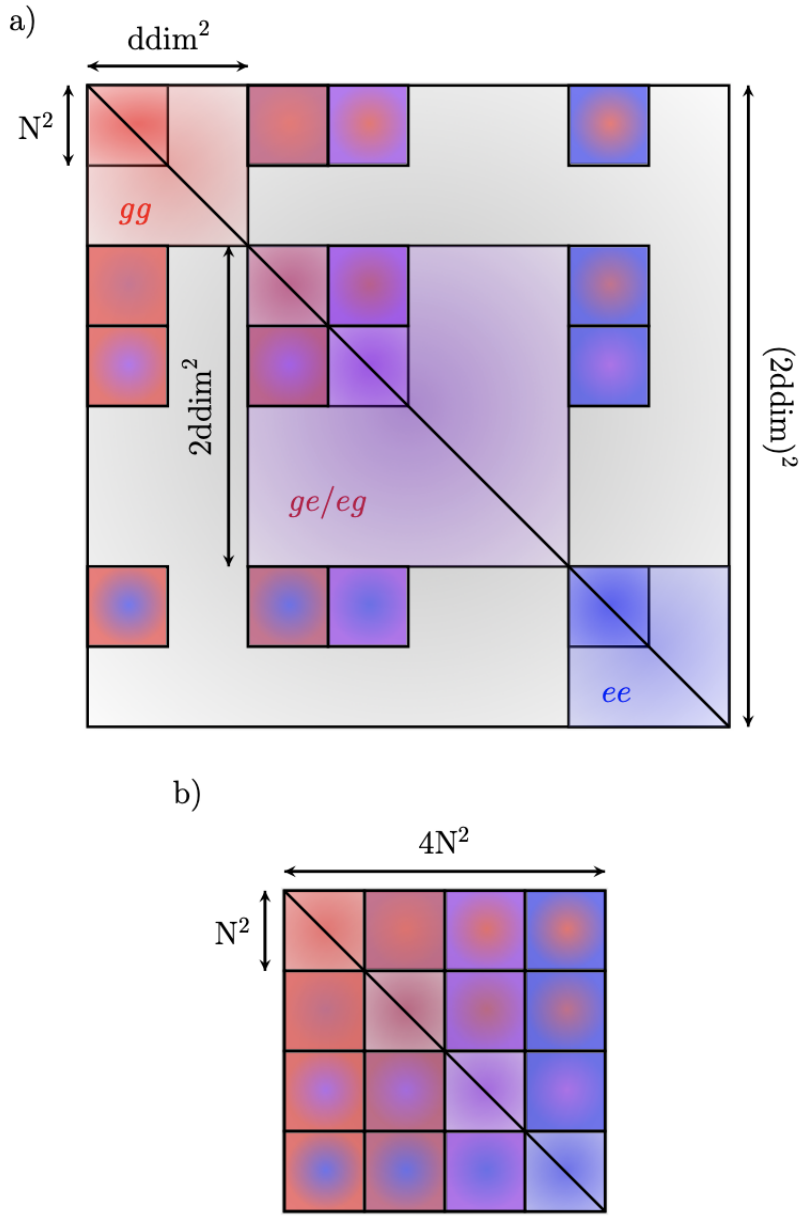

Figure I.1.1: a) The full dimer Hamiltonian, of dimensions $(2\mathrm{ddim})^2$, showing the size of each constituent part: doubly ground and excited states of dimension ddim^2, the single exciton manifold of dimension $2\mathrm{ddim}^2$ (one ddim^2 for each monomer), and N^2 truncated regions containing 'necessary' energy levels. The four singly coloured N^2 regions along the diagonal contain states of increasing energy, the other two-coloured regions denote coupling between the levels of colours which they share (e.g. the second square in row 1 is red and mauve and couples gg and the lowest N^2 levels of the single exciton manifold). b) shows the combination of all N^2 units into the truncated Hamiltonian and has dimension $4\mathrm{N}^2$.

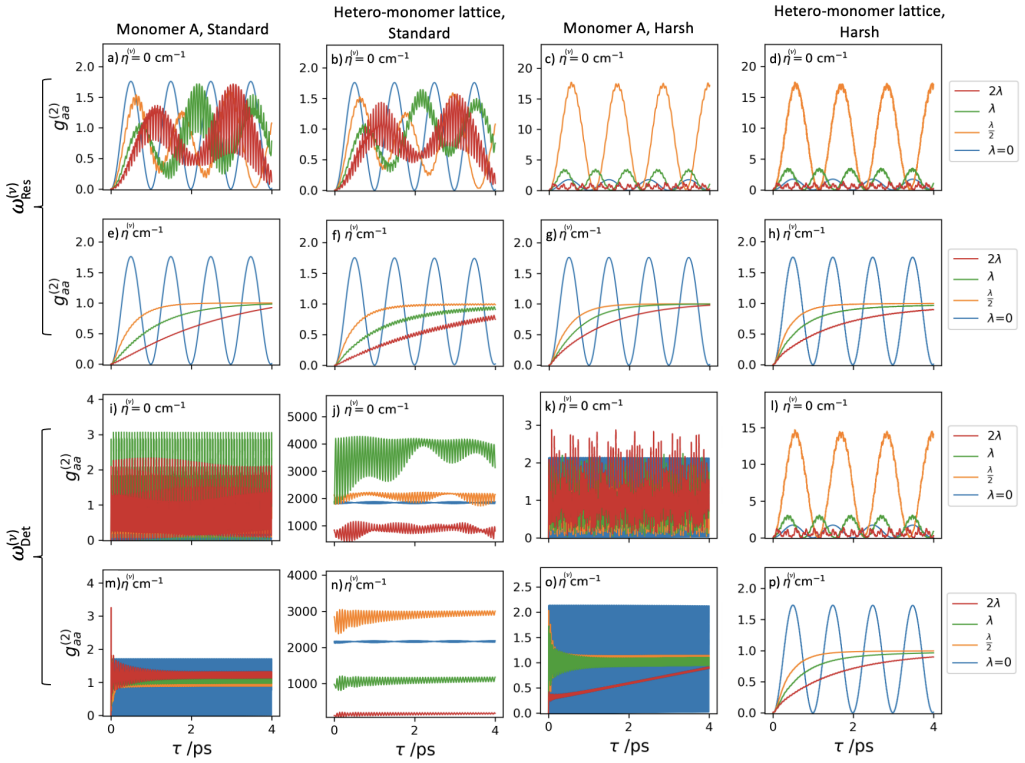

Figure I.1.2: Second order two-time photon correlations in the default and harsh truncation limits for a monomer and a hetero-monomer lattice. a), e) depict a monomer with $\mathrm{ddim} = 10$, $\mathrm{N} = 3$, with resonant field frequency $\omega^{(\nu)}_{eg\mathrm{A}}$ and i), m), have detuned frequency $\omega^{(\nu)}_{eg\mathrm{B}}$. b), f) depict the hetero-monomer lattice with $\mathrm{ddim} = 10$, $\mathrm{N} = 3$, with field frequency $\omega^{(\nu)}_{\mathrm{Res}}$ and j), n), have field frequency $\omega^{(\nu)}_{\mathrm{Det}}$. c), g) depict a monomer with $\mathrm{ddim} = \mathrm{N} = 3$, with resonant field frequency $\omega^{(\nu)}_{eg\mathrm{A}}$ and k), o), have detuned field frequency $\omega^{(\nu)}_{eg\mathrm{B}}$. d), h) depict the hetero-monomer lattice with $\mathrm{ddim} = \mathrm{N} = 3$, with field frequency $\omega^{(\nu)}_{\mathrm{Res}}$ and l), p), have field frequency $\omega^{(\nu)}_{\mathrm{Det}}$.

I.1.2 Correlation from harshly truncated Hamiltonians

In the hetero-monomer lattice, moving from an A resonant laser field to a B resonant laser field should show correlations move from one monomer to the other. This would appear as no change in correlation, as figure 4.4.2 demonstrates that correlations at differing frequencies result in equivalent signals. However, the A monomer energy levels are located within the first $2\mathrm{N}^2$ energy levels in the single exciton manifold, but the necessary B monomer energy levels are not. Additionally, the two monomer units are not sampled evenly, because of the non-degenerate energies, when $\mathrm{ddim} \neq \mathrm{N}$. This is demonstrated in columns 1 and 2, which have $\mathrm{ddim} = 10$ and $\mathrm{N} = 3$, of figure I.1.2 where monomer A is visible in the monomer-lattice, panel b) and f), but the B monomer is absent and electronic signals far from resonance of monomer A are detected in panels j) and n). Upon shifting to the harshly truncated regime

with $\mathrm{ddim} = \mathrm{N} = 3$ both monomer units are present within correlations. However, this comes at the expense of vibrational (phonon) signatures as a result of reduced ddim vibrational levels, and also an inability to model large system reorganisation energies. This is because large system reorganisation energies, as a consequence of large excited state displacement, induce transitions to highly vibrationally excited states which are either not present in the model or are strongly divergent due to computational error. This means, that while the results in columns 3 and 4 correctly demonstrate the desired correlation, only those data-sets with $\lambda \approx 0$ are reliable. Current computational restraints require the use of $\mathrm{ddim} = \{3, 10\}$, but these findings demonstrate that increasing to larger Hamiltonians warrants further investigation on the basis of correlations being strongly dependent on higher vibrational levels.

J Supplement to LDUO-HEOM Spectra

J.1 Phase Shifting in the LDUO-HEOM

As a supplement to the discussion in chapter 5 this appendix outlines the coupling, and broadening limits of the LDUO-HEOM linear spectra and discusses the phase flipping procedure employed to generate vibronic progressions.

Figure 5.1.4 shows uHEOM BVM spectra and the comparative LDUO-HEOM spectra. In all panels the phase is set to be $\phi_1 = 0^{\mathrm{c}}$ and therefore peaks close to the fundamental electronic transition frequency are split Lorentzians. a) and b) demonstrate a weak coupling to the undamped mode, with $\lambda_{\mathrm{UO}}^{(\nu)} = 1\ \mathrm{cm}^{-1}$, resulting in very small amplitude vibronic peaks at integer multiples of the vibrational mode frequency. As discussed in section 5, the oscillatory envelope of the response function gives rise to the vibronic progression and represents an interaction of vibrational and electronic degrees of freedom within the EOM. Each of the data sets in a) are run with a constant value of $\Gamma_{\mathrm{max}}^{(\nu)} = 1\,000\ \mathrm{cm}^{-1}$ leading to a balance between the overdamped environmental coupling and the undamped mode coupling in order to generate the vibronic progression. As the overdamped coupling strength increases, interaction with the pure undamped mode leads to a divergent response function which loses definition of the envelope function, for this specific hierarchy depth, which results in erroneous broadening of the spectral lineshape. This could additionally be improved by increasing the value of Γ_{max}. As discussed in section 2.5.6.2, the indefinite oscillations within the linear response function also lead to a vertical and horizontal stretching of the spectrum and the formation of satellite peaks from the Fourier transform of a continuous oscillation. In order to mitigate both of these effects, a Hamming apodisation function is applied to limit divergence and continual oscillation in the response function.

The results shown in c) and d) of figure 5.1.4 present results with an increased undamped mode coupling strength and the application of the Hamming window. Within the uHEOM BVM any increase in the coupling to the intramolecular vibration is accompanied by a large increase in the intrinsic canonical damping, as evidenced by the movement from $\eta^{(\nu)} = (50, 50)\ \mathrm{cm}^{-1}$ to $\eta^{(\nu)} = (300, 50)\ \mathrm{cm}^{-1}$. This both dramatically broadens the spectra and increases

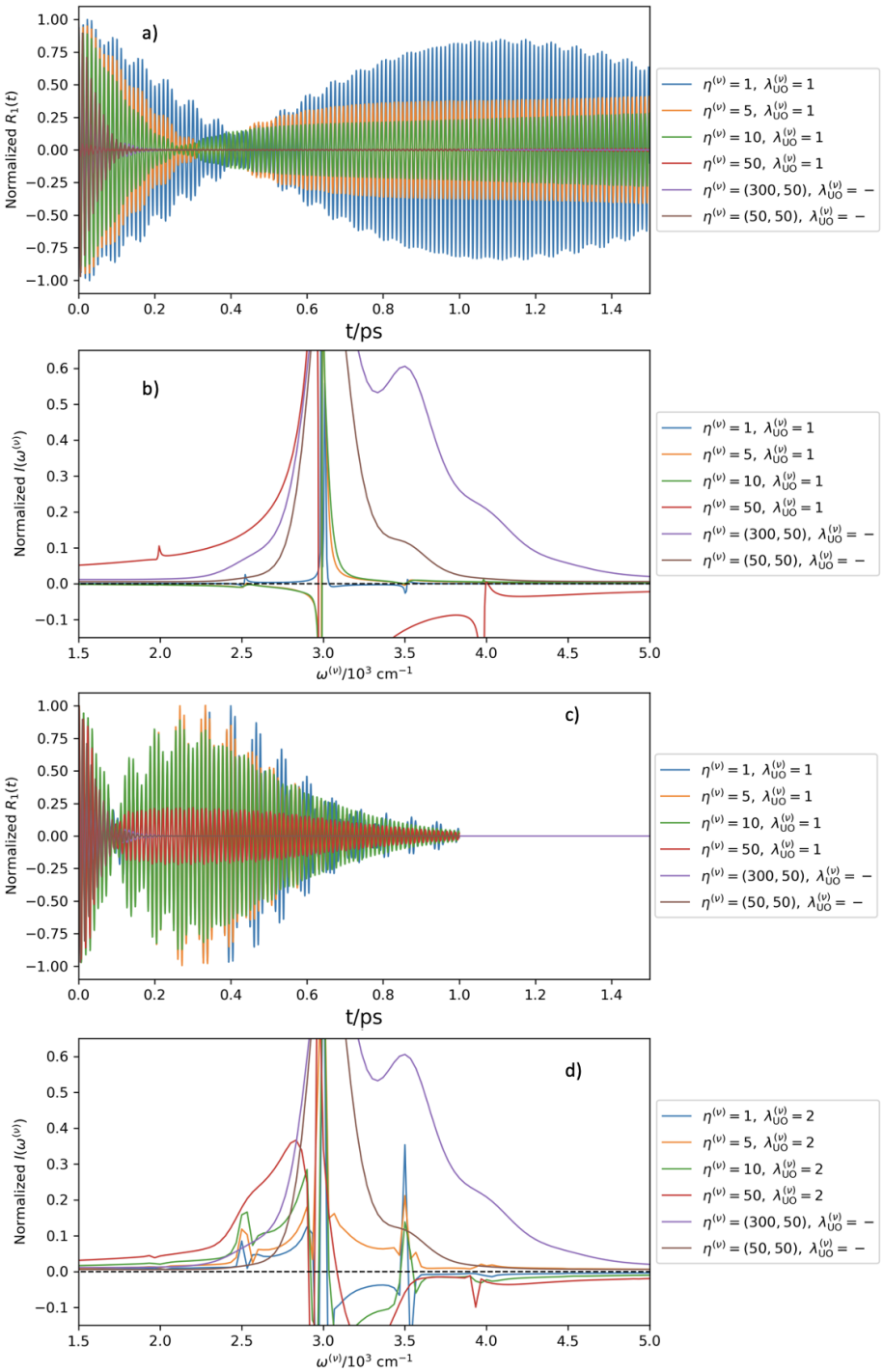

Figure J.1.1: A series of uHEOM BVM spectra and comparative LDUO-HEOM spectra. a) and b) present the linear response function and linear spectra of a system which is weakly coupled to the undamped mode with $\lambda_{\mathrm{UO}}^{(\nu)} = 1\ \mathrm{cm}^{-1}$. The response function is allowed to oscillate indefinitely resulting in infinitessimal peak widths. c) and d) depict an increase of the undamped coupling strength to $\lambda_{\mathrm{UO}}^{(\nu)} = 2\ \mathrm{cm}^{-1}$ and the application of a Hamming apodisation to limit the divergence of the response function and reduce the necessary Γ_{max} value. In both cases a constant phase of $\phi_1 = 0^{\mathrm{c}}$ is applied.

the amplitude of vibronic peaks. In the LDUO-HEOM vibronic peaks arise from coupling to a pure intramolecular oscillation, with zero damping, making it very sensitive to increased coupling. A small increase in $\lambda_{\mathrm{UO}}^{(\nu)}$ from $1\ \mathrm{cm}^{-1}$ to $2\ \mathrm{cm}^{-1}$ leads to a dramatic increase in the amplitude of vibronic peaks, along with the amplitude of the sinusoidal envelope of the response function, but in turn a dramatic increase in the speed of divergence for this value of Γ_{max}. This makes application of a Hamming window increasingly necessary in order to limit the intense changes to the response function induced by coupling to a pure undamped mode. However, it is clear that the LDUO-HEOM is able to model a range of vibrational coupling strengths through increasing the parameter $\lambda_{\mathrm{UO}}^{(\nu)}$. The lineshape of each of the data sets in panel d) show qualitative agreement with the strong and weakly coupled uHEOM BVM scenarios presented. In particular, there is good agreement in peak position, amplitude, and broadening between the LDUO-HEOM with $\eta^{(\nu)} = 10\ \mathrm{cm}^{-1}$, $\lambda_{\mathrm{UO}}^{(\nu)} = 2\ \mathrm{cm}^{-1}$, and the uHEOM BVM with $\eta^{(\nu)} = (50, 50)\ \mathrm{cm}^{-1}$.

On the right hand side of the fundamental transition, the broadening in the LDUO-HEOM occurs below the x-axis because of the negative value of absorptive spectrum generated from a single oscillatory mode rather than a wavepacket. As a result of energy considerations, discussed in section 5 we chose to make the absorptive component strictly positive, but rather than taking the absolute Fourier spectrum which would increase the lineshape broadening because of dispersive elements, phase is exploited. This is achieved by implementing a phase jump discontinuity centred at the fundamental electronic frequency. In the frequency domain this is achieved through multiplying the spectrum by $-H(\omega^{(\nu)} - \omega_{\mathrm{eg}}^{(\nu)})$, where H is the step function, which is equivalent to convoluting the response function with a time dependent phase of π^{c}. This ensures that the absorptive spectrum is strictly positive and broadened dependent on only the absorptive contributions to the spectrum. Results of this kind are shown in figure 5.1.4.

K

Acronyms

2DES 2D electronic spectroscopy.

2DEV 2D electronic-vibrational spectroscopy.

2DVE 2D vibrational-electronic spectroscopy.

2DIR 2D infrared spectroscopy.

2DOS 2D optical spectroscopy.

EOM equation of motion.

ODE ordinary differential equation.

ADO auxiliary density operator.

HEOM hierarchical equations of motion.

NLS nonlinear Schrödinger equation / Schrödinger equation.

QMC Quantum Monte-Carlo.

MCTDH Multi-Configuration time-dependent Hartree.

LVN(E) Liouville von-Neumann (equation).

FIs Feynman path integrals / Feynman integrals.

MEs master equations.

QMEs quantum master equations.

BRME Bloch-Redfield master equation.

LME / GKSL(E) Lindblad master equation / Gorini – Kossakowski – Sudarshan – Lindblad (equation).

NZE Nakajima-Zwanzig equation.

LE / QLE Langevin equation / quantum Langevin equation.

GLE generalised Langevin equation.

KSLE Kubo's stochastic Liouville equation.

SEs stochastic equations.

SSE stochastic Schrödinger equation.

pFPE perturbative Fokker-Planck equation.

FPE Fokker-Planck equation.

uHEOM underdamped HEOM.

PTQME polaron transformed quantum master equation.

ASD-HEOM arbitrary spectral density HEOM.

gHEOM generalised HEOM.

LDUO-HEOM Lorentz-Drude undamped oscillator HEOM.

CPTP completely positive trace preserving.

BLP Breuer, Laine, and Piilo.

EET excitation energy transfer.

ESA excited state absorption.

GSB ground state bleach.

FFT Fast Fourier Transform.

FWHM full-width-at-half-maximum.

HPC (ADA) High Performance Computing[a].

IVR intramolecular vibrational relaxation.

VR vibrational relaxation.

LO local oscillator.

MBO multimode brownian oscillator.

PES potential energy surface.

QED quantum electrodynamics.

RK4 fourth-order Runge-Kutta.

TLS two-level-system.

UEA University of East Anglia.

TBC to be confirmed.

[a] Synonymous with ADA, after Mathematician Ada Lovelace.

Bibliography

[1] D. Green, B. S. Humphries, A. G. Dijkstra, and G. A. Jones, J. Chem. Phys. **151**, 174112 (2019).

[2] B. S. Humphries, D. Green, and G. A. Jones, J. Chem. Phys. **156**, 084103 (2022).

[3] B. S. Humphries, D. Green, M. O. Borgh, and G. A. Jones, Phys. Rev. Lett. **131**, 143601 (2023).

[4] R. Feynman and F. Vernon, Ann. Phys. (N. Y). **24**, 118 (1963).

[5] L. Cacciapuoti et al., Phys. Rev. A **68**, 053612 (2003).

[6] R. H. Brown and R. Twiss, London, Edinburgh, Dublin Philos. Mag. J. Sci. **45**, 663 (1954).

[7] M. Kizmann, H. K. Yadalam, V. Y. Chernyak, and S. Mukamel, Proc. Natl. Acad. Sci. **120**, e2304737120 (2023).

[8] F. Poletti et al., Nat. Photonics **7**, 279 (2013).

[9] P. Kaushik, D. P. Singh, and S. Rajpoot, Fibre Optic Communication In 21 st Century, in *2020 Int. Conf. Intell. Eng. Manag.*, pages 125–129, IEEE, 2020.

[10] H. J. Carmichael and D. F. Walls, J. Phys. B At. Mol. Phys. **9**, 1199 (1976).

[11] H. Zheng, D. J. Gauthier, and H. U. Baranger, Phys. Rev. A - At. Mol. Opt. Phys. **85**, 043832 (2012).

[12] R. Avriller, Q. Schaeverbeke, T. Frederiksen, and F. Pistolesi, Phys. Rev. B **104**, L241403 (2021).

[13] K. Ishida and K. Nasu, J. Phys. Soc. Japan **81**, 2 (2012).

[14] A. Imamoğlu, H. Schmidt, G. Woods, and M. Deutsch, Phys. Rev. Lett. **79**, 1467 (1997).

[15] K. M. Birnbaum et al., Nature **436**, 87 (2005).

[16] C. Lang et al., Phys. Rev. Lett. **106**, 243601 (2011).

[17] W.-W. Deng, G.-X. Li, and H. Qin, Opt. Express **25**, 6767 (2017).

[18] B. Gu and S. Mukamel, ACS Photonics **9**, 938 (2021).

[19] Y. T. Guo, F. Zou, J. F. Huang, and J. Q. Liao, Phys. Rev. A **105** (2022).

[20] A. Ridolfo, M. Leib, S. Savasta, and M. J. Hartmann, Phys. Rev. Lett. **109**, 193602 (2012).

[21] A. Cidrim, T. S. do Espirito Santo, J. Schachenmayer, R. Kaiser, and R. Bachelard, Phys. Rev. Lett. **125**, 073601 (2020).

[22] L. A. Williamson, M. O. Borgh, and J. Ruostekoski, Phys. Rev. Lett. **125**, 73602 (2020).

[23] M. Chen, J. Tang, L. Tang, H. Wu, and K. Xia, Phys. Rev. Res. **4**, 033083 (2022).

[24] L. Medina-Dozal et al., arXiv, arxiv-2309.16087 (2023).

[25] M. Setodeh Kheirabady, E. Ghasemian, and M. K. Tavassoly, Ann. Phys. **535**, 2300024 (2023).

[26] M. C. Teich and G. J. Wolga, Phys. Rev. Lett. **16**, 625 (1966).

[27] V. Tamma and S. Laibacher, Phys. Rev. A - At. Mol. Opt. Phys. **90**, 063836 (2014).

[28] A. Labeyrie, P. Lipson, and P. Nisenson, *An Introduction to Optical Stellar Interferometry*, Cambridge University Press, Cambridge, 2006.

[29] W. Ruppel, P. Duerr, J. Ross, and W. Elsäßer, Appl. Phys. B **129**, 1 (2023).

[30] A. R. Thompson, J. M. Moran, and G. W. Swenson, *Interferometry and Synthesis in Radio Astronomy*, SpringerOpen, third edition, 2017.

[31] C. Foellmi, Astron. Astrophys. **507**, 1719 (2009).

[32] V. Corbin and N. J. Cornish, Class. Quantum Gravity **23**, 2435 (2006).

[33] R. Weiss, Annu. Rev. Astron. Astrophys. **18**, 489 (1980).

[34] A. S. Chou et al., Phys. Rev. D **95**, 063002 (2017).

[35] C. Arnau del Valle et al., J. Photochem. Photobiol. B Biol. **234** (2022).

[36] T. Brixner et al., Nature **434**, 625 (2005).

[37] S. Mukamel, *Principles of Nonlinear Optical Spectroscopy*, Oxford University Press, New York, 1995.

[38] P. Hamm and M. Zanni, *Concepts and Methods of 2D Infrared Spectroscopy*, Cambridge University Press, 2011.

[39] N. S. Ginsberg, Y.-C. Cheng, and G. R. Fleming, Acc. Chem. Res. **42**, 1352 (2009).

[40] M. Cho, Chem. Rev. **108**, 1331 (2008).

[41] D. A. Chin et al., Rev. Sci. Instrum. **94**, 013101 (2023).

[42] Y. Nam et al., Chem. Sci. **14**, 2971 (2023).

[43] S. M. Cavaletto et al., J. Chem. Theory Comput. **19**, 2327 (2023).

[44] S. Mukamel, Theory and Simulation of Ultrafast Multidimensional Nonlinear X-ray Spectroscopy of Molecules, Technical report, Chicago Operations Office, Argonne, IL (United States), 2023.

[45] N. H. Lewis et al., J. Phys. Chem. Lett. **7**, 4197 (2016).

[46] T. A. Oliver, R. Soc. Open Sci. **5**, 171425 (2018).

[47] T. L. Courtney, Z. W. Fox, K. M. Slenkamp, and M. Khalil, J. Chem. Phys. **143**, 154201 (2015).

[48] J. D. Gaynor and M. Khalil, J. Chem. Phys. **147**, 094202 (2017).

[49] E. C. Wu, E. A. Arsenault, P. Bhattacharyya, N. H. Lewis, and G. R. Fleming, Faraday Discuss. **216**, 116 (2019).

[50] P. Bhattacharyya and G. R. Fleming, J. Phys. Chem. Lett. **10**, 2081 (2019).

[51] T. Hansen, T. Bezriadina, and D. Popova-Gorelova, Molecules **28**, 4502 (2023).

[52] K. Zakutauskaitė, M. Mačernis, H. H. Nguyen, J. P. Ogilvie, and D. Abramavičius, J. Chem. Phys. **158**, 015103 (2023).

[53] J. O. Tollerud, C. R. Hall, and J. A. Davis, Opt. Express **22**, 6719 (2014).

[54] J. O. Tollerud, S. T. Cundiff, and J. A. Davis, Phys. Rev. Lett. **117**, 097401 (2016).

[55] A. Sharma et al., Light Sci. Appl. **9**, 1 (2020).

[56] N. H. Lewis, H. Dong, T. A. Oliver, and G. R. Fleming, J. Chem. Phys. **142**, 174202 (2015).

[57] H. Dong, N. H. Lewis, T. A. Oliver, and G. R. Fleming, J. Chem. Phys. **142**, 174201 (2015).

[58] K. W. Stone et al., Science **324**, 1169 (2009).

[59] B. P. Fingerhut, M. Richter, J. W. Luo, A. Zunger, and S. Mukamel, Ann. Phys. **525**, 31 (2013).

[60] E. Harel, S. M. Rupich, R. D. Schaller, D. V. Talapin, and G. S. Engel, Phys. Rev. B **86**, 075412 (2012).

[61] M. Righetto et al., Phys. Chem. Chem. Phys. **20**, 18176 (2018).

[62] Y. Wang et al., Phys. Rev. Appl. **17**, 024009 (2022).

[63] P. J. Brosseau et al., Commun. Phys. **6**, 1 (2023).

[64] J. Li, T. Zeng, Y. Zhai, Z. Qu, and H. Li, Phys. Chem. Chem. Phys. **25**, 24636 (2023).

[65] M. Katzer et al., Phys. Rev. B **107**, 035304 (2023).

[66] E. Meneghin et al., Nat. Commun. **9**, 1 (2018).

[67] T. Mančal et al., J. Phys. Chem. Lett. **3**, 1497 (2012).

[68] H. G. Duan, P. Nalbach, V. I. Prokhorenko, S. Mukamel, and M. Thorwart, New J. Phys. **17** (2015).

[69] R. Tempelaar et al., J. Phys. Chem. A **120**, 3042 (2016).

[70] M. S. Barclay et al., J. Chem. Phys. **158**, 035101 (2023).

[71] S. Freitas et al., Mar. Drugs **17**, 229 (2019).

[72] S. S. Senlik, V. R. Policht, and J. P. Ogilvie, J. Phys. Chem. Lett. **6**, 2413 (2015).

[73] R. Moca, S. R. Meech, and I. A. Heisler, J. Phys. Chem. B **119**, 8623 (2015).

[74] E. Meneghin, C. Leonardo, A. Volpato, L. Bolzonello, and E. Collini, Sci. Rep. **7**, 11389 (2017).

[75] S. Kopec, P. Ottiger, S. Leutwyler, and H. Köppel, J. Chem. Phys. **137**, 184312 (2012).

[76] P. Ottiger, S. Leutwyler, and H. Köppel, J. Chem. Phys. **136**, 174308 (2012).

[77] P. Ottiger, H. Köppel, and S. Leutwyler, Chem. Sci. **6**, 6059 (2015).

[78] V. Tiwari, W. K. Peters, and D. M. Jonas, Proc. Natl. Acad. Sci. **110**, 1203 (2013).

[79] V. Tiwari, W. K. Peters, and D. M. Jonas, J. Chem. Phys. **147**, 154308 (2017).

[80] V. Tiwari and D. M. Jonas, J. Chem. Phys. **148**, 084308 (2018).

[81] A. Chenu, N. Christensson, H. F. Kauffmann, and T. Mančal, Sci. Rep. **3**, 1 (2013).

[82] E. Romero, V. I. Novoderezhkin, and R. van Grondelle, Nature **543**, 355 (2017).

[83] V. I. Novoderezhkin, E. Romero, and R. van Grondelle, Phys. Chem. Chem. Phys. **17**, 30828 (2015).

[84] V. Perlík et al., J. Chem. Phys. **142**, 212434 (2015).

[85] P. Malý, O. J. Somsen, V. I. Novoderezhkin, T. Mančal, and R. Van Grondelle, ChemPhysChem **17**, 1356 (2016).

[86] P. Malý et al., Phys. Chem. Chem. Phys. **22**, 21222 (2020).

[87] V. R. Policht et al., Sci. Adv. **8**, 1 (2022).

[88] D. Giavazzi, S. Saseendran, F. Di Maiolo, and A. Painelli, J. Chem. Theory Comput. **19**, 436 (2022).

[89] A. Bose and N. Makri, J. Phys. Chem. B **124**, 5028 (2020).

[90] A. Nitzan, *The Spin–Boson Model*, Oxford University Press, 2006.

[91] H. G. Duan, M. Thorwart, and R. J. Miller, J. Chem. Phys. **151**, 114115 (2019).

[92] Y. Fujihashi, G. R. Fleming, and A. Ishizaki, J. Chem. Phys. **142**, 212403 (2015).

[93] D. M. Monahan, L. Whaley-Mayda, A. Ishizaki, and G. R. Fleming, J. Chem. Phys. **143**, 065101 (2015).

[94] V. Butkus, H. Dong, G. R. Fleming, D. Abramavicius, and L. Valkunas, J. Phys. Chem. Lett. **7**, 277 (2016).

[95] P. Kjellberg, B. Brüggemann, and T. Pullerits, Phys. Rev. B **74**, 024303 (2006).

[96] B. Brüggemann, P. Kjellberg, and T. Pullerits, Chem. Phys. Lett. **444**, 192 (2007).

[97] Y. Kim et al., Quantum Reports **3**, 80 (2021).

[98] H. G. Duan et al., Proc. Natl. Acad. Sci. U. S. A. **114**, 8493 (2017).

[99] S. M. Blau, D. I. Bennett, C. Kreisbeck, G. D. Scholes, and A. Aspuru-Guzik, Proc. Natl. Acad. Sci. U. S. A. **115**, E3342 (2018).

[100] D. I. Bennett, P. Malý, C. Kreisbeck, R. Van Grondelle, and A. Aspuru-Guzik, J. Phys. Chem. Lett. **9**, 2665 (2018).

[101] C. C. Jumper, S. Rafiq, S. Wang, and G. D. Scholes, Curr. Opin. Chem. Biol. **47**, 39 (2018).

[102] D. M. Jonas, Annu. Rev. Phys. Chem. **69**, 327 (2018).

[103] M. Maiuri, E. E. Ostroumov, R. G. Saer, R. E. Blankenship, and G. D. Scholes, Nat. Chem. **10**, 177 (2018).

[104] J. Cao et al., Sci. Adv. **6**, eaaz4888 (2020).

[105] T. R. Nelson et al., Chem. Rev. **120**, 2215 (2020).

[106] S. Biswas, J. W. Kim, X. Zhang, and G. D. Scholes, Chem. Rev. **122**, 4257 (2022).

[107] Y. Zhao and R. S. Knox, J. Phys. Chem. A **104**, 7751 (2000).

[108] X.-h. Tong, arXiv, arXiv.2211.04131 (2023).

[109] J. Sung and R. J. Silbey, J. Chem. Phys. **118**, 2443 (2003).

[110] S. Mukamel and D. Abramavicius, Chem. Rev. **104**, 2073 (2004).

[111] T. Brixner, T. Mančal, I. V. Stiopkin, and G. R. Fleming, J. Chem. Phys. **121**, 4221 (2004).

[112] U. Weiss, *Quantum Dissipative Systems*, World Scientific, 2012.

[113] H.-P. Breuer and F. Petruccione, *The Theory of Open Quantum Systems*, Oxford University Press, New York, 2007.

[114] W. P. de Boeij, M. S. Pshenichnikov, and D. A. Wiersma, J. Phys. Chem. **100**, 11806 (1996).

[115] Y. C. Cheng, G. S. Engel, and G. R. Fleming, Chem. Phys. **341**, 285 (2007).

[116] A. G. Dijkstra and Y. Tanimura, Phys. Rev. Lett. **104**, 250401 (2010).

[117] A. G. Dijkstra and Y. Tanimura, J. Phys. Soc. Japan **81**, 063301 (2012).

[118] Y. Tanimura, J. Chem. Phys. **153**, 020901 (2020).

[119] T. Joo, Y. Jia, J.-Y. Yu, M. J. Lang, and G. R. Fleming, J. Chem. Phys. **104**, 6089 (1996).

[120] J. Sue, Y. J. Yan, and S. Mukamel, J. Chem. Phys. **85**, 462 (1986).

[121] A. G. Redfield, Academic Press Inc. **1**, 1 (1965).

[122] D. O. Soares-Pinto et al., Phys. Rev. A **83**, 062336 (2011).

[123] T. V. Tscherbul and P. Brumer, J. Chem. Phys. **142**, 104107 (2015).

[124] R. Chetrite and K. Mallick, J. Stat. Phys. **148**, 480 (2012).

[125] D. Manzano, AIP Adv. **10**, 025106 (2020).

[126] A. S. Trushechkin, Proc. Steklov Inst. Math. **313**, 246 (2021).

[127] R. S. Whitney, J. Phys. A Math. Theor. **41**, 175304 (2008).

[128] S. Denk and M. Schweda, J. High Energy Phys. **7**, 703 (2003).

[129] O. Rubel, F. Tran, X. Rocquefelte, and P. Blaha, Comput. Phys. Commun. **261**, 107648 (2021).

[130] S. Nakajima, Prog. Theor. Phys. **20**, 948 (1958).

[131] R. Zwanzig, J. Chem. Phys. **33**, 1338 (1960).

[132] L. Chen, R. Zheng, Q. Shi, and Y. Yan, J. Chem. Phys. **132**, 024505 (2010).

[133] F. Šanda and S. Mukamel, J. Phys. Chem. B **112**, 14212 (2008).

[134] Z. Zhang, X. Nie, D. Lei, and S. Mukamel, Phys. Rev. Lett. **130**, 103001 (2023).

[135] M. T. Wong and Y.-C. Cheng, J. Chem. Phys. **154**, 154107 (2021).

[136] E. Cortés, B. J. West, and K. Lindenberg, J. Chem. Phys. **82**, 2708 (1985).

[137] J. I. Jiménez-Aquino and R. M. Velasco, Entropy **16**, 1917 (2014).

[138] Y. Tanimura, J. Phys. Soc. Japan **75**, 082001 (2006).

[139] T. Ikeda and G. D. Scholes, J. Chem. Phys. **152**, 204101 (2020).

[140] Y. Tanimura and T. Steffen, J. Phys. Soc. Japan **69**, 4095 (2000).

[141] F. Guarnieri, W. Moon, and J. S. Wettlaufer, J. Math. Phys. **58** (2017).

[142] T. Ikeda and Y. Tanimura, J. Chem. Theory Comput. **15**, 2517 (2019).

[143] A. Caldeira and A. Leggett, Phys. A Stat. Mech. its Appl. **121**, 587 (1983).

[144] R. P. Feynman, A. R. Hibbs, and G. H. Weiss, *Quantum Mechanics and Path Integrals*, volume 19, Dover Publications Ltd., 1966.

[145] D. Chruściński and A. Kossakowski, Phys. Rev. Lett. **104**, 070406 (2010).

[146] C. Meier and D. J. Tannor, J. Chem. Phys. **111**, 3365 (1999).

[147] Y. Tanimura and R. Kubo, J. Phys. Soc. Japan **58**, 101 (1989).

[148] I. de Vega and D. Alonso, Rev. Mod. Phys. **89**, 015001 (2017).

[149] Y. Tanimura, Phys. Rev. A **41**, 6676 (1990).

[150] A. Ishizaki and Y. Tanimura, J. Phys. Soc. Japan **74**, 3131 (2005).

[151] Y. Tanimura, J. Chem. Phys. **141**, 044114 (2014).

[152] Y. Tanimura, J. Chem. Phys. **142**, 144110 (2015).

[153] A. G. Dijkstra and Y. Tanimura, J. Chem. Phys. **142**, 212423 (2015).

[154] H. Liu, L. Zhu, S. Bai, and Q. Shi, J. Chem. Phys. **140**, 134106 (2014).

[155] A. Ishizaki and Y. Tanimura, Chem. Phys. **347**, 185 (2008).

[156] L. Chen, R. Zheng, Q. Shi, and Y. Yan, J. Chem. Phys. **131**, 094502 (2009).

[157] Y. Tanimura, J. Chem. Phys. **137**, 22A550 (2012).

[158] H. Takahashi and Y. Tanimura, J. Chem. Phys. **158**, 124108 (2023).

[159] A. Ishizaki and Y. Tanimura, J. Phys. Chem. A **111**, 9269 (2007).

[160] A. O. Atsango, A. Montoya-Castillo, and T. E. Markland, J. Chem. Phys. **158**, 074107 (2023).

[161] K. Polley and R. F. Loring, J. Chem. Phys. **156**, 204110 (2022).

[162] J. Fang, Z. H. Chen, Y. Wang, R. X. Xu, and Y. J. Yan, J. Chinese Chem. Soc. **70**, 662 (2023).

[163] N. Lorenzoni et al., arXiv, arxiv:2303.08982 , 1 (2023).

[164] M. Tanaka and Y. Tanimura, J. Phys. Soc. Japan **78**, 073802 (2009).

[165] F. Delgado and M. Enríquez, Int. J. Mol. Sci. **24**, 10862 (2023).

[166] M. Schröter et al., Phys. Rep. **567**, 1 (2015).

[167] C. Kreisbeck, T. Kramer, and A. Aspuru-Guzik, J. Chem. Theory Comput. **10**, 4045 (2014).

[168] J. Strümpfer and K. Schulten, J. Chem. Phys. **131**, 225101 (2009).

[169] S. H. Yeh, R. D. Hoehn, M. A. Allodi, G. S. Engel, and S. Kais, Proc. Natl. Acad. Sci. U. S. A. **116**, 18263 (2019).

[170] J. Iles-Smith, N. Lambert, and A. Nazir, Phys. Rev. A **90**, 032114 (2014).

[171] H. Maguire, J. Iles-Smith, and A. Nazir, Phys. Rev. Lett. **123**, 093601 (2019).

[172] C. McConnell and A. Nazir, J. Chem. Phys. **151** (2019).

[173] D. Green, *Modelling Ultrafast Two-Dimensional Spectroscopy of Vibronic Systems using non-Markovian Hierarchical Equations of Motion.*, PhD thesis, University of East Anglia, 2020.

[174] E. Jaynes and F. Cummings, Proc. IEEE **51**, 89 (1963).

[175] B. W. Shore and P. L. Knight, J. Mod. Opt. **40**, 1195 (1993).

[176] W. S. Teixeira, F. L. Semião, J. Tuorila, and M. Möttönen, New J. Phys. **24**, 013005 (2022).

[177] H. A. Kramers, Physica **7**, 284 (1940).

[178] H. Grabert, P. Schramm, and G. L. Ingold, Phys. Rep. **168**, 115 (1988).

[179] P. Kok, LibreTexts-Physics, https://phys.libretexts.org/Bookshelves/Quantum_Mechanics/Advanced_Quantum_Mechanics_(Kok)/06%3A_Evolution_of_Open_Quantum_Systems/6.02%3A_Positive_and_Completely_Positive_Maps, 2023–08–22 (2023).

[180] W. T. Pollard, S. Y. Lee, and R. A. Mathies, J. Chem. Phys. **92**, 4012 (1990).

[181] M. Gruebele and A. H. Zewail, J. Chem. Phys. **98**, 883 (1993).

[182] U. Chakraborty and D. Chruściński, New J. Phys. **23**, 013009 (2021).

[183] L. Li, M. J. Hall, and H. M. Wiseman, Phys. Rep. **759**, 1 (2018).

[184] J. Brugger, C. Dittel, and A. Buchleitner, Phys. Rev. Res. **5**, 023060 (2023).

[185] H.-P. Breuer, E.-M. Laine, J. Piilo, and B. Vacchini, Rev. Mod. Phys. **88**, 021002 (2016).

[186] M. A. Man'Ko and V. I. Man'Ko, Phys. Scr. **T160**, 014030 (2014).

[187] C. Helstrom, Phys. Lett. A **25**, 101 (1967).

[188] H.-P. Breuer, E.-M. Laine, J. Piilo, and B. Vacchini, **88**, 021002 (2015).

[189] C. P. Burgess, J. Hainge, G. Kaplanek, and M. Rummel, J. High Energy Phys. **2018**, 122 (2018).

[190] F. Nesi, E. Paladino, M. Thorwart, and M. Grifoni, Phys. Rev. B **76**, 155323 (2007).

[191] T. E. Li, H. T. Chen, and J. E. Subotnik, J. Chem. Theory Comput. **15**, 1957 (2019).

[192] F. Caycedo-Soler et al., Nat. Commun. **13**, 2912 (2022).

[193] D. Green, F. V. A. Camargo, I. A. Heisler, A. G. Dijkstra, and G. A. Jones, J. Phys. Chem. A **122**, 6206 (2018).

[194] S. Tomasi and I. Kassal, J. Phys. Chem. Lett. **11**, 2348 (2020).

[195] I. Kassal, J. Yuen-Zhou, and S. Rahimi-Keshari, J. Phys. Chem. Lett. **4**, 362 (2013).

[196] L. A. Nafie, J. Chem. Phys. **79**, 4950 (1983).

[197] M. Roche and H. H. Jaffé, J. Chem. Phys. **60**, 1193 (1974).

[198] A. T. Kumar, F. Rosca, A. Widom, and P. M. Champion, J. Chem. Phys. **114**, 6795 (2001).

[199] A. Chenu and G. D. Scholes, Annu. Rev. Phys. Chem. **66**, 69 (2015).

[200] J. E. Frost and G. A. Jones, New J. Phys. **16**, 113067 (2014).

[201] N. J. Hestand and F. C. Spano, Acc. Chem. Res. **50**, 341 (2017).

[202] G. Juzeliūnas and D. L. Andrews, Phys. Rev. B **49**, 8751 (1994).

[203] G. A. Jones and D. S. Bradshaw, Front. Phys. **7**, 1 (2019).

[204] D. L. Dexter, J. Chem. Phys. **21**, 836 (1953).

[205] N. J. Hestand and F. C. Spano, Chem. Rev. **118**, 7069 (2018).

[206] E. Thyrhaug et al., Nat. Chem. **10**, 780 (2018).

[207] J. S. Briggs and A. Eisfeld, Phys. Rev. E - Stat. Nonlinear, Soft Matter Phys. **83**, 4 (2011).

[208] T. Mančal, Chem. Phys. **532**, 110663 (2020).

[209] M. Kasha, Radiat. Res. **20**, 55 (1963).

[210] V. Butkus, D. Zigmantas, D. Abramavicius, and L. Valkunas, Chem. Phys. Lett. **587**, 93 (2013).

[211] H. Fidder, J. Knoester, and D. A. Wiersma, Chem. Phys. Lett. **171**, 529 (1990).

[212] G. Bressan et al., J. Phys. Chem. A **123**, 1594 (2019).

[213] M. I. S. Röhr et al., J. Phys. Chem. C **122**, 8082 (2018).

[214] A. Caldeira and A. Leggett, Phys. Rev. Lett. **49**, 1545 (1981).

[215] F. Levi, S. Mostarda, F. Rao, and F. Mintert, Reports Prog. Phys. **78**, 082001 (2015).

[216] Y. Tanimura and A. Ishizaki, Acc. Chem. Res. **42**, 1270 (2009).

[217] P. Vöhringer, D. C. Arnett, R. A. Westervelt, M. J. Feldstein, and N. F. Scherer, J. Chem. Phys. **102**, 4027 (1995).

[218] R. Kubo, Reports Prog. Phys. **29**, 306 (1966).

[219] A. G. Dijkstra and V. I. Prokhorenko, J. Chem. Phys. **147**, 064102 (2017).

[220] A. Kurt and R. Eryigit, Phys. Lett. Sect. A Gen. At. Solid State Phys. **382**, 1262 (2018).

[221] H. Imai, Y. Ohtsuki, and H. Kono, Chem. Phys. **446**, 134 (2015).

[222] G. L. Giorgi, A. Saharyan, S. Guérin, D. Sugny, and B. Bellomo, Phys. Rev. A **101**, 012122 (2020).

[223] M. Sala and D. Egorova, Chem. Phys. **481**, 206 (2016).

[224] E. Y. Wilner, H. Wang, M. Thoss, and E. Rabani, Phys. Rev. B - Condens. Matter Mater. Phys. **92**, 195143 (2015).

[225] Q.-S. Tan, W. Wu, L. Xu, J. Liu, and L.-M. Kuang, Phys. Rev. A **106**, 032602 (2022).

[226] S. Korsakas, J. Bučinskas, and D. Abramavicius, J. Chem. Phys. **152**, 244114 (2020).

[227] A. Rivas, S. F. Huelga, and M. B. Plenio, Phys. Rev. Lett. **105**, 1 (2010).

[228] A. S. Bondarenko, J. Knoester, and T. L. Jansen, Chem. Phys. **529**, 110478 (2020).

[229] A. S. Mazur, M. A. Vovk, and P. M. Tolstoy, Fullerenes Nanotub. Carbon Nanostructures **28**, 202 (2020).

[230] S. Mukamel, Annu. Rev. Phys. Chem. **41**, 647 (1990).

[231] V. Butkus, D. Zigmantas, L. Valkunas, and D. Abramavicius, Chem. Phys. Lett. **545**, 40 (2012).

[232] A. Tokmakoff, MIT Opencourseware, http://ocw.mit.edu/OcwWeb/Chemistry/5-74Spring-2005/CourseHome/index.html (2005).

[233] R. Kubo, *A Stochastic Theory of Line Shape*, Wiley, 1969.

[234] T. Mančal, A. V. Pisliakov, and G. R. Fleming, J. Chem. Phys. **124**, 234504 (2006).

[235] D. Egorova, M. F. Gelin, and W. Domcke, J. Chem. Phys. **126**, 074314 (2007).

[236] D. Egorova, J. Chem. Phys. **140**, 034314 (2014).

[237] G. S. Schlau-Cohen, A. Ishizaki, and G. R. Fleming, Chem. Phys. **386**, 1 (2011).

[238] X. Leng, S. Yue, Y. X. Weng, K. Song, and Q. Shi, Chem. Phys. Lett. **667**, 79 (2017).

[239] A. Anda and J. H. Cole, J. Chem. Phys. **154**, 114113 (2021).

[240] J. Sung and R. J. Silbey, J. Chem. Phys. **115**, 9266 (2001).

[241] T. N. Do, M. F. Gelin, and H. S. Tan, J. Chem. Phys. **147**, 144103 (2017).

[242] M. Khalil, N. Demirdöven, and A. Tokmakoff, J. Phys. Chem. A **107**, 5258 (2003).

[243] D. P. Craig and T. Thirunamachandran, *Molecular Quantum Electrodynamics: An Introduction to Radiation-molecule Interactions*, Courier Corporation, 1998.

[244] G. H. Richards, K. E. Wilk, P. M. Curmi, and J. A. Davis, J. Phys. Chem. Lett. **3**, 272 (2014).

[245] V. P. Singh et al., J. Chem. Phys. **142**, 212446 (2015).

[246] Y. Song et al., Rev. Sci. Instrum. **90**, 013108 (2019).

[247] S. Wolff, A. Sheikhan, and C. Kollath, SciPost Phys. Core **3**, 010 (2020).

[248] M. Ban, Eur. Phys. J. D **73**, 1 (2019).

[249] U. Fano, Am. J. Phys. **29**, 539 (1961).

[250] B. Bai et al., Sci. Rep. **7**, 2145 (2017).

[251] M. Dagenais and L. Mandel, Phys. Rev. A **18**, 2217 (1978).

[252] R. J. Glauber, Phys. Rev. **130**, 2529 (1963).

[253] M. Moslehi, H. R. Baghshahi, M. J. Faghihi, and S. Y. Mirafzali, Eur. Phys. J. Plus **137**, 777 (2022).

[254] T.-t. Ma, D. B. Horoshko, C.-s. Yu, and S. Y. Kilin, Phys. Rev. A **105**, 053718 (2022).

[255] S. Abo et al., Sci. Rep. **12**, 17655 (2022).

[256] J. K. Kalaga, W. Leoński, R. Szczęśniak, and J. Peřina, Entropy **24**, 324 (2022).

[257] H. Paul, Rev. Mod. Phys. **54**, 1061 (1982).

[258] S. Khan, B. K. Agarwalla, and S. Jain, Phys. Rev. A **106**, 022214 (2022).

[259] M. Lax, Phys. Rev. **129**, 2342 (1963).

[260] M. Lax, Phys. Rev. **157**, 213 (1967).

[261] H. J. Carmichael, *Statistical Methods in Quantum Optics 1*, Springer Berlin Heidelberg, Berlin, Heidelberg, 1999.

[262] B. R. Mollow, Phys. Rev. **188**, 1969 (1969).

[263] M. Hassani Nadiki and M. K. Tavassoly, Eur. Phys. J. D **76**, 1 (2022).

[264] Z. Y. Li, G. R. Jin, T. S. Yin, and A. Chen, Photonics **9**, 70 (2022).

[265] T. S. Yin, G. R. Jin, and A. Chen, Micromachines **13**, 591 (2022).

[266] S. Mukamel and D. Abramavicius, Chem. Rev. **104**, 2073 (2004).

[267] B. Dick, Chem. Phys. **113**, 131 (1987).

[268] M. Cho, N. F. Scherer, G. R. Fleming, and S. Mukamel, J. Chem. Phys. **96**, 5618 (1992).

[269] D. M. Jonas, Annu. Rev. Phys. Chem. **54**, 425 (2003).

[270] N. Christensson et al., J. Phys. Chem. B **115**, 5383 (2011).

[271] D. Paleček, P. Edlund, E. Gustavsson, S. Westenhoff, and D. Zigmantas, J. Chem. Phys. **151**, 024201 (2019).

[272] F. V. A. Camargo, *Unravelling Vibrational and Electronic Coherences via Two-Dimensional Electronic Spectroscopy of Zinc-Porphyrins*, PhD thesis, University of East Anglia, 2017.

[273] R. Borrego-Varillas et al., Chem. Sci. **10**, 9907 (2019).

[274] Y. C. Cheng and G. R. Fleming, J. Phys. Chem. A **112**, 4254 (2008).

[275] C. Y. Wong et al., Nat. Chem. **4**, 396 (2012).

[276] G. Panitchayangkoon et al., Proc. Natl. Acad. Sci. U. S. A. **107**, 12766 (2010).

[277] A. Gelzinis, R. Augulis, V. Butkus, B. Robert, and L. Valkunas, Biochim. Biophys. Acta - Bioenerg. **1860**, 271 (2019).

[278] R. Louden, *The Quantum Theory of Light*, Oxford University Press, Oxford, 3rd edition, 2000.

[279] A. Tokmakoff, J. Phys. Chem. A **104**, 4223 (2000).

[280] S. T. Roberts, J. J. Loparo, and A. Tokmakoff, J. Chem. Phys. **125**, 084502 (2006).

[281] M. Sebawe Abdalla and H. Eleuch, J. Appl. Phys. **115**, 234906 (2014).

[282] A. Trushechkin, Phys. Rev. A **103**, 062226 (2021).

[283] C. Smyth, F. Fassioli, and G. D. Scholes, Philos. Trans. R. Soc. A Math. Phys. Eng. Sci. **370**, 3728 (2012).

[284] M. Goldman, J. Magn. Reson. **149**, 160 (2001).

[285] M. Niknam and L.-S. Bouchard, arXiv, https://arxiv.org/abs/2310.00581 , 1 (2023).

[286] J. J. Ding, R. X. Xu, and Y. Yan, J. Chem. Phys. **136**, 224103 (2012).

[287] W. Wu, Phys. Rev. A **98**, 012110 (2018).

[288] Y. A. Yan and J. Shao, Front. Phys. **11**, 110309 (2016).

[289] J. Seibt and T. Mančal, Chem. Phys. **515**, 129 (2018).

[290] S. Yizhong and P. Xin, Proc. - 4th Int. Conf. Nat. Comput. ICNC 2008 **7**, 48 (2008).

[291] J. P. Lee and M. B. Comisarow, Appl. Spectrosc. **41**, 93 (1987).

[292] S. Yue, Z. Wang, X.-c. He, G.-b. Zhu, and Y.-x. Weng, Chinese J. Chem. Phys. **28**, 509 (2015).

[293] S. H. Rutherford et al., J. Chem. Phys. **157**, 205102 (2022).

[294] C. Lhoste et al., Prog. Nucl. Magn. Reson. Spectrosc. **130-131**, 1 (2022).

[295] L. D. Smith and A. G. Dijkstra, J. Chem. Phys. **151**, 164109 (2019).

[296] E. K. Irish, R. Gómez-Bombarelli, and B. W. Lovett, Phys. Rev. A - At. Mol. Opt. Phys. **90**, 012510 (2014).

[297] H. Mustroph et al., ChemPhysChem **10**, 835 (2009).

[298] O. Kühn, V. Rupasov, and S. Mukamel, J. Chem. Phys. **104**, 5821 (1996).

[299] P. J. Nowakowski, M. F. Khyasudeen, and H. S. Tan, Chem. Phys. **515**, 214 (2018).

[300] K. Lazonder, M. S. Pshenichnikov, and D. A. Wiersma, Opt. Lett. **31**, 3354 (2006).

[301] F. P. Diehl et al., J. Phys. Chem. Lett. **5**, 262 (2014).

[302] T. P. Fay, J. Chem. Phys. **157**, 054108 (2022).

[303] Y. Yan, M. Xu, T. Li, and Q. Shi, J. Chem. Phys. **154**, 194104 (2021).

[304] D. Zhang, X. Ding, H.-D. Zhang, X. Zheng, and Y. Yan, Chinese J. Chem. Phys. **34**, 905 (2021).

[305] X. Ding, D. Zhang, L. Ye, X. Zheng, and Y. Yan, J. Chem. Phys. **157**, 224107 (2022).

[306] L. Han, H. D. Zhang, X. Zheng, and Y. Yan, J. Chem. Phys. **148**, 234108 (2018).

[307] Q. Shi, L. Chen, G. Nan, R. Xu, and Y. Yan, J. Chem. Phys. **130**, 164518 (2009).

[308] M. R. Andrews et al., Science **273**, 84 (1996).

[309] A. Kurt, Quantum Inf. Process. **20**, 238 (2021).

[310] R. Carballeira, D. Dolgitzer, P. Zhao, D. Zeng, and Y. Chen, Sci. Rep. **11**, 11828 (2021).

[311] A. A. Alkathiri, S. A. Alsallami, N. Abdel-Wahab, S. Abdel-Khalek, and E. Khalil, Results Phys. **39**, 105739 (2022).

[312] M. Yang, M. Čufar, E. Pahl, and J. Brand, Condens. Matter **7**, 1 (2022).

[313] F. V. Camargo, H. L. Anderson, S. R. Meech, and I. A. Heisler, J. Phys. Chem. A **119**, 95 (2015).

[314] J. Lu, Y. Lee, and J. M. Anna, J. Phys. Chem. B **124**, 8857 (2020).

[315] E. Condon, Phys. Rev. **28**, 1182 (1926).

[316] M. O. Scully and M. S. Zubairy, *Quantum Optics*, Cambridge University Press, 1997.

[317] R. Wang, X. Y. Huang, C. F. Zhang, X. Y. Wang, and M. Xiao, Chinese J. Chem. Phys. **30**, 637 (2017).

[318] S. Mohammadnejad, P. Nosratkhah, and H. Arab, Quantum Inf. Process. **22**, 360 (2023).

[319] R. Hanbury Brown and R. Q. Twiss, J. Astrophys. Astron. **15**, 13 (1994).

[320] J. Schedlbauer et al., Adv. Opt. Mater. **10**, 2200092 (2022).

[321] A. Tiene, *Charged Polaritons in Two-Dimensional Semiconductors*, PhD thesis, Universidad Autonoma de Madrid, 2023.

[322] A. V. Shumilin, T. S. Shamirzaev, and D. S. Smirnov, arXiv, https://arxiv.org/abs/2306.12868 , 1 (2023).

[323] S. F. Völker et al., J. Phys. Chem. C **118**, 17467 (2014).

[324] J. Seibt and O. Kühn, J. Chem. Phys. **153**, 194112 (2020).

[325] J. Seibt and T. Mančal, Chem. Phys. **515**, 129 (2018).

[326] W. H. Press, S. A. Teukolsky, W. T. Vetterling, and B. Flannery, *Numerical Recipes 3rd Edition: The Art of Scientific Computing*, Cambridge University Press, Camridge, 3 edition, 2007.

[327] U. Mosel, *Path Integrals in Field Theory*, Advanced Texts in Physics, Springer Berlin Heidelberg, Berlin, Heidelberg, 2004.

[328] S. Efthimiades, arXiv, https://arxiv.org/abs/quant-ph/0607001 , 1 (2006).

[329] Y. E. Kuzovlev, arXiv, https://arxiv.org/pdf/0903.2061.pdf , 1 (2009).

[330] E. Nelson, Phys. Rev. **150**, 1079 (1966).

[331] D. Speiser, *Discovering the Principles of Mechanics 1600-1800*, Birkhauser, Basel, 2008.

[332] E. Rieffel and W. Polak, *Quantum Computing: A Gentle Introduction*, The MIT Press, 2011.

[333] F. Schwabl, *Statistical Mechanics*, Springer-Verlag Berlin Heidelberg, 2 edition, 2002.

[334] V. V. Ignatyuk and V. G. Morozov, arXiv, https://arxiv.org/abs/1911.12312 , 1 (2019).

[335] M. K. Singh, S. A. Sahu, A. Singhal, and S. Chaudhary, J. Intell. Mater. Syst. Struct. **29**, 3582 (2018).

[336] A. Smirne and B. Vacchini, Phys. Rev. A - At. Mol. Opt. Phys. **82**, 022110 (2010).

[337] X. Wang, Appl. Sci. **9**, 4512 (2019).

[338] P. Nation, J. Johanssen, A. Pitchford, C. Granade, and A. Grimsmo, Bloch-Redfield Equation - QuTip, 2017.

[339] V. Gorini, A. Kossakowski, and E. C. Sudarshan, J. Math. Phys. **17**, 821 (1975).

[340] N. Megier, A. Smirne, and B. Vacchini, New J. Phys. **22**, 083011 (2020).

[341] R. Hartmann and W. T. Strunz, Phys. Rev. A **101**, 012103 (2020).

[342] P. Ullersma, Physica **32**, 90 (1966).

[343] Y. Pomeau and J. Piasecki, Comptes Rendus Phys. **18**, 570 (2017).

[344] G. W. Ford and M. Kac, J. Stat. Phys. **46**, 803 (1987).

[345] G. W. Ford, M. Kac, and P. Mazur, J. Math. Phys. **6**, 504 (1965).

[346] G. W. Ford, J. T. Lewis, and R. F. Oconnell, Phys. Rev. A **37**, 4419 (1988).

[347] K. Kawasaki, J. Phys. A Gen. Phys. **6**, 1289 (1973).

[348] R. Dengler, arXiv, https://arxiv.org/abs/1506.02650 , 1 (2015).

[349] H. Kleinert and S. V. Shabanov, Phys. Lett. A **200**, 224 (1995).

[350] K. Tsusaka, Phys. Rev. E - Stat. Physics, Plasmas, Fluids, Relat. Interdiscip. Top. **59**, 4931 (1999).

[351] M. Rigo, F. Mota-Furtado, and P. F. O'Mahony, J. Phys. A. Math. Gen. **30**, 7557 (1997).

[352] N. Gisin, Phys. Rev. Lett. **52**, 1657 (1984).

[353] N. Gisin and I. C. Percival, J. Phys. A Gen. Phys. **25**, 5677 (1992).

[354] N. N. Bogolyubov and D. P. Sankovich, Russ. Math. Surv. **49**, 19 (1994).

[355] S. N. Sharma and H. G. Patel, *Stochastic Control*, IntechOpen, 2010.

[356] J. Zinn-Justin, *Quantum Field Theory and Critical Phenomena: Fifth Edition*, Oxford University Press, 2021.

[357] M. R. Rahimi Tabar, *Analysis and Data-Based Reconstruction of Complex Nonlinear Dynamical Systems*, Understanding Complex Systems, Springer International Publishing, Cham, 2019.

[358] N. Gisin, Helv. Phys. Acta **62**, 363 (1989).

[359] P. Hammerton, *Lecture Notes: Advanced Mathematical Techniques. UEA*, UEA, Norwich, 2018.

[360] D. M. Ceperley, Rev. Mod. Phys. **67**, 279 (1995).

[361] C. Chakravarty, Int. Rev. Phys. Chem. **16**, 421 (1997).

[362] A. Wipf, *Statistical Approach to Quantum Field Theory*, Springer, 2021.

[363] H. Bruus and K. Flensberg, *Many-Body Quantum Theory in Condensed Matter Physics—An Introduction*, Oxford University Press, Copenhagen, 2 edition, 2005.

[364] T. J. Hele, M. J. Willatt, A. Muolo, and S. C. Althorpe, J. Chem. Phys. **142**, 134103 (2015).

[365] M. E. Siemens, G. Moody, H. Li, A. D. Bristow, and S. T. Cundiff, Opt. InfoBase Conf. Pap. **18**, 445 (2010).